Interdigital Dielectrometry Sensor Design and Parameter Estimation Algorithms for Non-Destructive Materials Evaluation

by

Alexander V. Mamishev
B.S., Kiev Polytechnic Institute, 1992
M.S., Texas A&M University, 1994

Submitted to the Department of Electrical Engineering and Computer Science
in Partial Fulfillment of the Requirements for the Degree of
Doctor of Philosophy in Electrical Engineering and Computer Science

at the

Massachusetts Institute of Technology
May 1999

Signature of Author .....
Department of Electrical Engineering and Computer Science
May 8, 1999

Certified by .....
Markus Zahn
Professor of Electrical Engineering
Thesis Supervisor

Certified by .....
Bernard C. Lesieutre
Associate Professor of Electrical Engineering
Thesis Co-Supervisor

Accepted by .....
Arthur C. Smith
Chairman, Committee on Graduate Students
Department of Electrical Engineering and Computer Science

To my parents:

Valentin Mamishev

and

Leokadia Sokolovskaja

Interdigital Dielectrometry Sensor Design and Development of Parameter Estimation Algorithms for Non-Destructive Materials Evaluation

by
Alexander V. Mamishev

Submitted to the Department of Electrical Engineering and Computer Science on May 10, 1999 in partial fulfillment of the requirements for the degree of Doctor of Philosophy.

Abstract

The major objective of this thesis is to develop instrumentation and parameter estimation algorithms for nondestructive measurement of non-homogeneous material property profiles with fringing electric field dielectrometry sensors. The instrumentation includes interdigital sensors and sensor arrays, other types of fringing field sensors, electronic circuit boards for measurement of sensor signals, and mechanical setups for specific applications. The parameter estimation algorithms require solving forward and inverse problems of material property estimation. The forward problem implies calculation of the sensor admittance matrix as a function of geometry and material properties. The inverse problem, inherently more difficult than the forward problem, implies estimation of unknown geometry and material properties based on known properties and measured entries of the sensor admittance matrix. The developed instrumentation and algorithms are applied to practical problems which include monitoring of moisture dynamics in transformer pressboard, evaluation of the saturation state of chemical garments, detection of flaws in fiberglass flywheels, and detection of buried metal and plastic landmines.

The design strategy and fabrication practices are described for multiple penetration depth interdigital sensors designed for measurement of conductivity and permittivity of electrical insulation of power transformers. An extensive overview of interdigital electrode technology in other fields is given. A number of disturbance parameters that affect interdigital dielectrometry measurements is characterized and either eliminated or accounted for using empirical, analytical, and numerical simulation approaches. A new type of fringing field sensor has been developed to improve the cross-correlation between different fringing field patterns.

In most cases, the forward problem has been solved using commercial finite-element software *Maxwell* by Ansoft Corp. Other methods, such as a continuum model, analytical expressions, and direct calibration were used for comparison and to achieve greater accuracy in simple cases. A family of algorithms for solving inverse problems has been developed to address different applications. No single algorithm provides the most accurate and reliable results in all cases. The most appropriate algorithm for each given application should be chosen on the basis of required speed and accuracy, number of known and unknown parameters, type of distribution of material properties, contact conditions between the sensor head and the material, and a specific type of

sensor selected for the task. Major types of property estimation algorithms include direct calibration; use of empirically and numerically determined approximations; use of pre-computed lookup tables; iterative guesses at dielectric and geometry properties while solving the minimization problem of matching theoretical and measured entries of sensor admittance matrix; direct mapping between the sensor output and the physical variable of interest (not necessarily a dielectric property); pattern recognition in the dielectric spectroscopy signature; and search for signal characteristics in the sensor output due to material property variations. Each of these major types of algorithms has been implemented in one or more forms to achieve the desired results for each specific problem. One of the algorithmic approaches has been generalized to other types of problems by implementing it as a generic optimization tool.

Moisture dynamics in transformer pressboard has been studied extensively with numerical simulations of the forward and inverse problem. The developed algorithm has been applied to experimental data obtained by another graduate student, Yanqing Du, in a concurrent Ph.D. thesis. It has been demonstrated that a three-wavelength interdigital sensor can be used to measure time-dependent continuous smoothly varying moisture profiles in oil-impregnated power transformer pressboard. Ultimately, this technology is capable of preventing partial discharges and transformer failures due to flow electrification and static charging of the oil-pressboard interface.

Preliminary measurements also demonstrated adequate sensitivity and selectivity of fringing field sensors for the detection of flaws in fiberglass flywheels and detection and discrimination of buried plastic and metal landmines. The saturation state of chemical protective garments has been determined for relatively high levels of saturation. Additional work is needed to improve sensitivity in the low saturation region.

Thesis Supervisor: Professor Markus Zahn

Thesis Co-supervisor: Professor Bernard C. Lesieutre

Acknowledgments

I am infinitely grateful to my primary research advisor, Professor Markus Zahn, for inviting me to work in the Laboratory for Electromagnetic and Electronic Systems (LEES) and the High Voltage Research Laboratory (HVRL), supporting me throughout my stay, supervising my work day after day, and being always available for discussions, be it a research-related argument, brief lesson on electromagnetic theory, or a philosophical discourse.

My secondary thesis advisor, Professor Bernard Lesieutre, served me as a role model of a young faculty member and a great resource for the algorithm development portion of my research. He significantly contributed to almost all my publications that originated at MIT and supplied vigor and optimism at times of confusion. I would like to thank my thesis committee member Professor Lang and my academic advisors Professors Hagelstein and Kong for the encouragement and moral support of my research initiatives.

A significant portion of my time towards the end of the program was spent at Jentek Sensors, Inc. I have learned a lot from Jentek president, Dr. Neil Goldfine, and I am grateful to him for providing resources and ideas for further research and greatly appreciate his willingness to serve on my thesis committee. I would also like to acknowledge the help of other Jentek employees, namely, Andy Washabaugh, Bill Chepolis, Michelle McDevitt, Karen Walrath, and David Clark.

Several graduate students in LEES/HVRL participated in heated discussions on the core issues of interdigital dielectrometry and provided experimental data, computer code, ideas, and inspiration that proved invaluable for the development of this technology. Most of my research work was done together with Yanqing Du, whose exceptional diligence and creativity resulted in major contributions to this work. I also would like to express my gratitude to Darrell Schlicker, Yanko Sheiretov, Julio Castrillon, and Albert Lu and to visiting scientists Prof. Kang and Jean Rivenc, who worked on related projects at different times during my program. A lot of timely advice on general technical matters came from graduate students Robert Lyons, Afsin Ustundag, and Tza-Jing Gung with whom we shared office space and computer facilities.

Numerous experiments and computer simulations in this thesis were done by undergraduate students under my supervision, as a part of their Undergraduate Research Opportunities Program (UROP) at MIT. Their contributions are also pointed out separately in the body of the thesis. I would like to acknowledge (in chronological order) Boris Berdnikov, Binh Truong, John Miller, Christopher Lin, Andrew Takahashi, Gaurav Tewari, Jason Bau, Indrajeet (Ricky) Debnath, and Madhu Sarda for their diligence and creativity.

My thanks also go to lab technical staff Wayne Ryan for his assistance with computers, printers, experimental setups, and numerous devices, gadgets, instruments, fixtures, tools, apparatus, and mechanisms that had to be conquered, tamed, and

brought to life over the years in the lab.

I am happy to thank MIT secretaries Kathy McCue, Barbara Smith-Connolly, Vivian Mizuno, Sara Wolfson, Karin Janson-Strasswimmer of MIT, as well as Maria Stark and Jennifer DeGeorge of Jentek Sensors, Inc. for providing valuable assistance and always managing to squeeze my meetings into busy schedules of my superiors.

Also, I would like to congratulate the departmental administrative officers Peggy Carney, Marilyn Pierce, and Monica Bell with their efficient and flexible management of my files, especially when I was lost in the multitude of blue, yellow, pink, white, and green forms that marked important milestones of my Ph.D. program.

On a larger scale, the research projects covered in this thesis were supported by Electric Power Research Institute, grant number WO 8619-01, managed by Mr. Stan Lindgren, National Science Foundation, grant no. ECS-9523128, and Fibertek-Humanitarian Demining project No. 116000-MIT-01. Thanks to Ansoft Corp. for donation of the finite-element method software package *Maxwell*.

On a smaller scale, the financial support of my Ph.D. studies came in many forms, and I am happy to acknowledge my sponsors here. I am honored to have received the IEEE Dielectrics and Electrical Insulation Fellowship and ISEI (International Symposium on Electrical Insulation) and CEIDP (Conference on Electrical Insulation and Dielectric Phenomena) Scholarships; Travel Grants from the IEEE Power Engineering Society, Materials Research Society, National Science Foundation, and MIT Graduate Student Council; American Public Power Association Demonstration of Energy-efficient Developments Scholarship; Link Foundation Energy Fellowship; and American Vacuum Society Graduate Research Award.

On a personal level, I would like to thank my Master's program adviser, B. Don Russell of Texas A&M University and his wife, Becky Russell, for their support, love, and care, which carried me through my first difficult years in a foreign country. I also express my gratitude to my secondary advisors, Professors Robert Nevels and James Hennigan of Texas A&M University, Professor Stan Grzybowsky of Mississippi State University, and Professor Stanislav Sokolovsky of Kiev Polytechnic Institute, who shared much of their wisdom with me and helped me to stay afloat during my education.

I want to thank my friends Alexey and Alla Terentieva, Alexander Mazurenko (TRex), Sergej Lilitchenko, Nikolai Stolin, Olya Gutman, and John and Jeanie Seffel, who cheered me up when I needed it (usually) and helped me when I was in trouble (often).

I would like to thank my parents and my brother's family for their love and moral support, long letters and brief, by necessity, phone calls, and ability to remember tiny details after not seeing each other for so many years. Many thanks to Alexander Podlipenets, who provided a vitally important emergency email connection with my family. And finally, I would like to express my gratitude and love to my wonderful wife, Krystyna Szul, whose patience and tolerance exceeded any reasonable limits and who makes it all worthwhile.

Contents

List of Figures

List of Tables

Chapter 1

Introduction

1.1 Interdigital Dielectrometry

1.1.1 Historical Perspective

The literature sources listed in this section are also referenced individually in this thesis, but they are entered in groups in the introduction to bring order to a large number of references. This thesis builds on previous work that is represented in the sequence of MIT theses [2–12]. Among other elements, it includes material from a number of publications by the author [13–40]. It also includes material from undergraduate and visiting scientist internal reports written under my supervision [1, 41–49]. Several documents by Jentek Sensors, Inc. have been used [38, 50, 51]. The following patents are directly related to this technology [52–57].

While interdigital electrode structures have been used since the beginning of the century, the application of multiple penetration depth electric fields started in the 1960s [58]. Later, independent dielectrometry studies with single [59], and multiple (see Figure 17 of [60] and [61] as some of the first references) penetration depths using interdigital electrodes have continued and provided the groundwork for this thesis. Commercialization of the multiple penetration depth dielectrometry in the United States had been initiated in the early 1990s [62].

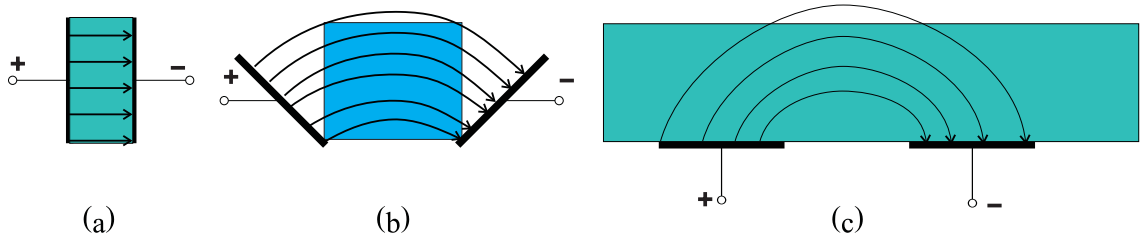

Figure 1.1: A fringing field dielectrometry sensor can be visualized as a parallel plate capacitor whose electrodes open up to provide a one-sided access to material under test.

A fringing field dielectrometry sensor performs essentially the same functions as a more conventional parallel plate capacitor, but it does not require two-sided access to the material under test. Figure 1.1 shows a gradual transition from the parallel plate capacitor to a fringing field capacitor. In all cases, electric field lines pass through the material under test, therefore the capacitance between the two electrodes depends on the material dielectric properties as well as on the electrode and material geometry.

Usually, the capacitance between two co-planar strips, as shown in Figure 1.1(c), is comparable to the stray capacitance of the leads (conductors that connect the electrodes with the electrical excitation source). Therefore, in order to build-up an easily measurable electrode structure, the coplanar strips pattern may be repeated several times. The term "interdigital" refers to digit-like or finger-like periodic pattern of parallel in-plane electrodes used to build up the capacitance associated with the electric fields that penetrate into a material sample. Figure 1.2 illustrates this analogy.

1.1.2 Imposed Frequency-Wavenumber ($\omega - k$ Sensing)

A variety of interdigital sensors are used for a number of research and commercial applications to measure material properties [63, 64], control manufacturing processes [65,66], monitor chemical and physical changes of fluid and solid dielectrics [67,68], etc. In many cases, the interpretation of the sensor response depends on simple calibration procedures, yet in other cases, it requires sophisticated signal processing algorithms [69] and deep understanding of the physics and chemistry of the dynamic processes that

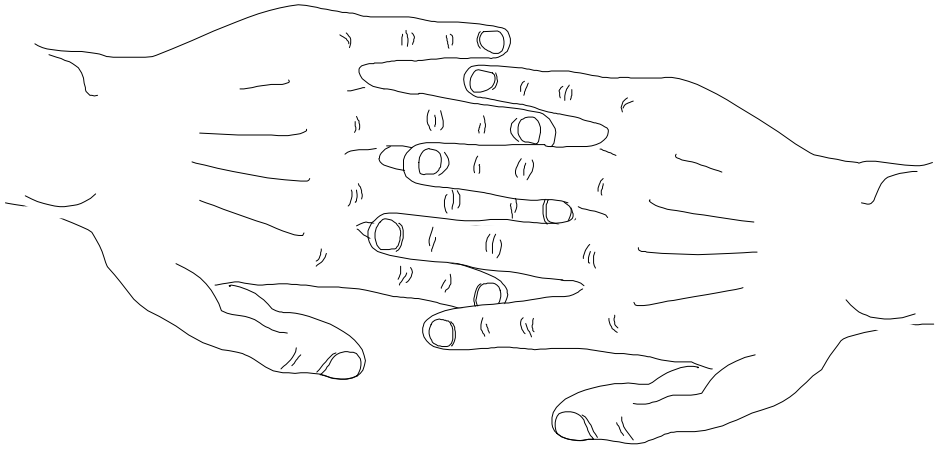

Figure 1.2: The term "interdigital" refers to the pattern of fingers or "digits" that is resembled by the shape and relative position of electrodes.

are being monitored [14].

Interdigital dielectrometry is a subset of interdigital electrode sensor applications that relies on direct measurement of dielectric properties of insulating and semi-insulating materials from one side [70–72]. The basic idea is to apply a spatially periodic electrical potential to the surface of the material under test. The combination of signals produced by variation of the spatial period of the interdigital comb electrodes combined with the variation of electrical excitation frequency potentially provides a plethora of information about the spatial profiles and dielectric spectroscopy of the material under test. Since the changes in the dielectric properties are usually induced by changes in various physical, chemical, or structural properties of materials, the dielectrometry measurements provide effective means for indirect non-destructive evaluation of vital parameters in a variety of industrial and scientific applications [62, 73].

The task of interpreting sensor signals is fulfilled by parameter estimation algorithms, whose complexity, precision, accuracy, and reliability vary considerably depending on the experimental conditions and available computation time. The amount of information about material properties that can be extracted from dielectrometry measurements is limited by the number of independent equations and boundary conditions that can be solved using interdigital sensors and auxiliary instrumentation. The

simplest experimental setup contains a single stationary interdigital sensor in contact with a studied material. In this case, one can only determine dielectric properties of a single homogeneous layer of known thickness, or, alternatively, one can determine the thickness of that layer if the dielectric properties are known in advance. In order to measure a larger number of unknown parameters, additional equations must be supplied to parameter estimation algorithms. These equations come from the auxiliary instrumentation, physical and numerical models of monitored processes (e.g. diffusion process), and, finally, from additional interdigital electrode pairs of different periodicities.

The art and science of designing sensors with multiple interdigital electrode pairs and processing the output signals to gain knowledge about the material under test is the subject of interdigital frequency-wavelength ($\omega - k$) dielectrometry. The penetration depth of the fringing electric fields above the interdigital electrodes is proportional to the spacing between the centerlines of the sensing and the driven fingers and is independent of frequency. Multi-wavelength interdigital dielectrometry, also known as frequency-wavenumber ($\omega - k$) dielectrometry, has been under development for about two decades. Overviews of important concepts related to this technology are available in [7, 8, 10, 27, 56, 63, 74, 75].

One of the most attractive features of multi-wavelength dielectrometry is the ability to measure from one side complex spatially inhomogeneous distributions of properties. As the complexity of spatial distribution grows and the number of unknown variables in each experiment increases, the parameter estimation algorithms become more complicated, computationally intensive, and less accurate and reliable. Ultimately, every major type of spatial distribution of material properties requires a different parameter estimation algorithm. The types of spatial distributions include, but are not limited to, homogeneous materials, multiple layer materials, local discontinuities (such as cracks and electrical trees), global discontinuities of micro-structure (such as grains or fibers forming the material), and, finally, the type extensively addressed in this thesis, smoothly varying properties. On the electrical properties side, materials under test

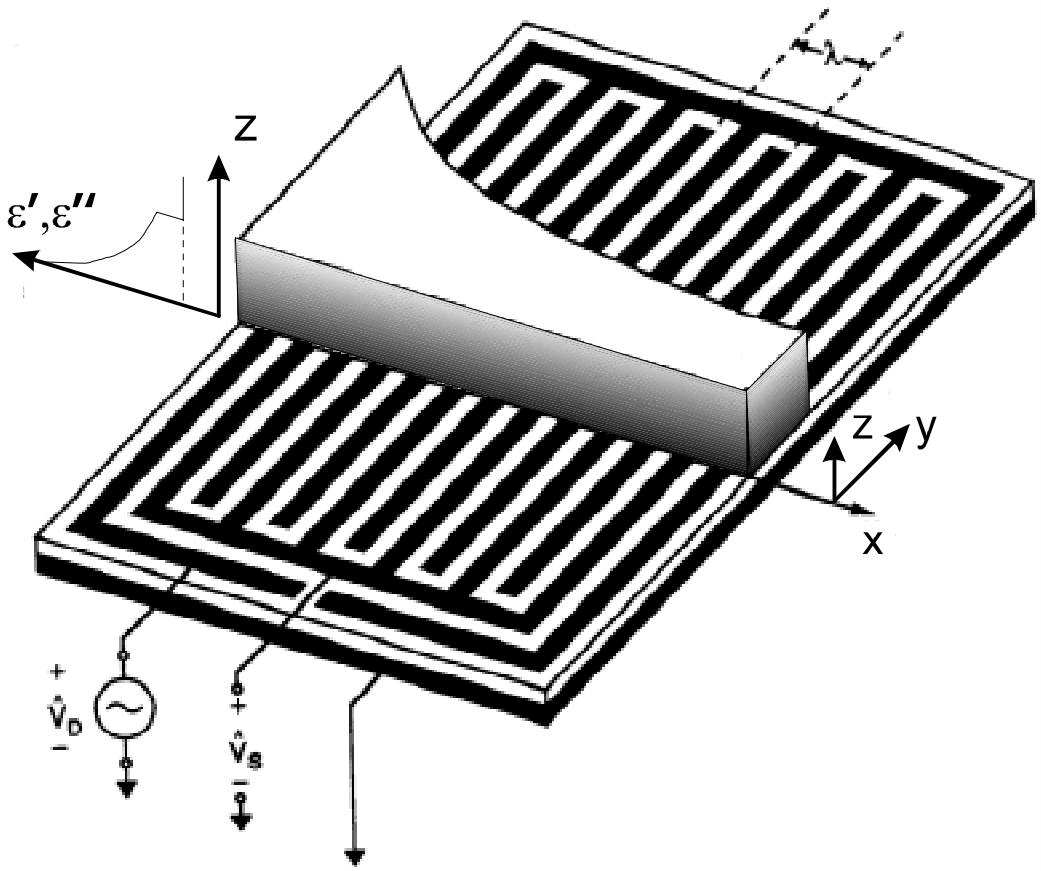

Figure 1.3: A generic interdigital dielectrometry sensor [8, 9].

may be purely insulating or weakly conductive. Various phenomena may affect sensor response, including frequency dispersion, electrode polarization due to an electrochemical double layer, quality of interfacial contact, and many others.

A conceptual schematic of $\omega - k$ dielectrometry is presented in Figure 1.3. For a homogeneous medium of semi-infinite extent, periodic variation of electric potential along the surface in the x direction produces an exponentially decaying pattern of electric fields penetrating into the medium in the z direction. The variation of shade in the material under test indicates the possible variation of material properties and thus variations in the complex dielectric permittivity ε^* with the distance z from the surface. For multi-layered systems the required model is developed in Appendix B.

Concepts of the forward and the inverse problems are widely used in the literature

related to this technology. Here, the forward problem is defined as the task of determining the electric field distribution and the interelectrode admittance matrix when the geometry, material properties, and external excitations are given. Correspondingly, the inverse problem requires determining either material properties or associated geometry, or both, when the imposed excitations and experimental values of the sensor admittance matrix are available. Each application that involves theoretical modeling usually requires solving the forward problem.

The forward problem can be solved using several approaches. One of them is to use a continuum model as developed in Appendix B of this thesis [76]. From the electroquasistatic field point of view, in a homogeneous dielectric, the electric scalar potential of the field excited by the driven electrode is a solution to Laplace's equation. At any constant z position, the electric field distribution far away from the sensor edges is periodic in the x direction and assumed uniform in the y direction. For a homogeneous dielectric of semi-infinite extent, the scalar potential can be written as an infinite series of sinusoidal Fourier modes of fundamental spatial wavelength λ that decays away in the z direction:

$$\Phi = \sum_{n=0}^{\infty} \Phi_n e^{-k_n z}(A_n \sin k_n x + B_n \cos k_n x), \quad z \geq 0 \tag{1.1}$$

where $k_n = 2\pi n/\lambda$ is the wavenumber of each mode. For $e^{j\omega t}$ excitations at radian frequency ω, such that $\Phi_n = \Re\widehat{\Phi}_n e^{j\omega\, t}$, the complex surface capacitance density $\hat{C}_n$ relates $\varepsilon^*\hat{E}_{zn}$ at a planar surface $z = constant$ to the potential $\hat{\Phi}_n$ at that surface for the n-th Fourier mode in the following way:

$$\hat{C}_n = \frac{\varepsilon^*\hat{E}_{zn}}{\hat{\Phi}_n} = \varepsilon^* k_n, \tag{1.2}$$

where

$$\varepsilon^* = \varepsilon - j\frac{\sigma}{\omega} \tag{1.3}$$

is the complex permittivity with ε as material dielectric permittivity and σ as ohmic conductivity. Appendix B generalizes (1.1)-(1.3) for the case of superposed homogeneous layers. Then, knowledge of $\hat{C}_n$ at the electrode surface lets us calculate the

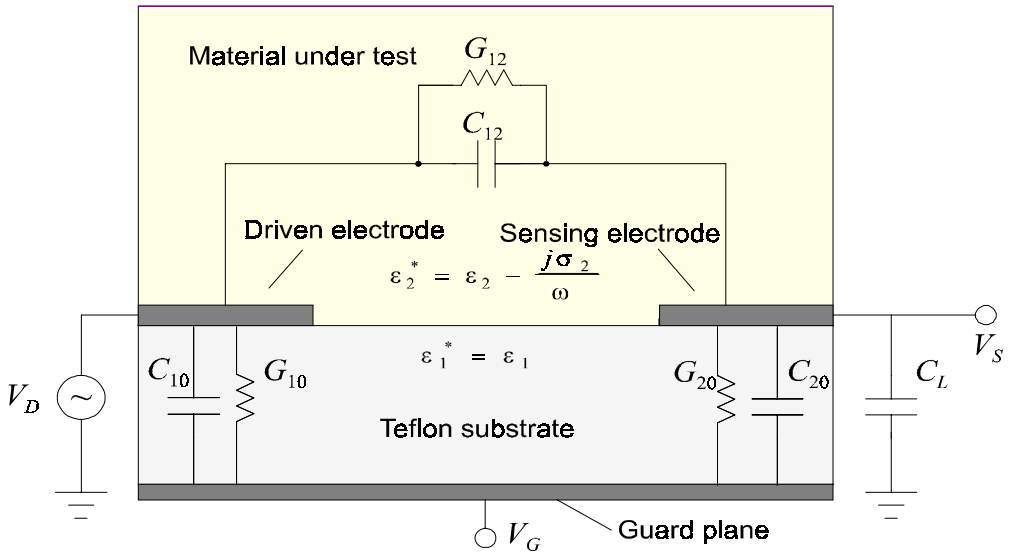

Figure 1.4: Half-wavelength cross-section with a superimposed equivalent circuit model.

terminal current from the potential distribution at that surface. It is also possible to solve the forward problem with commercial finite-element software [18], with finite-difference techniques, or by using analytical approximations [77].

Figure 1.4 shows the equivalent circuit of the sensor superimposed onto the schematic view of a half-wavelength cell. Note that each wavelength has an opposite conducting guard plane at the bottom of the substrate. For each wavelength, a follower op-amp drives the guard plane at the substrate bottom at the voltage $V_G = V_S$, thus eliminating any current between the sensing and guard electrodes.

The concept of imposed frequency-wavenumber $(\omega - k)$ goes beyond dielectrometry applications. Earlier studies by Professor J. R. Melcher employed interdigital electrodes to study electrohydrodynamic surface waves and instabilities [78], effects on static electrification in insulating liquids [79, 80], and electromechanics of electrochemical double layers in liquid electrolytes [81].

The penetration depth of the fringing electric fields above the interdigital electrodes is proportional to the spacing $\lambda/2$ between the centerlines of the sensing and the driven

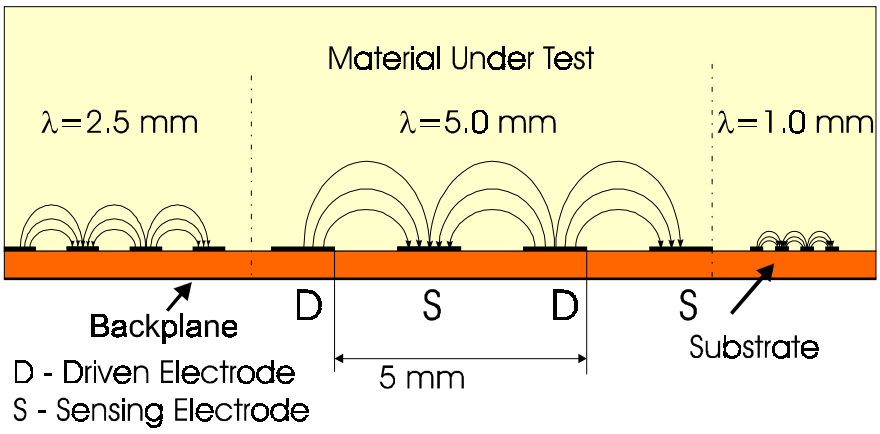

Figure 1.5: A conceptual view of multi-wavelength dielectrometry.

fingers. Figure 1.5 illustrates the idea of multiple penetration depths for a three-wavelength sensor. The variation of the material properties across the thickness of the material under test in the z direction can be found by simultaneously solving three complex equations describing this three-wavelength experimental arrangement.

1.1.3 Generic Measurement Setup

A typical measurement setup with dielectrometry sensors requires that a dielectrometry interface circuit be connected between the controller measurement/data acquisition unit and the sensor. The main purpose of the interface circuit is to provide a very high input resistance of the measurement circuit, otherwise, it is not possible to evaluate the effects of conduction currents in weakly conducting materials. Figure 1.6 shows the setup most frequently used in the measurements presented throughout this thesis. Dielectric properties are highly dependent on temperature and humidity of the ambient, therefore monitoring of these quantities is crucially important in many cases. Many industrial designs incorporate a temperature probe in the sensor head. The specific applications explored in this thesis did not require such a feature.

The setup shown in Figure 1.6 is not the only one possible. The choice of the custom-made measurement instrumentation was made on the basis of available hardware, keeping in mind the desire to sweep frequencies into the millihertz range. Analogous studies

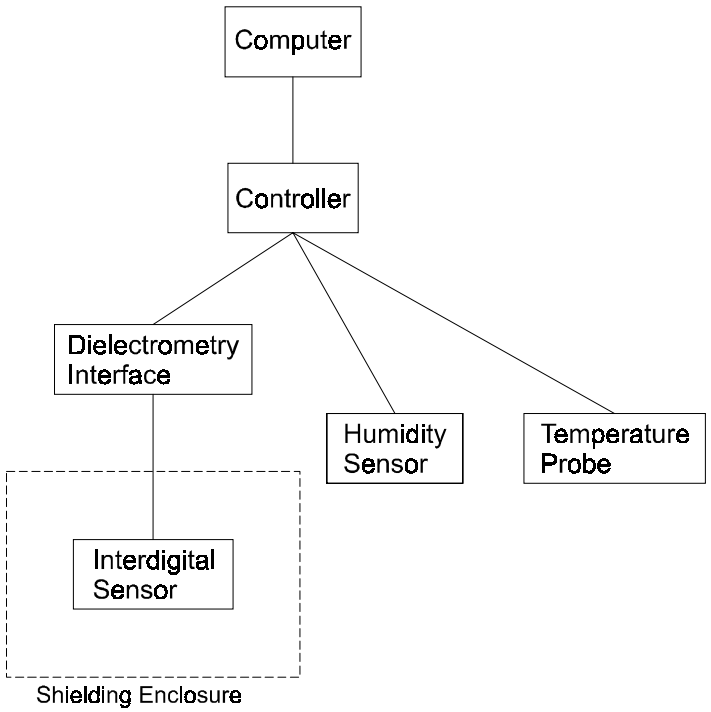

Figure 1.6: Generic measurement setup.

by other groups [67] have successfully used commercially available equipment.

1.2 Scope of the Thesis

1.2.1 NDE Perspective

All innovations in the field of non-destructive material evaluation can be subdivided into several major categories [82] (five categories in the original citation):

1) New types of physical phenomena used for sensing purposes. For example, introducing x-rays for medical imaging after their initial discovery.

2) New types of sensors that use known physical mechanisms in an original way, for example, by drastically modifying the geometry or other aspects of the sensor design, or by combining several known mechanisms into a single instrument.

3) Using existing sensors for new applications. For example, using commercial

piezoelectric sensors to sense vibrations of electric power cables (assuming that it was not done before).

4) New algorithms for processing of the signals from the sensors in order to gain additional information about the measured specimen. For example, using wavelet analysis to detect the presence of discontinuities in material properties.

5) New ways to visualize information from the sensors. For example, creation of a three-dimensional thermal map of the human body.

6) Optimization of sensor performance through incremental changes in the manufacturing processes, measurement procedures, etc.

As we step from higher to lower categories, we move from the realms of science into applied science into engineering into product development. The work presented in this thesis covers categories 2 through 6. Contributions in each category can be loosely traced through the chapters of this thesis.

Thus, the major purpose of this thesis to develop the field of fringing electric field dielectrometry into a fairly rigorous discipline for non-destructive measurements.

1.2.2 Parameter Estimation Algorithms

Non-destructive testing is a relatively mature discipline. However, model based fringing electric field sensing is one of the less developed methods of non-destructive testing. For that reason, most existing studies did not go far beyond preliminary measurements and conceptual verifications. It has been demonstrated in numerous applications that information about bulk and surface material properties can be obtained, in principle, with this technology. Yet, a reliable and accurate estimation of non-homogeneous distributions of material properties still presents substantial difficulties. Generally speaking, each task and application requires a different version of a parameter estimation algorithm. Among the major tasks of this thesis is the development of a suite of generic parameter estimation algorithms with widely varying characteristics, so that only an easy modification of the most appropriate generic algorithm would be needed to accommodate new applications.

The types of distinctively different parameter estimation algorithms include:

- iterative algorithms which require computationally expensive electric field simulations for each set of measurement data points;

- pre-computed lookup tables which require offline calculations of discretized solution spaces;

- closed form algebraic solutions which are available for selected cases;

- empirical calibration curves obtained with known materials and used to estimate properties of unknown materials;

- simplifying assumptions about the relationships between the sensor output and the variables of interest (such as linear or quadratic relationships).

There is no best approach, as each algorithm type has a number of advantages and drawbacks, whose significance varies with the sensor type and specific application. Properties and implementations of every major type of parameter estimation algorithms are discussed throughout this thesis.

1.3 Thesis Objectives

The main objectives of this thesis research are:

1. To evaluate the significance of a variety of factors that influence the response of interdigital sensors that were not taken into account or assumed to be negligible in the course of previous research. These factors include variations in the geometry of the sensor itself and the experimental setup, interfacial effects, uniqueness of response, adequacy of a two-dimensional model, and error propagation effects.

2. On the basis of this analysis, to design, fabricate, characterize, and test alternative designs of interdigital sensors optimized for the best performance under given environmental conditions determined by each specific application.

3. To measure dielectric properties of a large number of solid and liquid materials and to relate these properties to other physical variables of interest, which may include, but are not limited to moisture content, thickness of layers, structural integrity, and

concentration of chemical impurities.

4. To explore various aspects of dielectric spectroscopy from the point of view of interdigital dielectrometry; to identify characteristic signatures associated with material structure, chemical content, sensor to specimen contact conditions, and the nature of the electrochemical double layer.

5. To perform a variety of simulations as related to the problem of landmine detection with the purpose of finding promising technical dielectrometry approaches for discrimination of buried plastic and metal landmines.

6. To unify and generalize principles of fringing field dielectrometry sensor design and parameter estimation algorithms.

7. As an incremental effort to the adaptive search inverse problem algorithm, to develop a general tool for optimization of electromagnetic devices.

8. To use fringing field dielectrometry in numerous applications.

1.4 Previous Work

The focus of direct prior research in this area was concentrated mainly on the development of analytical and numerical tools for the computation of the sensor response under idealized conditions of the perfectly stratified multi-layer medium adjacent to the sensor electrodes [6,8]. Fairly complex algorithms were developed to measure both thickness and complex dielectric permittivity of insulating material layers [6,71]. Also, several sensors were designed to implement the core ideas of frequency-wavelength dielectrometry [70, 83]. If these measurements were fully successful, this thesis would have not been necessary. Experiments quickly revealed significant differences between theoretical calculations and real measurements [9]. In the search of the source of these differences, it was suggested that the thickness of electrodes is the major contributor to the measurement error. Finite element computer simulations and a semi-empirical model were developed to account for this error [9]. Subsequent measurements [10] indicated that such a model was insufficient and that other effects were also important.

Sometimes, in trying to fit models to measurements the thickness of the electrodes could be evaluated to non-physical negative values.

Due to a high sensitivity of existing parameter estimation algorithms to the variations in the sensor output, even a small error in a single parameter could propagate through the algorithm and lead to entirely erroneous estimations. At this point, work presented in this thesis was initiated with an ultimate goal of improving the precision, reliability, stability, and practicality of the fringing field dielectrometry technology. Experimental work with power transformer insulation revealed a number of problems that must be resolved before an adequate parameter estimation can be achieved.

1.4.1 Measurement of Moisture Distribution in Power Transformer Pressboard

The service life of power transformer pressboard insulation is reduced by excessive concentration of moisture in transformer oil. The ability to withstand high electric fields and thermal stresses that is critical for operation of the power transformer is compromised by high moisture levels. The failure of the electrical insulation can sometimes lead to explosions, which have adverse economic effects on the power industry and endanger the health and life of utility personnel. A conventional technique to evaluate the equilibrium concentration of moisture in the pressboard is to use moisture equilibrium curves, which relate easily measurable moisture concentration in the oil to the moisture concentration in the pressboard. Since the characteristic times to achieve equilibrium conditions in a large transformer are on the order of days and weeks, the conventional approach introduces significant errors. Other ways to measure the concentration of moisture include measurement of the average moisture ratio in impregnated paper insulation with the help of a voltage recovery meter [9], Karl Fischer reaction method [10], and pressure gauge method [11]. It is very attractive to be able to monitor moisture diffusion processes in the pressboard on-line and based on that draw recommendations regarding the further operation of the transformer.

1.4.2 Detection of Buried Landmines

There are more than 100 million landmines installed in the world. About 10,000 people die annually from landmine explosions. About 100,000 landmines are cleared per year worldwide, and about one million new ones are installed during the same time. Currently used detection procedures for demining are slow and fairly inefficient and are generally limited to metal landmines. False alarm rates can be as high at 1,000 to 1, and real mines sometimes remain undetected. Plastic landmines with no or very little metal content present the major problem, as they are generally undetectable by conventional metal detectors used to detect metallic landmines.

Detection and discrimination of buried landmines can be accomplished using interdigital dielectrometry technology. In general, dielectrometry is capable of detecting and discriminating both plastic and metal objects in the ground, as the presence of low dielectric constant plastic landmines in a high dielectric constant sand will decrease the measured capacitance while a metal landmine would increase the capacitance for most configurations. Further improvements in measurement selectivity will be gained from low frequency measurement of terminal conductance as well as capacitance and their variation with frequency. Signatures from dielectrometry frequency spectroscopy measurements can be used to enhance detection sensitivity and to minimize false alarms. Computer based models can relate sensor terminal admittance measurements to identification of the size, location, and material of buried objects. Measurements show good agreement with computer simulations.

1.5 Past and Present Research

The purpose of this section is to list in an organized fashion publications on prior work conducted by prominent research groups worldwide. A more detailed analysis of their findings is available in the following two chapters and throughout the entire thesis, where the same references are mentioned in the specific context relevant to the issue under consideration.

Several other groups also have conducted intensive research developing novel sensors, measurement circuitry, and parameter estimation algorithms for fringing electric field dielectrometry. The overlap of conceptual approaches and ideas between different groups is very significant. Unfortunately, the lack of technical communication is clearly visible throughout published results based on the work conducted at different locations. The priority to the same or very similar approaches and concepts has been claimed by different groups with a time difference of as much as 20 years. One of the reasons for that lack of communication is that fringing field dielectrometry developments have been multidisciplinary and are not hosted by one or two technical societies or journals. Instead, it is spread across many societies and disciplines and is being developed in different contexts using a widely varying terminology. Hopefully, this thesis will bring some clarity, unity, and structure to the accumulated information.

The longest and the most extensive research in the area of fringing electric field dielectrometry has been conducted in Latvia since the 1960s [52, 53, 58, 84–117]. In the United States, interdigital sensors are developed in dozens of locations. Interdigital dielectrometry could be viewed as a separate field on the basis of fundamental analysis of dielectric properties. The research work on single wavelength sensors, mostly for monitoring of moisture concentration and resin cure state, at MIT and by MIT graduates, has been conducted since the 1970s [59, 60, 65, 66, 72, 74, 77, 118–145]. Both theoretical and practical aspects of multiple penetration depth sensors with separate sensor heads of varying size, dubbed frequency-wavenumber $\omega - k$ dielectrometry, have been studied since the early 1980s [61, 63, 70, 71, 73, 75, 76, 83, 146–151]. The results of research work of other groups is described in a specific context elsewhere in this thesis.

1.6 Thesis Outline

Chapter 1 provides a general introduction to central concepts and terminology, lists key references, determines thesis objectives and describes previous work directly related to the topics of this thesis. Chapter 2 provides theoretical background on dielectric

theory concepts and measurements of moisture in transformer pressboard insulation. Background information about flow electrification related phenomena that initially motivated this research project is given. Chapter 3 is dedicated exclusively to interdigital sensors. It gives an extensive overview of interdigital sensors used in different technical fields, including humidity monitoring, control of polymer cure processes, chemical and biological sensors, piezoelectric sensors, microelectromechanical systems, and sensor arrays.

The first part of Chapter 4 gives an overview of material selection and manufacturing techniques used for fabrication of interdigital sensors. Then, all sensors built in the course of this research work are described and compared. Electronic circuitry issues that affect measurement and sensor design practices are considered next. Chapter 4 ends with discussion of specific and most relevant fabrication and design issues.

Chapter 5 introduces and illustrates a number of subtle issues that affect interdigital dielectrometry measurement results. It also describes guarded parallel-plate capacitor cells built for independent verification of material properties. In general, this chapter describes tools and approaches for diagnostics of electronic equipment and sensor performance. Chapter 6 lists and documents major disturbance factors that affect dielectrometry measurements and describes ways to eliminate, minimize, or account for such factors.

Chapters 7 and 8 treat parameter estimation algorithms in the framework of forward and inverse problems of material characterization. Chapter 7 provides an overview of forward problem solution algorithms, in which the sensor admittance matrix must be determined as a function of geometry and material properties. The inverse problem is inherently more complex. It requires determination of geometry or material properties based on measured admittance matrix entries. Chapter 8 provides description of several inverse problem algorithms of varying generality, flexibility, and accuracy. It also provides explanation for terminal negative transcapacitance and transconductance values frequently observed in interdigital dielectrometry measurements. Chapter 9 also deals with the inverse problem, but in the context of optimization theory, in

which it can be approached as a generic minimization problem. In this case, it can be generalized to other optimization problems, not necessarily involving determination of material properties. The development of a general optimization tool on the basis of Ansoft *Maxwell* software and the Matlab optimization toolbox is described in Chapter 9.

Chapter 10 is dedicated entirely to visualization of dielectric spectroscopy data, in preparation for critical analysis of simulations and measurement data in the remaining chapters. Generally speaking, a graphical representation that provides the best picture of salient features of a data array in a given experiment should be selected.

Chapter 11 deals exclusively with moisture dynamics in transformer pressboard. Parameter estimation algorithms are applied to a benchmark problem and to experimental results. A correct estimation of spatial moisture profiles during a transient diffusion process is one of the major results of this thesis.

Chapter 12 lists preliminary and exploratory simulations and measurements for detection of plastic landmines with fringing field dielectrometry. A more extensive treatment of this subject will become a thesis topic for the next generations of graduate students. Chapter 13 provides a brief overview of practical applications of interdigital dielectrometry. Selected cases of experimental data for measurement of the saturation state of chemical protective garments and detection of flaws in fiberglass flywheels are presented. These studies are part of the commercialization process of interdigital dielectrometry. Chapter 14 gives an overview of major results, draws conclusions, and outlines directions of future work.

Appendix A is an extensive set of instructions for ultrasonic cleaning of sensors fabricated with copper coated Teflon® material (CuFlon®). Appendix B provides mathematical background of the continuum model developed by previous research students and included here for completeness. Appendices C and D provide documentation for interface and controller electronics used throughout this thesis research. Appendix E summarizes know-how accumulated over the last several years regarding practical use of *Maxwell* software.

Appendix F gives listings of some of the C and Matlab codes used for data acquisition and data processing. Appendix G gives a listing of Matlab code for different parameter estimation algorithms. Appendix H gives a listing of Matlab code for the graphical user interface for generic optimization with *Maxwell*. Finally, the bibliography, author's biography, and alphabetical index of terms are included.

Chapter 2

Background and Motivation

2.1 Basics of Dielectrometry

2.1.1 Core Literature

Understanding of dielectrometry requires prior background knowledge of basic electromagnetism. Numerous introductory texts are available on the subject of electrostatics and electrodynamics, for example [152, 153]. Introductory texts and classic research monographs on dielectrometry include [154–164]. Dielectric spectroscopy, which is the subject of Chapter 10 of this thesis is treated extensively in [165–167]. Specialized monographs cover advanced areas of dielectric science, such as Schottky and Poole processes [168], anisotropic dielectrics [169], electrets [170, 171], analysis of dielectric and viscoelastic material properties [172]. An advanced text on continuum electromechanics [173], among other relevant topics, explores analytical solutions for electrical and mechanical perturbations of multi-layered media.

2.1.2 Debye Model

The Debye dielectric relaxation model [154] is the simplest way to analyze polarization processes in insulating materials. It assumes that dielectric relaxation processes are governed by first-order dynamics and, thus, can be characterized with a single time

constant. The Debye model can be derived from basic polarization and conduction laws [166] using the following argument.

The current density (Amp/m^2) in a lossy dielectric ohmic material with ohmic conductivity σ_0 is equal to:

$$\mathbf{J} = \sigma_0 \mathbf{E} + \frac{\partial \mathbf{D}}{\partial t} \tag{2.1}$$

The first term is the conduction current and is associated with translational drift motion of mobile charge carriers due to the local electric field intensity $\mathbf{E}$, whereas the second term is the displacement current density associated with motion of electrical dipoles due to changing electrical displacement field $\mathbf{D}$ defined as

$$\mathbf{D} = \varepsilon_0 \mathbf{E} + \mathbf{P} \tag{2.2}$$

where $\varepsilon_0 \approx 8.854 \times 10^{-12}$ Farads/m is the permittivity of free space and $\mathbf{P}$ is the polarization vector. The Debye model deals with displacement current density, represented by the second term in (2.1).

In the simplest case of linear dielectrics, the polarization of an insulating material ($\sigma_0 = 0$) stressed by an electric field is linearly proportional to the electric field and occurs on two sufficiently distinct time scales. The high frequency polarization is due to ionic vibrations and also due to deformation of the electron cloud under the influence of electric field (so that the center of the electron cloud no longer coincides with the nucleus). These processes determine the value of the so-called high frequency *dielectric susceptibility* χ_∞ defined as:

$$\mathbf{P}_\infty = \varepsilon_0 \chi_\infty \mathbf{E} \tag{2.3}$$

as well as the high frequency relative dielectric permittivity ε_∞:

$$\varepsilon_\infty = 1 + \frac{\mathbf{P}_\infty}{\varepsilon_0 \mathbf{E}} = 1 + \chi_\infty \tag{2.4}$$

The time constants associated with these processes fall in the range 10^{-14} s to 10^{-16} s, so, they become important for high frequency excitations with f $> 10^{14}$ Hz.

The low frequency polarization is due to reorientation of dipoles formed by polar molecules in the changing electric field. In the extreme, the polarization due to a

constant static field is characterized by the static dielectric susceptibility χ_s defined as

$$\mathbf{P}_s = \varepsilon_0 \chi_s \mathbf{E} \tag{2.5}$$

and relative static dielectric constant ε_s:

$$\varepsilon_s = 1 + \frac{\mathbf{P}_s}{\varepsilon_0 \mathbf{E}} = 1 + \chi_s \tag{2.6}$$

Since the polarization $\mathbf{P}$ at intermediate frequencies is usually lower than the static polarization $\mathbf{P}_s$ but higher than the nearly instantaneous high frequency polarization $\mathbf{P}_\infty$, it is convenient to define a time-dependent polarization $\mathbf{P}_t = \mathbf{P} - \mathbf{P}_\infty$. The transition from $\mathbf{P}_\infty$ to $\mathbf{P}_s$ is gradual, and the difference between the two can be denoted as a frequency dependent (or, equivalently, time-dependent) polarization at $t = \infty$:

$$\mathbf{P}_t(t = \infty) = \mathbf{P}_s - \mathbf{P}_\infty, \tag{2.7}$$

where $\mathbf{P}_\infty$ is a nearly instantaneous polarization due to the displacement of the electron cloud.

According to our earlier assumption about the first-order dynamics, the rate of growth of time-dependent polarization for each moment of time is proportional to the difference between the time-dependent polarization $\mathbf{P}$ and the static polarization $\mathbf{P}_s$:

$$\frac{d\mathbf{P}_t\,(t)}{dt} = \frac{\mathbf{P}_s - \mathbf{P}\,(t)}{\tau}. \tag{2.8}$$

The polarization due to a step electrical field with magnitude $E = E_0 u(t)$ is

$$\mathbf{P} = \left[\mathbf{P}_s(1 - e^{-t/\tau}) + \mathbf{P}_\infty e^{-t/\tau}\right] u(t) \tag{2.9}$$

The displacement current density of (2.1) with $\sigma_0 = 0$ is:

$$\mathbf{J}\,(t) = \frac{d}{dt}\left(\varepsilon_0 \mathbf{E} u(t) + \mathbf{P}(t)\right) = (\varepsilon_0 \mathbf{E}_0 + \mathbf{P}_\infty)\delta\,(t) + (\mathbf{P}_s - \mathbf{P}_\infty)\,\frac{e^{-t/\tau}}{\tau} u(t) \tag{2.10}$$

For sinusoidal steady state fields of the form $\mathbf{J} = \Re\left[\hat{\mathbf{J}} e^{j\omega t}\right]$ and $\mathbf{E} = \Re\left[\hat{\mathbf{E}} e^{j\omega t}\right]$ we find the complex relative dielectric constant from (2.1) with $\sigma_0 = 0$ and (2.8) as:

$$\varepsilon^* = \frac{1}{j\omega\varepsilon_0}\frac{\hat{\mathbf{J}}}{\hat{\mathbf{E}}} = \frac{j\omega\left[\varepsilon_0 \hat{\mathbf{E}} + \hat{\mathbf{P}}\right]}{j\omega\varepsilon_0 \hat{\mathbf{E}}} = \varepsilon' - j\varepsilon''. \tag{2.11}$$

From (2.8), one can derive the expression for polarization:

$$\hat{\mathbf{P}} = \frac{\hat{\mathbf{P}}_s + j\omega\tau\hat{\mathbf{P}}_\infty}{j\omega\tau + 1} = \frac{\chi_s + j\omega\tau\chi_\infty}{j\omega\tau + 1}\varepsilon_0\hat{\mathbf{E}}. \tag{2.12}$$

Substitution of (2.12) into (2.11) yields:

$$\varepsilon^* = \varepsilon_\infty + (\varepsilon_s - \varepsilon_\infty)\frac{1}{j\omega\tau + 1} \tag{2.13}$$

To separate real and imaginary parts, the numerator and denominator of the rightmost term in (2.13) are first multiplied by its complex conjugate, so that:

$$\varepsilon^* = \varepsilon_\infty + \frac{(\varepsilon_s - \varepsilon_\infty)(1 - j\omega\tau)}{1 + (\omega\tau)^2}, \tag{2.14}$$

or, in a conventionally used form:

$$\varepsilon^* - \varepsilon_\infty = \frac{(\varepsilon_s - \varepsilon_\infty)}{1 + (\omega\tau)^2} - j\frac{\omega\tau(\varepsilon_s - \varepsilon_\infty)}{1 + (\omega\tau)^2}, \tag{2.15}$$

The real and imaginary parts of (2.15) are the Debye dispersion relations, which are also restated in subsequent sections for reference in another widely used form. It is worthwhile noticing that the frequency response suggested by this relationship of $j\omega\varepsilon^* A/d$ corresponds exactly to the admittance frequency response of the simple lumped-element circuit shown in Figure 2.1(a) for a parallel plate electrode geometry with area A and gap d. The equivalency between the dielectric constants and the lumped element values for a voltage source is given by

$$C_P = \varepsilon_0\varepsilon_\infty A/d, \tag{2.16}$$

$$C_S = \varepsilon_0(\varepsilon_s - \varepsilon_\infty)A/d, \tag{2.17}$$

$$\tau = R_S C_S. \tag{2.18}$$

It should be noted that the complex dielectric permittivity may have an appreciable imaginary part even if no dc conductivity is present. The imaginary part arises from the energy dissipation process due to dipole re-orientation. Translational motion of

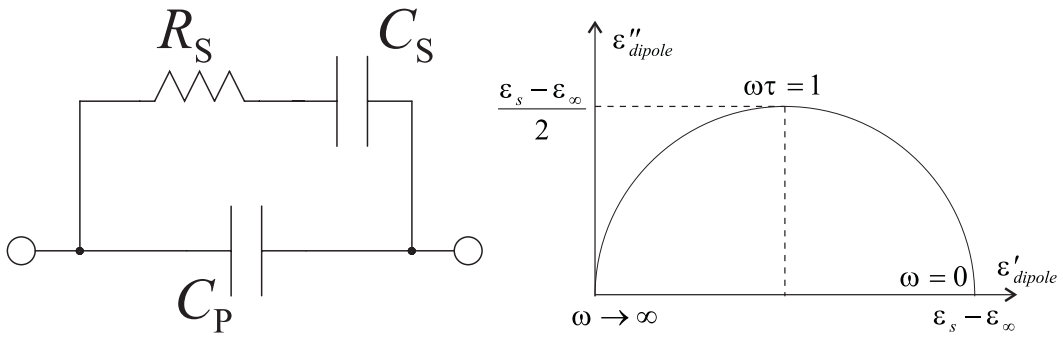

(a) equivalent circuit (b) graphical representation

Figure 2.1: The Debye model for time-dependent polarization.

charge carriers also leads to energy dissipation. The expressions (2.1) and (2.15) can be combined to include ohmic conductivity and Debye polarization as:

$$\varepsilon' = \varepsilon_\infty + \varepsilon'_{dipole} \tag{2.19}$$

$$\varepsilon'' = \frac{\sigma_0}{\omega} + \varepsilon''_{dipole} \tag{2.20}$$

$$\varepsilon'_{dipole} = \frac{(\varepsilon_s - \varepsilon_\infty)}{1 + (\omega\tau)^2} \tag{2.21}$$

and

$$\varepsilon''_{dipole} = \frac{(\varepsilon_s - \varepsilon_\infty)\omega\tau}{1 + (\omega\tau)^2} \tag{2.22}$$

A convenient presentation of (2.19)-(2.22) is the Cole-Cole plot [174] shown in Figure 2.1(b) which plots ε' vs. ε'' with frequency ω as an independent parameter and is an exact semicircle. Note that for $\omega\tau$=1, ε'_{dipole} and ε''_{dipole} are half of $(\varepsilon_s - \varepsilon_\infty)$ and ε''_{dipole} assumes its maximum value.

2.2 Distribution of Relaxation Times

In reality, dielectric materials usually do not obey a simple model which assumes a single relaxation time. To analyze experimental data, a certain distribution of relaxation times over the frequency range of interest is assumed. A number of modifications

to the original Debye model have been proposed. One of the most commonly used for polar liquid and solid dielectrics is by Cole and Cole [174], in which the center of semicircular arcs in the ε''-ε' plane shifts below the horizontal axis. According to this model, the dielectric relaxation is described by the equation

$$\varepsilon * - \varepsilon_\infty = \frac{\varepsilon_s - \varepsilon_\infty}{1 + (j\omega\tau)^{1-\alpha}} \tag{2.23}$$

with $0 < \alpha < 1$ where $(\alpha\pi)/2$ is the angle between the real axis and the line that connects the semicircle center with the high frequency intercept.

Sometimes, the experimental data is not symmetric with respect to the center of the arc (semicircle for $\alpha = 0$) in the $\varepsilon'' - \varepsilon'$ plane. For example, the Davidson-Cole distribution function [175] results in a tilted arc, which approximates the original semicircle at low frequencies, but flattens out at high frequencies. The rate of distortion from the original shape is controlled by the parameter β in the Davidson-Cole equation:

$$\varepsilon * - \varepsilon_\infty = \frac{\varepsilon_s - \varepsilon_\infty}{(1 + j\omega\tau)^{\beta}} \tag{2.24}$$

where $0 < \beta < 1$. This function is a perfect semicircle when $\beta = 1$. Many other distribution functions and other extensions of the original Cole-Cole theory have been proposed. The most commonly used include those by Kirkwood and Fuoss [176] and Williams and Watts [177, 178].

2.3 Double Layer Interface

The results of admittance spectroscopy measurements of dielectric materials are often strongly altered by the characteristics of a space-charge layer that forms at the metal-dielectric interface. This layer, often referred to as a double layer, plays a critical role in flow electrification phenomena [9]. In the electrical double layer, oppositely charged ions effectively neutralize each other in the bulk. At electrode boundaries, however, there is a preferential absorption of one species with an opposite polarity carrier diffusely distributed over a thin boundary region equal to the Debye length.

The degree of net charge and the depth to which it penetrates into the liquid volume are related to the balance of ion diffusion and migration, as well as convection for the case of circulating electrolyte. The charge on the liquid side of the double layer can be entrained in a liquid flow and can accumulate on insulating or isolated surfaces. If the rate of charge accumulation is faster than the rate of charge relaxation, the electric field can become larger than the material's breakdown strength. Resulting spark discharges can lead to system failure.

Thus, a deep understanding of charge dynamics as related to the electrochemical nature of the double layer is critically important. The significance of this phenomenon has long been recognized by electrical engineers [128]. Interdigital dielectrometry measurements help to evaluate the double-layer characteristics by using relatively simple models [73]. However, a deep understanding of all consequences of the double layer formation requires the conceptual framework of electrochemical physics [179].

Multi-wavelength interdigital dielectrometry sensors have been used to determine various electrochemical parameters of dielectric interfaces. Preliminary experiments have measured the Debye length, zeta potential, molecular diffusion coefficient and the mobility of positive and negative charge carriers in a liquid dielectric [9].

Energy storage and conversion devices represent an enabling technology for a broad range of applications. Electric vehicle development, for example, is dependent upon improvements in energy storage and conversion. Current understanding of interfacial electrochemical processes is largely limited to application of microscopic thermodynamic and kinetic concepts. Multi-wavelength dielectrometry has the potential to significantly expand our understanding of electrochemical processes in boundary layers. The potential also exists to use installed dielectrometry sensors to provide active control of boundary layer processes by applying voltages on the order of the thermal voltage, kT/q, to drive the electrical double layer out of equilibrium. Large-scale efforts have already improved battery performance but a better understanding of fundamental electrochemical behavior, especially at interfaces, can lead to new ways for future battery improvements.

A metal electrode transfers charge to an adjacent dielectric solid even under zero electric field conditions [125]. The double layer thickness λ_D, known as the Debye length, at solid-liquid interfaces varies as

$$\lambda_D \approx \sqrt{\varepsilon D/\sigma}, \tag{2.25}$$

where D is the molecular diffusivity, and λ_D can be comparable with the sensor feature size at the micron and submillimeter scales [8].

In equilibrium, the interface between pressboard and transformer oil is characterized by the Debye length λ_D and by zeta potential, ζ. The analysis of double layer formation and dynamics affected by laminar and turbulent flows of liquid dielectrics is available in [180–182].

Multi-wavelength interdigital dielectrometry sensors have been used to determine various electrochemical parameters of dielectric interfaces. Preliminary experiments have measured the Debye length, zeta potential, molecular diffusion coefficient and the mobility of positive and negative charge carriers in a liquid dielectric [9].

The results of admittance spectroscopy measurements of dielectric materials are often strongly altered by the characteristics of a space-charge layer that forms at the metal-dielectric interface. This layer, often referred to as a double layer, plays a critical role in flow electrification phenomena [9]. In the electrical double layer, oppositely charged ions effectively neutralize each other in the bulk. At electrode boundaries, however, there is a preferential absorption of one species with an opposite polarity carrier diffusely distributed over a thin boundary region equal to the Debye length. The degree of net charge and the depth to which it penetrates into the liquid volume are related to the balance of ion diffusion and migration, as well as convection for the case of circulating electrolyte. The charge on the liquid side of the double layer can be entrained in a liquid flow and can accumulate on insulating or isolated surfaces. If the rate of charge accumulation is faster than the rate of charge relaxation, the electric field can become larger than the material's breakdown strength. Resulting spark discharges can lead to system failure.

Thus, a deep understanding of charge dynamics as related to the electrochemical nature of the double layer is critically important. The significance of this phenomenon has long been recognized by electrical engineers [128]. Interdigital dielectrometry measurements help to evaluate the double-layer characteristics by using relatively simple models [73]. However, a deep understanding of all consequences of the double layer formation requires the conceptual framework of electrochemical physics [179].

The space-charge polarization is most conspicuous at the low frequencies of dielectrometry admittance spectroscopy. At high frequencies, the double layer remains almost invisible to the alternating current. At low frequencies, the bulk of the moderately conductive dielectric looks like a short circuit from the terminal point of view. As a result, the terminal capacitance between the electrodes becomes extremely high. If double layer effects are not taken into account properly, the estimated dielectric permittivity assumes an unreasonably high value [14]; and the estimated conductivity has little correlation with the ohmic conductivity of the material.

Double layer parameters can be obtained from measurements using Cole-Cole plots, which plot the real part of the complex permittivity versus the imaginary part. In the absence of a double layer, the Cole-Cole plot is a semi-circle. Deviations from a semi-circle provide information on the Debye length and molecular diffusion coefficient.

2.4 On-line Measurement of Moisture in Transformer Pressboard

2.4.1 Motivation

Failures of large power transformers are fairly infrequent, however, since each failure induces multi-million dollar losses and potentially endangers lives, they cannot be ignored. A substantial amount of effort in the power industry worldwide has been directed towards developing on-line monitoring systems to optimize transformer performance and prevent failures.

Various characteristic pre-failure processes in transformer insulation can be monitored using chemical, acoustical, electrical, magnetic, dielectric, and other types of measurements. Complementary information from various measurements can be integrated in a unified monitoring system to increase the reliability and accuracy of performance evaluation. An on-line monitoring and internal diagnostics system of a power transformer involves prediction of future performance through trend analysis and detection of anomalous behavior [183, 184].

2.4.2 Effects of Moisture

Pressboard

Dielectric properties of transformer insulation vary with the presence of contaminant materials and additives. Since moisture is always present in the environment, it plays an important role in evaluating operational characteristics of a power transformer. Transformer pressboard, being a highly hydrophilic fibrous material, is particularly strongly affected by moisture [185–187], which also makes it a good candidate for property monitoring through dielectrometry measurements [188, 189]. Somewhat paralleling corrosion processes in metals, moisture accelerates pressboard insulation aging due to thermal, mechanical, and electrical degradation of the cellulose base [190–192]. It has been observed that the practical lifetime of cellulose insulation is inversely pro-

portional to its average moisture content [193]. Extensive review of properties of transformer pressboard, and related measurement, modeling, and application issues is given in [194, 195].

At normal atmospheric conditions, pressboard naturally contains about five percent of water by weight [196, 197]. During transformer operation, very small amounts of water should normally be present within the transformer enclosure. Transformers are subjected to drying cycles using nitrogen and vacuum pumps to remove most of the moisture before operation [198–201]. After that, they are filled with dry transformer oil, which, after a certain period of time, establishes a moisture concentration equilibrium with pressboard.

Transformer Oil

An extensive up-to-date overview of transformer oil properties is given in [202, 203]. Like most other oils, transformer oil is a hydrophobic liquid. It usually contains a much smaller percentage of water than pressboard, therefore the transformer oil dielectric permittivity and conductivity are not strongly affected by the presence of typical amounts of moisture. At the same time, the electric field intensity breakdown strength of transformer oil drops dramatically when the moisture in oil concentration exceeds allowable levels [204]. Chemical additives and impurities may form in oil due to manufacturing processes, oxidation, partial discharging, and other aging-related processes. These impurities, together with moisture and charged ion species from the oil-pressboard double layer form a complex electrochemical system that determines the reliability and efficiency of transformer operation [205].

2.4.3 Flow Electrification

Moisture dynamics between oil and transformer pressboard as a function of temperature is very important in power transformer operation. For example, if the temperature were to drop too quickly before the moisture in the oil could diffuse into pressboard, oil

moisture would exceed the saturation value at this temperature, resulting in free water in the oil. Such free water in the high voltage region of the transformer could result in catastrophic electric breakdown and transformer failure. Another transformer failure mode dependent on moisture dynamics is flow electrification, which often arises when a transformer that has been out of service is being recommissioned. A plausible scenario is that as the transformer heats up, moisture is driven out of the pressboard insulation into the oil. The moisture first comes from near the pressboard interface, leaving a very dry interface that is also highly insulating. Any accumulating surface charge has no leakage and thus the surface charge density can increase until spark tracking discharges occur. These sparks cause gas formation, which can rise into the high electric field region causing a high-energy discharge that causes transformer failure. If failure does not occur during the early times of the recommissioning process, the moisture deeper in the pressboard diffuses to the surface, reaching equilibrium with the oil moisture. The moisture diffusion time can easily be a few weeks, but once there is no longer an interfacial dry zone, there is a leakage path for interfacial surface charge so that the surface charge density cannot rise to electric field strengths beyond the breakdown strength of oil and pressboard. Thus, once the transformer is in moisture equilibrium, this flow electrification hazard is minimized.

Flow electrification is believed to play an important role in mass transport of water molecules by affecting properties of the pressboard/oil interface [206]. Continuous monitoring of the moisture diffusion process has an immediate application in the electric power industry. Flow static electrification of transformer pressboard sometimes leads to catastrophic explosions of large power transformers. The charge buildup processes in the course of electrification depend on the surface and volume conductivity of pressboard. The conductivity of the cellulose based pressboard is a function of two major factors: temperature and moisture content. Thus, research monitoring of the pressboard state helps to understand, predict, and prevent spark discharges due to significant charge accumulation with negligible leakage when a highly insulating surface dry zone forms as increase in temperature at the pressboard drives moisture out of the

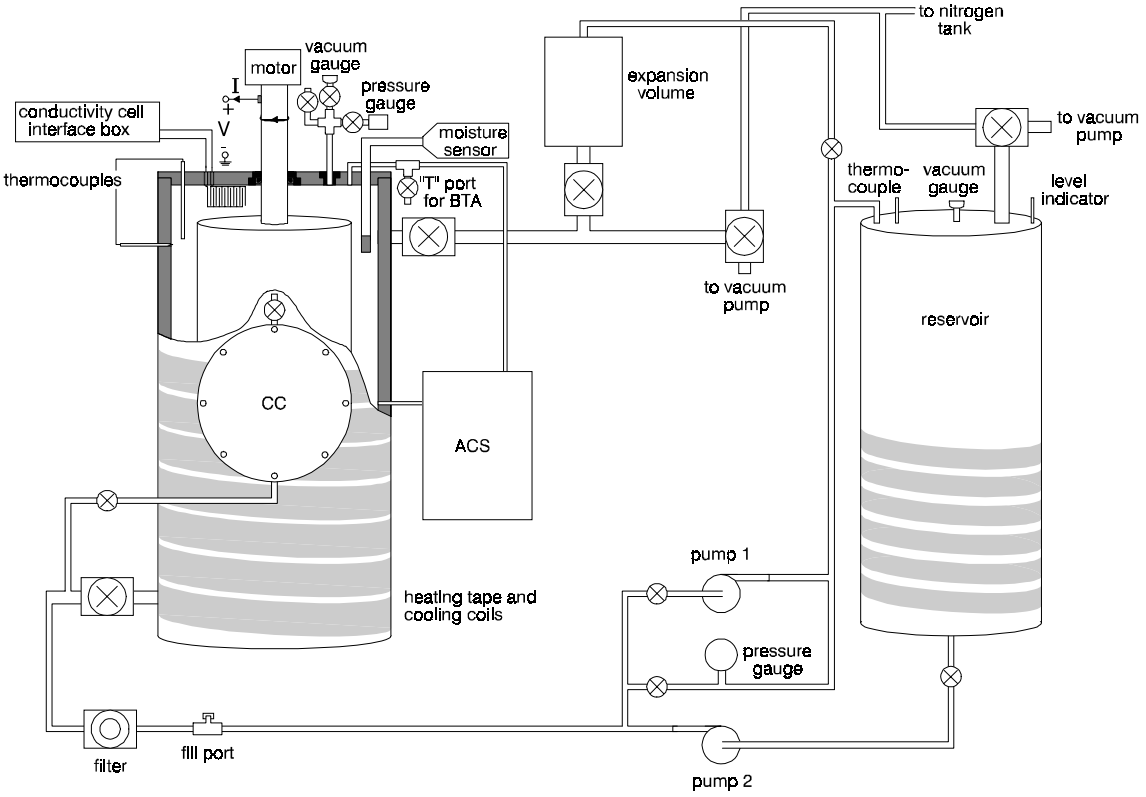

Figure 2.2: Couette Facility for simulating a variety of interdependent electrodynamic, electrochemical, thermodynamic, and hydrodynamic phenomena in the power transformer environment [207–209].

pressboard into the oil. Each failed transformer entails financial losses of millions of dollars, which include the costs of transformer repair or replacement, transformer oil spill cleanup, and purchase of replacement power.

Figure 2.2 shows the apparatus for experimental work with flow electrification-related phenomena used at the MIT High Voltage Research Laboratory for a number of years. It comprises a reservoir, the experimental chamber itself, and an extensive set of auxiliary equipment for sensing and control of relevant physical parameters. The experimental chamber consists of a pair of co-axial cylinders. The rotation of the inner cylinder by an electric motor produces viscous flow that entrains electrical double layer charge at the interfaces that may lead to significant flow electrification and, ultimately, to electrical breakdown.

2.4.4 Moisture Dynamics

The electric power load of a large power transformer changes continuously with time of the day and month of the year, depending on customer needs. Transient processes with time constants ranging from milliseconds through weeks constantly take place. In other words, the transformer is never in equilibrium, which makes measurement of the moisture concentration in transformer pressboard particularly complicated.

It is inherently easier to measure moisture content in liquids than in solid insulation. Significant experience has been accumulated in measuring moisture content in pressboard indirectly, by using the empirical equilibrium relationship with the moisture content in transformer oil [197, 210–212]. The relative humidity of the pressboard and the transformer oil at the oil-pressboard interface boundary is the same at thermal equilibrium [213]. However, the absolute value of moisture concentration is drastically different on two sides of the interface due to the large difference in saturation levels of moisture uptake.

Chapter 3

State of the Art

3.1 Introduction

The linear dimensions of interdigital electrodes in existing designs vary over several orders of magnitude. For example, the widths of electrodes of 24 nm [214], 50 nm [215], 1 μm [216], 2 μm [217], 14 μm [218], 250 μm [17], 1.25 mm [17], and 20 cm [26] have been reported.

The analysis of signals from interdigital sensors can be as involved as required by the application. On the low end of the complexity spectrum are simple calibration techniques that assume a linear relationship between the physical variable of interest and the sensor output. On the high end of the complexity spectrum are sophisticated parameter estimation algorithms that use the full power of modern data analysis techniques, such as neural networks [69, 219], Wiener kernel estimation [220], weighted fault-tolerant least squares analysis, to name a few.

Naturally, interdigital electrodes is only one of many possible shapes of electrode arrangements. Not surprisingly, the results of measurements with interdigital electrodes are often compared with measurements with the same sensitive materials but different shapes, for example, pellet sensors [221], parallel plate sensors, spiral sensor electrodes, etc.

Database	INSPEC	USPTO
"interdigital"	2345	42
"interdigitated"	931	41
"interdigital" AND "sensor"	144	3
"interdigitated" AND "sensor"	81	5
"interdigital" AND "transducer"	928	11
"interdigitated" AND "transducer"	34	5
"interdigital" AND "electrode"	415	8
"interdigitated" AND "electrode"	165	4
"finger" AND "array"	124	18

Table 3.1: Results of literature search using INSPEC database for technical papers and the United States Patent and Trademarks Office (USPTO) database for patent search.

3.2 Interdigital Structures

A lack of coordination of research efforts is quite characteristic of this field. For example, theoretical expressions obtained for capacitance of interdigital piezoelectric sensors are rarely used in dielectrometry; researchers in one country are often unaware of efforts in other countries. Ambiguity of terminology does not help this situation: not everyone associates periodic microstrip electrode structures with interdigital patterns. Moreover, the word itself, "interdigital", does not have direct analogs in other languages. Table 3.1 indicates that the volume of literature on this subject is very large. The literature cited in this manuscript presents the most complete account of relevant literature sources known to the author, as related to interdigital dielectrometry and to the broader subject of interdigital sensors and transducers.

3.2.1 Microdielectrometry

3.2.2 External Capacitive Probes

Charge-Flow Transistor

The technology later named "microdielectrometry" started more than 20 years ago as a modification of the Charge-Flow Transistor (CFT), originally developed for monitoring the sheet resistance of thin-film materials [59]. The CFT was an MOS-compatible

device based on contemporary principles of transistor electronics [118, 121]. In this device, the time delay between the application of the gate voltage and a complete inversion of the channel region is dependent on the sheet resistance of the material under test. Subsequent experiments demonstrated that bulk conduction effects can be separated from surface conduction. The separation of these two phenomena gives additional valuable insights into the properties of materials under test.

Humidity Sensors

The idea of monitoring the surface conductance of thin dielectric films under changing environmental conditions was actively used in the development of several generations of capacitive humidity sensors [60]. The precision of measurement was limited by hysteresis of moisture adsorption. An accuracy of 7% of relative humidity in the range 17% to 65% relative humidity, and better accuracy at higher humidity values, was achieved. A shielding element was inserted between the fingers of a capacitance sensor in order to maximize the sensitivity due to the changes of dielectric properties in the sensitive layer deposited over the interdigital electrodes. The sensor was coated using chemical vapor deposition with a thin film of SiO_2. It is well-known that the sheet resistance of silicon dioxide is a strong function of ambient moisture. An interesting feature of measurements reported in [60] is so-called "moisture hysteresis": the capacitance between the electrodes was dependent not only on the moisture level but also on the direction of moisture change. The capacitance at the same moisture level was lower when the moisture was increasing and higher when the moisture was decreasing. Most probably, the moisture dynamics in the bulk of the sensitive layer is responsible for this phenomenon. The equivalent circuit that was used to model changes in the sheet resistance of the sensitive layer was a classic distributed RC transmission line. Humidity-capacitance hysteresis has also been observed in another study [222], where a one μm thick layer of cross-linked cellulose acetate butyrate (CAB) polymer was used as a sensitive layer whose dielectric permittivity changes with relative humidity.

An important application that developed from the original concept of the charge-

flow transistor [118] was a currently commercialized technique of microdielectrometry [65, 74, 119, 124, 134]. In fact, earlier work in this area served as a foundation of some of the studies presented in this thesis.

An integrated design that combined the sensor, electrical buffer, oscillator, and decoder presented in [77] used different types of moisture-sensitive films, specifically, poly(*p*-aminophenylacetylene) (PAPA) and polyethylene oxide (PEO). Another moisture sensitive material, aluminum oxide, being exploited as the sensitive layer exhibited a quicker response to the changes of the ambient relative humidity [122]. While this work demonstrated significant potential of the general approach, the reproducibility of measurements was quite low. An expression for the admittance of an interdigital capacitor or, in the original citation, "lock and key device," is given in [77]. See subsection 7.6.1 for relevant analysis.

A typical frequency range for microdielectrometry measurements is from 1 Hz to 10 kHz. This range is appropriate for measuring sheet resistance in the range of 10^9 to $10^{16}\Omega$/square. The absorption of water on $MgCr_2O_4$-TiO_2 porous ceramic that results in rapid and reversible changes of electrical conductivity was investigated for high temperature applications (up to 550°C) [123]. The electrical resistance of this multi-functional ceramic sensor decreases with an increase in relative humidity and increases with an increase in reducing gas content in the ambient atmosphere. A simultaneous and independent measurement or both ambient temperature and humidity is recommended.

Further advances in humidity measurement techniques involved the inclusion of moisture diffusion processes into the model of the Kapton sensor response [130]. The moisture diffusion coefficient was extracted from the dew point cycle measurements. The moisture diffusion coefficient in Kapton was evaluated to be on the order of 5.0 $\times 10^{-9}$ cm^2/sec at room temperature. A weak dependence of the diffusion coefficient on moisture concentration was observed as an asymmetry in the sorption and desorption kinetics. Design optimization of the moisture sensitive capacitance sensor is discussed in [133]. The advantages of linearity of sensor response had been investigated in [132].

A remarkable analysis of moisture diffusion processes is described in [138, 141]. In this investigation, the moisture diffusion coefficients are measured in thin polymer films through monitoring changes in permittivity with micro-dielectric sensors. The dielectric properties are measured within the first 10 μm of the film thickness. The total film thickness is about 100 μm. By 1992, the frequency range of operation was extended over the range from 0.001 Hz to 100 kHz. The alternation of wet and dry environments allows measurement of diffusion coefficients for both absorption and desorption. Because of electrode polarization double layer effects, after the initial experimentation, the measurement was limited to the single frequency of 10 kHz. The dynamics analysis relies on the evidence available from the literature that the dielectric constant changes linearly with moisture content in polyimides [130] and epoxies [137]. A one-dimensional diffusion process is modeled with the traditional solution to Fick's law [223].

An application of highly hydrophilic materials other than polyimide films opens doors for various biomedical applications. Usage of a water-swelling polymer as a sensitive layer over interdigitated electrodes that changes both conductivity and thickness with moisture absorption is discussed in [142].

The environmental stability and moisture effects related to various polyimide films, including Kapton®, Upilex®R, and HQDEA/4-BDAF are investigated in depth in [145].

Monitoring of Cure Processes

Dielectric properties change dramatically during the curing process of thermosetting resin matrix composite materials when the resin transforms from a monomeric liquid into a cross-linked insoluble solid material [224].

Advantages of using lower frequency excitation for dielectrometry measurements were explored in [119]. The core application of the microdielectrometer "chip" was to monitor the dielectric properties of thermosetting resin both during and after the curing process. The microdielectrometer was using the same principles as the more conventional parallel-plate measurement approach. The advantages were smaller sensor size and on-chip amplification that eliminated the need for electrical shielding.

It is pointed out in [74] that a parallel-plate capacitor is susceptible to expansion and contraction of the material under test. The microdielectrometer "chip" is more reliable in this sense, as long as it stays in intimate contact with the material under test.

Using results of the two-dimensional numerical solution to Laplace's equation [3], one can calculate the sensor's response in the entire range of possible values of the real and imaginary parts of complex dielectric permittivity. The sensor's response is measured in terms of the gain and phase of the logarithm of the ratio between the floating (sensing) and driving voltages (see section 4.6.1 for more details). The dielectric properties are found by plotting the Gain/Phase measurement point on the chart and interpolating between the nearest values of the real and imaginary parts of complex dielectric permittivity. Analysis of the experimental data has indicated an excellent fit with the Debye model for dipole orientation by using Cole-Cole plots with frequency as the plotting parameter [174]. An inherently low precision of measurement of the dielectric permittivity (ε') for high-loss materials and the dielectric loss factor (ε'') for low-loss materials is shown in terms of spacing between the lines of constant dielectric permittivity.

A more advanced measurement approach involves simultaneous measurement of temperature as well as the complex dielectric permittivity [124]. On-chip amplifiers and off-chip electronic circuitry of the microdielectrometer sensor permitted measurement of interelectrode capacitance down to 0.1 pF with acceptable accuracy. The authors point out that the separation of ε' and ε'' is always possible because the sensor dimensions are stable with respect to temperature and pressure variations. Interpretation of the dielectric analysis data is proposed based on the Debye model for dipole relaxation [154].

Another combination of sensing techniques, microdielectrometry and differential scanning calorimetry has been used to study cure processes in epoxy resins [127]. In this paper, the frequency sweep approach had been replaced by a so-called "Fourier Transform Digital Correlator," which allows interpretations of measurements in the

frequency range from 0.005 Hz to 10 kHz. A domination of ionic conductivity in the early stage of the cure process had been observed (also see [126]). The ionic conduction can be correlated with viscosity during the early stages of resin cure. Later stages of cure can be analyzed using the loss factor as a sensitive measure of the cross-linking [135].

With the introduction of lower frequency measurements, the double layer effects became particularly important. The role of the double layer in both parallel plate measurements and microdielectrometry measurements was studied in [128]. Aluminum and gold electrodes in contact with commercial resins exhibited a drastic increase of apparent dielectric permittivity at low frequencies. A polarization model was developed to explain this phenomenon. An analytical treatment of the double-layer impedance based on the continuum-model simulations of [8] is presented in [143].

Mapping techniques have often been used in microdielectrometry. An expression that relates viscosity and ionic conductivity has been proposed in [72]. Experiments demonstrated a high correlation between theory and measurements.

An industry oriented overview of microdielectrometry given in [66] compares dielectrometry measurements with several other, more traditional, manufacturing process monitoring techniques, including differential scanning calorimetry (DSC), rheological dynamic spectroscopy, and mechanical viscosity measurement. It also presents the critical point control (CPC) software designed for characterization of curing processes based on process phenomenology and correlation with other process monitoring techniques. Additional insights into correlation of data from various property estimation methodologies are presented in [144].

3.2.3 Dielectrometry Sensors

This subsection contains a review of research work on interdigital dielectrometry sensors by different groups not directly associated with the microdielectrometry developers, whose results were covered in subsection 3.2.1. Humidity detection in solar panel encapsulations with interdigital electrodes screen-printed over glass and Tedlar® films

was accomplished by electrochemical impedance spectroscopy [225].

3.2.4 Chemical Sensors

Chemical sensors constitute a large portion of all interdigital sensors described in the literature. A typical chemical interdigital sensor design includes a thin layer of material above the interdigital electrodes that is sensitive to the concentration of chemicals present in the ambient. The main effort in the development of such sensors is in the chemistry and materials science aspects, rather than electromagnetics and parameter estimation. A wide variety of sensitive materials is available and being developed for detection of various gases, chemicals, moisture, organic impurities, etc. The analysis of the chemical sensors output rarely involves full-scale modeling of the electric field distribution. Instead, impedance spectroscopy, analysis of double layer and doping related phenomena, and direct calibration are used. An in-depth analysis of all issues related to chemical sensors is beyond the scope of this manuscript, however, the literature review contains pointers to the most conspicuous features of different categories of sensor design, manufacturing, and signal processing practices described elsewhere.

Undoped, Pd-doped, and Pt-doped SnO_2-based thin-film chemical sensors have been used to monitor changes in the concentration of NO_2, CO, CH_4, and H_2 [226]. The impedance spectroscopy analysis of the sensors output separates contact, surface, bulk, and grain boundary contributions to the sensor admittance at different frequencies of electrical excitation.

Doped and undoped substrates of Bi_2O_3 (a p-type semiconductor material) had been used to detect concentrations of NO from 10 to 1000 ppm in exhaust gases [227]. The sensitivity of substrates to various challenge gases in this case was monitored using simple two-terminal resistive measurements.

The impedance spectroscopy has also been used successfully to detect parts-per-billion (ppb) concentrations of NO_2 and diisopropyl methylphosphonate (DIMP) [67].

Detection of CO_2 has been given considerable attention due to recent concerns about the emission of CO_2 as a global warming factor [228]. A variety of commercial and

laboratory sensors have been developed to detect CO_2 and differentiate between the signal changes due to CO_2 and due to other gases, humidity, and temperature [221,228].

The influence of humidity can be accounted for by compensating the signal shift using an empirical mathematical model, as long as humidity is measured independently by an auxiliary sensor [229]. The detection of sulfur dioxide (SO_2) with a classic interdigital sensor is reported in [230,231]. The 0.6 μm thick layer of heteropolysiloxane (HPS) exhibited a high sensitivity to SO_2 combined with a low cross-sensitivity to other gases. Visualization of the sensor response with impedance spectroscopy Cole-Cole plots help to distinguish between surface and bulk property changes. The electrode processes were described with Warburg impedance and double layer capacitance phenomena.

Measurement of mass and dielectric changes of cellulose products, namely ethylcellulose, cellulose-acetate, and cellulose-propionate, as they absorb various organic compounds in the gas phase (ketones, alkanes, alcohols, aromatic and chlorinated hydrocarbons) was reported in [218].

3.2.5 Biological Applications

Biosensors are self-contained, portable electronic devices which utilize biological events at the molecular level to detect and quantify chemical and biological substances [232]. With recent advances in biotechnology, it is natural to expect an increasing number of applications of interdigital dielectrometry sensors for monitoring of physiological processes, for example, through the characterization of electrochemical parameters of body fluids. An interdigital sensor for characterization of the ionic content of body fluids has been planted *in vivo* to monitor the conductivity of the tracheal fluid of mongrel dogs [233].

Many biological and chemical sensors use selective membranes above sensitive layers that respond to the changes in concentration of the chemical substance being detected. A penicillin sensor coated with a polypyrolle-deposited array device with a cross-linked penicillinase membrane was used as a pH-sensitive device, since the electrical conductivity of polypyrolle changes with the pH of the solution [234].

Differential sensor design (when the active sensor signal is subtracted from the reference sensor signal) results in particularly high sensitivity. An acetylcholine receptor-based biosensor was reported to detect nanogram quantities of cholinergic ligands per ml [232].

A miniature conductance biosensor that responds to changes in the electrode double layer capacitance [235] was formed with electrodes that were both serpentine and interdigital. Moreover, three sets of electrodes with different sensitive layers were used to determine concentration of three distinct reaction products.

3.2.6 Piezoelectric SAW Devices

Background

One of the most active areas of interdigital electrode research applications is the acoustic measurement of material properties with surface acoustic wave (SAW) devices. The interdigital transducer (IDT) is the most important component of SAW devices [236]. Electroacoustic waves are generated with SAW transducers by the contractions and expansions of the piezoelectric substrate material by using interdigital electrodes deposited on the substrate surface. The frequency range of operation of such transducers is between 50 MHz and several GHz [237]. The velocity of these waves depend on the dielectric and mass dependent properties of the material under test. The phase shift of the transducer signal is proportional to the wave speed, v, and frequency of excitation ω, and inversely proportional to the length of the transducer [238]. Normally, the electroacoustic wave propagation characteristics are only weakly influenced by the dielectric properties of the sensitive layer or material under test [238].

Two categories of sensors may be identified, depending on whether the interaction between the sensor and the environment takes place on the surface (SAW devices) or in the bulk (BAW devices). In the case of homogeneous resonators, the entire substrate is affected. This type of sensor is used for temperature and stress measurement. Composite resonators include additional materials, usually a thin sensitive coating to perform a

variety of tasks, such as measurement of mass density, film thickness, molecular weight of polymers, viscosity of liquids, etc [237].

Comparison of sensitivities of an interdigital sensor and a SAW transducer demonstrated higher sensitivity of the latter to the changes in the mass absorption properties than the former of the changes in the dielectric permittivity of the sensitive layer [238]. The two sensors demonstrated a different relative sensitivity to SO_2 and to H_2O. This characteristic of sensors exposed to identical environments makes them a good candidate for sensor array applications.

Combination of SAW and Interdigital Capacitors

Several books contain chapters dedicated to surface acoustic wave devices that use interdigital structures [236, 239–242]. Both interdigital dielectrometry sensors and surface acoustic wave devices have essentially identical electrode topology, but they use different physical phenomena to detect changes in the material under test. Each technology has inherent advantages and drawbacks. Depending on the details of the specific application, fringing electric field sensing compares favorably [67] or unfavorably [238] to bulk-wave piezoelectric quartz crystal microbalances and surface acoustic wave devices. The natural step in the sensor development is to combine positive aspects of each sensing technology in a single design. One such design, shown in Figure 3.1 used SO_2-sensitive material (heteropolysilaxane, NND/PTMS) to reduce the overall cross-sensitivity of the sensor to humidity interference [238].

Potential Pitfalls

The currents in microdielectrometry measurements can be as low as tens of fA. At such low levels, the reduction of electrical noise through electromagnetic shielding and digital filtering of the sensor output signal becomes particularly important [136]. A strong dependence of dielectric properties of polyimides on ambient moisture concentration introduces difficulties to some applications of microdielectrometry. The control of ambient moisture may be necessary for achieving reproducible results with sensors

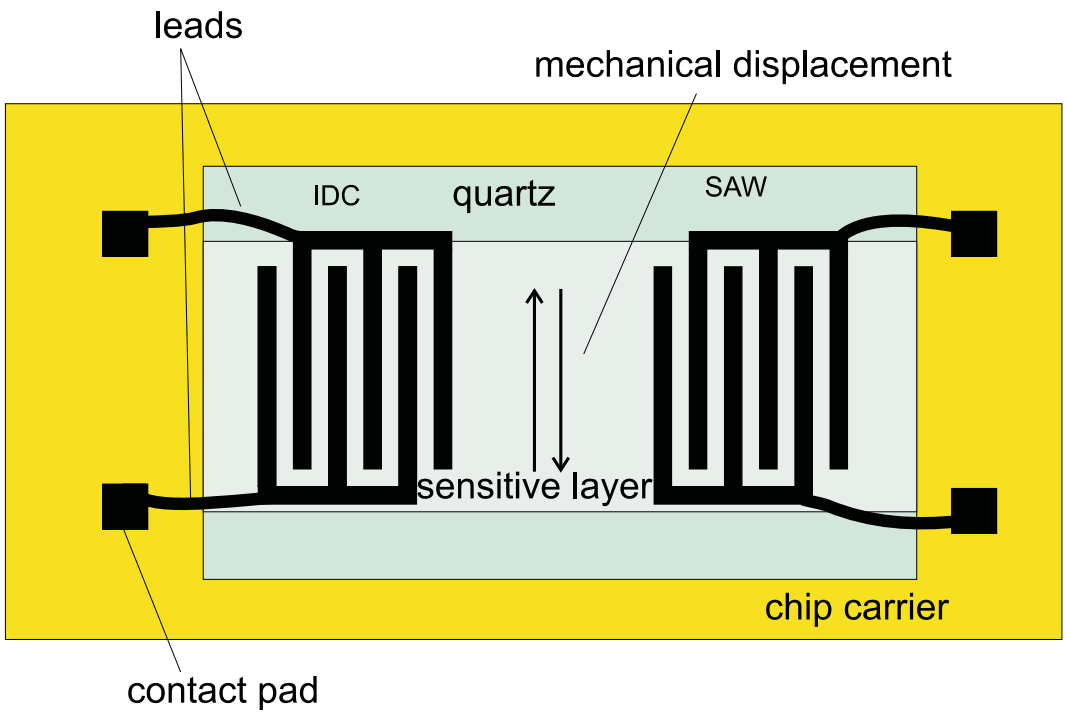

Figure 3.1: A combined sensor that comprises a SAW transducer and an interdigital capacitor (IDC) on a single chip (Adapted from [238]).

that use a Kapton substrate [136]. An extensive review of the dependence of Kapton properties on moisture and ionic contaminants is provided in [139].

A wide class of phenomena are referred to as "history" or "memory" effects in the polymer literature. Sometimes, history effects arise because charge accumulation in the previous experiment can influence the current distribution in subsequent experiments [136].

3.2.7 Interdigital Electrode Structures in Microelectromechanical Systems (MEMS)

Microelectromechanical systems (MEMS) have recently gained considerable interest due to numerous potential benefits in sensing, mechanical, biomedical, automotive, military, and aerospace applications. Typical micromachined motors and actuators today occupy area less than 1 mm^2 and weight a few milligrams. Conceptual overviews

of MEMS technology are given in [243–246]. The major advantage of using electrostatic forces as opposed to magnetic forces is that a very high energy density can be achieved when the distance between the adjacent electrodes becomes small [247].

Interdigital comb drives are commonly used in linear microactuators to produce linear movement of machine parts using fringing electric fields at the tips of the comb fingers. In a typical layout of a linear comb drive of a lateral resonator the interdigital capacitors perform a dual function: supply force for linear movement of the load and sense the current position of the load with respect to stationary parts. Several properties of interdigital electrodes makes them attractive for use with microelectromechanical resonators. The interelectrode capacitance changes linearly with displacement. Consequently, the electrostatic drive force is independent of the vibration amplitude, which can be significantly higher than those observed in the structures which move normal to the surface of the substrate [248].

The presence of a ground plane underneath the interdigital electrodes causes an asymmetry in the electrical field distribution, which eventually leads to levitation induced by an electrostatic attraction force [248, 249]. The ground plane is necessary to shield the interdigital electrodes from external electrical fields [250].

Potential applications of linear electrostatic motors formed with interdigital capacitors include friction test structures [251], microgrippers [252], force-balanced accelerometers [253], and positioning of components with submicron precision [254]. A large number of applications has been explored with MicroSurface Acoustical Wave (MSAW) devices and similar interdigital sensors, including sensing and control of drag and skin friction in aerospace and underwater structures [255], aircraft flex beam deflection and acceleration, ice formation monitoring on aircraft wings [256], noise suppression in buildings [64], and early warning from collapsing bridges [64, 257].

Force Calculation

The longitudinal electrostatic force in a comb drive is generated due to fringing fields at the ends of interdigital electrodes. Thus, this force is independent of the finger length

and is proportional to electrode height. Ignoring fringing field effects, the capacitance of the interdigital finger with overlap length x is

$$C = \varepsilon_0 \frac{2nxb}{w} \tag{3.1}$$

where b is electrode height, w is the gap between electrodes, and n is the number of electrode fingers. Then the force developed by the finger interaction with application of voltage V is equal to [258]:

$$F = \frac{1}{2} V^2 \frac{dC}{dx} = \frac{V^2 \varepsilon_0 bn}{w} \tag{3.2}$$

This force becomes significant at micron and submicron scales.

3.3 Sensor Arrays

One may choose to differentiate sensor arrays and array sensors, as follows: a combination of sensors with different operating principles in a single system is called a *sensor array*, whereas the combination of the sensing elements of the same type in the single device is called an *array sensor*. The above terminology is not universally accepted, but it is used here to clarify the distinct features of each design.

It is relatively safe to say that sensor arrays represent one of the most likely directions of research in the field. Information from different types of sensors integrated into a single monitoring system can be used to monitor, control, and predict performance of all kinds of experimental setups, apparatuses, and systems. One of the very promising applications of multi-sensor single chip technology is multi-component gas chemical analysis [259].

Processing and interpretation of data from multiple sensor arrays is a wide area that involves a full arsenal of digital and analog signal processing, neural networks, wavelets, statistical analysis, etc. The full coverage of this topic is beyond the scope offered here, however, some general features related to most sensor array applications are described in this section.

A sensor array device (SAD) that includes six polymer-coated interdigital sensors on a silicone nitride membrane combined with built-in thin film thermometer/heaters has been manufactured to measure concentration of toluene, n-propanol, and n-octane [259].

The technology of multiple interdigital electrode array measurement is still in its inception stage. While the advantages of such arrays are widely recognized, they're not yet being used to their full potential. Relatively complex multi-layer structures can be formed using modern technology. Small modifications of a basic design permit a variety of sensing principles to be combined within a single array. An interdigital sensor array that uses conductivity, piezoelectricity, and voltage/current electrochemical sensing principles was reported in [260]. In addition to these principles, thin-film sensitive coatings of ZnO_x and lipid bilayers were used.

3.3.1 Capacitive Sensor Arrays

Naturally, the shape of coplanar microstrips does not have to be limited to pairs of interdigital combs. In fact, any pair of coplanar electrodes can be used to generate fringing electric fields. Provided that the measurement sensitivity is adequate, the information about material properties can be extracted from such measurements. A simple example, extracted from [111], is shown in Figure 3.2. The excitation of one of the electrodes of the capacitive array produces fringing field patterns which contribute to capacitance matrix entries associated with the given array. The total number M of independent two-electrode measurements is:

$$M = \frac{N(N-1)}{2}, \tag{3.3}$$

where N is the number of electrodes in the array. For example, the 3-sensor system allows 3 independent measurement, and the 8-sensor system allows 28 independent measurements.

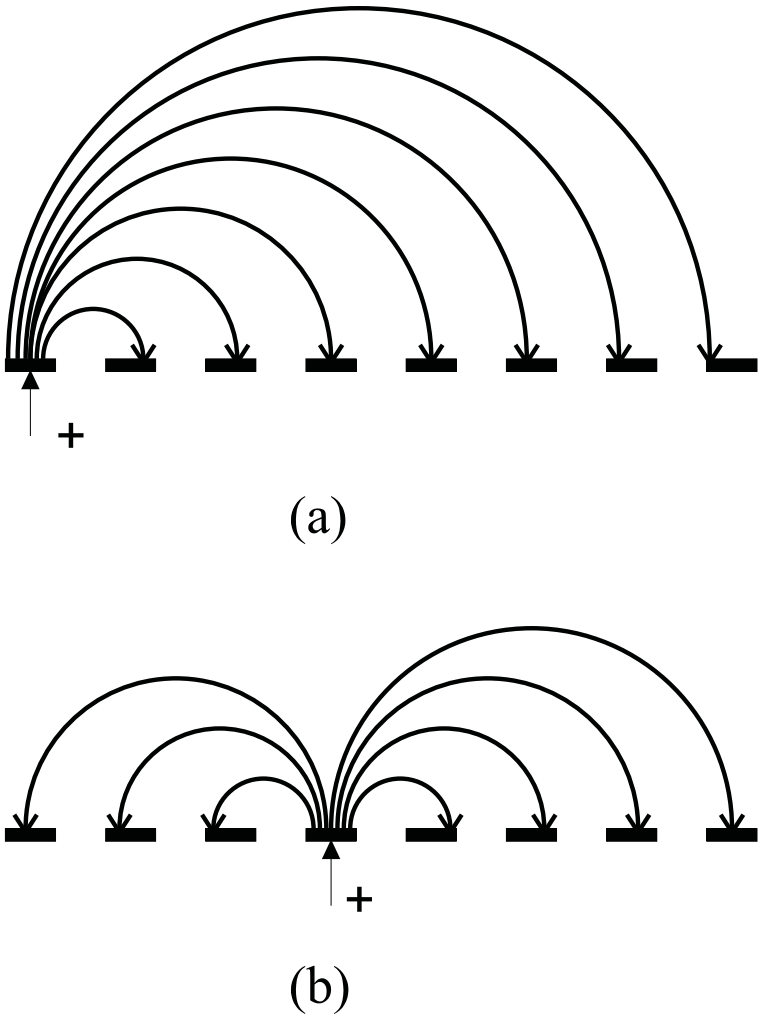

Figure 3.2: Schematic excitation patterns for a linear sensor array: (a) the leftmost electrode is excited, the rest are grounded (b) the fourth from the left electrode is excited, the rest are grounded. (Adapted from [111]).

3.3.2 Combination of Different Sensor Types

Monitoring of temperature of the material under test provides crucial information for a correct interpretation of the dielectrometry sensor response. For that reason, a temperature sensitive resistor is often placed on the same chip with the dielectrometry interdigital sensor [123, 233].

Combination of interdigital sensors with auxiliary instrumentation provides numerous advantages. For example, wireless communication with an interdigital trans-

ducer can be implemented by connecting the transducer with a small microwave antenna [261, 262]. This duo is particularly advantageous when the sensor is placed on the moving part (such an aircraft rotor), and wired communication with the rest of hardware is technically cumbersome.

Chapter 4

Sensor Design and Parameter Estimation Algorithms

4.1 Introduction

It is not possible, at the current state of technology, to develop a universal sensor and a universal parameter estimation algorithm that will provide adequate and best possible information about material properties for all applications. Therefore, each application requires a judicious choice of sensor design and associated parameter estimation algorithms. As a technical system develops, the requirements for each element become more clear and affect the requirements for other elements of the trinity shown in Figure 4.1. For example, it may become clear during the development stage that the one-sided access to the material under test is an artificial requirement that would be easily bypassed by simple design modifications. In that case, it is not wise to limit the design to interdigital structures only. The dual-sided access has advantages of larger, easily measurable capacitances and a more uniform field distribution. The examples of appropriate matching of sensors and parameter estimation algorithms to each application are encountered throughout this thesis.

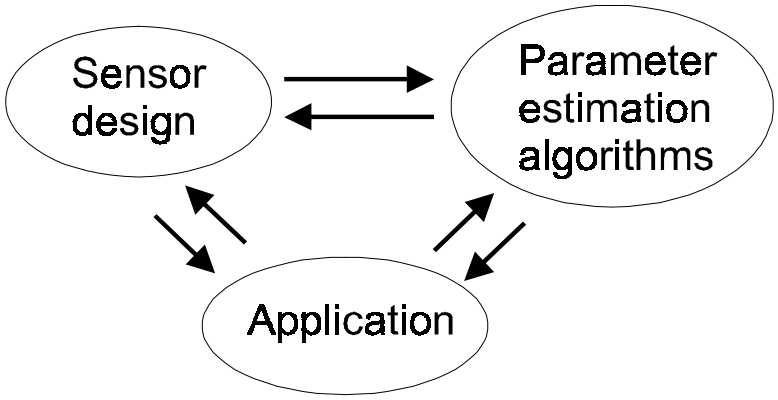

Figure 4.1: Every sensing application requires an optimum combination of inherently dependent elements of the measurement system comprising sensor design and parameter estimation algorithms.

4.2 Choice of Substrate

4.2.1 Flexible versus Rigid

The choice of substrate thickness and degree of flexibility depends on the application. Flexible substrates with thin electrodes are advantageous when the sensor head is expected to conform to the surface of the material under test. Representative applications of such a design include measurements performed at an airfoil surface, turbine blades, aircraft rotor blades [256], and curved transformer pressboard insulation [26].

On the other hand, rigid substrates or rigid electrode designs are advantageous in non-contact measurements. In this case, it is important to maintain a well-defined geometry of the electrode structure in order to be able to take advantage of model-based parameter estimation algorithms.

4.2.2 Glass Substrate

Borosilicate glass substrate [143] and silica glass substrate [238] are common materials in thin-film technology. Recent developments in interdigital dielectrometry indicate a strong correlation between surface condition properties and sensor response. For

measurements with highly insulating materials, the surface conductivity control is extremely important. Contaminated surface conditions can be detected by measurements in dry air or vacuum, prior to application of the sensor to the surface of the material under test. Organic contaminants can be removed from the glass surface using acid based cleaners, such as "piranha" (3:1, H_2SO_4:H_2O_2) [143].

The glass substrate can be made hydrophobic by immersing into octadecyltriethoxysilane/benzene solution [234]. Usually the glass substrates are brittle, which makes them unsuitable for those applications where conformity to the sample surface is essential. However, these substrates perform very well in fluid environments.

4.2.3 Kapton®

Polyimide is a frequent choice of the sensor substrate, especially for flexible sensor heads. Polyimides are omnipresent in the modern printed circuit board industry, the manufacturing techniques for them are well-developed, and their properties have been investigated under many different conditions and reported in a large number of publications. Examples of designs and use of sensors manufactured with polyimide substrates are reported in [8, 9, 70, 83, 146, 233].

Polyimide sensors can operate in temperatures up to 350°C, which makes them an attractive choice for a transformer environment where operating temperatures reach 100°C [263]. Polyimide is a highly hydrophobic material, being able to absorb moisture up to 3% of its dry weight [9, 264]. Because of the high dielectric permittivity of water ($\varepsilon_r \approx 80$) in comparison with the dielectric permittivity of dry polyimide ($\varepsilon_r \approx 3$), even such relatively small amounts of water increase the dielectric permittivity of polyimide by as much as 30% [130, 265]. Table 4.1 shows the variation of the electrical properties of Kapton with relative humidity at room temperature, assuming that the material has been allowed enough time to achieve moisture concentration equilibrium with the ambient. For calculations involving absolute water content at room temperature, 50% RH in this study is equal to 1.8% water in the film and 100% RH is equal to 2.8% water, the maximum adsorption possible regardless of the driving force.

Relative humidity,%	**Dielectric Strength, AC, (kV/mm)**	**Dielectric constant, ε_r**	**Dissipation factor, tan δ**
0	339	3.0	0.0015
30	315	3.3	0.0017
50	303	3.5	0.0020
80	280	3.7	0.0027
100	268	3.8	0.0035

Table 4.1: Relative humidity vs. electrical properties of Kapton at room temperature. Type HN film, 25 μm (1 mil) [265].

While the hydrophilic nature of polyimide creates problems due to moisture interference with many sensor applications, it can be used for the detection of moisture itself. A number of studies reported successful results with capacitive humidity sensors that use polyimide as a sensitive substrate [55, 266–268].

4.2.4 Teflon®

Polyflon manufactures copper-clad PTFE substrates, including CuFlon®, using a proprietary electroplating process to produce a dielectric substrate with exceptional insulation and hydrophobic characteristics. Representative properties are listed in Table 4.2. This process ensures a strong molecular bond between the PTFE dielectric and conductive metal layer. Electroplated PTFE withstands continuous temperatures of 175°C and 225°C short term without damage to the plated material, dielectric, or the bond between them. Electroplated PTFE also performs well at low temperatures, even under cryogenic conditions [269].

Standard thicknesses of boards available from Polyflon in mils are 0.25 thru 5 for standard sheet size of 9 inches by 9 inches and 10 mils to 125 mils for standard sheet sizes of 12 inches by 18 inches. CuFlon is the dominant substrate material for the dielectrometry sensors used in the research of this thesis.

Property	Units	Typical Value	Test Method
Relative Dielectric Constant, 18GHz	-	2.10	ASTM D 3380
Dissipation Factor, 18GHz	-	.00045	ASTM D 3380
Dielectric Strength, 5 mils	V/mil	2000	ASTM D 149
Volume Resistivity	ohm-cm	$1{\cdot}10^{16}$	ASTM D 257
Tensile Strength	psi	3500	ASTM D638
Peel Strength	lb/in	8	MIL-S-13949
Water Absorption, 24hrs @23 °C	%	$< .01\%$	ASTD D 570
Coefficient of Thermal Expansion	ppm/C	129	ASTM E 831

Table 4.2: CuFlon microwave substrate data sheet [269].

4.2.5 Kapton Sealed with Teflon

DuPont has recently introduced a new type of insulating substrate for flexible circuits, Kapton Type FN . In this product, a thin layer Kapton film is sandwiched between Teflon FEP fluorocarbon resin coatings. The Kapton core provides mechanical strength and improves thermal stability, whereas the Teflon layers prevent moisture absorption by the film. Potentially, this material could be used in dielectric sensing applications without fear of measurement results being contaminated by moisture absorption. At this point, however, adhesion of copper to the Teflon coatings has not been developed.

4.2.6 G10 Board

A regular fiberglass circuit board used for most electronics applications is suitable for dielectrometry sensor heads when a rigid design is advantageous and the low frequency losses are not of concern. Since masking and patterning of regular circuit boards is most economical in an industrial environment, it can be used for rapid prototype development. The G10 circuit board has proven to be too conductive for our dielectrometry measurements.

4.2.7 Silicon

Common materials in the semiconductor industry, oxidized silicon and silicone nitride are very likely candidates for small size sensors or sensor arrays built on the same chip.

The details of manufacturing of interdigital sensors with the silicon dioxide substrate are available in [233]. The resistivity of the high quality silicon dioxide is greater than 10^{14} Ohm·cm.

4.2.8 Other Substrates

Many other substrate materials are becoming available as the semiconductor industry, polymer industry, and basic chemical engineering and science research adopt new technologies. A separate manuscript could be written to cover every major possible substrate material, and it would become outdated within a couple of years. We would like to mention one particularly promising material: aluminum oxide. Thick film printing on Al_2O_3 with a gold electrodes is an inexpensive conventional process well-suited for manufacturing of chemical gas sensors [228].

4.3 Choice of Coating

4.3.1 General Requirements

The sensor coating or the substrate itself can be used as a selective sensitive layer that responds to the changes in the concentration of certain specific types of molecules and ions present in the ambient fluid through adsorption and absorption processes, possibly combined with diffusion and mass transfer.

The reversibility of sensor response is of major concern when the sensitive layer or substrate are being used. Irreversible changes, sometimes referred to as film poisoning [68] reduce sensor lifetime and reliability. In some cases, recycling of previously used sensors is possible by vacuum, temperature, or chemical [232] treatment.

4.3.2 Parylene Coating

Parylene is a generic name for members of a unique polymer series. The basic member of the series, called parylene N, is poly-p-xylylene, a completely linear, highly crystalline

	Parylene N	**Parylene C**	**ParyleneD**
Dielectric strength, short time, volts/mil at 1 mil	7,000	5,600	5,500
Volume resistivity, 23°C, 50% RH, ohm·cm	1×10^{17}	6×10^{16}	2×10^{16}
Surface Resistivity,			
23°C, 50% RH, ohms	1×10^{13}	1×10^{14}	5×10^{16}
Dielectric constant			
60 Hz	2.65	3.15	2.84
1 kHz	2.65	3.10	2.82
1 MHz	2.65	2.95	2.80
Dissipation factor			
60 Hz	0.0002	0.020	0.004
1 kHz	0.0002	0.019	0.003
1 MHz	0.0006	0.013	0.002

Table 4.3: Typical electrical properties of parylene [270].

material. Parylene C, the second member of the series, is produced by the same monomer modified only by the substitution of a chlorine atom for one of the aromatic hydrogens. The third member of the series is parylene D and contains two, or dual, chlorine atoms on the benzene ring [270].

Parylene N is a primary dielectric, exhibiting a very low dissipation factor, high dielectric strength and a dielectric constant invariant with frequency. Parylene C has a useful combination of electrical and physical properties plus a very low permeability to moisture and other corrosive substances. Along with its ability to provide a true pinhole-free conformal insulation, parylene C is the material of choice for the coating of critical electronic assemblies. Parylene D forms the hardest surface, and it has the least elongation ability and the greatest temperature stability. Its molecular structure also gives it the best chemical resistance. Due to the uniqueness of the vapor phase deposition, the parylene polymers can be formed as structurally continuous films from as thin as a fraction of a micron to as thick as many mils.

Most conformal coatings are sprayed or dipped and have a tendency to pull away from edges, bridge components or wick into unwanted locales. Parylene goes on void free and pinhole-free. It will not edge, bridge or gap and because it is not line-of-sight, everything within the chamber gets coated uniformly.

The Parylene process involves several aspects. After proper cleaning, activation and masking, the product to be coated is placed in the deposition chamber. The product will remain at room temperature during the coating process. Dimer is placed on the glass tube at the opposite end from the deposition chamber in an aluminum foil cup called a "boat". The coating thickness is controlled by the amount of raw Dimer placed in the boat and usually weighed out in grams.

An end cap is then placed over the tube and the process started. The vaporizer radiant heater cycles on and off with a pressure safety interlock to ensure safe operating limits; the Dimer changes from a solid to a vapor and the molecules move down the tube by virtue of the reduced pressure at the opposite end. The Dimer now moves into the pyrolysis zone which is at 680°C and the high temperature cleaves the Dimer into two divalent radical monomers. The monomer molecules enter the deposition chamber and re-form as a long chain polymer on all surfaces within the chamber. Studies show that each molecule makes an average of l0,000 collisions and because of the short mean free path of the vapor molecule (less than l mm) the coating forms slowly and uniformly over surfaces with both sharp edges and deep crevices with no pin holes. The chamber walls are coated with a release agent to prevent the film from forming a tight bond and after 3 or 4 runs the film is peeled off and discarded.

A cold trap is used between the deposition chamber and the vacuum pump. The cold trap use is twofold.

1. It prevents Parylene molecules that have not deposited in the chamber from getting into the vacuum pump.

2. It prevents the oil molecules from "backstreaming" into the deposition chamber. The cold trap should be cleaned weekly to dispose of Parylene and oil film.

4.3.3 Hydrogels

Highly hydrophilic polymer gels (hydrogels) have been used as the sensitive layer for a conductimetric interdigital micro-sensor [142]. In this case, the hydrogel itself has to be characterized for its water content, which may vary from 30 percent to 99 percent by

mass. Hydrogels undergo reversible swelling with moisture uptake, so that conductivity and linear dimensions of the layer change during the experiment. Due to an increasing use of such materials for medical and biological applications, *in vivo* applications of auxiliary interdigital sensors for biological and chemical parameter monitoring is of great potential interest.

4.3.4 Other Materials

Numerous advanced sensing applications are based on the use of so-called "smart materials," applied to the sensor surface as an active coating. This coating changes its material properties, geometry, mechanical or electromagnetic characteristics in response to changes in the environment [255].

Semiconductive thin films based on ZnO_x were used to detect the presence of oxygen in a gas mixture [271]. A sensitive layer of an electron-beam evaporated copper phthalocyanine (CuPc) thin film has been used to detect part-per-billion concentration levels of nitrogen dioxide (NO_2) and diisopropyl methylphosphonate (DIMP) [67]. Another hygroscopic polymer, cross-linked cellulose acetate butyrate (CAB), has been used for humidity sensing [222]. A combination of CuO, $BaTiO_3$, La_2O_3 and $CaCO_3$ has been used to detect CO_2 concentration changes [228]. A frequently used SO_2-sensitive material heteropolysiloxane (NND/PTMS) has been used with a great success in combined dielectrometry and piezoacoustic measurements [238] as well as in impedance spectroscopy measurements [231].

Porous cellulose products, such as ethylcellulose, cellulose-acetate, and cellulose-propionate are good sensitive layer candidates for detection of organic compounds (ketones, alkanes, alcohols, aromatic and chlorinated hydrocarbons) in the gas phase. Absorption of organic molecules changes density and bulk dielectric permittivity that can be detected with microbalance oscillators and interdigital capacitors [218]. Particularly successful experimental results were obtained with ethylcellulose interacting with chloroform, tetrachloromethane, trichloroethylene, tetrachloroethylene, tetrachloroethane, octane, benzene, toluene, and nitrobenzene. Other sensitive low conduction polymers

include polyethylcellulose, polycyanomethylsiloxilane, and polyurethane [272].

Increasing success of biotechnology applications is exhibited in a variety of still exotic sensor applications. Lipid bilayers, which constitute the basic structure of all biological membranes, have been used to monitor pH changes in surrounding fluids [260]. A thin layer of polypyrrole coating was found to change its conductivity with the concentration of penicillin that affected the pH response of penicillinase membrane [234].

4.4 Electrodes

The choice of manufacturing technique for electrode fabrication depends on the required feature size of the electrode mask, substrate material properties, expected environmental working conditions, such as temperature, acidity, and pressure, economical factors, and limitations of parameter estimation algorithms. The latter may put restrictions on certain electrode features. For example, the earlier continuum model by Zaretsky [8] required the electrodes to be nearly infinitely thin. In general, the entire manufacturing arsenal of the electronics industry is available to the designer at a fairly low cost. Extensive sources dedicated to the description of various manufacturing technologies are available (e.g. [273]). The following selective overview is not intended to cover every manufacturing technique available. Instead, it emphasizes characteristic features of a few commonly used manufacturing technologies that lead to successful designs of interdigital sensors.

Screen-printing of electrodes with silver and silver-palladium inks on thick films makes possible deposition of interdigital structures on the material under test. The advantage of this approach is an intimate contact between the electrodes and the substrate, which in this case also serves as a sensitive layer [225]. An electron beam thermal evaporation process followed by a conventional mask etching allows control of both the deposition rate and the thickness of the films [67, 143]. Gold and platinum electrodes normally used in the electronics industry offer the advantage of being inert

and flexible [274]. Silver and NiCr electrodes may also be used [260].

4.4.1 Electroplating

Electroplating has been used by Polyflon to deposit a uniform layer of copper on the surface of the CuFlon substrate. This particular technique is highly proprietary, it involves pre-process surface treatment, and provides uniformity of the copper layer adequate for most applications explored in our laboratory. Additional electroplating with nickel and gold has been used in several cases to prevent corrosion of the electrode surface. The additional thickness due to the gold layer did not exceed one μm. Since most technical applications did not involve highly corrosive environments, the gold plating has not been used at later steps of this thesis research.

4.4.2 Micron and Submicron Technology

Electrode patterns can be formed from coatings produced with various sputtered and vaporized metal coatings. The materials currently used include Al, NiCr, Au [230, 238], Pt [234], etc. Photolithography followed by electroplating are the most common manufacturing techniques for this scale. The spin-coating technique is preferred for formation of very thin layers of material [217].

Nanotechnology advances permit fabrication of conductor strips as narrow as a few nanometers, with interdigital capacitors being no exception. An electrode width as small as 24 nm has been reported a decade ago [214].

4.5 The Gallery of Sensors

4.5.1 Single-Wavelength Sensor with Kapton Substrate

Figure 4.2 shows one of the first interdigital sensors developed in the Laboratory for Electromagnetic and Electronic Systems [9]. The sensor contains 50 spatial 1 mm wavelengths. The thickness of the Kapton substrate is 1 mil (25.4 μm). In order to prevent moisture absorption by the substrate, a 5 μm thick layer of Parylene encapsulates the entire surface area.

A relatively large sensing area of 2 in. $\times$ 2 in. (approximately 5 cm $\times$ 5 cm) resulted in a sufficiently high capacitance value (C_{12} = 10.4 pF in air) so that the additional capacitance between the leads could be safely ignored in most cases. It should be remembered that the capacitance between the leads may be a major contributor to the discrepancies between the theoretical and measured values.

The functions of electrodes can be described through listing of the functions of sensor leads, from top to bottom, as shown in Figure 4.2: driven, ground, shield, sensing, sensing, shield, ground, driven. The details of the manufacturing process, cleaning procedures, and electrical excitation are similar to those described in the following subsection for the three-wavelength sensor [9]. After several diagnostic experiments, the single-wavelength sensor was replaced by the three-wavelength sensor described in the following subsection.

4.5.2 Three-Wavelength Sensor with Kapton Substrate

The earlier design of the three-wavelength sensor has been thoroughly described in [9, 10, 13, 75, 83]. The planar view of this design is shown in Figure 4.3. This sensor consists of three sets of copper electrodes on a flexible polyimide substrate (Kapton) with wavelengths of 1.0 mm, 2.5 mm, and 5.0 mm. The sensing electrodes are shielded in the plane of the sensor by guard electrodes driven by a buffer stage in the interface circuit, and the guard electrodes are shielded by ground electrodes. As discussed

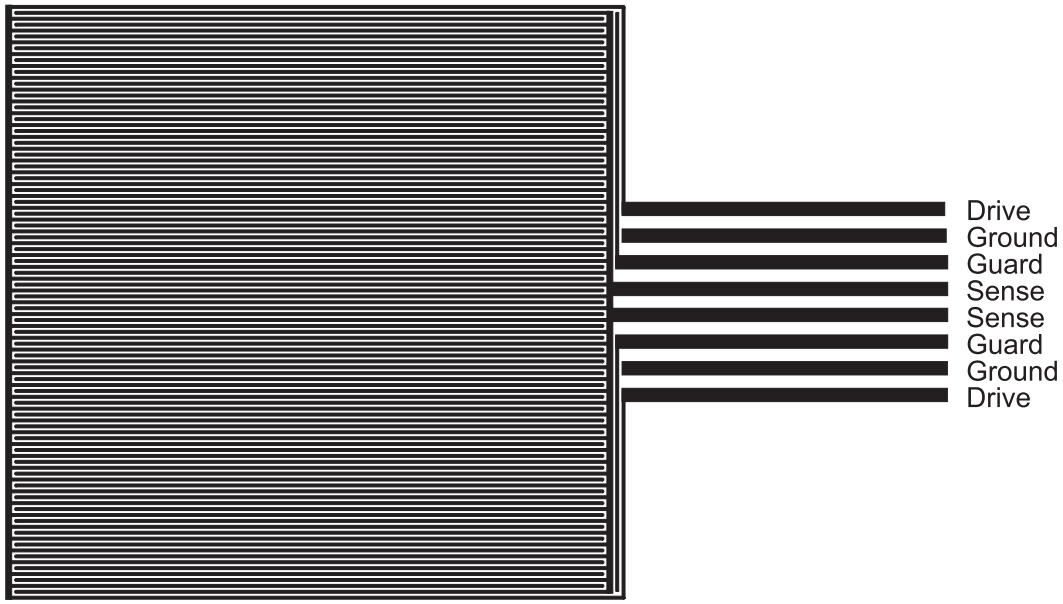

Figure 4.2: Single-wavelength flexible sensor on a Kapton substrate with a spatial wavelength of 1 mm. Adapted from [9].

in section 6.2, the in-plane shielding of the sensor leads is not sufficient when the capacitance C_{12} between the sensing and driven electrodes is relatively low.

A thin passivating layer of parylene (5 μm) covers the sensor on both sides to prevent moisture absorption by the hydrophilic Kapton substrate. In general, the presence of moisture in the volume of Kapton causes significant variations in its complex dielectric permittivity (see subsection 4.2.3). A grounded backplane deposited on the bottom side of the substrate provides shielding from external perturbations, defines ground potential, and predominantly confines the electric field to the upper half-space.

The idealized model, for which closed form expressions for the electric field exist, requires the electrodes to be modeled as an infinitely long and wide array of zero height metal microstrips placed on the surface of the insulating substrate. The most important contributors to the discrepancies between the theoretical model and real measurement data are the finite length and finite number of the finger electrodes, the capacitance of the leads of the electrodes to ground and to each other, the metallization ratio (described as the ratio of the area covered with copper to the total area of the sensor), and the fluid (typically air or liquid dielectric) trapped between the sensor's

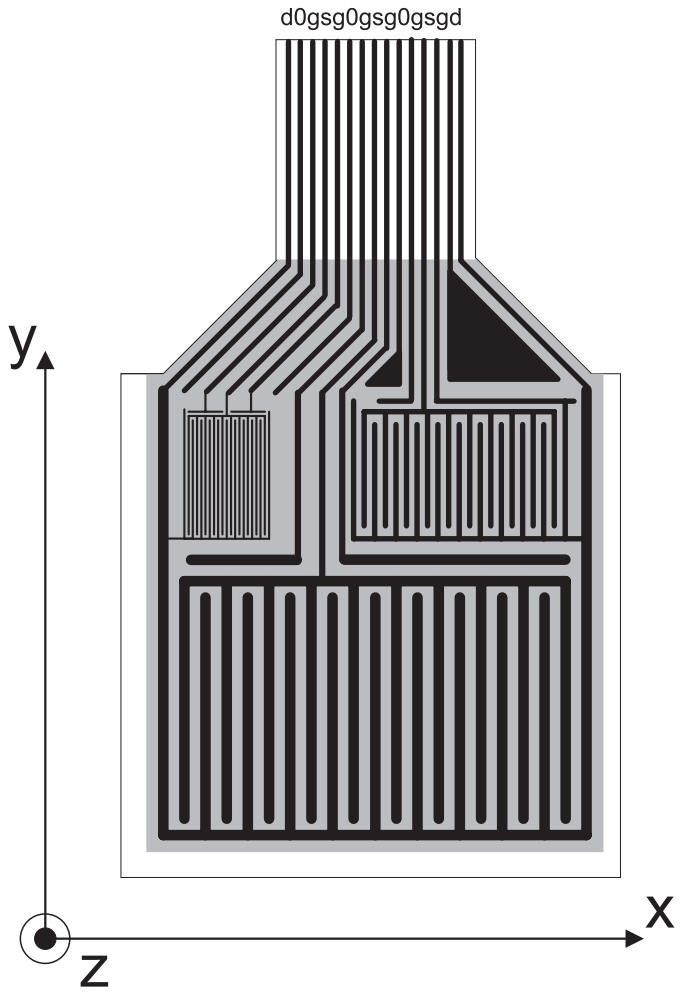

Figure 4.3: The three-wavelength Kapton substrate sensor with wavelengths of 1, 2.5, and 5 mm. Legend of electrode contacts: d - driven, 0 - ground, g - guard, s - sensing [9].

surface and the surface of the tested specimen. The finite thickness of the copper electrodes (35 μm or 17.5 μm for different sensor designs) may also contribute to these differences, however, recent computational models take the thickness of electrodes into account.

Comparisons given in Table 4.4 for the three-wavelength sensor in air demonstrate that although the continuum model of the interdigital sensor is theoretically adequate, the results of actual measurements may differ from predicted values by more than 30 percent. Several factors contribute to this, such as finite size of the interdigitated

	$\lambda = 1.0$ mm		$\lambda = 2.5$ mm		$\lambda = 5.0$ mm	
Capacitance(pF)	C_{20}	C_{12}	C_{20}	C_{12}	C_{20}	C_{12}
Continuum Model	11.8	1.19	24.6	0.54	89.1	0.8
FEM (*Maxwell*)	10.7	1.01	23.4	0.56	88.8	0.8
Direct Measurement	17.1	1.24	32.8	0.67	112	0.82

Table 4.4: Comparisons of three-wavelength sensor capacitance matrix in air from Fourier series continuum model, finite-element simulation, and measurements. Definitions of capacitances C_{12} and C_{20} and direct capacitance measurement procedure are given in section 4.6.2, details about the continuum model approach are given in section 7.3, and the finite-element simulation is described in Section 7.3.

electrodes, non-zero metallization thickness of the electrodes, and, sometimes, poor contact between the materials on the sensor-specimen boundary.

An intermediate design that marks the first attempt to measure capacitance and conductance between the sensing and the driven electrodes directly is shown in Figure 4.4. The ground backplane has been separated into three independent electrodes, so that the voltage on each of the planes could be set equal to the corresponding voltage of the sensing electrode above. Section 4.6 provides additional information about the differences between these two approaches. This sensor was made using in-lab capabilities from a Kapton sensor without a ground plane. Measurements confirmed the hypotheses regarding significant cross-coupling and end effects and justified fabrication of the new generation of three-wavelength sensors described in the next section.

4.5.3 Three-Wavelength Sensor with Teflon Substrate

Several problems with the Kapton sensor were resolved by introducing a new design. The improved design structure of the three-wavelength interdigital sensor used in most of the experiments of this thesis is shown in Figure 4.5. The major parameters, namely, the number of wavelengths (three) and their spatial periodicities of 1.0 mm, 2.5 mm, and 5.0 mm, were kept the same as in the previous Kapton sensor design. The substrate material was changed from Kapton to Teflon. The superior hydrophobic characteristics of Teflon necessitated this choice, as it eliminated the need of the moisture barrier coating (such as parylene), although Kapton outperforms Teflon in its thermal endurance

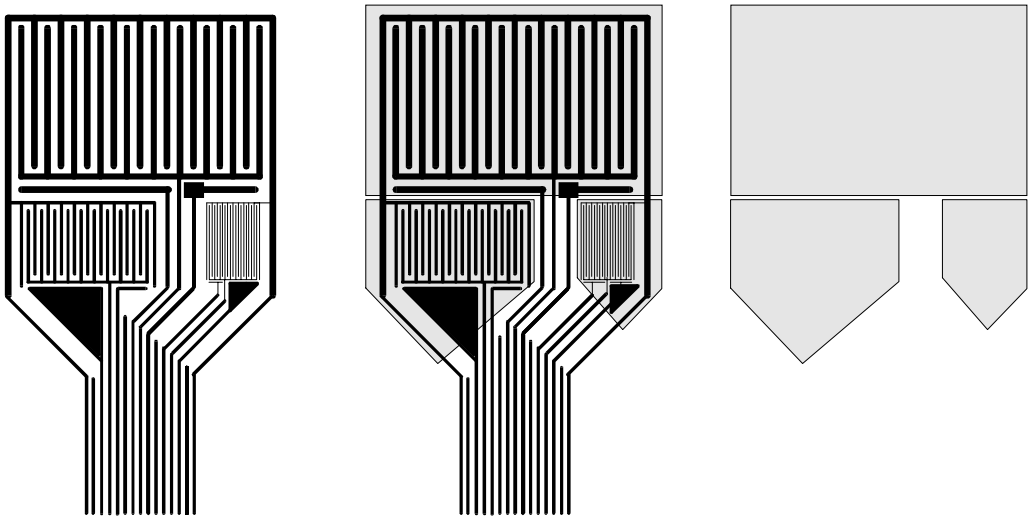

Figure 4.4: Intermediate design of the three-wavelength sensor with separate backplane electrodes that can be used as separate guards for each wavelength. The top interdigital electrode pattern is shown on the left, the backplane pattern is shown on the right, and their superimposed image is in the middle.

and mechanical stability. The recent introduction by DuPont of Kapton-F material, which consists of a Kapton core with a Teflon-like coating, may make it possible to manufacture a sensor on a substrate that combines advantages of both materials (see subsection 4.2.5).

Guard fingers are introduced on each side of the active sensing area to make the sensor look "infinite" in the x direction. The nominal meander length represents the total length of the meandering dielectric path between the sensing and the driven electrodes, which is approximately equal to twice the total length of the sensor electrode fingers.

The guard electrodes are also known to be used as a guard ring to minimize stray surface leakage currents [67]. Our application did not require a guard ring because of the high surface resistance of the Teflon substrate under experimental conditions reported here.

The dielectrometry interface circuitry has been redesigned with the purpose of increasing precision of measurements, mitigating the cross-coupling effects (described in

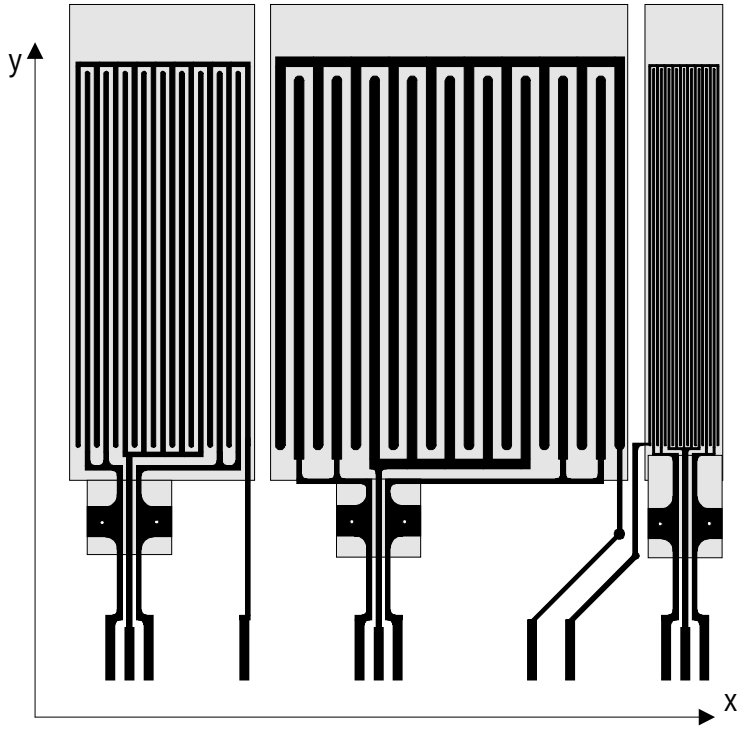

Figure 4.5: Improved design of the three-wavelength interdigital sensor using a Teflon substrate. Scale 1:1. In this design, the finger length to wavelength aspect ratio is increased, the cross-coupling between the wavelengths is reduced by moving them farther apart and adding guard electrodes, the infinite periodicity is approximated with guard fingers, and the substrate material was changed from hydrophilic Kapton to hydrophobic Teflon. The three separate guard planes on the back surface replaced the single ground plane in order to facilitate independent measurements of each wavelength.

section 6.2), and measuring individual entries of the sensor admittance matrix directly and independently. Section 4.6 provides details of the dielectrometry interface design and its relationship to parameter estimation algorithms.

4.5.4 Variations of Basic Three-Wavelength Design

Figures 4.6 and Figure 4.7 show variations of the basic three-wavelength interdigital sensor built to increase the capacitance of each channel and the working area of the sensor head. Another motivation is a closer agreement with the theoretical model which implies infinite periodicity and infinite extent of the electrode fingers. These design modifications were made for large surface area experiments with the cylindrical electrode Couette facility, however they were not used in subsequent experiments.

4.5.5 Curved Interdigital Sensor

A curved interdigital sensor shown in Figure 4.8 has been developed for flaw detection applications briefly described in Section 13.2 in a Jentek Sensors, Inc. research project. The sensor has three driven electrode fingers and two sensing electrode fingers. The curvature is intended to follow the radius of the flywheel that has potential cracks due to centripetal force acting on the material.

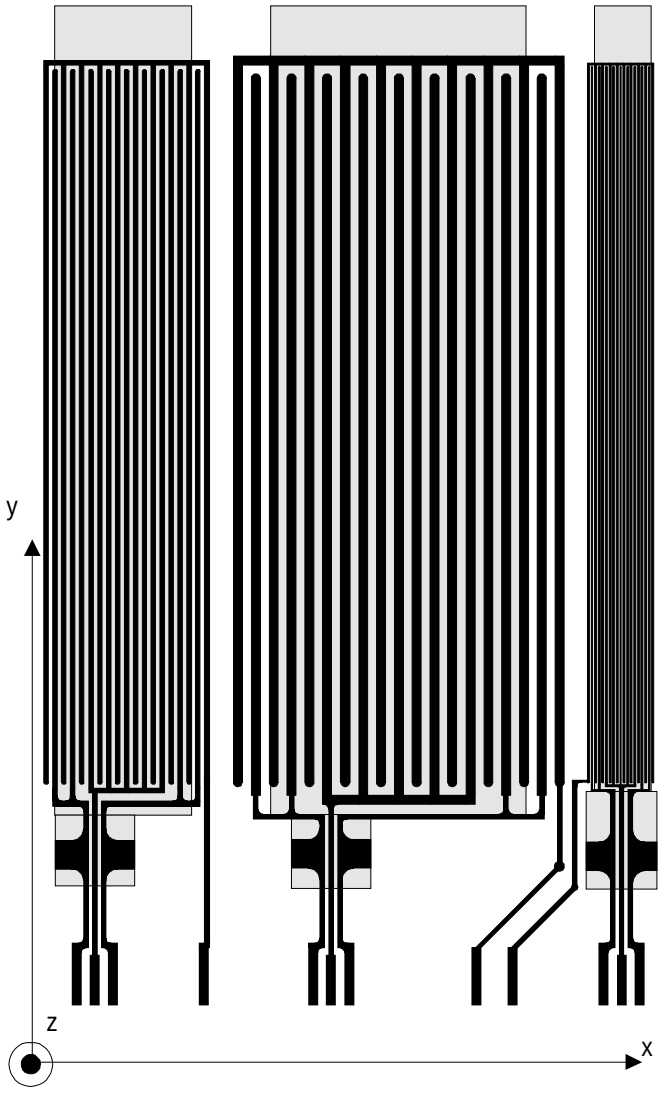

Figure 4.6: Teflon three-wavelength sensor with a larger length-to-width aspect ratio than that of the basic design in Figure 4.5.

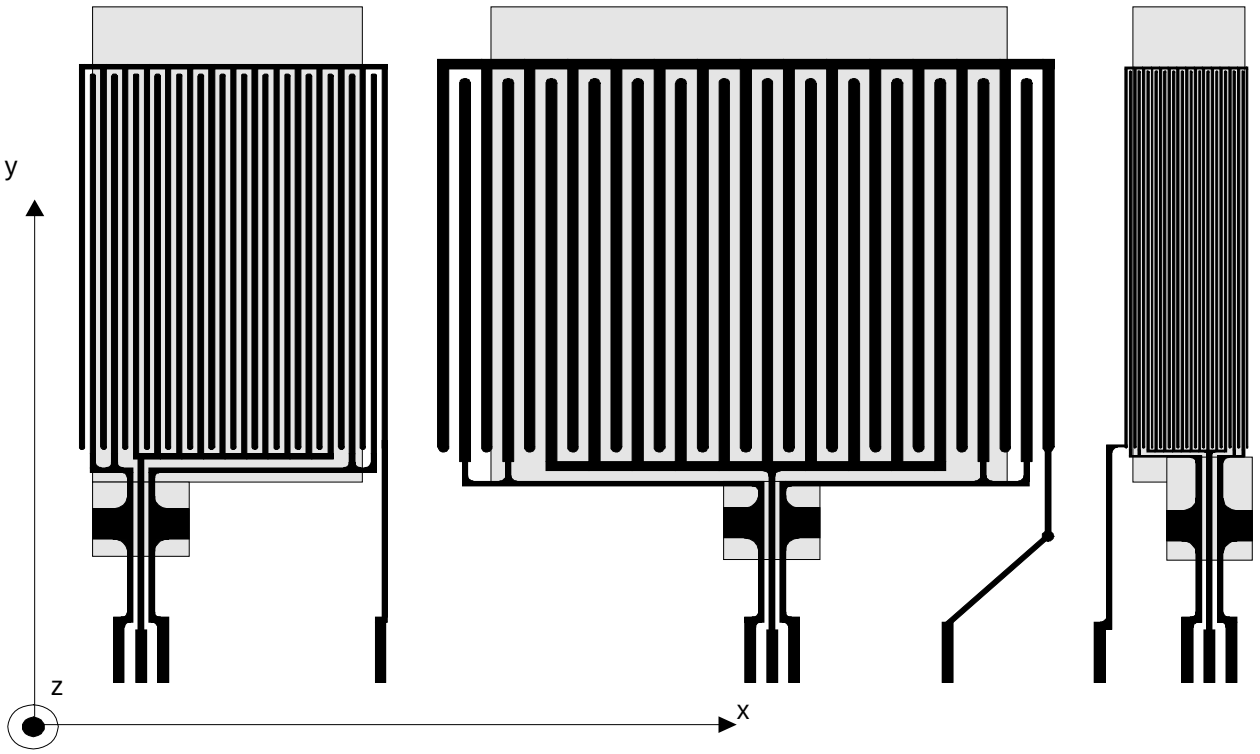

Figure 4.7: Teflon three-wavelength sensor with a smaller length-to-width aspect ratio than that of the basic design in Figure 4.5.

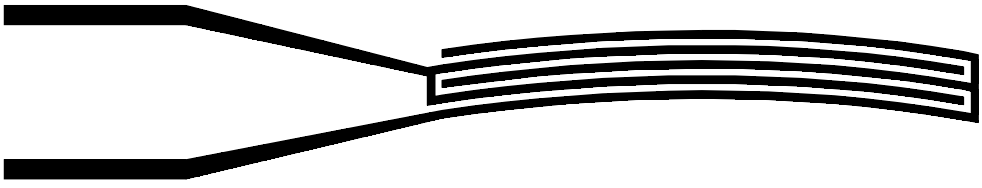

Figure 4.8: Curved sensor for detection of structural flaws in flywheel inspection.

4.5.6 Comb-Serpentine-Comb (CSC) Sensor

Motivation

Multi-wavelength interdigital dielectrometry is highly susceptible to the quality of contact between the sensor and the material under test. It has been determined that the change of capacitance due to the contact quality is far more significant than the change due to the finite thickness of the electrodes. Numerical simulations and measurements demonstrated that the equivalent air gap has to be as high as 20 to 50 microns in order to produce the reduction in the capacitance indicated by differences between the theoretical and the measured values.

This problem is known to exist in many fields, including the usage of ultrasonic transducers, eddy current sensors, high voltage electrodes, and magnetometry sensors. Experience from other fields of engineering shows that it is unlikely to completely eliminate the micro-gaps that form between the sensor electrodes and the material under test. Current techniques to reduce the error introduced by the micro-gaps including increase of the contact force, using a flexible substrate and/or rubber padding, allowing a uniform time period for mechanical relaxation, and standard statistical analysis. Some of the material presented in this section is based on the patent application of the author during his employment by Jentek Sensors [38].

At this point, the conventional multi-wavelength measurement practice suggests that an "equivalent gap" between the electrodes and the sample can be used to account for surface contact properties. This gap can be measured by postulating the existence of an additional layer in the direct vicinity to the sensor. Then, its thickness can be evaluated by considering additional equations, so that the number of equations is greater than or equal to the number of unknowns. Even though this approach is useful for the measurements of stratified media, it is bound to perform poorly because the distribution of micro-gaps is not the same across all wavelengths on the sensor head.

Figure 4.9(a) shows the conceptual picture of the alternative design proposed in this document. The arrangement of the electrodes shown in this diagram allows connection

of excitation and measurement circuits of the interface box to the electrodes using only single plane connections. That is, there is no need to drill holes through the substrate except for the ground/guard backplane hookup. The guard or ground names for the backplane are used interchangeably in this document, based on the discussion in Section 4.6.

Ideally, the interface circuit should provide independent switching for each electrode, so that each electrode can serve in the capacity of the driven, sensing, or guard electrode. Each penetration depth requires a unique combination of these roles. For each measurement, one of the electrodes is driven, one is sensing, and one is guard. This type of switching is quite cumbersome for highly insulating measurements, because a large number of reed relays would have to be employed. However, for the measurements at higher frequency, solid-state switches can be used, which would significantly simplify the design of the interface circuit.

Two wavelengths, rather than one wavelength, would detect any discontinuity, such as the presence of a dust particle several microns in diameter. As a result, the properties of the material layers will be determined more precisely. Three wavelengths provide even greater capabilities. Figure 4.9(b) shows another version of the sensor, also built on the rigid highly insulating substrate that was used in preliminary measurements. The substrate TLY-5-0620 by Taconic Plastics Ltd. is also Teflon-based and can be recommended for applications where flexibility is not desirable.

Figure 4.10 shows the final design of the CSC sensor built on the flexible Teflon substrate. Preliminary experiments with the sensor indicated high levels of cross-correlation of sensor gain between individual electrode pairs for a series of measurements affected by statistically varying disturbance factors. Refer to section 6.5 for a discussion on cross-correlation.

Golden Section Design

One feature that comes with this type of design and that is not present in the conventional three-wavelength sensor of Figures 4.3 and 4.5 is that the penetration depths

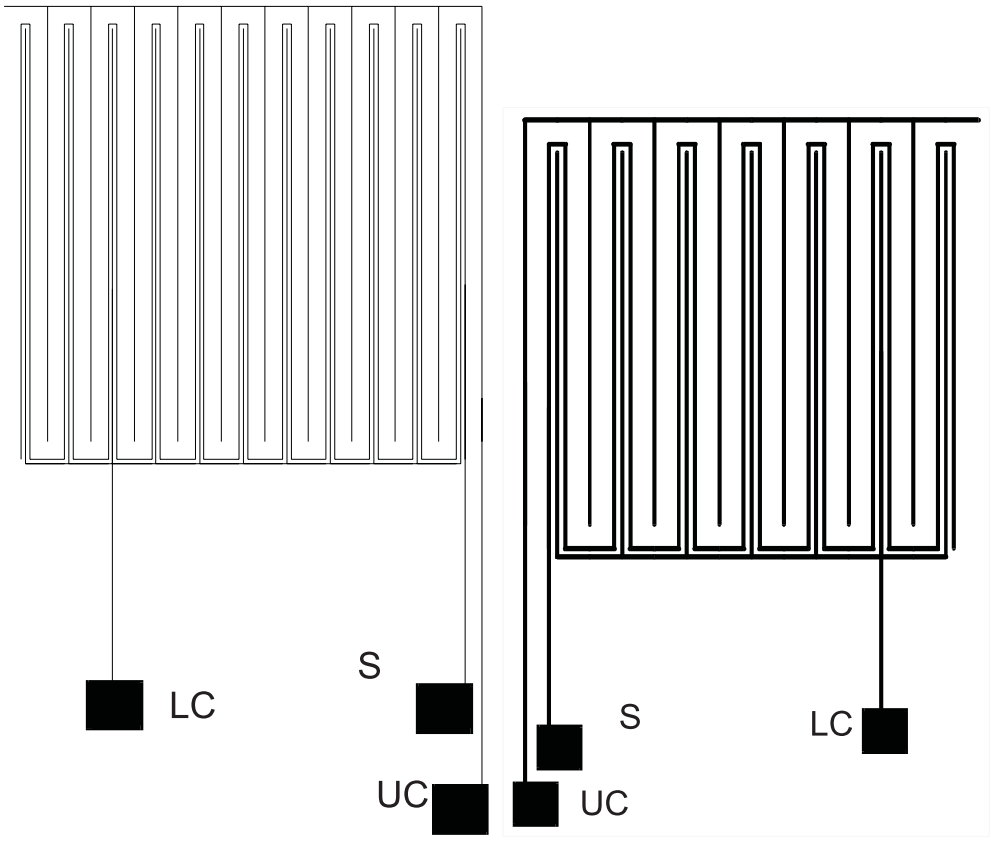

(a) 5 mm periodicity, 0.25 mm finger width

(b) 8 mm periodicity, 0.5 mm finger width

Figure 4.9: Double-driven sensors with capability of better measurement of air gap effects due to higher cross-correlation between different electrode pair signals. Legend: LC - lower comb, UC - upper comb, S - serpentine.

are no longer independent of each other. More accurately, a two-wavelength sensor based on this design can be built with any ratio of penetration depths. However, the third penetration depth would not be independent of the other two. For that reason, a golden section design is advocated here as the optimal three-wavelength layout for the proposed topology, so that the third wavelength has maximum separation from the other two wavelengths. Figure 4.11 illustrates the concept of the golden section. The definition given in [275] is:

"If a is a positive real number, then a partition of a into two positive summands x and $a-x$ such that x is the geometric mean of a and $a-x$, is called the golden section

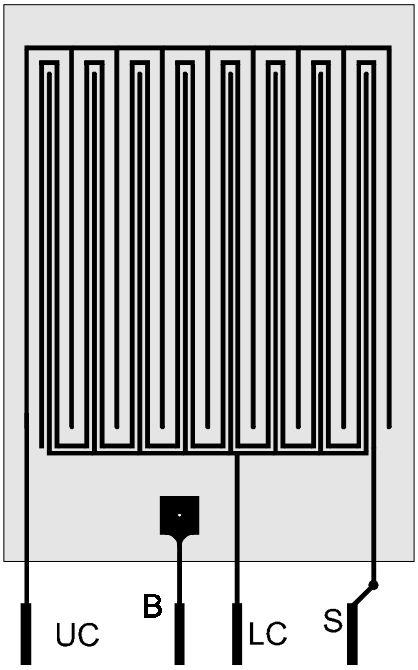

Figure 4.10: Comb-Serpentine-Comb (CSC) sensor with 0.5 mm finger width and 6 mm fundamental wavelength. Scale 1:1. Legend: LC - lower comb, UC - upper comb, S - serpentine, B - backplane.

of a. The ratio of a to x is called the golden ratio. It follows from $x = \sqrt{a(a-x)}$ that $x = \frac{\sqrt{5}-1}{2}a \approx 0.618a$."

It is useful to slightly alter the parameters from their "ideal" values because otherwise the designer would have to deal with transcendental dimensions.

Let us present the demonstration that the effective penetration depth is approximately equal to the distance between the centerlines of the respective electrodes. Consider a sensor layout with the topology as shown in Figure 4.10. The width of the electrodes is 500 μm and the distances between the centerlines in the half-wavelength arrangement that corresponds to Figures 4.10 and 4.11 are : AB = 1530 μm, AC = 4000 μm, substrate thickness 254 μm, electrode thickness 17 μm, and substrate relative permittivity 2.2 (Teflon-based substrate). Let us assume that an insulating material with the relative permittivity of 3.0, moves away from the sensor-material interface leaving

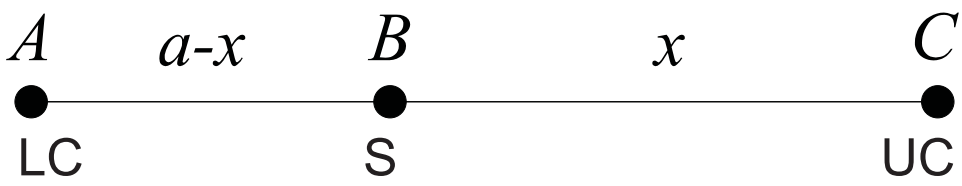

Figure 4.11: The illustration of the golden section concept. The ratio $BC/AB = x/(a-x)$ must be equal to the ratio of $AC/BC = a/x$, so that $x = \frac{\sqrt{5}-1}{2}a \approx 0.618a$.

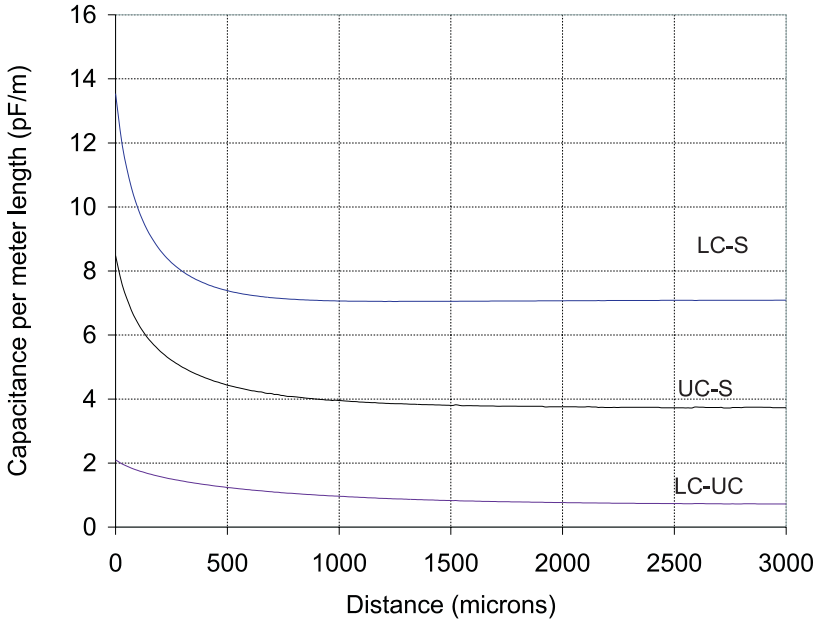

Figure 4.12: Calculated capacitance per unit length of the sensor to the movement of the dielectric with the relative permittivity of 3.0 away from the sensor so that the air gap is increasing.

an air gap. The response of the sensor to this movement in the units of capacitance per meter length is shown in Figure 4.12 for each electrode pair combination of lower comb to serpentine electrode (LC-S), upper comb to serpentine electrode (UC-S), and lower comb to upper comb (LC-UC). The change in the interelectrode capacitance is obvious, but since the amplitude of the capacitances are different, it is hard to compare the results. To make the comparison easier, one can draw the normalized capacitance, as shown in Figure 4.13. The zero value corresponds to the dielectric filling the region above the sensor, and 100 percent corresponds to air above the sensor.

Many ways can be used to define the effective penetration depth. If we choose $\gamma_{3\%}$ as the measure of the penetration depth (the difference between the asymptotic value

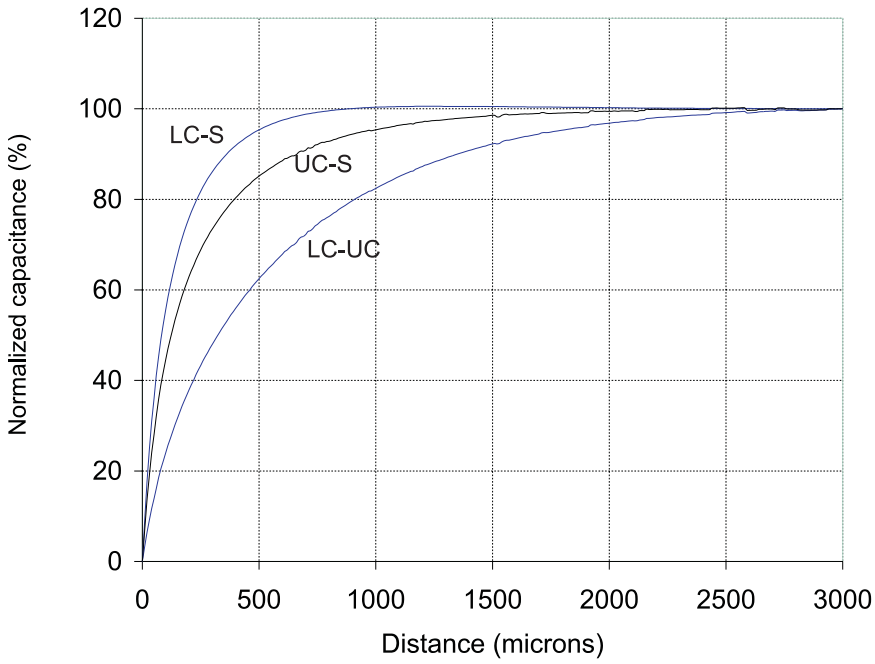

Figure 4.13: Normalized capacitance as a function of air gap. In the normalization, the zero distance value is accepted as 0%, the infinite thickness value is taken as 100%, and the intermediate values are mapped linearly.

and the measured value is 3%), we can now compare the effective penetration depth on the same basis. Figure 4.14 shows the same plot as Figure 4.13, but with the current normalized capacitance value subtracted from the 97% base line. The zero crossing indicates the $\gamma_{3\%}$ penetration depth. As seen from Figure 4.14, the $\gamma_{3\%}$ penetration depths are: 570, 1180, and 2020 μm.

4.5.7 Alternative Layouts

Possible layouts of planar electrodes are endless. Ultimately, planar electrodes of any shape generate some sort of fringing fields that penetrate into the material under test. Why would anyone want to explore shapes different from the classic interdigital electrode design? One reason may be to increase the amount of capacitance per unit area. Another possible reason is to concentrate the lines of electric field in a specific location. Also, one may want to redistribute the relative magnitude of spatial Fourier components of the electric potential in order to change the effective penetration depth.

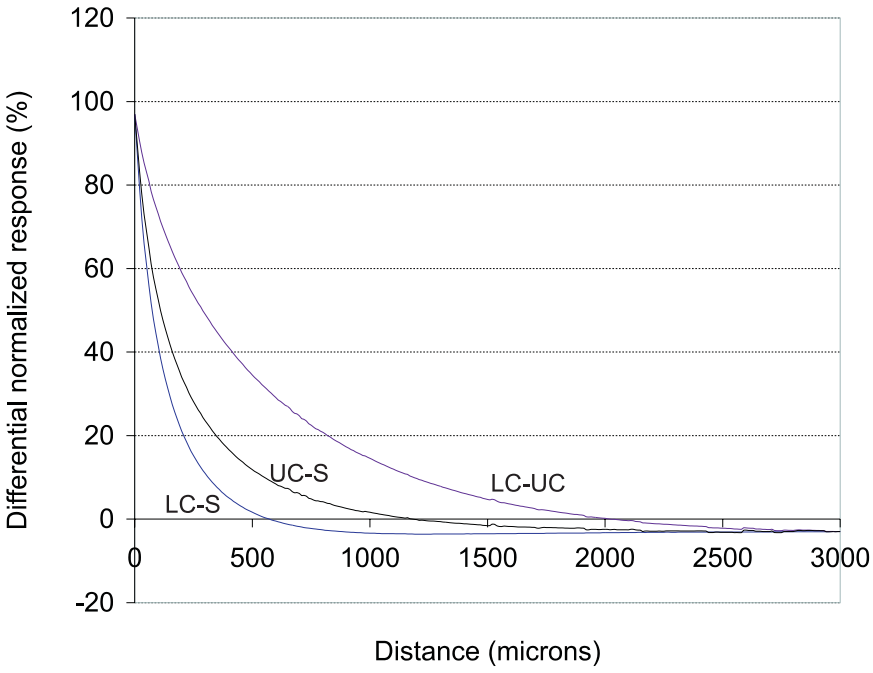

Figure 4.14: The 97 percent value minus the normalized capacitance. The zero crossings show the effective penetration depth of each electrode pair combination.

The departure from the classic shape may require a three-dimensional, as opposed to two-dimensional modeling. For example, planar coaxial and planar square spiral electrode layouts were modeled with three-dimensional finite element software and compared to the interdigital layout of the same area [224]. The square spiral electrode layout had a slightly higher interelectrode capacitance due to a higher influence of end effects.

4.6 Electronic Circuitry

Aside from specifying what functions should be performed by the electronic circuitry, one has to select an optimum partitioning between on-board and off-board design [134]. This decision is particularly important for sensors based on semiconductor technology. Signal processing electronics placed in the same housing as the sensing elements offers advantages of removing lead parasitic effects, reducing measurement noise [124], or providing wireless communication with the data acquisition system [255]. The major

disadvantage in this case is the increased complexity of chip design and vulnerability of the sensor.

Figure 1.6 shows that the dielectrometry interface connects the interdigital sensor with the controller. It serves two purposes: to increase the input impedance of the measurement circuit and to buffer the weak sensing signal with an operational amplifier so that it can be sent to the controller without being contaminated with noise. Appendix D features schematics of several generations of interface circuits.

Under any type of sensor geometric arrangement and electronic control, the dielectric properties of materials are evaluated by measuring terminal quantities defined by an equivalent lumped-element circuit and relating these quantities to the distributions of complex dielectric permittivity. The measurement of profiles of other physical variables, e.g. the distribution of moisture concentration, requires a calibration mapping that relates the complex permittivity to the physical variable. Appropriate choice of measurable quantities may significantly simplify this task. Possible variations of the measurement setup compared in this section are:

- Floating voltage measurement with backplane held at earth ground potential.

- Floating voltage measurement with backplane and guard fingers (if existing) held at guard potential.

- Short circuit current measurement with backplane and guard fingers (if existing) held at virtual ground potential.

- Combinations of the above three approaches.

The following sections provides a detailed description of each approach, along with their inherent advantages and disadvantages.

4.6.1 Floating Voltage with Ground Plane

The circuit schematic for this measurement mode is presented in Figure 4.15. Node 1 corresponds to the driven electrode, and node 2 to the sensing electrode. Basically, an impedance divider is formed by the sensor's equivalent lumped elements and by the known load capacitance C_L. Strictly speaking, the load capacitance is not necessary,

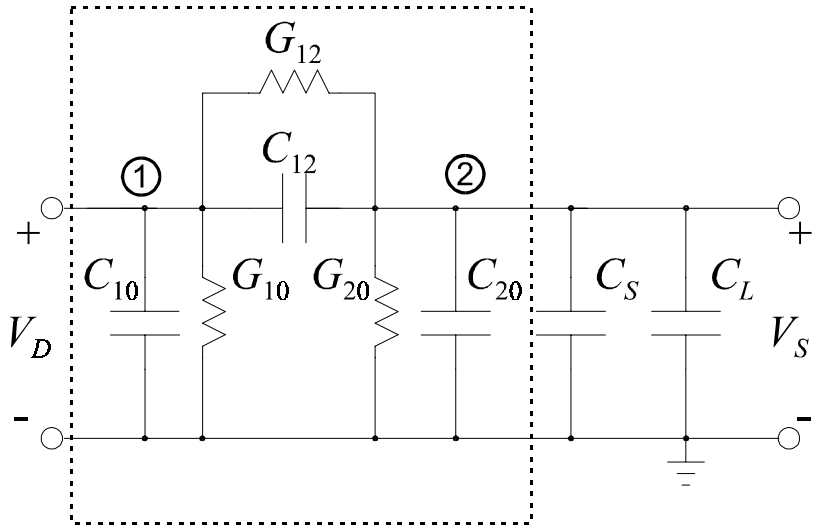

Figure 4.15: Floating voltage measurement with a grounded backplane and an impedance divider.

since the admittance to the ground plane is connected in parallel. However, it is useful to minimize the effects of the unknown stray capacitance C_S, to optimize the amplitude of the complex gain, and to select the frequency breakpoint between high and low frequency behavior. The complex gain between the driven and the sensing voltage at frequency ω is given by

$$\hat{G} = \frac{\hat{V}_S}{\hat{V}_D} = \frac{G_{12} + j\omega C_{12}}{G_{12} + G_{20} + j\omega\left(C_{12} + C_{20}\right) + j\omega\left(C_L + C_S\right)} \tag{4.1}$$

where $\hat{V}_S$ is the phasor voltage of the sensing electrode, and $\hat{V}_D$ is the phasor voltage of the driven electrode. It should be remembered that elements G_{12}, G_{20}, C_{12}, and C_{20} are frequency-dependent, as they represent an equivalent network of distributed elements that differs topologically from the actual sensor. C_S represents the combined effects of the stray capacitance of the sensor leads, gate of the operational amplifier, fringing fields to the surrounding objects, etc. The sum (C_{20}+C_L) is usually one or two orders of magnitude larger than C_S.

One disadvantage of this measurement approach is that the complex gain values cannot be converted in a straightforward way to the equivalent network element values. One complex equation can be solved for at most two real unknowns, while equation

((4.1)) has four unknowns (G_{12}, G_{20}, C_{12}, and C_{20}) when the complex gain is known from measurements. Even though G_{20} and C_{20} may be predominantly determined by known substrate properties, fringing fields through the unknown material have a significant effect on G_{20} and C_{20}.

A similar argument applies to the high frequency limit, where equivalent conductances G_{12}, G_{20} can be ignored compared to the imaginary part of all admittances. In this case, only one equation with two unknowns is available:

$$G = \frac{V_S}{V_D} = \frac{C_{12}}{C_{12} + C_{20} + C'_L}, \tag{4.2}$$

where the gain G is now real and C_S was incorporated into $C'_L = C_L + C_S$.

Although the number of equations is not sufficient to solve for equivalent capacitances and conductances directly, the solution can be found by iterative solution of the electric potential distribution either by a continuum model or by finite-element techniques. That is, the solution to the inverse problem can still be found, by employing two additional implicit functional dependencies, $G_{12}(\varepsilon, \sigma, \omega)$ and $C_{12}(\varepsilon, \sigma, \omega)$ found by theory. This approach is not necessarily reliable, due to a high sensitivity to the error and possible existence of multiple solutions.

One way to simplify the relationships between measurable quantities and equivalent admittance values is to drive the backplane at the same potential as the sensing voltage. A detailed description of this approach follows.

4.6.2 Floating Voltage with Guard Plane

Generic Equivalent Circuit

When a potential equal to that of the floating sensing electrode is applied to the backplane, $V_G = V_S$, as shown in Figure 4.16, the equivalent circuit elements G_{20} and C_{20} no longer affect the complex gain of the impedance divider, so that (4.1) reduces to:

$$\hat{G} = \frac{\hat{V}_S}{\hat{V}_D} = \frac{G_{12} + j\omega C_{12}}{G_{12} + j\omega C_{12} + j\omega \left(C_L + C_S\right)} \tag{4.3}$$

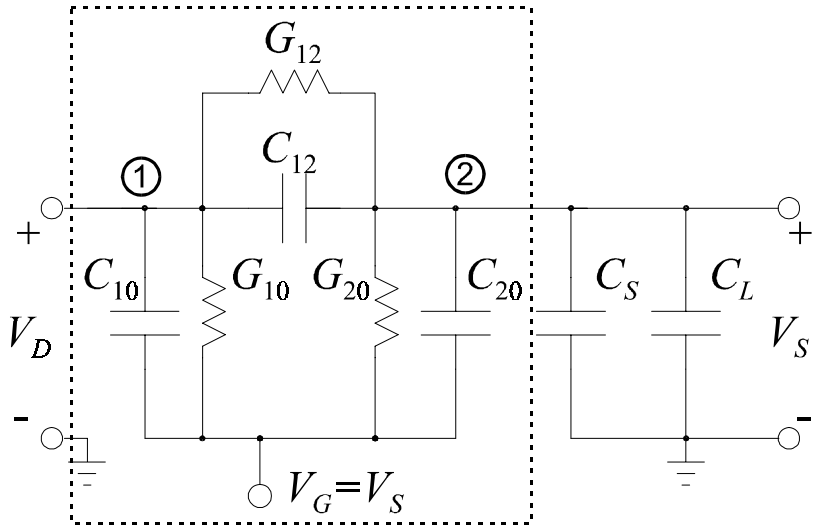

Figure 4.16: Floating voltage mode measurement of gain, phase, C_{12}, and G_{12} with actively driven backplane voltage equal to the sensing voltage.

This simplification allows the sequence of the inverse problem solution process to be changed. The equivalent admittance between the driven and sensing electrodes can now easily be found by solving a system of two linear equations with two unknowns. Relating the value of the complex interelectrode admittance to the complex dielectric permittivity ε^* of the tested material can be achieved in several ways, which are discussed in the appropriate following sections.

There are several consequences of the change of the measurement approach, which affect the design of the sensor. Since the backplane has to be driven at the guard voltage, and this voltage is different for each wavelength, it is no longer possible to have a common backplane, as was implemented in the previous design. This is why the new design has three separate backplanes, shown in gray in Figure 4.5. Also, any grounded electrodes, such as a shielding case, must be placed sufficiently far from the sensing electrode, so that the elimination of C_{20} in (4.3) is valid. In addition, separation of the driven electrode for each of the three wavelengths units is desirable if precise measurements are needed by avoiding cross-coupling with other wavelengths. In this case, only one wavelength at a time performs active measurements, and all other wavelengths are held at the guard potential of the active one.

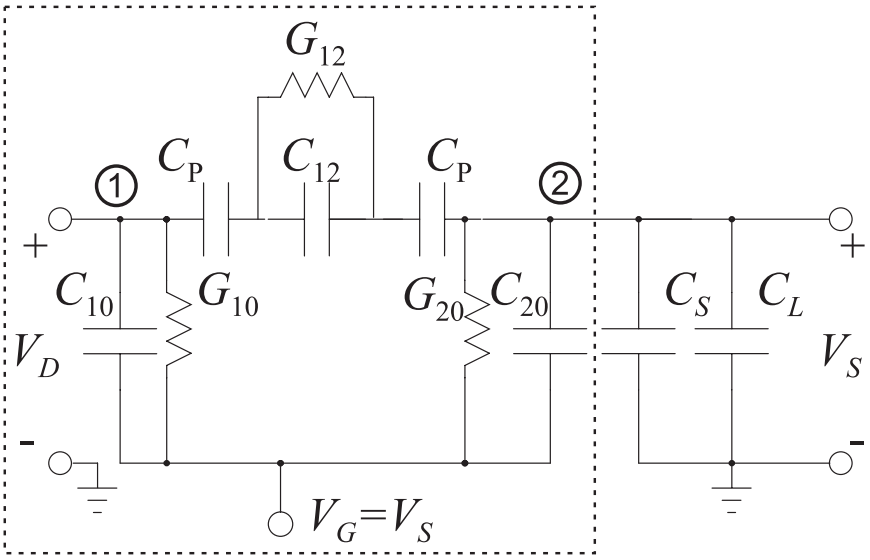

Figure 4.17: When a coating layer (such as Parylene) is relatively thin, it can be modeled as a series capacitor C_P.

Separation of Parylene in the Model

When the sensor surface is covered with Parylene (see section 4.3.2), it may be worthwhile to separate the effects of Parylene from the effects of the properties of the material under test. The presence of highly insulating Parylene may be modeled as a series capacitor C_P between each electrode and material characterized by capacitance C_{12} and conductance G_{12}, as shown in Figure 4.17. Then, (4.3) transforms to

$$\hat{G} = \frac{\hat{V}_S}{\hat{V}_D} = \frac{G_{12} + j\omega C_{12}}{G_{12}(1+\alpha_R) + j\omega C_{12}(1+\alpha_R) + j\omega\left(C_L + C_S\right)} \tag{4.4}$$

where

$$\alpha_R = \frac{2\left(C_L + C_S\right)}{C_P} \tag{4.5}$$

4.6.3 Short Circuit Current With Virtual Ground

A measurement setup [11] which combines advantages of both guard plane and ground plane approaches is presented in Figure 4.18. In this case, the voltage gain measured by the controller is $G = V_O/V_D$. Effectively, the measurement of the current I_t and

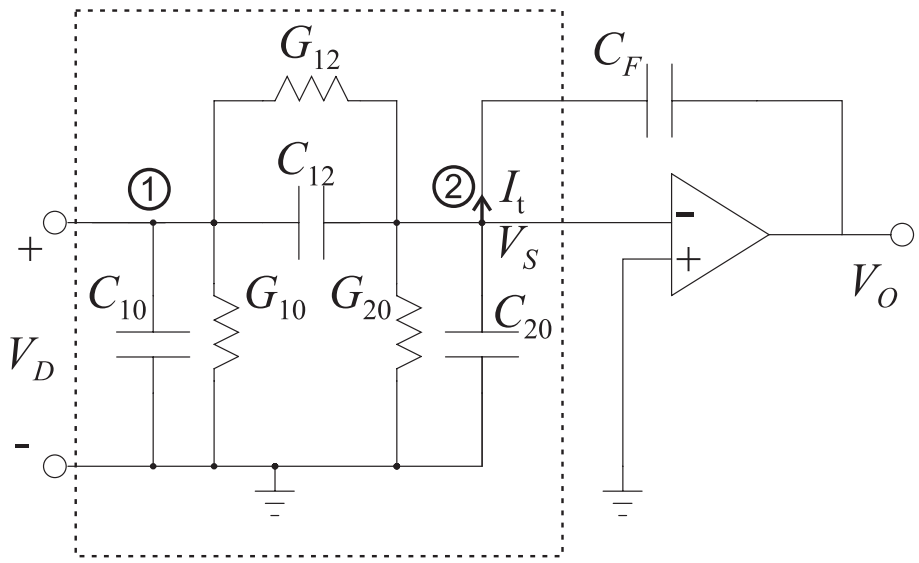

Figure 4.18: Short-circuit mode measurement of sensor electrode current I_t, C_{12}, and G_{12} by current integration with grounded backplane.

knowledge of the voltage V_D provides the sought information about the properties of the circuit elements G_{12} and C_{12}:

$$G_{12}(\omega) = \Re e\left(\frac{\hat{I}_t}{\hat{V}_D}\right), \tag{4.6}$$

$$C_{12}(\omega) = \frac{1}{\omega}\Im m\left(\frac{\hat{I}_t}{\hat{V}_D}\right) \tag{4.7}$$

In this case, the backplane, as well as all surrounding electrodes are always held at ground potential. At very low frequencies, the voltage build-up of the operational amplifier input may exceed the saturation voltage, in which case the value of the feedback loop capacitor C_F needs to be increased. Automatic switching of the feedback capacitor to avoid low frequency saturation is implemented electronically (there are two possible values of the feedback capacitor to select from, different for each channel and varying from one interface to another based on the application). The other floating voltage mode interfaces require manual replacement of the load capacitance C_L to avoid signal saturation.

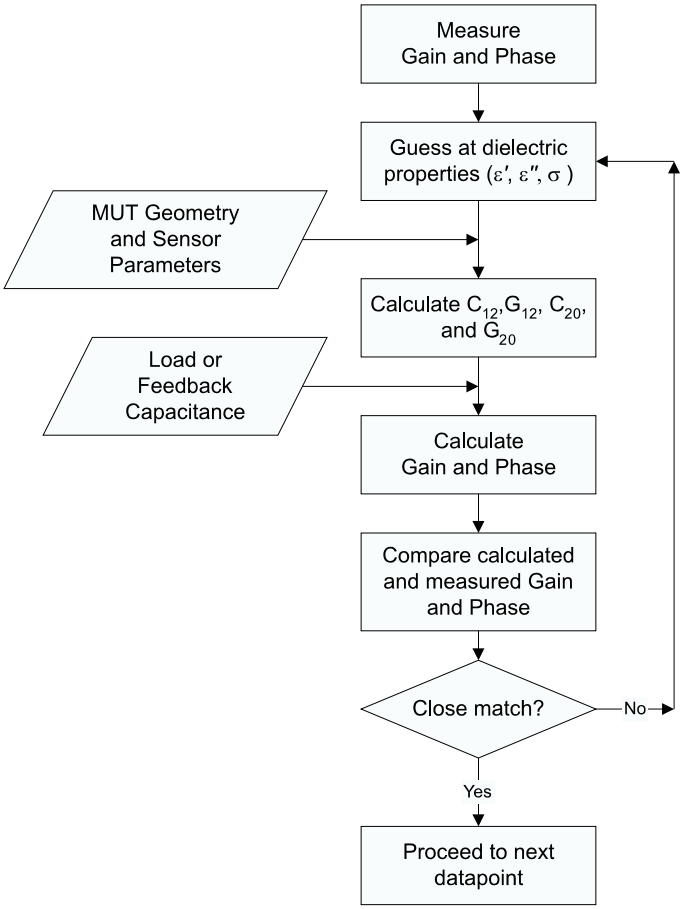

Figure 4.19: The comparison of measured and calculated gain and phase for grounded backplane measurements is necessary as C_{12} and G_{12} cannot be evaluated directly. MUT stands for "material under test."

4.6.4 Summary of Conceptual Approaches

Based on the discussion of various measurement circuits, one could summarize various approaches to parameter estimation through the diagrams shown in Figures 4.19 and 4.20. When the direct measurement of capacitance and conductance between the sensing and driven electrodes is not possible, the determination of dielectric properties requires matching of the measured and calculated gain and phase values. Figure 4.19 illustrates this concept. On the other hand, when it is possible to measure C_{12} and G_{12} directly, fewer equations must be solved simultaneously, and the estimation of material properties is somewhat simplified.

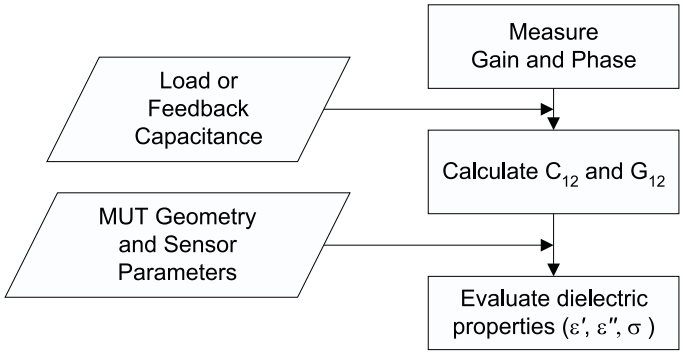

Figure 4.20: Guarded backplane circuitry allows the direct measurement of C_{12} and G_{12}, which greatly simplifies the parameter estimation process.

4.7 Manufacturing Process

Crane Polyflon [269] manufactured sensors according to the drawings supplied to them. As an example, Figure 4.21 shows a downscaled version of the top layer of one of the sensor batches. Figure 4.22 shows the bottom part of the same drawing, and Figure 4.23 shows the third page of the same drawing, which indicates the location of copper-plated through holes. In most cases, the drawings were done in CorelDraw.

4.7.1 Plating

Polyflon has developed a proprietary plating process for electroplating directly onto PTFE. This unique process ensures a strong molecular bond between the PTFE dielectric and conductive metal layer. Electroplated PTFE withstands continuous temperatures of 175°C and 225°C short term without damage to the plated material, dielectric, or the bond between them. Electroplated PTFE also performs well at low temperatures, even under cryogenic conditions [269].

4.7.2 Etching and Cleaning

Etching according to the supplied pattern has been done by Polyflon on Teflon flexible substrates, by Tech-Etch [276] on Kapton flexible substrates, and using MIT HVRL in-house capabilities on rigid substrates. The quality of etching in terms of uniformity

and the adherence to given specifications varied widely across manufacturers and even across individual batches. Undoubtedly, the accuracy of patterning will improve in the future following the overall trends of the electronics industry. The necessary cleaning procedures of the sensors after their arrival from the manufacturer are described in Appendix A.

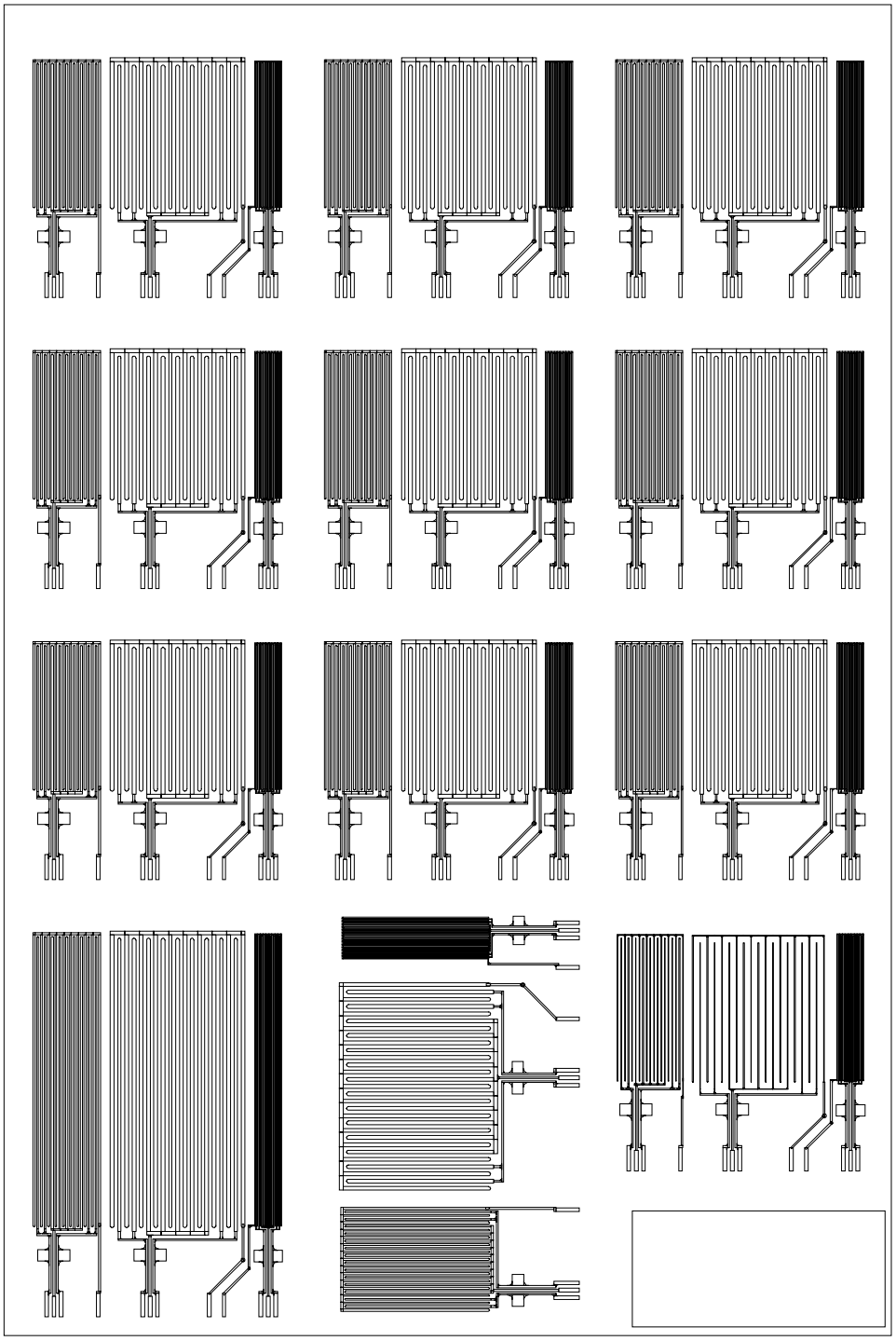

Figure 4.21: Top of the drawing supplied to the manufacturer.

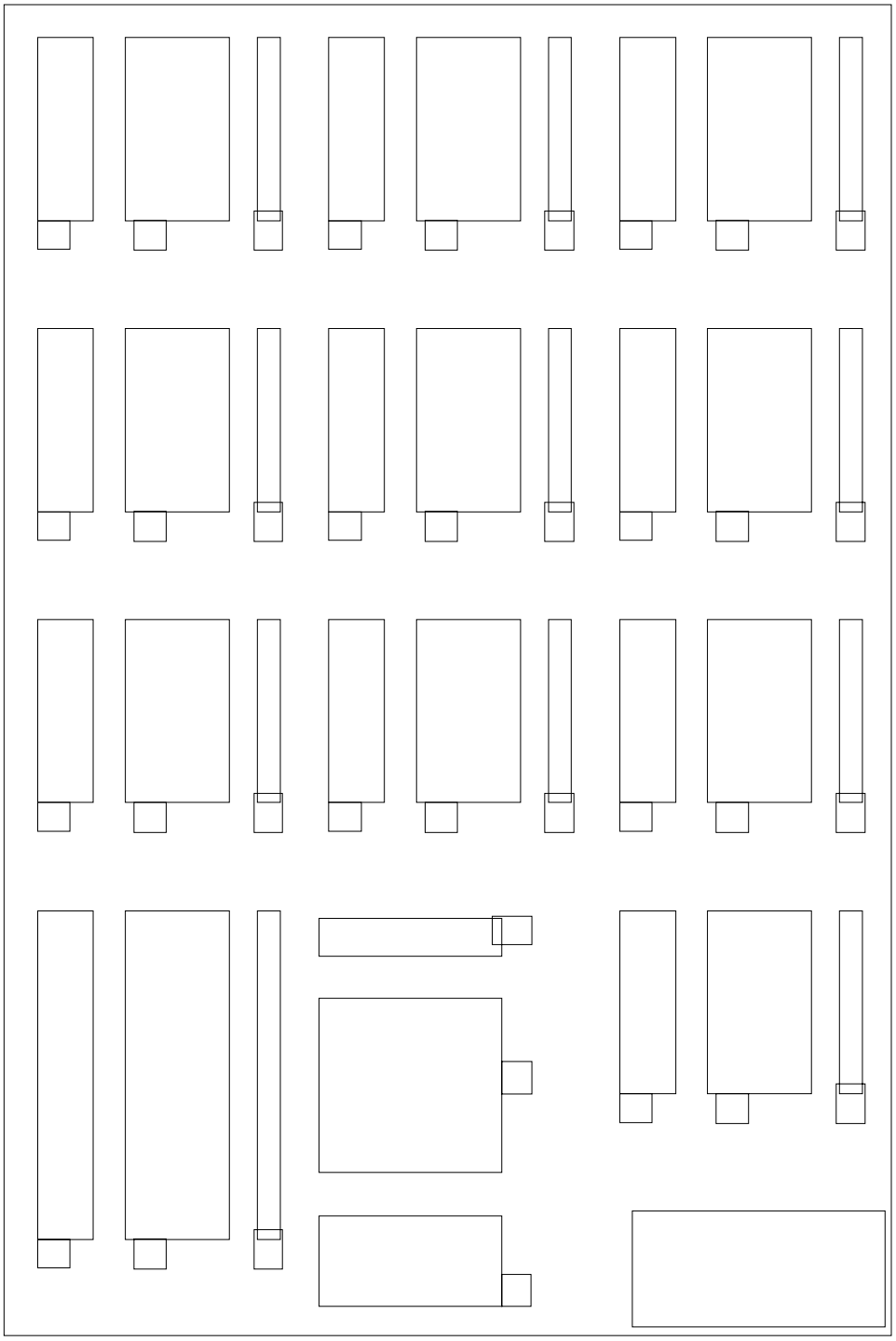

Figure 4.22: Bottom of the drawing supplied to the manufacturer.

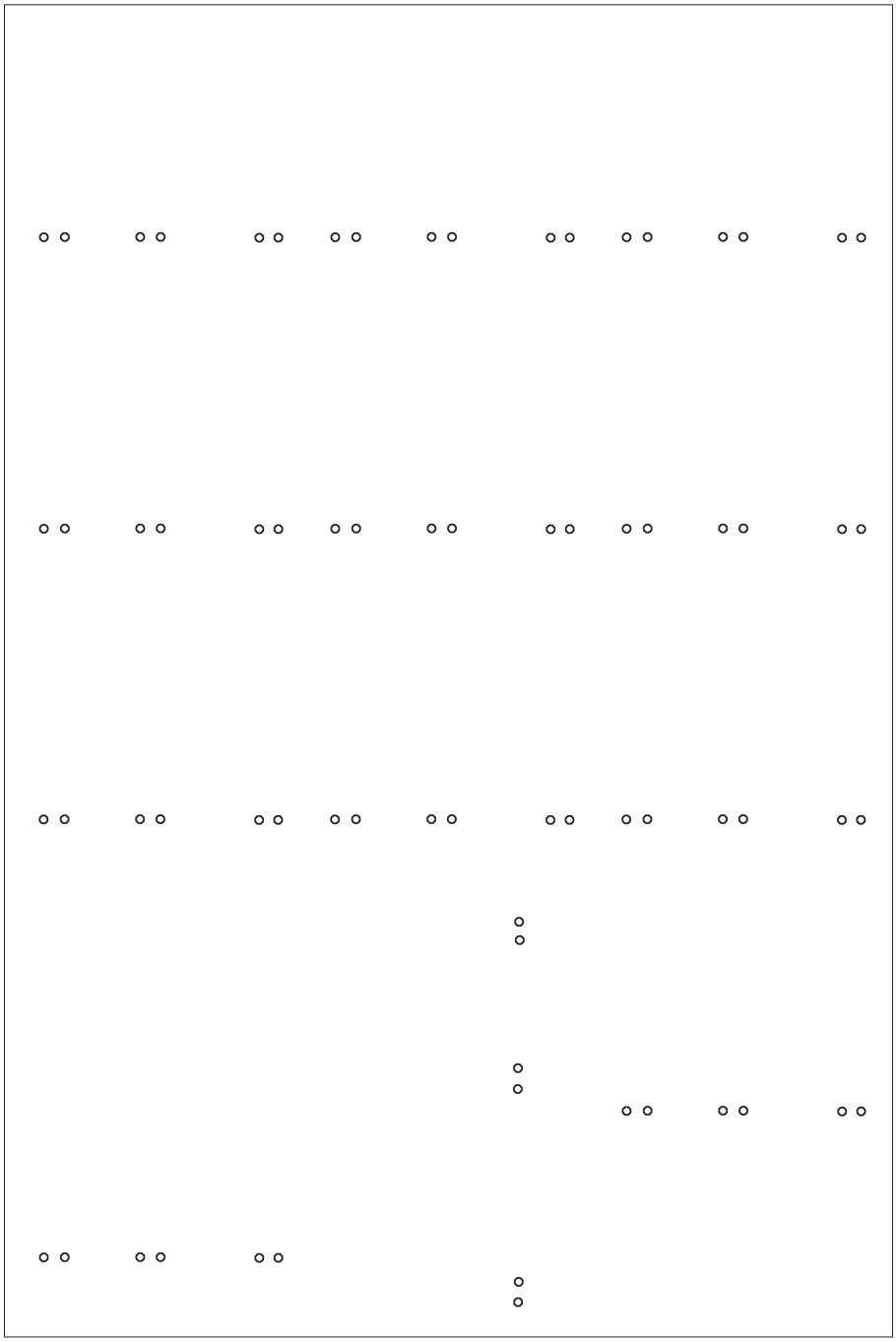

Figure 4.23: Holes specification of the drawing supplied to the manufacturer.

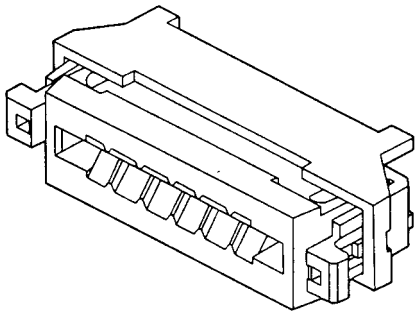

Figure 4.24: Right angle ZIF flex circuit-to-board connector 90500 by Molex® [277].

4.8 Mechanical Design

A number of fixtures and holders have been designed and built for different applications. The factors that determined each specific design included curved and straight surfaces in contact with the sensor, tight spacing around the material sample, access of chemicals and moisture to the opposite side of the sample, required pressure, texture of the sensor surface, and the need to test a large number of samples (as opposed to a single specimen) subjected to environmental effects. The details of each design are included with the application descriptions in the following chapters.

In some cases, the leads that connect the sensor and the interface box had been soldered onto the connecting pads. More often, however, zero-insertion-force (ZIF) connectors by Molex had been used for this purpose. Figure 4.24 shows a typical right angle ZIF flex circuit-to-board latch connector. These connectors are fragile and should be handled with care. In many cases, a single connector would not be wide enough to accommodate all necessary connections. In this case, two conductors were used in parallel, as shown in Figure 4.25. An indentation in the sensor head is then necessary to provide spacing for latches.

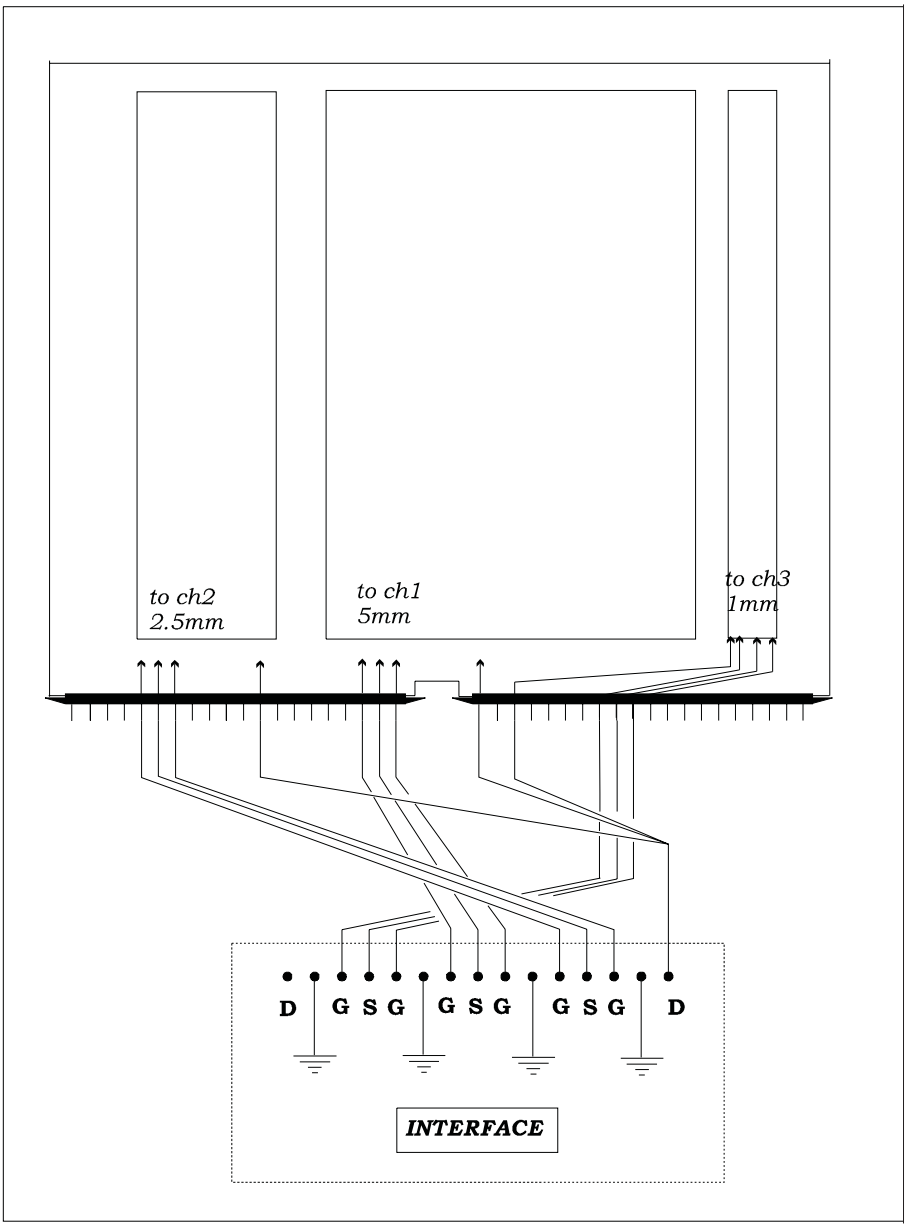

Figure 4.25: Two zero-insertion-force connectors had been used in parallel with the basic design of the three-wavelength sensor. Legend: D - driven electrode, G - guard electrode, S - sensing electrode [1].

4.9 Penetration Depth

There is no single number that adequately reflects the penetration depth of fringing electric fields into the material under all conditions. Depending on simulation strategy and required sensitivity of measurement, the effective penetration depth is evaluated to be one-third [142], 0.3 [9] [26], one-fourth, or one-fifth [20], of the fundamental wavelength λ.

Also in order to determine the spatial profiles of relative permittivity and conductivity within a sample, the detection limits of the sensors had to be determined. This task was achieved by conducting a *Maxwell* 2D finite element computer simulation with the appropriate sensor geometries. A sample was modeled as a thin layer on top of the sensor. The thickness of this layer was set as a constraint in the model which could be swept in the parametric solver. The sample was treated as a liquid sample in a sense that it filled the gap between the finite height electrodes. The background for these simulations was set to vacuum.

Sweeps were conducted from 0 μm to 4000 μm on the thickness of the sample. The excitation of backplane (guarded vs. grounded) is not relevant to calculations because capacitance is not a function of electrical excitation in the linear quasistatic regime. Conductance and capacitance were calculated. However, for the simulations run on this experiment the samples were selected as perfect insulators with conductivity of zero. This selection means that all conductances were zero and that the only signal was from capacitance. As expected for thin layers, the measured C_{12} was determined by the combination of properties of the thin layer and the surrounding fluid. For sufficiently thick layers, the measured C_{12} was dependent only on the sample permittivity. The point at which C_{12} reached an asymptotic value was defined as the point of signal saturation. The data from the simulations on the three-wavelength (TWS) and CSC sensors are presented in Tables 4.5-4.7. The percentages reported are the percent capacitance normalized to the difference between maximum and minimum capacitances, $C_{max} - C_{min}$.

	$\lambda/5$	$\lambda/4$	0.3λ	$\lambda/3$		at 80 %	at 90%	at 95%
5.0 mm	85.27%	91.60%	95.95%	96.95%		870.8 μm	1164.8 μm	1445.7 μm
2.5 mm	87.83%	93.41%	96.14%	97.46%		393.5 μm	540.4 μm	686.8 μm
1.0 mm	89.34%	94.27%	96.53%	97.49%		146.6 μm	205.4 μm	265.5 μm
	(a)					(b)		

Table 4.5: The percent change of capacitance weighted to the difference between the maximum and minimum capacitance values, $C_{max} - C_{min}$, for penetration depth data for TWS with a test relative permittivity of 2.1 for (a) selected sample thickness and (b) sample thickness for selected percent change in capacitance.

	$\lambda/5$	$\lambda/4$	0.3λ	$\lambda/3$		at 80 %	at 90%	at 95%
5.0 mm	84.54%	91.88%	95.35%	96.87%		891.9 μm	1183.1$\mu\mu$m	1471.6 μm
2.5 mm	87.15%	92.95%	96.06%	97.22%		405.4 μm	553.1 μm	701.2 μm
1.0 mm	88.61%	93.83%	96.47%	97.66%		152.7 μm	212.6 μm	271.9 μm
	(a)					(b)		

Table 4.6: The percent change of capacitance weighted to the difference between the maximum and minimum capacitance values, $C_{max} - C_{min}$, for penetration depth data for TWS with a test relative permittivity of of 3.1 for (a) selected sample thickness and (b) sample thickness for selected percent change in capacitance.

	$\lambda/5$	$\lambda/4$	0.3λ	$\lambda/3$		at 80 %	at 90%	at 95%
UC-LC (8.0 mm)	82.84%	90.79%	95.36%	96.87%		1497.7 μm	1953.3 μm	2361.4 μm
UC-S (6.0mm)	86.86%	91.92%	95.14%	96.57%		945.1 μm	1350.1 μm	1785.0 μm
S-LC (2.0 mm)	89.66%	94.60%	97.44%	98.38%		291.5 μm	405.2 μm	511.3 μm
	(a)					(b)		

Table 4.7: The percent change of capacitance weighted to the difference between the maximum and minimum capacitance values, $C_{max} - C_{min}$, for penetration depth data for CSC sensor with a test relative permittivity of 2.1 for (a) selected sample thickness and (b) sample thickness for selected percent change in capacitance. Legend: LC - lower comb, UC - upper comb, S - serpentine.

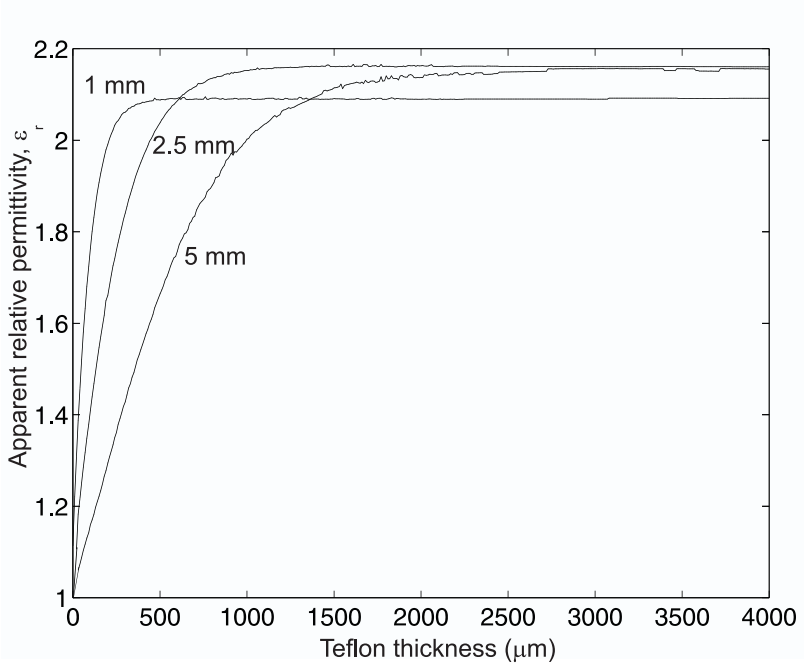

Figure 4.26: Calculated apparent relative permittivity of Teflon ($\varepsilon = 2.1$) using the calculated capacitances as a function of Teflon thickness for 1.0 mm, 2.5 mm, and 5 mm wavelengths.

The simulation data from the signal penetration depth experiment also provided an excellent test vector for the portion of the continuous spatial property profiling program that converts capacitance-conductance data to relative permittivity and conductivity. The results of passing the signal penetration test vectors through the *convertGCtoES.m* program listed in Appendix G are shown in Figure 4.26. The expanding air region data equivalent to the expanding Teflon block data are given in Figures 4.27 and Figure 4.28.

These simulations were run with a sample relative permittivity of 2.1, therefore the expected asymptotic value of apparent relative permittivity is also 2.1. However, the estimate of dielectric permittivity at the curve saturation generated by *convertGC-toES.m* is not exactly 2.1. This mismatch is mostly due to the linear interpolation in the program from the previously generated solution spaces. In this synthetic case, the level of discretization of the Maxwell generated solution space is the limiting factor in the accuracy of the final value for relative permittivity.

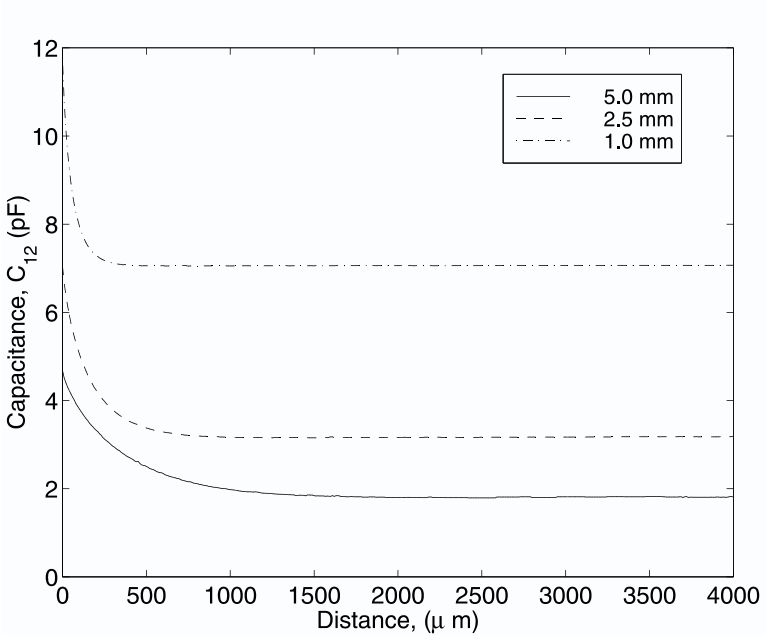

Figure 4.27: Calculated capacitance per one meter length for 1, 2.5, and 5 mm wavelengths with an expanding air gap separating sensor to dielectric with $\varepsilon_r = 2.1$.

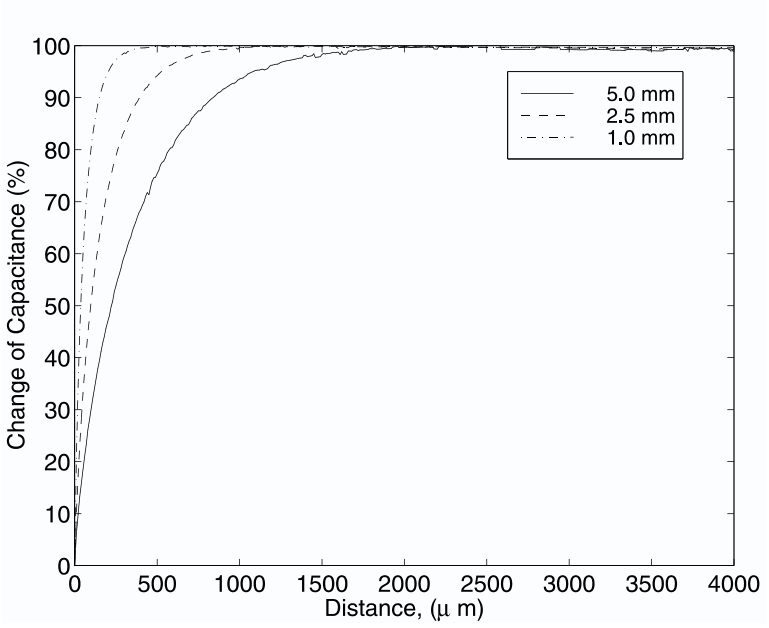

Figure 4.28: Calculated percentage change of capacitance for 1, 2.5, and 5 mm wavelengths with an expanding air gap separating sensor to dielectric with $\varepsilon_r = 2.1$.

	Previous design	**New design**
Material of substrate	Kapton (ε_r=3.05)	Teflon (ε_r=2.1)
Moisture barrier coating	Parylene (5 μm thick)	none
Thickness of substrate	5 mil (127 μm)	10 mil (254 μm)
Metallization ratio	0.5	0.5
Measured quantity	Floating voltage	Floating voltage or short-circuit current
Mode of operation,	All wavelengths simultaneously	Either simultaneous or separate
Nominal meander length (m)	0.3/ 0.3/ 0.6	0.5/ 0.5/ 0.5
Thickness of electrodes	35 μm or 17 μm	14 μm
Number of sensing electrode fingers per wavelength	10	5
Connection	Flat cable	Coaxial cable
Backplane	Common(Grounded)	Separate(Grounded/Guarded)

Table 4.8: Differences between the first (Kapton substrate) and new (Teflon substrate) design of the three-wavelength interdigital sensor.

4.10 Summary of Improvements

Table 4.8 gives the summary or improvements between the three-wavelength Kapton sensor of Figure 4.3 and the three-wavelength Teflon sensor of Figure 4.5. These improvements were adequate to accommodate many of the applications explored in the course of this thesis work, including moisture dynamics measurements in transformer pressboard, measurements of properties of two insulating material layers, flaw detection measurements, concentration of toluene in chemical garments, and measurements with liquid dielectrics. At the same time, these modifications were not sufficient to provide reliable information about the distribution of dielectric properties in materials with more than two distinct layers. The CSC sensor is the first step towards this goal.

Chapter 5

Diagnostic and Proof-of-Concept Measurements

5.1 Introduction

Development of a diagnostic measurement arsenal is a significant portion of this thesis. To avoid confusion, distinction should be made between *Dielectric Diagnostics* [278] and *diagnostics of dielectric measurements*. The former is a synonym for "non-destructive dielectrometry" and the latter is a set of procedures for troubleshooting of electronic equipment and measurement setup. This chapter concentrates on the second case, whereas the thesis itself is dedicated to the general subject of non-destructive dielectrometry measurements.

The diagnostic measurements are extremely important for all aspects of dielectrometry. The choice of the diagnostics technique depends on the specifics of application. During the development stage of a particular sensor, the diagnostics are especially complicated because it is difficult to predict which phenomena might degrade the sensor and the system performance. This chapter presents a variety of diagnostic procedures and provides comments regarding their usefulness during different stages of the technology development process and troubleshooting of various experimental setups.

5.2 Cleaning

The quality of cleaning required for each application varies significantly. Most frequently encountered contaminants include dust particles, oil (usually from fingertips), and moisture. The contamination may be both surface and bulk.

It is sometimes desirable to skip the ultrasound cleaning in order to avoid negative mechanical impact of ultrasound waves. The sensor surface can be considered adequately clean if a frequency sweep in air produces a variation of the signal phase of less than one degree for the entire range of the frequencies of interest, typically 0.005 Hz to 10 kHz. For the newly manufactured with CuFlon technology sensors, the ultrasound cleaning with bleach is not necessary (the phase is sufficiently low) as long as the sensor operating frequency is expected to be above 1 Hz.

Figure 5.1 shows the diagnostic frequency sweep of the CuFlon sensor after cleaning with methanol and drying in an oven for two hours at 60 °C. At the lowest frequency, the phase departs from zero by more than two degrees. However, the response is reasonably flat above 0.1 Hz. Figure 5.2 shows the results of the frequency sweep of the same sensor after ultrasound cleaning in accordance with the procedures outlined in Appendix A.

5.3 Electronics

5.3.1 Load Capacitance

Accurate values of the load capacitance C_L for each channel (wavelength) can be determined by using a known capacitor as C_{12} connected between the sensing and driven electrode contacts of the interface box. Since the conductance of the test capacitor is negligible, it follows from (4.3) that the load capacitance C_L for the floating voltage interface is:

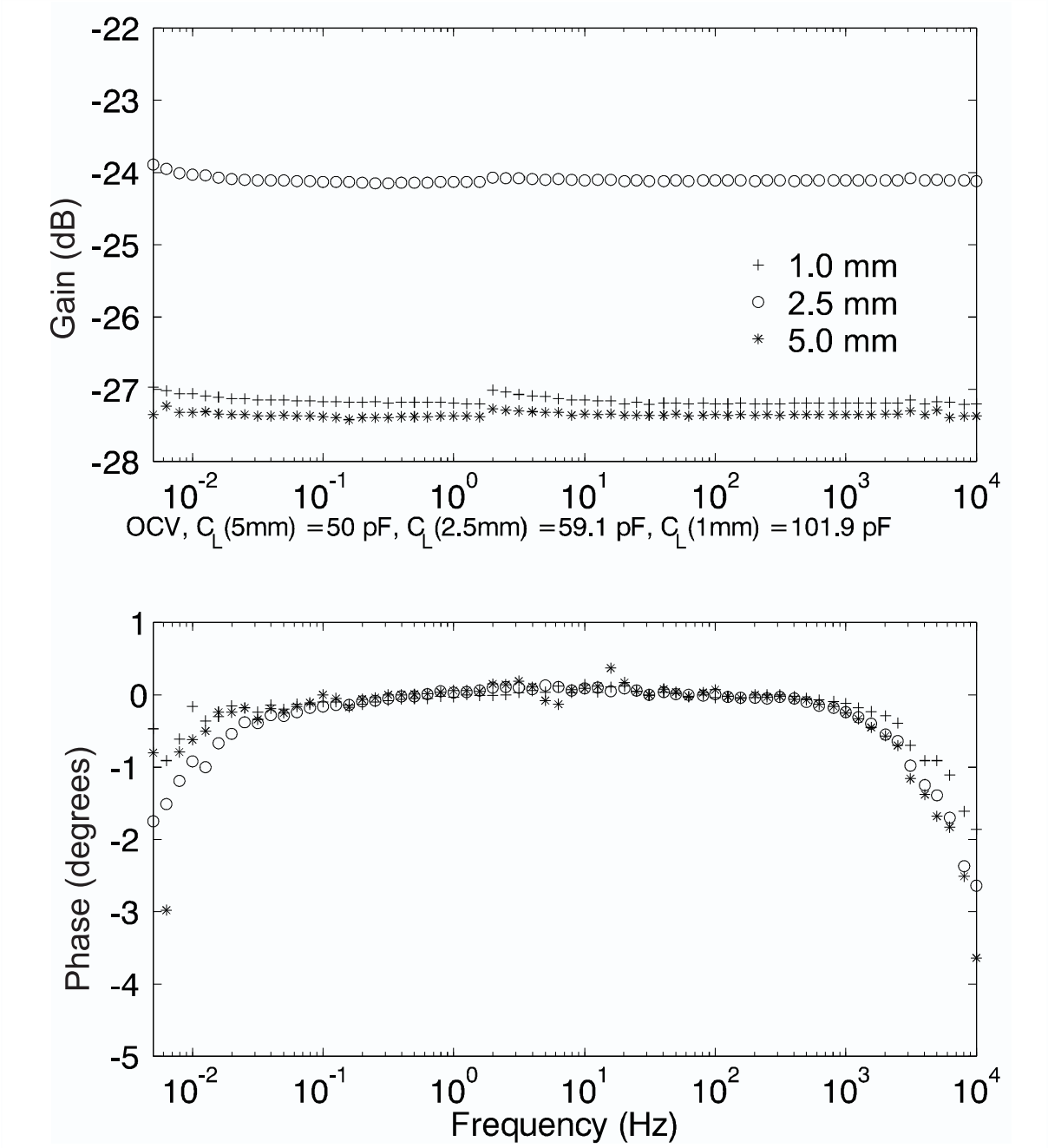

Figure 5.1: CuFlon floating voltage mode circuit gain/phase sensor response in air after regular cleaning but before ultrasound. At this point, the sensor surface is brownish and it is not suitable for very low frequency measurements (below 10^{-1} Hz). The high frequency roll-off is due to the speed limitations of the high input impedance operational amplifier (AD549). It can be accounted for in software.

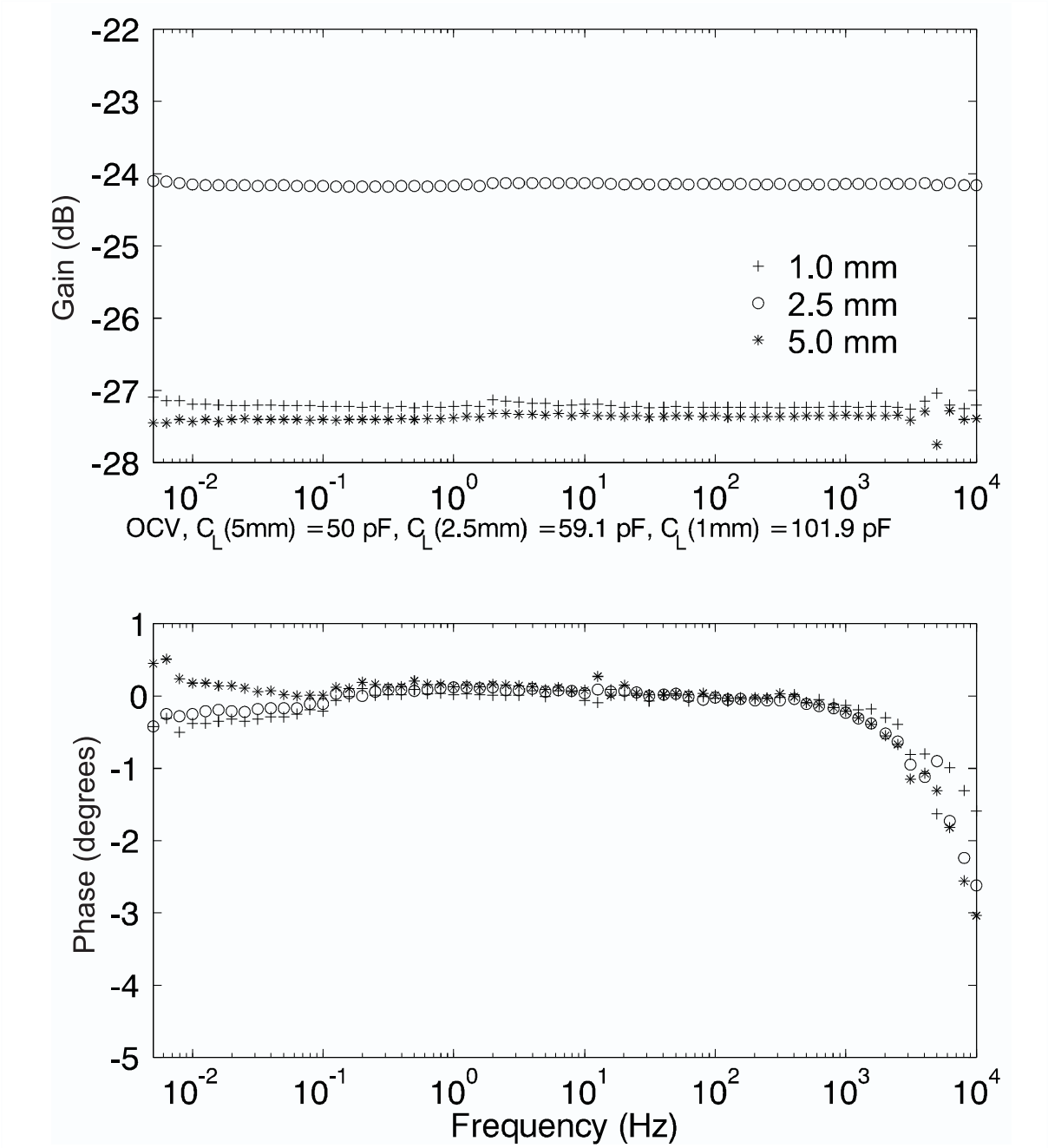

Figure 5.2: CuFlon floating voltage mode circuit gain/phase sensor response in air after ultrasound treatment described in Appendix A. The sensor surface is paper-white, and the gain/phase response is sufficiently flat for the entire range of frequencies.

Wavelength	λ= 1.0 mm		λ= 2.5 mm		λ= 5.0 mm	
Load cap, pF	Nominal	Measured	Nominal	Measured	Nominal	Measured
Kapton sensor	56.0	59.7	20.0	23.3	0	3.3
Teflon sensor	100.0	98.6	47.0	47.4	47.0	49.2

Table 5.1: Typical values of load capacitances for many of the reported measurements, using procedure described in Section 5.3.1. The difference between nominal and measured values is due to precision limitations of test capacitors themselves, stray capacitance of the leads, and the gate capacitance of the operational amplifier.

$$C_L = \frac{(1 - G_V)}{G_V} C_{12}^t \tag{5.1}$$

where C_{12}^t is the known test capacitance and the voltage gain in volts V_S/V_D in terms of the voltage gain in dB ($G_{dB} = 20log(V_S/V_D)$) is equal to

$$G_V = 10^{G_{dB}/20}. \tag{5.2}$$

Then, the calculated value of the load capacitance can be used to determine the value of the capacitance between the driven and sensing electrodes of each wavelength for the material under test.

$$C_{12} = \frac{G_V}{(1 - G_V)} C_L. \tag{5.3}$$

5.3.2 Measurement of Interelectrode Capacitances

With the wavelength of the interdigital structure being on the order of millimeters, the capacitance C_{12} between the driven and the sensing electrodes is around one pF, while the capacitance C_{20} between the sensing electrode and the ground plane is on the order of tens of pF. If the material above the interelectrode structure is highly insulating ($\omega C_{12} \gg G_{12}$), the gain G in (4.1) is real, and it provides only one equation for two unknowns (C_{20} and C_{12}). Similarly, if the test material is sufficiently conductive ($G_{12} \gg \omega C_{12}$) to cause a phase shift in the divider's response, only two equations are available for the four unknowns (C_{20}, C_{12}, G_{20}, and G_{12}).

In the case of very low conduction, one may try to add a resistor or a capacitor of known value to either branch in order to provide additional equations with the same

unknowns. However, the precision of such an approach proved to be low because the nominal values of circuit elements must be very precise to give reproducible results. A sufficiently precise and practical procedure for measuring the capacitance of interest follows. Since the capacitance C_{20} is relatively high, it can be measured using a conventional impedance meter in a standard three-terminal connection scheme where drive and sense electrodes are driven at the same potential with respect to the ground plane electrode.

Since the value of C_{12} is too low for conventional meters, it can be determined using (4.2) for the existing capacitive divider after C_{20} has been found. Alternatively, C_{20} can be eliminated in this part of the measurement by connecting it to a guard electrode, whose voltage follows the voltage on the sensing electrode. The measurements of G_{20} and G_{12} are performed in the same fashion, except for the fact that the equation for the gain becomes complex instead of real.

5.3.3 Surface Conductivity

Almost any residue on the sensor surface gives rise to surface conductivity. In most cases, this is an undesirable effect as it introduces an uncontrollable phase shift into the sensor signal, such as the one shown in Figure 5.1. Possible reasons for this residue are fingerprints, condensed moisture, contaminants from solvents that remain on the surface after evaporation of the volatile liquids, corrosion sub-products, and dust.

5.3.4 Circuit Performance With Lumped Elements

When the distributed electrodes of the sensor are physically replaced with lumped elements (resistors and capacitors), the solution of both forward and inverse problems is very simple. If, in addition, C_{20} is considered a known, so that it lumps with C_L, the solution is trivial. Such a substitution of elements provides good benchmark cases for testing overall performance of the measurement circuitry. Another advantage is brought by simultaneous use of the lumped elements and the sensor in the resistive-capacitive

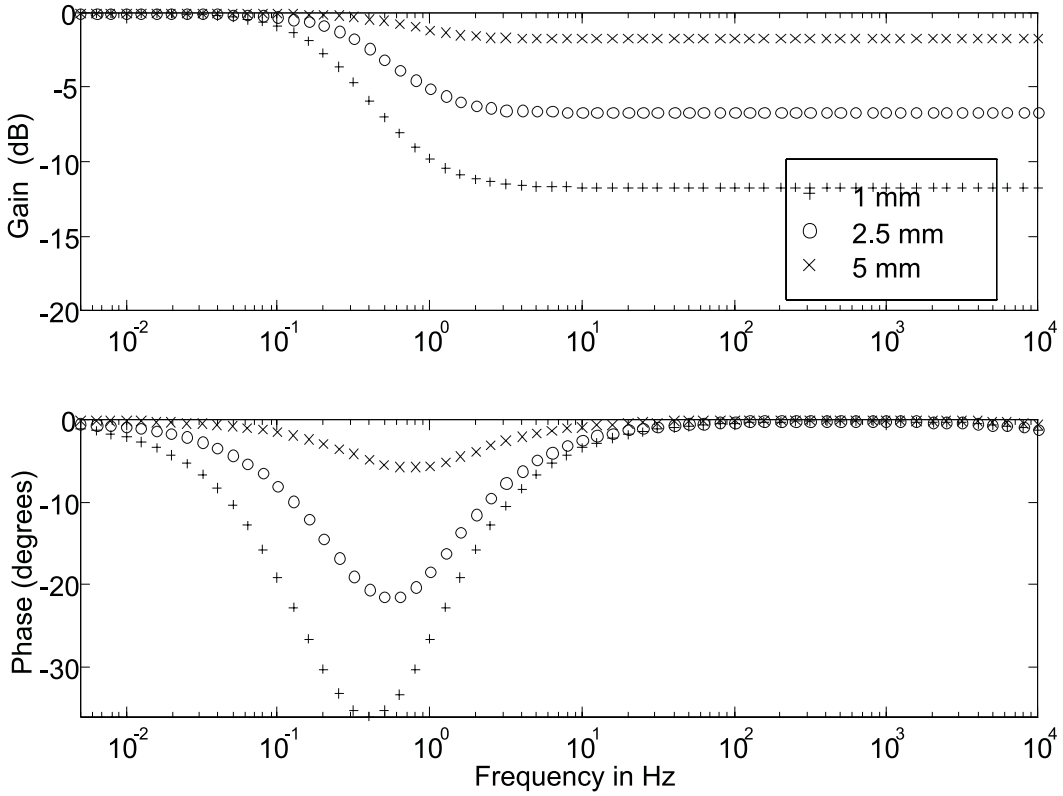

Figure 5.3: Results of the frequency sweep when ≈9.8 Gohm resistor and ≈20 pF capacitor are connected in parallel, between each sensing and driven electrode terminals. The legend gives correspondence to the interface channels that are normally used for the connection of the indicated wavelengths.

divider. Such a combination provides extra equations necessary for analyzing aberrant behavior of the sensor response, which occurs in many cases when the experiments are performed with conductive liquids or liquid-impregnated materials. The circuit response for each channel shown in Figure 5.3 is given simply to illustrate adequate performance of the measurement system and a basis for a calibration-based inversion algorithm. The theoretical Bode plots for given values of the resistors and capacitors show excellent agreement with experimental data.

Table 5.2(a) gives the values of resistors (nominal resistance 9.8 GΩ) estimated using a multivariable fit assuming that the independently measured values of the test capacitors C_{12} are correct. Table 5.2(b) shows the results of the same process except that R_{12} were considered known in this case.

(a)			(b)		
	C_{12} - given	R_{12} - estimated		R_{12} - given	C_{12} - estimated
1 mm	21.5 pF	9.5 GΩ	1 mm	9.8 GΩ	20.7 pF
2.5 mm	20.7 pF	9.5 GΩ	2.5 mm	9.8 GΩ	20.2 pF
5 mm	20.8 pF	9.2 GΩ	5 mm	9.8 GΩ	19.5 pF

Table 5.2: Testing of measurement circuitry using known lumped elements. C_{12} was independently measured and the nominal resistance of R_{12} of 9.8 Gohm was estimated using a multivariable fit. Then, R_{12} was independently measured and the nominal capacitance of C_{12} was estimated using a multivariable fit.

5.4 Shielding

Proper shielding is important for accurate measurements in the frequency range close to the 60 Hz power frequency, especially when the signal level is weak. Figure 5.4 shows an example of a fairly noisy measurement with the Kapton sensor placed on the top of a workbench, without any metal shielding around it. Signal noise can be greatly reduced using a highly conducting shielding material whose thickness is unimportant at these frequencies. Common aluminum foil is perfectly adequate. The shielding of the sensor leads is a separate issue. It is desirable that a grounded or guarded coaxial cable delivers the signal from the sensor head to the interface in order to avoid excessive noise and crosstalk between the channels.

5.5 Time Domain Measurements

5.5.1 Start-up Transients of Sinusoidal Signals

When a sinusoidal drive signal is turned on, an initial transient process takes place. While time domain measurements represent a separate field of research, their simplest use is for diagnostics of the measurement equipment. A controller command of the form `[GP, -1.3, -1.5, 1, E, D, D, D, E, D]` can be used to record the time-domain signals. This command initiates a frequency sweep over three frequencies, $10^{-1.3}$ Hz, $10^{-1.4}$ Hz, and $10^{-1.5}$ Hz and enables data recording on the first channel of the controller

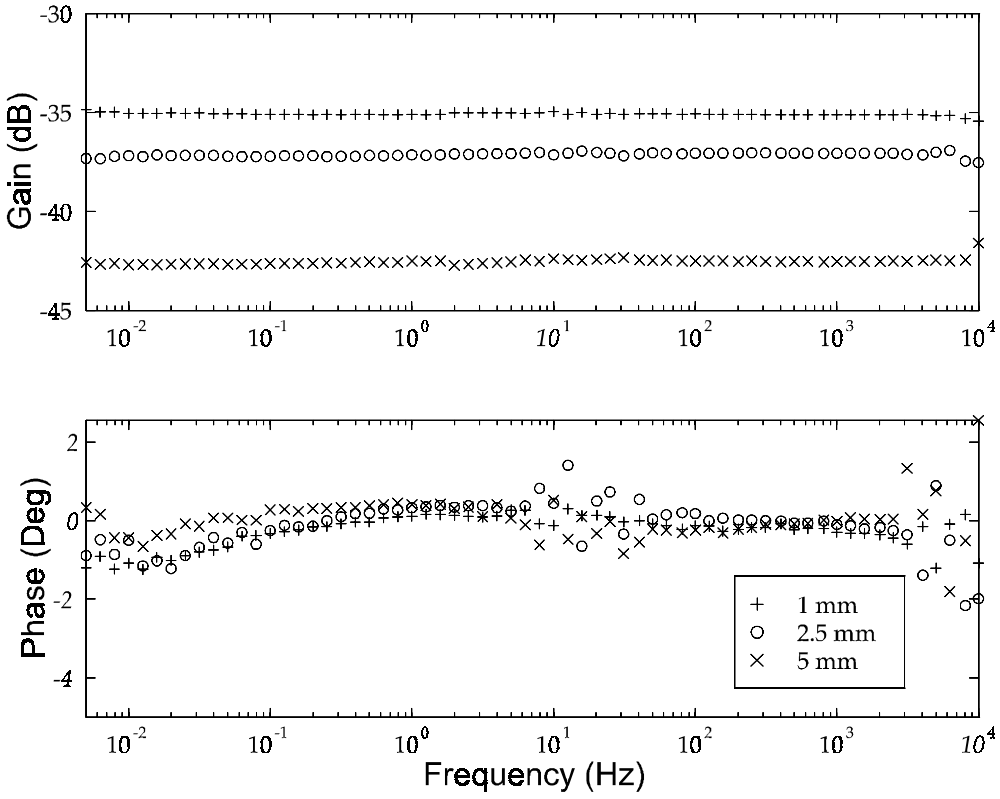

Figure 5.4: Unshielded Kapton sensor - full frequency sweep in air. Values of load capacitances are given in Table 5.1. Phase is close to zero and the gain is flat over the entire frequency range since the interelectrode admittance is purely imaginary and frequency independent. The noise around 60 Hz is due to the lack of shielding.

in the diagnostic mode. This command is used to record the transient signals. See Appendix C for definitions of controller commands.

Illustrative time-domain measurement data are shown in Figure 5.5 and Figure 5.6 during a three data point interval of the frequency sweep at approximately 0.05 ($10^{-1.3}$) Hz, 0.04 ($10^{-1.4}$) Hz, and 0.03 ($10^{-1.5}$) Hz on the 5 mm wavelength sensor immersed in corn oil. Data are taken at a sampling frequency of 10 Hz divided over two channels (drive and guard electrodes), that is a new data point is taken every 0.2 seconds. One can see that the switching transient is of a very short duration for the driven voltage in Figure 5.5. The voltage on the sensing electrode cannot be measured directly, because the measurement current itself would load the signal in such a high impedance

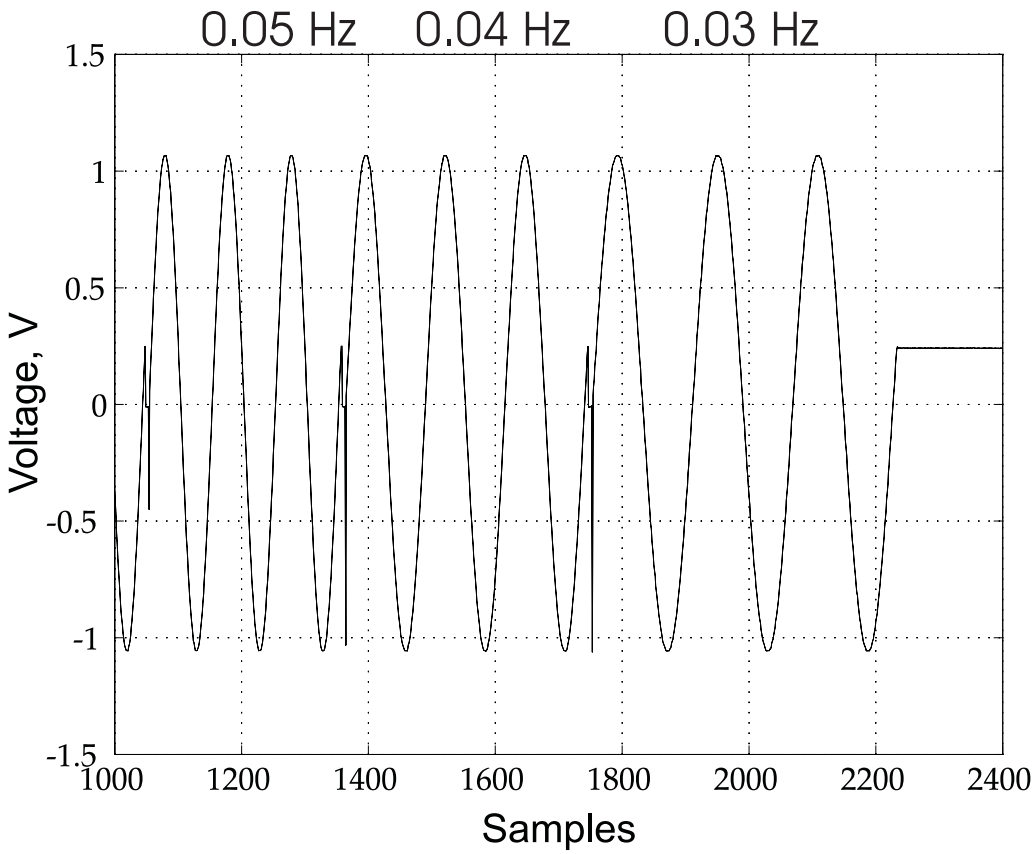

Figure 5.5: Driven electrode time-domain sinusoids with three measurement points taken at 0.05 Hz, 0.04 Hz, and 0.03 Hz. The time interval between samples is 0.2 seconds.

application. The guard voltage, equal to the sensing electrode voltage, is shown in Figure 5.6. The sensing electrode voltage can be viewed as a combination of particular and homogeneous solutions of a differential equation approximately describing the distributed circuit of the sensor. Sinusoidal steady state is nearly achieved by the end of the third cycle, which is used for measurement of gain and phase of a capacitive divider. The residual DC offset is accounted for in associated controller firmware by subtracting an estimated value of residual DC offset from the signal during the third cycle of the measurement.

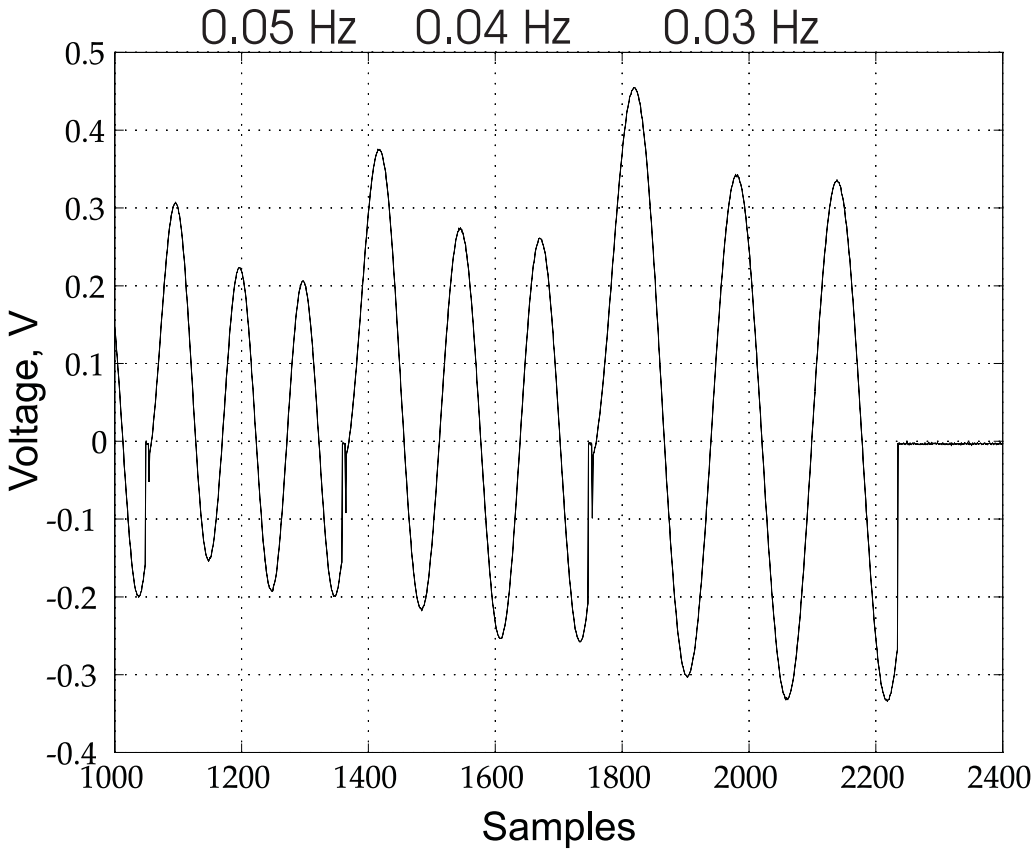

Figure 5.6: The 5 mm wavelength guard electrode time-domain response in corn oil for the driven electrode signal shown in Figure 5.5. The time interval between samples is 0.2 seconds.

5.5.2 Time-domain Response to a Step or Pulse Excitation

It would be an interesting project to apply a step or pulse voltage to the electrode structure and to relate the time-domain response to the frequency sweep data. Advantages of using a step voltage include possible information about short relaxation time phenomena and increased speed of measurements, important in such applications as landmine detection and surface inspection of plastic components. A single step, pulse, or impulse voltage contains information from all frequencies and may be a more effective excitation than to perform many separate measurements over a wide frequency range.

Theoretically, the same information about the material under test can be extracted

from the frequency sweep, step, pulse, or impulse excitations. Some impedance spectroscopy analyzers operate in this regime. A Fast Fourier Transform is often used to relate the frequency sweep response to the step response. One advantage of the pulse excitation vs. frequency sweep is that the measurement time is significantly reduced in the former case. The total measurement time is a critical parameter for a large number of field applications, where the sensor is used to scan large areas. It is also important for the measurement of fast-changing properties, for example, a drying process that lasts a few minutes. On the other hand, the pulse excitation entails a significant computational burden and may also lead to ambiguity in the interpretation of results. Ever increasing speed of computers and sophistication of signal processing algorithms will probably eventually leverage for pulse excitations.

Figure 5.7 shows the 5 mm wavelength interdigital sensor sensing and guard response to a drive voltage step down excitation. In this experiment, the sensor is immersed in transformer oil. Potentially, step or impulse responses contain as much information about material properties as do the frequency sweeps. Application of time domain spectroscopy techniques to interdigital dielectrometry is a valuable topic for future research.

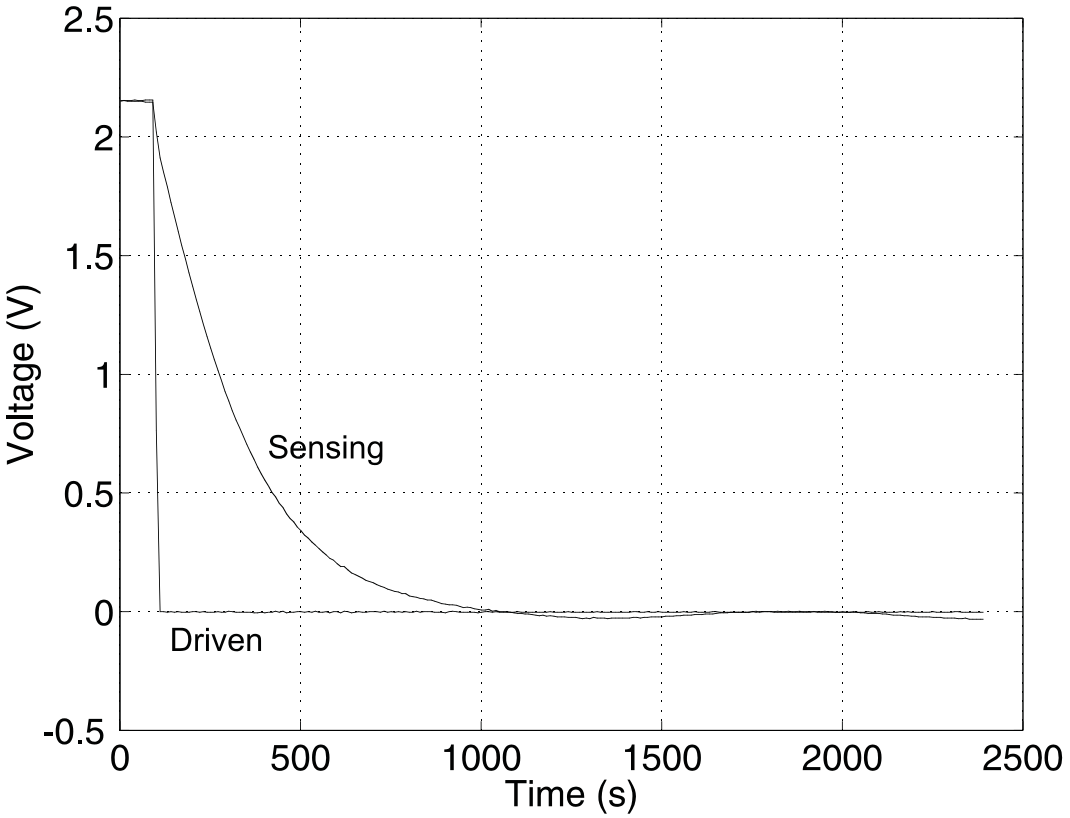

Figure 5.7: The 5 mm wavelength interdigital sensor response to a step excitation. A DC voltage of 2.15 V on the drive electrode is stepped down to zero V causing an exponential decay of electric potential on the sensing and guard electrodes. The sensor is immersed in transformer oil, whose dielectric properties ($\varepsilon_r = 2.2$, $\sigma \approx 10^{-13}$ S/m) determine the dynamics of the exponential decay. The small oscillatory trail behavior is characteristic and could be studied closer in the future.

5.6 Parallel Plate Capacitor Cells

5.6.1 Background

The parallel plate capacitor cells are classic in dielectrometry. An overwhelming majority of studies of dielectrics in materials science, semiconductors, electrochemistry, and polymer science involve parallel plate capacitors. Their major advantage is uniformity of the applied electric field and simplicity of equations that relate material properties with terminal electrical parameters. For homogeneous material with dielectric permittivity ε and conductivity σ that fills a parallel plate capacitor with electrode area A and a distance between the plates d, the capacitance is equal to

$$C = \frac{\varepsilon A}{d} \tag{5.4}$$

and the conductance is equal to

$$G = \frac{\sigma A}{d} \tag{5.5}$$

It is important to recognize that the measurement error introduced by changes in geometrical parameters in a parallel plate cell affects equally the estimated values of the dielectric permittivity (ε') and the dielectric loss factor (ε''). For this reason, the loss tangent ($\varepsilon''/\varepsilon'$) is often used for conventional parallel plate measurements [65].

5.6.2 Design

Several parallel plate capacitors had been designed to characterize insulating materials of interest. Figure 5.8 shows a parallel plate capacitor built by Yanko Sheiretov [10] for measurements of the complex dielectric constant of solid, elastic, and liquid material samples with thickness on the order of several mm. It is a classic design in which sensing electrodes are surrounded by a guard electrode, at the same potential as the sensing electrodes in order to guarantee a uniform electric field across the plates. Later, the sensor was replaced with a mechanically simpler and topologically equivalent design shown in Figure 5.9. The top and bottom views of the latter capacitor are shown in

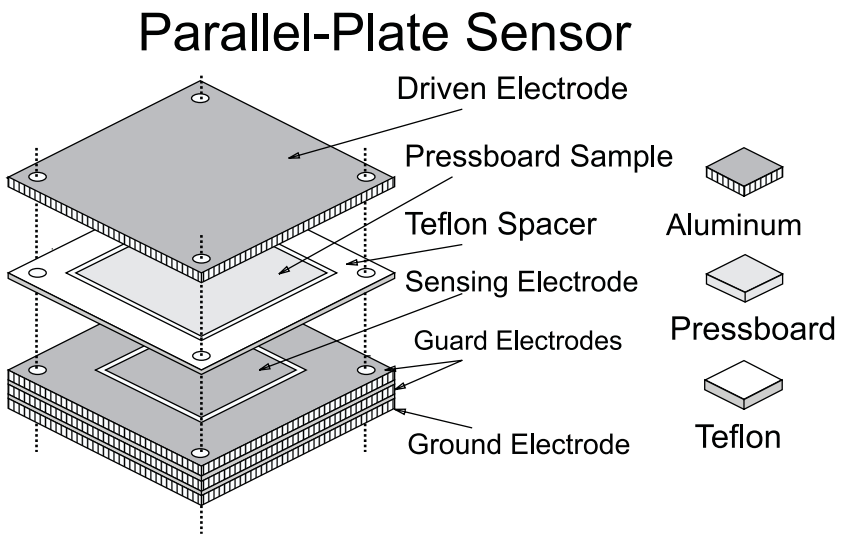

Figure 5.8: Guarded parallel-plate capacitor with surrounding guard electrodes to improve shielding [10].

Figure 5.10. These capacitors perform well with fluid, elastic, and granular dielectrics, where the appropriate contact between the capacitor plates and the material can be achieved. However, solid materials almost always incur a small air gap, which introduces an error to the measurements. Therefore, the dielectric properties of solid materials in this thesis have been measured using either a conductive adhesive copper tape or by spraying the sample surface with a conductive paint and forming appropriate electrodes by grooving the resulting layer of paint. Figure 5.11 shows an example of such a parallel plate capacitor formed on the sample of polymer material. In some cases it was desirable to build up the surface of parallel plates in order to increase the measured capacitance and conductance. Figure 5.12 shows a variable capacitor used for measurements with several liquid dielectrics.

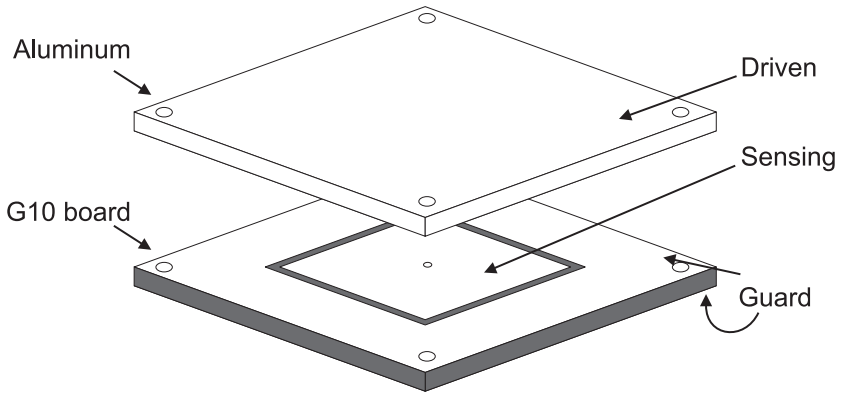

Figure 5.9: Simpler guarded parallel-plate capacitor constructed by manually removing a rectangular insulation strip to separate guard and sensing electrodes.

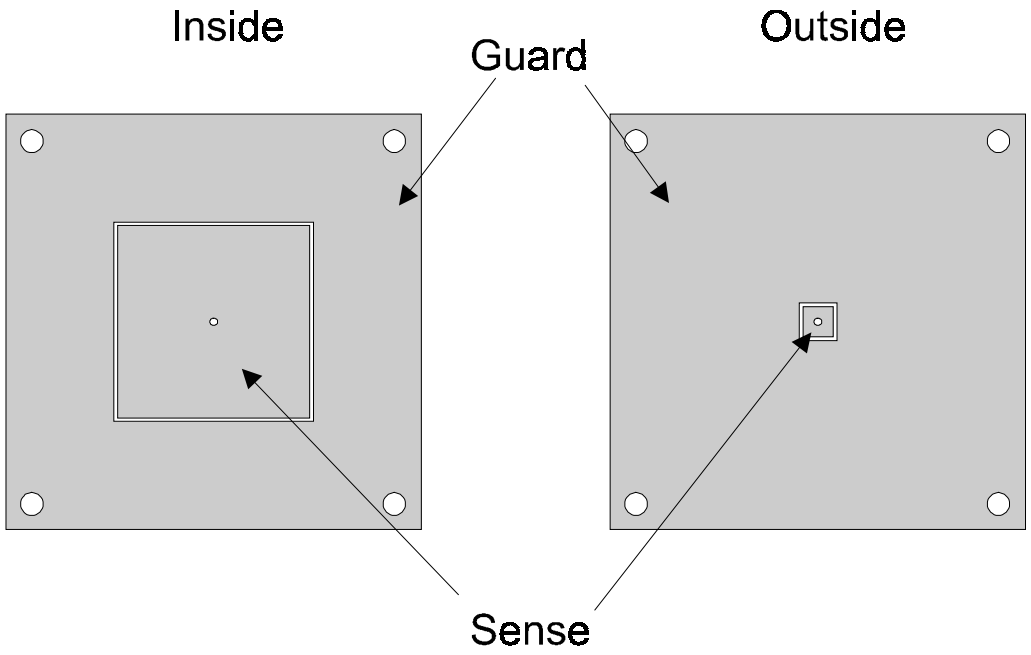

Figure 5.10: Top and bottom views of the guarded parallel-plate capacitor of Figure 5.9. The through hole at the center connects the guarded sensing electrode lead to the sensing electrode.

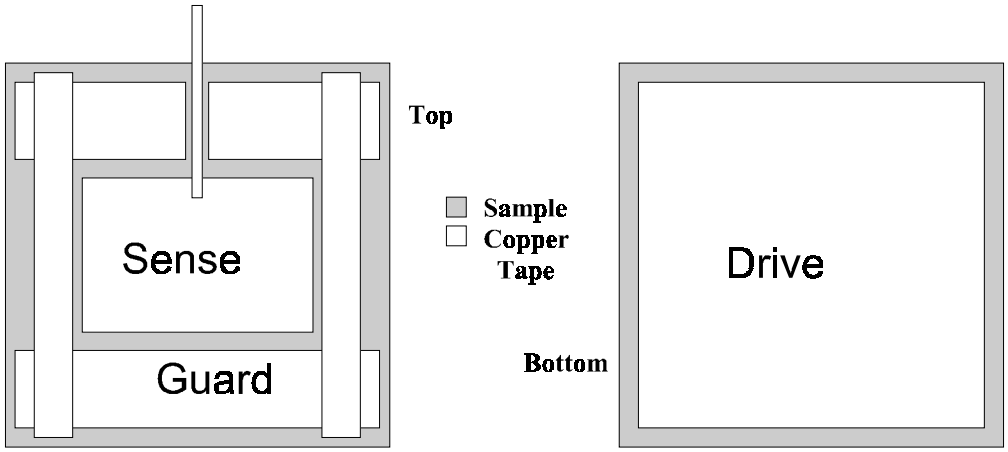

Figure 5.11: A guarded parallel plate capacitor formed with conductive tape (to achieve good surface contact) on the slab of a solid polymer.

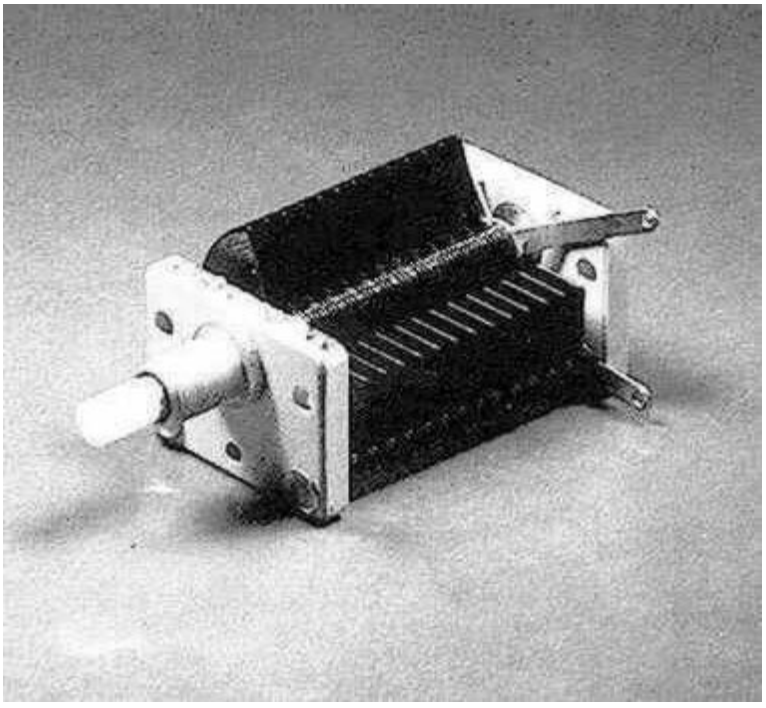

Figure 5.12: A variable tuning capacitor used as a parallel plate cell in measurements with fluid dielectrics [279].

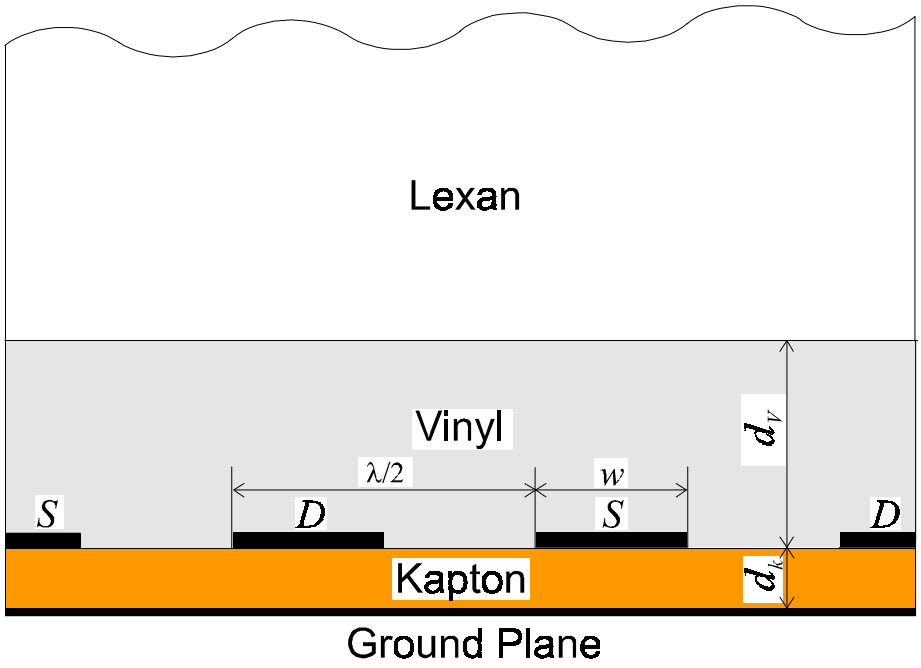

Figure 5.13: The cross-section of the interdigital sensor with two layers of materials above it.

5.7 Early Measurements with the Kapton Sensor

The goal of the series of experiments presented in this section is to test the dependence of the sensor response on the thickness of the material above the sensor. Figure 5.13 depicts the cross-section of the experimental setup. Two materials with known properties form a two-layer medium. When the thickness of the lower material is reduced, the interlayer boundary moves down, and the influence of the upper material increases. The upper material is thick enough to be considered infinitely thick.

Two commercially available insulating polymers, monolithic 1/2 inch thick pieces of Lexan®(GE polycarbonate brand name) and 0.19 mm thick vinyl, had been used. The thin film enables us to control the thickness of the test sample by changing the number of sheets of vinyl. In order to press the whole structure together and provide a good contact between the materials, a heavy slab of lead had been positioned on top of the test cell. In general, highly conductive metal would strongly affect the distribution of

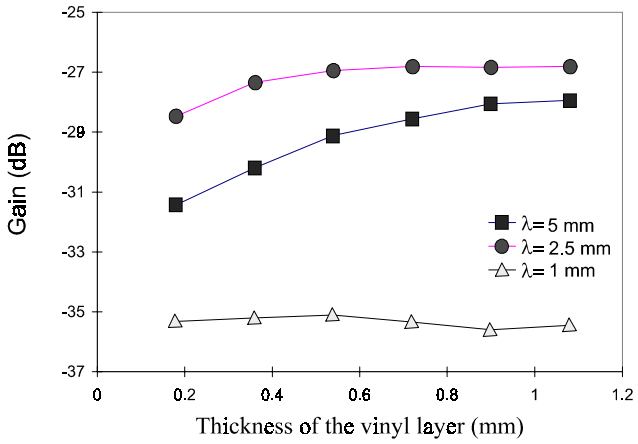

Figure 5.14: Experimental estimation of the effective penetration depth of the three-wavelength sensor as the thickness of the vinyl layer in Figure 5.13 is increased.

the electric field in the studied region, unless it was sufficiently far from the strong field region. It can be seen from (1.1) that the electric potential induced by the sensor dies away exponentially in the vertical position with the penetration depth of $\lambda/3$ (except for the zero order spatial harmonic). Let us denote the distance at which the electric field potential reduces by one order of magnitude as an effective penetration depth of our sensor. The total thickness of Lexan was 17 mm, which is about 10 times the effective penetration depth of the largest wavelength.

The schematic view of the experimental setup in Figure 5.13 shows one and a half periods of the interdigitated electrodes. The character D refers to the driven electrode and S refers to the sensing electrode. A one volt peak sinusoidal voltage was applied to the driven electrode. The voltage magnitude and phase of the sensing electrode was measured and recorded. As the distance d_v becomes smaller the influence of dielectric properties of the Lexan becomes stronger, which is illustrated in the following sections.

The dielectric permittivity of the materials was also determined using a parallel-plate capacitor of known geometrical dimensions with (5.6), which is approximately

valid for a rectangular sample with no guard electrodes:

$$\varepsilon_a = \frac{\pi \cdot C}{L + W + W \ln\left(\frac{\pi L}{d}\right) + L \ln\left(\frac{\pi W}{d}\right) + \frac{\pi L W}{d}}, \tag{5.6}$$

where L and W are the length and width of the parallel-plate capacitor, d is the distance between the plates, and C is its capacitance. Equation (5.6) takes into account the fringing fields of a parallel-plate capacitor and is derived using a Schwarz-Christoffel transformation [280].

The relative dielectric permittivity of the polycarbonate Lexan sheet has originally been estimated using (5.6) to be equal to 2.6, and that of vinyl film to equal 3.8. These estimates were done at the very beginning of the project, and the values of dielectric permittivity are lower than they should be. A better estimate for Lexan is $\varepsilon_r = 3.01$, and the estimate for vinyl remains the same. The reason for this error was the air gap between the solid electrodes of the parallel plate capacitor and the solid surface of the samples. In the subsequent measurements, the dielectric permittivity of these materials had been determined with much greater accuracy, and the prior values had no effect on this study. The conductivity of Lexan is on the order of 10^{-15} S/m and in our frequency range its effect is negligible. The conductivity of vinyl is on the order of 10^{-9} S/m, and the vinyl appears to be a dispersive material. Only qualitative discussion of conductivity effects is given in this section.

As discussed above, according to the idealized model, the effective penetration depth of an interdigital sensor is about one-third of the sensor's spatial wavelength λ. For the sensor used in this experiment, the metallization ratio was close to 0.5 for 5 mm and 2.5 mm wavelengths, and it was about 0.36 for the 1 mm wavelength due to manufacturing imprecision. The measured gain at high frequency (1 kHz) is shown in Figure 5.14 for all three wavelengths. A good correspondence with the theory can be observed. The smallest wavelength does not respond to the changes of the thickness because in almost all cases it exceeds one-third of 1 mm. The response of the 2.5 mm structure flattens off at about 0.7 mm, and for 5 mm at about 1.2 mm. It should be noted, however, that since the distinction must be made between levels of attenuation which differ only

by 1 or 2 dB, the sensitivity to the error in such measurements is relatively high. Of course, if the difference between the values of the dielectric permittivity of the two materials was larger, the effect of the movement of the interlayer boundary would have been more observable.

As seen from Figure 5.14, given the geometrical dimensions of this setup, the measurements with the 5 mm wavelength are the most descriptive in terms of sensitivity of the sensor to the position of the interlayer boundary. The results of the frequency scans of setups with varying thickness are shown in Figures 5.15 and 5.16.

Since the dielectric permittivity of vinyl is higher than that of Lexan, the equivalent capacitance measured by the sensor becomes smaller as the distance d_v decreases. Thus, the gain shifts towards the flat gain of the non-conductive Lexan-insulated interdigital capacitor. As the frequency is lowered, the slightly conductive vinyl makes the test cell behave like a first order system with one pole and one zero in the transfer function. It has a minimum in the phase-frequency curve whose position is determined by the location of the pole and zero (see Figure 5.16). It should be noted that depending on the ratio of interelectrode capacitances and conductances, and the load capacitance, the phase minima may shift either to the left or to the right, since the conductivity of Lexan is lower, and the dielectric permittivity is lower than that of vinyl.

In the curves shown in Figure 5.15, the small negative phase-shift is not considered, primarily because it does not affect the overall estimation of the effective penetration depth. In the graphs shown in Figure 5.17, the gain, measured at the frequency of 10 kHz (the right-most data points in Figure 5.15, curve 1), is compared with the gain calculated with a finite-element electric and magnetic field calculation package *Maxwell* from Ansoft Corp. (curve 2). The slight irregularity of the shape of the experimental curve 1 is mostly due to the operational amplifier speed limitation at 10 kHz. The highest frequency of the sweep had been used to reduce effects of the conductivity on the output data.

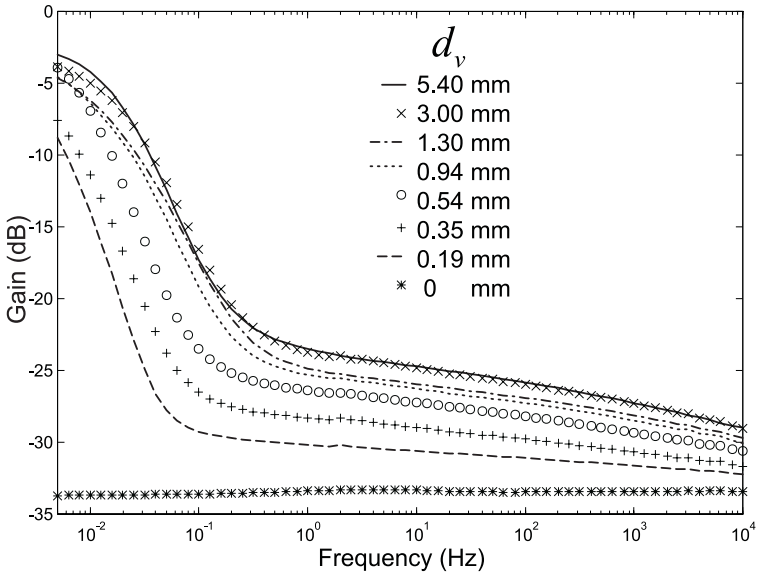

Figure 5.15: Measured response of the circuit gain to the movement of the interlayer boundary by increasing the thickness of the vinyl layer, d_v, as shown in Figure 5.13.

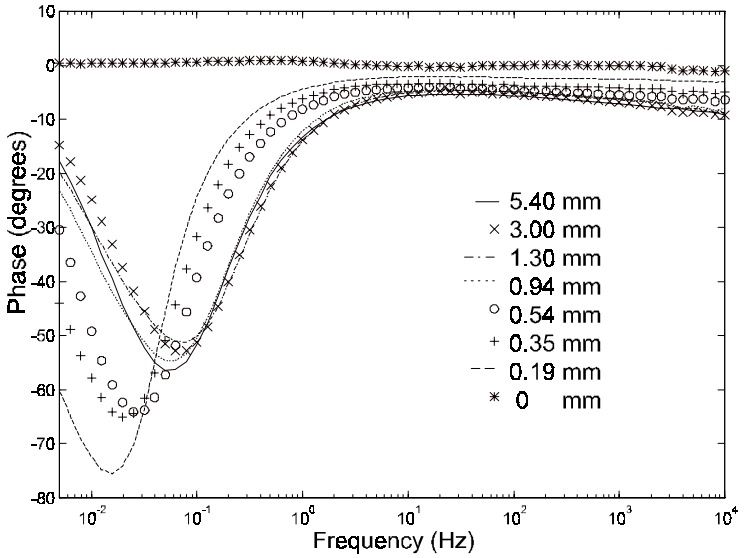

Figure 5.16: Measured response of the circuit phase to the movement of the interlayer boundary by increasing the thickness of the vinyl layer, d_v, as shown in Figure 5.13.

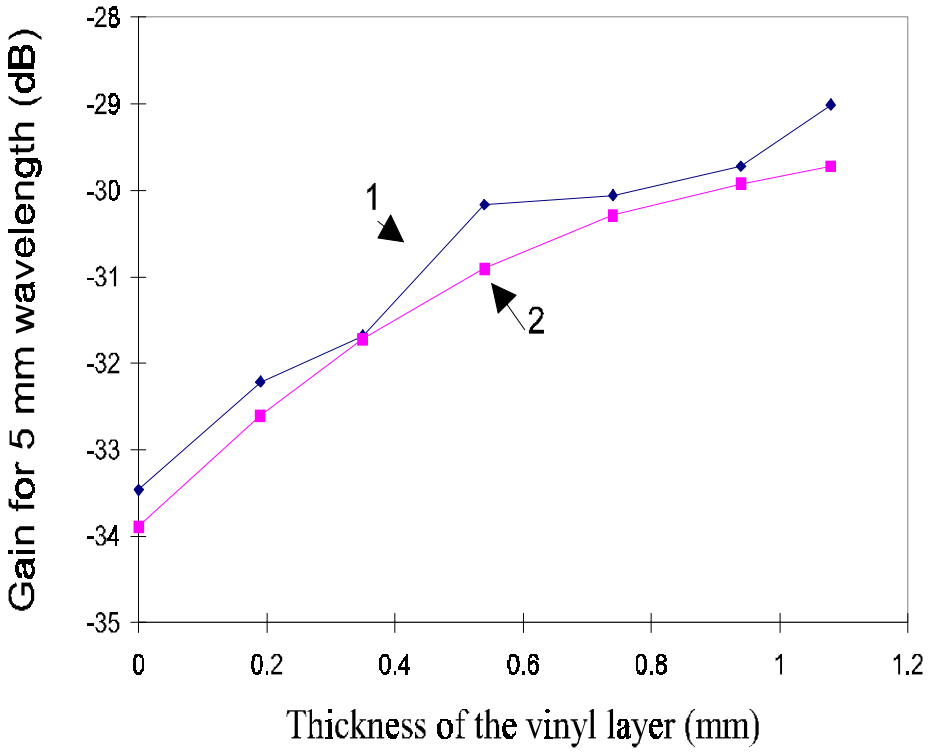

Figure 5.17: Comparison of the measured (1) and theoretical ($\varepsilon_r = 2.6$ for Lexan and $\varepsilon_r = 3.8$ for vinyl) (2) response of the 5 mm interdigital sensor at 10 kHz.

5.8 CSC Sensor versus Three-Wavelength Sensor

5.8.1 Motivation

Model-based multi-wavelength interdigital dielectrometry parameter estimation algorithms require a good agreement between theory and measurements. Research data indicate that the agreement is high for measurement of the properties of fluid dielectrics or the sensor substrate. However, the non-ideality of the surface contact between the sensor and solid materials creates significant differences between the idealized model and experimental results. One solution to this problem is to evaluate surface contact conditions for every measurement and account for them in software. Two alternative

sensor designs are compared in this section in their ability to provide reliable measurement data that can be used by parameter estimation algorithms. Measurement of dielectric and conduction properties of both fluids and solid dielectrics are considered. It is shown that the distribution of the electric field excitation over the entire multi-wavelength sensor head, as opposed to using separate electrode wavelengths, leads to reduction of errors in parameter estimation.

Recent work with interdigital dielectrometry sensors demonstrated that measurements of the fluid properties and the sensor substrate properties can be modeled accurately in most cases [17]. However, the parameter estimation of solid dielectrics is more complicated due to the presence of microcavities formed when the sensor and the material under test are brought into direct contact [18]. Conceivably, it is possible to treat this layer of microcavities as an additional layer whose properties and effective thickness must be estimated. Early implementations of such an approach with a three-wavelength interdigital sensor demonstrated that the parameter estimation based on the assumption of a homogeneous microcavity layer tends to produce inaccurate results because the distributed sensor electrode structures had different thicknesses of the microcavity layer at different sensor locations. While the measurement error due to the microcavities may not be critical for simple tasks, such as measurement of properties of homogeneous materials, it plays an increasingly important role in the estimation of non-uniform material properties.

This paper offers a comparative analysis of performance of two different multiple penetration depth sensors. The first design, the three-wavelength sensor (TWS) offers the advantage of being able to choose any penetration depth combination in a single sensor head by varying appropriately the spatial periodicity of each electrode pair. The second design, the comb-serpentine-comb (CSC) sensor, restricts the choice of the combination of penetration depths, but has the advantage of confining fringing fields at different penetration depths to the same area of the material under test.

5.8.2 Topology of Both Sensors

The top view of the three-wavelength sensor used in this study is shown in Figure 4.5. It consists of three sets of topologically identical interdigital electrodes etched on a common flexible substrate with electrode spatial periodicities of 1.0 mm, 2.5 mm, and 5.0 mm. Each sensing electrode has five 50 mm long fingers. The gray shaded area indicates guard backplanes on the reverse side of the substrate. The highly hydrophobic Teflon substrate is 254 μm thick and has a relative dielectric permittivity ε_r of 2.1. The transconductance and transcapacitance between electrode combs is measured by driving one of them with a sinusoidal voltage signal and measuring the voltage at the other electrode, which is capacitively loaded.

Figure 4.9 shows the planar view of the comb-serpentine-comb (CSC) sensor. The top side of this sensor has three electrodes (upper comb, serpentine, and lower comb), all in the same plane, etched on the surface of a rigid substrate. The sensor was fabricated in the lab using a simple decal hot image transfer and etching with $FeCl_3$. The backplane electrode on the opposite side of the substrate covers the entire surface of the sensor head. The substrate material is fiber-glass reinforced Teflon with measured relative dielectric permittivity of 2.2. The thickness of the substrate is 1.57 mm and the thickness of the electrodes is 17 μm. The width of each electrode strip is 0.5 mm. Each digit of the sensor is 50 mm in length. The overlapping length of the line per half wavelength is 47 mm. The fundamental spatial wavelength of the sensor is 8 mm. The sensor used in these experiments contained 13 half wavelengths for a total meandering length of 611 mm. A floating voltage with guarded backplane mode has been used in measurements.

5.8.3 Quality of Contact

As already mentioned, quality of contact at the electrode-specimen interface is of great importance for many types of dielectric measurements. For example, in order to ensure an intimate contact in parallel plate measurements, standard procedures suggest

painting the electrodes onto the specimen surface with adhesive conductive paint or using liquid electrodes [281].

The importance of the surface and electrode effects in interdigital dielectrometry has been recognized for a long time [65]. Figure 6.20 shows a schematic half-wavelength wide cross-section view of the interdigital sensor in contact with a solid material under test. The cavities that form between the electrodes and the material under test affect the capacitance between the driven and the sensing electrodes. Several solutions were proposed to account for the cavities. An earlier approach to parameter estimation assumed that the effect of microcavities between the electrodes and the material under test is negligible. A quantitative analysis of these effects is available in [18]. Among other results, this analysis demonstrates that the equivalent air gap between the electrodes and the material under test would have to be on the order of 30 μm in order to offset the capacitance between the electrodes to the level indicated by measurements. In that analysis, the air cavity due to the thickness of electrodes is accounted for separately by calibration of the sensor signal.

It should be noted that the surface roughness of the electrodes and the material under test itself is significantly smaller than the evaluated equivalent air gap. Figure 6.21 shows the results of a surface scan with a profilometer over a 1 mm wavelength electrode. The difference between the highs and lows of each electrode section is on the order of 1 μm, which is clearly not sufficient to account for the difference between the theoretical and measured capacitance. This argument leads us to conclude that the total air gap is primarily due to a few irregularities, which may be electrode scratches or dust particles, as well as due to a global deformation of the sensor surface. It is possible to improve the contact by refining sensor attachment techniques, using more flexible substrates, etc. However, this will only alleviate the problem but will not remove it completely. A separate experiment indicated that no amount of pressure applied to the sensor can eliminate the contact quality effects.

Once surface effects are recognized as unavoidable, the next logical step is to account for them in software. If the experimental conditions, including pressure, temper-

ature, stiffness of the specimen, and the levels of air contamination and humidity stay approximately stable, the offset of the signal due to the air cavities stays within a sufficiently narrow range to be considered constant for each wavelength electrode. Then, this constant offset signal can be measured and built into the parameter estimation algorithms [21].

On the other hand, when the sensor is expected to operate in a variety of experimental setups, the offset due to air cavities varies significantly from one setup to another. The nature of multi-wavelength dielectrometry suggests that the equivalent thickness of the cavity layer can be measured in the same way that it is done for any other layer of a stratified specimen. However, the layer of cavities differs from the other layers of the stratified materials because the thickness of the layer is non-uniform, and it depends on the local contact conditions.

Theoretically, it is possible to estimate the thickness of the equivalent air gap using data from two wavelengths if the material under test is homogeneous. Thus, a three-wavelength sensor can produce three distinct numbers for the equivalent layer thickness. A number of experiments has shown that these numbers do not agree with each other. The discrepancy is due to differences in the actual cavity size across the sensor. The CSC sensor was developed to address this problem. In the CSC sensor, the entire head area is used for the measurement with different penetration depths, so that the micro-cavity geometry is the same for each penetration depth.

5.8.4 Computer Simulation

Penetration Depth

The concept of multiple penetration depths can be better understood by considering the following example. Imagine that we put a slab of a solid homogeneous perfectly insulating dielectric in air over the sensor head. Initially, the specimen and the sensor are in intimate contact (ideally). The cavity between the electrodes is filled with the same dielectric. Since the dielectric permittivity of the specimen is higher than

that of air, the capacitance between the two interdigitated electrodes increases with the thickness of the material layer. This process was simulated with finite element software, assuming that the relative dielectric permittivity of the specimen is $\varepsilon_r = 2.1$ (Teflon). Figure 5.18 shows the calculated change of capacitance in each of the three wavelengths of the three-wavelength sensor shown in Figure 4.5. The results of the simulation of the same experiment but with the CSC sensor are shown in Figure 5.19.

It is hard to judge from Figures 5.18 and 5.19 what is the effective penetration depth for each case. In order to better visualize the change of the sensor signal we plot the normalized change of capacitance with zero percent being the lowest value of the capacitance (corresponding to the zero thickness of the dielectric) and hundred percent being the highest capacitance value (when the increase of the thickness of the dielectric material no longer affects the capacitance). Figure 5.20 shows the normalized plot for the three-wavelength sensor. The change of capacitance reaches a 90 percent level at approximately one-fifth of the corresponding wavelength.

The fundamental wavelength of the CSC sensor is 8 mm. Because the arrangement of electrodes is no longer strictly interdigital, we may replace the wavelength of the previous case with the centerline distance between the corresponding pairs of electrodes. Then, the expected effective penetration depths for the CSC sensor are 400 μm, 1200 μm, and 1600 μm. Figure 5.21 confirms these expectations.

In-Plane Shielding

A potential disadvantage of the CSC sensor is a partial shielding of the electric field lines from the upper comb to the lower comb by the serpentine electrode. As a result, the capacitance between the upper and lower combs becomes smaller and, consequently, more difficult to measure accurately. Thus, it is beneficial to evaluate the reduction of capacitance caused by the partial, or in-plane shielding. Table 5.3 shows the capacitance matrix for the CSC sensor in air, with the serpentine electrode in place. Table 5.4 shows the capacitance matrix for the same case, but with the serpentine

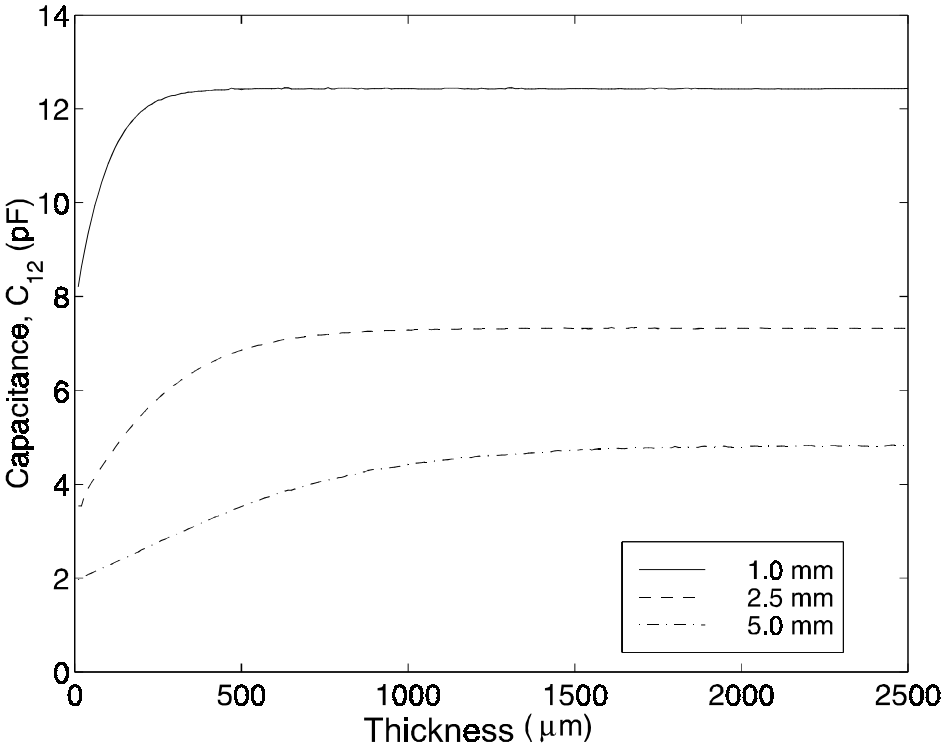

Figure 5.18: Calculated change of the interelectrode capacitance C_{12} with the increase of the dielectric thickness ($\varepsilon_r = 2.1$), with air above it, for each wavelength of the three-wavelength sensor.

electrode completely removed. The capacitance between the upper comb and lower comb changes by approximately a factor of 2.5. The effect of the in-plane shielding is significant, however, the reduced capacitance remains within a detectable range.

Measurements with Fluid Dielectrics

Measurements with fluid dielectrics are useful for verification of the numerical model of the sensor as they fill all cavities. They also provide calibration data for subsequent experiments. Figure 5.22 shows the results of the frequency sweep of the CSC sensor in air compared to the simulation data from the finite element software. The agreement between the theory and the measurements for all three pairs of electrodes at all frequencies except for the slightly noisy data around the power frequency is guaranteed by the nature of the calibration procedure. The electrode meander length was chosen

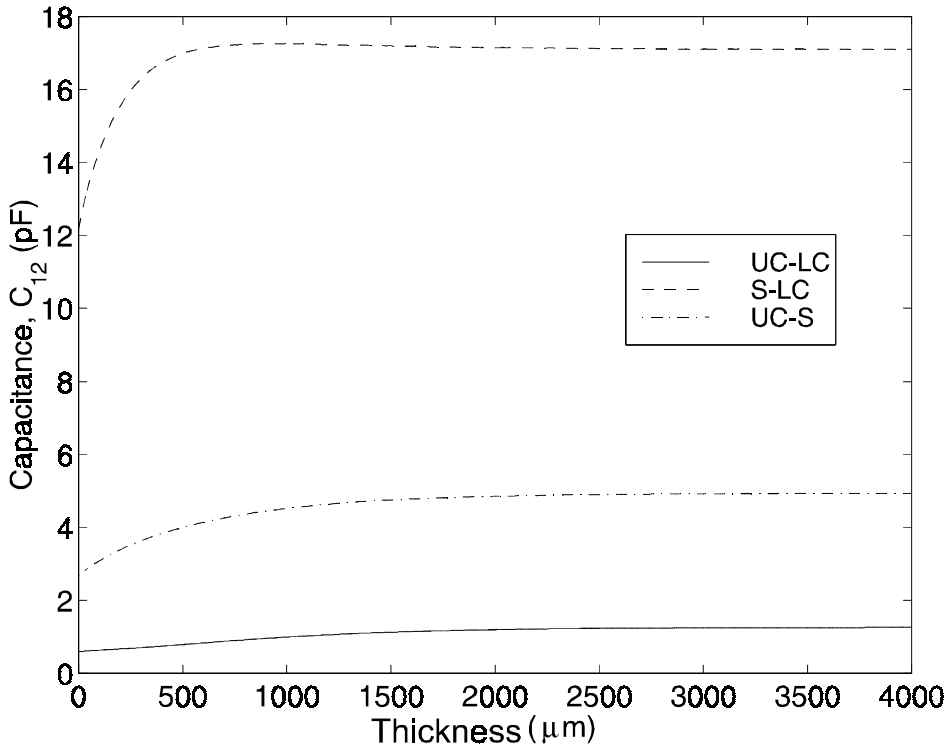

Figure 5.19: Calculated change of the interelectrode capacitance C_{12} with the increase of the dielectric thickness ($\varepsilon_r = 2.1$), with air above it, for each pair of electrodes of the CSC sensor. Legend: UC - upper comb, S - serpentine, LC - lower comb, as described in section 5.8.2.

to be the adjustable parameter. The values of 0.672, 0.670, and 0.639 m were chosen for the electrode pairs UC-S, UC-LC, and S-LC, respectively. These values exceed the previously mentioned nominal meander length of 0.611 m because the end effects at the edges of the sensor area and the sensor leads contribute to the increase of interelectrode capacitance.

Figure 5.23 shows the frequency sweep of the same CSC sensor immersed in transformer oil with $\varepsilon_r = 2.2$. Again, the agreement between the simulation and the measurement is very good for the S-LS pair and for the UC-LC pair. Measured capacitance is slightly lower than predicted for the UC-S pair, which is exactly what was expected in this case. Originally, this CSC sensor was not designed for measurements between the upper comb and serpentine electrodes because at that stage of research two pen-

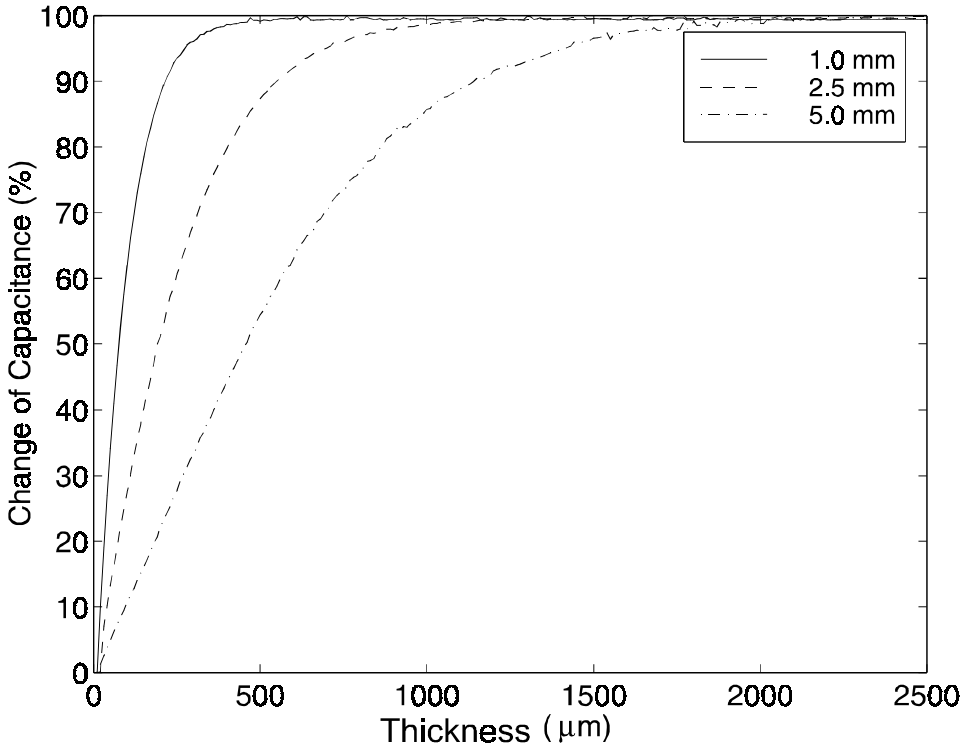

Figure 5.20: Calculated change of the interelectrode capacitance C_{12} of the three-wavelength sensor normalized to the highest and lowest capacitance values ($\delta C = (C - C_{min})/(C_{max} - C_{min})$) clearly illustrates the variation of the effective penetration depth with sensor wavelength as the $\varepsilon_r = 2.1$ dielectric thickness increases.

etration depths were sufficient. Because of that, the contact leads of the upper comb and the serpentine electrodes were placed close to each other (see Figure 4.9). The capacitance between the leads contributes to the total interelectrode capacitance in the capacitance matrix shown in Table 5.3. When the sensor is submerged in transformer oil to cover the sensor head, part of the contacts and leads remain in air. Thus, the proportional increase in the interelectrode capacitance was slightly smaller for the UC-S pair than would be expected from the theoretical model.

The results of similar measurements with the three-wavelength sensor are reported in [18] and in Section 6.4.3 of this thesis. They indicated good agreement between theory and measurements for all wavelengths at all measured frequencies.

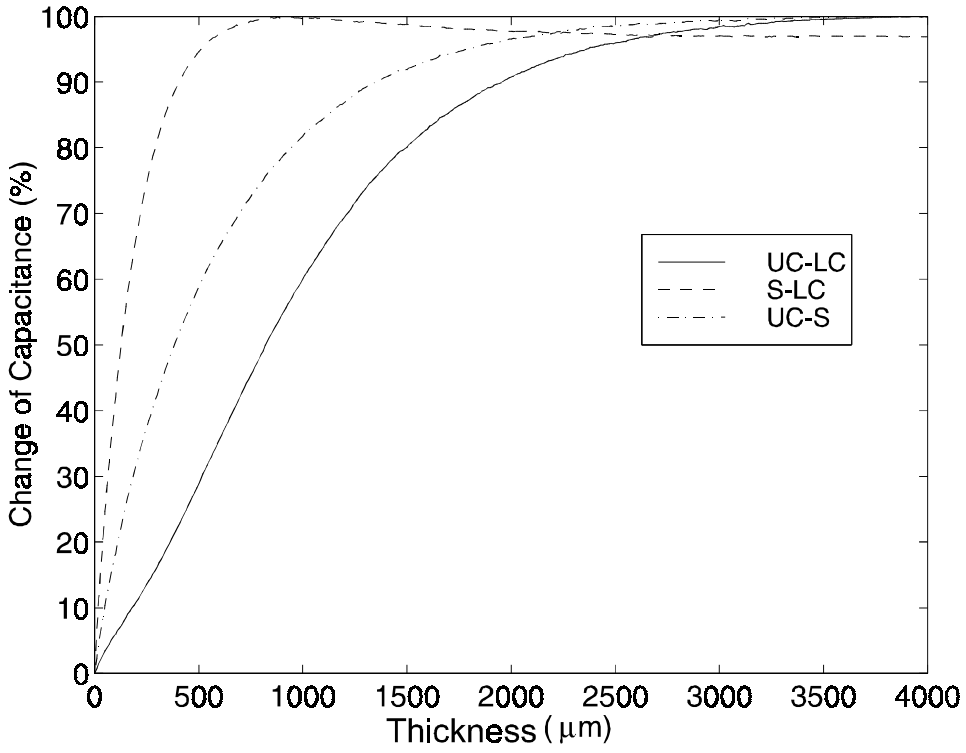

Figure 5.21: Calculated change of the interelectrode capacitance C_{12} of the CSC sensor normalized to the highest and lowest capacitance values also indicates the variation of the effective penetration depth as the $\varepsilon_r = 2.1$ dielectric thickness increases. Legend: UC - upper comb, S - serpentine, LC - lower comb.

5.8.5 Cross-correlation

Having demonstrated an adequate performance of both sensors with fluid dielectrics, we would like to evaluate one of the sources of errors that contribute to inaccurate estimates of the dielectric permittivity of solid dielectrics. The goal of this section is to present a statistical analysis of performance of the two types of multi-wavelength sensors, CSC and TWS, with a solid dielectric.

Figure 5.24 shows the results of 64 consecutive measurements with the same dielectric under slightly varying conditions. A block of Teflon was placed over the three-wavelength sensor and pressed down with a 10 kg weight. The Teflon sample was rotated 90 degrees between each of the 16 consecutive tests shown in Figure 5.24. Each of the 16 test groups contained four measurements triggered with approximately

	Lower Comb	Backplane	Serpentine	Upper Comb
Lower Comb	19.65	-6.95	-12.08	-0.624
Backplane	-6.95	36.54	-17.95	-11.64
Serpentine	-12.08	-17.95	32.72	-2.69
Upper Comb	-0.624	-11.64	-2.69	14.95

Table 5.3: Calculated capacitance matrix of the full CSC sensor of Figure 4.9. All capacitances are in pF/m. The comparison of selected calculated and measured values is in Section 5.8.4.

	Lower Comb	Backplane	Upper Comb
Lower Comb	14.74	-13.21	-1.534
Backplane	-13.21	26.38	-13.17
Upper Comb	-1.534	-13.17	14.71

Table 5.4: Calculated capacitance matrix of a CSC sensor with the serpentine electrode removed. All capacitances are in pF/m.

10 second intervals. The purpose of such sequencing was to differentiate and compare the instrumentation noise with the variation of this signal due to the specimen positioning. In addition, the surface of the sample was slightly roughened in order to bring the signal variation on both sensors to approximately the same range of values.

The signal variation within each of the 16 test groups did not exceed 1% of the normalized voltage. With this in mind, the potential accuracy of the estimation of the equivalent air gap depends mainly on the cross correlation between the signals from electrode pairs with different penetration depths.

Figure 5.25 shows 15 tests taken under the same conditions as described for the three-wavelength sensor data in Figure 5.24. Only two penetration depths were used in this experiment because the CSC sensor interface electronics was not yet designed for three penetration depths operation. Later, it was modified to allow three penetration depths. Visual inspection shows that the signals from the CSC sensor are better correlated than those from the three-wavelength sensor. Table 5.5 lists the cross-correlation coefficients for all considered cases. The cross-correlation coefficient between data series X and Y is

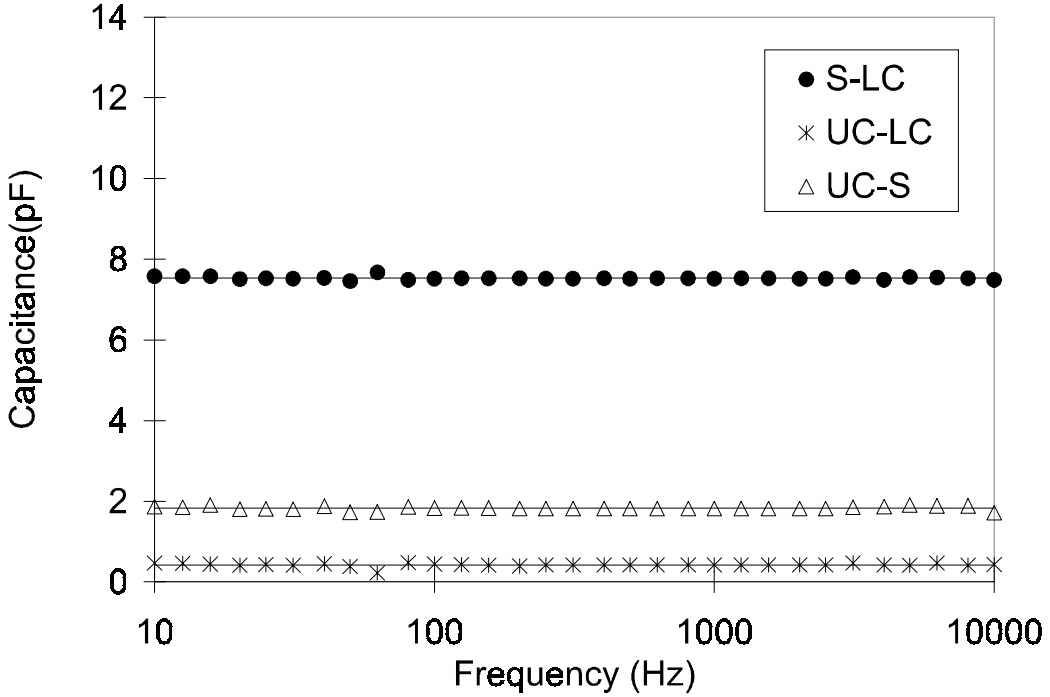

Figure 5.22: Capacitance values for the frequency sweep of the CSC sensor in air. A good agreement between the theory (solid lines) and measurements is observed for all pair combinations of electrodes.

$$\rho_{X,Y} = \frac{\mathrm{Cov}(X,Y)}{\sigma_X \cdot \sigma_Y}, \tag{5.7}$$

where σ is the standard deviation and

$$\mathrm{Cov}(X,Y) = \frac{1}{n}\sum_{i=1}^{n}(x_i - \mu_x)\cdot(y_i - \mu_y), \tag{5.8}$$

where μ is the mean of the data series.

Another way to visualize the sensor performance is to plot the difference between the sensed voltage normalized to the average sensed voltage for each pair of signals. The smaller the differential signal the higher is the expected accuracy of measurements. Figure 5.26 shows the difference between normalized voltages for all considered pairs of penetration depths. Again, the CSC sensor has the smallest and the most stable differential voltage. It should be noted that the differential voltage does not have to

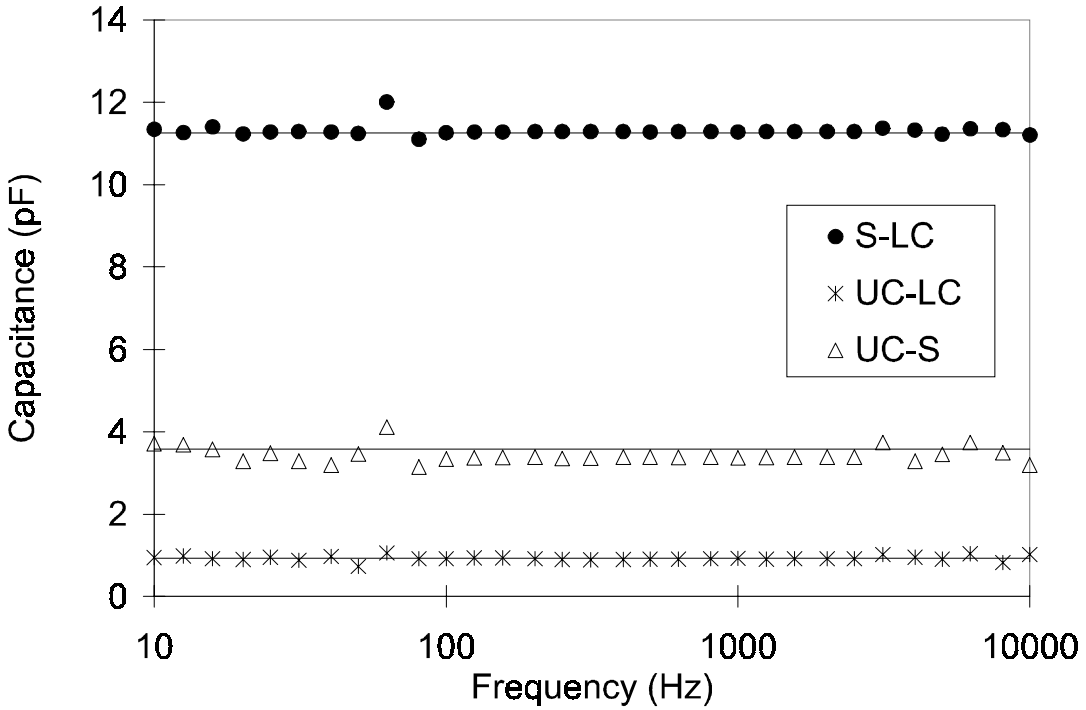

Figure 5.23: Capacitance values for the frequency sweep of the CSC sensor in transformer oil ($\varepsilon_r = 2.2$). A good agreement between the theory (solid lines) and measurements is observed for S-LC and UC-LC pairs. The UC-S pair measurement value is slightly lower than theory because of the close placement of a non-submerged section of contact leads.

be exactly zero even for the ideal performance, because the same air gap affects the response from the electrode combinations of different penetration depths to a different degree, as illustrated in Figures 5.20 and 5.21.

5.8.6 Summary

Two designs of penetrating fringing field dielectrometry sensors were compared in this section. Both sensors are adequate for measuring spatially inhomogeneous distributions of physical properties in insulating materials. The signal variation due to the effects of the surface contact quality between the sensor and a solid dielectric material has been studied. It is shown that a thin layer of cavities between the two surfaces is considerably inhomogeneous across the area of the sensor head. The CSC sensor

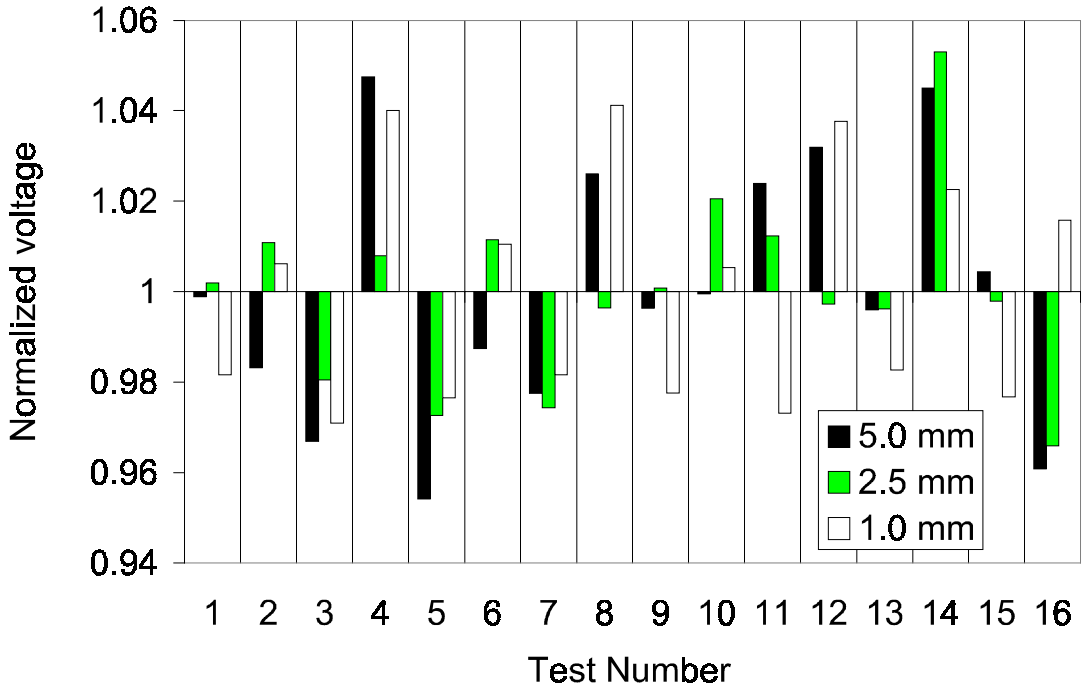

Figure 5.24: Sensed voltage normalized to the average sensed voltage in the experiments with the three-wavelength sensor. The cross-correlation of values between the data series is fairly low (see Table 5.5).

exhibited better performance than the three-wavelength sensor in a statistical study of these effects with a solid dielectric because each discontinuity of geometry is reflected in all signals in the CSC sensor instead of only one wavelength signal in the TWS. For the fluid dielectrics, both sensors had an excellent agreement between the interelectrode capacitances computed with finite element software and from measurements.

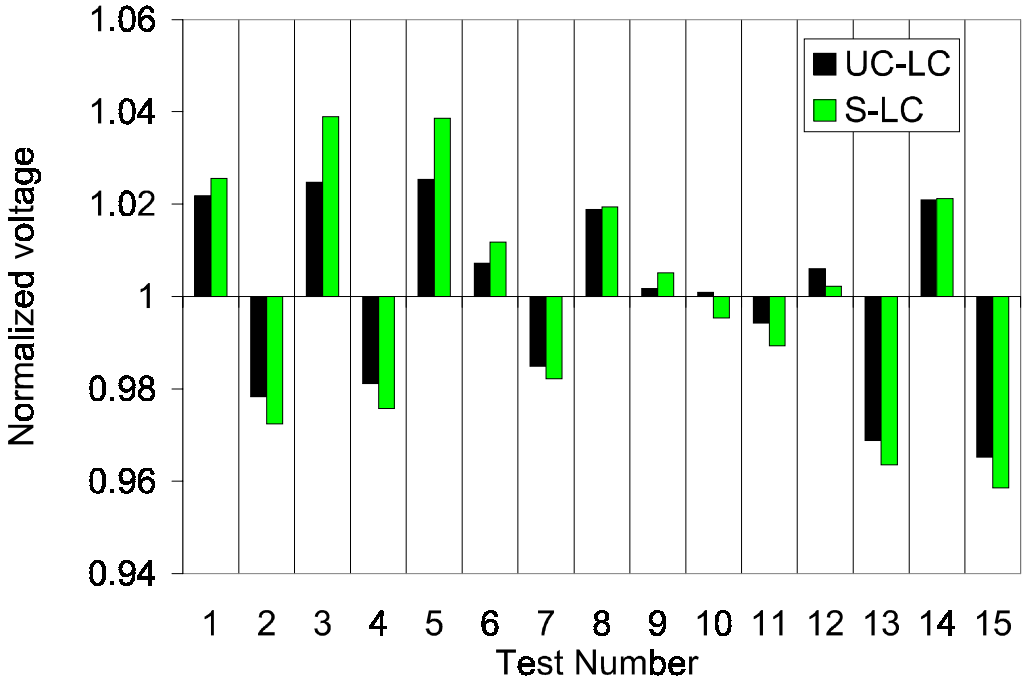

Figure 5.25: Normalized voltage values in the experiments with the CSC sensor. The cross-correlation between the data series is high (see Table 5.5).

	Cross-correlation coefficient	Probability that data is not linearly correlated
Three-wavelength sensor		
5.0 mm to 2.5 mm	0.707	<0.3%
2.5 mm to 1.0 mm	0.303	<26%
1.0 mm to 5.0 mm	0.559	<4.9%
CSC sensor		
UC-LC to S-LC	0.987	<0.05%

Table 5.5: Correlation coefficients for different cases.

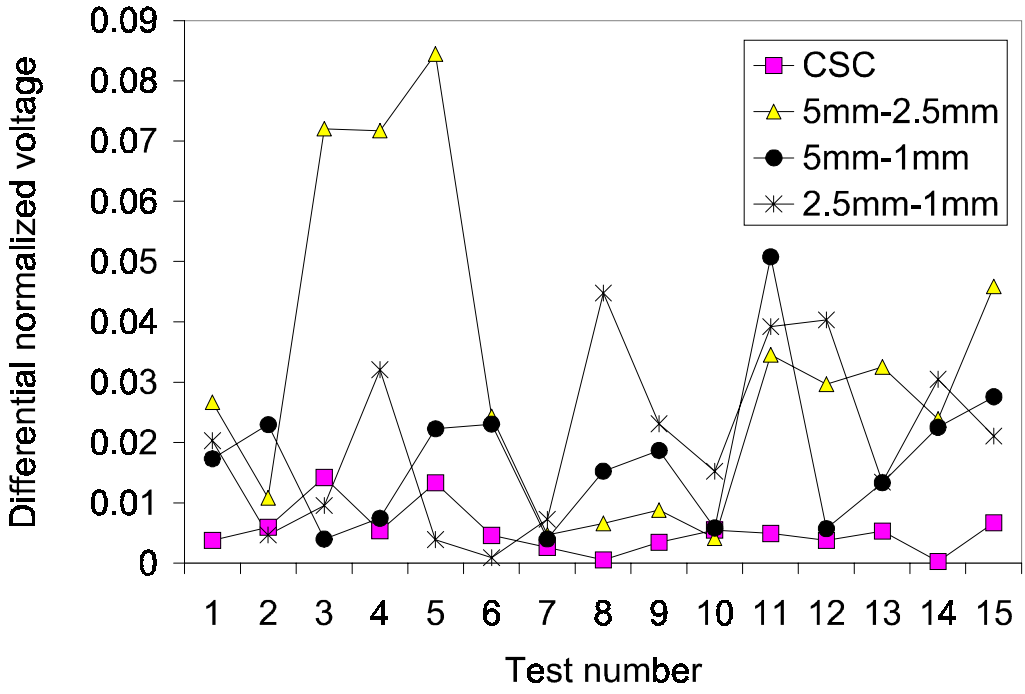

Figure 5.26: The difference in normalized voltage for all presented data series pairs. The CSC sensor indicates a greater likelihood of generating high accuracy data.

Chapter 6

Disturbance Factors

6.1 Introduction

The term "disturbance factors" is widely used in inverse problem theory, usually to differentiate between the input parameters that affect the measurement output and are of interest and the input parameters that affect the measurement output, but their exact values are not of interest. In some cases, the disturbance parameters should be converted into input variables in the problem formulation. In other cases, their influence can be eliminated or reduced through changes in sensor design, measurement practices, or parameter estimation algorithms. The analysis and control of disturbance factors is probably the most important area of non-destructive testing in general and of interdigital dielectrometry in particular. An attempt is made in this chapter to classify, evaluate, and account for several types of disturbance factors, including cross-coupling effects, limitations of a theoretical model, artifacts of numerical simulations, manufacturing tolerances, geometrical imprecision of experimental setups, and instrumentation noise.

6.2 Cross-Coupling

In general, if sensing elements of different interdigital pairs are placed sufficiently far from each other, and the signal amplitude is comparable in all channels, the cross-talk is negligible, as observed, for example, in [235].

In the initial design of the three-wavelength sensor, shown in Figure 4.3, the driven electrode was shared between the three sensing electrodes of different spatial periodicity. Consequently, the excitation of all wavelengths and measurement of their response was done simultaneously. Due to close placement and the limitations of two-dimensional in-plane (as opposed to the three-dimensional) shielding of the leads, the voltage induced on the sensing electrode (and associated shielding circuitry) of one wavelength affected the response of the others. This effect was significantly reduced in the consecutive design shown in Figure 4.5. Additional reduction of the cross-coupling effects may be possible by further optimization of the electrode geometry.

Figure 6.1 shows a frequency sweep of the Kapton sensor in air. This sweep should be compared to a similar one, shown in Figure 6.2, where 9.8 Gohm resistors were connected in parallel with each 2.5 and 1 mm wavelength sensor electrode. Since no changes were made on the 5 mm wavelength channel, the response for this wavelength should remain the same as in Figure 6.1 at all frequencies. However, Figure 6.2 shows that both gain and phase of the 5 mm wavelength channel undergo transition in the mid-frequency range, caused by cross-coupling from the other two wavelengths revealed by the sensor electrode loading by 9.8 Gohm resistors. An equivalent pair of frequency sweeps for the new Teflon sensor is shown in Figure 6.3 and Figure 6.4. In this case, the effect of cross-coupling is practically negligible. In many cases with the Teflon sensor, especially when properties of materials do not have a strong variation in space, cross-coupling effects are negligible, and the measurements can be performed simultaneously on all wavelengths. Cases where the variation of the complex dielectric permittivity in space is strong sometimes require independent, non-simultaneous measurements.

Table 6.1 shows the variation of gain and capacitance among measurements under

Channel	All (dB)	1mm(dB)	2.5mm(dB)	5mm(dB)	C_{12} All(pF)	C_{12} One(pF)
CH 1 ($\lambda = 5$)	-32.75	-52.95	-51.74	-33.44	1.16	1.07
CH 2 ($\lambda = 2.5$)	-29.99	-52.83	-30.09	-54.42	1.93	1.91
CH 3 ($\lambda = 1$)	-28.01	-28.12	-54.89	-54.89	4.06	4.01
CH 1 ($\lambda = 5$)	-32.75	-52.93	-51.82	-33.44	1.16	1.07
CH 2 ($\lambda = 2.5$)	-29.99	-52.92	-30.1	-54.39	1.93	1.91
CH 3 ($\lambda = 1$)	-28.01	-28.12	-54.96	-54.96	4.06	4.01
CH 1 ($\lambda = 5$)	-32.74	-52.98	-51.73	-33.45	1.16	1.07
CH 2 ($\lambda = 2.5$)	-29.99	-53.01	-30.1	-54.32	1.93	1.91
CH 3 ($\lambda = 1$)	-28.01	-28.12	-54.96	-54.85	4.06	4.01
CH 1 ($\lambda = 5$)	-32.74	-52.96	-51.83	-33.44	1.16	1.07
CH 2 ($\lambda = 2.5$)	-29.99	-52.98	-30.1	-54.39	1.93	1.91
CH 3 ($\lambda = 1$)	-28.01	-28.11	-54.92	-54.89	4.06	4.01
CH 1 ($\lambda = 5$)	-32.74	-52.99	-51.74	-33.45	1.16	1.07
CH 2 ($\lambda = 2.5$)	-29.99	-52.95	-30.1	-54.32	1.93	1.91
CH 3 ($\lambda = 1$)	-28.01	-28.12	-54.85	-54.85	4.06	4.01

Table 6.1: Gain and measured capacitances in air of the Teflon three-wavelength sensor at 1 kHz for five identical sets of measurements with all drive electrodes simultaneously excited (All, columns 2 and 6) and each drive electrode excited one at a time (columns 3-5 and 7).

the same conditions in air and between two cases. For these two cases, a separate sensor has been built, which resembled very closely the one shown in Figure 4.5, except that the driven electrodes had an option of independent excitation for each wavelength. The first case (All) is when all driven electrodes are excited simultaneously, the second case (One) is when they were excited individually. The discrepancy between the two cases indicates the remaining cross-coupling between individual wavelengths. Note in Table 6.1 that for the single tests, when a given wavelength is excited , that the other two wavelengths have pick-up signals about 20-26 dB lower.

6.3 Fringing Field Effects

A two-dimensional model of the interdigital structure assumes an infinite periodicity and infinite length of the electrode fingers. In reality, the effects of the finite size of the interdigital structure become important when the number of fingers is relatively small and/or when the length of the fingers with respect to the spatial wavelength of the interdigital structure is relatively small. In other words, two types of end discontinuities

in Figure 1.3 must be considered: the finite number of fingers along the y axis, and the finite length of the electrodes along the x axis. The effect of the former is alleviated by adding additional guard fingers on both sides of each wavelength, as shown in Figure 4.5. A visualization of the field enhancement regions at the edges of the sensor head of an interdigital capacitor is available in [216].

6.3.1 Infinite Length Assumption

Evaluation of the end effects along the x-axis can be accomplished in several ways. Several authors have developed closed-form solutions as well as empirical models of interdigital sensor discontinuities, for example see [17]. At the same time, the precise geometry of the end areas usually differs from the idealized models. A relatively simple experimental procedure was developed in order to approximately measure the equivalent capacitance of the end area.

The geometry of the end area of the 5 mm wavelength is shown in Figure 6.5. A piece of Lexan (GE polycarbonate) with measured relative dielectric constant ε_r=3.17 was placed in contact with the sensor so that the y-z plane (as defined by Figure 1.3) containing the air-Lexan boundary goes through $x = 0$ in Figure 6.5. The Lexan sample was then repositioned in 0.25 mm increments in the direction of x, so that it gradually covers the electrode. Naturally, the equivalent capacitance C_{12} increases as the Lexan moves along the x axis. The change in capacitance during this measurement is shown in Figure 6.6. The growth becomes approximately linear when the Lexan slab position exceeds $x = 3.125$ mm. The equivalent meander length of the end area can now be found by subtracting the capacitance at the point $x = 3.125$ mm and at $x = 0$ mm and relating it to the linear function for $x > 3.125$ mm. After taking the end effects into account and proper scaling of variables, the total meander lengths were empirically found to obey the relation $50+1.2\lambda$ cm for each wavelength, where λ is expressed in centimeters.

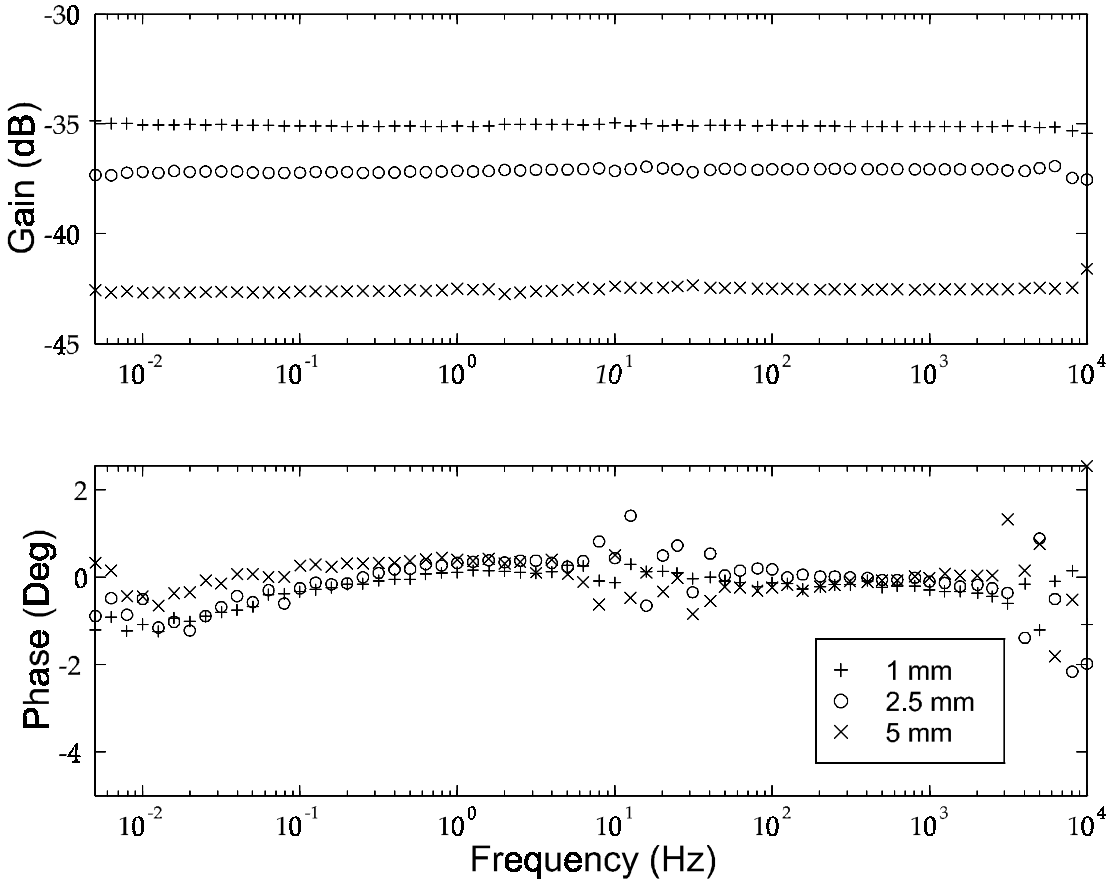

Figure 6.1: Kapton sensor, floating voltage mode with grounded backplane full frequency sweep in air. Values of load capacitances are $C_L(1mm) = 59.66$ pF, $C_L(2.5mm) = 23.3$ pF, $C_L(5mm) = 3.28$ pF. Phase is close to zero and the gain is flat over the entire frequency range since the interelectrode admittance is purely imaginary and frequency independent.

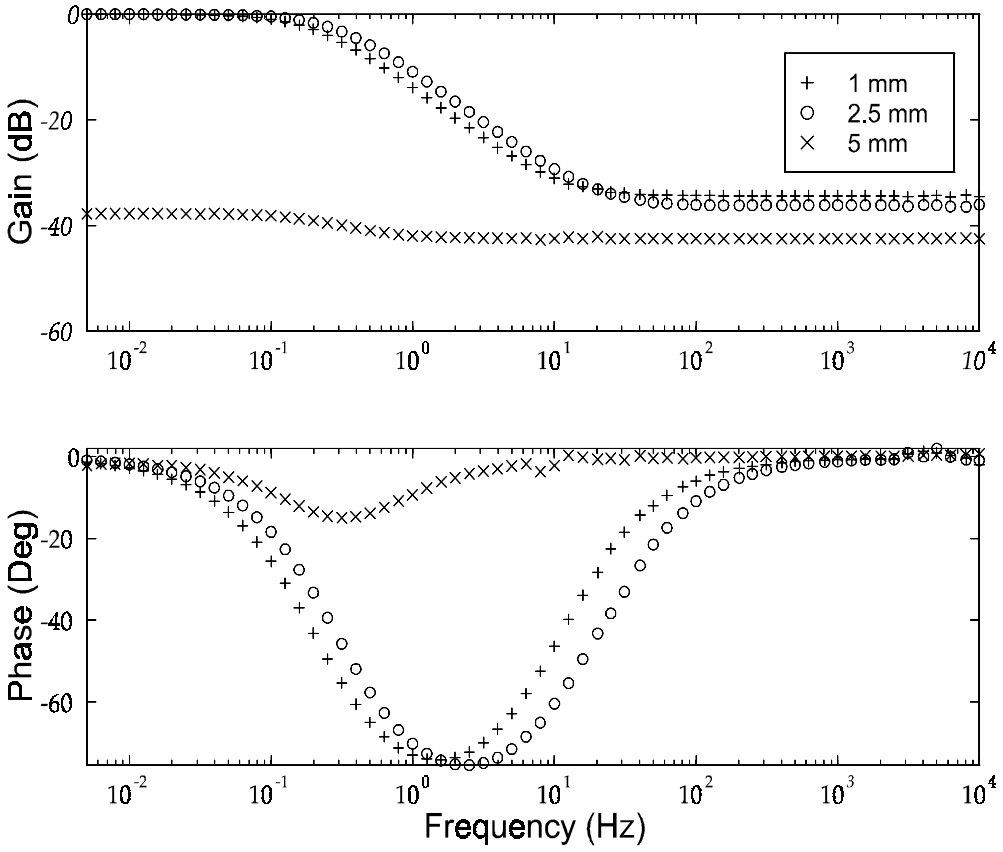

Figure 6.2: Kapton sensor, floating voltage mode with grounded backplane full frequency sweep in air. Two resistors of 9.8 Gohm each are separately connected in parallel with 1 mm and 2.5 mm wavelengths. Ideally, the response of the 5 mm wavelength should remain unchanged from that shown in Figure 6.1. However, the phase peaks to ≈-15 degrees and the gain increases by about 4 dB at low frequencies due to cross-coupling between channels.

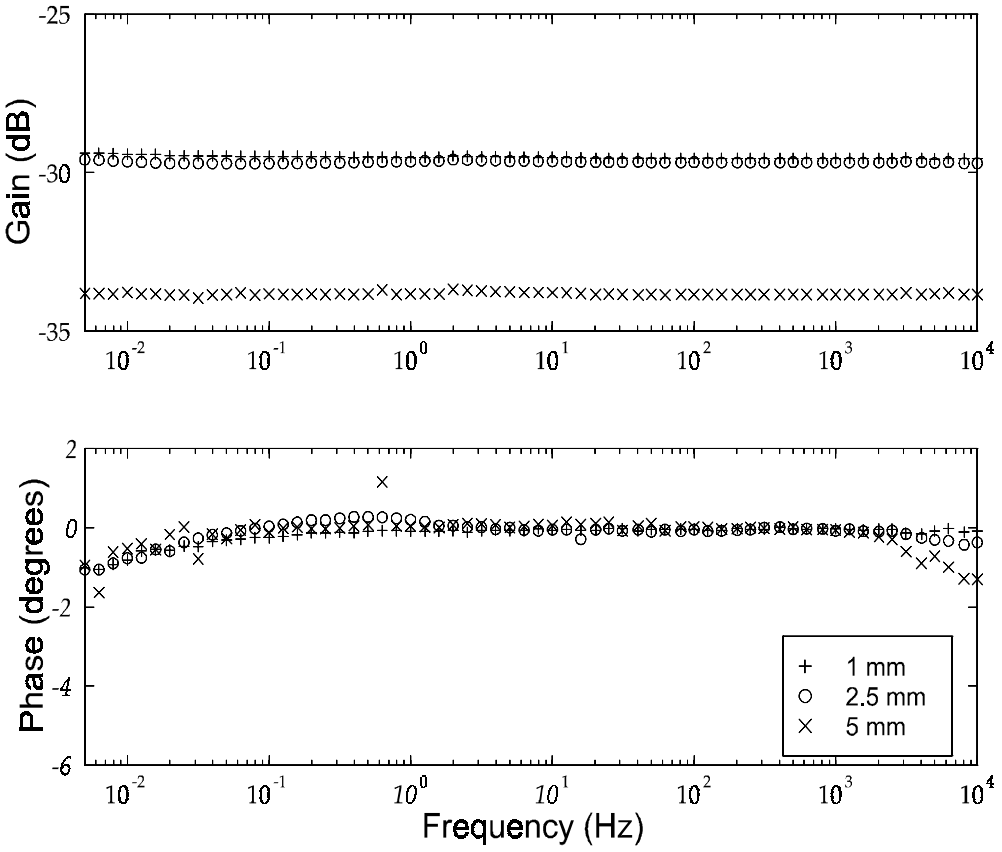

Figure 6.3: Clean Teflon sensor, floating voltage mode with grounded backplane full frequency sweep in air. Values of load capacitances $C_L(1\text{mm}) = 59.66$ pF, $C_L(2.5\text{mm}) = 23.3$ pF, $C_L(5\text{mm}) = 3.28$ pF. The slight decrease in phase at low frequencies sometimes takes place due to residual contamination and existence of conduction paths in the electronic circuitry, but can be ignored for most practical measurements as long as it stays within the noise level bounds.

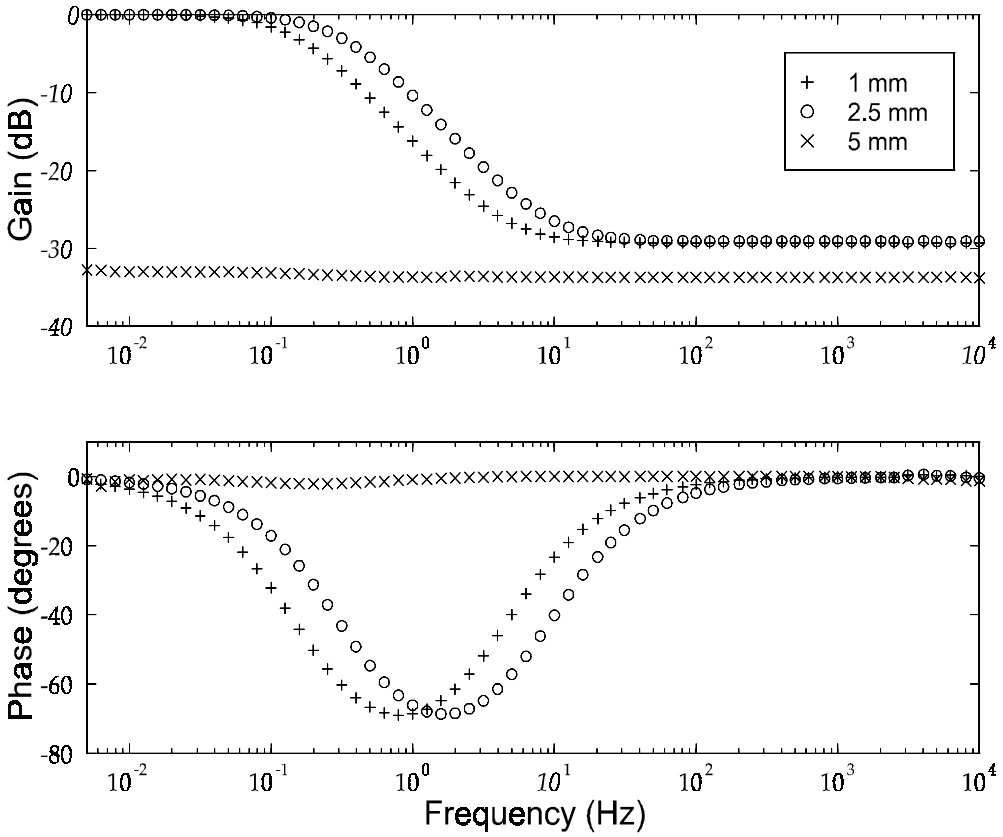

Figure 6.4: A floating voltage mode with grounded backplane full frequency sweep in air with the Teflon sensor to be compared to the Kapton sensor data in Figure 6.2. Two resistors of 9.8 Gohm each are separately connected in parallel with 1 mm and 2.5 mm wavelength sensing electrodes. The response of the 5 mm wavelength is practically unaffected by the other two wavelengths.

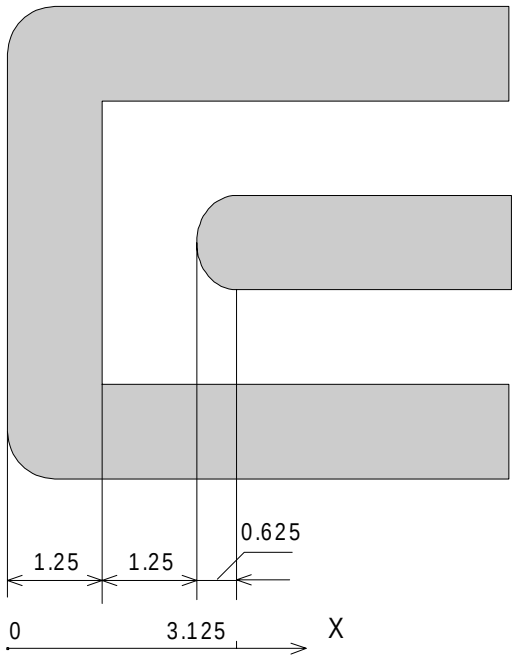

Figure 6.5: An enlarged image of the end area of the individual finger of the 5.0 mm wavelength sensing electrode.

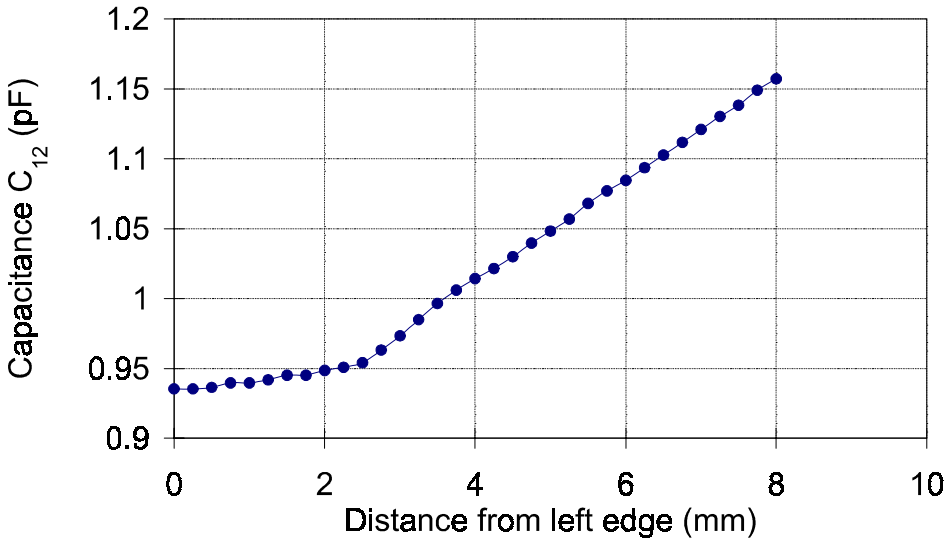

Figure 6.6: Measured sensor's response to the linear movement of a Lexan ($\varepsilon_r = 3.17$) slab over the 5 mm wavelength sensor end area shown in Figure 6.5.

6.3.2 Infinite Periodicity Assumption

It is the infinite periodicity assumption that makes interdigital sensors one of the most popular structures for the design of fringing field sensors, be it piezoelectric, dielectric, conductivity, capacitance, or any other measurement principle that is used. In most cases, there is no physical reason to form an interdigital structure, as any other planar geometry pattern would also generate fields that penetrate into the material. The advantage of the interdigital structure is that only a small part of the entire geometry has to be modeled. The assumption of infinite periodicity allows modeling of the entire array through a mere two-dimensional half-wavelength cell, as shown, for example, in Figure 1.4. The admittance per meter length predicted by computer simulation must be multiplied by the total finger length to be compared with measurement results.

When the number of fingers of each electrode is large, only a small error due to the fact that the number of fingers is not infinite would result. For example, the sensor shown in Figure 4.2, which has 50 fingers on the sensing electrode, would have a very small error of the capacitance estimation even under the infinite periodicity assumption. On the other hand, the estimation of the capacitance of the sensor shown in Figure 4.8 would have, among other sources of error, a larger departure from the true answer because of the small number of fingers.

One way to reduce the error due to the finite number of fingers is to introduce guard fingers on each side of the sensing electrode. Guard fingers maintain the periodicity of the spatial distribution of electric potential at the electrode edges in the x direction, as specified by Figure 4.5. A natural question arises: how many guard fingers are sufficient to satisfy the infinite periodicity assumption within a requested accuracy of computation? One way to find the answer to this question is to model a finite number of fingers in the interdigital structure and compare to an analogous modeling result from the simulation with the half-wavelength cell. The problem with this approach is the computational complexity of the task. Generation of closed form theoretical expressions for edge effects of a non-periodic structure is yet to be achieved. On the other hand,

the numerical simulation with finite element or finite difference techniques would suffer from low computational precision due to a very small ratio of the smallest feature size to overall dimensions of the modeled region stemming from the large number of modeled fingers. Since small differences between capacitances are being analyzed, it is desirable to achieve a high accuracy of estimation. In addition to the above reasons, even if the theoretical modeling was an acceptable choice, the experimental verification would still be required.

A simple experiment has been conducted to analyze the effects of the finite number of electrodes. First, a "sacrificial" single-wavelength sensor with a large number of guard electrode fingers has been manufactured. Figure 6.7 shows the sensor manufactured using the same materials and technology as described in detail for the three-wavelength sensor shown in Figure 4.5. The term "sacrificial" is used here to reflect the fact that the sensor is destroyed in the course of experiment. The sacrificial sensor comprises a sensing electrode with five fingers with two four-finger guard electrodes on each side, and a driven electrode over the entire width of the sensor.

To clarify subsequent analysis, the fingers in Figure 6.7 are numbered from 1 to 27, from left to right. In the course of the experiment, the fingers were removed (cut-off with a razor blade) alternately from each side in the following sequence: 27, 1, 26, 2, 25, 3, 24, 4, 23, 5, 22, 6, 21, 7, 20, 8, 19, 9. The capacitance C_{12} between driven and sensing electrode was measured before the experiment and after removal of each subsequent finger. Five consecutive measurements were recorded at each position. Figure 6.8 shows the average value of voltage gain in dB plotted against the left vertical axis. One can see that the removal of eight outer guard and drive fingers (four from each side) had practically no effect on the sensor response. The removal of the last two drive fingers had a very significant effect. Figure 6.9 visualizes the same process by plotting the measured capacitance against the finger position in an array. The increase of capacitance from finger 2 to finger 6 data points and from finger 7 to finger 8 data points is not measurement noise. This discontinuity is entirely valid because as the guard finger is removed, a larger number of electric field lines extends from the driven

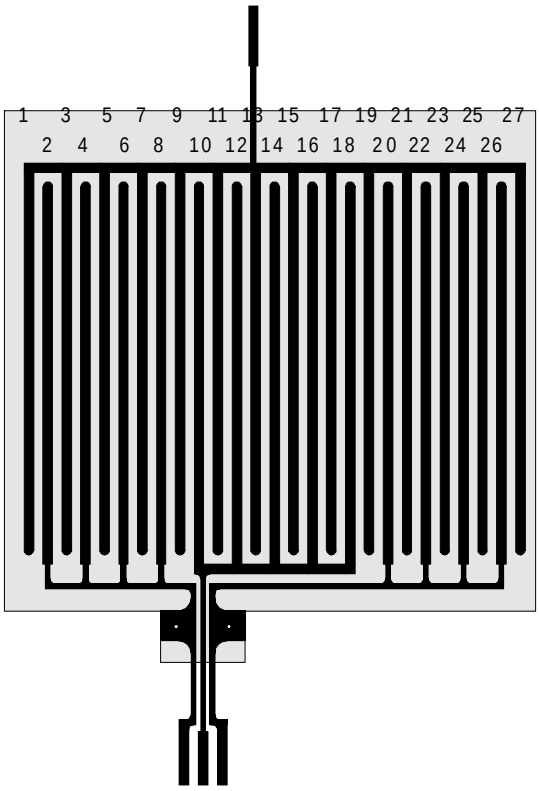

Figure 6.7: A sacrificial sensor with additional guard fingers on each side of the sensing electrode. Side fingers were removed one by one until no guard fingers were present in order to quantify the effects of the finite sensor width.

electrode to the sensing electrode. There are no analogous jumps on the right side of this graph because of the sequence of finger removal: there is at least one left side driven electrode finger removed between the data points above 20 that correspond to the removal of the right side driven finger.

Figure 6.10 presents the same results as in Figure 6.9, but in the form of the percentage capacitance difference with respect to the nominal capacitance. One can see that the maximum does not exceed 3%. However, even a 3% error may have a very large effect on the results of the inverse problem. The gray rhombuses correspond to the cases where the sensor is completely symmetric with drive electrode fingers at both left and right ends. The black symbols correspond to either a symmetric sensor with guard electrode fingers at left and right ends or a non-symmetric sensor with a drive

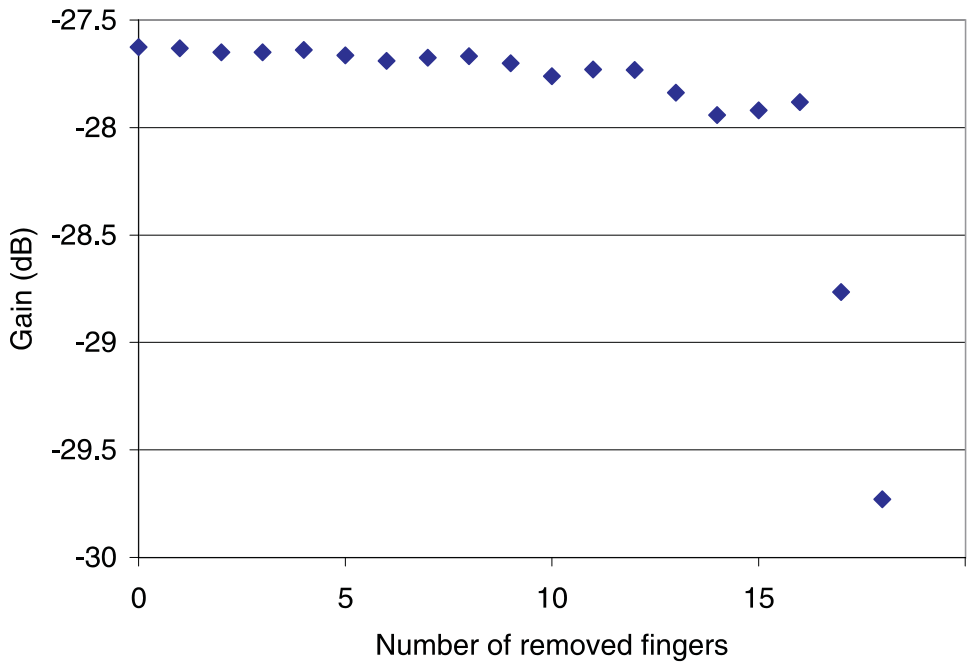

Figure 6.8: Measured change of sensor gain with the number of removed fingers from the sensor shown in Figure 6.7.

electrode finger at one end and a guard electrode finger at the other end.

Naturally, as the number of sensor electrode fingers grows, the relative edge effect becomes less significant, because the same absolute errors of capacitance estimation due to missing electrode fingers are compared to a larger capacitance between driven and sensing electrodes. Figure 6.11 shows the estimated error for different numbers of the guard finger pairs and different total numbers of sensing electrode fingers. The error was estimated using the following argument.

The absolute sensing electrode capacitance is proportional to the number of the sensing electrode fingers, whereas the absolute capacitance error due to end effects is only a function of the number of guard finger pairs and is not a function of the number of sensing electrode fingers. Therefore, the percent error due to end effects reduces with the number of the sensor electrode fingers increase and also reduces with the number of the guard finger pairs. The measurements with five sensing electrode fingers and zero to four guard electrode finger pairs is taken as a baseline (triangles in Figure 6.11), and the other data points are computed on the basis of the sensing electrode finger ratio.

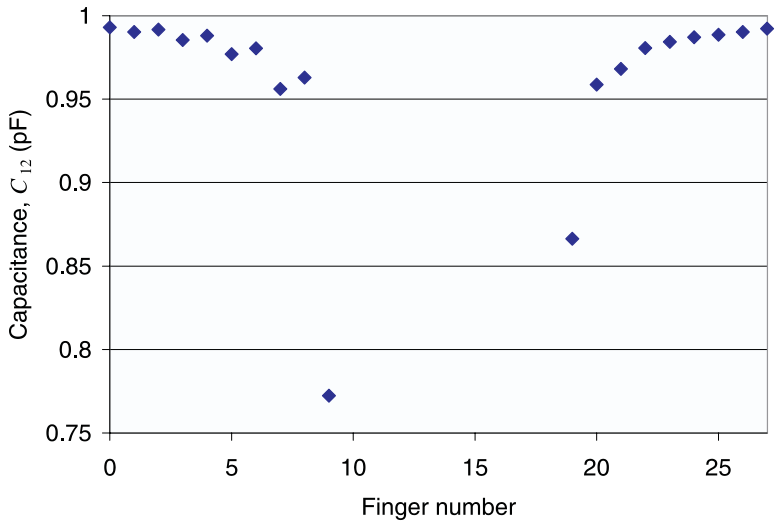

Figure 6.9: Measured change of sensor capacitance with the number and position of the removed finger from the sensor shown in Figure 6.7.

For example, the percent error for 10 finger sensing electrodes is half of that for the five finger sensing electrode.

6.4 Geometry

6.4.1 Electrode Thickness

In some cases, it is desirable to make electrodes as thin as technologically possible without sacrificing mechanical strength. Yet in other cases, very thick electrodes (with respect to the electrode width) are the preferred choice. Thicker electrodes have higher interelectrode admittance and generate higher electromechanical forces. Thus, one may achieve higher sensitivity and signal to noise ratio by using thicker electrodes. A three-dimensional design of an interdigital structure was reported in [217].

The thickness of the electrodes introduces a significant variation of the capacitance. Figure 6.12 shows that the total capacitance increase, called the parasitic capacitance in air, defined here as the difference between the capacitance of the electrodes of finite height and the infinitely thin ones, is an approximately linear function of the thickness of the electrodes. Additional analysis of the effects of the parasitic capacitance is given

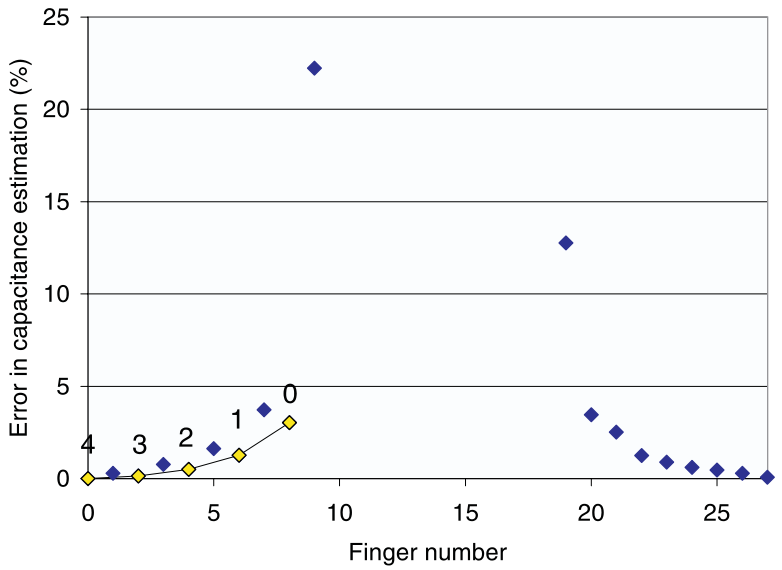

Figure 6.10: The measured percentage error in capacitance estimation as a function of the number and position of the removed fingers. The gray rhombuses connected by a line correspond to the number of complete guard electrode finger pairs, indicated above each rhombus.

in the following section.

6.4.2 Electrode Width

The variation on electrode width should be differentiated from the variation of the spatial wavelength. The width of each individual finger may vary even if the spatial wavelength remains the same. In this case, the amplitude of individual spatial harmonics of the electric potential distribution becomes different for each width. At least two cases of the width variation should be considered. First, it may be desirable to intentionally alter the design to achieve better sensitivity or selectivity of sensor signals. Second, it may not be possible to control the width to the exact specified parameter due to manufacturing limitations. In this case, the potential error introduced by imperfection of manufacturing should be estimated. Assuming that the electrode structure is periodic, it is convenient to define the metallization ratio, β, as the ratio of the sensor head area covered by metal to the total area. An alternative definition is the ratio of the spatial half-wavelength to the width of an individual finger (assuming

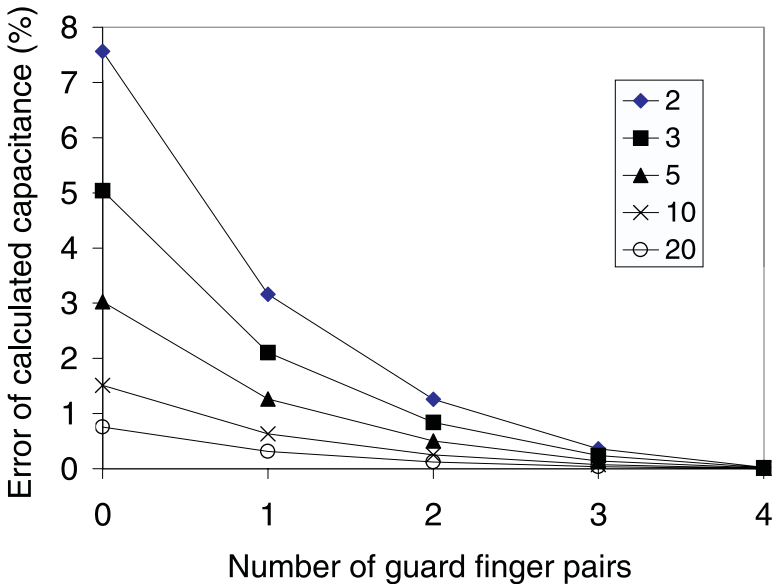

Figure 6.11: The error in capacitance estimation as a function of present guard finger pairs for different number of sensor electrode fingers. The legend numbers for different curves correspond to the number of sensing electrode fingers. The result of simulation is intuitive. The larger the number of sensing electrode fingers the smaller is the error due to the infinite periodicity assumption. Increasing the number of guard fingers reduces the error as well. This effect can be compensated in software.

that the sensing and driven fingers have equal width). Figure 6.14 shows a microscope photograph of 1 mm wavelength electrodes on a Teflon sensor with a metallization ratio of 0.41. The metallization ratio specified for the manufacturer was 0.5, but it was not achieved in the first batch. Figure 6.15 shows the same set electrodes under a larger magnification which confirms that the electrode edges are adequately smooth in our manufacturing process.

Figure 6.16 shows how the calculated capacitance between the driven and sensing electrodes changes with the metallization ratio for the Teflon sensor. This data has been computed with the finite element software *Maxwell*. A faster-than-linear increase of capacitance is logical and can be thought of in the following way. As the edges of the driven and sensing electrodes move closer towards each other, most of the electric field energy is stored at these edges. For comparison, the distance between the edges is inversely proportional to the metallization ratio. As a cylindrical analogy, the ca-

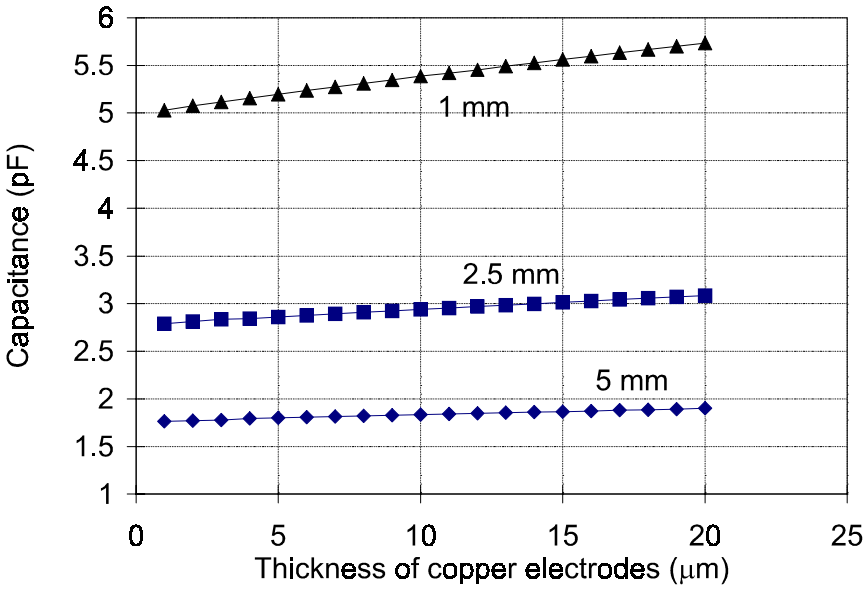

Figure 6.12: Calculated interelectrode capacitance C_{12} for the Teflon sensor as a function of the thickness of copper electrodes, approaching zero thickness values of 1.7 pF, 2.7 pF, and 4.9 pF for 5 mm, 2.5 mm, and 1 mm wavelengths, respectively.

pacitance per unit length C between two infinitely long thin cylindrical conductors of radius R with centers separated by the distance D is [153]

$$C = \frac{\pi\varepsilon_0}{\cosh^{-1}[D/2R]} \tag{6.1}$$

As D decreases, so that the cylinders become closer, the capacitance increases. Of course, viewing the capacitive energy stored at the edges of electrodes is a gross approximation of the true field distribution. However, it does provide a correct qualitative picture of field dependence and develops intuition for sensor design.

Because the ratio of the substrate thickness to the wavelength is different for each wavelength, the percent change of the capacitance is also different. Figure 6.16 shows that on a percentage basis the longest, 5 mm wavelength, is the one most strongly affected by the metallization ratio, and the smallest, 1 mm wavelength, is least affected. The slope around 50 percent metallization ratio, where all three curves intersect, is important for analysis of the sensor signal sensitivity to the disturbance factor introduced by the metallization ratio and may be used in future studies.

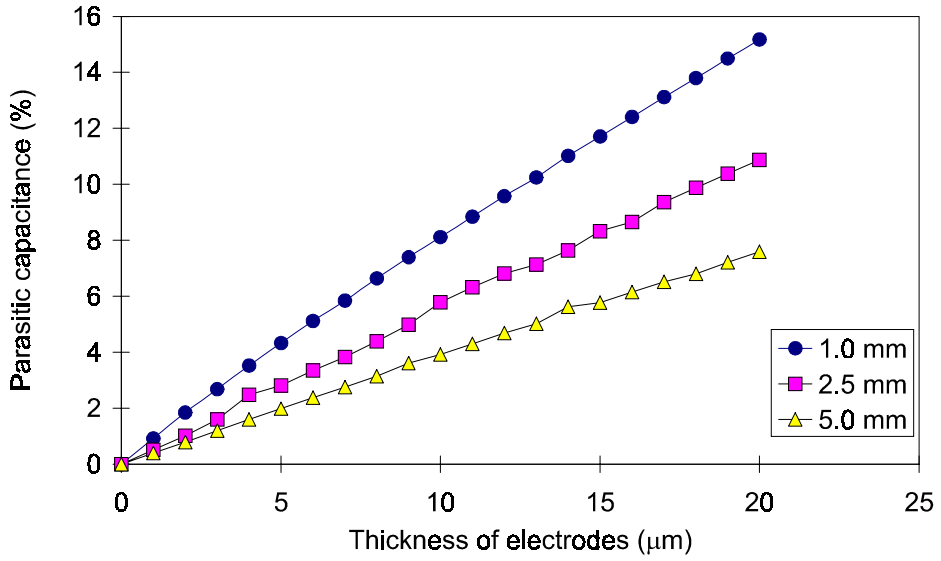

Figure 6.13: Calculated percent ratio of the parasitic capacitances with respect to the nominal capacitance of each wavelength of the Teflon sensor as a function of the electrode thickness, $C_{\%} = C_{par}/C_{nom} \times 100$.

The capacitance between the sensing electrode and the backplane through the substrate, on the other hand, varies nearly linearly with the metallization ratio, as shown in Figure 6.18. Intuition confirms this trend, because this situation is similar to that of a parallel plate capacitor, given by (5.4). Again, the relative changes of each capacitance are larger for larger wavelengths, as shown in Figure 6.19. As already stated, this information is useful for two reasons. The resolution of the etching process on a flexible substrate is not always sufficient to ensure precise dimensions of the smaller wavelength, but even if this limitation is overcome, it may be useful to change the metallization ratio in order to extract additional information about the properties of the dielectric sample by altering the relative amplitudes of the Fourier components of the sensor surface voltage distribution. The numerical values of capacitance per meter length for the most frequently used case of the 50/50 metallization ratio computed with Maxwell for the Teflon sensor of Figure 4.5 in air are given in Table 6.2.

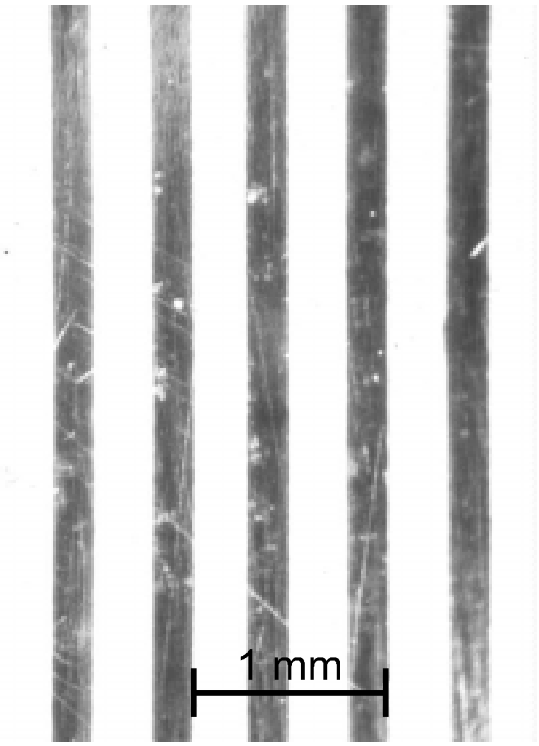

Figure 6.14: The metallization ratio is not always easy to control. The measured metallization ratio for the 1 mm wavelength electrodes of the Teflon sensor is 0.41, whereas the specified metallization ratio was 0.5. The visible scratches are due to the manufacturing process and are less than one micron deep.

6.4.3 Effects of Surface Contact Quality

Surface Deformation

Many applications require that interdigital sensors operate over a wide range of temperatures. Several precautions should be taken to ensure an adequate performance. One side effect of varying the environment temperature is the surface deformation of flexible interdigital sensors. Consider the case of sensors that use CuFlon substrate. The coefficient of thermal expansion of pure PTFE is 129 ppm/K [269], whereas the coefficient of thermal expansion of copper is 17 ppm/K [282]. Not surprisingly, the continuous copper backplane bulges out when the sensor is exposed to low temperatures. Another possible reason for surface deformation is absorption of moisture or chemicals in the volume of the material under test. In several cases, with significant moisture

Figure 6.15: Larger magnification optical microscope photograph of the 1 mm wavelength electrodes in Figure 6.14 showing edge sharpness of the Teflon sensor.

	Capacitance, pF/m	
wavelength	C_{12}	C_{20}
λ= 1.0 mm	7.14	16.1
λ= 2.5 mm	3.33	34.4
λ= 5.0 mm	2.03	60.2

Table 6.2: Calculated values of C_{12} and C_{20} per meter length for the Teflon sensor in air.

absorption of more than 100% by weight, the transformer pressboard used in our experiments would increase its thickness by more than a factor of two and lose its original flatness. This introduced an undesirable air gap between the sensor and pressboard, which decreased the accuracy of measurements. Such a large increase of pressboard thickness and weight would normally occur only for pressboard not impregnated with oil. In this case, water was supplied by a wick in direct contact with pressboard rather than being absorbed directly from air.

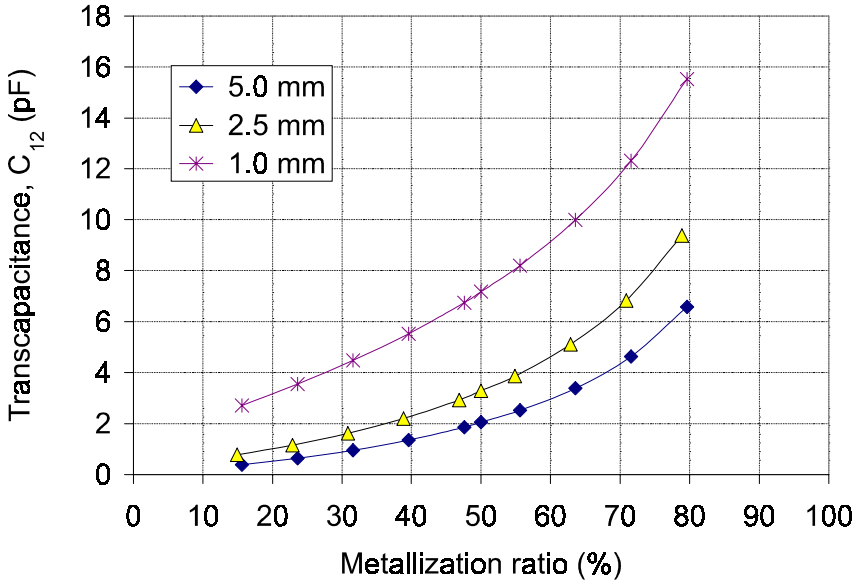

Figure 6.16: Calculated dependence of capacitance per meter length C_{12} of the Teflon sensor on the metallization ratio.

Surface Roughness

A schematic view of a half-wavelength cross-section of the sensor is shown in Figure 6.20. Several void regions can be identified. The cavity due to thickness of electrodes gives rise to the so-called parasitic capacitance described in [9] and in Section 6.4.1 of this thesis. In addition, some voids are formed above the electrodes, due to roughness and non-flatness of the electrodes and the tested material, as well as due to variations of the contact quality, which depends on the distribution of pressure above the specimen, which may be rigid or elastic.

A representative profilometer scan of the sensor's surface in Figure 6.21 shows that variation of the nominally 14 μm electrode thickness is nearly negligible, on the order of 1 μm. The surfaces of the solid dielectric materials used in this study are even smoother for most cases. This leads us to conclude that the primary surface contact effect is due to non-flat surface deformations of the solid dielectrics and the sensor.

It is very difficult to achieve an adequate contact with a solid material sample. The distribution of pressure is usually inhomogeneous due to local compressions and

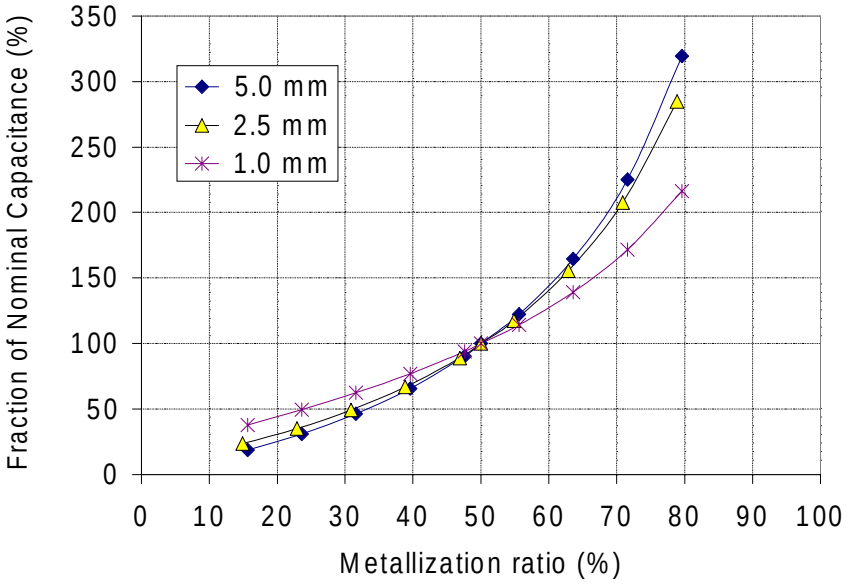

Figure 6.17: Calculated percent change of capacitance C_{12} of the Teflon sensor normalized with respect to $\beta = 50\%$ capacitance value $C_{12\%} = C_{12}/C_{12}(50\%)$ vs metallization ratio.

surface deformations. Figure 6.22 shows an image of the sensor left in a pressure sensitive film [283]. The sensor was squeezed in the vice with 1 inch thick lexan layers on each side of the sensor. It can be seen that even a 1 inch layer was not sufficient to redistribute pressure from the vice surface pattern into a homogeneous distribution.

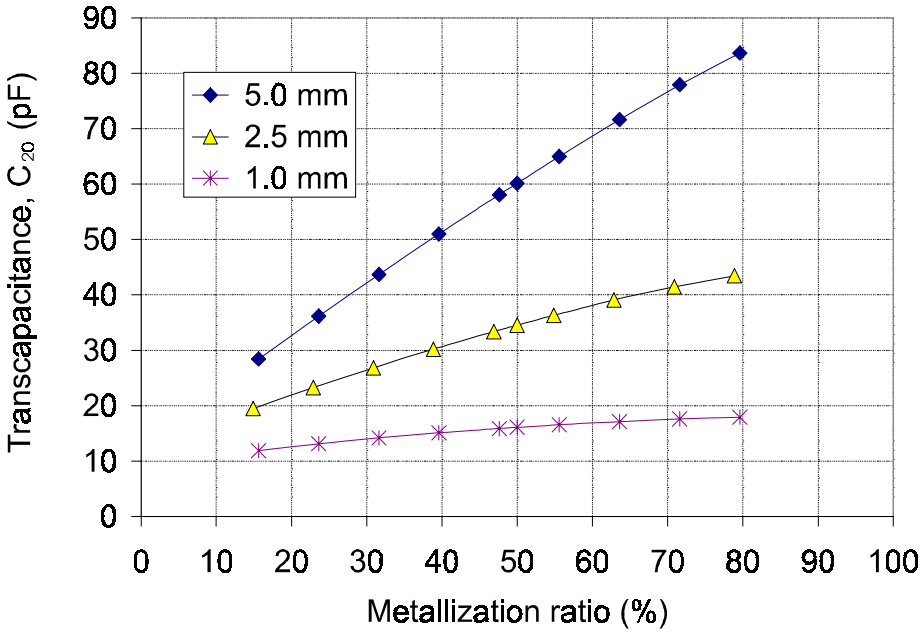

Figure 6.18: Calculated change of the sensing electrode-to-backplane capacitance per meter length C_{20} of the Teflon sensor as a function of the metallization ratio.

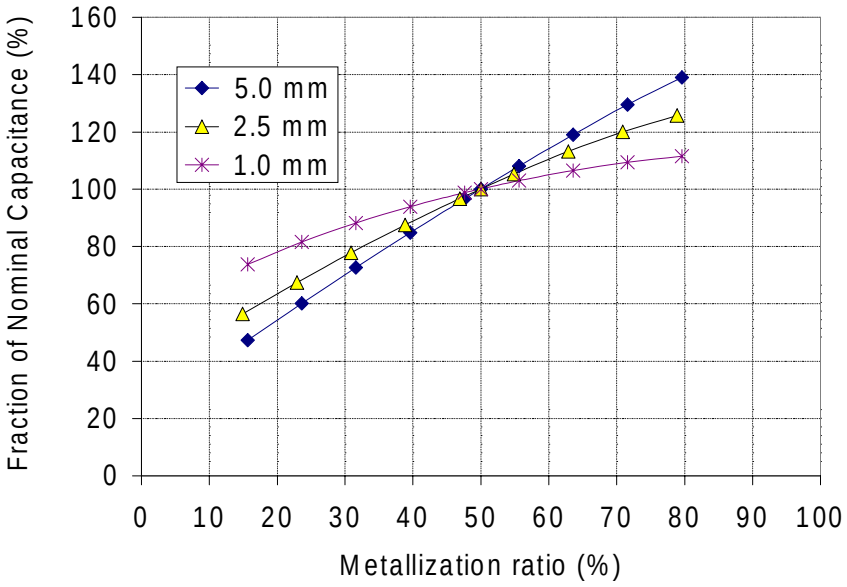

Figure 6.19: Calculated percent change of the sensing electrode-to-guard plane capacitance $C_{20\%} = C_{20}/C_{20}(50\%)$ of the Teflon sensor as a function of the metallization ratio.

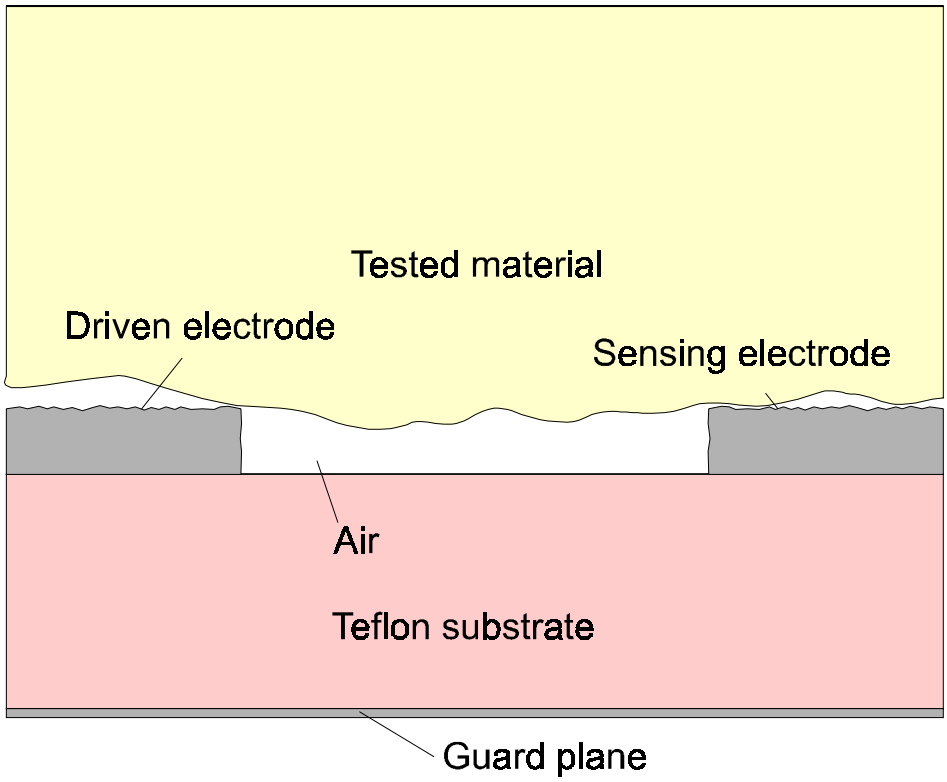

Figure 6.20: Air layer trapped between the drive and the sensing electrodes during measurements with solid materials due to electrode height, surface roughness, and surface non-flatness. For all calculations the electrode height is 14 μm, the Teflon substrate has thickness 254 μm and ε_r=2.1, and the tested material has infinite thickness.

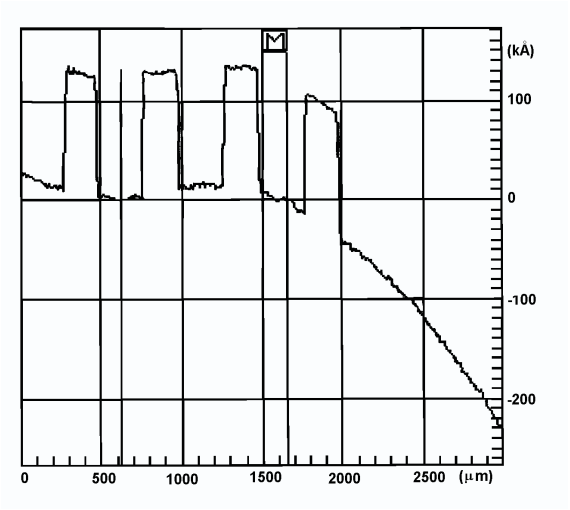

(a) 1 mm wavelength

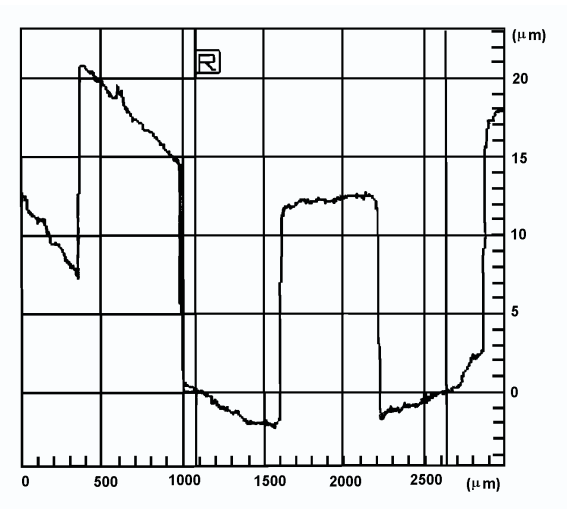

(b) 2.5 mm wavelength

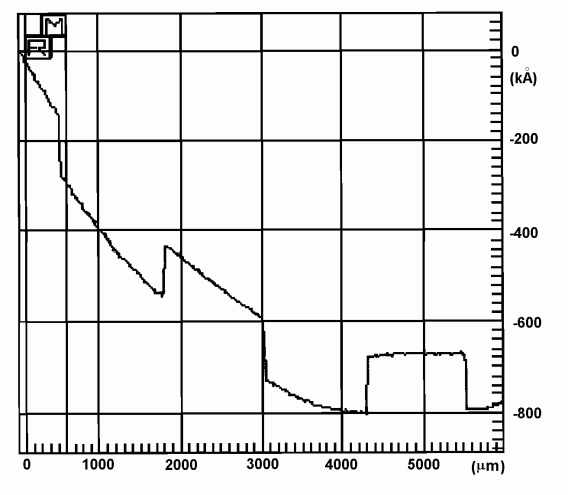

(c) 5 mm wavelength

Figure 6.21: Profilometer scan of the electrode surface for each wavelength. The overall slope of the Teflon sensor surface due to the global surface deformation of the flexible substrate is software corrected in selected regions denoted by vertical lines and characters R and M in (a) and (b) and is the flat baseline region around 5000 μm in (c). The scans show that the electrode height is about 14 μm whereas the surface roughness is on the order of one μm.

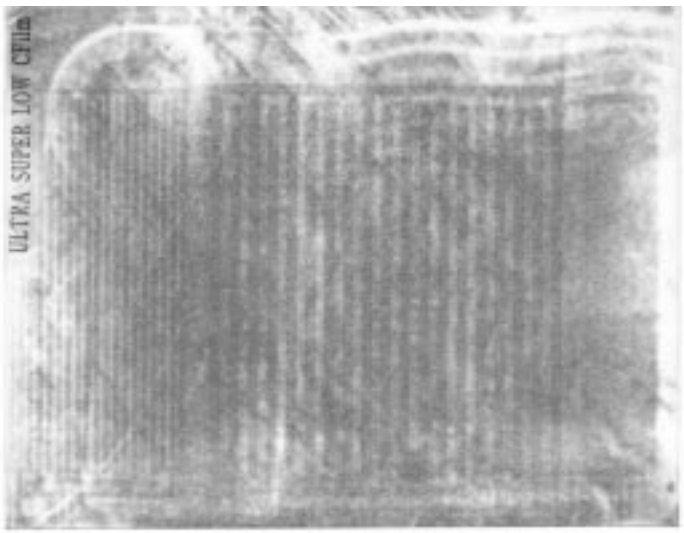

Figure 6.22: Pressure-sensitive film image with the Teflon sensor pressed against the Lexan slab demonstrates that the pressure distribution tends to be nonuniform and the air gap characteristics should not be regarded homogeneous across the sensor head.

Experiments

Paraffin wax

The first set of measurements, serves to demonstrate the dramatic dependence of sensor output on the quality of contact with the specimen. Paraffin wax (ε_r=2.1, $\sigma \approx$0 for frequency 1 kHz, melting temperature 57°C) was first formed into a solid rectangular slab and placed directly contacting the sensor. Then, it was melted, poured over the sensor, and allowed to re-harden with paraffin wax filling the air cavities. After room temperature was reached and the paraffin wax solidified, measurement of interelectrode capacitance was made and compared to that of the pre-melted case. The results are summarized in Table 6.3. The increase in C_{12} after re-hardening from the melt is in good agreement with calculated values from a finite-element computer simulation which indicates that the paraffin wax has flowed into air cavities.

Hyzod and corn oil

A similar experiment was conducted to further demonstrate the strong effect of air cavities and to explore the possibility of using matching dielectric constant liquids

	Capacitance, C_{12} (pF)		
wavelength	pre-melted	re-hardened after melt	calculated, no air cavities
λ= 1.0 mm	3.63	6.36	6.29
λ= 2.5 mm	2.18	3.96	3.73
λ= 5.0 mm	1.32	2.38	2.35

Table 6.3: Comparison of measured capacitance C_{12} with pre-melted and re-hardened paraffin wax using the Teflon three-wavelength sensor.

for high-precision measurements with irregularly shaped specimens. The approach to this measurement originates from a common technique of liquid displacement in dielectrometry measurements, (for example, see [284]). In this technique, two materials, solid and liquid, whose values of dielectric permittivity are very close, are used in such a way that displacement of the liquid by the solid material does not change the response of the measurement circuit. Thus, the knowledge of properties of the liquid allows determination of the properties of the solid without making intricate electrodes.

Dielectric properties of all materials used in this paper were measured using parallel-plate capacitive structures recommended in [284]. Liquid corn oil (ε_r=3.015) and solid polycarbonate Hyzod (ε_r=3.00, about 1 inch thick) were used in this experiment. Four consecutive steps of measurements at a frequency of 1 kHz were taken:

1) Solid Hyzod is pressed against the Teflon sensor trapping a layer of air between the Hyzod and the sensor's surface.

2) Corn oil is then poured over the Hyzod, but since oil is quite viscous and air cavities are very small, the viscous oil did not fill in the cavities.

3) Hyzod specimen is then lifted so that oil can fill all cavities, after which the Hyzod is returned to its original position.

4) Hyzod is removed and measurements are taken with corn oil only.

Table 6.4 shows that the interelectrode capacitance C_{12} increases from a low to a high value as we go from step 1 to step 4 showing the importance of sample contact. The computer simulation assumes that the dielectric with relative permittivity ε_r=3.015 fills the entire space above the sensor, corresponding to step 4. We would have expected steps 3 and 4 to have about the same capacitances. We believe that a change in the

	Capacitance, C_{12} (pF)				
wavelength	step 1	step 2	step 3	step 4	simulation
λ= 1.0 mm	5.14	5.39	7.99	8.29	8.50
λ= 2.5 mm	3.96	3.96	5.25	5.61	5.59
λ= 5.0 mm	3.17	3.22	3.80	4.17	4.07

Table 6.4: Measured values of C_{12} with oil ($\varepsilon_r = 3.015$) and Hyzod ($\varepsilon_r = 3.00$), which have almost identical relative dielectric permittivities.

electrical double layer for the two cases in steps 3 and 4 may be the cause of the slight capacitance change.

It was observed that increase of the contact pressure and flexibility of the sensor does not lead to significant reduction of this effect. The quality of contact needs to be incorporated into the parameter estimation software relating measured gain and phase to calculate dielectric permittivity and conductivity.

Calculations

Observations on the strong effects of air cavities on the transcapacitance with solid samples made in the previous subsection lead to the need to distinguish between solid and liquid dielectrics when solving the inverse problem of material characterization from complex gain measurements. Calibration curves computed by finite-element simulation are compared to the experimental results in Figure 6.23 for various liquid and solid dielectrics.

Two lines correspond to two modeled cases – when the cavity between the electrodes is filled with dielectric ("liquids-simulation"), and when it is filled with air ("solids-simulation"). For all simulations the dielectric material and electrodes are assumed to be perfectly flat. The effect of the cavity becomes smaller as the wavelength increases. For the case $\lambda = 5$ mm it is hardly noticeable. At the same time, measurements show a large difference between solids and liquids for all wavelengths. Note that this difference far exceeds the effect of electrode height determined by simulation. This phenomena is attributed to the air trapped between the electrodes and the sample surfaces (as was shown schematically in Figure 6.20).

The presumed equivalent air gap was simulated numerically (Figure 6.24). In this simulation, the material with ε_r=2.1 (Teflon, paraffin wax) is initially in ideal flat contact with the electrodes. The interelectrode capacitance decreases as the tested material moves away from the electrodes leaving behind the planar gap filled with air. In order to achieve a reduction of capacitance equal to that measured, the equivalent gap has to be on the order of 40 μm (not including the electrode height), about three times the thickness of electrodes.

A calibration program has been developed to include information about type of contact, surface roughness and surface deformation. One approach is to use redundant information from three independent measurements using the three-wavelength sensor to determine the equivalent planar air gap thickness.

a) $\lambda = 1.0\mu$m

b) $\lambda = 2.5\mu$m

c)$\lambda = 5.0\mu$m

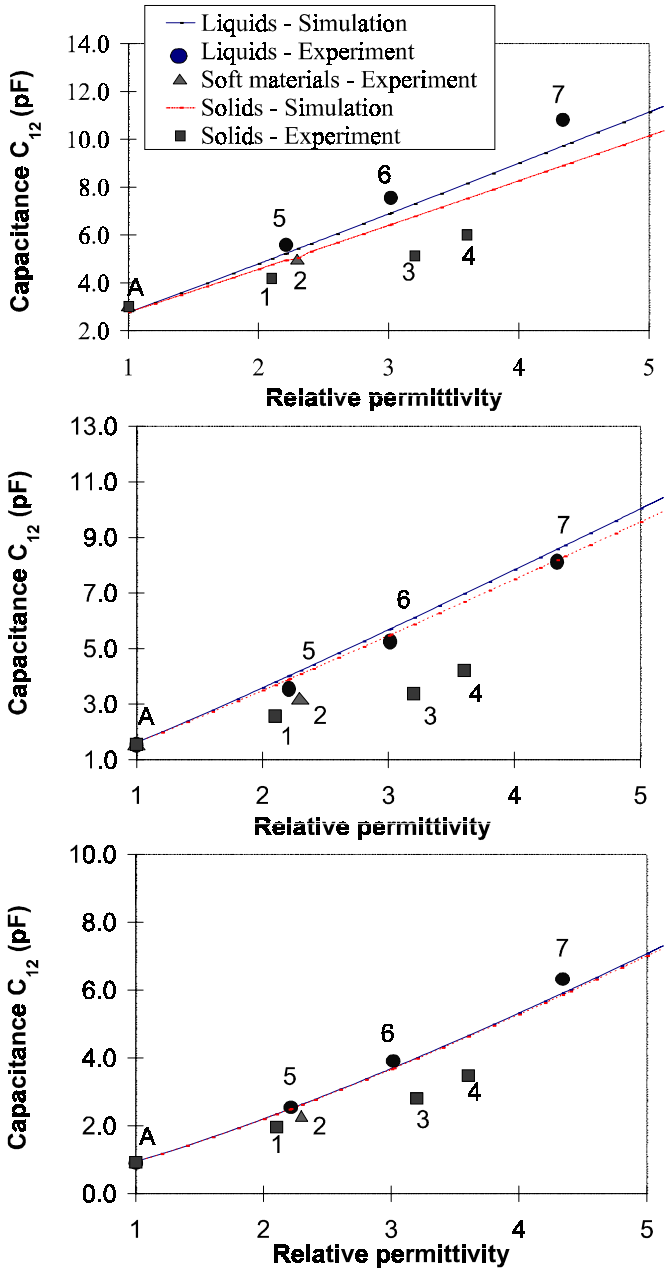

Figure 6.23: Measured and calculated interelectrode capacitance C_{12} for air, liquid, and solid dielectrics for each of the sensor's three wavelengths. The metallization ratio significantly smaller than the nominal value of 0.5 results in lower than nominal values of capacitance. Legend: A: Air, 1:Teflon, 2:Polyethylene, 3:Lexan, 4:Delrin, 5:Transformer Oil, 6:Corn Oil, 7:Castor Oil.

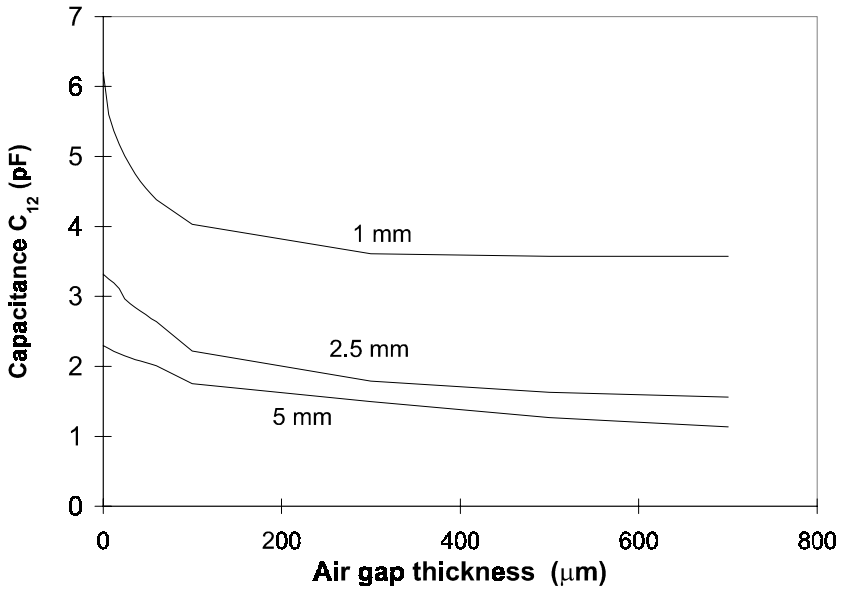

Figure 6.24: Simulation of the air gap thickness effect for all three wavelengths of the Teflon sensor, assuming the test dielectric has ε_r=2.1.

6.5 Cross-Correlation Between Wavelengths

6.5.1 Background

Experiments were conducted to measure the air gap created at the contact surface between the material layer and an interdigital three-wavelength sensor while making dielectrometry measurements. Simulations with Ansoft *Maxwell* software were used to compute the interelectrode capacitances in the three-wavelength Teflon sensor for measurements with a Teflon solid with an air gap ranging from 0 to 60 microns at the contact surface. The simulation results were normalized with an appropriate ratio to enable comparison with measured results. Measurements of the interelectrode capacitance were made using a "Short-circuit mode" Interface box and equivalent air gaps between Teflon and the sensor head were calculated by comparing with and interpolating simulated results. The cross-correlation between the equivalent air gaps for the three wavelengths in the interdigital three-wavelength sensor was found to be much less than 1 in magnitude. This implies that the three equivalent air gaps for each of the

three wavelengths have to be considered as separate parameters while solving for the dielectric properties of an unknown material using the interdigital three-wavelength sensor. This study was conducted together with an undergraduate student Madhu Sarda and this section is based on his Advanced Undergraduate Project report [49].

The micro-level undulations of the sensor surface and the material surface create an air gap between the two surfaces when they are pressed together. The air gap is not constant over the entire surface of the interface between the sensor and the material. Multi-wavelength dielectrometry can be used to measure the thickness of an "equivalent" air-gap for each of the different wavelengths for known materials. This air gap is a "disturbance parameter" in dielectromety measurements. It is an extra parameter to be solved for along with the conductivity and the permittivity of the material being measured. Multi-wavelength dielectrometry provides a tool for measurement of the equivalent air gap for an unknown material. For each wavelength, the measured impedances provide two independent equations with three parameters: the conductivity, the permittivity, and the equivalent air gap. Since the conductivity and the permittivity for the different wavelengths are correlated, a correlation between the equivalent air gaps over the different wavelengths can be determined if it exists. This section describes experiments conducted to measure the equivalent air gaps between Teflon and an interdigital three-wavelength Teflon sensor when they are pressed together for dielectrometry measurements. It shows the degree of correlation between equivalent air gaps between any two of the three wavelengths.

6.5.2 Computer Simulations

A finite element software program, *Maxwell* from Ansoft Corp., was used to separately simulate measurements with Teflon for each of the three wavelengths of the interdigital three-wavelength Teflon sensor.

Simulations with Teflon

Figure 6.25 shows the geometry used to simulate the electrode structure of the sensor. It shows a portion of the width of the electrode geometry equal to half the spatial periodicity of the electrodes for the corresponding wavelength. Different widths and spacings of electrodes were used to simulate different wavelengths. For example, for an electrode spatial periodicity of 1.0 mm, the half-width of the electrodes chosen was 125 μm with a horizontal spacing of 250 μm in between. An arrangement of these units placed side by side results in an electrode spatial periodicity of 1.0 mm as required. Thus, to simulate electrode spatial periodicities of 2.5 mm and 5.0 mm, electrode half-widths of 312.5 μm and 625 μm respectively, and electrode spacings of 625 μm and 1250 μm respectively were used for the electrode structure geometry. For each simulation, the thickness of the guard plane was 14 μm, the substrate was 254 μm thick, and the thickness of the drive and sense electrodes was 14 μm. These dimensions are the same as those of the three-wavelength sensor.

The guard plane was assigned infinite conductivity. The substrate was assigned a relative permittivity, ϵ_r, value of 2.1 (Teflon). The material for the drive and sense electrodes for both measurements and simulations was copper. The material on top of the sensor was assigned the relative permittivity value of Teflon. The thickness of the material layer was chosen to be significantly greater than the penetration depth of the electric field for each wavelength. The background was chosen to be vacuum.

A variable air gap between the sensor surface and the material layer was introduced in the simulations. The air gap, measured from the electrode surface to the material layer, was varied from 0 to 60 μm in increments of 1 μm. For each value of the air gap, the simulation produced values of the drive-sensing transcapacitance and the capacitance of the drive electrode relative to guard.

Figure 6.26 shows graphs of the transcapacitances vs. the air gap for the three wavelengths. Since the dielectric permittivity of the material layer is higher than that of air, the capacitance between the two interdigitated electrodes decreases with the

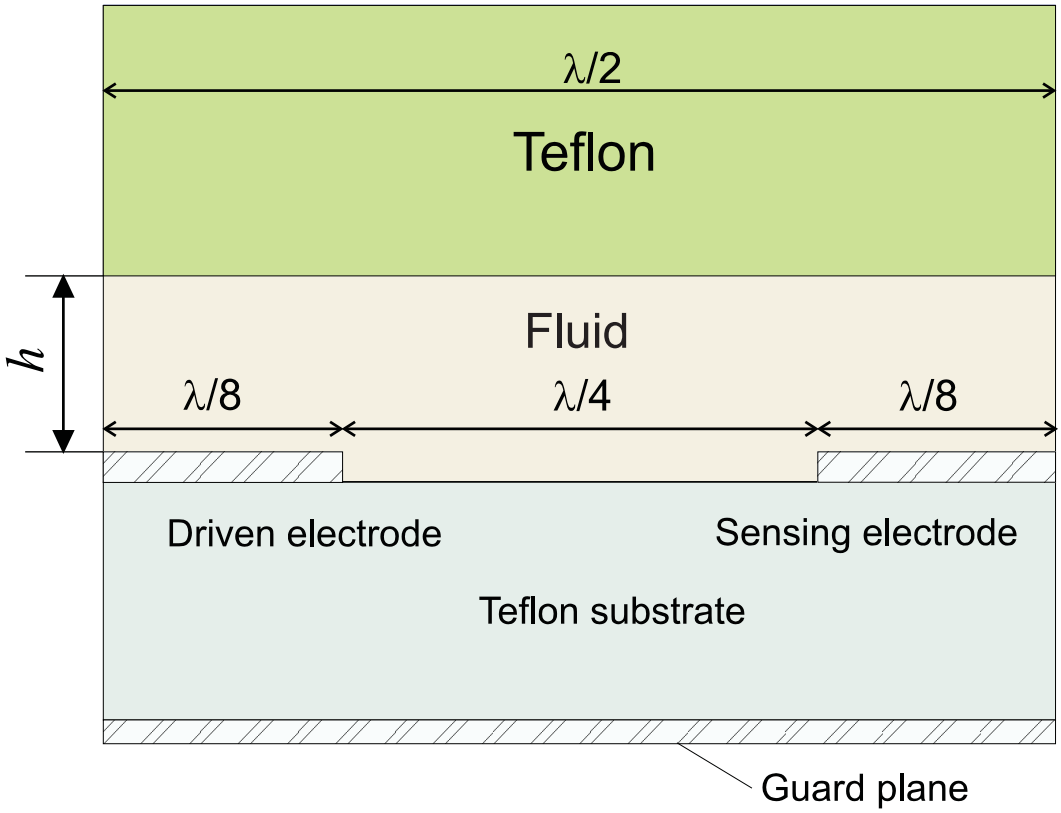

Figure 6.25: The Maxwell half-wavelength model geometry used to simulate the interdigital three-wavelength sensor electrode structure.

thickness of the air gap.

Simulations with Air

For simulations in air, the models used for different wavelengths were the same as for Teflon, except that the material layer was replaced by air. The thickness of the air layer was large enough to accommodate the penetration depth for each wavelength. Table 6.5 lists the interelectrode capacitance, $C[drive, sense]$, and the drive to guard capacitance, $C[drive, guard]$, calculated by the simulation for each wavelength.

Wavelength	$C[drive, sense]$ (pF/m)	$C[drive, guard]$ (pF/m)
1.0 mm	7.1512	16.111
2.5 mm	3.3302	34.49
5.0 mm	2.0289	60.162

Table 6.5: Capacitance values in air produced from Maxwell simulations. $C[drive, sense]$ is the transcapacitance and $C[drive, guard]$ is the capacitance of the drive electrode relative to the guard.

6.5.3 Measurements with Interdigital Three-Wavelength Teflon Sensor

Experimental Setup

Data was collected for measurements made on Teflon using the interdigital three-wavelength sensor. The interdigital three-wavelength sensor was connected to a dielectrometry interface box. The output of the interface box was fed to a controller box which is in turn connected to a computer for data retrieval. The interface box in this case was operating in a short-circuit mode, described in section 4.6.3 to measure the sensor electrode current I_t. It measures the circuit capacitance, C_{12}, and conductance, G_{12}, from knowledge of the driving voltage, V_D, and by current integration with a grounded backplane. The feedback capacitances, C_F, in the Interface Box for the 1.0 mm, 2.5 mm, and 5.0 mm were measured to be 27.5 pF, 221 pF, and 100 pF respectively. Figure 4.18 shows the short circuit current with virtual ground approach of measuring the transcapacitance and transconductance.

A rectangular Teflon slab of uniform thickness 13 mm was used as the material layer over the sensor head. The other dimensions of the slab were big enough to fully cover the electrodes etched on the sensor as its position over the sensor was varied. A metal weight of 10 kg was put on the Teflon slab to improve its contact with the sensor surface. The weight was uniformly distributed over the sensor surface. Additionally, three Teflon pieces of similar dimensions to the Teflon slab used as the material layer above the sensor were placed between the first Teflon layer and the weight so that the metal weight was far enough from the sensor electric field to not

influence dielectrometry measurements. A thin layer of rubber was used underneath the sensor substrate and backplane to improve contact between the electrode surface and the material layer.

The circuit was driven with a sinusoidal voltage of amplitude 1 V peak and measurements were made at a frequency of 1000 Hz for which the system output was most stable. The sensor was housed in an aluminum box and covered with an aluminum lid to provide shielding from external electric fields. The backplane guard electrode was grounded to the aluminum box.

Procedure

The goal of the experiments with Teflon was to obtain at least a twenty-point data set of equivalent air gaps for the three wavelengths. Many experiments were done to ascertain that the level of noise was insignificant and that the air gap between Teflon and the sensor surface was reduced to within 60 microns. The interface box had to be changed from the "floating-voltage type" to the "short-circuit current type," because the former, being an earlier design, produced significant electrical noise. The air gap was reduced to the desired range by pressing the material and the sensor together with a 10 kg weight and by placing a rubber layer of appropriate thickness underneath the substrate layer of the sensor to improve contact of the sensor head with the material layer.

Circuit impedance measurements were taken at 1000 Hz for all three wavelengths for four angular positions of Teflon on the sensor head - 0°, 90°, 180° and 270°. After each measurement Teflon was rotated by 90° on the sensor head. Thus a 24-point data set for each wavelength consisted of six repeated measurements for each of the four positions.

Measurements in Air

Measurement of air dielectrics were made by removing the weight and the Teflon layers. The circuit capacitances measured for the different wavelengths at a driving frequency

Wavelength	$C[drive, sense]$ (pF)
1.0 mm	4.9812
2.5 mm	1.7494
5.0 mm	1.0092

Table 6.6: Measured capacitance values in air using the interdigital three-wavelength sensor. $C[drive, sense]$ is the transcapacitance.

of 1000 Hz are shown in Table 6.6.

Results

The ratio of the air capacitance values obtained from measurements using the interdigital three-wavelength sensor to the values obtained from *Maxwell* simulations was used to normalize the values obtained for simulations with Teflon for comparison with measured data. An additional factor of 1/2 was included in the normalization ratio to account for the fact that the total electrode lengths in the three-wavelength sensors are 0.5 m whereas the simulated values are computed on per meter length basis.

6.5.4 Equivalent Airgaps and Correlation Coefficients

The equivalent airgaps in the sensor structure for different wavelengths were computed from the measured capacitances, C_{12}, by interpolating the normalized $C[drive, sense]$ vs the air gap, h, graphs obtained from the simulations with Teflon and shown in Figure 6.26.

Figures 6.27 through 6.29 are scatter plots showing the cross-correlations between the equivalent air gaps for the three wavelengths for all measurements taken at the four positions of the Teflon sample above the sensor. The correlation coefficients for any two wavelengths are tabulated in Table 6.7.

Table 6.7 shows that the magnitudes of the correlation coefficients for the 24-point data set of equivalent air gaps for three wavelengths are much lower than one. This implies that the equivalent air gaps for the three wavelengths have only a weak correlation.

	$h_{1.0mm}$	$h_{2.5mm}$	$h_{5.0mm}$
$h_{1.0mm}$	1.0000	0.0600	-0.2762
$h_{2.5mm}$	0.0600	1.0000	0.2024
$h_{5.0mm}$	-0.2762	0.2024	1.0000

Table 6.7: Correlation coefficients of the three wavelengths for all measurements computed using the Matlab function corrcoef.

The low correlation coefficients for the 24-point data set means that the equivalent air gaps for the different wavelengths have to be treated as separate parameters while solving for the dielectric properties of an unknown material in the interdigital three-wavelength sensor. This implies that there are too many parameters to be solved for in the inverse problem of computing material and geometrical properties from measurements of circuit elements. The number of independent relations that can be obtained from dielectrometry measurements using the interdigital three-wavelength sensor were less than the number of unknown parameters.

6.5.5 Conclusions

The cross-correlation of data sets from individual wavelengths is critical for reducing the influence of an erratic air gap between the sensor and the solid specimen on multiple penetration depth parameter estimation. The experimental data of this section demonstrates that such cross-correlation is not adequate for selected experimental procedures. The error introduced by the air gap as a major disturbance factor is greatly amplified in the "marching" algorithm, as shown in Section 8.7. The experimental data presented in this Section, in conjunction with the experimental data presented in Section 5.8.5 should serve as an illustration of measurement artifacts that should be taken into account, either in software or, preferably, during the sensor design stage.

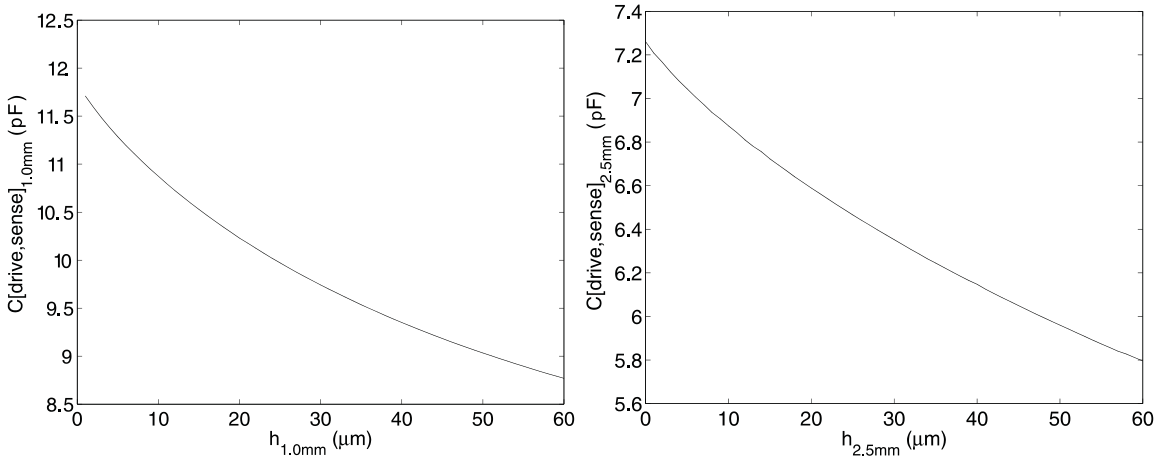

(a) 1 mm wavelength

(b) 2.5 mm wavelength

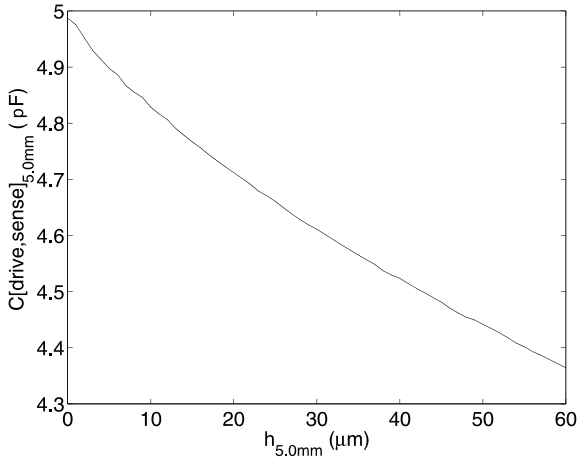

(c) 5 mm wavelength

Figure 6.26: Calculated graphs of the transcapacitances, $C[drive, sense]$ per one meter length, vs the air gap, h, for spatial electrode periodicities of 1 mm, 2.5 mm, and 5 mm.

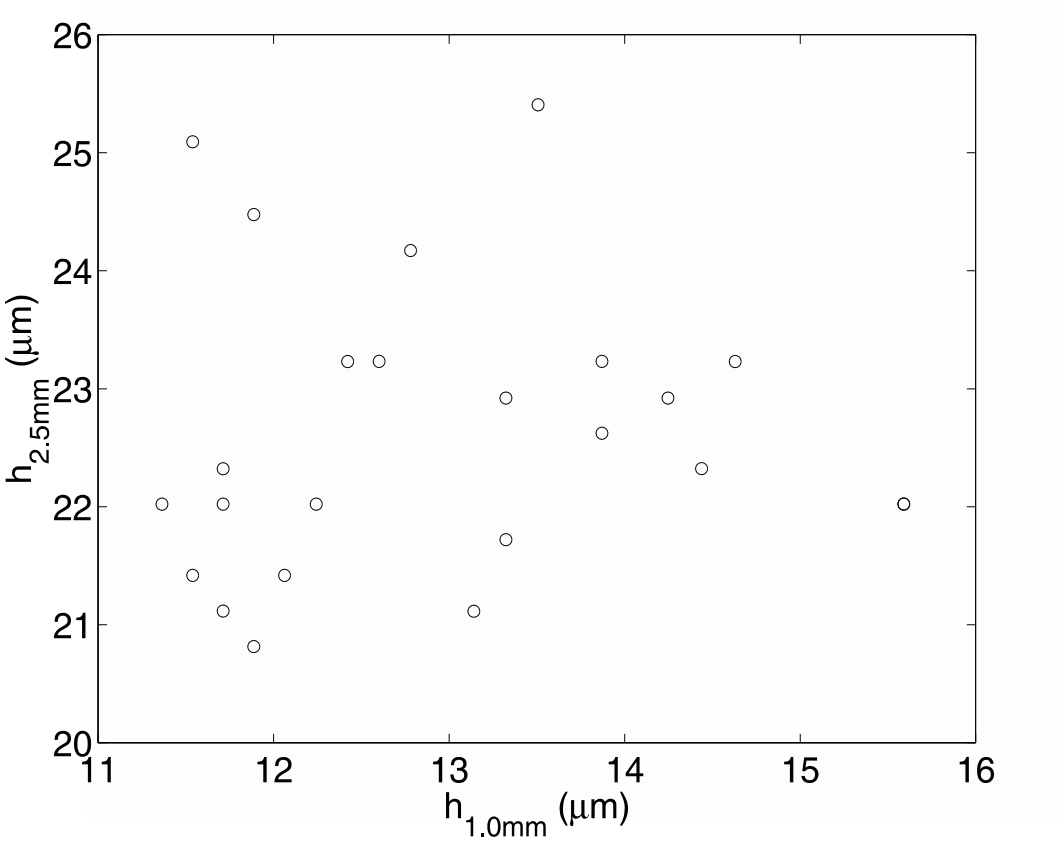

Figure 6.27: A scatter plot of the calculated equivalent air gap from measurements for the 1.0 mm wavelength, $h_{1.0mm}$, vs the equivalent air gap for the 2.5 mm wavelength, $h_{2.5mm}$, for all four positions of the Teflon sample above the sensor.

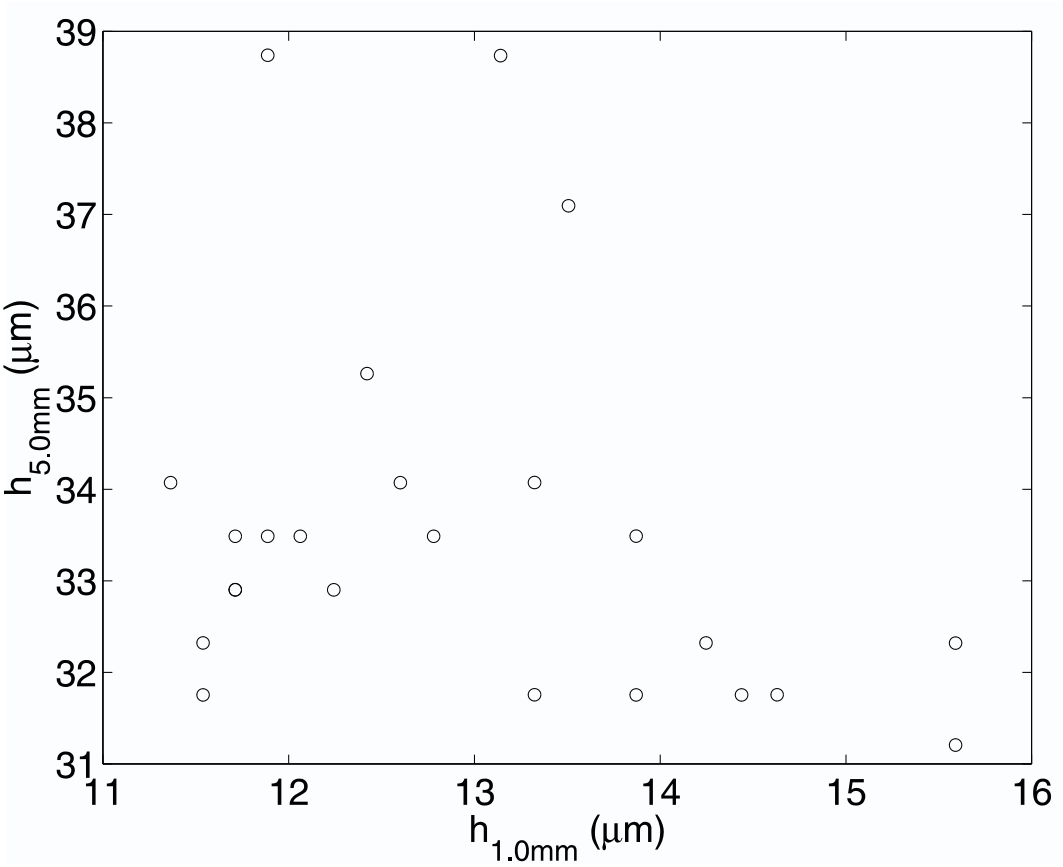

Figure 6.28: A scatter plot of the calculated equivalent air gap from measurements for the 1.0 mm wavelength, $h_{1.0mm}$, vs the equivalent air gap for the 5.0 mm wavelength, $h_{5.0mm}$, for all four positions of the Teflon sample above the sensor.

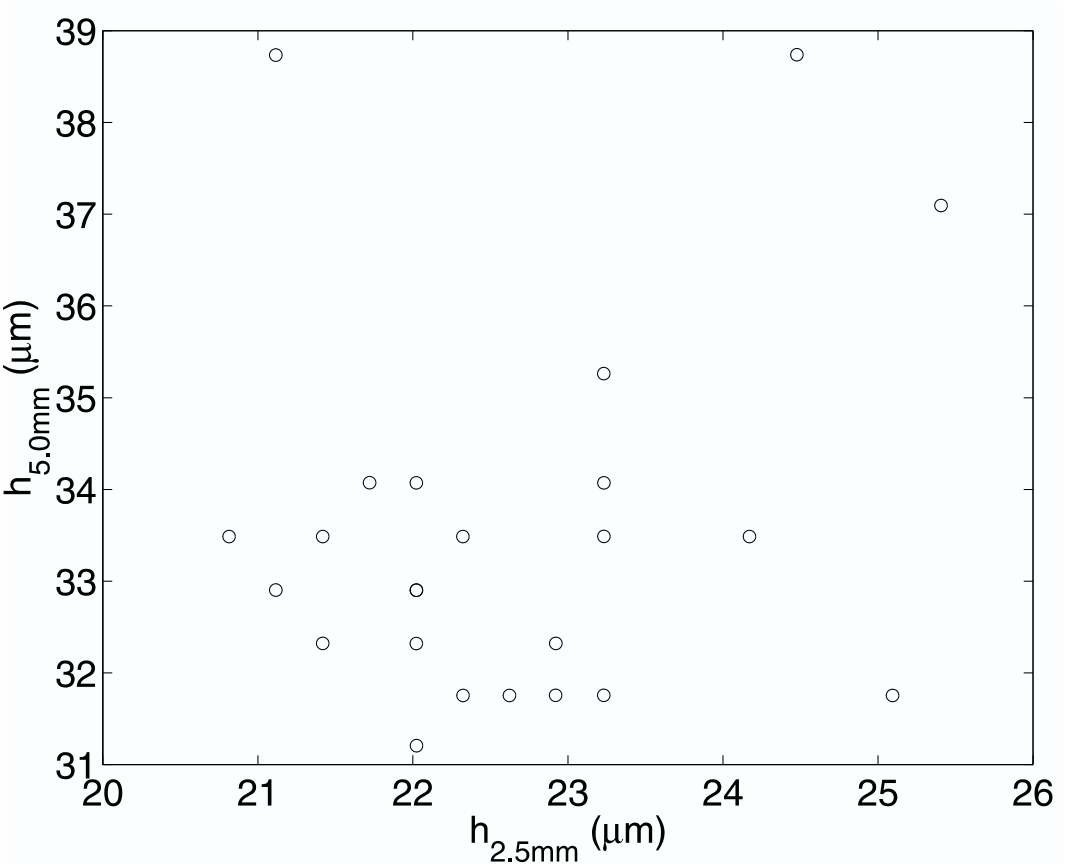

Figure 6.29: A scatter plot of the calculated equivalent air gap from measurements for the 2.5 mm wavelength, $h_{2.5mm}$, vs the equivalent air gap for the 5.0 mm wavelength, $h_{5.0mm}$, for all four positions of the Teflon sample above the sensor.

Chapter 7

Forward Problem

7.1 Significance of Forward and Inverse Problems

Most non-destructive measurement techniques are often viewed in the framework of inverse problem theory. This framework helps to utilize relevant concepts from linear algebra, integral equation applications, and other mathematical fields in an organized and concise manner. In our case, the definition of forward and inverse problems can be presented as shown in Figure 7.1. The forward problem is defined as an electromagnetic calculation problem where transcapacitance and transconductance between sensor electrodes are calculated as a function of material properties and geometric parameters of the given electrode system. Given enough information about material properties and geometric dimensions, this problem can be solved numerically, analytically, or through calibration, depending on the complexity of the task.

For most applications, the inverse problem is inherently more difficult. It requires solving for unknown properties given a known subset of material and geometrical properties and measured transcapacitance and transconductance. The forward problem usually has a unique solution, whereas the inverse problem does not necessarily have a unique or any solution. Furthermore, even if a unique and exact mathematical solution exists for a given set of input the values, it may have no resemblance to the true physical parameters because of the effects of measurement noise.

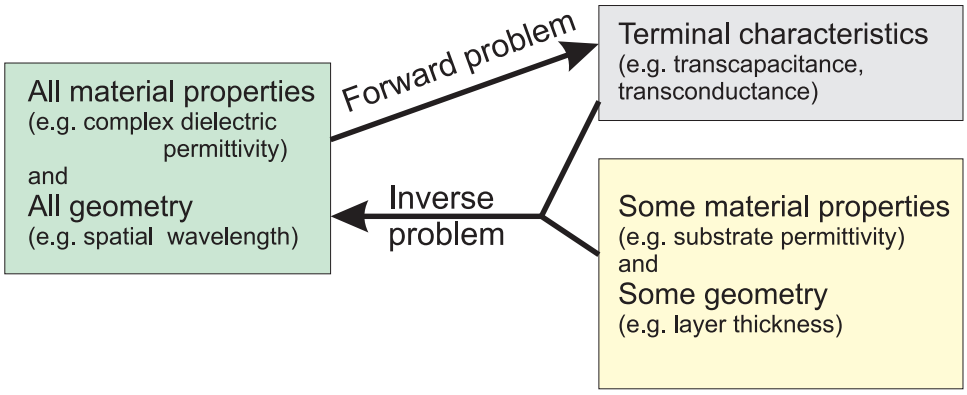

Figure 7.1: The conceptual representation of forward and inverse problems in the framework of dielectrometry.

7.2 2D vs. 3D

For the purpose of this thesis, the *forward problem* is defined as computation of inter-electrode complex transadmittance given geometrical parameters and dielectric properties of materials in a region that includes the sensor itself and material under test. For a more extended discussion on forward and inverse problems, see Section 8.1.

With new geometric designs emerging, the dilemma of choice between the 2D and 3D simulation arises. For the case of dielectrometry, it is advantageous to stay with the 2D simulation. Tens of thousands of finite-elements are needed to simulate the electric fields surrounding even a relatively simple 3D object with reasonable precision (energy error on the order of 1 %).

A three-dimensional finite element analysis has been explored in [224]; exact solutions were successfully approximated with empirical expressions and also compared to measurements. With the stratified geometry of materials, 2D simulation was apparently reasonable and advantageous, especially after the end effects were either reduced, taken into account, or estimated to be insignificant. On the contrary, the presence of confined objects in the high field region seemingly suggests the use of the 3D simulation techniques. In our experience, the computational cost may be prohibitive even for some 2D case simulations, especially in the adaptive simulation approaches.

A compromise solution is proposed and implemented in the simulations in this

thesis. According to this approach, a 3D simulation is replaced with a combination of two 2D simulations. This is possible when the shape of the electrodes remains highly ordered, and the shape of the 3D objects above the sensor is approximately symmetric.

Since the two-dimensional capacitances are calculated on a per unit length basis, one can approximately predict the three dimensional capacitance by multiplying each material's two-dimensional capacitance by its depth in the three-dimensional configuration. If a sensor of length L_D adjacent to a homogeneous dielectric with no object has a 2D simulated admittance per unit length of Y_D, and with an object in the material of length L_O has a 2D simulated admittance per unit length of Y_O, the total sensor admittance due to the object of length L_O in a dielectric material of length L_D is $Y = Y_D(L_D - L_O) + Y_O L_O$. For example, in the case of a 10 cm long object centered within a 1 meter long sensor, the total three dimensional capacitance would be (0.1*object capacitance per unit length)+(0.9*dielectric medium capacitance per unit length) + fringing field capacitance at the electrode ends. This fringing field capacitance is approximately calculated by taking the total 3D capacitance of dielectric only and subtracting the 2D capacitance of dielectric only times the 1 meter length. A side note associated with this technique: Given a 3D object and variable length of the sensing electrode, the sensitivity to the presence of the object is inversely proportional to the length of the sensing electrode.

There is an important difference between distributed parallel circuits in XY and in RZ planes. In the case of the XY plane, the length ratio coefficient which multiplies entries of the admittance matrix is independent of the position of the 3D object, while in the case of the RZ plane, this coefficient is dependent on the radial coordinate of the 3D object with respect to the center of the sensor. This radial dependence should augment sensitivity of the sensor to the differential signal reflecting local inclusion in the uniform medium.

7.3 Continuum Model

From the electroquasistatic field point of view, in a homogeneous medium the electric scalar potential of the field excited by the driven electrodes is a solution to Laplace's equation. At any constant z position, the electric field distribution far away from the sensor edges is periodic in the x direction and assumed uniform in the y direction. In this case, the scalar potential can be written as an infinite series of sinusoidal Fourier modes of fundamental spatial wavelength. The mathematical description of this approach to calculate transcapacitance and transconductance between the sensor electrodes is introduced in Section 1.1.2 and further developed in Appendix B. This approach, called the "continuum model" was developed in the 1980s [8]. The representation of electric potential with spatial Fourier modes falls between closed form analytical solutions and numerical techniques, such as finite element and finite difference calculations. It is less computationally expensive than traditional numerical approaches, but it does not offer analytical expressions suitable for extensive manipulation, for example, to calculate the analytical form of a Jacobian matrix associated with a given electrode geometry. Being limited to multiple layer problems, the continuum model does not possess the generality of numerical techniques that allow computation of electric fields associated with arbitrary shapes. On the other hand, it is easier to incorporate a problem specific individually written computer code implementation of a continuum model as a subroutine to a variety of inverse problem algorithms.

The continuum model has not been used for practical purposes in this thesis because of the simplicity and the versatility of the finite element code *Maxwell*. Ultimately, every approach for the forward problem produces the same answer. The use of the continuum model requires a significant overhead of programming and debugging effort that steals attention and limited resources from critical problems of interdigital dielectrometry, which include, among others, well-posedness of the inverse problem, cross-correlation between signals from interdigital channels, correctness of the representation of dielectric properties on the macroscale, design of signal conditioning electronics, and

analysis of time-frequency relationships in dielectric spectroscopy data.

7.4 Finite Element Simulation

7.4.1 Example of Field Calculations

The *Maxwell* finite element method software package by Ansoft Corp. has been used extensively for calculation of capacitance and conductance matrices throughout this thesis. Figure 7.2 shows a typical half-wavelength cross-section of an interdigital sensor with a triangular finite element mesh superimposed with the electrode structure. The density of finite elements is higher in the higher electric field regions. Generally, a denser mesh results in a more accurate solution, however, it is also more computationally expensive.

Figures 7.3-7.8 visualize the solution for electromagnetic quantities for two specific cases, at very low frequency and at high frequency with respect to the ratio of conductivity and dielectric permittivity of the material under test. In all cases of this example, the driven electrode is held at one volt peak sinusoidal excitation, and the sensing and guard electrodes are held at zero volts. This example is useful for developing intuition for correctness of computed field distributions and and for visualization of physical processes in the bulk of material. The break frequency of $\omega_c \approx \sigma/\epsilon \approx 5$ rad/s determines reasonable values for high $\omega \gg \omega_c$ and low $\omega \ll \omega_c$ frequency approximations.

By comparing Figure 7.3 and Figure 7.4 one can see that at a very low frequency (Figure 7.3) the direction of electric field is tangential to the substrate-corn oil interface above the interface and orthogonal to it below the interface. This happens because the conduction currents in this corn oil case are much higher than the capacitive currents. In the high frequency case, the normal component of displacement field is continuous across the interface because both materials (corn oil and Teflon substrate) appear to be insulating. In both cases, the electric field intensity in the gap between the guard and sensing electrodes is very low because they are at the same potential. The scaling

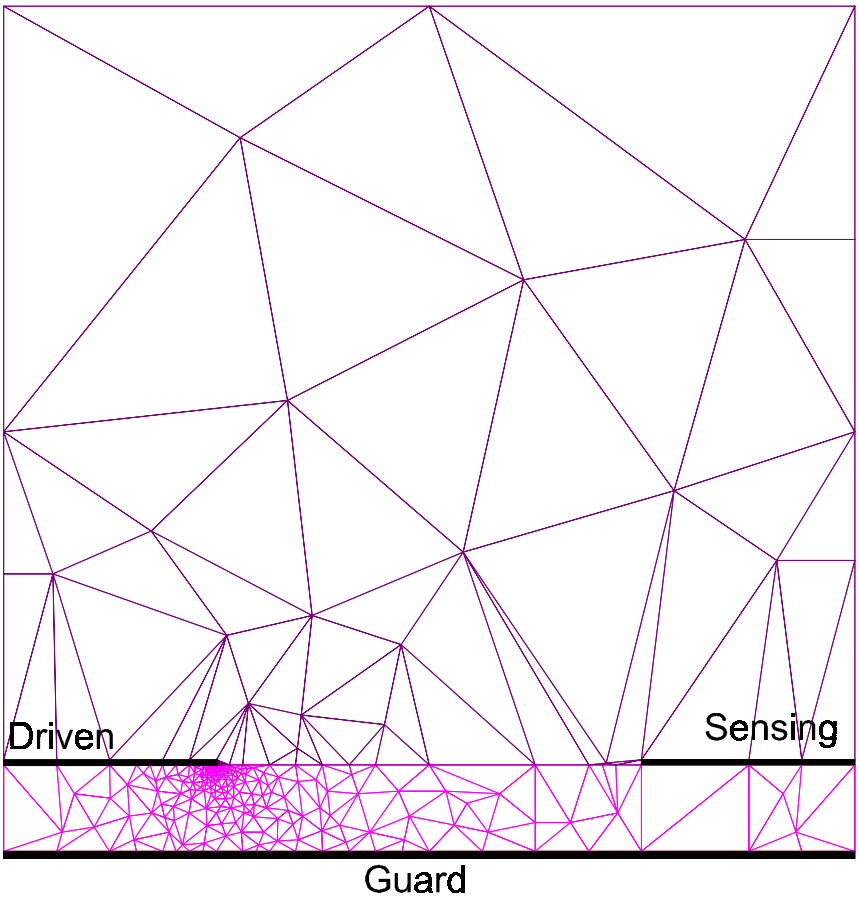

Figure 7.2: An example of a triangular mesh used for computation of capacitance and conductance matrices associated with an interdigital structure.

of the field line arrows with respect to field intensity is logarithmic, therefore their size reduces approximately linearly, rather than exponentially, with the increase of the distance to the sensor head in the upward direction. The field arrows are tangential to the left and right side boundaries due to the even periodicity of the electrode structure with respect to these boundaries.

Figures 7.5 and 7.6 show the distribution of conduction currents for the same two cases. There are no conduction currents in the sensor substrate because it is assumed to be perfectly insulating. Similar observations can be made about the direction of the current density vector arrows as for the electric field arrows.

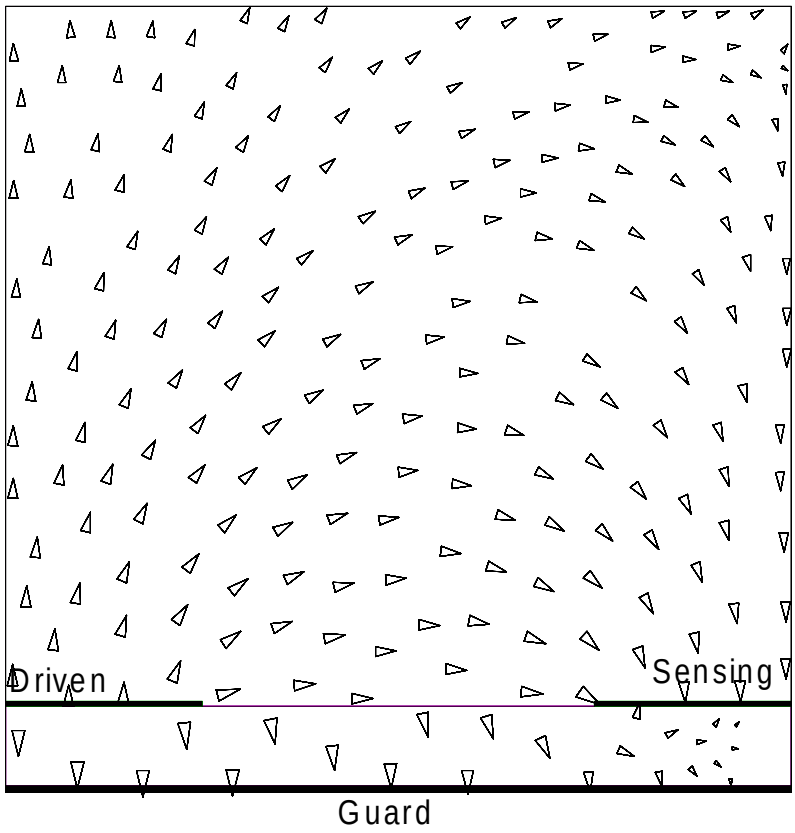

Figure 7.3: The arrows indicate the direction and magnitude of the electric field at an excitation frequency of 0.005 Hz. The relative dielectric permittivity of the material under test (corn oil) is $\epsilon_r = 3.015$ and the conductivity is $\sigma = 3.2 \times 10^{-11}$ S/m. Note the direction of the electric field arrows at the oil-substrate interface.

Figures 7.7 and 7.8 show the equipotential lines for the same two cases. Since the equipotential lines are perpendicular to the electric field lines, one can predict that they will come perpendicularly from above to the corn oil-Teflon interface at low frequency, at an angle to the same interface at high frequency, and perpendicular to the left and right region boundaries.

Finally, Figure 7.9 shows the calculated distribution of the electric potential along the corn oil-Teflon interface. One can see that the gradient of potential is higher near the electrodes, which corresponds to higher intensity of the electric field.

The distribution of electric potential above the interdigital electrodes can also be measured experimentally by using a needle probe. Naturally, the lateral and longi-

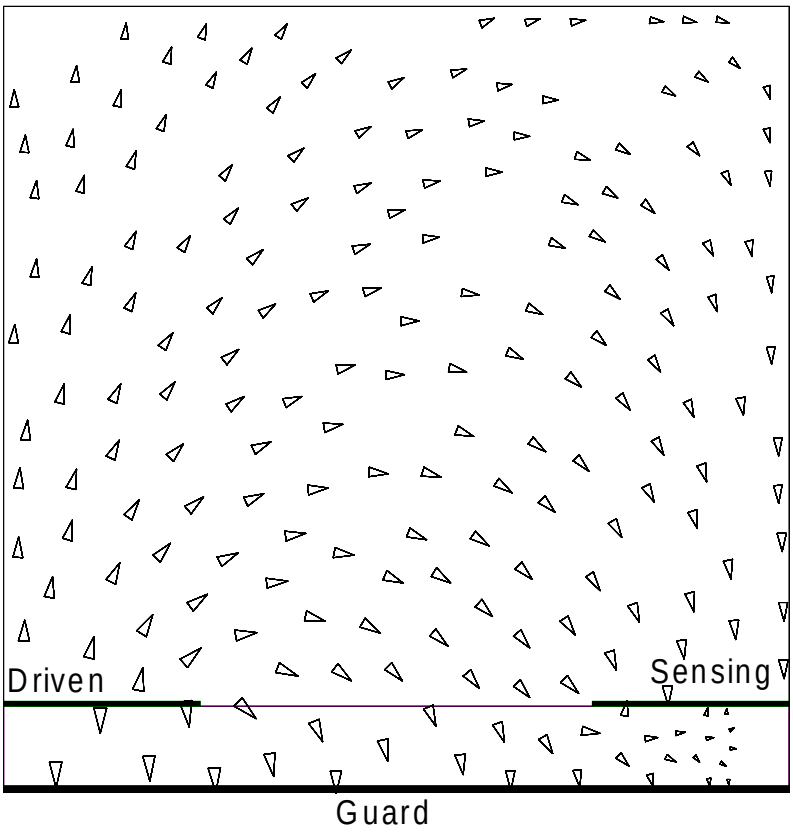

Figure 7.4: The arrows indicate the direction and magnitude of the electric field at an excitation frequency of 60 Hz. The relative dielectric permittivity of the material under test (corn oil) is $\epsilon_r = 3.015$ and the conductivity is $\sigma = 3.2 \times 10^{-11}$ S/m. Note the direction of the electric field arrows at the oil-substrate interface.

tudinal electric field components can be computed from the potential distribution by partial differentiation. The highest resolution of such measurements reported to date is in the submicron region [216].

7.4.2 Non-dimensionalized Plot of Capacitances

Additional work was undertaken with MIT undergraduate student Jason Bau to produce a non-dimensionalized plot of calculated capacitances between drive and sense and drive and backplane as a function of normalized substrate thickness, d/λ, and normalized dielectric constant, $\varepsilon_m/\varepsilon_s$, where d is the substrate thickness, ε_m is the

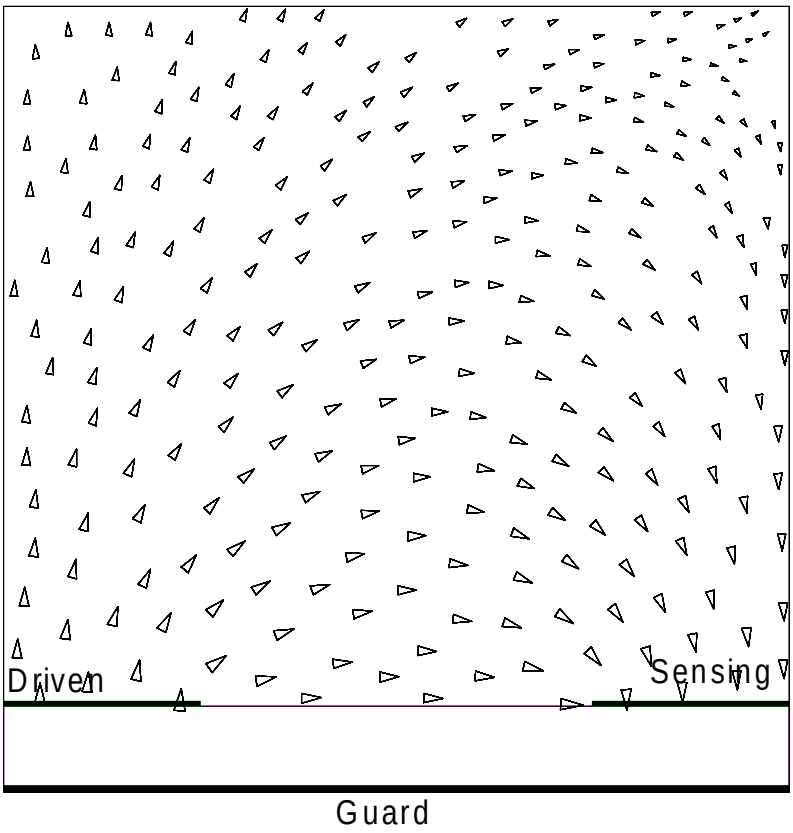

Figure 7.5: The arrows indicate the direction and magnitude of conduction currents at an excitation frequency of 0.005 Hz. The relative dielectric permittivity of the material under test (corn oil) is $\epsilon_r = 3.015$ and the conductivity is $\sigma = 3.2 \times 10^{-11}$ S/m.

dielectric permittivity of material under test of infinite thickness, and ε_s is the dielectric permittivity of the substrate. This required a *Maxwell* parametric sweep of two variables, one of which was spatial in varying the thickness of the substrate from 20 microns to 2000 microns with a total height of 4000 microns. The other variable was the relative permittivity of the material, which was varied from 2 to 100, while the permittivity of the substrate was kept at 10 to permit the ratio $\varepsilon_m/\varepsilon_s$ to have values above and below 1. To save calculation time, the permittivity sweep was done at each point in the distance sweep to prevent the calculation of a new mesh at every point. Once the data was simulated, it was processed within *Matlab* to produce 3-d mesh graphs shown in Figure 7.10 as well as contour plots. Also, a third-order polynomial

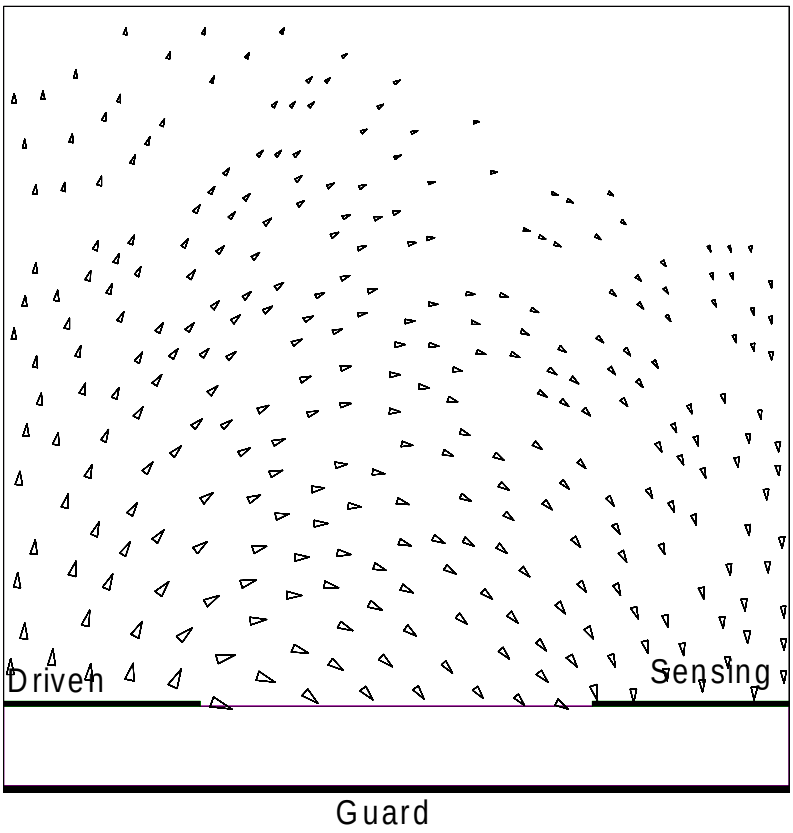

Figure 7.6: The arrows indicate the direction and magnitude of conduction currents at an excitation frequency of 60 Hz. The relative dielectric permittivity of the material under test (corn oil) is $\epsilon_r = 3.015$ and the conductivity is $\sigma = 3.2 \times 10^{-11}$ S/m.

fit was calculated for this data, and the percentage error was calculated and plotted, with the error at most points being less than 2%, as shown in Figure 7.11. The code for all these manipulations and plots is available in Appendix H. Table 7.1 lists the coefficients of the two-variable third-order polynomial-fit of this data, according to the equation

$$\frac{C_{12}}{\varepsilon_S} = \sum_{\substack{i=0,3 \\ j=0,3}} x^i y^j, \tag{7.1}$$

where x=d/λ (substrate thickness/wavelength) and y=$\varepsilon_m/\varepsilon_s$ (material dielectric constant/ substrate dielectric constant).

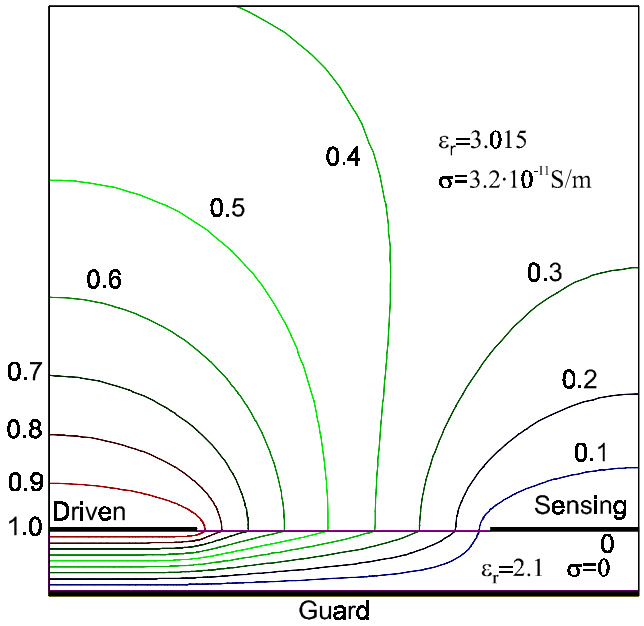

Figure 7.7: Equipotential lines at an excitation frequency of 0.005 Hz. The relative dielectric permittivity of the material under test (corn oil) is $\epsilon_r = 3.015$ *and the conductivity is* $\sigma = 3.2 \times 10^{-11}$ *S/m.*

	x^3	x^2	x	1
y^3	3.8977676e-002	-8.5779518e-001	6.9341789e+000	4.3670077e+000
y^2	-7.6134189e-002	1.6695304e+000	-1.3413833e+001	-1.2547746e+001
y	4.6964771e-002	-1.0239383e+000	8.1446603e+000	1.3133535e+001
1	-9.2907431e-003	2.0048778e-001	2.8965208e+000	-1.5943268e+000

Table 7.1: Polynomial coefficients a_{ij} *for* x=d/λ *(substrate thickness/wavelength) and* y=$\varepsilon_m/\varepsilon_s$ *(material dielectric constant/ substrate dielectric constant).*

7.5 Other Methods

Of course, other numerical methods can be used for the calculation of capacitance and conductance matrices of interdigital sensors. Finite difference simulation is treated in [3] and in [233]; a heat-conduction equivalence approach is used in [224]; another finite element package, ANSYS, has been used in [285]; multipole-accelerated fast capacitance extraction is used in [140], and RC-transmission line equivalency in [60].

7.6 Approximating Expressions

7.6.1 Lock and Key Device

An approximate expression for the admittance of an interdigital structure (called lock and key device in the original source) has been derived in the 1970s and later reported in [77]. The admittance Y of the device immersed in an infinitely thick layer of resin, as shown in Figure 7.12 is

$$Y = G + j\omega C \tag{7.2}$$

where

$$G = \frac{4\sqrt{2NW}}{\pi^2}\left[\sigma_{resin} + \sigma_{sub} + \frac{\pi T}{L}\sigma_{ox} + \frac{\pi}{L}\left(\kappa_{ox} + \kappa_{sub}\right)\right], \tag{7.3}$$

$$C = \frac{4\sqrt{2NW}}{\pi^2}\left[\varepsilon_{resin} + \varepsilon_{sub} + \frac{\pi T}{L}\varepsilon_{ox}\right], \tag{7.4}$$

and N is a total number of interelectrode gaps, W is the length of electrodes, L is the interelectrode separation, T is the oxide layer thickness, σ is conductivity, ε is dielectric permittivity, κ_{ox} is the surface conductivity at the oxide-resin interface, and κ_{sub} is the surface conductivity at the substrate-oxide interface. This model is different from the sensor designs used in this thesis, but is included here for future reference.

7.6.2 Conformal Mapping

Another potentially useful approach for the calculation of interdigital electrode capacitance stems from conformal mapping. Conformal mapping is one of the most frequently used approaches for calculation of the capacitance of interdigital structures, especially when the imaginary part of the complex dielectric permittivity of all materials is small enough to be neglected. Typical examples of such equations are given in [230,286] for a case of interdigital electrodes of thickness h located on the boundary of two layers with relative permittivities ε_1 and ε_2 (no substrate). The layer of thickness h with relative permittivity ε_3 fills the gap due to the electrode thickness (see Figure 7.13). Using a complete elliptic integral of the first kind $K[x]$, the sum of the capacitances per unit

length C_1 and C_2 due to relative dielectric permittivities ε_1 and ε_2 is found as:

$$C_1 + C_2 = \varepsilon_0 \frac{(\varepsilon_1 + \varepsilon_2)}{2} \frac{K\left[\sqrt{1 - \left(\frac{a}{b}\right)^2}\right]}{K\left[\frac{a}{b}\right]}, \tag{7.5}$$

where a is the distance between inner edges and b is the distance between outer edges of electrodes in the half-wavelength representation of Figure 7.13. The capacitance per unit length due to the volume of thickness h between the electrodes filled with relative dielectric permittivity ε_3 could be approximated as that of a parallel plate capacitor:

$$C_3 = \varepsilon_0 \varepsilon_3 \frac{h}{a} \tag{7.6}$$

Then, the total capacitance between the driven and sensing electrodes is:

$$C_{12} = C_1 + C_2 + C_3 \tag{7.7}$$

7.7 Summary

The techniques used in this chapter serve to calculate the admittance matrix associated with the sensor electrode system for different levels of modeling complexity. Although analytical models are generally most attractive due to their inherent accuracy and suitability for theoretical analysis, they are only available for the simplest electrode and material property combinations. A semi-analytical continuum model is faster than finite element or finite difference calculations, but is exceedingly complex to produce closed form analytical expressions. A speed-up of the forward problem calculation can also be achieved by pre-computing large arrays of discretized variables of interest in the region of interest. Then, these solutions may be either stored in computer memory in the form of lookup tables or approximated with polynomial expressions. When the physics of the underlying phenomena is not fully understood and, thus, is not adequate for modeling, a brute force calibration may help to build an adequately large database for the forward and inverse problem transformations. The choice of a specific technique depends on the application and the requirements of the inverse problem.

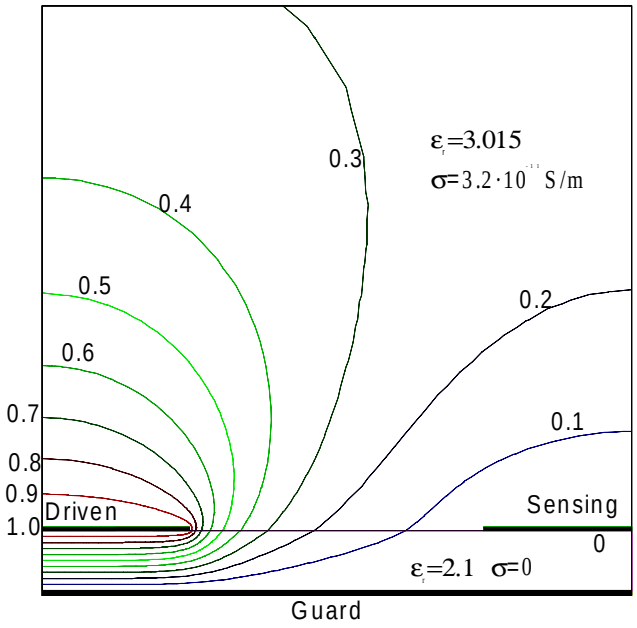

Figure 7.8: Equipotential lines at an excitation frequency of 60 Hz. The relative dielectric permittivity of the material under test (corn oil) is $\epsilon_r = 3.015$ and the conductivity is $\sigma = 3.2 \times 10^{-11}$ S/m.

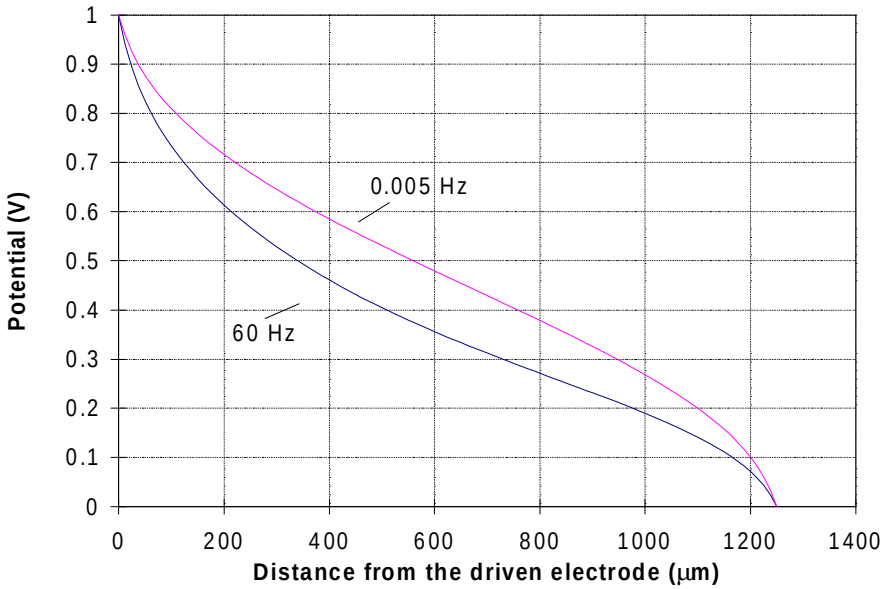

Figure 7.9: Calculated distribution of the potential along the substrate-specimen interface between the driven and sensing electrodes.

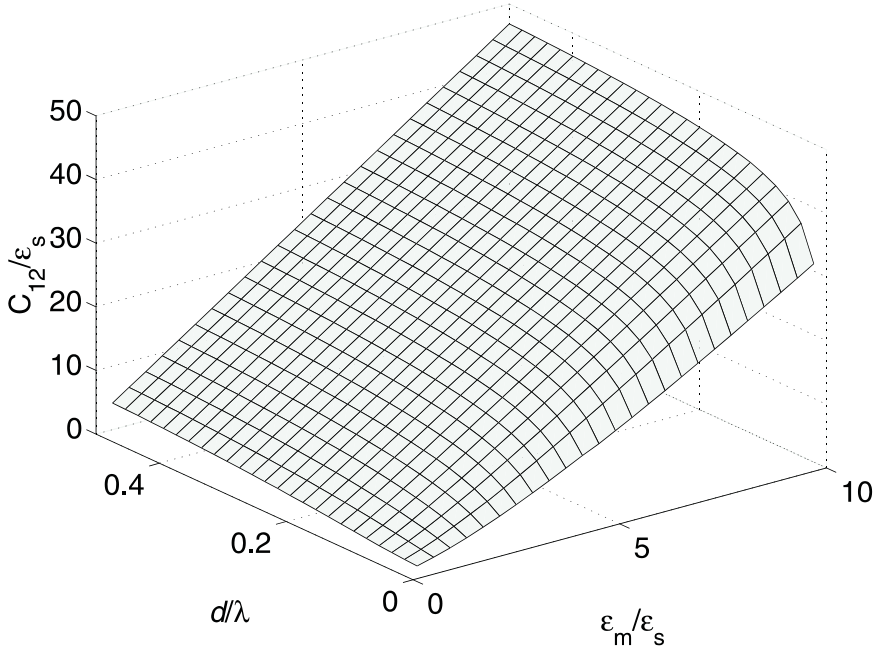

Figure 7.10: C_{12}/ε_s vs. normalized dielectric constant and normalized substrate thickness. This function can be used to predict the range of capacitance values in future sensor designs.

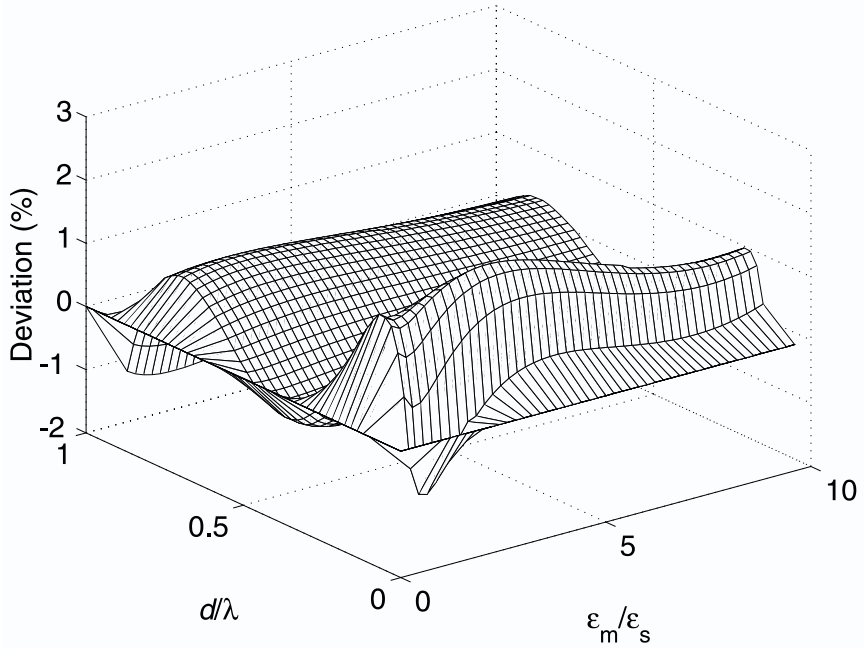

Figure 7.11: Error between the 3rd order polynomial approximation and a calculated function shown in Figure 7.10.

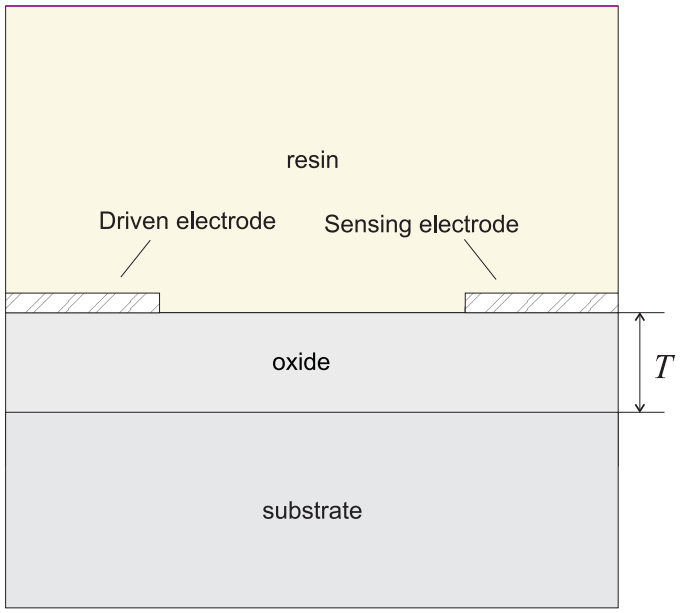

Figure 7.12: A half-wavelength cross-section of the interdigital electrode structure whose conductance and capacitance are approximated with (7.3) and (7.4).

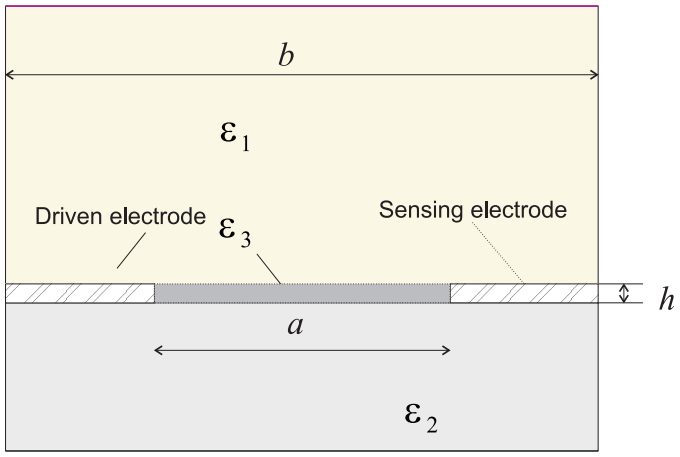

Figure 7.13: A half-wavelength cross-section of the interdigital electrode structure whose conductance and capacitance are approximated with (7.5) and (7.6).

Chapter 8

Inverse Problem

8.1 Introduction

From a purely mathematical perspective, both the forward and inverse problems postulated in this thesis can be considered the inverse to each other [287]. Conventionally, a simpler problem is chosen to be called a *forward problem*, and the more complicated one is called an *inverse problem*. However, distinction between the two goes beyond mere simplicity considerations. The forward problem is usually determined by the nature of the physical phenomena behind the mathematical formulation [288]. For example, determining the response of a physical system to a set of external excitations logically falls into a category of a forward problem, whereas determining what the external excitations and internal parameters of the system should be in order to provide the measured response is treated more naturally as an inverse problem. The latter example is sometimes classified as a *parameter identification* or *parameter estimation* problem. Another example of problems inverse to each other is differentiation and integration. In the context of this thesis, to solve the forward problem is to calculate the entries of the admittance matrix (most often C_{12} and G_{12}) of the sensor given the geometry and material properties. To solve the inverse problem is then to find geometry and material properties given the measured values of the admittance matrix entries and, possibly, some of the geometry and material properties.

Real world physical inverse problems often lead to *ill-posed* (improperly posed) mathematical problems, which means, among other things, that their solution is highly sensitive to input data perturbations [288]. The source of data perturbations in interdigital dielectrometry includes most phenomena listed in Chapter 6 as well as such general perturbations as experimental noise, numerical precision of calculation, and analog-to-digital conversion errors. Regularization methods allow solving ill-posed problems through a system of techniques that take advantage of additional information available about the system. Regularization methods tend to balance accuracy and stability, sacrificing one for the sake of the other to achieve an acceptable performance of parameter estimation algorithms.

Ill-posed problems do not fulfill one of the three requirements in Hadamard's definition of well-posedness [288]:

$$\text{For all admissible data, a solution exists.} \tag{8.1}$$

$$\text{For all admissible data, the solution is unique.} \tag{8.2}$$

$$\text{The solution depends continuously on the data.} \tag{8.3}$$

The same problem may be considered well-posed or ill-posed depending on what data are considered admissible, what is the criterion of continuity, and what is the expected accuracy of solution.

The requirements (8.1) and (8.2) are of concern when solving interdigital dielectrometry problems. It may be difficult to distinguish admissible data from erroneous unless a fair amount of information about the system is available. In simple cases, the uniqueness of solution can be verified by computing all possible cases with reasonable discretization. In more complex cases, even when the number of equations provided by a sensor array exceeds the number of unknown variables, there is no guarantee that the solution is going to be unique or that it exists.

The discretization often introduces non-uniqueness to the inverse problem. Several levels of discretization are normally present in dielectrometry algorithms. The

three wavelengths themselves in the TWS or CSC sensor constitute crude discretization of penetration depth of electric field into the material. The algorithms which use pre-computed solution spaces use parameter discretization to speed up solution of the inverse problem. Forward problem computation algorithms, unless they are based on analytical solutions available for the simplest cases, also use some type of spatial discretization in representation of material geometry. For example, the continuum model uses a finite number of collocation points and a finite number of spatial Fourier components; finite element and finite difference software spatially discretize the entire simulated region; multi-layer models that describe continuously varying material properties are limited by the number of discrete layers; etc.

8.2 Negative Capacitance and Conductance

8.2.1 Literature Survey

Experimental data from interdigital dielectrometry measurements with semi-insulating solid and liquid dielectrics often have negative values of capacitance and conductance between the driven and sensing electrodes of an interdigital sensor [21, 27]. In light of other reported cases of negative capacitance [164, 289–293] and negative conductance (or resistance) [294–300], especially in parallel plate geometry, the readers sometimes misinterpret the reported data from the interdigital dielectrometry measurements and associate it with other known cases. The goal of this section is to provide necessary background for proper interpretation of such cases, and, through illustrative experimental and theoretical examples, to set the ground for differentiation between various scenarios that lead to the negative values of interelectrode capacitance and conductance. A basic explanation was made in [27], but it only covered the negative capacitance effect without going into details. Anticipating future work where negative values of interelectrode capacitance and conductance will appear in different situations, this section analyzes the issue from several viewpoints and provides the connection of

results from dielectrometry to other technical fields, such as semiconductor electronics [301–305] and piezoacoustic transducers [306].

In many cases, the negative values are not a result of an unmodeled physical phenomena, but simply a valid lumped-element circuit representation of a given electrode geometry at the specified frequency of electrical excitation. Earlier work on interdigital dielectrometry parameter estimation algorithms used voltage gain and phase of the admittance divider formed by the interdigital electrodes and the test admittance (or the closed-loop integrator [5, 11, 27]) to estimate dielectric properties of the material under test [5, 8, 10, 65, 71, 83]. This type of sensor response representation is dependent not only on the sensor parameters and material properties but also on the parameters of the measurement electronics, most notably load or feedback capacitors for voltage or current mode measurements, respectively. It is desirable to decouple the sensor response from the measurement parameters, because it improves signal linearity, better reflects frequency dependence of material properties, and, in some cases, guarantees the uniqueness of the inverse problem [19]. The last condition means that sometimes gain and phase data may not be unique with respect to material properties while the capacitance and conductance data for the same combination of material properties is unique. In the specific implementation of this thesis, C_{12} and G_{12} are independent of C_L and C_F while gain and phase depend on C_L and C_F. The definition of these circuit elements is given in Section 4.6.

8.2.2 Experimental Results

Representative corn oil gain and phase measurements with the capacitive divider for guarded floating voltage mode measurements are shown in Figure 8.1, and the results of conversion to the admittance matrix entries are shown in Figure 8.2.

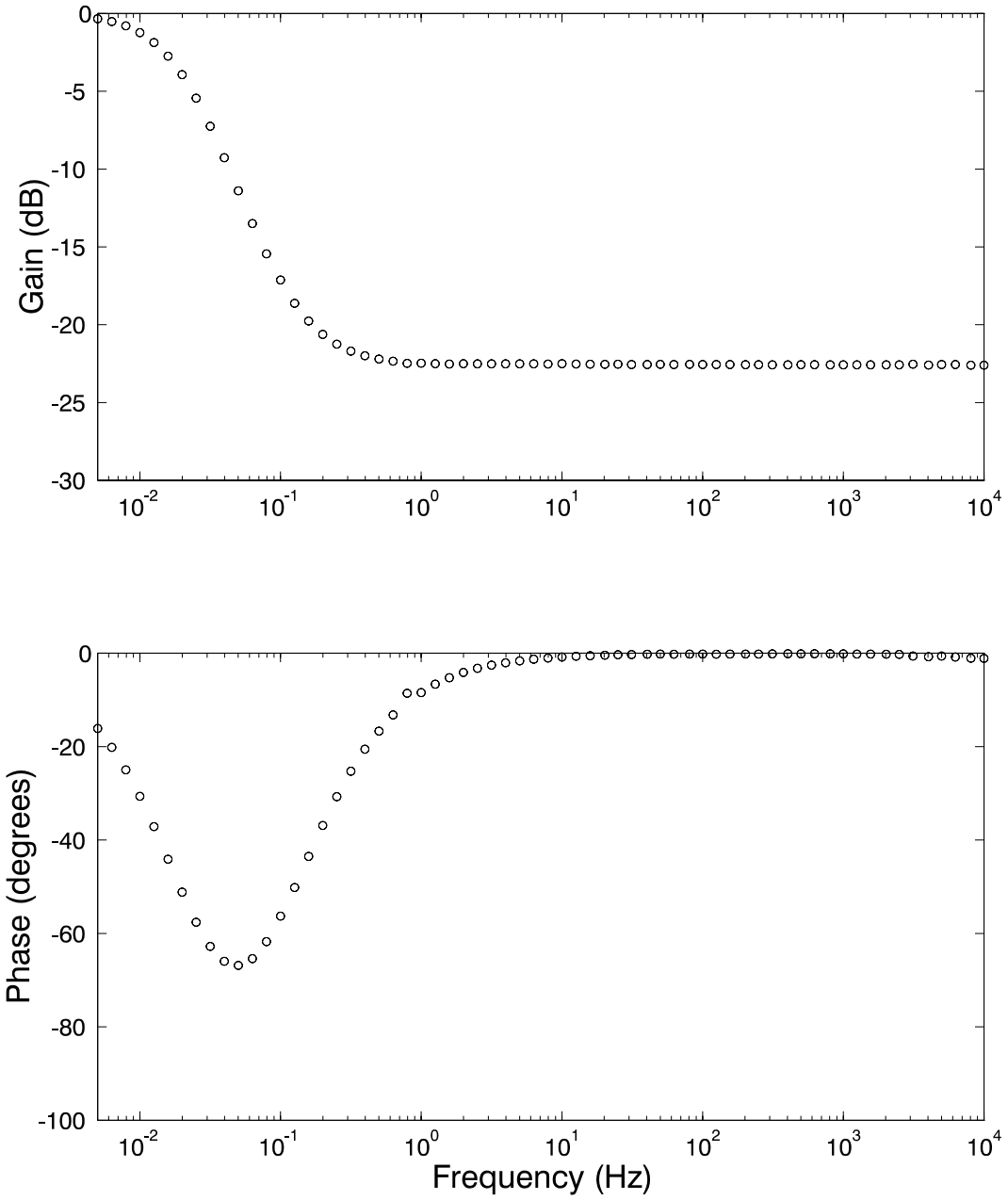

Figure 8.1: Gain and phase measurements of corn oil with a floating voltage with guard plane method, 5 mm wavelength, load capacitance $C_L = 47.4$ pF.

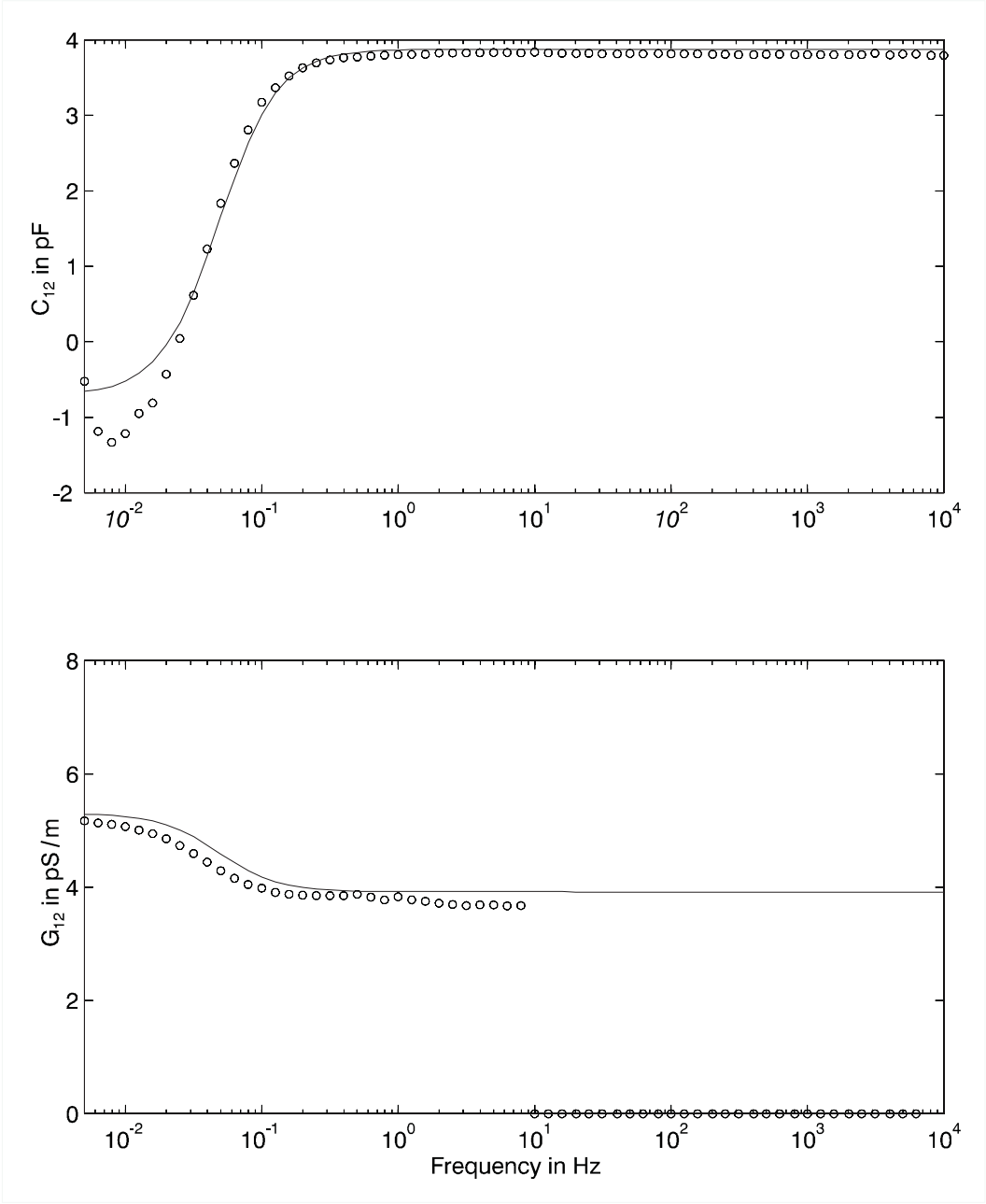

Figure 8.2: Interelectrode capacitance and conductance for the gain/phase measurements in Figure 8.1 for the corn oil experiment with 5 mm wavelength, $C_L = 47.4$ pF (circles) and simulation (with $\varepsilon_r = 3.25$ and $\sigma = 23$ pS/m) of the frequency dependent admittance matrix entries with finite-element software (lines).

The gain is near zero for very low frequencies, which indicates a predominantly resistive behavior of the interelectrode admittance. To a first look, the overall gain-phase behavior looks very reasonable for the system with constant coefficients, one pole and one zero.

This measurement was done with the first generation of Teflon sensors (it has poorer etching tolerances than the second generation). In Figure 8.1, the gain is flat and phase is zero for high frequencies, which indicates a dominant capacitive behavior of the interelectrode admittance.

The measurement and calculation of admittance matrix entries shown in Figure 8.2 shows that this gain-phase behavior corresponds to a system with frequency dependent coefficients, moreover, the capacitive part of the interelectrode admittance becomes negative at low frequencies. The simulation (solid line) is done assuming for corn oil $\varepsilon_r = 3.25$ and $\sigma = 23$ pS/m. There are usually slight ambient temperature variations during the experiments, and the conductivity is strongly dependent on temperature. Measurements with a parallel plate capacitor indicate that the conductivity of corn oil approximately doubles with every 10°C temperature increase. For example, the conductivity of corn oil in ambient laboratory environment at 15°C is about 16 pS/m and at 25°C is about 32 pS/m. In both cases the conductivity is measurable only at frequencies less than 1 Hz and is not frequency dispersive.

8.2.3 Simplified Equivalent Circuit

It is appropriate to pause to discuss the calculated negative values of capacitance as it may not be immediately apparent to the reader how any lossy dielectric material can admit these values. Basic circuit theory can be used to help explain the measured negative capacitances. To understand the apparent negative capacitance in a more elementary setting consider the circuit shown in Figure 8.3 that approximately models the sensor topology in Figure 1.4. Suppose that we do not have the ability to measure the voltage at node c, and we are only interested in the circuit characteristics at nodes a, b, and ground. Then we can use the pi-equivalent circuit shown in Figure 8.4 which

exhibits identical steady-state behavior as the circuit shown in Figure 8.3 from the terminals of interest. The circuit parameters in Figure 8.4 are related to those of Figure 8.3 by:

$$G_{12} = 2G_1 \frac{\omega^2 C_1(C_2 + C_1) + G_1^2}{\omega^2(2C_1 + C_2)^2 + 4G_1^2}, \tag{8.4}$$

$$C_{12} = \frac{\omega^2 C_1^2(2C_1 + C_2) + G_1^2(2C_1 - C_2)}{\omega^2(2C_1 + C_2)^2 + 4G_1^2}, \tag{8.5}$$

$$G_{10} = G_{20} = G_1 - 2G_{12} = \frac{\omega^2 C_2^2 G_1}{\omega^2(2C_1 + C_2)^2 + 4G_1^2}, \tag{8.6}$$

and

$$C_{10} = C_{20} = C_1 - 2C_{12} = C_2 \frac{\omega^2 C_1(2C_1 + C_2) + 2G_1^2}{\omega^2(2C_1 + C_2)^2 + 4G_1^2}. \tag{8.7}$$

Each parallel combination of G_1 and C_1 approximately represents the effective lossy layer of dielectric along the interface between driven and sensing electrodes, while C_2 represents the shunt capacitance through the substrate from substrate/material interface to ground. Note that the capacitance C_{12} is negative at low frequencies if $C_2 > 2C_1$. The other three parameters (G_{12}, G_{11}, and C_{11}) are positive definite for all frequencies. We would like to emphasize a few points.

1. In theory, we can represent our distributed system well by a (possibly dense) network of resistors and capacitors which have a direct physical correspondence to the electrical properties of the material and sensor topology on an incremental scale. When we represent the same system by fewer elements while retaining the voltage/current terminal characteristics, the general equivalent circuit may include frequency dependent capacitors or resistors that can become negative over a range of frequency.

2. This is only possible in circuits with more than two terminals. In our case, we have the driving, sensing, and backplane electrodes. In a two-terminal circuit it is straightforward to prove (using Tellegen's theorem [307]) that any circuit containing only resistors and capacitors will appear from the terminals as a lossy capacitive system with no negative capacitors. As a consequence of this, in our circuits the driving point impedance seen by the source at the driven electrode will always be positively capacitive (and lossy).

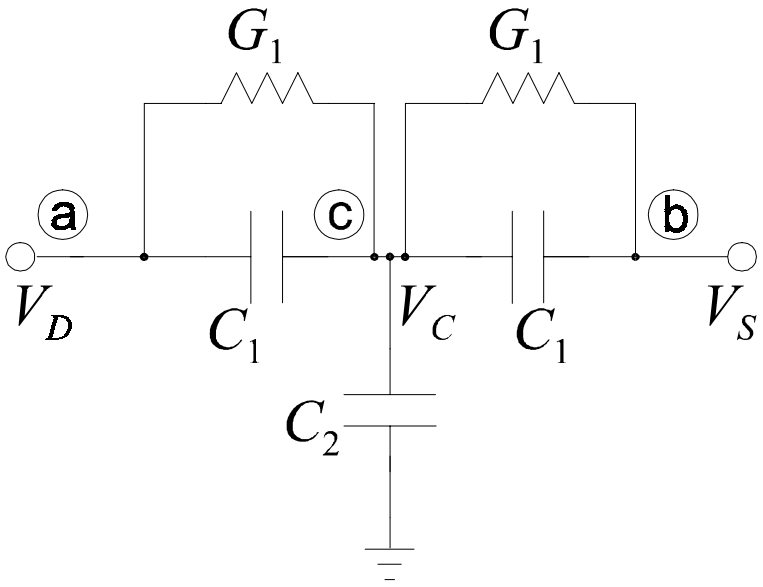

Figure 8.3: Justification of the negative transcapacitance values for C_{12} in Figure 8.4. Equivalent circuit of a sensor that approximately models sensor topology.

3. Our elementary circuit example explains why the transcapacitances shown in Figure 8.2 have negative values at low frequencies but does not explain why the capacitance value is increasing at the very low frequencies for the experimental data (circles) in Figure 8.2. This occurs due to a separate phenomenon, the formation of an electrical double-layer capacitance [73], which has been discussed in Section 2.3. Since *Maxwell* software was not set up to account for such phenomena, the computer simulated capacitance does not increase at low frequencies but remains negative. An illustrative simulation of the frequency response agreed well with laboratory measurements as shown in Figure 8.5.

A similar argument for negative transconductance is taken from [308]. A minor additional modification of a simplified distributed circuit shown in Figure 8.6, as well as many other possible distributed element circuit combinations can make the transconductance negative. The equivalent conductance G_{12} in terms of distributed elements is

$$G_{12} = \frac{2G_1(G_1^2 + \omega^2 C_1(C_1 + C_2)) + G_2(G_1^2 - \omega^2 C_1^2)}{(2G_1 + G_2)^2 + \omega^2(2C_1 + C_2)^2}. \tag{8.8}$$

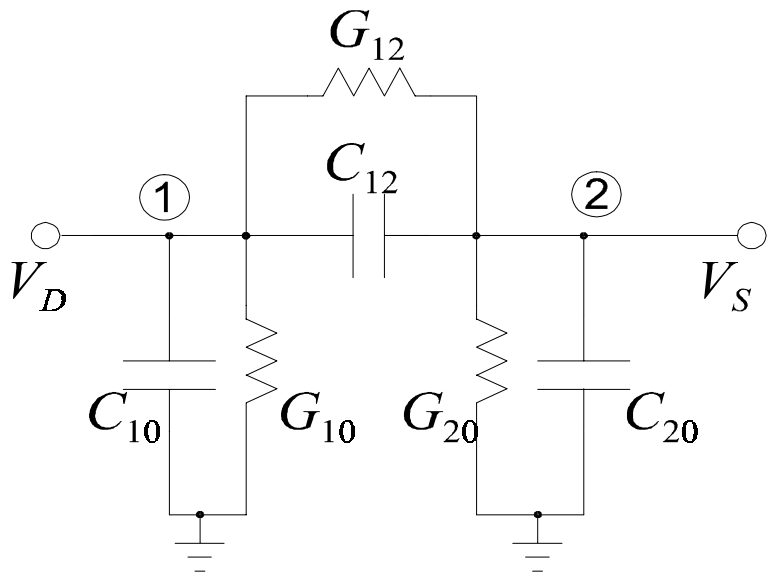

Figure 8.4: Simple π-equivalent circuit with identical terminal characteristics as in Figure 8.3 can result in negative values of C_{12} at low frequency.

So when the term after the negative sign in Equation 8.8 is greater than the sum of all positive terms, G_{12} could be negative. Another model is shown in Figure 8.7. The corresponding G_{12} is

$$G_{12} = \frac{G_1\left[G_1^2(3G_1^2 - \omega^2C_2^2 + 6\omega^2C_1^2 + 8\omega^2C_1C_2) + \omega^4C_1^2\left(3C_2^2 + 3C_1^2 + 8C_1C_2\right)\right]}{\left(3G_1^2 - \omega^2(C_2^2 + 3C_1^2 + 4C_1C_2)\right)^2 + 4\omega^2G_1^2(3C_1 + 2C_2)^2}. \tag{8.9}$$

Again, when the magnitude of the negative term in the numerator is greater than the sum of all the positive terms, G_{12} is negative. The denominator of (8.9) is always positive as a sum of squares.

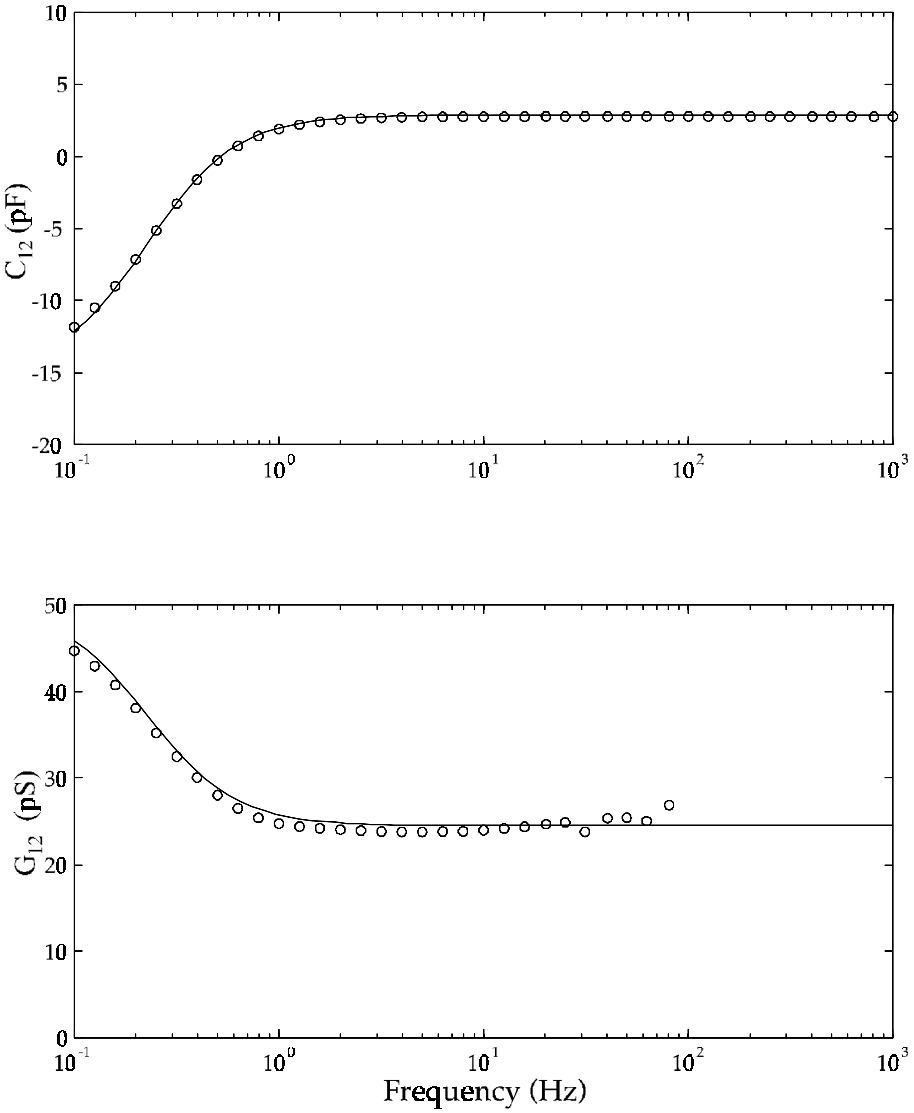

Figure 8.5: The measured and theoretical frequency response of the interelectrode capacitance C_{12} and conductance G_{12} for element values in Figure 8.3 of G_1=9.8 Gohm, C_1=20 pF, and C_2=100 pF.

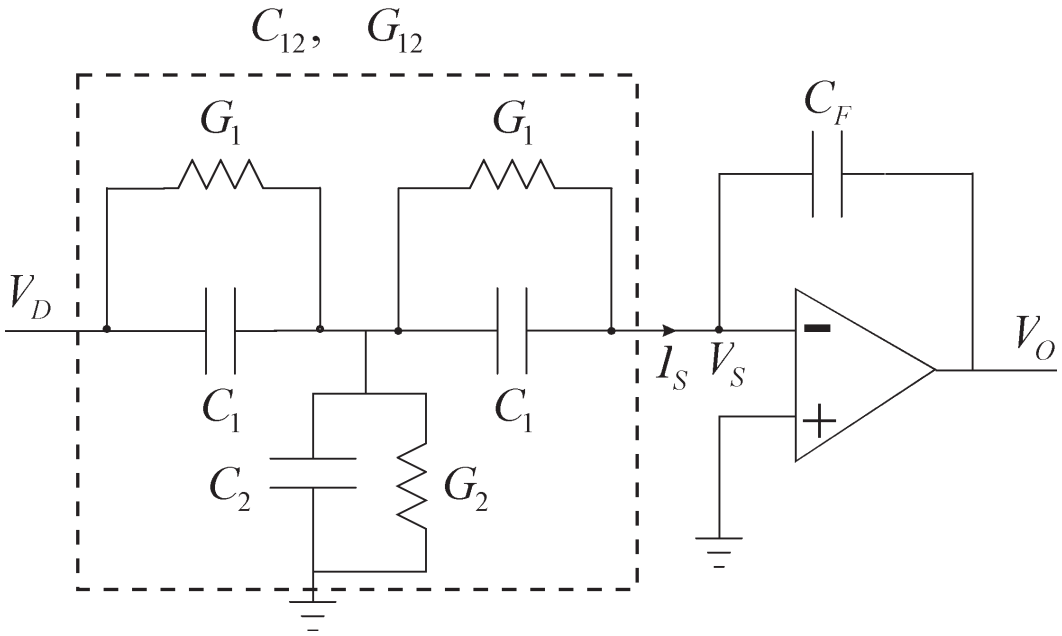

Figure 8.6: The distributed element circuit model for possible negative transconductance G_{12}.

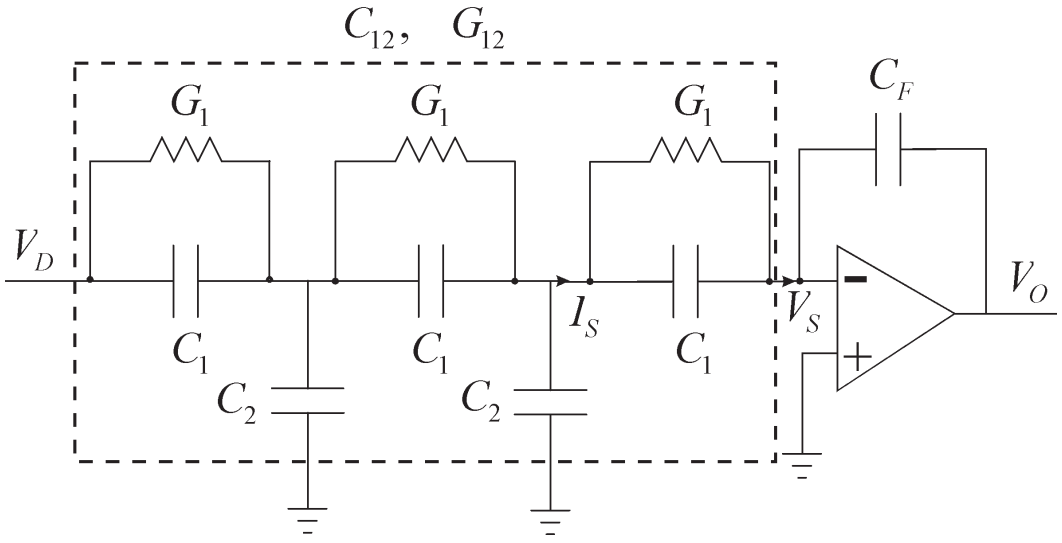

Figure 8.7: Another distributed element circuit model for possible negative transconductance G_{12}.

8.3 Calibration-Based Algorithms

8.3.1 Calibration Process

Teflon, being a chemically inert and hydrophobic material, was chosen as the substrate for most sensors used throughout this thesis. However, the mechanical properties of Teflon are less attractive than those of some other polymers; cold flow, thermal expansion, and softness, although moderate, limit the precision of the geometric dimensions of the electrodes. In addition, erosion, friction, and corrosion slightly reduce the width and thickness of the electrodes with time. Because of all these factors, the average metallization ratio, defined here as the ratio of the sum of the widths of the driven and sensing electrodes to the wavelength of an interdigital comb, can rarely be exactly the designed 50% of the wavelength. In our experience, the metallization ratio of CuFlon sensors, measured from microscope photographs, varied from 45% to 55%.

A number of geometric differences between the computer simulation and real experiment can be taken into account by a calibration process. The calibration might involve several stages, taking into account physics, chemistry, environmental conditions, and other elements that influence the sensor response. Except for the simplest cases, the calibration was found necessary for dielectrometry measurements at all frequency ranges. Figure 8.8 shows a flow chart of the parameter estimation process with non-iterative calibration procedures. In this specific case, the phenomena to account for include whether the dielectric is fluid or solid, contact quality, densification of material under test with pressure, electrochemical double layer effects, and natural inhomogeneous structure of the material.

The presented algorithm requires that the metallization ratio, β, is found by the calibration of the sensor in air prior to measurements. This is done for each wavelength by locating the measured interelectrode capacitance C_{12} on the pre-computed theoretical curve that represents a functional dependence of the metallization ratio on the interelectrode capacitance for each of the three wavelengths of the Teflon sensor of Figure 4.5. Figure 8.9 shows this dependence for all three wavelengths for a Teflon

substrate with dielectric permittivity $\varepsilon = 2.1$ and thickness of 254 μm. These curves were generated with the nominal computational error of 0.01% using finite-element software Maxwell by Ansoft Corp. The functional form of each curve shown in Figure 8.9 is approximated with the following expression (nearly linear function with reducing slope):

$$\beta = a_2\sqrt{C_{12}} + a_1 C_{12} + a_0 \tag{8.10}$$

where the empirical coefficients found by the best fit for each wavelength with C_{12} having units of pF are given in (8.11)-(8.13) respectively for 1.0 mm, 2.5 mm, and 5.0 mm wavelengths:

$$\beta = 0.7934\sqrt{C_{12}} - 0.0966C_{12} - 0.6502 \qquad \lambda = 1.0 \text{ mm} \tag{8.11}$$

$$\beta = 0.8419\sqrt{C_{12}} - 0.1545C_{12} - 0.3157 \qquad \lambda = 2.5 \text{ mm} \tag{8.12}$$

$$\beta = 0.9099\sqrt{C_{12}} - 0.1954C_{12} - 0.2040 \qquad \lambda = 5.0 \text{ mm} \tag{8.13}$$

Theoretical models, numerical simulations, and experimental data indicate that the capacitance between driven and sensor electrodes is a nearly linear function of dielectric permittivity of the material under test when the real part of the admittance between these two electrodes is negligible. Figure 8.10 shows the theoretical dependence of transcapacitance C_{12} for a half-meter meander length. Obviously, when the accuracy of the parameter estimation is limited not by the precision of the finite element simulation but by the experimental data, the description of the functional dependence of capacitance C_{12} on the dielectric permittivity ε_r is adequate.

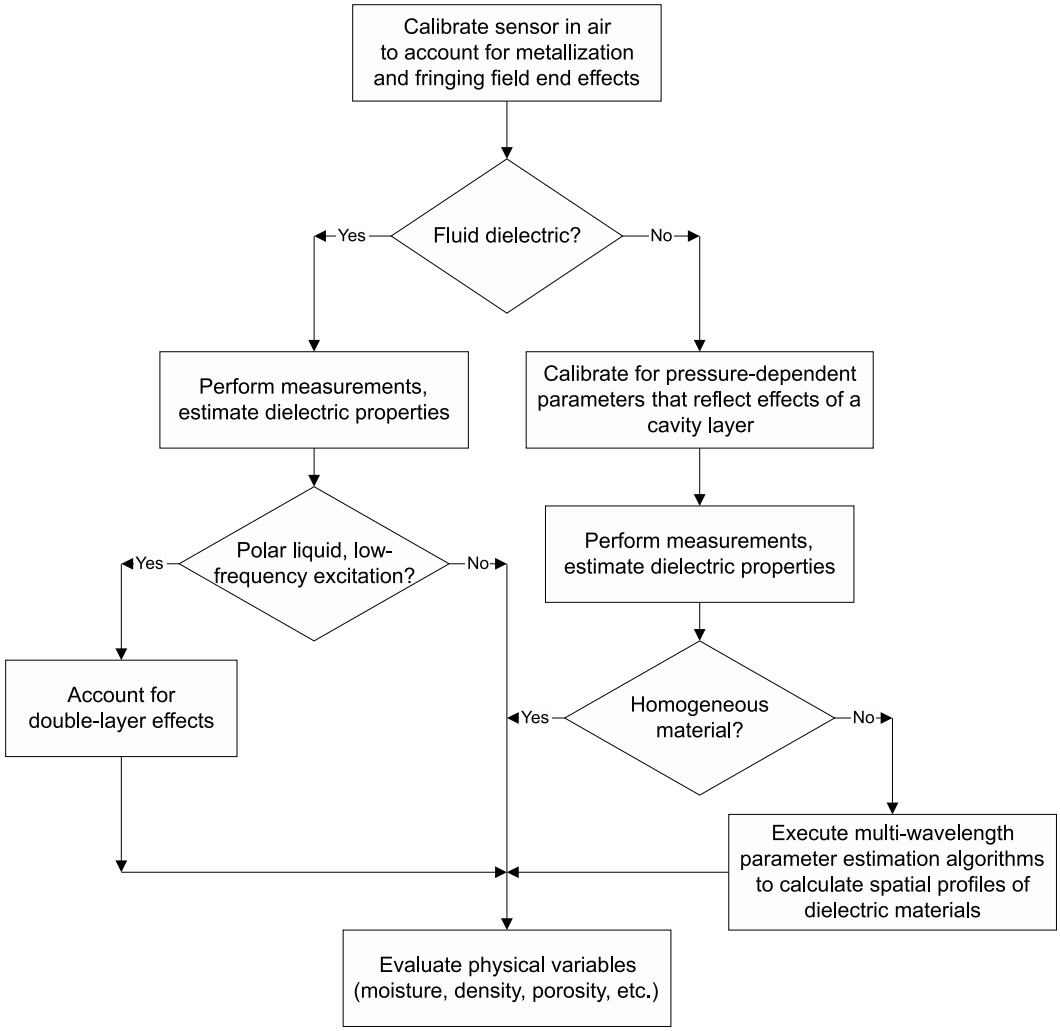

Figure 8.8: Model-based parameter estimation algorithms differentiate between solid and fluid dielectrics, homogeneous and non-homogeneous materials, take into account pressure and manufacturing tolerances of the sensor head, and compute volume distributions of several physical variables.

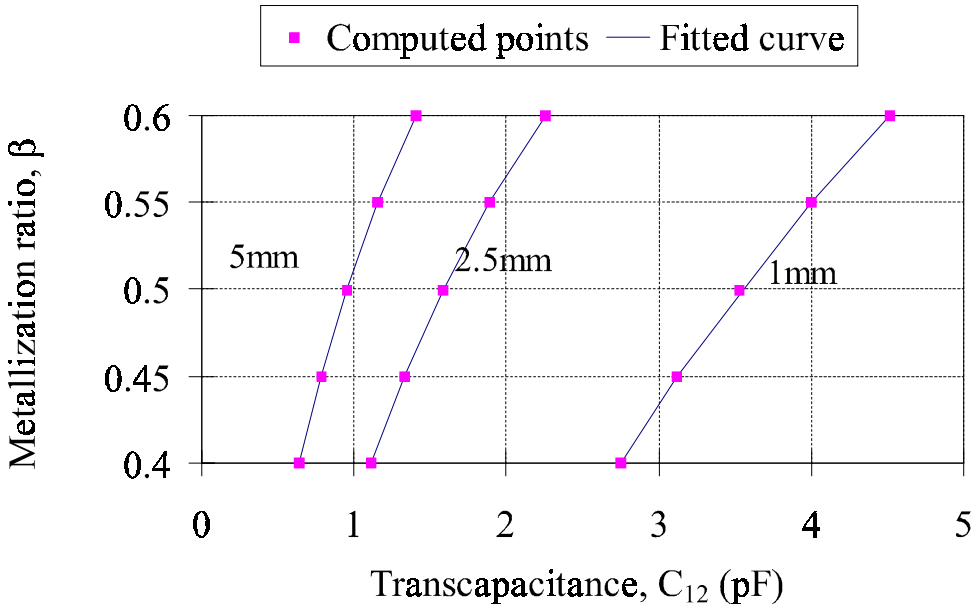

Figure 8.9: For all wavelengths, the interelectrode transcapacitance grows with the metallization ratio.

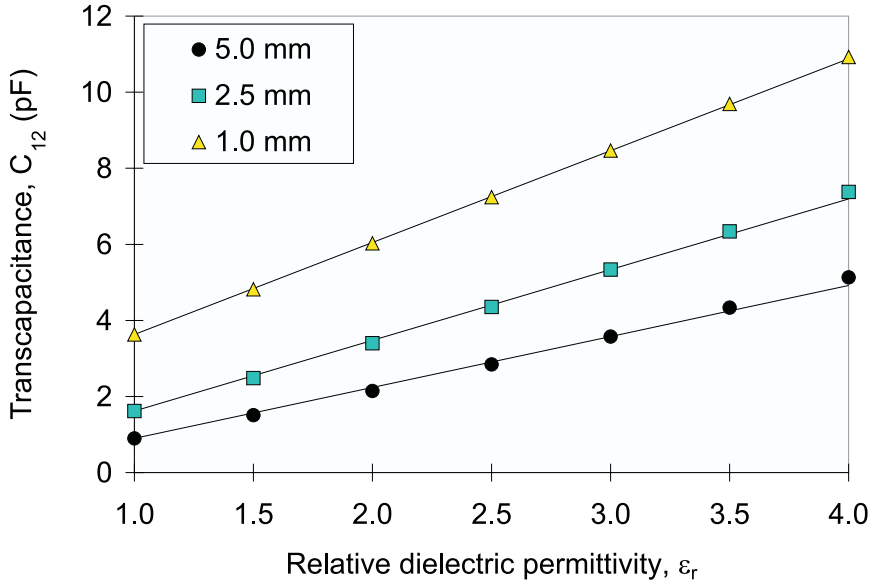

Figure 8.10: Simulated data with linear least squares fit lines plotted for the 50 percent metallization ratio case for 0.5 m meander length.

	Metallization ratio, β	
	Measured	Calculated
Sensor 1, $\lambda = 1.0$ mm	59%	55%
Sensor 1, $\lambda = 2.5$ mm	53%	55%
Sensor 1, $\lambda = 5.0$ mm	54%	55%
Sensor 2, $\lambda = 1.0$ mm	56%	54%
Sensor 2, $\lambda = 2.5$ mm	55%	53%
Sensor 2, $\lambda = 5.0$ mm	50%	51%

Table 8.1: Measured with a microscope and computed from measured air capacitance metallization ratios of two randomly selected three-wavelength sensors.

Table 8.1 compares metallization ratio for two randomly selected sensors, manufactured by Polyflon using the 254 μm (10 mil) thick CuFlon substrate. The measured values were obtained from air capacitance measurements and from microscope photographs, whereas the calculated values were determined using (8.11)-(8.13). Naturally, under the same precision of manufacturing process, the smaller wavelengths' metallization ratio differs more from the ideal 50% then that of larger wavelengths. The calculated estimates of the metallization ratio were generated with Matlab routine *se.m* (Sigma-Epsilon) (See Appendix G).

8.3.2 Interpolation Curves

After the metallization ratio, β, is determined, the sensor is ready for measurements. Let us first consider the simplest case: a thick layer of non-conducting homogenous fluid surrounding the sensor. For each wavelength, one can calculate the dependence of the capacitance on the relative dielectric permittivity, ε_r, of the material under test. Figure 8.11 (a) shows the inverse dependence $\varepsilon_r(C_{12})$ plotted for several values of the metallization ratio β for the 1 mm wavelength. The curves for the other two wavelengths have very similar shapes, and are shown in Figures 8.11 (b) and (c).

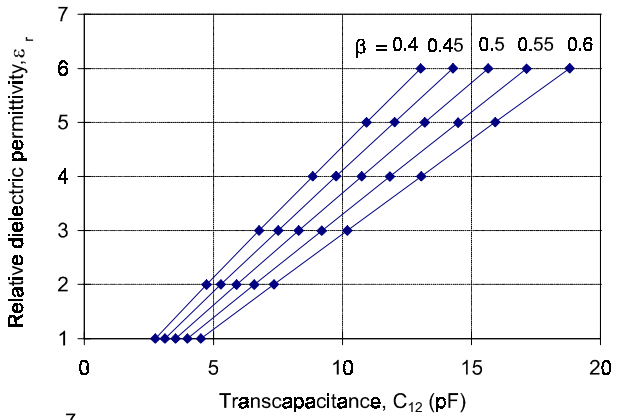

(a) $\lambda = 1.0$ mm

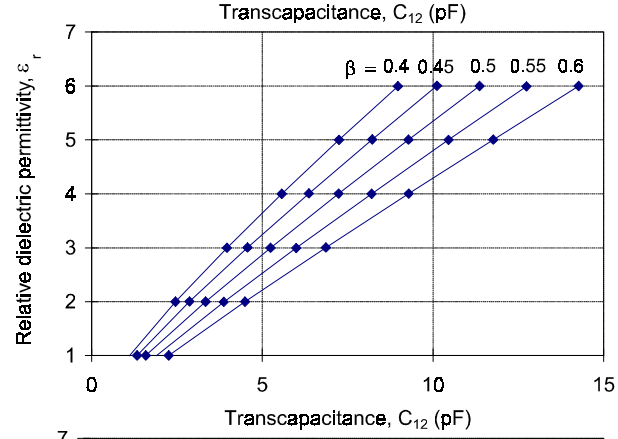

(b) $\lambda = 2.5$ mm

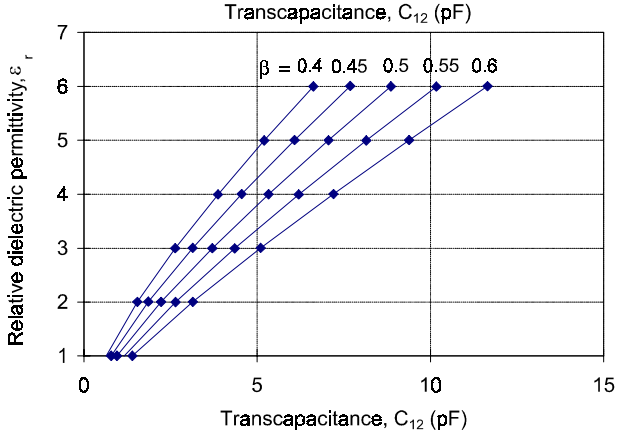

(c) $\lambda = 5.0$ mm

Figure 8.11: Families of calibration curves for the capacitance per half-meter length for three distinct spatial periodicities. The response becomes less linear with increasing wavelength because the guard plane becomes proportionally closer to the electrodes when the substrate thickness is held constant (the substrate thickness is the only dimension that does not scale in these simulations).

Thus, since the numerical value of β is known from the calibration in air, one can easily find the relative dielectric permittivity ε_r from the measured value of C_{12} by interpolating the curves in Figure 8.11. The choice of the interpolation technique is not crucial. A functional approximation has been used here, although other methods, such as look-up tables, could have been used. For each wavelength, the family of curves such as shown in Figure 8.11 is approximated by the following equation:

$$\varepsilon_r = b_2(\beta)\sqrt{C_{12}} + b_1(\beta)C_{12} + b_0(\beta) \tag{8.14}$$

where the variable coefficients $b_2(\beta)$, $b_1(\beta)$, and $b_0(\beta)$ are found from the finite-element simulation. These coefficients, in turn, are approximated with the second-degree polynomial:

$$b_i = c_{2,i}\beta^2 + c_{1,i}\beta + c_{0,i} \tag{8.15}$$

Figure 8.12 shows the functional dependencies of these coefficients on the metallization ratio β for the 1 mm wavelength. The functions, shown in Figures 8.13 and 8.14 have similar shapes and can be found using the coefficients listed in Table 8.2. The expressions (8.14) and (8.15) are only applicable for fluid dielectrics. The fluid gap, which forms between the sensor and the surface of the solid material, reduces the interelectrode capacitance. Figure 8.15 shows the effect of the air gap on the inverse functional dependence $\varepsilon_r(C_{12})$. This effect is accounted for by using equations (8.14) and (8.15) for the fluids, and a linear fit of the $\varepsilon_r(C_{12})$ function for the solids. The intercept of the linear fit and the fluid curves at ε_r=1 are the same, and the slope is based on the derivative of the fluids curve at the point where $\varepsilon_r = 1$. The angle α between the tangent of the fluids curve and the solid materials curve is 0.096 rad, 0.041 rad and 0.0002 rad for 1.0 mm, 2.5 mm, and 5.0 mm wavelengths, respectively.

Calibration techniques and estimation of dielectric permittivity based on fitting of pre-computed data has been implemented as a stand-alone parameter estimation algorithm. However, this approach has other uses. Most notably, the capacitive-only parameter estimation has been used as a backup branch of the sophisticated multi-layer parameter estimation when the local function approximation using non-dimensional so-

	$\lambda = 1.0$ mm			$\lambda = 2.5$ mm			$\lambda = 5.0$ mm		
	b_2	b_1	b_0	b_2	b_1	b_0	b_2	b_1	b_0
c_2	0.929	0.209	-0.126	2.299	0.186	-0.268	3.511	0.187	0.931
c_1	-1.773	-0.715	-0.247	-4.594	-0.617	0.396	-7.109	-0.575	-0.428
c_0	0.801	0.693	-0.490	2.277	0.653	-0.451	3.718	0.610	-0.394

Table 8.2: Coefficients of (8.15) for the three-wavelengths to be used in the ε_r vs C_{12} relationship (8.14) generated for fluid dielectrics by se.m.

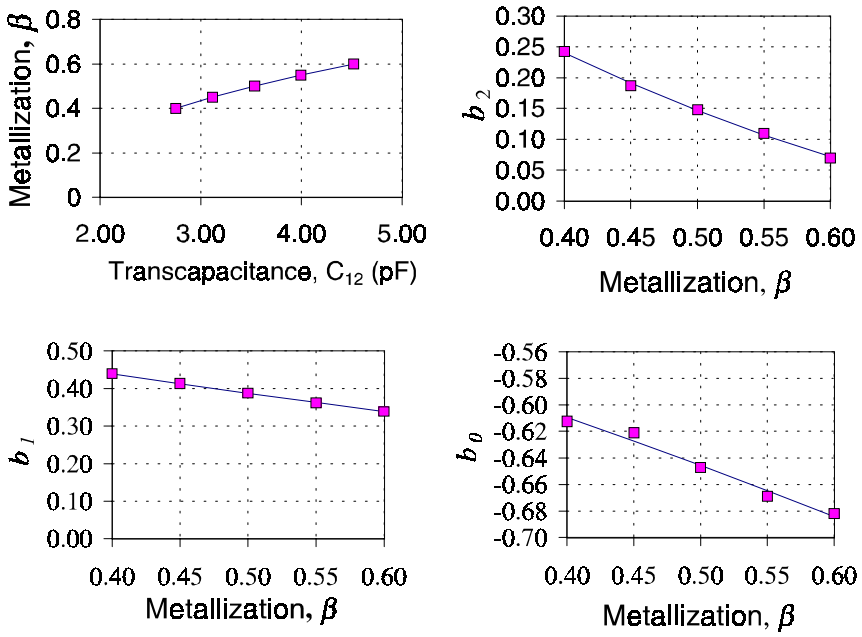

Figure 8.12: Calculated coefficients used in (8.14) and (8.15) for 1.0 mm wavelength.

lution spaces discussed in Section 8.6 fails due to constraints imposed by the interpolation routine. That is, the solution space discretization assumes only physically possible values of material properties, and a small estimation at the boundary of the solution space requires special handling. For example, the relative dielectric permittivity of any material cannot be less than 1, but a dielectric permittivity of a gas estimated to 0.99 is not unreasonable if the true permittivity is 1.02, and if we expect an accuracy of ±3 percent.

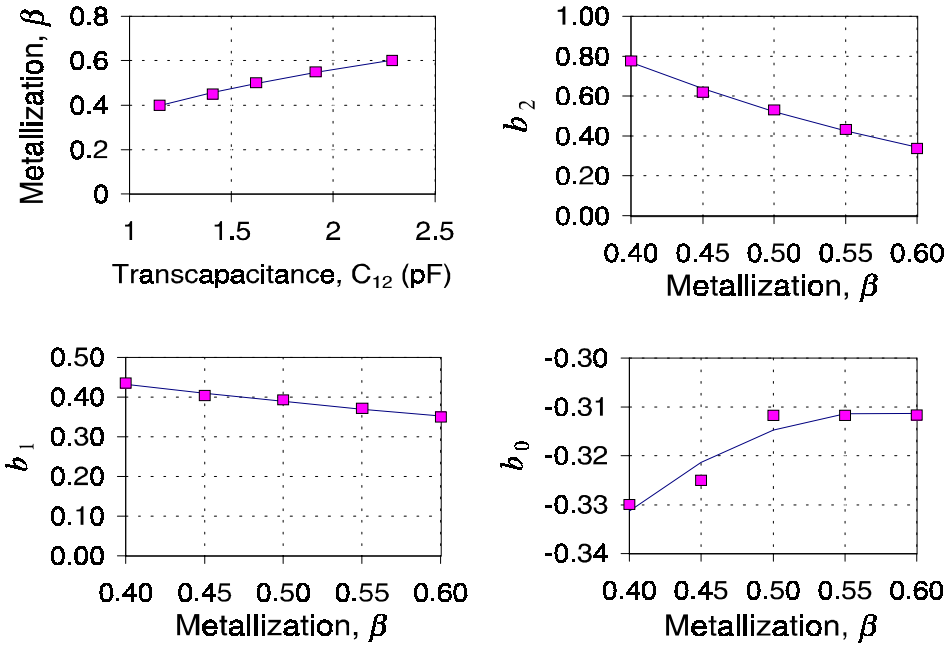

Figure 8.13: Calculated coefficients used in (8.14) and (8.15) for 2.5 mm wavelength.

8.3.3 Purely Capacitive Measurements

The measurement of the real part of the complex dielectric permittivity with the imaginary part being negligible is a conceptually simple task. However, previous measurements with interdigital sensors indicated significant differences between the predicted and the measured values. The performance of the sensor with low conductivity dielectrics is described here.

Table 8.3 lists the results of measurements made on a variety of fluid and solid homogeneous dielectrics. For a homogeneous material, all three wavelengths should indicate equal values of ε_r, and each of them should be equal to the value found with the parallel plate capacitor measurements. For solid materials, parallel-plate measurements were done with guard ring electrodes deposited on the surface of specimens in accordance with ASTM standard [281]; and for liquid materials, they were done by immersing a parallel plate capacitor into the liquid. The air measurement is guaranteed to be perfect by the nature of the metallization ratio adjustment calibration procedure, discussed in Section 8.3.1.

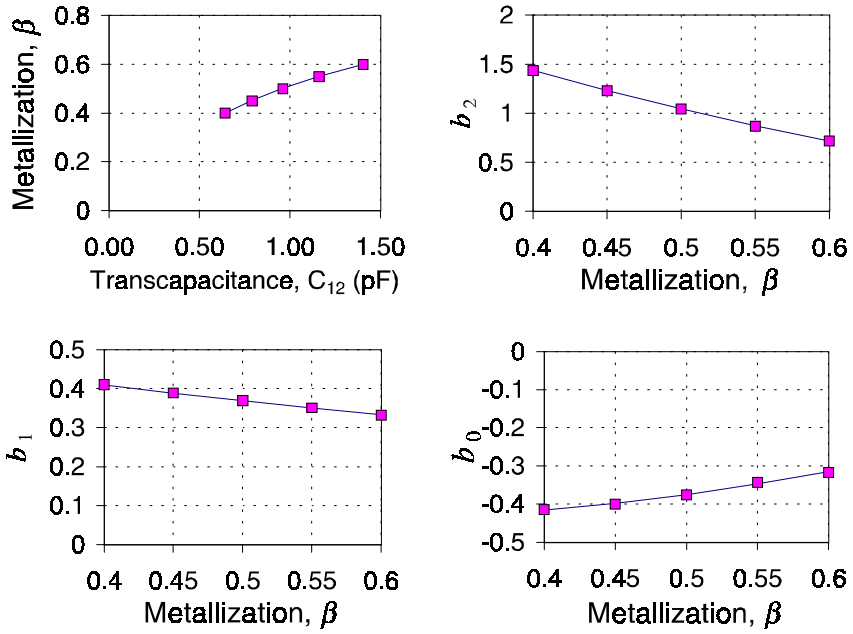

Figure 8.14: Calculated coefficients used in (8.14) and (8.15) for 5.0 mm wavelength.

Clearly, the precision of measurements shown in Table 8.3 is significantly lower than could be achieved with standard parallel plate measurements, especially for solid dielectrics. The main source of error in this case is the variation of air gap across the sensor head. Notably, it is easier to measure the dielectric permittivity of liquid dielectrics than that of solid ones, at least in the high frequency regime because the contact between the sensor and material is guaranteed to be perfect for liquids.

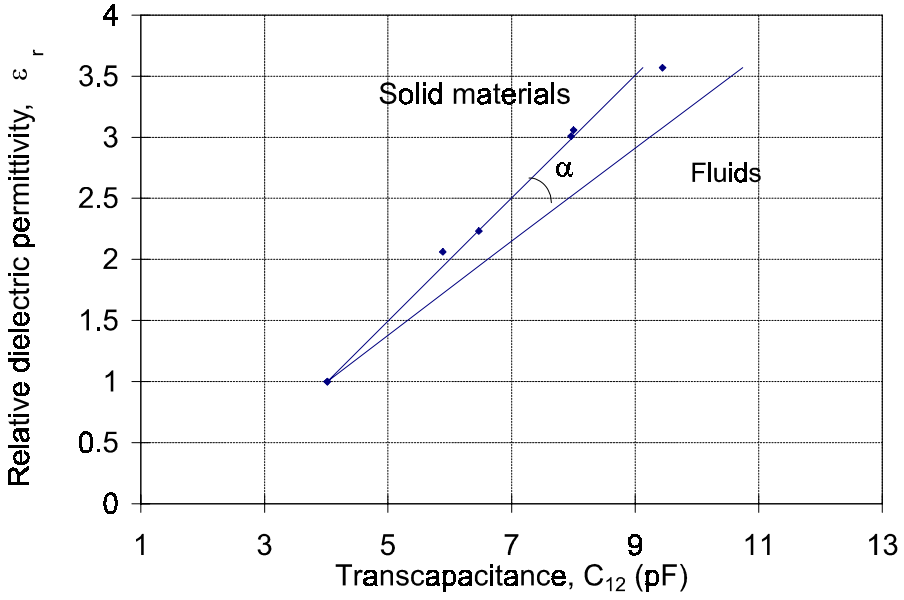

Figure 8.15: Influence of air at a solid/sensor interface for a 1 mm wavelength sensor is accounted for by assuming a small angle α between the two linear approximations of the sensor response. The "Fluids" line is found by finite-element simulations and the "Solid materials" is empirical. The experimentally determined value of α for each wavelength is $\alpha(\lambda = 1\ mm) = 0.096$ rad, $\alpha(\lambda = 2.5\ mm) = 0.041$ rad, and $\alpha(\lambda = 5\ mm) = 0.0002$ rad.

Material	**1 mm**	**2.5 mm**	**5 mm**	**Average**	**Parallel plate**
Air	1.00	1.00	1.00	1.00	1.00
Teflon	1.92	2.03	2.02	1.99	2.06
Transformer oil	2.23	2.29	2.27	2.26	2.20
Polyethylene	2.24	2.26	2.29	2.26	2.23
Polypropylene	2.35	2.35	2.29	2.33	2.35
HD Polyethylene	2.38	2.44	2.38	2.40	2.36
Lexan	3.11	3.04	3.11	3.09	3.01
Corn Oil	3.09	3.19	3.10	3.13	3.10
PVC	3.30	3.23	3.45	3.32	3.35
Delrin (white)	3.36	3.49	3.77	3.54	3.63

Table 8.3: Measurement of relative dielectric permittivity of non-conductive materials in the 100 Hz - 10 kHz range.

8.3.4 Simulation and Measurements for a Wide Frequency Range

Simultaneous Measurements with Two Parallel Plate Sensors

During the course of this study, a number of experiments with transformer oil and transformer pressboard have been conducted in an uncontrolled environment. In this case, both temperature and relative humidity follow the ambient and may contribute to the dynamics of the experiment. Variation of the dielectric permittivity and conductivity of corn oil at the constant frequency of $10^{-1.2} \approx 0.063$ Hz has been measured using two parallel plate sensors, namely, a guarded ring plate sensor shown in Figure 5.8 and a variable tuning capacitor shown in Figure 5.12.

Theoretically, both sensors should provide the same values of the dielectric permittivity and conductivity. Figure 8.16 shows that while the estimated permittivity values differ by less than two percent, estimated conductivity values differ by about 30 percent. This difference can not be assigned to the error in the geometric factor of the two parallel plate capacitors, because it would require the difference of the estimated parameters to be about the same fraction of the signal. Subsequent investigation revealed several factors that contributed to the observed difference. The dielectric permittivity at the constant frequency of $10^{-1.2} \approx 0.063$ Hz was estimated higher using the data from the tuning capacitor (TC) because of the high-permittivity ceramic holders present in the fringing field region. The conductivity estimated with the parallel plate capacitor (PPC) was higher because it was placed in slightly warmer location, several centimeters above the TC in the same container. A temperature increase of about one degree from the bottom to the top of the ≈ 20 cm high container has been observed. A strong dependence of conductivity on ambient temperature contributed to the observed difference. The conductivity may change significantly during a single experiment due to a heating, oxidation, or effect of chemical additives. According to measurements with a parallel plate capacitor cell in natural ambient environment, the corn oil conductivity approximately doubles for every 10°C. For that reason, the con-

ductivity, or, alternatively, loss factor are often plotted on a logarithmic scale, in which case the differences between simulation and measurements are much less conspicuous. Another source of difference is attributed to the double layer effects (see Section 2.3). Since the separation between the PPC and TC electrodes and the conditions of the electrodes surface is not the same, the electrochemical diffuse double layer affects the measurement results to a different degree. At this point, no additional effort has been made to characterize the above phenomena in detail. Instead, they were minimized by a careful positioning of parallel plate sensors and the increase of electrode separation in subsequent experiments.

Simultanous Measurements with Parallel Plate and Interdigital Sensors

Figure 8.17 shows the experimental results obtained with corn oil and the computer simulation of the driving voltage frequency sweep from 10 kHz to 0.005 Hz. This plot contains several features frequently encountered in dielectrometry measurements. A reasonable agreement between the measurements and the theory is achieved at all frequencies except for the lowest (below 0.03 Hz). The rise of capacitance C_{12} at low frequencies is due to electrochemical double layer formation at the metal-dielectric interface. It is possible to account for the double layer effects (discussed in Section 2.3), and even evaluate its properties [14]. The simulations in Figure 8.17 did not account for the double layer and to maintain the focus of the study they show the ideal theoretical response of a non-dispersive liquid dielectric. There is little experimental data for the transconductance at frequencies above 5 Hz because the capacitive currents at these frequencies dominate the conductance currents and the accurate measurement of the real part of the transadmittance becomes very difficult.

The values of the relative dielectric permittivity $\varepsilon_r = 3.15$ and conductivity $\sigma = 60$ pS/m, 53 pS/m, and 14.2 pS/m for 1.0 mm, 2.5 mm, and 5 mm wavelengths, respectively, used in the simulation were measured separately with a parallel plate sensor. The values of the conductivity differ because the measurement with each wavelength were taken at different moments of time and at different ambient temperatures be-

tween 10°C and 30°C (about 30°C for a 1 mm wavelength, about 27°C for 2.5 mm wavelength, and about 13°C for a 5 mm wavelength).

The reader might want to inquire why corn oil was selected for the tests. Even though corn oil is sometimes considered a potential insulator for use in the power industry in developing countries [309], the presented measurements have no direct relation to practical engineering uses of corn oil. Here, corn oil was selected due to its dielectric properties in order to conveniently benchmark performance of the sensors (rather than study properties of an unknown liquid dielectric). Since the relaxation time of corn oil is on the order of one second, its loss peak lies in the middle of the applied frequency range. A more extensive analysis of dielectric properties of corn oil is available in [310, 311]. These sources confirm high temperature dependence of conductivity and provide the following physical properties for food-grade Mazola corn oil at 25°C: density $\rho = 936$ kg/m^3, viscosity $\eta = 45$ mPa s, relative dielectric constant $\varepsilon = 3.34$, and conductivity $\sigma = 40 \times 10^{-12}$ S/m at room temperature. Conductivity of corn oil approximately doubles for every 10°C increase in temperature.

Corn oil is non-dispersive in this frequency range (0.005 Hz to 10 kHz). A good agreement between the experimental and the theoretical values is achieved. Low frequency data differ due to the capacitive double-layer effect, which is currently not included in the model. The negative value of the transcapacitance at low frequencies is due to the actively driven three-terminal arrangement, and does not contradict any circuit laws (see Section 8.2).

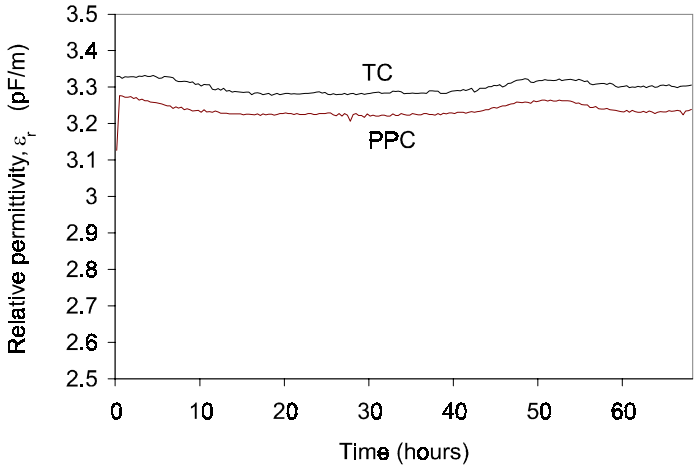

(a)

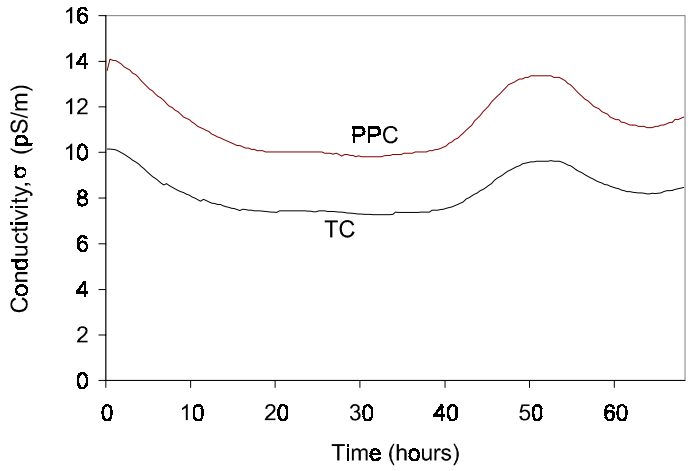

(b)

Figure 8.16: Variation of dielectric permittivity and conductivity of corn oil in natural laboratory environment at the constant frequency of $10^{-1.2} \approx 0.063$ *Hz. Measurements points were taken at 20 minute intervals during a 70 hour experiment using the tuning capacitor (TC) and a parallel plate capacitor (PPC) shown in Figures 5.8 and 5.12.*

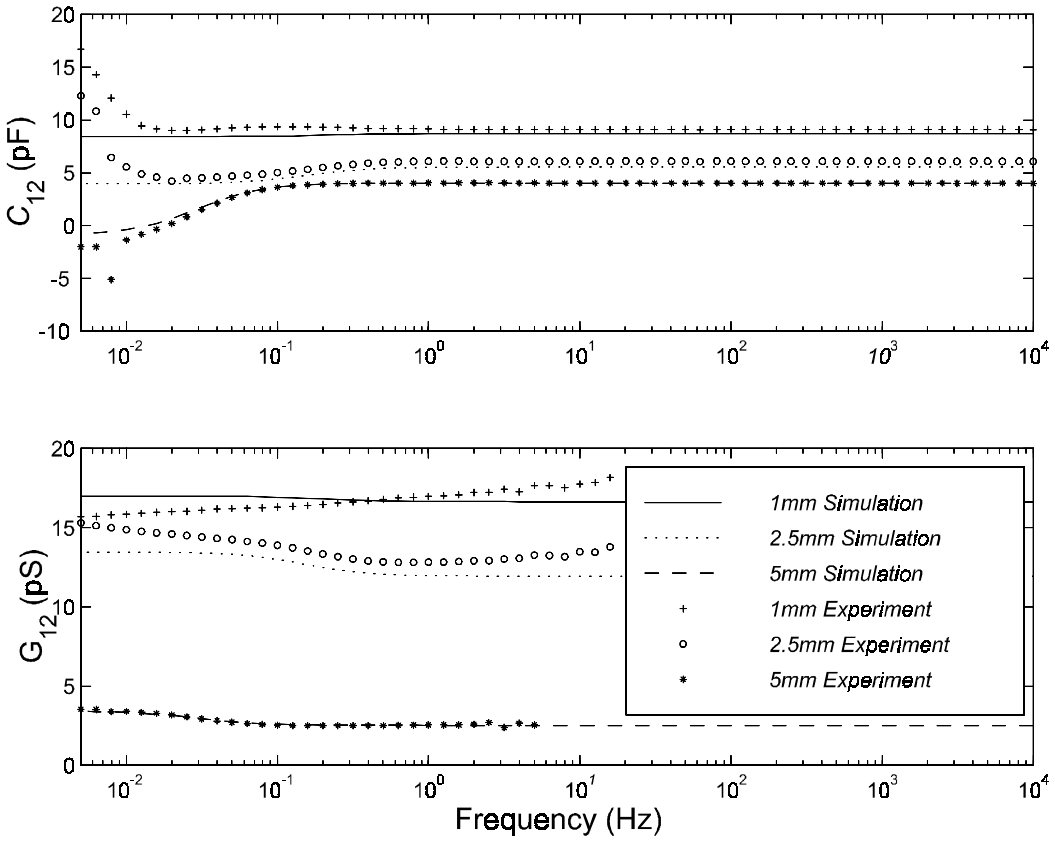

Figure 8.17: Comparison of measured and calculated interelectrode transcapacitance C_{12} and transadmittance G_{12} for the experiments with corn oil. A very good agreement is observed for the entire frequency range except the lowest frequencies. The discrepancy at the lowest frequencies is due to electric double layer effects.

8.3.5 Measurements with Solid Dielectrics

Many solid and fluid dielectrics have been tested in order to gain confidence in sensor performance and accuracy of parameter estimation algorithms. The relationship ε_r vs. C_{12} for solid materials was first determined empirically using several samples of plastics. The measurement setup was positioned in a metal enclosure electrically connected to ground. Figure 8.18 shows a schematic of the experimental setup for basic measurements with solid materials. The electrically grounded metal enclosure with aluminum foil layer at the bottom was sufficient to guarantee shielding from electrical noise generated by nearby computers and fluorescent lights. The acrylic layer served to provide a hard surface against which the sensor could be effectively pressed. A paper towel protected the bottom of the sensor from unnecessary contact with the hard acrylic beneath it. The sample was placed directly on top of the sensor. The samples were typically 1.2 cm thick. Four slabs of acrylic were then placed on top of the sample and the sensor (to provide sufficient insulation distance to the metal weight). A paper towel was placed between the 10 kg mass and the highest piece of acrylic to prevent scratching. The weight was left electrically floating since casual experiments indicated that the difference between grounding the mass and leaving it floating were insignificant. Although guarding the weight and placing the weight higher did not significantly affect the measurements, other factors did; for example, the softness of material that was placed beneath the sensor.

The initial calibration curve shown in Figure 8.19 was generated using only air ($\varepsilon_r = 1$), Delrin (black) ($\varepsilon_r = 3.6$), Lexan ($\varepsilon_r = 3.01$), Plexiglas (generic)($\varepsilon_r = 3.1$), polyethylene($\varepsilon_r = 2.23$), and Teflon ($\varepsilon_r = 2.1$). Table 8.3 includes results of these measurements for ε_r and C_{12}. These points, along with their linear least squares (LLS) fit and the liquids and solids curves for the appropriate metallization, were all plotted on the same axes. The solids curve differs from the best fit primarily because of the black Delrin whose measured capacitance is consistently too high, possibly due high carbon content.

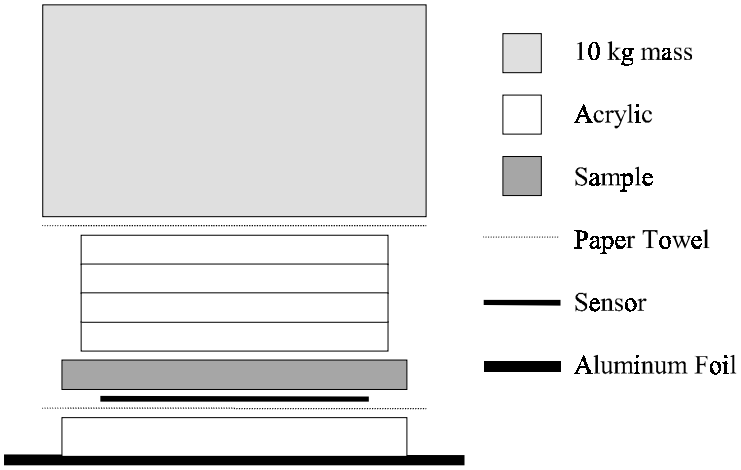

Figure 8.18: Schematic of the experimental setup for measurement of high frequency dielectric permittivity of solid samples.

The program *se.m*, listed in Appendix G was expanded to handle solids by empirically determining an offset angle between the liquids curve and the solids line. This angle is fixed and is not a function of other parameters. This approximation should suffice for most designs since actual metallizations range from only 45% to 60%. To test the program, eight different plastics were measured. Their high frequency dielectric permittivity was measured separately using a copper tape guarded parallel plate capacitor (Figure 5.11). Two different sensors were used (designated A and B in the following plots).

Figures 8.20 through 8.25 show experimental results obtained in the narrow high frequency range from 100 Hz to 10 kHz. In all cases, experimental data above 5 kHz contains instrumentation noise due to frequency limitations of the interface box operational amplifier. In addition to experimental data, a horizontal line is plotted for each material, which indicates the dielectric permittivity of the same sample measured separately using a parallel plate capacitor with a guard ring made in accordance with [281]. In most cases, measurements are reported for two samples and two distinct, although nominally equivalent, sensors. All estimations had been performed using the

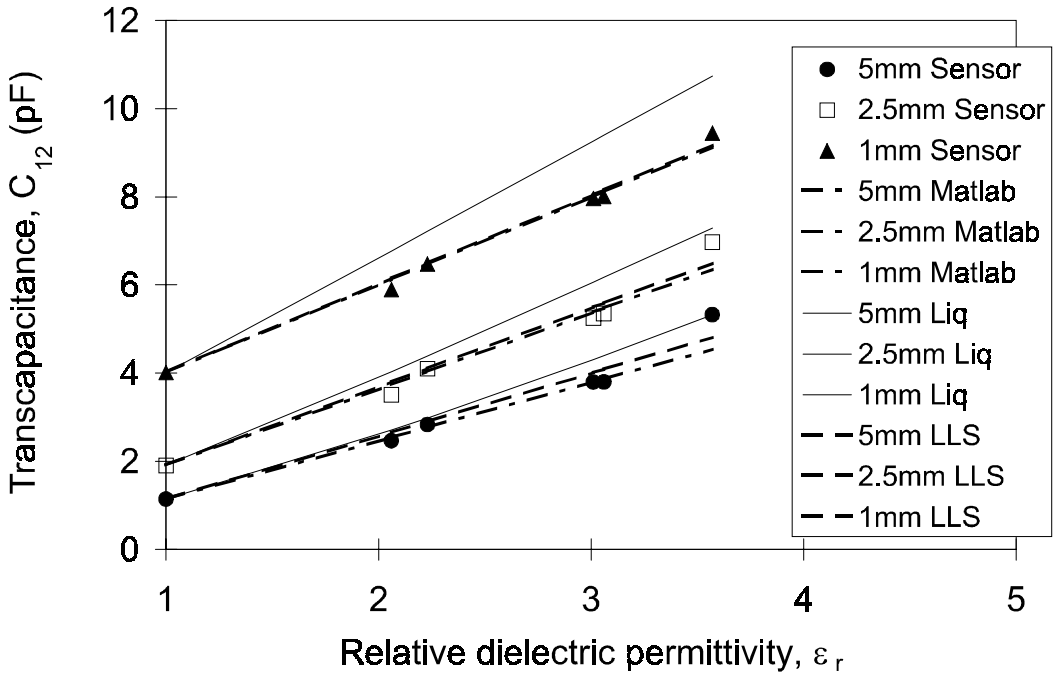

Figure 8.19: Linear least squares fit (LLS, dashed lines) of measurements with solid materials (shapes) with the three-wavelength sensor compared to theoretical simulation (solid line) and later used for sensor calibration (dash-dot line).

parameter estimation code *se.m* (Appendix G), which requires sensor calibration prior to measurements.

Due to the nature of the calibration process of the metallization ratio adjustment described in Section 8.3.1, estimates of permittivity of air shown in Figure 8.20 are very close to experimental data, with precision limited only by the instrumentation noise. On the other hand, the estimation of the dielectric permittivity of Sintra, also shown in Figure 8.20, is one of the least successful among those presented here. Sintra is a slightly compressible coated polymeric foam; the coating makes it non-homogeneous. Since the assumption in this subsection is that all materials are homogeneous, the dielectric permittivity of Sintra is overestimated with the three-wavelength sensor. Not surprisingly, the overestimation increases as the wavelength decreases as the denser coating has a higher dielectric permittivity than the foam, and thus the coating occupies

a proportionally larger volume for the smaller wavelength's measurements. Although measurements with the parallel plate capacitor include the effect of the coating, the response is still determined largely by the thick layer of foam.

Figure 8.21 shows measurements with two well-behaving materials, Teflon and polyethylene. For both materials, the estimations fall within about five percent of the correct value, whereas the measurements of the dielectric permittivity of solid homogeneous samples with the parallel plate capacitor are normally within 1 percent of the true value. This range of accuracy represents an intermediate stage in the interdigital dielectrometry measurements. A number of subsequent improvements in the design of the sensor and the experimental procedures served to improve the accuracy.

Figure 8.22 shows results of measurements with several other commonly available polymers. The dielectric permittivity of the highly insulating polypropylene was estimated with the same accuracy that was achieved for other insulating polymers. On the other hand, plastics that indicate significant conductivity in the frequency range of interest could not have been evaluated precisely using this approach, because calibration was done for non-conductive materials only. For weakly conductive materials, there usually exists a frequency range where calibrated dielectric permittivity estimation is reasonable. For acrylic, the estimation with a reasonable match between the parallel plate and interdigital sensor data is observed at 1 kHz, the frequency at which the parallel plate measurements were taken. A highly negative phase (not shown here) in the frequency sweep signals for nylon made purely capacitive estimation of the dielectric permittivity meaningless. This data illustrates the potential pitfall for many non-destructive measurement applications, where an undetected increase of conductivity with time may lead to an incorrect interpretation of experimental data due to inadequacy of the selected parameter estimation algorithm.

Figure 8.23 shows the results of measurements with two samples of Lexan. The dielectric permittivity of Lexan obtained with parallel plate measurements slightly differs from the three-wavelength sensor data, but is usually within three percent of the nominal value. The fact that the values of the dielectric permittivity obtained

with the three-wavelength sensor are higher than those obtained from parallel plate measurements is a positive indication of the three-wavelength sensor performance. The apparent frequency dispersion of the dielectric permittivity of Plexiglas is due to bulk conductivity of the sample.

Figure 8.24 shows the results of measurements with another two relatively well behaved materials, high-density polyethylene and polyvinylchloride (PVC). It is typical that the relative error of measurements between different wavelengths increases with the dielectric constant, as can be seen for the PVC data as well as for the Delrin measurements shown in Figure 8.25. Putting it more generally, the error increases with the difference between the dielectric constant of the solid material and the fluid environment of measurements because the linear calibration is only valid for a fairly narrow range of dielectric constants.

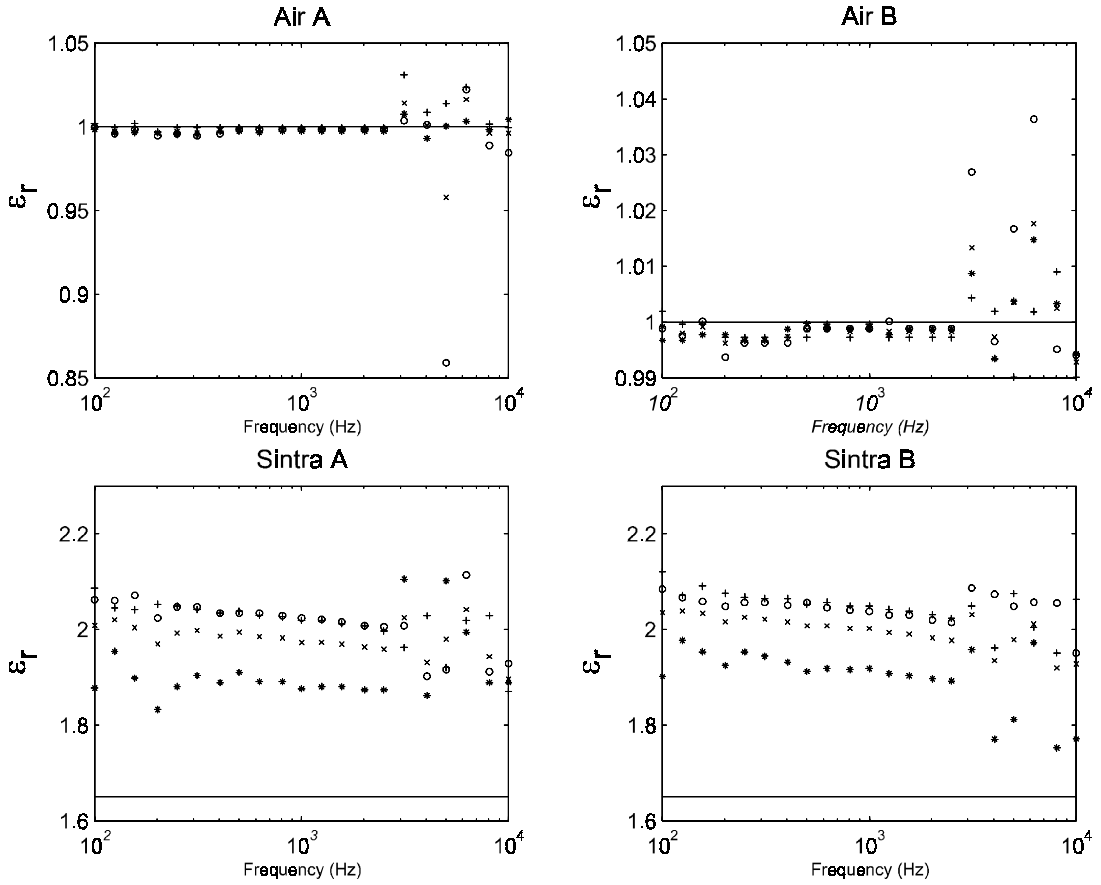

Figure 8.20: Relative dielectric permittivity of air and Sintra estimated with parallel plate capacitor and with three-wavelength sensor using calibration and α parameter defined in Figure 8.15. Legend: "+" - 1.0 mm, "o" - 2.5 mm, "" - 5.0 mm, "x" - average of the three, "–" - parallel plate measurement. The experimental data above 5 kHz contains instrumentation noise due to frequency limitations of the interface box operational amplifier.*

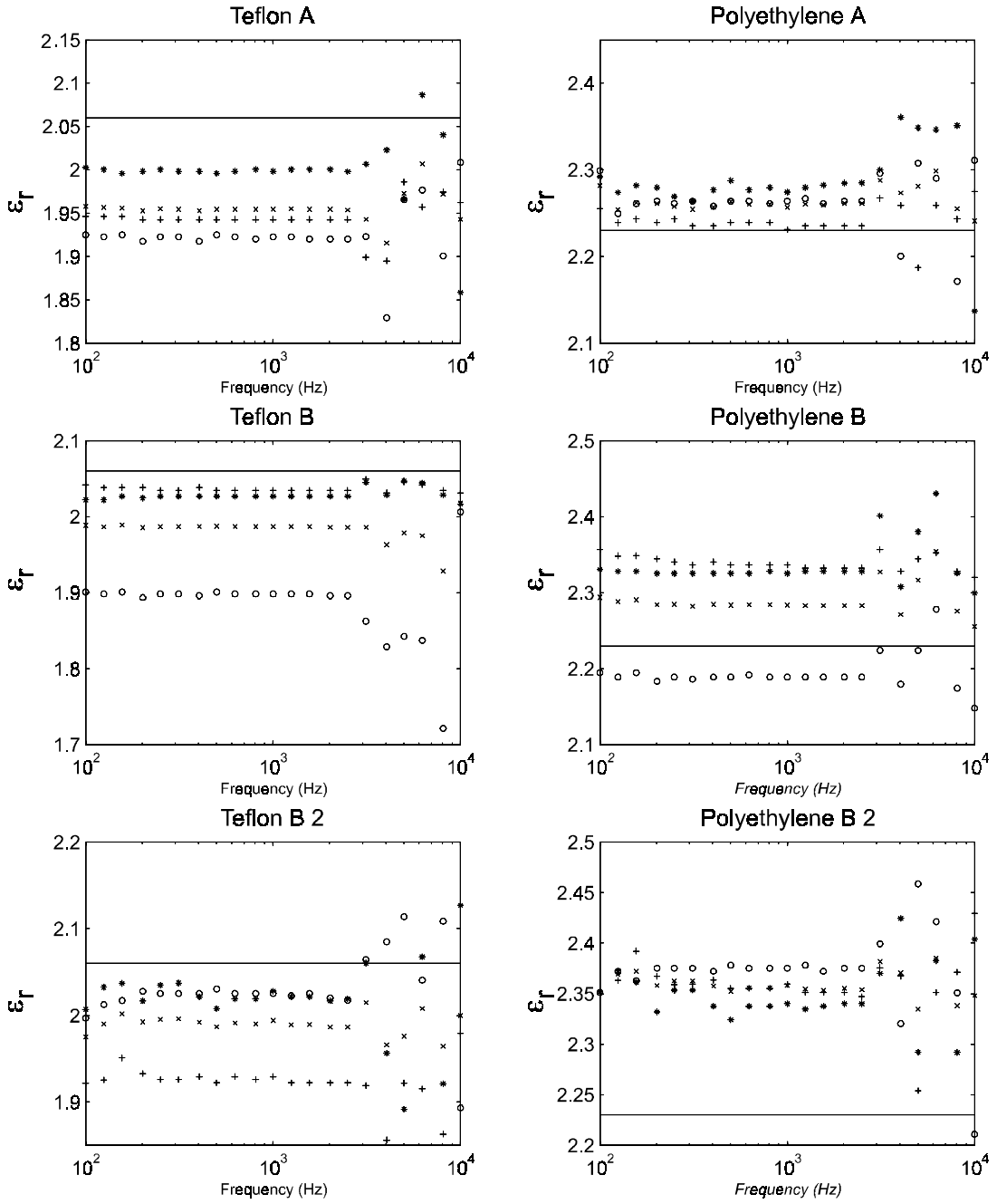

Figure 8.21: Relative dielectric permittivity of Teflon and polyethylene estimated with parallel plate capacitor and with three-wavelength sensor using calibration and α parameter. Legend: "+" - 1.0 mm, "o" - 2.5 mm, "" - 5.0 mm, "x" - average of the three, "–" - parallel plate measurement.*

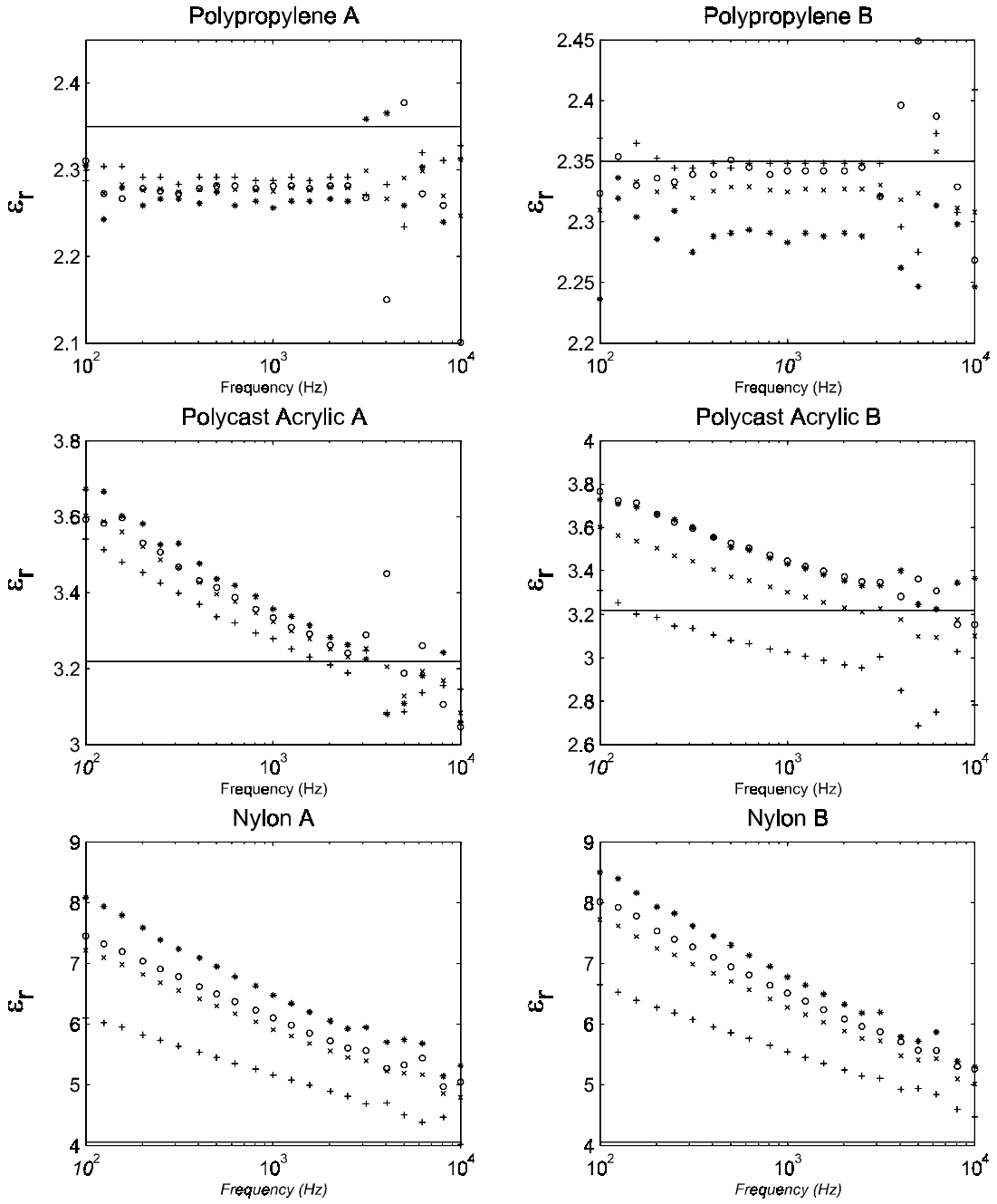

Figure 8.22: Relative dielectric permittivity of polypropylene, acrylic, and Nylon estimated with parallel plate capacitor and with three-wavelength sensor using calibration and α parameter. Legend: "+" - 1.0 mm, "o" - 2.5 mm, "" - 5.0 mm, "x" - average of the three, "–" - parallel plate measurement.*

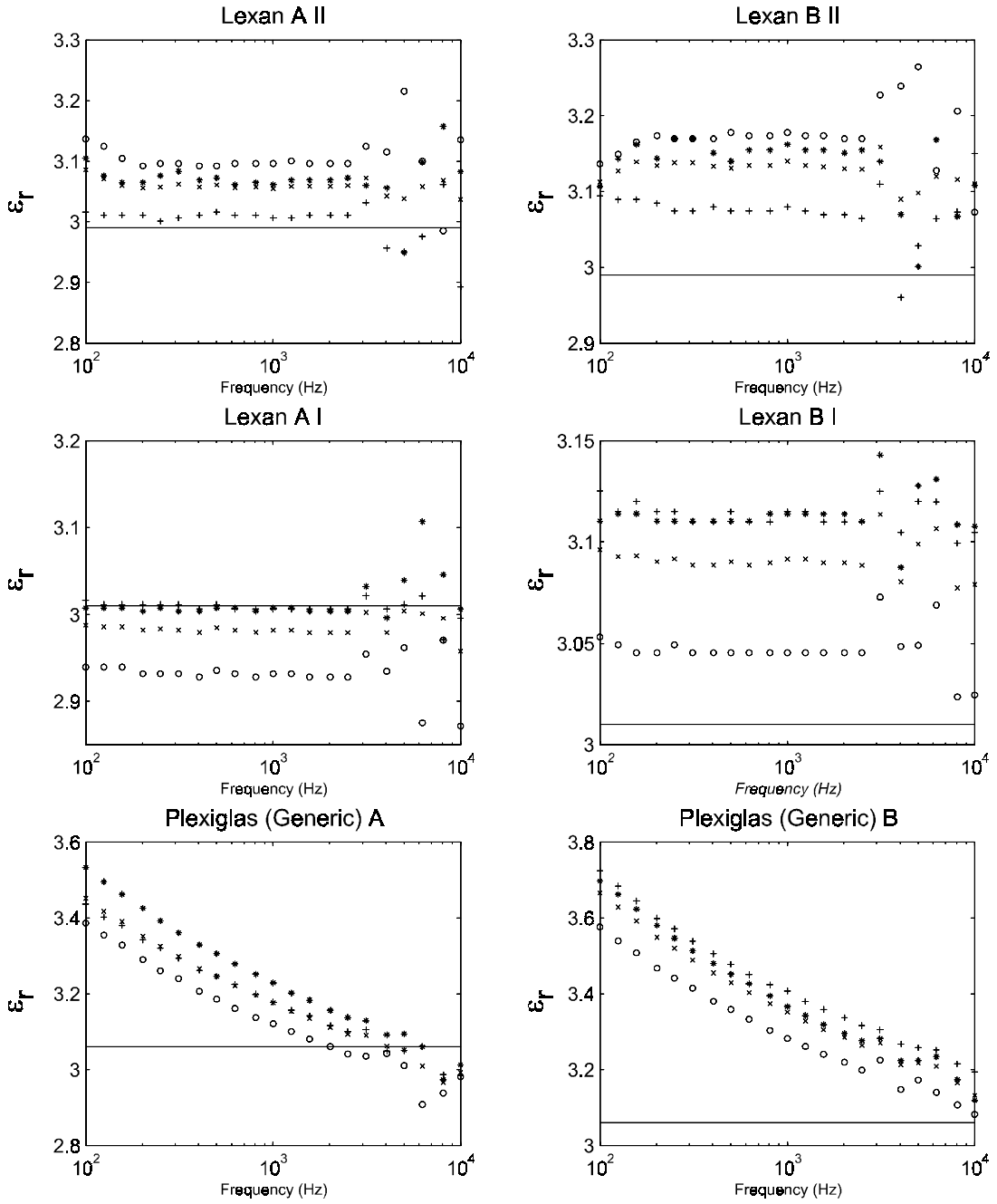

Figure 8.23: Relative dielectric permittivity of Lexan and Plexiglas estimated with parallel plate capacitor and with three-wavelength sensor using calibration and α parameter. Legend: "+" - 1.0 mm, "o" - 2.5 mm, "" - 5.0 mm, "x" - average of the three, "–" - parallel plate measurement.*

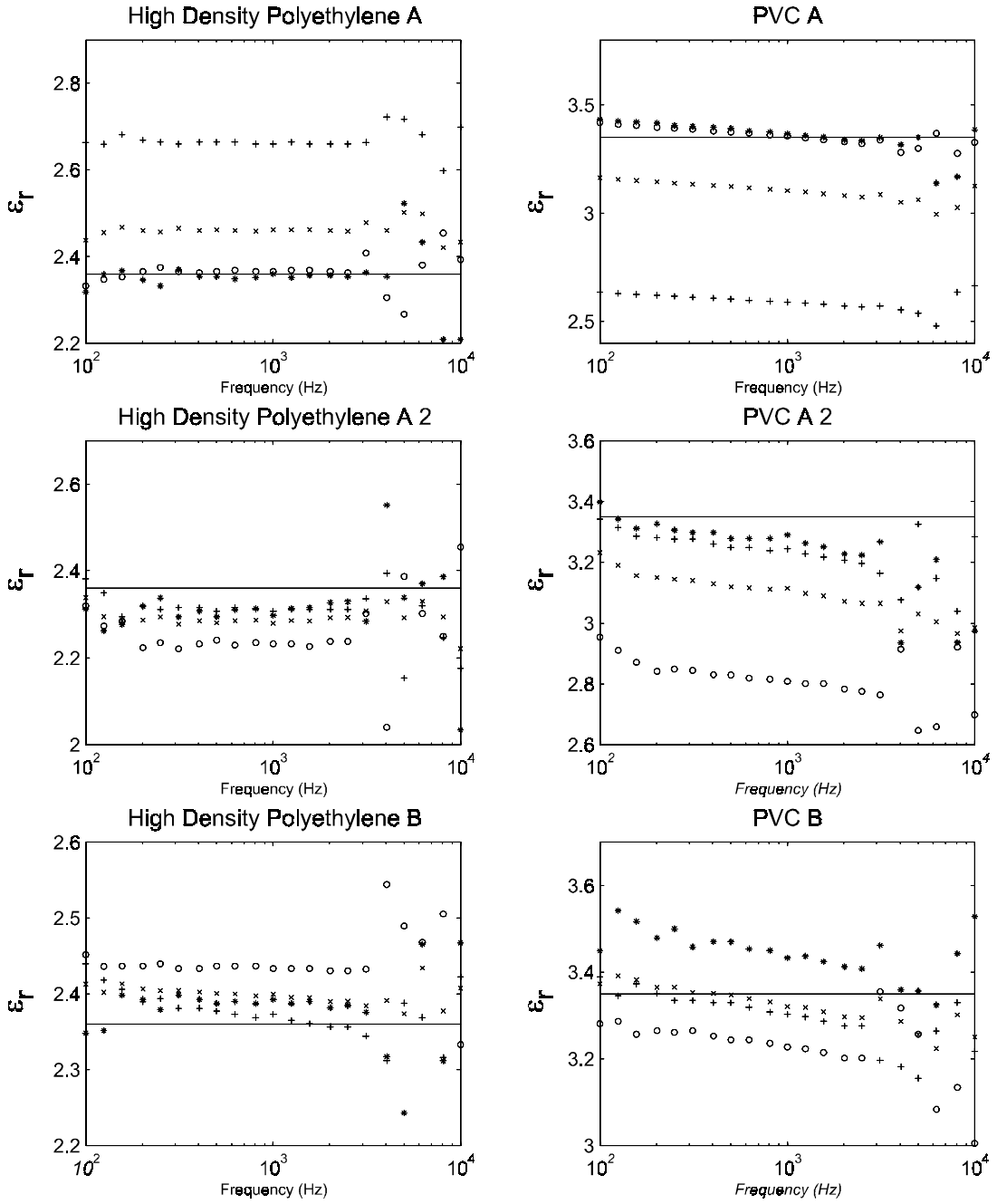

Figure 8.24: Relative dielectric permittivity of HD polyethylene and polyvinylchloride estimated with parallel plate capacitor and with three-wavelength sensor using calibration and α parameter. Legend: "+" - 1.0 mm, "o" - 2.5 mm, "" - 5.0 mm, "x" - average of the three, "–" - parallel plate measurement.*

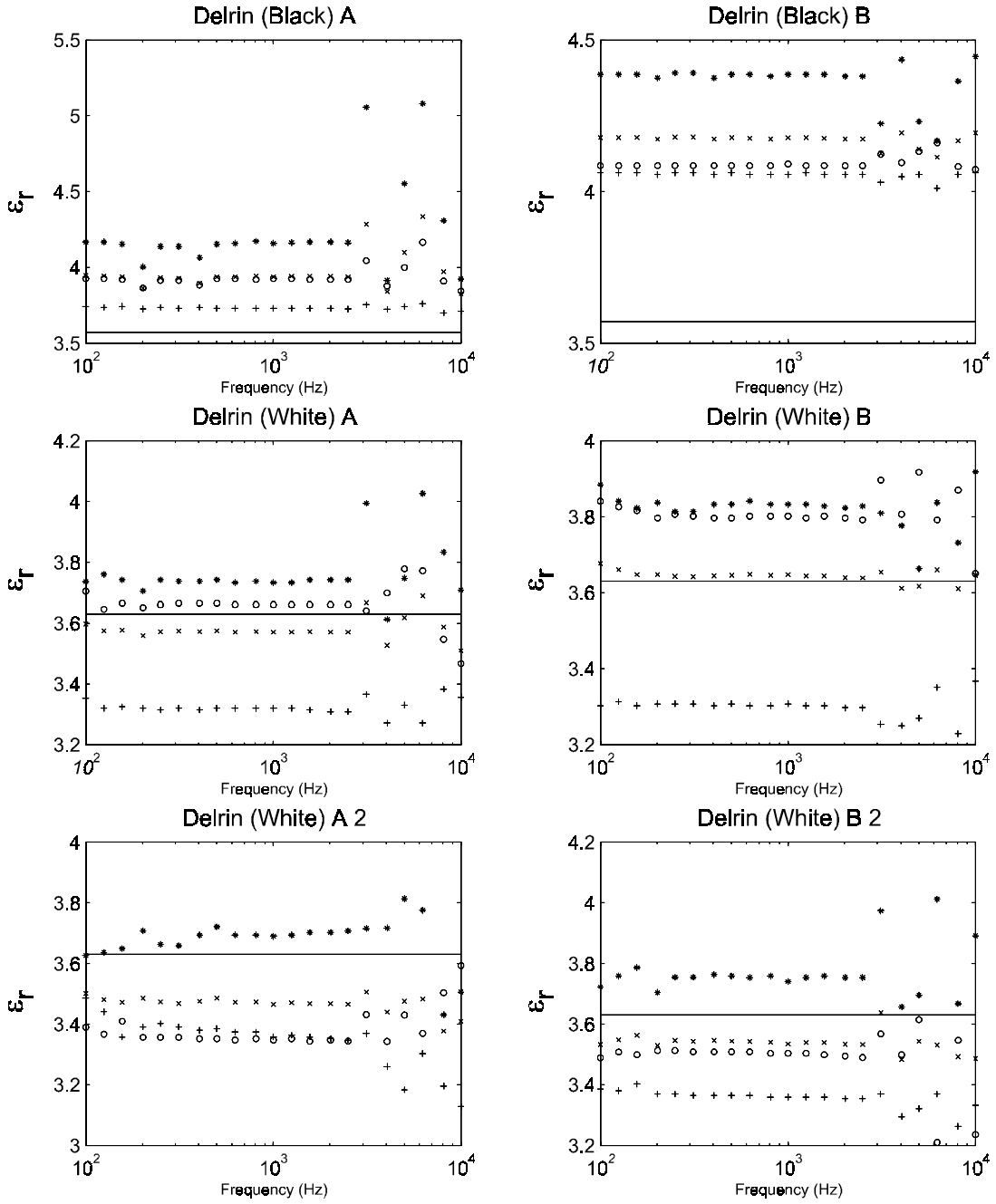

Figure 8.25: Relative dielectric permittivity of Delrin estimated with parallel plate capacitor and with three-wavelength sensor using calibration and α parameter. Legend: "+" - 1.0 mm, "o" - 2.5 mm, "" - 5.0 mm, "x" - average of the three, "–" - parallel plate measurement.*

8.3.6 Measurements with Liquid Dielectrics

For these experiments, a large plastic container was filled with about a gallon of corn oil. This same oil was used for all the experiments except for a little that was added from time to time to ensure that everything was fully submerged. The devices were immersed and connected to the interface box. The 5.0 mm sensor was connected to channel 1, PPC was connected to channel 2, and the TC was connected to channel 3. Even with this simultaneous setup, the measurements of G_{12} and σ (for the two capacitors) were not consistent. It should be noted that the shielding of the experiment was tried both at ground and at the guard voltage of the 5.0 mm sensor. Running the shield at the sensor's guard gave better results.

In the process of running these tests, it was discovered that oil had leaked into the interface box by a combination of capillary action and gravity. Some of the components (particularly the relays and SMA connectors) were damaged. The relays were replaced and the rest of the board was cleaned with methanol. One should be careful to avoid penetration of oil inside the interface circuit enclosure.

The high frequency relative dielectric permittivity of two liquid dielectrics, corn oil and transformer oil, has been estimated using data from a calibrated three-wavelength sensor and a parameter estimation routine *se.m*. An excellent agreement (within $\pm 2\%$) has been achieved among all three wavelengths as well as the parallel plate capacitor data. The permittivity of transformer oil was estimated to be 2.2, and the permittivity of corn oil was estimated to be 3.1 for this batch.

8.4 Matching Fluid Approach

If various secondary effects are neglected, it is possible to estimate the dielectric properties of irregularly shaped solid materials by positioning them between the electrodes of the test cell, which can be, for example, a parallel-plate capacitor or a coaxial cylindrical capacitor. If the dielectric permittivity of the solid material under test is uniform, it can be determined in the following way. Two identical test cells are positioned in

the same container filled with some kind of a dielectric liquid. One cell contains only this liquid, and the other cell contains the solid material under test surrounded by the same dielectric liquid. The capacitances between the corresponding pairs of electrodes are equal when the dielectric permittivity of the liquid is equal to the dielectric permittivity of the solid sample. Initially, the capacitances of each cell are different, but by varying the dielectric permittivity of the liquid, one can bring them to be equal. The easiest way to estimate the dielectric permittivity of the filler dielectric is to gradually mix two miscible dielectric liquids with approximately equal specific gravity, as was done in [312] to measure the dielectric permittivity of various grains. For this type of measurement, it is necessary that the relative dielectric permittivity of the filler be between the dielectric permittivities of the two liquids.

Similar to the liquid displacement approach described in [313], the two-fluid method provides a potentially higher accuracy of measurements, especially with irregularly shaped material surfaces. This project evaluated the applicability of two-fluid methods to determine ε_r with a greater accuracy then could be achieved otherwise. Two nearly identical single wavelength sensors (identical in terms of metallization and capacitance) were submerged in a liquid composed of transformer oil and corn oil and, later, transformer oil and castor oil (as shown in Figure 8.26). A solid sample was placed on one of the two single wavelength sensors. The sensors were placed on a piece of Lexan to ensure good contact with the solid sample since the bottom of the basin was flexible and not flat. Additionally, a parallel plate capacitor (either TC or PPC) was used to give another measure of the permittivity of the liquid. The second liquid was mixed into the transformer oil until both sensors measured the same capacitance (adjusted for the small difference in metallization) and permittivity. At this point, a value for the permittivity of the solid sample could be obtained. Although the only necessary stopping criterion is that the measured dielectric permittivity be the same, the equality of the capacitance provided an additional check. The collected data were processed using the program *twoliq.m* written for Matlab 5.0 (Appendix G).

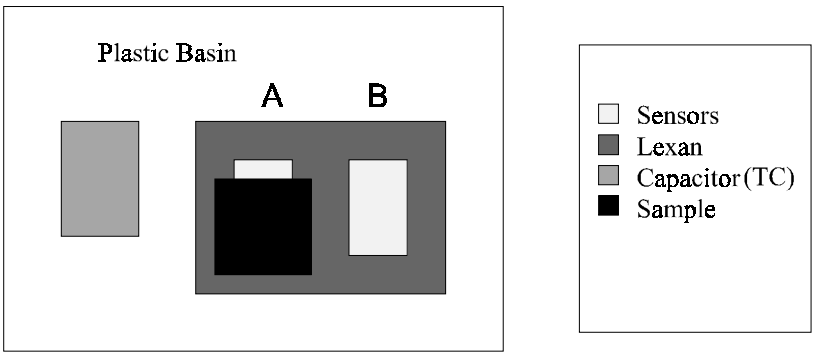

Figure 8.26: Schematic of the measurement setup for two fluids measurement. A parallel plate capacitor on the left is used to measure the dielectric permittivity of the liquid mixture.

8.4.1 Transformer Oil and Corn Oil

Two selected sensors, designated sensor A and sensor B, had very similar values for the interelectrode capacitance. Both sensors were 2.5 mm wavelength sections of two Teflon three-wavelength sensors. Sensor A was pressed against the sample while sensor B was measuring the properties of the fluid only, as shown in Figure 8.26. Since the two capacitance values for sensors in air were not exactly equal (C_A/C_B ratio of 1.016), the correct solution point was assumed to occur when the ratio of measured capacitance values in the liquid was the same as the ratio in air. The C_{12} vs. ε curves for both sensors was determined and the capacitance ratio (Sensor A: Sensor B) vs. ε curve was plotted. That is, the ratio criterion was used instead of the equality criterion. The sensors and TC were submerged in 3500 ml of transformer oil, $\varepsilon_r = 2.2$. Corn oil ($\varepsilon_r = 3.1$) was added in increments of 100 mL and mixed very well with the transformer oil. The dielectric permittivity of the liquids was determined with a parallel plate tuning capacitor ε_{TC} as the ratio of the capacitance in the liquid dielectric C_{fluid} and capacitance in air C_{air}:

$$\varepsilon_{TC} = \frac{C_{fluid}}{C_{air}}. \tag{8.16}$$

Tables 8.4 and 8.5 show that even though the dielectric permittivity of materials under test can be determined using this approach, the achieved accuracy does not

Filename	Transformer Oil	Corn Oil	Notes
nosample	3500 mL	0 mL	No sample
polyeth0000	3500 mL	0 mL	polyethylene on sensor A
polyeth0100	3500 mL	100 mL	
polyeth0200	3500 mL	200 mL	
polyeth0300	3500 mL	300 mL	
polyeth0400	3500 mL	400 mL	

Table 8.4: Absolute oil volumes and filenames for repeated two-fluid iterations on polyethylene.

Filename	ε_{TC}	ε_A	ε_B	C_A	C_B	C_A/C_B
nosample	2.1478	2.2093	2.2224	4.2166	4.2005	1.0038
polyeth0000	2.1446	2.2425	2.2305	4.2849	4.2172	1.0161
polyeth0100	2.1777	2.2516	2.2465	4.3037	4.2499	1.0127
polyeth0200	2.1952	2.2603	2.3289	4.3216	4.4187	0.978
polyeth0300	2.2106	2.2845	2.3513	4.3716	4.4647	0.9791
polyeth0400	2.2391	2.2986	2.3419	4.4007	4.4454	0.9899

Table 8.5: Relative permittivity and capacitance measurements corresponding to Table 8.4. Capacitance in air was 1.92 pF for sensor A and 1.95 pF for sensor B. The ratio of 1.016 should mark the match, however, the accuracy achieved here is not as high as the small percentage variation of the last column values suggests.

significantly exceed the accuracy of experiments in air. Candidate liquids for this type of experiment should be highly miscible. Also, this approach is more likely to perform well in non-contact measurements, that is when the sensor is not in direct contact with the solid specimen and has a known gap.

Tables 8.6 and 8.7 show that even though the dielectric permittivity of polypropylene was determined correctly, the accuracy was not sufficient to distinguish between the polypropylene ($\varepsilon_r = 2.36$, measured with a parallel plate capacitor) and polyethylene ($\varepsilon_r = 2.23$, measured with a parallel plate capacitor) based on these measurements only.

8.4.2 Transformer Oil and Castor Oil

Since the mixtures of transformer oil and corn oil trials did not succeed in providing enough precision, mixtures of transformer oil and castor oil were also tried to verify

Filename	Transformer Oil	Corn Oil	Notes
nosample	3500 mL	0 mL	No sample
polypro0000	3500 mL	0 mL	polypropylene on sensor A
polypro0100	3500 mL	100 mL	
polypro0200	3500 mL	200 mL	
polypro0300	3500 mL	300 mL	
polypro0400	3500 mL	400 mL	

Table 8.6: Absolute oil volumes and filenames for two-fluid iterations on polypropylene.

Filename	ε_{TC}	ε_A	ε_B	C_A	C_B	C_A/C_B
nosample	2.1478	2.2093	2.2224	4.2166	4.2005	1.0038
polypro0000	2.1474	2.2195	2.224	4.2375	4.2038	1.008
polypro0100	2.1685	2.2336	2.2546	4.2666	4.2663	1.0001
polypro0200	2.1972	2.2563	2.3186	4.3134	4.3976	0.9809
polypro0300	2.2111	2.2883	2.3434	4.3794	4.4485	0.9845
polypro0400	2.2362	2.2983	2.3321	4.4001	4.4253	0.9943

Table 8.7: Permittivity and capacitance measurements corresponding to Table 8.6. The ratio of capacitances has been varied in very narrow brackets. Since the ratio 1.016 has not been achieved due to a small systematic error, the intersection of the curves is not sufficiently close to the permittivity measured with the parallel plate capacitor.

the applicability of the proposed approach when the dielectric permittivity of the two fluids differ significantly. The relative dielectric permittivity of transformer oil is about 2.2, whereas corn oil has a relative dielectric permittivity of about 3.1, and castor oil has a relative dielectric permittivity of about 4.5. By using castor oil instead of corn oil, measurements could be performed on Lexan ($\varepsilon \approx 3.0$). This range should have been sufficient to permit an accurate measurement of this value as well as to illustrate the changes of value during this process. A 1/4 inch thick piece of Hyzod (also a polycarbonate produced by a different manufacturer) was used.

The results of these trials were not very successful because castor oil mixes very poorly with transformer oil. Even with the magnetic stirrer, it was impossible to know if adequate mixing had occurred. Castor oil is denser and more viscous than transformer oil. Both fluids would separate immediately after interruption of vigorous mixing. For completeness, the results are shown in Tables 8.8 and 8.9. The variation of the ratio of capacitance of the two sensors is shown in Figure 8.27.

Filename	Transformer Oil	Castor Oil	Comment
castor0000ns	2000 mL	0 mL	No sample
castor0000	2000 mL	0 mL	Lexan on sensor A
castor0500	2000 mL	500 mL	castor oil and transformer oil not miscible
castor1000	2000 mL	1000 mL	
castor1000a	2000 mL	1000 mL	
castor1000b	2000 mL	1000 mL	
castor1500	2000 mL	1500 mL	

Table 8.8: Absolute oil volumes and filenames for two-fluid measurements with Lexan using castor oil ($\varepsilon_r = 4.5$) and transformer oil ($\varepsilon_r = 2.2$).

Filename	ε_{TC}	ε_A	ε_B	C_A	C_B	C_A/C_B
castor0000ns	2.1382	2.1959	2.2053	4.1891	4.1656	1.0056
castor0000	2.1424	2.4829	2.1985	4.7853	4.1519	1.1521
castor0500	2.4856	2.8849	2.7523	5.6296	5.2974	1.0627
castor1000	2.7598	2.9066	3.196	5.6756	6.2355	0.9102
castor1000a	2.7998	3.0649	3.4098	6.0129	6.6927	0.8984
castor1000b	2.8114	3.0668	2.9014	6.017	5.611	1.0724
average 1000	2.7903	3.0128	3.1691	5.9018	6.1797	0.955
castor1500	2.9964	3.0455	3.2753	5.9714	6.4046	0.955

Table 8.9: Permittivity and capacitance measurements corresponding to Table 8.8. The capacitances C_A and C_B are the drive-sense interelectrode capacitance C_{12}.

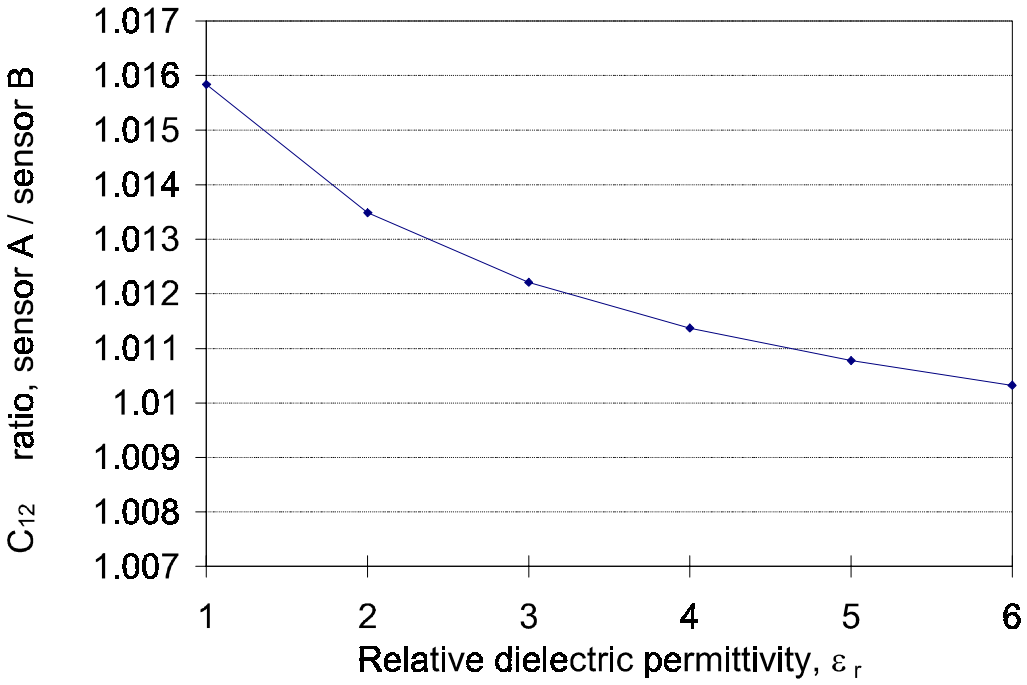

Figure 8.27: Calculated with finite-element software, the ratio of C_{12} values for the 2.5 mm sensors "A" and "B" as a function of ε_r used in the two fluid experiment. The metallization ratio of sensor A is 53.2% and the metallization ratio of sensor B is 52.7%.

Figure 8.28 shows the change of apparent relative dielectric permittivity computed from measurements under the assumption that the sensor head is in contact with a homogeneous dielectric medium. The two lines intersect at the correct value of the Lexan relative dielectric permittivity $\varepsilon_r = 3.0$ when the amount of added castor oil is equal to 1000 ml.

The estimation of the relative dielectric permittivity plotted in Figure 8.28 requires either calibration of interdigital sensors or a model-based inverse problem algorithm. It is also possible to bypass modeling by adding the measurement data from the parallel-plate capacitor to the analysis. The ratio of capacitances of the two interdigital sensors is plotted in Figure 8.29 against the relative dielectric permittivity measured by the parallel-plate capacitor. The intersection of the measured capacitance ratio curve with the equal capacitance curve gives the estimate of the relative dielectric permittivity of

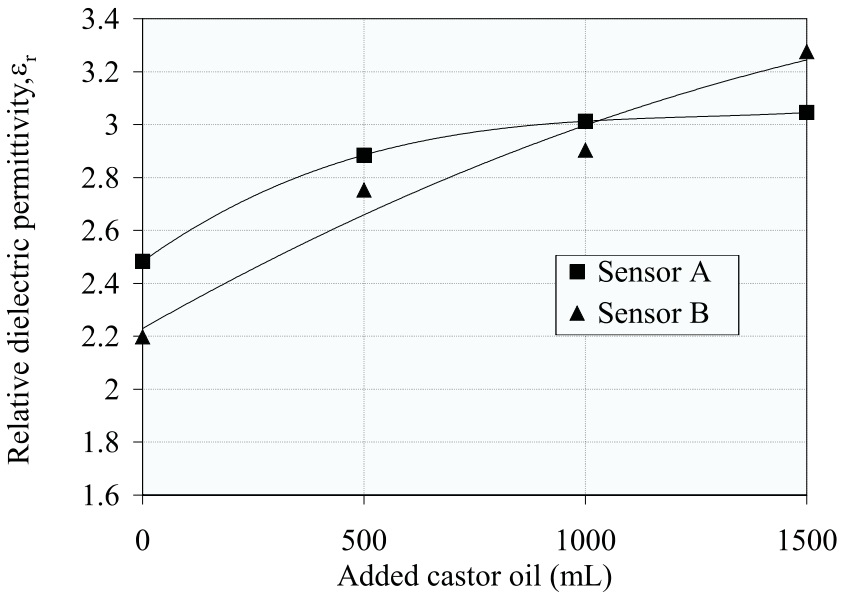

Figure 8.28: Apparent relative dielectric permittivity measured by two nearly identical 2.5 mm wavelength interdigital sensors as a function of added castor oil volume. The transformer oil volume is 2000 ml. Both sensors are immersed in the oil mixture with Sensor A also pressed against the Lexan sample. Solid lines are a third order polynomial fit to the experimental data.

material under test ($\varepsilon_r = 2.95$). The equal capacitance curve comes from the measurement of the capacitance of each interdigital sensor in air; the values are not exactly 1.0 because the sensors are not completely identical due to inherent manufacturing imprecision of flexible circuits.

Further refinement of this experimental technique is recommended. At this point, further investigation with the liquid measurements was not pursued because the principle has been demonstrated and no specific application at the moment required using it. Otherwise, this approach would have been fine-tuned for a specific application.

8.4.3 Filled Air Gap Measurements

In order to gain insight into how the air gap affects measurements with the TWS, different solid materials were coated with non-conductive grease or oil so that the cavity space between the sensor and the material under test that would have been otherwise filled with air, would now be filled with a material with a different permittivity than air.

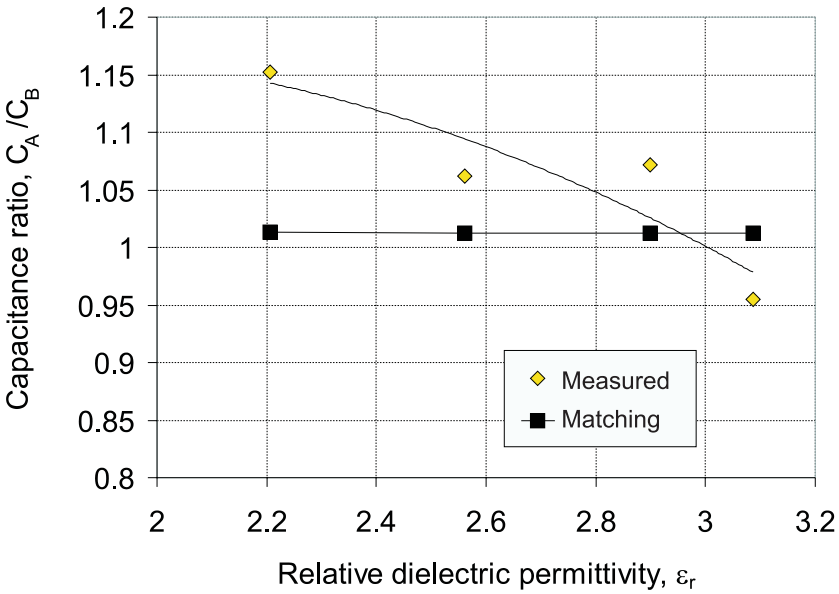

Figure 8.29: Relative dielectric permittivity of material under test determined through the capacitance ratio. The "Matching" line represents the calibration-based simulated data for two slightly different sensors immersed in a homogeneous dielectric. All points on this line would be at the capacitance ratio of 1.0 for identical sensors.

The same set-up described in the previous section was used except that measurements were conducted in air and both the sensor and the sample were coated with a grease or oil. Observations and trials with Lexan (which is transparent) indicated that the greases did not distribute properly so that the gap was larger than it would have been had air only been present. The oil experiments were more successful. Table 8.10 lists values of interelectrode capacitances obtained with different fillers which were significantly different than air only measurements with no filler. Table 8.11 lists the dielectric permittivity of both fillers and test materials. A selected subset of data from this table is analyzed in the following section.

8.5 Multiple Wavelength Measurement Sensitivity

The major interest that drives multiple wavelength measurement technique development stands from the ability to determine several material properties with a single device. Such an approach also implies a possibility to increase measurement accuracy of properties of interest by reducing the effect of measurement perturbations. The

	1mm	2.5mm	5mm	Filename	Notes
Metallization	52.88%	53.53%	53.40%		
Air					
Teflon	5.78 pF	3.29 pF	2.40 pF	teflonb1	
Polyethylene	6.36 pF	3.77 pF	2.78 pF	polyb1	
Polypropylene	6.38 pF	4.02 pF	2.73 pF	polyprob	
Lexan	7.86 pF	5.18 pF	3.79 pF	lexanb1	
Nylon	12.5 pF	10.9 pF	8.45 pF	nylonb	phase present
Corn Oil					
Teflon	7.04 pF	4.39 pF	2.69pF	tefloncorn2	
Polyethylene	7.76 pF	4.56 pF	3.01 pF	polyethcorn	
Polypropylene	7.40 pF	4.51 pF	3.01 pF	polyprocorn	
Lexan	9.08 pF	6.12 pF	4.28 pF	lexancorn	no trapped air bubbles
Nylon	13.4 pF	11.3 pF	8.25 pF	nyloncorn	phase present
Castor Oil					
Teflon	10.7 pF	5.72 pF	3.43 pF	tefloncastor	
Polyethylene	9.66 pF	5.77 pF	3.53 pF	polyethcastor	
Polypropylene	11.0 pF	5.92 pF	3.88 pF	polyprocastor	
Lexan	11.8 pF	7.19 pF	4.88 pF	lexancastor	few air bubbles
Nylon	13.4 pF	11.5 pF	8.32 pF	nyloncastor	phase present
Ultra Lube					
Polyethylene	8.71 pF	5.46 pF	3.63 pF	polyethgrease	too viscous
Polypropylene	7.38 pF	4.68 pF	2.86 pF	polyprogrease	too viscous
Nylon	8.44 pF	6.50 pF	5.03 pF	nylongrease	too viscous, phase
Silicone Grease					
Teflon	6.98 pF	4.20 pF	2.96 pF	teflonsili	too viscous
Polyethylene	6.39 pF	4.86 pF	3.11 pF	polyethsili	too viscous
Lexan	8.30 pF	5.53 pF	3.89 pF	lexansili	too viscous

Table 8.10: Measured C_{12} values from filled air gap measurements. Each solid material sample is at least 1/4 inch thick. Non-zero phase present in high frequency measurements indicates that the dielectric permittivity estimation is not accurate. Lexan, being transparent, allows visual observation of the contact quality.

Fillers, from sensor measuremts	ε_r	Samples, parallel plate measurments	ε_r
Air	1	Teflon	2.06
Silicone Grease	2.7	Polyethylene	2.23
UltraLube	2.9	Polypropylene	2.36
Corn Oil	3.15	Lexan	3.01
Castor Oil	4.5	Nylon	4.05

Table 8.11: Relative permittivity of test materials and fillers used in Table 8.10.

	1 mm	2.5 mm	5 mm
Air	6.07	4.72	4
Castor oil	10.5	6.7	4.4

Table 8.12: Calculated capacitance in pF for different wavelengths and filler materials for the operating point ($(\varepsilon_r = 3.0,\ h = 30\ \mu m)$) shown in Figure 8.30.

following example shows that filling the gap between the sensor head and the solid material under test may improve selectivity of the measurement. The gap is modeled here as an ideally flat one. This representation is adequate for purely capacitive cases with no significant conduction currents. Figure 8.30 shows lines of equal capacitance computed with finite element simulation for a specific point in a two-variable (ε_r and h) solution space. The values of relative dielectric permittivity ε_r and equivalent air gap h can be found from two measurements with different spatial wavelengths, different ambient media, or both. The angle between the iso-capacitance lines should be as close as possible to 90 degrees in order to provide the best selectivity with respect to both variables, ε_r and h.

One of the ambient media in this simulation is castor oil, marked with the letter C in Figure 8.30, and the other one is air, marked with the letter A. Since the dielectric permittivity of air is smaller than that of Lexan, all three iso-capacitance lines given in Table 8.12 lie in the first and third quadrants (if the origin is placed at the operation point, where all lines intersect). Similarly, since the dielectric permittivity of castor oil is larger than that of Lexan, all three iso-capacitance lines for castor oil lie in the second and fourth quadrants. Therefore, it is theoretically impossible to obtain a 90 degree angle between iso-capacitance lines for the same media. Also, since the absolute value of the derivative grows with spatial wavelength, it is reasonable to expect that the accuracy of measurement is better for a combination of more distant spatial wavelengths.

Table 8.13 shows the results of measurements with selected pairs of spatial wavelengths for the same case. The measurements confirm the general trend of improved accuracy when the angle between the iso-capacitance lines approaches 90 degrees.

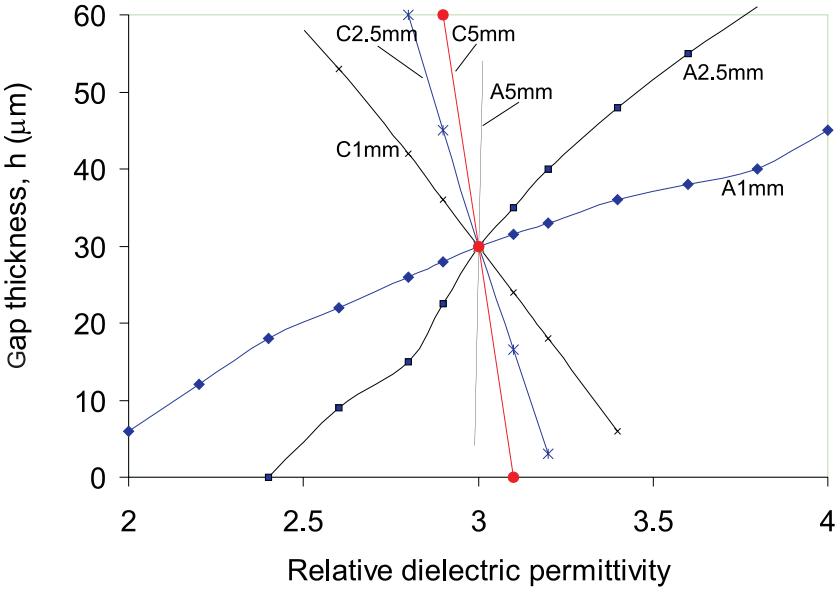

Figure 8.30: Calculated lines of equal capacitance for different levels of perturbation from the operating point ($\varepsilon_r = 3.0$, $h = 30$ μm) for each of the three wavelengths of the sensor shown in Figure 4.5 with air (A) and castor oil (C) filling the gap. The values for each iso-capacitance line are listed in Table 8.12.

Combination	Permittivity	Relative error (%)
A1-A2.5	2.6	-13.33
A1-A5	2.9	-3.33
A2.5-A5	2.8	-6.67
A1-C5	2.95	-1.67
A2.5-C2.5	3.0	0.00
A2.5-C1	3.1	3.33
C1-C2.5	2.75	-8.33
C1-C5	3.05	1.67
C2.5-C5	3.2	6.67

Table 8.13: Measured dielectric permittivity of Lexan ($\varepsilon_r = 3.0$) using different pairs of spatial wavelengths and gap-filling fluid. The accuracy of measurement generally improves with the increasing angle between the iso-capacitance lines shown in Figure 8.30.

8.6 Interpolation Using Solution Spaces

The fundamental feature of $\omega - k$ interdigital dielectrometry is the one-sided application of sets of interdigital electrodes of different spatial periodicity to measure property profiles of dielectric materials at different depths from the material surface. Apart from the property-versus-depth profiling features, $\omega - k$ dielectrometry is similar to other dielectrometry measurement methodologies because it uses electrodes excited by a time-varying voltage signal. Indeed, admittance spectroscopy is commonly used to measure properties of frequency-dispersive materials. However, the electrode structure in more conventional techniques is usually either parallel plates or coaxial cylinders. Simple shapes offer the advantage of having closed-form algebraic solutions for the interelectrode admittance. When dealing with interdigital electrodes, the task of computing the admittance matrix of the sensor is more difficult. Finite element simulation allows the computation of the admittance matrix given the inhomogeneous distribution of material properties and the sensor geometry in several seconds using modern personal computers. While this computational time is acceptable for the forward problem (computation of electric fields and terminal admittance matrix), it may be prohibitively long for the inverse problem of determining unknown material properties or geometry from dielectrometry measurements.

The algorithms that are used for the estimation of material properties are computationally expensive because model-based material property estimation (as opposed to straightforward calibration) is required in order to extract the maximum amount of information about the material. Even modern computers do not have sufficient speed required for online or manual measurements if each measurement were to be followed by a full-scale computer simulation of the tested region.

One efficient solution to speed up the process is to compute the response of the sensor for all possible values of the measured parameters with a reasonable degree of discretization. Then, each measurement point can be interpolated using the results of the prior calculations. With a small number of unknown parameters, this approach

works reasonably well. However, as the number of unknown parameters grows, the computational space quickly becomes unacceptably large. Several techniques are available to reduce the number of points that have to be computed in advance. One of the techniques explored in this section exploits the property that the frequency-dependent terminal admittance of a homogeneous ohmic non-dispersive dielectric material can be predicted from a single frequency measurement [8, 65]. The proposed normalization allows mapping the results of measurements at one frequency to the results of measurements at a different frequency. As illustrated later in the text, this technique is applicable for evaluation of material properties even when they are frequency dispersive. Non-dispersive material properties always map onto the same point in the base computational space, while the frequency-dispersive material properties map onto different points in the base space for different frequencies [19]. Although the presented methodology is valid for any geometry, parallel plate electrode cases that have analytical solutions are considered in this section for illustrative purposes.

8.6.1 Maxwell Capacitor

Let us first consider the simplest case of a Maxwell capacitor, which has the two series dielectrics topology similar to the interdigital sensor structure considered in the next section, but has an easily understood analytical solution. Figure 8.31 shows the schematic of the parallel-plate capacitor test cell and equivalent lumped-element circuit. The lower layer is a perfect insulator ($\sigma_b = 0$). Suppose that the dielectric permittivity of the lower layer, ϵ_b, is known, and our task is to determine the dielectric properties of the upper layer, ϵ_a and σ_a, from parallel-plate admittance measurements. This is a realistic arrangement that takes place when the parallel-plate test cell is in air and the test dielectric is inserted between the electrodes. Except for possible interfacial effects not considered here, it makes no difference whether the air gap is on one side of the dielectric or both sides.

One can express the admittance as a complex number, and represent the real part of it as conductance G, and the imaginary part as the product of the angular frequency

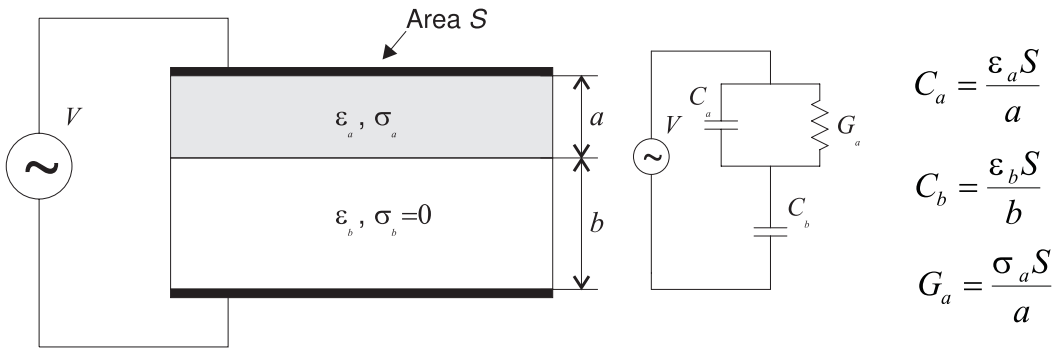

Figure 8.31: Maxwell parallel plate capacitor and equivalent circuit.

ω of a sinusoidal voltage excitation times the capacitance C:

$$Y = Y_r + jY_i = G + j\omega C. \tag{8.17}$$

It is possible to relate the material properties and geometric parameters of the Maxwell capacitor test cell to the terminal conductance and capacitance as

$$\frac{G}{\omega C_b} = \frac{\frac{\sigma_a S}{a\omega}\left(\frac{\varepsilon_b S}{b}\right)}{\left(\frac{\varepsilon_a S}{a} + \frac{\varepsilon_b S}{b}\right)^2 + \left(\frac{\sigma_a S}{a\omega}\right)^2} = \frac{\frac{G_a}{\omega C_b}}{\left(1 + \frac{C_a}{C_b}\right)^2 + \left(\frac{G_a}{\omega C_b}\right)^2} \tag{8.18}$$

and

$$\frac{C}{C_b} = \frac{\frac{\varepsilon_a S}{a}\left(\frac{\varepsilon_a S}{a} + \frac{\varepsilon_b S}{b}\right) + \left(\frac{\sigma_a S}{a\omega}\right)^2}{\left(\frac{\varepsilon_a S}{a} + \frac{\varepsilon_b S}{b}\right)^2 + \left(\frac{\sigma_a S}{a\omega}\right)^2} = \frac{\frac{C_a}{C_b}\left(1 + \frac{C_a}{C_b}\right)^2 + \left(\frac{G_a}{\omega C_b}\right)^2}{\left(1 + \frac{C_a}{C_b}\right)^2 + \left(\frac{G_a}{\omega C_b}\right)^2}, \tag{8.19}$$

where S is the area of the parallel plate capacitor and the equivalent conductance and capacitances are

$$C_a = \frac{\varepsilon_a S}{a}, \qquad C_b = \frac{\varepsilon_b S}{b}, \qquad G_a = \frac{\sigma_a S}{a}. \tag{8.20}$$

This formulation is the forward problem of computing terminal capacitance C and conductance G from properties and dimensions of each layer. The determination of an unknown C_a and G_a in terms of the known C_b and from terminal measurements of C and G is obtained by inverting (8.18) and (8.19) to

$$\frac{G_a}{\omega C_b} = \frac{\frac{G}{\omega C_b}}{\left(\frac{G}{\omega C_b}\right)^2 + \left(1 - \frac{C}{C_b}\right)^2} \tag{8.21}$$

and

$$\frac{C_a}{C_b} = \frac{\frac{C}{C_b}\left(1 - \frac{C}{C_b}\right) - \left(\frac{G}{\omega C_b}\right)^2}{\left(\frac{G}{\omega C_b}\right)^2 + \left(1 - \frac{C}{C_b}\right)^2}. \tag{8.22}$$

We can visualize the functions described in (8.18) through (8.22) by discretizing the solution space determined by the unknown variables. Figure 8.32(a) shows the solution space of $G/\omega C_b$ that corresponds to the forward problem solutions of (8.18). The ratio C_a/C_b varies linearly from 0 to 20 and the ratio $G_a/\omega C_b$ varies logarithmically from 10^{-3} (high frequency) to 10^3 (low frequency). Such a wide range of values is needed to accommodate the wide range of frequencies in dielectrometry spectroscopy studies (in our experiments the frequency is usually varied from 10 kHz to 0.005 Hz). This and all subsequent plots use a logarithmic scale for non-dimensional conductances of the general form $G/\omega C$. The normalized terminal admittance real component $G/\omega C_b$ remains less than 1 (negative on logarithmic scale) for all frequencies. It assumes its highest values when $G_a/\omega C_b$ is close to 1 (0 on logarithmic scale), that is, when the capacitive and conductive currents in the dielectric "*a*" are of comparable magnitude. Figure 8.32(b) shows a contour plot of the same solution space that was shown in Figure 8.32(a). Both plots indicate that the real part of the normalized terminal admittance attains its highest values when the conductance G_a is of the same order of magnitude as the product ωC_b and approaches zero when they are significantly different. When the layer "*a*" is essentially insulating ($G_a/\omega C_b << 1$), the entire system becomes a capacitor consisting of two capacitors formed by the layers "*a*" and "*b*" in series. In the other extreme, when the layer "*a*" is essentially a conductor ($G_a/\omega C_b >> 1$), it can be seen as the extension of the upper electrode, and the entire system reduces to the capacitor formed by the layer "*b*".

Keeping in mind the previous discussion, one can interpret the solution space for the imaginary part of the normalized terminal admittance, C/C_b, that is shown in

Figure 8.33(a) as a three-dimensional function of the normalized layer "a" properties and also repeated in Figure 8.33(b) as a contour plot. High values of capacitance C_a have the same effect on the total capacitance value as high values of G_a: they bring C/C_b closer to unity.

The inverse problem relations of (8.21) and (8.22) are plotted in Figures 8.34 and and 8.35, allowing determination of an unknown C_a/C_b in terms of measured terminal variables C/C_b and $G/\omega C_b$. The dielectric permittivity ε_a and conductivity σ_a can be determined directly from C_a and G_a in parallel plate geometry.

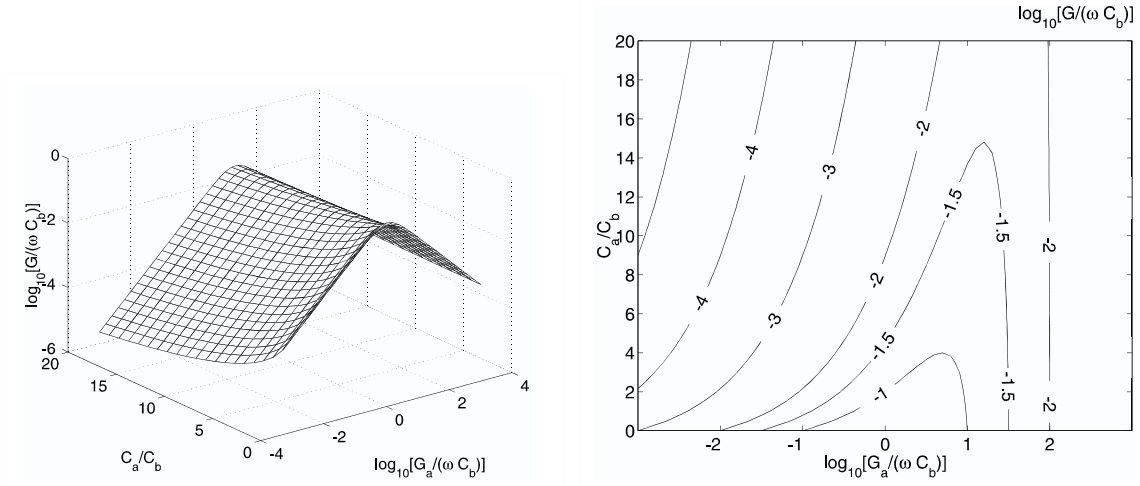

(a) (b)

Figure 8.32: A three-dimensional view (a) and a plot of the forward problem solution space iso-contours (b) for the normalized terminal conductance of the Maxwell capacitor in terms of normalized capacitance and conductance of the upper "a" layer.

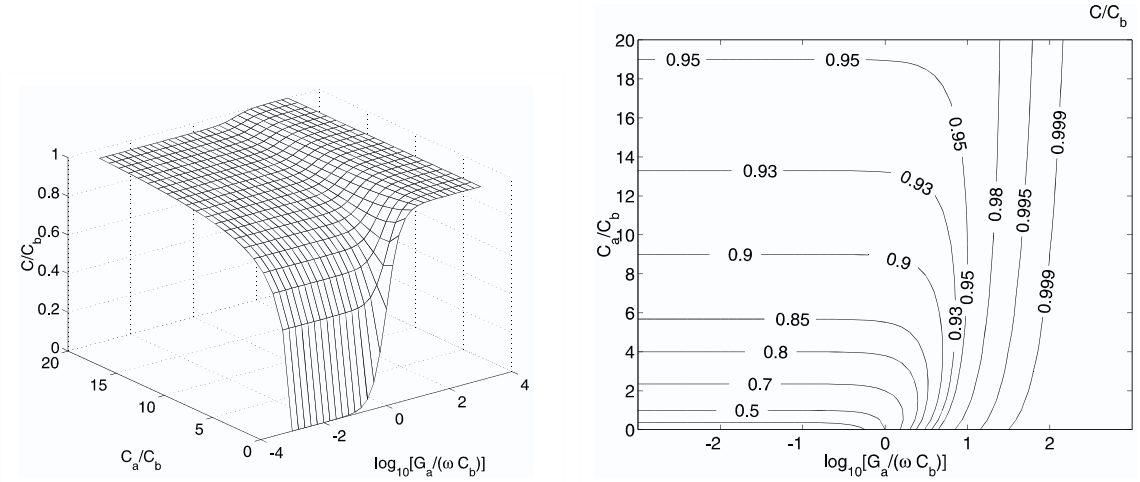

(a) (b)

Figure 8.33: A three-dimensional view (a) and a contour plot (b) of the forward problem solution space for the normalized terminal capacitance in terms of normalized capacitance and conductance of the upper "a" layer.

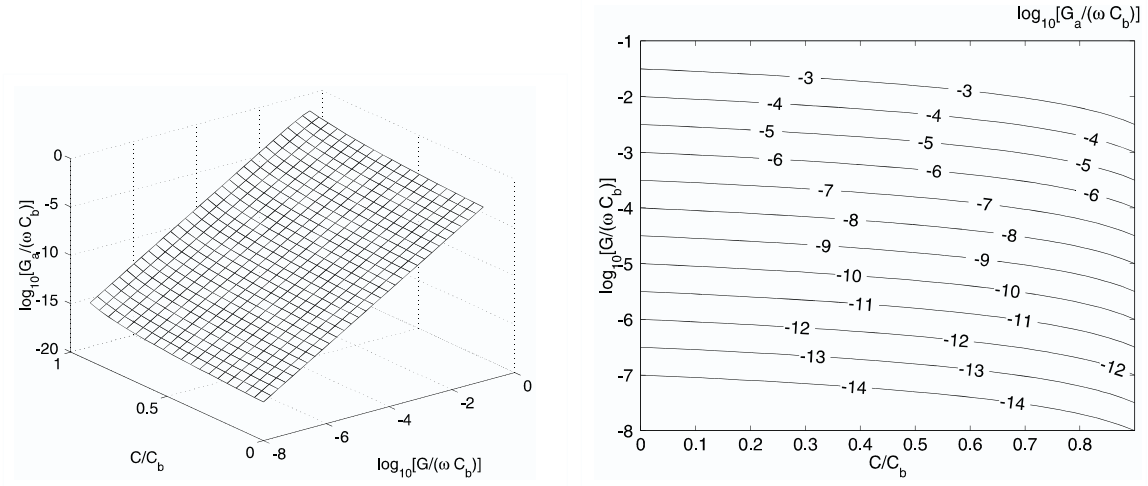

(a) (b)

Figure 8.34: A three-dimensional view (a) and a plot of the inverse problem solution space iso-contours (b) for the normalized conductance of the upper "a" layer in the Maxwell capacitor of Figure 8.31.

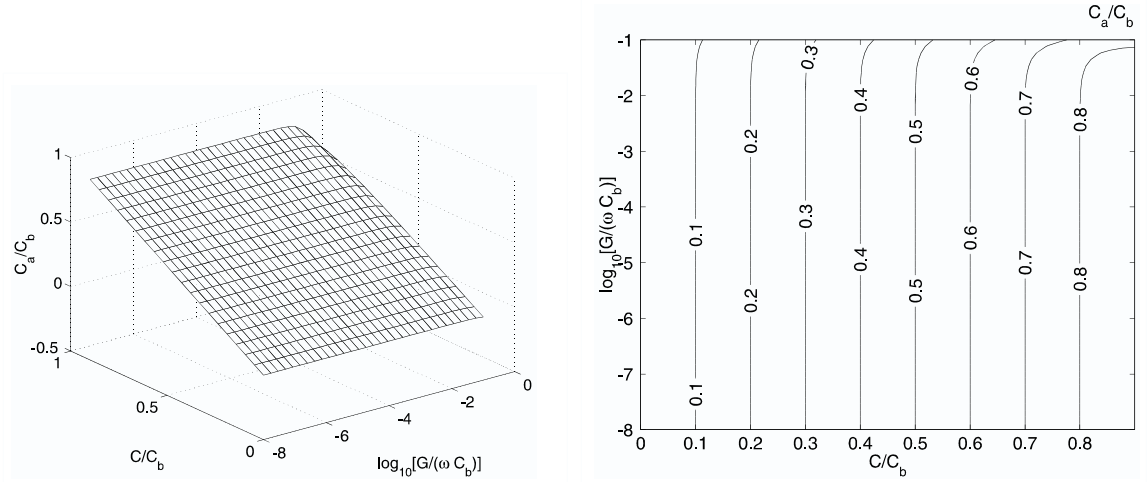

(a) (b)

Figure 8.35: A three-dimensional view (a) and a plot of the inverse problem solution space iso-contours (b) for the normalized capacitance of the upper "a" layer in the Maxwell capacitor of Figure 8.31.

8.6.2 Three-Wavelength Sensor Solution Spaces

5.0 mm Wavelength

The following plots of the solution spaces are computed for the three-wavelength sensor assuming an infinitely thick homogeneous material under test next to the sensor with Teflon substrate (ε_r=2.1) 254 μm thick. They follow the same pattern that was used for the Maxwell capacitor. Figure 8.36(a) shows the three-dimensional view of the 5 mm wavelength forward problem solution space for the real part of the normalized terminal transadmittance (conductance) per unit length computed with finite-element software. The normalization is with respect to the product of the dielectric permittivity of the Teflon substrate ($\varepsilon_s/\varepsilon_0 = 2.1$) and the frequency of excitation. A more conventional way to represent loss would be to use the loss factor $\varepsilon'' = \sigma/\omega$, but this representation was chosen to relate to our experimental data which is usually presented in terms of conductivity. Figure 8.36(b) shows a contour plot of the same solution space. Figure 8.37 shows the forward problem solution space for the normalized transcapacitance per unit length. Notice that the transcapacitance may take on negative values at low frequencies.

Unlike the Maxwell capacitor example, an exact closed form solution is not available for the terminal transadmittance of the interdigital sensor. In order to visualize the inverse functions of interest, the solution for the forward program is stored in computer memory in the form of a table that consists of columns ε, σ, G_{12}, and C_{12}. Figures 8.38(a) and 8.39(a) show the three-dimensional representation of the inverse problem solution space for the entire range of values of normalized permittivity and conductivity values of the material under test. Each calculation point is shown as a dot in a three-dimensional space. The uniqueness of solution is evident for all combinations of the variable values. Figures 8.38(b) and 8.39(b) show contour plots for the same solution space.

When the permittivity ε of the material under test is high, most of the field lines connecting the sensing and the driven electrodes go through the test material rather

than through the substrate. In that case, the response of the sensor approaches that of a parallel plate sensor, and the inverted value of ε becomes almost independent of transconductance, as can be seen in Figure 8.39(a).

The measurement data is interpolated using these solution spaces to find values of material properties. The solution spaces for the interdigital sensor presented in this section are not dependent on measurement electronics and are only functions of the sensor geometry and material properties.

The responses of Maxwell capacitor and interdigital sensor are similar at high frequency and differ significantly at low frequency because the Maxwell capacitor with $\sigma_b = 0$ has no DC conduction path whereas the interdigital sensor has a DC conduction path through the lossy material under test.

The measurements at different excitation frequencies can be mapped onto corresponding solution spaces presented in this section. If the material is not frequency-dispersive, the entire frequency sweep maps onto a single point in the non-dimensional solution space. A properly executed measurement of dielectric properties of dispersive materials at different frequencies mapped onto the same non-dimensional solution space produces a sequence of points that move from one measurement point to another forming a curve that falls entirely within the boundaries of the solution space. The drift of data for non-dispersive material measurements indicates shortcomings in the physical model of the simulated measurement setup. For example, the presence of a non-modeled electrochemical double layer at the electrode-dielectric interface results in very high values of effective dielectric permittivity at low frequencies due to double layer capacitance. The example of measurements of slightly dispersive material properties and parameter estimation with these solution spaces is given in Section 8.7.

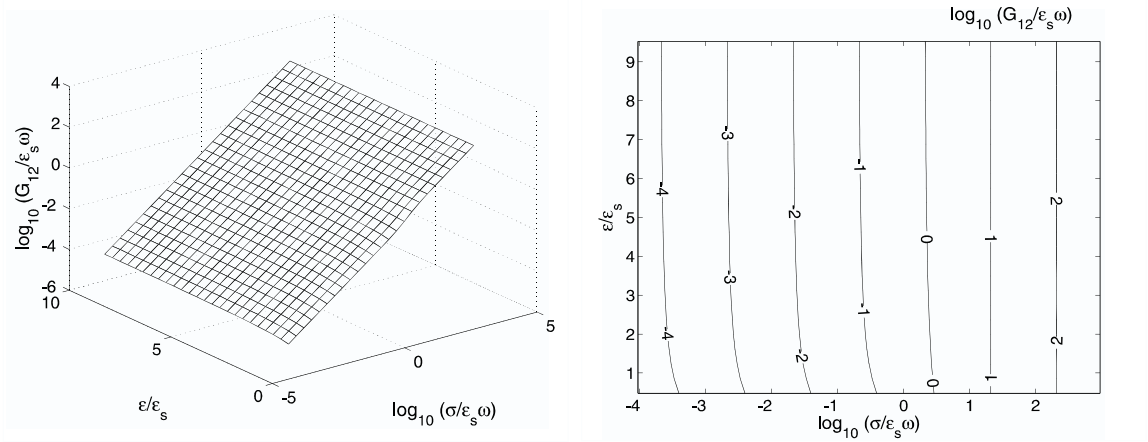

(a) (b)

Figure 8.36: A three-dimensional view (a) and a plot of the forward problem solution space iso-contours (b) for the normalized terminal transconductance per unit length for the 5.0 mm wavelength of the interdigital dielectrometry sensor in Figure 4.5 as a function of the normalized permittivity and conductivity of the material under test.

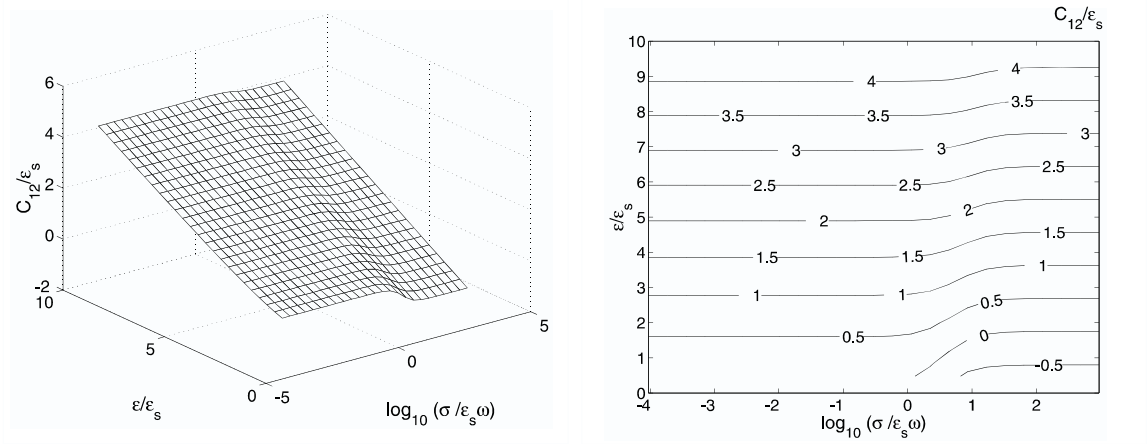

(a) (b)

Figure 8.37: A three-dimensional view (a) and a plot of the forward problem solution space iso-contours (b) for the normalized terminal transcapacitance per unit length for the 5.0 mm wavelength of the interdigital dielectrometry sensor in Figure 4.5 as a function of the normalized permittivity and conductivity of the material under test.

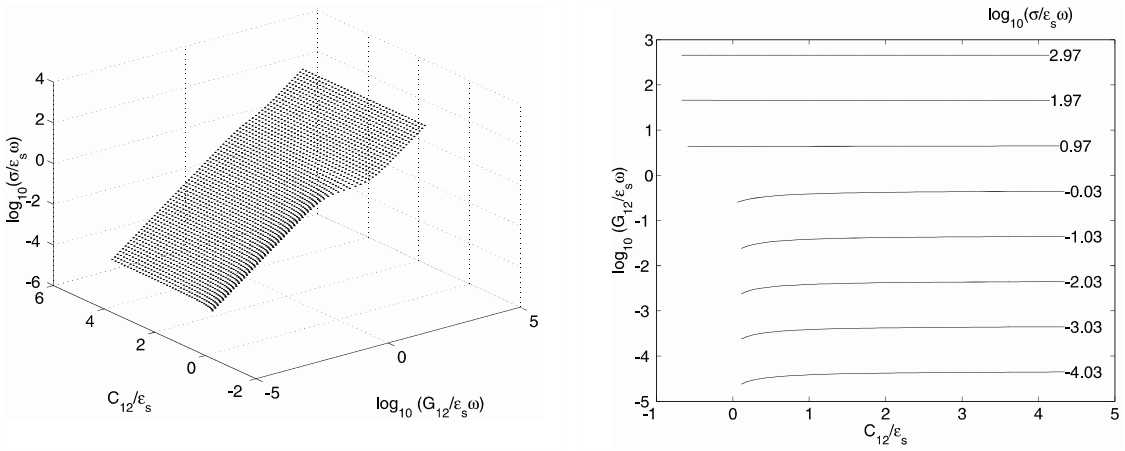

(a) (b)

Figure 8.38: A three-dimensional view (a) and a plot of the inverse problem solution space iso-contours (b) for the normalized material conductivity for the 5.0 mm wavelength in terms of normalized terminal transcapacitance and transconductance per unit length.

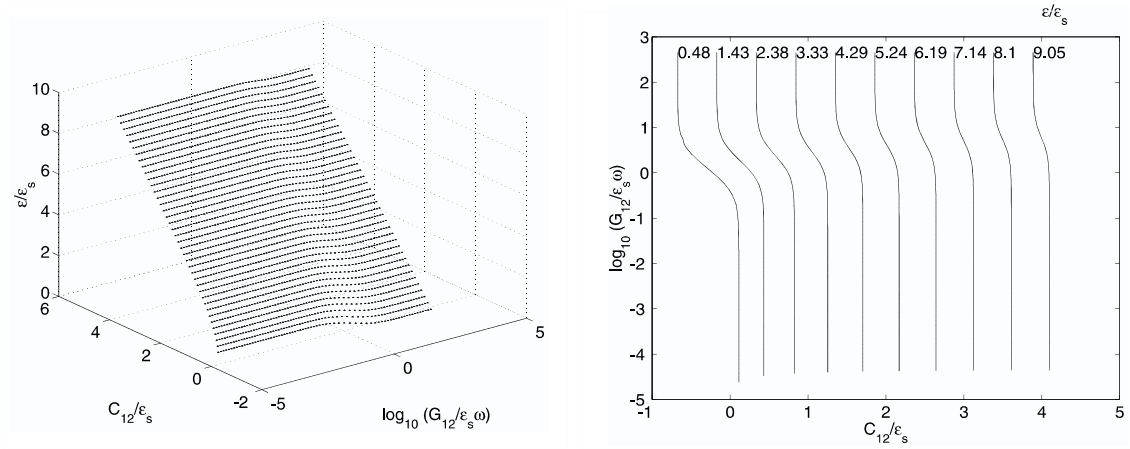

(a) (b)

Figure 8.39: A three-dimensional view (a) of the inverse problem solution space for the normalized material permittivity for the 5.0 mm wavelength and a plot of the inverse problem solution space iso-contours (b) for the normalized material permittivity.

2.5 mm Wavelength

The solutions for the 2.5 mm wavelength have essentially the same features as those for the 5 mm wavelength, already presented. The graphical representation of these solution spaces (Figures 8.40-8.43 for 2.5 mm wavelength) is included here for completeness.

1.0 mm Wavelength

The solutions for the 1.0 mm wavelength have essentially the same features as those for the 5 mm wavelength and 2.5 mm wavelength, already presented. The graphical representation of these solution spaces (Figures 8.44-8.47 for 1 mm wavelength) is included here for completeness. Naturally, the material layer directly adjacent to the sensor does not have to be of infinite thickness in order for these solution spaces to be applicable. These solutions are valid or approximately valid as long as the first layer thickness is larger then the penetration depth over a given wavelength.

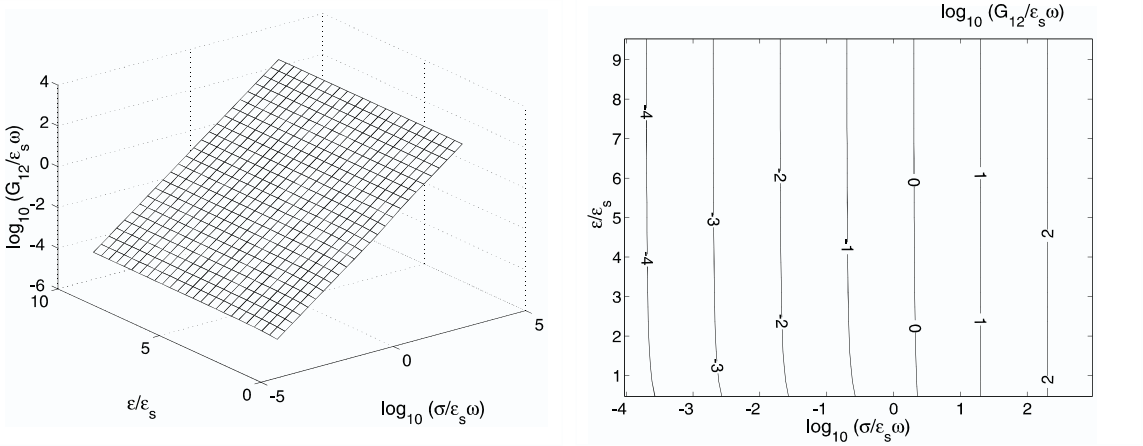

(a) (b)

Figure 8.40: A three-dimensional view (a) and a plot of the forward problem solution space iso-contours (b) for the normalized terminal transconductance per unit length for the 2.5 mm wavelength of the interdigital dielectrometry sensor in Figure 4.5 as a function of the normalized permittivity and conductivity of the material under test.

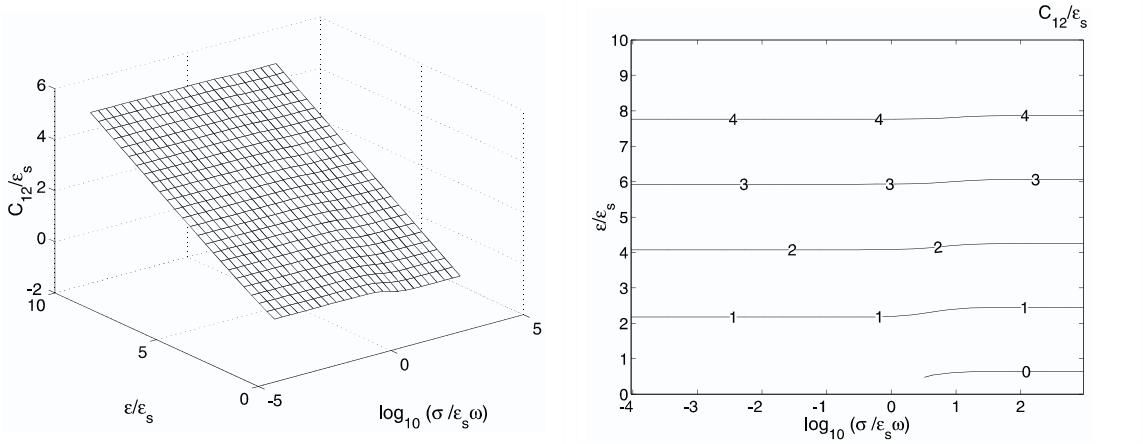

(a) (b)

Figure 8.41: A three-dimensional view (a) and a plot of the forward problem solution space iso-contours (b) for the normalized terminal transcapacitance per unit length for the 2.5 mm wavelength of the interdigital dielectrometry sensor in Figure 4.5 as a function of the normalized permittivity and conductivity of the material under test.

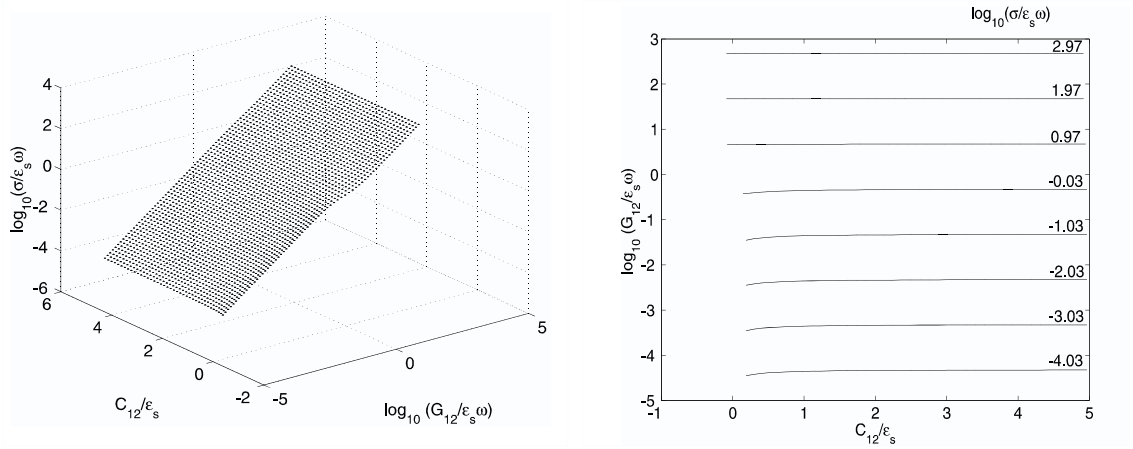

(a) (b)

Figure 8.42: A three-dimensional view (a) of the inverse problem solution space and (b) a plot of the inverse problem solution space iso-contours for the normalized material conductivity of the 2.5 mm wavelength in terms of normalized terminal transcapacitance and transconductance per unit length.

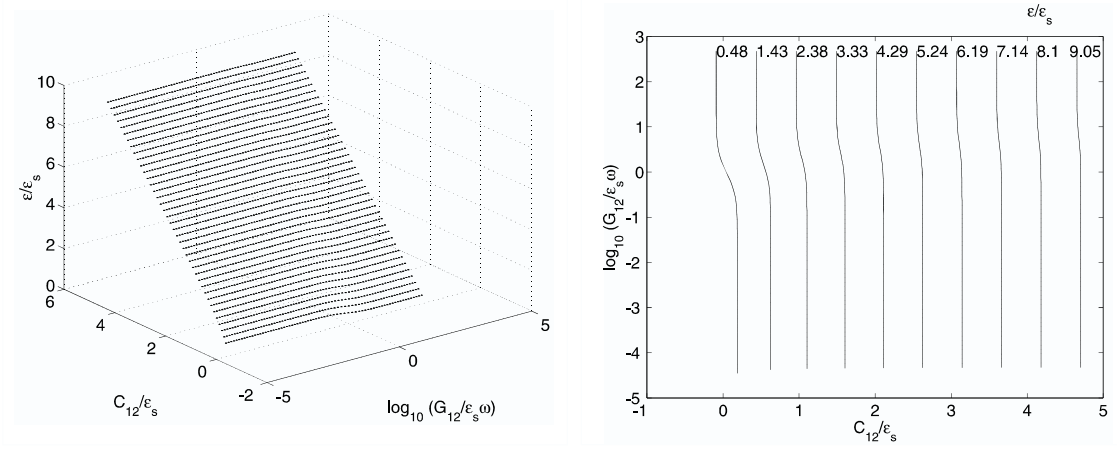

(a) (b)

Figure 8.43: A three-dimensional view (a) of the inverse problem solution space for the normalized material permittivity for the 1.0 mm wavelength and a plot of the inverse problem solution space iso-contours (b) for the normalized material permittivity.

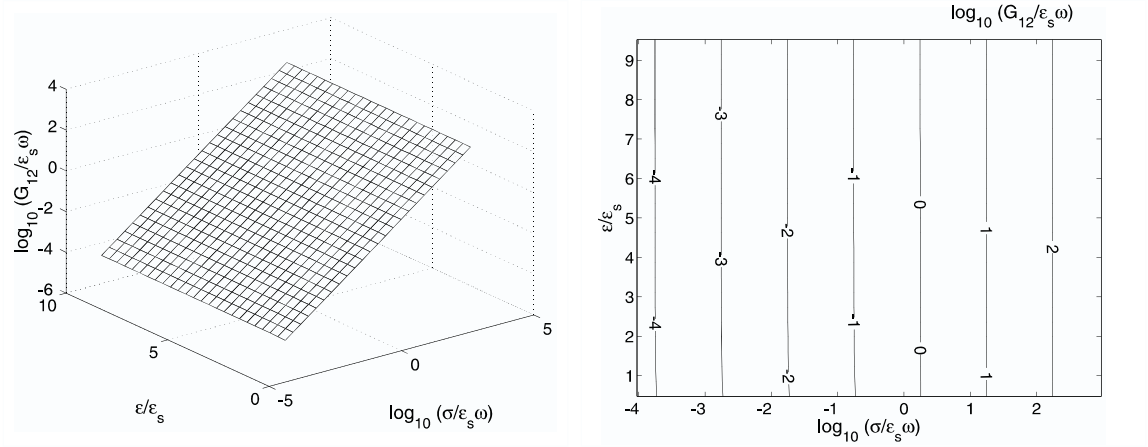

(a) (b)

Figure 8.44: A three-dimensional view (a) and a plot of the forward problem solution space iso-contours (b) for the normalized terminal transconductance per unit length for the 1.0 mm wavelength of the interdigital dielectrometry sensor in Figure 4.5 as a function of the normalized permittivity and conductivity of the material under test.

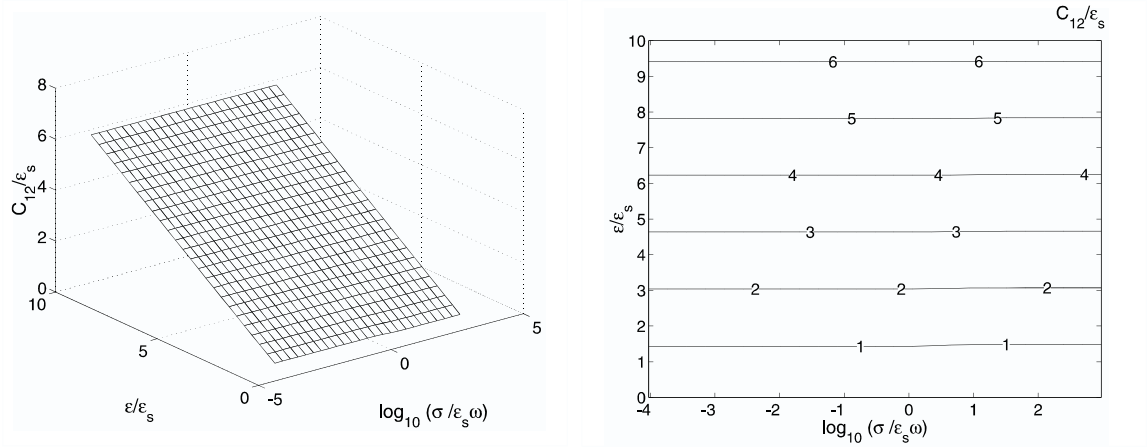

(a) (b)

Figure 8.45: A three-dimensional view (a) and a plot of the forward problem solution space iso-contours (b) for the normalized terminal transcapacitance per unit length for the 1.0 mm wavelength of the interdigital dielectrometry sensor in Figure 4.5 as a function of the normalized permittivity and conductivity of the material under test.

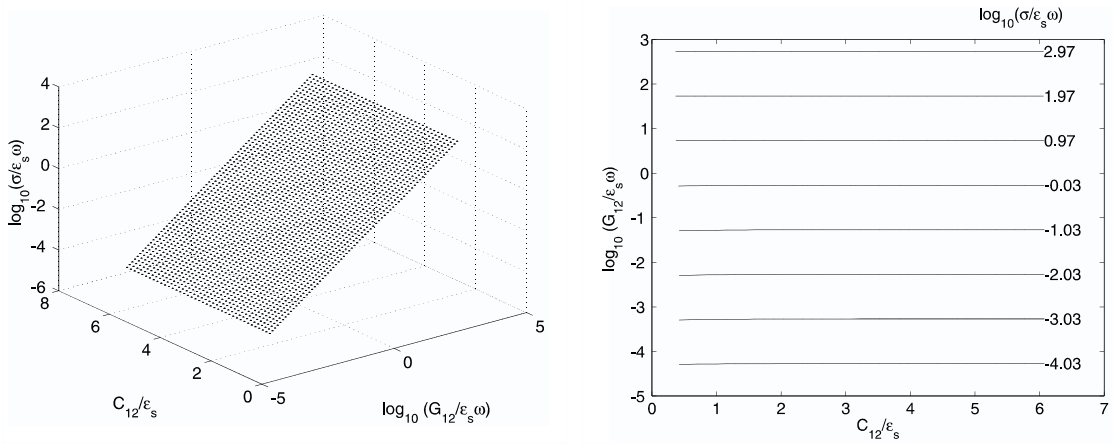

(a) (b)

Figure 8.46: A three-dimensional view (a) of the inverse problem solution space and (b) a plot of the inverse problem solution space iso-contours for the normalized material conductivity of the 1.0 mm wavelength in terms of normalized terminal transcapacitance and transconductance per unit length.

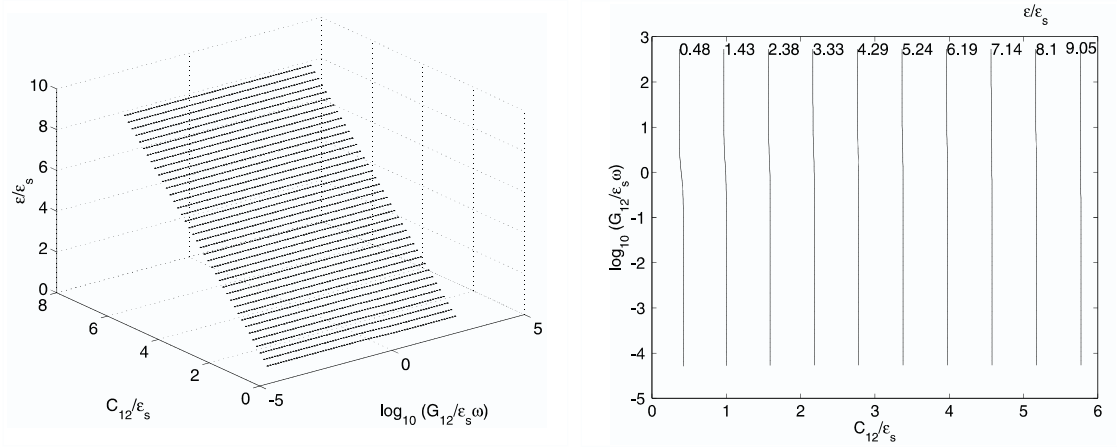

(a) (b)

Figure 8.47: A plot of the inverse problem solution space iso-contours for the normalized material permittivity for the 1.0 mm wavelength.

8.6.3 Frequency Conversion of Calculated Results

Consider an interdigital sensor immersed into a homogeneous material with unknown dielectric permittivity ε_2 and conductivity σ_2. Suppose that at some well-chosen reference frequency f_r the capacitance and conductance was tabulated for all ε_2 and σ_2. Then consider a test on an unknown sample whose properties are not known but are to be determined. From a practical point of view, we would like to run an experiment at a drive frequency such that there is appreciable phase in the response to be able to accurately distinguish σ_2 and ε_2. Furthermore, the material may be dispersive and as such its properties will change with frequency. For these reasons the test might not be conducted at the reference frequency. Nevertheless, given the measurement frequency f_i, the response and tabulated results from computer simulation at the reference frequency f_r we can estimate the parameters σ_2 and ε_2 at frequency f_i. Specifically, for each G_{12}-C_{12} (transconductance-transcapacitance) pair determined at frequency f_i, one can identify the corresponding ε_2 and σ_2 at the reference frequency that would give this response. Note that σ_i=$\sigma_r(f_i/f_r)$ so that σ_2 at the frequency f_i can readily be obtained.

Let's introduce the $\sigma - f$ normalization which allows one to find the values of G_{12} and C_{12} for any value frequency f and any given pair of ε and σ. For capacitances, the normalization is:

$$C\left[f_r, \sigma_i f_r/f_i, \varepsilon\right] = C\left[f_i, \sigma_i, \varepsilon\right] \tag{8.23}$$

where σ_i is the conductivity of interest, f_i is the measurement frequency of interest, and f_r is the reference frequency. Similarly, for conductances, the normalization is:

$$G\left[f_r, \sigma_i f_r/f_i, \varepsilon\right] = \frac{f_r}{f_i} G\left[f_i, \sigma_i, \varepsilon\right] \tag{8.24}$$

To best visualize the variation of conductance with conductivity, it is convenient to plot the conductance normalized to σ/σ_r, where σ_r can be chosen arbitrarily.

The following algorithm is used for estimation of complex dielectric permittivity from measurements with the interdigital sensor:

1) Convert the values of gain and phase measured at frequency f_i to G_{12} and C_{12}.

2) Normalize to f_r by applying (8.23) and (8.24).

3) By interpolation, find the values of ε and σ on the calibration surfaces that correspond to the reference frequency values of G_{12} and C_{12}.

4) Calculate the conductivity value at measurement frequency f_i by applying the relationship $\sigma_i{=}\sigma_r(f_i/f_r)$.

These steps are performed for each distinct measurement frequency separately. Note that this procedure does not require any iterations and extensive computations, so, the inversion is performed nearly instantly once the look up table at the reference frequency has been computed.

The range of calibration should be selected so that the ratio $\omega\varepsilon/\sigma$ is between 10^{-3} and 10^3. Outside of this range the influence of one of the variables on the output is insignificant.

8.7 Measurement and Error Propagation Analysis for Multiple-Layer Profiles

Measurement of multilayer material properties with fringing electric field dielectrometry sensors requires processing terminal admittance data from multiple electrode pairs. The choice of the algorithmic approach for data analysis is critically important because of a high sensitivity to small measurement errors. While individual channel errors are usually within a reasonable instrumentation range, measurement of properties of multiple material layers fails unless special techniques are used to prevent numerical instabilities. This section demonstrates the mechanism of error propagation in a successive stair-step property estimation in which the estimate of one layer's properties are used to estimate the subsequent layer's properties. Three-wavelength measurements of dielectric permittivity and conductivity illustrate the problem in two-layer experimental setups. Limitations of the stair-step approach and possible future improvements are discussed.

The multiple penetration depth fringing electric field dielectrometry sensor used in this study is shown in Figure 4.5. It consists of three sets of topologically identical interdigital electrodes etched on a common flexible Teflon substrate. The gray shaded area indicates guard backplanes on the reverse side of the substrate. Measurement of material properties at different depths from the surface is achieved through variation of spatial periodicity of interdigital electrode pairs. The larger the distance between the electrode centerlines the deeper is the effective penetration depth. Ideally, appropriate processing of signals from all pairs should provide an adequate picture of material property distributions that only vary with the z coordinate and do not change with x or y coordinates across the sensor head. The transadmittance between electrode pairs is measured by driving one electrode with a known sinusoidal voltage signal and measuring the terminal current on the other electrode. In our normal practice, the frequency of this signal varies between 0.005 Hz and 10 kHz. Several parameter estimation algorithms have been constructed to relate transadmittance values to dielectric permittivity and conductivity of a material layer under test at different depths in a multi-layer system. The solution spaces from Section 8.6.2 have been used here for parameter estimation.

This sensor has been used in several preliminary studies aimed at measurements of moisture diffusion through electric insulation of power transformers [24, 25], some of which are included in Chapter 11 of this thesis. Since no other experimental technique is currently available for verification of measured distributions of moisture concentration, the estimation of sensitivity and potential measurement error becomes particularly important. Many theoretical and experimental approaches are available for sensitivity analysis. The goal of this section is to present results of simulations and measurements that are directly applicable to the stair-step inversion algorithm. In this algorithm, dielectric properties close to the sensor are estimated first, and then used to estimate properties of consecutive layers [73, 76].

This section treats issues related to sensitivity and accuracy of parameter estimations from interdigital dielectrometry measurements. The influence of small distur-

bance factors of non-destructive measurements grows dramatically with the number of unknown variables that characterize materials under test. In the framework of inverse problem theory it means that the problem of material characterization is ill-posed, because a high variation in output parameters occurs due to the small variation of input parameters. To justify this claim, a numerical example of error propagation is presented here and then followed by measurement verification. The results of measurements also illustrate the potential of this technological approach and indicate its current limitations.

8.7.1 Error Propagation

General Procedure

Finite element method computer simulations are used to estimate error propagation for a specific case of perfectly insulating three-layer media. The results of these simulations show how an accumulation of small measurement errors may lead to a completely incorrect estimation of material properties. The limitations of the stair-step inverse problem approach arise mostly from this phenomena.

Consider the three layer system shown in Figure 8.48. Ideally, using a three-wavelength sensor with penetration depths comparable to the interface positions of the three layers, one should be able to determine the dielectric properties of each layer. For simplicity, let us consider a non-conducting case, so that σ_1, σ_2, and σ_3 are equal to zero. Then, the three permittivities to be determined from the three-wavelength measurements are ε_1, ε_2, and ε_3. For the purpose of this numerical example, the distance between the top of the sensor electrodes and the interfacial boundaries of the corresponding layers is chosen to be 0.3 of the spatial wavelength. So, the thickness of the first layer is 300 μm, the thickness of the second layer is 750-300=450 μm, and the thickness of the third layer is assumed to be infinite. To start, we assume all three layers have identical relative permittivity, $\varepsilon_1 = \varepsilon_2 = \varepsilon_3 = \varepsilon$, so that the transcapacitance of each wavelength is only a function of ε. For a particular operating point we

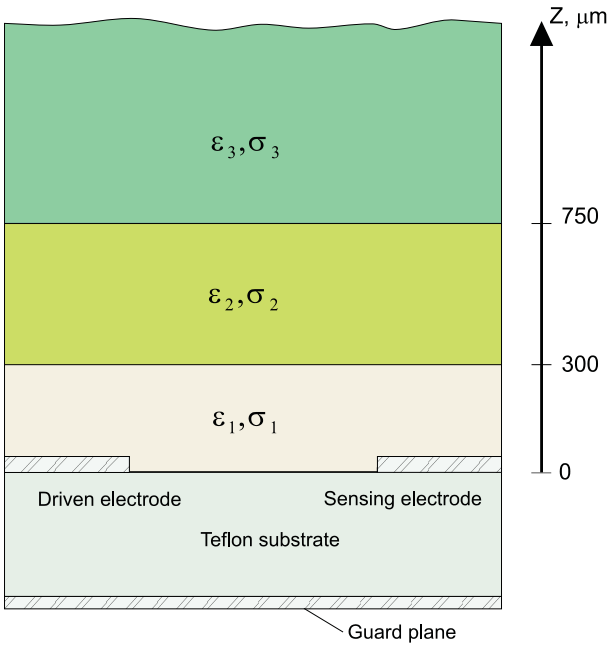

Figure 8.48: Three layers with unknown permittivity and conductivity can be characterized by a half-wavelength model.

use Teflon with $\varepsilon = 2.1$.

Whenever an infinite homogeneous layer is used in the simulations below, the dielectric permittivity of the layer or layers close to the sensor determines and is equal to the dielectric permittivity of the upper layers. The infinite homogeneous layer always starts at the penetration depth (0.3 λ) of the simulated wavelength. For clarity, these assumptions are stated at each figure caption. The combined layers are described with the permittivity subscripts of each of the layers, for example, the combined first and second layers measured by the 2.5 mm wavelength are described with the permittivity ε_{12}, where $\varepsilon_{12} = \varepsilon_1 = \varepsilon_2$.

One-layer Parameter Estimation

Figure 8.49 shows the transcapacitance for the 1 mm wavelength computed on a per meter length basis for an infinitely thick layer of relative permittivity $\varepsilon = \varepsilon_1$. It is nearly linear, and the ±3% error bounds in the measurement of interelectrode capacitance leads to ±3.8% error in the estimated value of relative dielectric permittivity

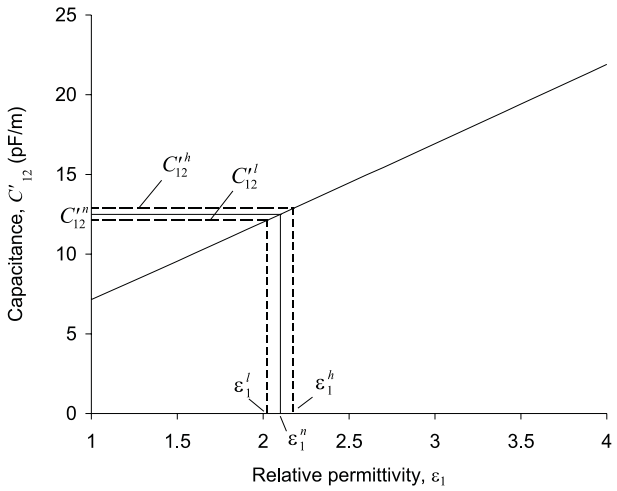

Figure 8.49: Error brackets of the relative dielectric permittivity $\varepsilon = \varepsilon_1$ around $\varepsilon_1 = 2.1$ of the first layer (with $\varepsilon_3 = \varepsilon_2 = \varepsilon_1 = \varepsilon$) calculated assuming a ±3% error of the 1 mm wavelength interelectrode capacitance per meter length C'_{12} due to a combined influence of all disturbance factors and the measurement noise.

around $\varepsilon_1 = 2.1$. The three percent error bound is an assumption based on a statistical description of our extensive experimental data. The worst case error depends on application. It combines known and unknown disturbance factors, including electronic equipment noise, round-off due to A/D conversion, manufacturing tolerances of the sensor itself, accuracy of known geometric parameters, effects of the finite length and width of the sensor head not included in the 2D half-wavelength cell model shown in Figure 8.48, and others. Figure 8.50 shows the transcapacitance for the 2.5 mm wavelength, again, assuming an infinitely thick layer of material with $\varepsilon = \varepsilon_{12}$. The ±3% error in the estimation of the interelectrode capacitance C_{12} leads to a ±2.7% error in the estimated value of ε. Figure 8.51 shows results of the same type of calculation for the 5 mm wavelength, with the error in the estimated value of $\varepsilon = \varepsilon_{123}$ being equal to ±2.4%. Given the assumed ±3% measurement error, the accuracy of material property estimation for a single layer of infinite extent is acceptable in all the above cases. However, as will be shown, as the number of unknowns grows in a multi-layer system, the uncertainty of measurements very quickly becomes unreasonably high.

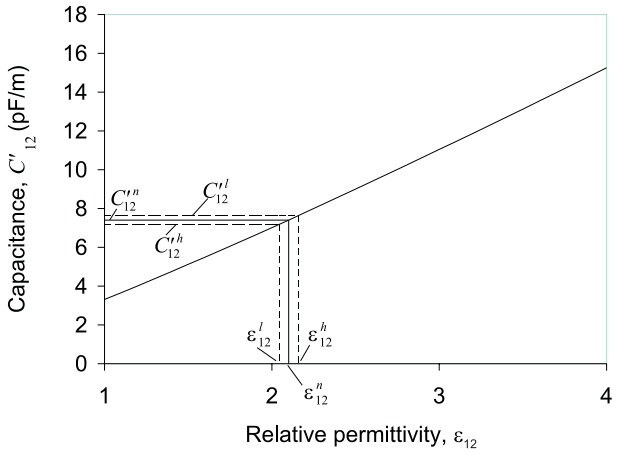

Figure 8.50: Error brackets of the relative dielectric permittivity $\varepsilon = \varepsilon_{12}$ of the first two layers (with $\varepsilon_3 = \varepsilon_2 = \varepsilon_1 = \varepsilon$) calculated assuming a ±3% error of the 2.5 mm wavelength interelectrode capacitance per meter length C'_{12} due to a combined influence of all disturbance factors and the measurement noise.

Two-layer Parameter Estimation

Suppose that we want to measure properties of a two-layer material under test and consider two cases. In the first case, the results of measurements with two neighboring (by size) wavelengths, 1 mm and 2.5 mm are used to estimate material properties. In the second case, the two spatial wavelengths are more dissimilar (1 mm vs 5 mm). The results of simulations for the first case are shown in Figure 8.52. The top and bottom curves in this figure represent the extreme cases of the relative dielectric permittivity of the first layer ($\varepsilon_1^l = 2.02$ and $\varepsilon_1^h = 2.18$) estimated based on the measurements with a 1 mm wavelength, shown in Figure 8.49. The middle curve is the capacitance of the 2.5 mm wavelength channel computed assuming the correct dielectric permittivity ($\varepsilon_1^n = 2.1$) of the first layer. The dashed lines indicate the maximum error brackets assuming that the error in the measured values of capacitance of the 2.5 mm wavelength channel due to a combination of all disturbance factors does not exceed ±3%. One can see immediately that the error brackets for the relative dielectric permittivity of the second layer, ε_2, are unacceptably high, from -22% to +29% of the nominal value $\varepsilon_2^n = 2.1$ ($\varepsilon_2^l = 1.63$, $\varepsilon_2^h = 2.70$).

In the second case with the 1 mm and 5 mm wavelengths, shown in Figure 8.53, the

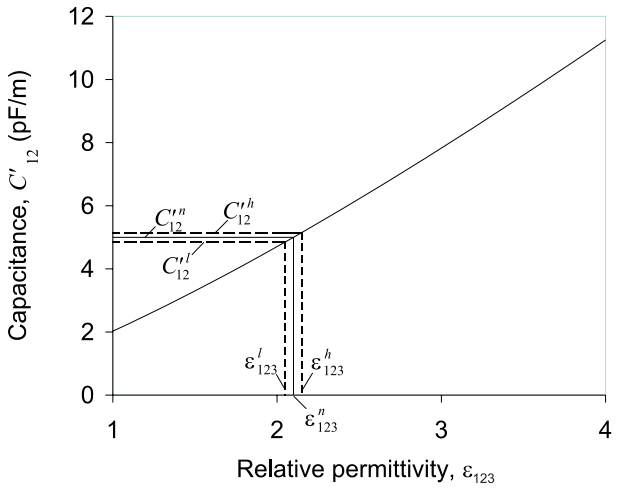

Figure 8.51: Error brackets of the relative dielectric permittivity $\varepsilon = \varepsilon_{123}$ of the first three layers (with $\varepsilon_3 = \varepsilon_2 = \varepsilon_1 = \varepsilon$) calculated assuming a ±3% error of the 5 mm wavelength interelectrode capacitance per meter length C'_{12} due to a combined influence of all disturbance factors and the measurement noise.

error brackets of the relative dielectric permittivity estimation are significantly more narrow, about ±8% of the nominal value $\varepsilon_2^n = 2.1$ ($\varepsilon_2^l = 1.93$, $\varepsilon_2^h = 2.27$).

Three-layer Parameter Estimation

A three-layer parameter estimation using a straightforward stair-step algorithm results in very large error brackets. Figure 8.54 shows the error brackets for the relative dielectric permittivity of the third layer, ε_3, computed using previously estimated values of dielectric permittivities of the first and second layers, ε_1 and ε_2, respectively, found in Figures 8.49 and 8.52. Since for this electrode geometry the interelectrode capacitance grows with the individual dielectric permittivities of each layer, the curves of the extreme cases use a combination of both highest (ε_1^h, ε_2^h) or both lowest (ε_1^l, ε_2^l) dielectric permittivities. This ±3% error of the measured capacitance of the 5 mm wavelength channel results in a -52% and +114% error in the value of third layer permittivity around $\varepsilon_3^n = 2.1$ ($\varepsilon_3^l = 1.0$, $\varepsilon_3^h = 4.45$).

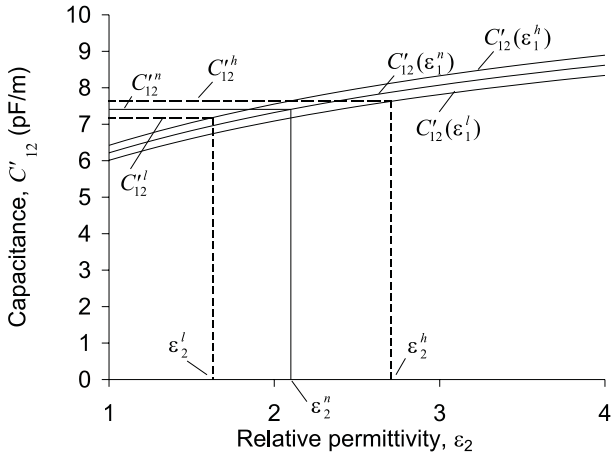

Figure 8.52: Error brackets of the relative dielectric permittivity around $\varepsilon_2 = 2.1$ (with $\varepsilon_2 = \varepsilon_3$) of the second layer calculated assuming a $\pm 3\%$ error of the 2.5 mm wavelength interelectrode capacitance per meter length C'_{12} due to a combined influence of all disturbance factors and measurement noise for first layer permittivity values $\varepsilon^l_1 = 1.63$, $\varepsilon^n_1 = 2.1$, and $\varepsilon^h_1 = 2.70$.

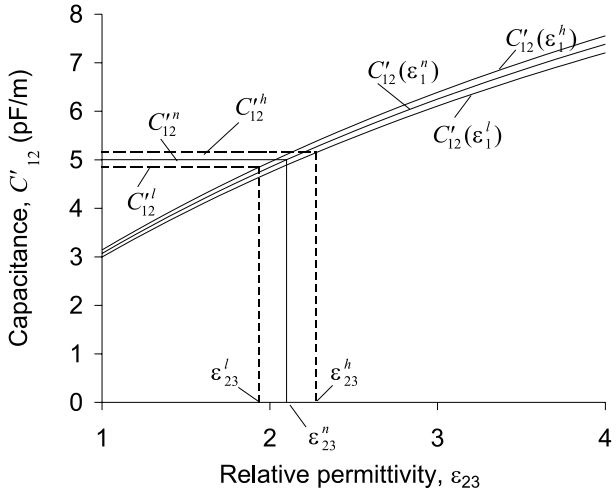

Figure 8.53: Error brackets of the relative dielectric permittivity (with $\varepsilon_2 = \varepsilon_3$) of the second and third layers calculated assuming a $\pm 3\%$ error of the 5 mm wavelength interelectrode capacitance per meter length C'_{12} due to a combined influence of all disturbance factors and measurement noise for first layer permittivity values $\varepsilon^l_1 = 1.93$, $\varepsilon^n_1 = 2.1$, and $\varepsilon^h_1 = 2.27$.

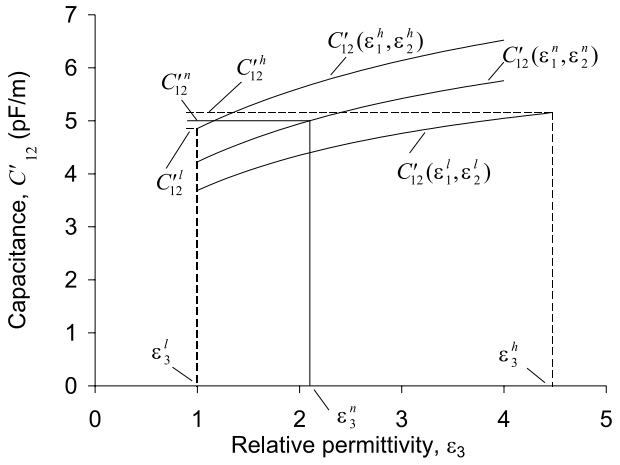

Figure 8.54: Error brackets of the relative dielectric permittivity of the third layer calculated assuming a ±3% error of the 5 mm wavelength interelectrode capacitance per meter length C'_{12} due to a combined influence of all disturbance factors and measurement noise for first and second layer permittivity values ($\varepsilon_1^l = 2.02$, $\varepsilon_2^l = 1.93$), ($\varepsilon_1^n = 2.1$, $\varepsilon_2^n = 2.1$), and ($\varepsilon_1^h = 2.18$, $\varepsilon_2^h = 2.27$.)

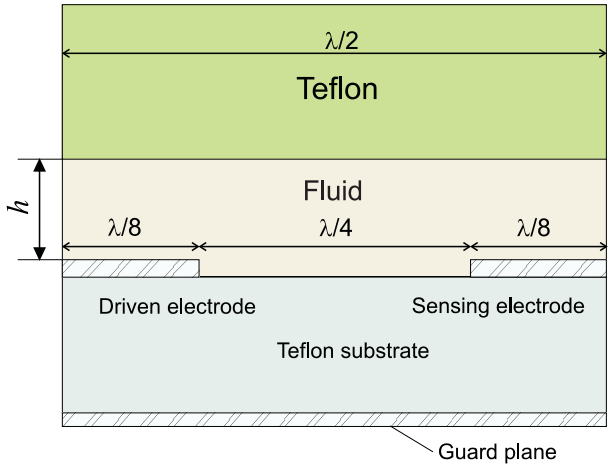

Figure 8.55: A generic two-layer test sample with two unknown dielectric layers used in this experiment series.

8.7.2 Experimental Results

Description of Setups

The dielectric properties of insulating materials have been determined experimentally for several cases, all of which can be described by the general diagram in Figure 8.55. The fluid material adjacent to the sensor in this series of experiments ensures a perfect contact between the sensor head and the material under test. Since the theoretical analysis of the previous solutions shows that the combination of the 1 mm and the 5 mm wavelengths is more accurate than other combinations for a two-layer system, this combination is used for the two-layer analysis below.

The properties of each layer are summarized at the top part of Table 8.14. In cases 3, 4, and 5 we assume that the conductivity of the second layer is known to be negligible.

Case 1. Sensor in air. This single infinite layer case is used for calibration to account for fringing field effects, manufacturing imperfections, stray lead capacitances, and other sources of small experimental errors. One unknown ε_0 ($\varepsilon_1 = \varepsilon_2 = \varepsilon_0$, $\sigma_1 = \sigma_2 = 0$), which can be checked against the theoretical value.

Case 2. Sensor in single infinite layer of corn oil. Two unknowns ($\varepsilon_1 = \varepsilon_2 = \varepsilon$,

$\sigma_1 = \sigma_2 = \sigma$).

Case 3. First h =500 μm thick layer – air, second infinite layer – Lexan. Two unknowns (ε_1, ε_2, $\sigma_1 = \sigma_2 = 0$).

Case 4. First h =500 μm thick layer – corn oil, second infinite layer – Lexan. Three unknowns (ε_1, ε_2, σ_1, $\sigma_2 = 0$).

Case 5. First h =500 μm thick layer – corn oil, second infinite layer – Teflon. Three unknowns (ε_1, ε_2, σ_1, $\sigma_2 = 0$).

Estimation Algorithm

As a first step, the dielectric permittivity and conductivity of the first layer (fluid layer) is determined from 1 mm wavelength admittance measurements together with precalculated solution spaces discussed in [28] and Section 8.6.2 of this thesis. This method assumes that the material above the sensor is homogeneous and is of semi-infinite extent. This assumption is approximately valid for the 1 mm wavelength (penetration depth about 300 μm) and a first layer thickness of h =500 μm.

As a second step, the dielectric permittivity of the second layer is calculated using the 5 mm wavelength data. For cases of dissimilar materials, the conductivity of the second layer material was zero, $\sigma_2 = 0$. The permittivity of the second layer was found by standard minimization techniques, with the cost function v defined as:

$$v = \sqrt{\left(\frac{G_{12}^m - G_{12}^c}{G_{12}^c}\right)^2 + \left(\frac{C_{12}^m - C_{12}^c}{C_{12}^c}\right)^2} \tag{8.25}$$

where G_{12}^m and C_{12}^m are measured values of transconductance and transcapacitance, and G_{12}^c and C_{12}^c are the values of transconductance and transcapacitance calculated under the assumption that the first layer values of dielectric permittivity and conductivity have been determined correctly from the 1 mm wavelength measurements. The cost function is minimized with respect to ε and σ which adjust C_{12}^c and G_{12}^c in (8.25).

The cost functions for the cases which require their calculations are shown in Figures 8.56 and 8.57. Figure 8.56 shows that the dielectric permittivity of Lexan has been found with an absolute value of error of no more than 3.6 percent for $\varepsilon_2 = 3.01$

Dielectric properties measured with guarded parallel-plate capacitor at 1 Hz and 1000 Hz								
	Air	Corn Oil		Air/Lexan	Corn Oil/Lexan		Corn Oil/Teflon	
	Case 1	Case 2a	Case 2b	Case 3a	Case 4a	Case 4b	Case 5a	Case 5b
f (Hz)	1000	1000	1	1000	1000	1	1000	1
ε_1^e	1.0	3.13	3.16	1.0	3.13	3.16	3.13	3.16
σ_1^e(pS/m)	0	-	29.18	0	-	29.18	-	29.18
ε_2^e	1.0	3.13	3.16	3.01	3.01	3.01	2.1	2.1
Measured C_{12} and G_{12} for each of three wavelengths								
C_{12}(1mm),pF	3.8641	9.1004	9.1806	3.7791	9.1525	9.3109	9.1952	9.4916
G_{12} (1mm),pS	0	0	8.5282	0	0	8.9939	0	8.3603
C_{12} (2.5mm),pF	1.6983	5.7795	5.8019	1.7734	5.7060	5.8289	5.7068	5.8011
G_{12} (2.5mm),pS	0	0	6.7499	0	0	7.0063	0	6.2959
C_{12} (5mm),pF	1.0081	4.1257	4.1259	1.4478	3.9811	4.0872	3.6349	3.7040
G_{12} (5mm),pS	0	0	5.4772	0	0	4.1410	0	3.3039
Estimations of one layer parameters								
ε_1(1mm)	1.00	3.07	3.12	1.005	3.09	3.14	3.11	3.22
σ_1(1mm)	0	-	28.83	0	-	30.32	-	28.26
ε_{12}(2.5mm)	1.00	3.09	3.11	1.05	3.06	3.18	3.06	3.11
σ_{12}(2.5mm)	0	-	28.50	0	-	32.95	-	26.58
ε_{123}(5mm)	1.00	3.13	3.15	1.34	3.05	3.18	2.81	2.88
σ_{123}(5mm)	0	-	29.14	0	-	24.35	-	18.04
Final estimated values of ε and σ for each layer								
ε_1^m	1.00(0)	3.07(2.0)	3.12(1.3)	1.005(0.5)	3.09(1.0)	3.14(0.6)	3.11(0.6)	3.22(1.9)
$\sigma_1^m(pS/m)$	0(0)	-	28.83(1.2)	0(0)	-	30.32(3.7)	-	28.26(3.2)
ε_2^m	1.00(0)	3.07(2.0)	3.12(1.3)	2.90(3.6)	3.01(0.0)	3.10(2.9)	2.17(3.3)	2.03(3.3)

Table 8.14: The two layer dielectrometry measurements using the geometry in Figure 8.55 with air or corn oil as layer 1 and air, corn oil, Lexan, or Teflon as layer 2. The numbers in parentheses for final estimated values indicate the percent difference from the measured parallel plate values. The corn oil conductance is not estimated at 1000 Hz (marked with "-") when the sensitivity of the measurement is known to be insufficient.

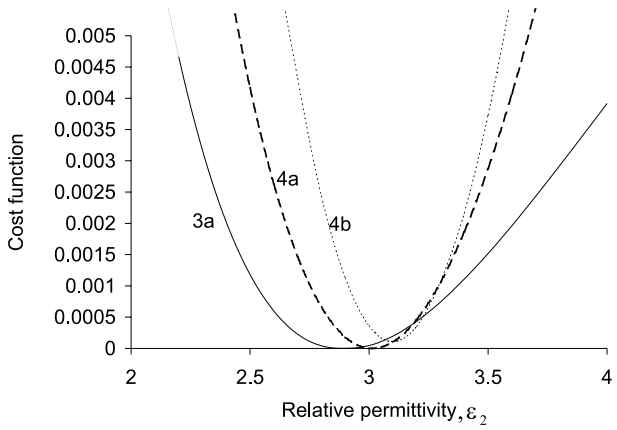

Figure 8.56: Cost functions for cases 3a, 4a, and 4b (air or corn oil as first layer, Lexan as the second layer).

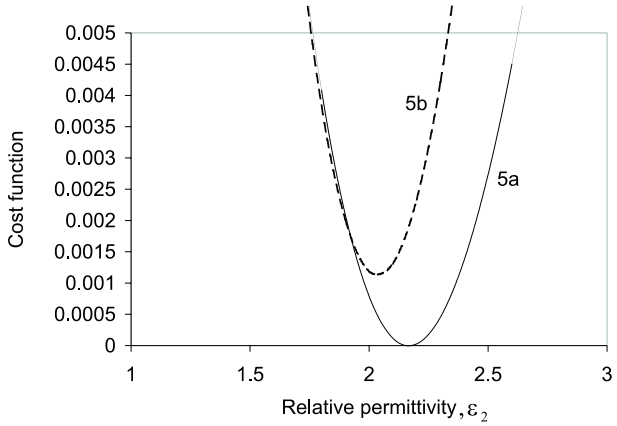

Figure 8.57: Cost functions for cases 5a and 5b (corn oil as first layer, Teflon as the second layer).

measured with the guarded parallel-plate cell, and that both the transcapacitance and the transconductance measured and calculated values were in close agreement at the cost function minimum, as indicated by a very low magnitude of the cost function at minimum. The agreement between individual components of transadmittance for measurements with Teflon as the second layer was not as good for the low frequency measurement point (case 5b), which is shown in Figure 8.57. Nevertheless, the measurement error did not exceed 3.3 percent for $\varepsilon_2 = 2.1$. The cost function does not go to zero because of errors in the estimation of the dielectric properties of the first layer and measurement errors in the 5 mm wavelength channel.

8.7.3 Conclusions

The dielectric properties of one and two-layer configurations have been accurately measured using two wavelengths of a three-wavelength interdigital dielectrometry sensor. The focus of this work is on sensitivity analysis and measurement error evaluation for the stair-step parameter estimation algorithm. It is important to highlight the error propagation phenomena in order to further improve parameter estimation algorithms and design of fringing field instrumentation. Computer simulations indicate that the measurement error builds up very quickly as the number of unknowns in the system increases. On the basis of such simulations, the decision can be made whether the electronic and dielectrometry instrumentation is adequate in every specific situation. Future efforts should concentrate on the reduction of the magnitude of disturbance factors and noise sources in dielectrometry measurements and on the development of more sophisticated and generic procedures to characterize the accuracy of fringing electric field sensors.

Chapter 9

Optimization

9.1 Introduction

9.1.1 Parameter Estimation As a Minimization Problem

One of the parameter estimation algorithms explored in the course of the thesis was implemented using *Maxwell*. The methodology used for parameter estimation had proven to be readily generalizable for other types of problems. This chapter describes efforts of implementing the parameter estimation algorithm as a general optimization tool. This project stands on its own, but many results are available for non-destructive testing with interdigital dielectrometry, the major topic of this thesis. This software has been developed jointly with several undergraduate students: Binh Truong, John Miller, Gaurav Tewari, and Jason Bau, who worked under my supervision during their MIT UROP assignments. Most of this chapter is based on their undergraduate project reports.

The development of design optimization strategy, algorithms, and software for power equipment is described. The task of design optimization is formulated as a generic inverse problem. That is, the question asked by the engineer is: what are the geometric parameters and material properties which result in the optimum performance of the device? One way to solve this problem is to make iterative guesses at the

design variables, and to compute repeatedly the goal variables until the optimum is achieved. The presented software tool for solving optimization problems is designed as an add-on to the commercial finite-element program *Maxwell*. An interface to a library of optimization algorithms in Matlab is provided. Results of the optimization process are presented.

In most cases, the geometrical and physical properties of a device can be defined parametrically. The principle of operation of the device itself is known in advance, and the task of an engineer is to find a set of parameters, which would provide its optimum performance. Analytical techniques are useful and provide intuition for best solutions, however, these techniques are usually limited to classical simple shapes and geometries. For more complicated cases, numerical modeling is necessary.

9.1.2 Motivation

There is significant interest worldwide in studies of this type. Optimization, combined with finite-element simulation, is considered to be one of the highly promising areas of technology. Previously, the speed and memory limitations of computers made such an approach infeasible. Recently, the exponential improvements in the computer industry induced shifts towards numerical algorithms.

On the software side, there are currently no tools capable of performing the tasks described in this document. Several leading international electromagnetic simulation companies (Ansoft, Infolytica, Magsoft, Vector Fields) offer tools for parametric sweeps and demonstrations of more advanced applications. In some cases, these packages are incorporated into shells by third-party customers and are executed in batch mode. However, no general tool is available at the time of writing this thesis.

No special training in electromagnetic field theory is needed for a large group of the optimization design projects when finite-element analysis is used. A quick study can be conducted with such software by any utility engineer with basic knowledge of electromagnetism. An equivalent theoretical analysis of the same problem would often require the knowledge of leading experts. For example, it will become possible for an

engineer with basic training to design electric power equipment for maximum energy efficiency by finding an optimal set of key design criteria when the number of possible variations of design far exceeds computational capabilities of modern computers.

9.1.3 Optimization in General

The computer-based optimization design and associated software finds numerous applications in the power industry as well as in many other technical fields. Significant efforts are directed by industry and academics worldwide towards the development of new optimization algorithms. The increasing speed and memory capabilities of modern computers make possible algorithmic approaches which could not be implemented ten years ago.

This project aims at the development of a versatile optimization design technology for electric power equipment, such as transmission lines, generators, high voltage insulators, and transformers. The geometric parameters and the electrical properties of manufacturing materials serve as the design variables and constraints. The goals and definitions of the optimal design can vary from one application to another. The software developed in the course of this project makes it possible to specify various optimization goals based either on electric or magnetic field values in a specified region, or the dependent electrical and electromechanical quantities, such as force, torque, capacitance, and conductance between electrodes. For example, the highest possible torque of a motor, the lowest electric field in the field enhancement region, or the smallest possible weight of the device can be found by changing the design variables while satisfying the constraints chosen by the engineer.

In most cases, the geometrical and physical properties of a device can be defined parametrically. The principle of operation of the device itself is known in advance, and the task of an engineer is to find a set of parameters, which would provide its optimum performance. Analytical techniques are useful and provide intuition for best solutions, however, these techniques are usually limited to classical simple shapes and geometries. For more complicated cases, numerical modeling is necessary.

9.1.4 Relation to Inverse Problem

For most applications of the electrical insulation design, the "fitness function", which quantifies the quality of the design, is inherently computationally expensive because electric or magnetic fields must be found throughout the regions which contain multiple, probably non-linear or frequency dispersive materials. The time needed to compute the field distributions for each set of values of design parameters may vary from seconds to hours, depending on the complexity of the arrangement, precision required, and presence of non-linear materials. In such cases, exhaustive searches and random improvement techniques (such as genetic algorithms, for example), are hardly applicable. Instead, more traditional root-solving and hill-climbing optimization algorithms should be used. Sufficient flexibility is one of the goals.

9.1.5 Non-destructive Testing of Transformer Insulation

High-power transformers are subjected to high levels of electrical and thermal stress during regular usage. In order to guarantee that the system works under varying environmental factors, measurements must be taken to record its characteristics under these conditions. For example, one can obtain records of a material's dielectric spectrum, which includes dielectric permittivity and conductivity as functions of electrical excitation frequency. From this information, one can more accurately predict the material's behavior at various temperatures and spatial distributions of moisture.

The dielectric spectrum can be found using several experimental techniques. In the case of interdigital dielectrometry, estimation of the material's properties requires extensive computations since the inverse problem of material characterization must be solved by iteration. Normally, measured values of the admittance matrix of the system of electrodes are used as input parameters. A complex dielectric permittivity as a function of frequency is computed on the basis of these values and then, by separate calibration, is related to other physical properties, such as moisture content, porosity, density, etc.

One application of the *Maxwell 2D Field Simulator* by Ansoft Corporation is to calculate admittance matrices when the geometry and dielectric properties of materials are specified. This particular application can also be utilized in the reverse manner to determine material properties given the admittance matrix and geometry. This is done by supplying proper initial guesses of material properties to the *Maxwell* software, which calculates a resultant admittance matrix, from which a refinement of the initial guess of material properties can be made. This process can be iterated until the admittance matrix calculated by *Maxwell* matches that determined experimentally.

The optimization toolbox of *Matlab* by MathWorks, Inc., can be utilized in this process of refining inputs to *Maxwell* to produce the desired admittance matrix. Some work has been done on this specific problem of finding the conductivity and permittivity of the materials from the capacitance and conductance of the system. However, the iterative process by which this reverse problem is solved is not problem specific and can be generalized as calls to *Matlab*'s optimization toolbox employing *Maxwell* as a subroutine. Thus, other applications of *Maxwell*, such as torque calculation, can also be optimized using the same process without any modifications to software, save the Maxwell project itself. The primary goal then is to develop an appealing and easy-to-use graphical user interface which would facilitate this general use of *Matlab*'s optimization functions on any of *Maxwell*'s applications.

9.2 Overall Strategy

In most cases, the geometrical and physical properties of a device can be defined parametrically. In this scenario, the operation principles of the device itself are known in advance, and the engineer's task is to find a set of parameters, that would provide the optimum performance. Analytical techniques are useful and may provide intuition as well as best theoretical solutions. However, these techniques are usually limited to classical simple shapes and geometric arrangements. For more complicated cases, numerical simulation is necessary.

If the software discussed in this project were to be written starting from the fundamental laws, the accomplishment of the first objective would have taken many man-years of work. However, the goals have been achieved within the scope of this project because readily available software modules will be used as the building blocks in the proposed project. They include *Maxwell* 2D and 3D simulation modules, Parametric Analysis Module, and *Matlab* Optimization Toolbox.

9.2.1 Maxwell - FEM Electromagnetics Package

One of the most versatile electromagnetic simulation software packages available today, *Maxwell*, by Ansoft Corp. has been taken as the basic numerical simulation package. Finite element meshes can be generated in both two-dimensional and three-dimensional geometry. The two-dimensional cases can be either in axisymmetric or in rectangular coordinates. Voltage and current excitations in dc and ac modes are available. One of the most attractive and well-implemented features of *Maxwell* is the ability to describe the problem of interest parametrically. This saves time in considering various design options, running sensitivity analysis, etc.

9.2.2 Parametric Analysis Module

The parametrized variables include linear and angular dimensions of the physical objects, the dielectric and magnetic properties of all materials, the distribution of voltage, charge, and current excitations, and the frequency of operation. Each of these variables can be either a simple independent variable or a function dependent on other user-defined variables. A sweep of variables is possible with the Parametric Analysis Module.

All the above features are already provided by Maxwell. The goal of the first part of the project was to augment the existing features with a new module. This module makes possible the adaptive variation of the variables during the execution of the optimization program. The choice of the new values of the variables comes from

the optimization library.

9.2.3 Matlab

Data manipulation, system calls, visualization of the output and related tasks have been implemented in Matlab. In addition, the Matlab Optimization Toolbox has been interfaced with Maxwell in such a way that a variety of optimization methods could be tried for each specific project. A user-friendly interface has been developed in the Matlab GUIDE (Graphical User Interface Development Environment) with help of undergraduate students Gaurav Tewari and Jason Bau.

9.3 Software Implementation

9.3.1 Overview

Figure 9.1 shows the relationship of the developed interface to commercial software packages and to types of problems it can solve. To achieve maximum flexibility, the optimization routines and functions are implemented within the Matlab environment. The changes to the *Maxwell* input files allow automatic variation of design parameters during the optimization process without entering the actual *Maxwell* interface. The field computations are initiated by system function calls. Figure 9.2 shows the details of a generic optimization process itself, as dictated by the *Maxwell* interface. The first five steps are executed within *Maxwell* environment, and the last four are executed within Matlab environment. The list of input variables and cost function components may be expanded using indirect computation of variables of interest.

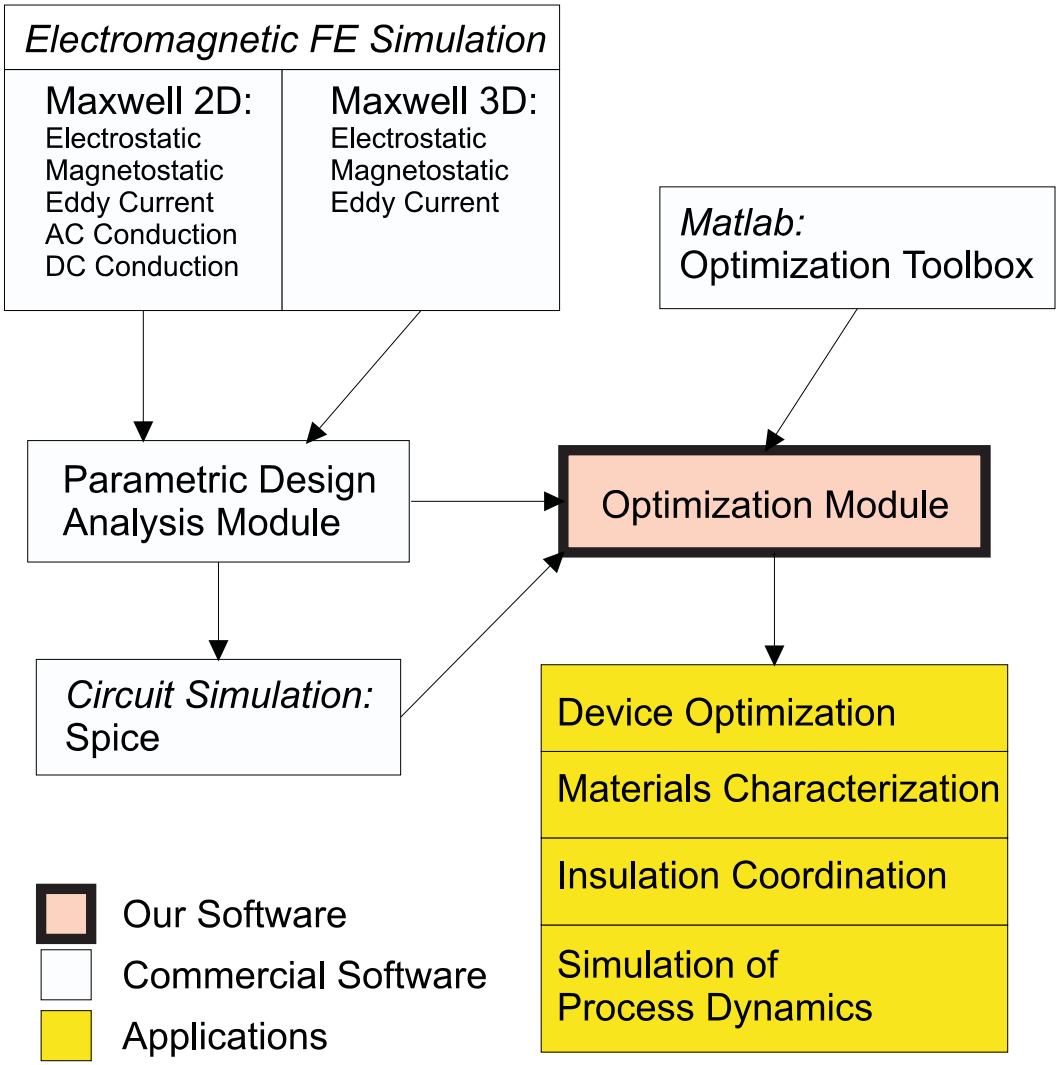

Figure 9.1: The module for solving optimization and inverse problems interfaces several software packages. Interfacing with Maxwell is implemented through system calls and input file manipulation.

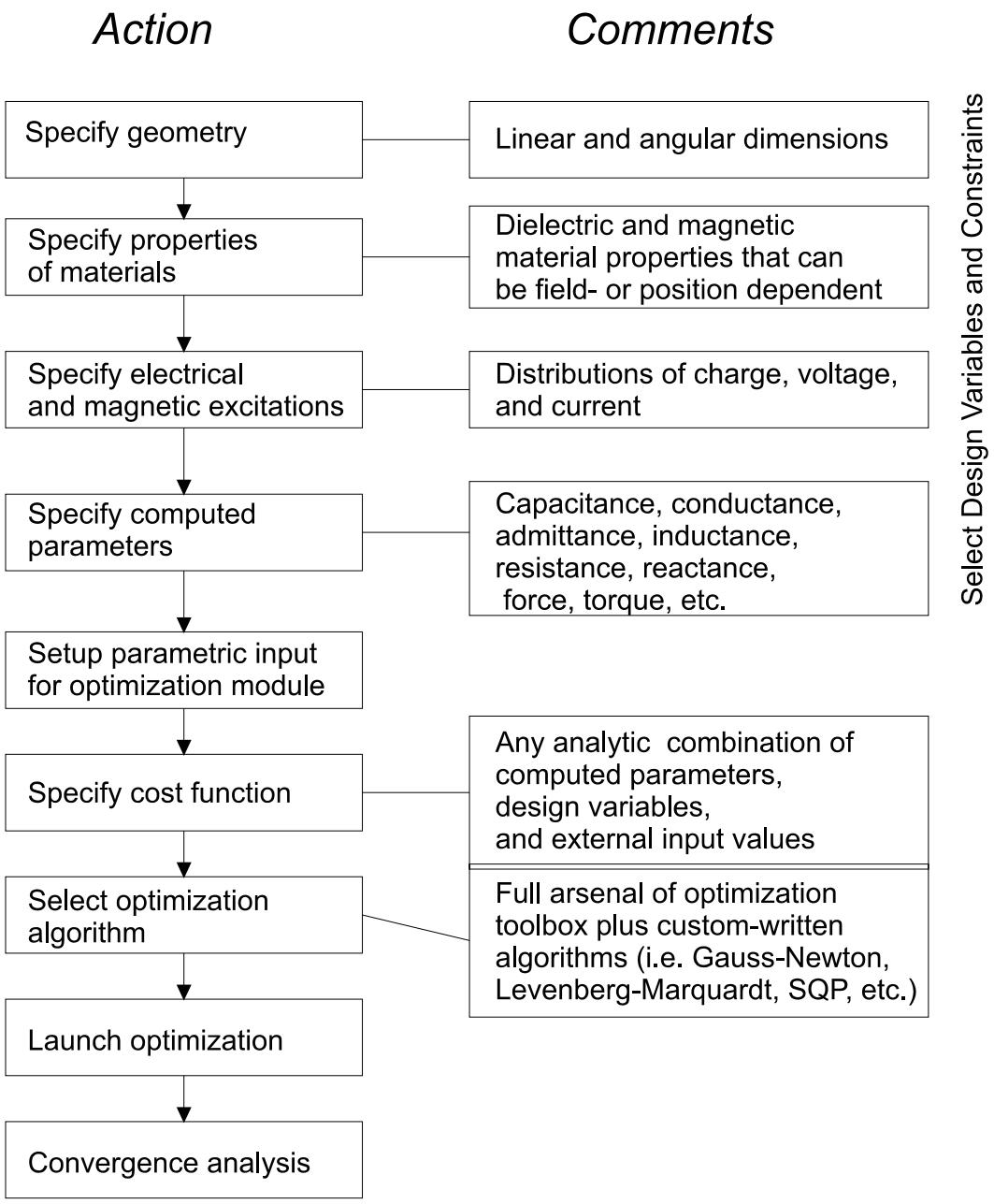

Figure 9.2: A sequence of optimization processes possible with the new interface.

9.3.2 Problem-Specific Version

The first version of the interface, developed during the early stages of this project, was specific to solving non-destructive testing problems with multiple wavelength interdigital dielectrometry. In this case, the measured and the calculated values of conductance and capacitance between pairs of interdigitated electrodes must be compared. The calculated values depend on material properties and geometric parameters of the experimental setup. Provided that the solution is unique, an iterative procedure for determining material properties involves guessing at them until the calculated and the measured terminal characteristics match.

Commercial software makes it possible to simulate the field behavior of an electric system through finite-element analysis. Given any number of material properties such as conductivity ("σ"), permittivity ("ε"), magnetization, or geometric dimensions, software like *Maxwell 2D Field Simulator* by Ansoft solves for the appropriate values of capacitance, conductance, inductance, resistance, force, and torque, which are the goals of the forward problem. However, the solution to the inverse problem in all of these cases, in particular finding σ and ε of materials from certain conductance G and capacitance C values, is not as easily found. One technique of achieving this solution is through iteratively refining guesses for the σ and ε values until they produce the correct G and C values.

One efficient way to implement this method of solution is to utilize pre-existing optimization packages, such as those in *Matlab*'s optimization toolbox, to perform the iterative solution-search process. These optimization routines work by taking an initial guess as an input and then calculating the result of a cost function of output variables. The cost function in this case is the error in the solution, that is, the absolute difference between the calculated values of G and C and values of G and C for which we wish to determine the σ and ε. After determining this error, the optimization routine then makes another guess as to the input values in order to minimize the cost function and again determines the error in the solution. This process is repeated until the error is

minimized and the proper input values have been determined.

Individual Frequency Sweeps

In conducting a frequency sweep the program calculates values of σ and ε for every frequency in a given range. The program takes values for frequency, G and C from input data and uses that information to solve for σ and ε. The program makes an initial guess as to what σ and ε might be. These values, along with the value of the frequency, are written to the .ptd file (the extension possibly stands for something like"Parametric Table Data") used by the *Maxwell* project. These values are used by *Maxwell* to calculate G and C values. The values calculated by *Maxwell* are then compared to those input to the program. The optimization routine continues to guess new values of σ and ε until they yield values for G and C which are close enough to the input values that the percent error for both is under one percent. This process is outlined in Figure 9.3.

Frequency Sweeps for All Wavelengths

This program can be used to start up to three frequency sweeps. The program completes a frequency sweep with one wavelength model then proceeds to the next wavelength until the values of σ and ε have been solved for all three wavelengths at all frequencies. Figure 9.4 charts this procedure. This approach to parameter estimation is essentially the same as was implemented by Dr. Zaretsky in his thesis [8]. Since this approach has been found very sensitive to small measurement errors in the sensor signals, it has not been used after it was implemented. If, however, future researchers are interest in reviving this approach, they should be able to use the software developed in the course of this thesis research. Alternatively, a generic optimization module could be used.

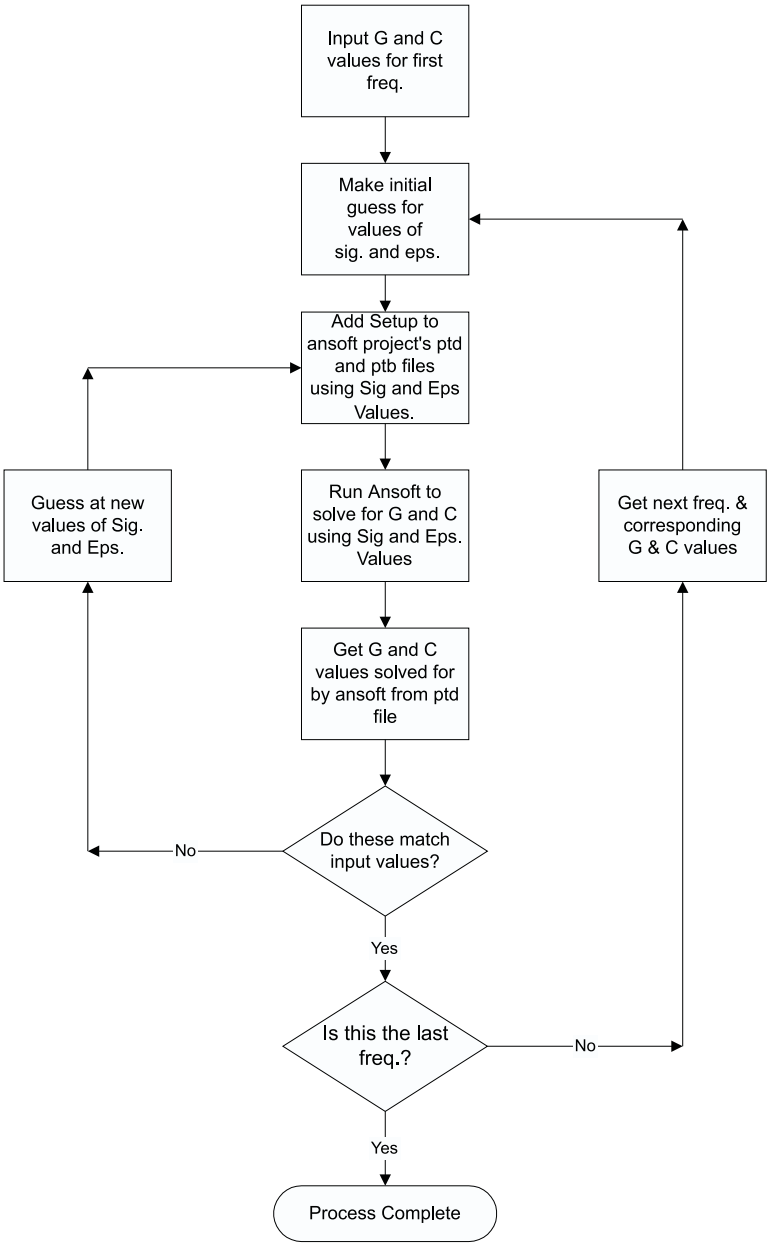

Figure 9.3: Flow chart for individual frequency sweep process. With the GUI, however, only one frequency is considered, and the σ and ε values are directly input by the user. This structure is presented because of its generality.

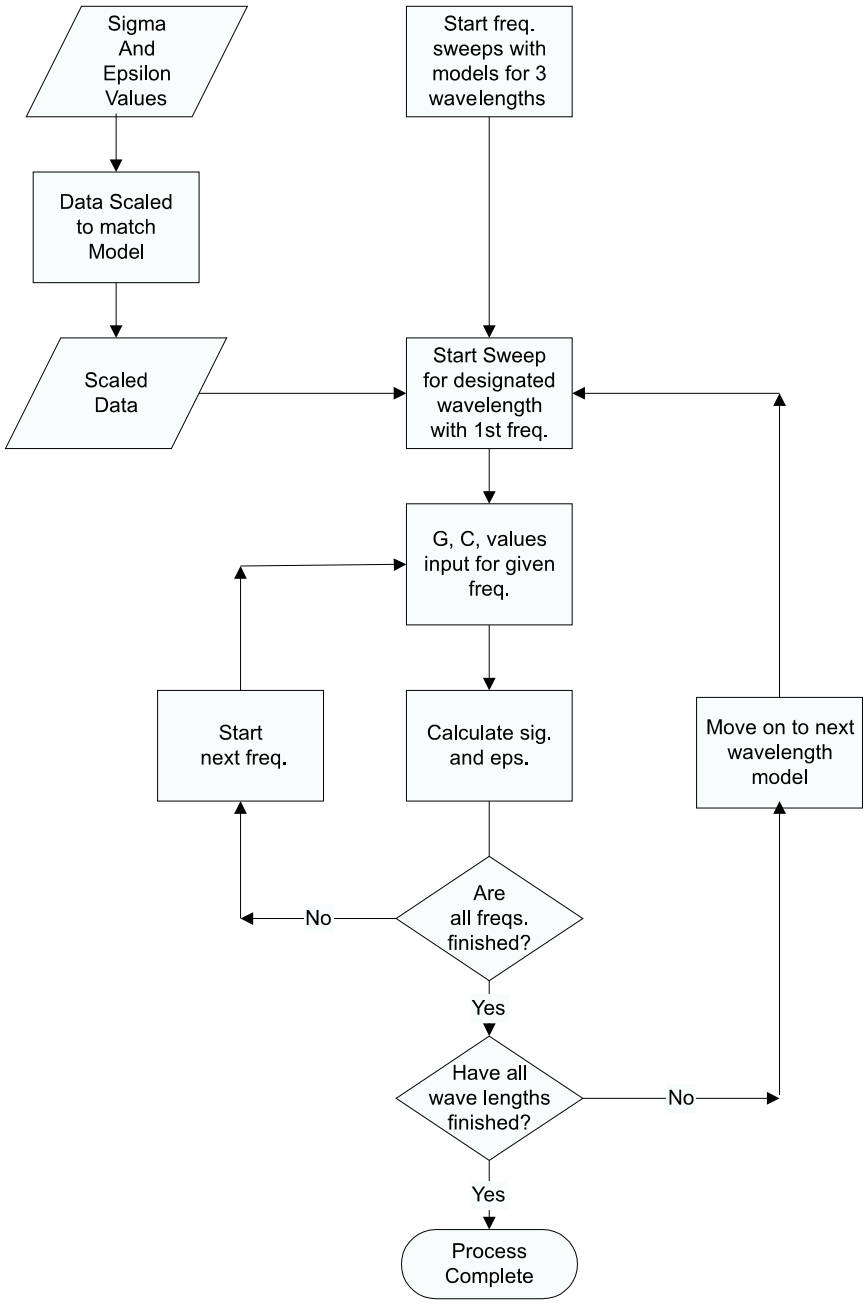

Figure 9.4: Flow chart for frequency sweeps for multiple wavelengths.

9.3.3 General Version

The screenshot of the final version of the graphical user interface is shown in Figure 9.5 and its flowchart is shown in Figure 9.6. The new interface results from the effort to generalize use of *Matlab*'s optimization routines with *Maxwell* projects. Explicit references to specific files and directories are eliminated, and all dependence upon the specific two-variable optimizations of ε and σ have now been removed. Any number of *Maxwell* parameters can now be chosen as variables to be optimized, and their initial values can be specified through the interface. An option of excluding specific variables from the optimization has also been added to complement this change. Furthermore, all of the optimization algorithms offered by *Matlab* are available to solve various user-specified cost functions. Finally, the writing of these cost functions has been simplified to exclude any need to explicitly call *Maxwell*. They are now simple *Matlab* functions of vector input and output.

Previous stages have already demonstrated the viability of this method of solution via the *Matlab* routines "fsolve" and "fmins". In addition, the graphical user interface to facilitate the easy use of these optimization routines to solve for permittivity and conductivity has been built. They had also generalized the underlying program path structure so that it was possible to interface with different *Maxwell* projects just by entering their path. The project detailed here extends the previous work. The most important of the changes is the generalization of the variable names and also their number above and beyond the two, σ and ε, of the original problem. This allows the optimization module to be used with more than just permittivity and conductivity calculations but instead all the applications of *Maxwell*, including force and torque calculations. Other improvements were also made to the graphical user interface, such as an expansion to include all *Matlab* algorithms as well as simplifying the writing of cost functions. The ability to exclude variables from the optimization was also added along with the ability to include constraints in the optimization problem.

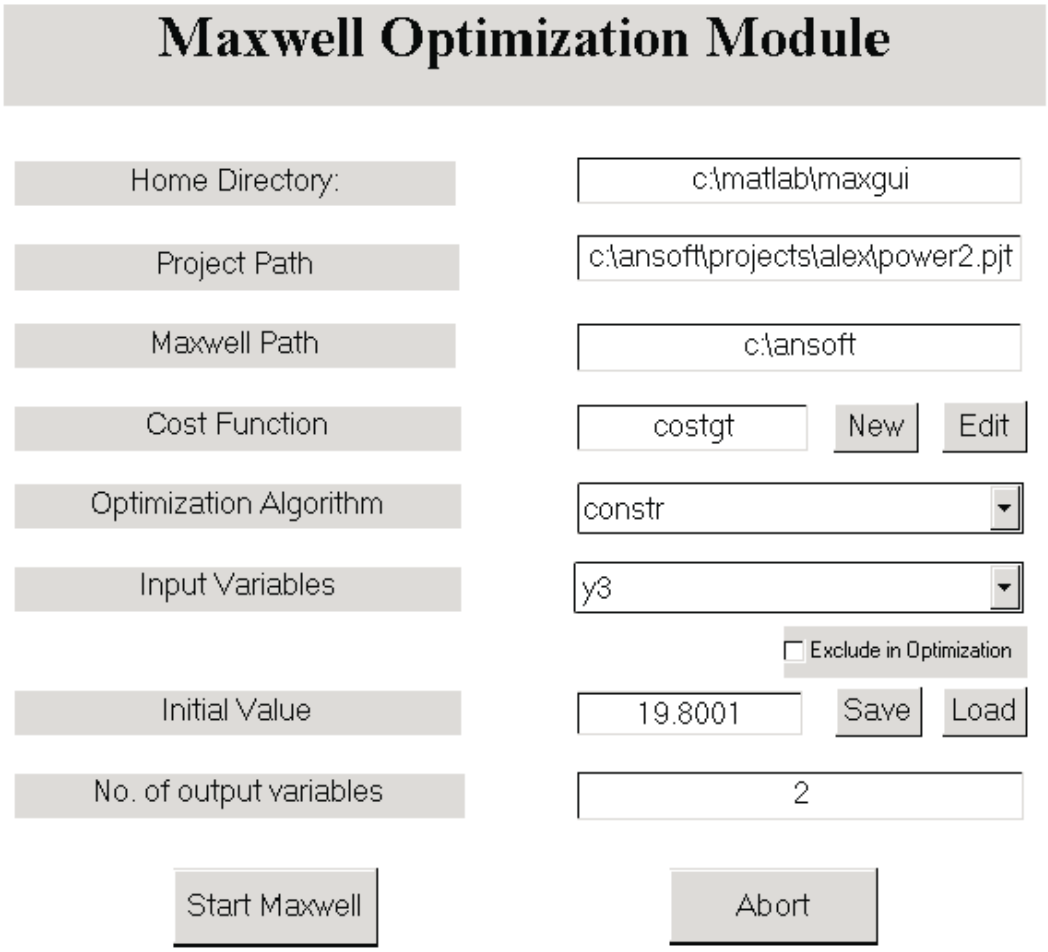

Figure 9.5: Screenshot of GUI Module.

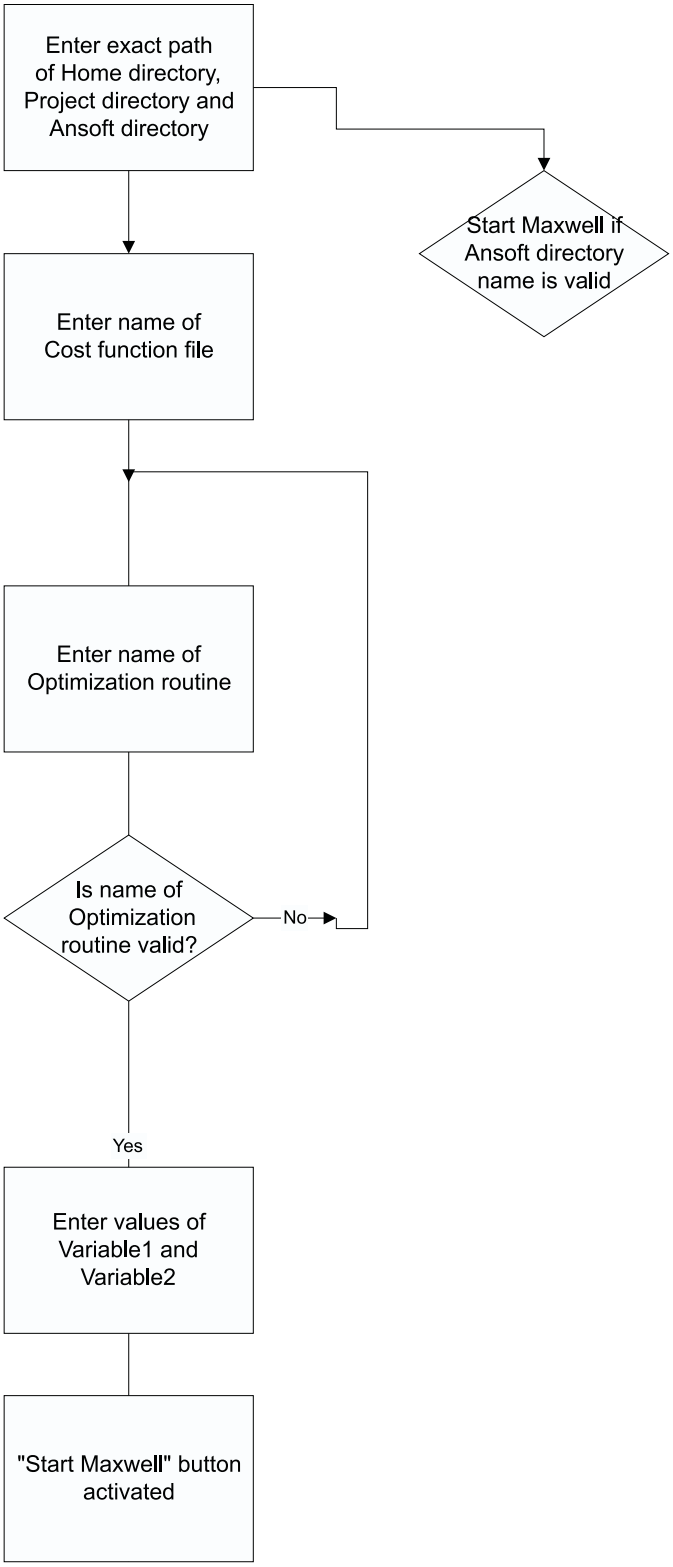

Figure 9.6: Schematic depiction of GUI organization.

9.3.4 Generalization of the Variables

Initial Guesses for the Variables

The list of variable names has been made into a list-menu, and as the user selects the variable name, the initial values can be entered in the editable textbox below the variable name field. This was implemented by reading the index of the selected variable name in the vector variable "varnames" and then editing the appropriate entry in the vector variable "varvals". In order to assure that the textbox would display the proper initial value for the variable name, the textbox was refreshed every time an entry of the list-menu was selected. The default initial value is zero, which is automatically entered every time a new *Maxwell* project is selected. As the process of re-entering initial values for every variable can become tedious, save and load buttons were provided so that the initial values can be retrieved at one click. This is simply implemented by saving and loading the variable "varvals" in the *Maxwell* project directory.

The previous implementation of the optimization module was still problem specific. Explicit references to σ and ε remained hard-coded in the program, and the number of variables that can be optimized was limited to two. To correct this, all the explicit references to σ and ε, including the global variables "sig_init" and "eps_init", were removed. These two global variables were replaced with the vector variables 'varvals"and "varnames", which represent the values of the variables and their respective names.

One technical difficulty which arose at this stage was the correlation between the variable names in the *Maxwell* project and this GUI module. Previously, since we were limited to only "σ" and "ε", there was no problem identifying the inputs into the GUI module with the actual variables in the *Maxwell* files. By generalizing the GUI module, we no longer knew the exact name of the variables. This information would now have to be obtained from the project-specific files. Our implementation of the solution takes advantage of the structure of the ".ptb" files in the *Maxwell* project directory, where the names of every variable in the parametric sweep is listed. Thus, by scanning the ".ptb"file for all the variables before "Solved", we can know all of the

parametric variables within the *Maxwell* project.

A small nuance with the *Maxwell* AC Conduction solver caused the addition of another feature to the GUI module. Within the solver's parametric mode, "frequency" was always a variable, even though it would not be varied in the reverse solution search. This left the choice of either explicitly ignoring the "frequency" variable while doing the scan of the ".ptd" file, or creating a more general way to deal with such a situation. In earlier implementations of the module, the explicitly ignoring method was chosen. However, it was later decided that a more creative method existed which would also add functionality to the module. This method was to remove the explicit avoidance of "frequency" and to include it in the list of optimizable variables. To avoid including "frequency" in the optimization, however, a checkbox was created which allowed variables to be excluded in the optimization calculations. By checking this box, the particular variable is excluded from the *Matlab* cost function upon which the optimization routines operated, thus it is kept from varying. Its initial value specified in the module will remain the same throughout all the calculations. This gives added functionality to the optimization module in providing the ability to reduce dimensions from the original optimization problem to yield a simpler problem.

The previous iteration of the *Maxwell* optimization module did not effectively implement a usable user-specified cost function. The difficulty which exists here involves the desire to shield the user from having to make direct calls to *Maxwell* as a subroutine in their *Matlab* cost function. The input to the *Matlab* optimization routines involves vectorized inputs and outputs, which in our case would be the parametric variables of *Maxwell* (σ, ε) and their dependent quantities (G, C), respectively. The problem arises in that *Maxwell* must be called as a subroutine to accomplish this, thus adding a level of complexity which would be undesirable for the user. Thus, to solve this problem, the present code asks the user for the number of output variables, and then passes those variables in a vector format, in the order of the *Maxwell* parametric module columns, into a user-specified *Matlab* function file as inputs. The user can then specify a function from the input vector, with the output being another vector, the one

which is passed straight back to the *Matlab* optimization routine. This allows the user to deal with a simple *Matlab* vector input-output function, thus removing them from having to deal with calling *Maxwell* as a subroutine. The ability to edit and create a new cost function file has also been added in the GUI module.

Addition of All Matlab Optimization Routines, Including Constrained Optimization

The earlier iterations of the GUI module provided only one *Matlab* routine to conduct the optimization solution search process. Originally, the routine implemented was "fmins", the simplex search method. This was changed to a quasi-Newton method of solution in the next iteration, which implemented the *Matlab* routine "fsolve." It was then decided that the user should have the flexibility to use whatever routine *Matlab* allows. Thus, the choice of all optimization algorithms along with all their various forms of implementation were made available. A previous implementation was done by way of a editable textbox, by which the user could enter the name of the *Matlab* optimization algorithm. This method required the user to recall the actual name of the functions in *Matlab*, which was thought to be disadvantageous. Thus, this present implementation utilizes a list-menu to provide the user the choices of algorithm and function. Figure 9.5 provides a screenshot of the implementation.

With the addition of all the *Matlab* optimization algorithms, the ability to specify constraints to an optimization setup became available. The *Matlab* routine "constr" was chosen to handle the constrained optimization calculations. The format of the inputs to "constr" requires a *Matlab* cost function of two vector outputs, one being the actual calculations of the cost function, and the other the calculation of a constraint function, which is to be kept less than zero. Thus, the cost function "iter" which calls *Maxwell* as a subroutine has been modified to pass back two vector values. Accordingly, the user-defined simplified cost function must be modified when using constraints. It should take in inputs as before, a vector of user specified length in the same order as the *Maxwell* columns, but the outputs should be modified to include the two specified

by "constr", the cost function output and the constraint output.

In addition to the ability to specify functional constraints, the ability to specify absolute min-max boundaries for each of the variables included in the optimization has also been implemented. When "constr" is selected from the list-menu of optimization algorithms, a dialogue-box appears, from where the absolute min-max boundaries can be specified by entering two vectors, one for all the minimum boundaries for the included variables, and one for all the maximum boundaries. The order of the vector components should be the same as that of the variables list. Finally, the code to handle constraints is in place but has not been tested, thus leaving something for the next improvement of this project.

9.3.5 Minor Code Revisions and Improvements

Auto-normalization of the Input Variables

In order for the *Matlab* optimization functions to work effectively, it is best if they are of the same order of magnitude. This issue was raised in the original problem by the disparity of relative permittivity, typically on the order of 10^0, and conductivity, typically on the order of 10^{-11} S/m. Originally, the orders of normalization had been hard-coded into the problem-specific routines which ran the optimizer. But in the interest of generality, these were removed and a new function was written to normalize any number of vectorized inputs. Thus, before passing the input variables into the *Matlab* optimization function, the code calls a separate normalization program which outputs the normalized arguments along with their original order of magnitude as a global variable. The normalized arguments are then passed to the *Matlab* optimization routine, to ensure effective functionality. Before the call to *Maxwell* is made, however, the arguments are restored to their original order through the global variable so that the *Maxwell* calculations are correct.

Added Functionality to .ptb Scans

The extraction of the calculated result from the *Maxwell* .ptd files was specifically defined under the original problem. One only had to read the final complex column (admittance) in order to obtain the conductance and the capacitance. In the general case, however, the desired result could conceivably be a single scalar, such as torque, or even multiple complex numbers, such as admittances between various electrodes. Thus, it was decided that it would be advantageous for the user to specify the number of output variables, and to have the program automated to extract these different forms of variables. Thus, the entry box, "Number of Output Variables", was added to the interface. Also, since the .ptd file contained both ordered pairs (for complex numbers) and scalars, the need to derive a form with which the .ptd could be read arose. This was solved by scanning the .ptb files, which told the variable types (real, complex, boolean, etc.) along with their names. Thus, the form with which the .ptd files could be read by "fscanf" was created by scanning the .ptb file for the specific variable types. Once read into a matrix, the user-selected number of variables were extracted from the lower-right of the matrix, where the output variables reside, and passed into the user-defined cost function. This allows for the general extraction of output variables of the *Maxwell* project.

Aside from the fact that they yielded the variable types for extraction of output variables, .ptb files were also scanned to provide the actual variable names for the "Variables" list-menu. Thus, they were scanned every time a new project directory was entered, and the list-menu became automatically updated.

9.4 Zero Order Issues

9.4.1 Running a project from MS-DOS

A project in *Maxwell* 2D can be solved without using the *Maxwell* Control Panel. To solve a project in DOS (Nominal Problem), issue the following command:

```
path m2dfs -batch <project>
```

where path is the drive and directory path of the Maxwell executables and <project> is the drive, directory path, and name of the desired project. To solve for the variables of a project, use the command:

```
path m2dfs -batch variables <project>
```

For example, to solve for the variables of a project named 1mmt.pjt in

```
d:\ansoft\projects\binh\1mmt.pjt,
```

use the command:

```
m2dfs -batch variables d:\ansoft\projects\binh\1mmt.pjt &
```

9.4.2 Changing Parametric Setup in Maxwell

Automatic File Changes by Maxwell

During the process of setting up a project to find a solution, certain files in the project's directory are updated when specific features of the project are changed. By examining which files are updated and how they change, a method of changing the project's features without directly accessing the Maxwell Control Panel can be found. When a project has not been opened, *Maxwell* denotes it in the Maxwell Projects window as unlocked. After a project is opened, *Maxwell* locks the project and a checkmark appears inside the "Locked" box. A file named lock.inf is created when a project is locked, and the deletion of this file unlocks the project.

In examining the step-by-step procedure of creating a project, an arbitrary project named 1mmcntrl will be considered. When the project's model has been defined, as indicated by a checkmark beside "Define Model" in the Maxwell 2D Field Simulator window, the message Model2DComplete is added to a file called mfs2.stt. When Setup Materials has been completed, files such as 1mmcntrl.asn and 1mmcntrl are created and Mfs2.stt is updated with the message MaterialSetupComplete. After completing the SetupBoundaries/Sources procedure, 1mmcntrl.bnd is created and BoundaryConditionsComplete is added to mfs2.stt. When Setup Solution is done, *Maxwell* further

updates three important files. ParametricSetupDone is added to mfs2.stt. The file 1mmcntrl.ptb is updated with information about the variables added. The first piece of information contains the name of the variables. For instance, if σ and ε were added, then

```
B_COLUMN 1002
 Type DBL
 Name epsilon
 Width 12
E_COLUMN
B_COLUMN 1003
 Type DBL
 Name sigma
 Width 12
E_COLUMN
```

would be inserted at the top of the file. Secondly, information about the number of setups is added to the file as well. The following lines,

```
B_ROW -5 33

E_ROW
B_ROW -6 33
E_ROW
B_ROW -7 33

E_ROW
```

are added to the bottom of the file before the line

```
E_DATA.
```

A file called 1mmctrl.ptd is also updated. Information that is needed in the solutions table, such as the number of setups, the data sweep, and values to be calculated, is added to this file. The information is formatted in the following manner (assuming that there are three setups):
setup1 1500 1E-009 F F T 0 0 0 (0 , 0) (0 , 0) 0 0 0 0
setup2 1500 5E-009 F F T 0 0 0 (0 , 0) (0 , 0) 0 0 0 0
setup3 1500 1E-008 F F T 0 0 0 (0 , 0) (0 , 0) 0 0 0 0

When these changes have been made, the information will be included in the solutions table of *Maxwell*, such as the one below.

Setup Table from *Maxwell*

At this point, the variables are ready to be solved. After solving the problem, mfs2.stt is updated with ParametricSolveComplete. 1mmcntrl.ptb changes only slightly with

```
B_ROW -5 41
E_ROW
B_ROW -6 41
E_ROW
B_ROW -7 41

E_ROW
```

where "33" changed to "41" (significance of the numbers is unknown). Also, the file 1mmcntrl.ptd is updated with the solved calculations and with changes in the Boolean values of fields like "Solved," "Save Fields," and "Solve." An example is shown below:
setup1 1500 1E-009 T F F 259 4.3025E-009 0.218528 (0,0) (0,0) 0 0 2.1353E-010
setup2 1500 5E-009 T F F 259 4.3025E-009 0.218528 (0,0) (0,0) 0 0 1.1744E-009
setup3 1500 1E-008 T F F 259 4.3025E-009 0.218528 (0,0) (0,0) 0 0 2.1353E-009
The first line shows that setup 1 is for the first variable value 1500, second variable

value 1e-9, project has been solved (True), field solutions should not be saved (False), project should not be solved (False), there are 259 triangles in the mesh, energy is at 4.3025E-009 with an energy error of 0.218528. The remaining entries vary depending on the solver type and requested integral variables. The last number is the interelectrode capacitance requested from *Maxwell*. Refer to Setup Solution/Variables menu option in *Maxwell* for exact correspondence of each entry. Many other files are created and updated throughout this process, but only the files important for parametric changes have been discussed.

Manual File Changes by User

In order to manually change the variables so that *Maxwell* can solve them, certain files in the project's directory must be changed. The most important files are 1mmctrl.ptb and 1mmctrl.ptd. In order to add a setup to the solutions table, both of these files must be updated with the desired information. First, 1mmcntrl.ptb must be updated with the following lines inserted at the end of the file:

```
B_ROW # 33


E_ROW
```

where $< \# >$ is replaced by adding negative one (-1) to the number in the previous setup. An important note is that it seems the 33 in the B_ROWis necessary for *Maxwell* to solve the problem (i.e., not to think that the solution has converged). It also seems that these lines must be added at the end of the list in order for *Maxwell* to recognize them. In order to add a new variable to the table, the following must be added to the top of the file (1mmcntrl.ptb):

```
B_COLUMN <column#>
 Type DBL
 Name <var>
 Width 12
```

```
E_COLUMN
```

where

```
<column#>
```

is the column number (one more than the column number of the previous setup) and <var> is the name of the variable to be added. The information contained in Type indicates the precision, such as double-precision (DBL). In addition to the changes in 1mmcntrl.ptb, the file 1mmcntrl.ptd must be updated with the following:
setup<#> var1 var2 F F T 0 0 0 (0 , 0) (0 , 0) 0 0 0 0
where <#> is the setup number, var1 is the value of the first variable, and var2 is the value of the second variable. When updating these files, save them only in text mode. Also, in order to view the changes in the solutions table in Maxwell, the project must first be closed and then opened after the changes to the files are made. The following table describes a few of the files that *Maxwell* creates in a project's directory.

9.4.3 File Description

The following files have been identified.
lock.inf: (.inf - information) File is created when a project is in use (or locked).
mfs2.stt: File is updated every time a process has been completed (such as Define Model, Setup Materials, etc.).
(project).ptb: Contains the variable names, the column labels, and setup information (Energy, Triangles, etc.).
(project).ptd: (.ptd - parametric table data) Contains the data for each setup.
(project).sm2 Contains specifications for the project model (object name, coordinates, etc.). Created after Define Model is performed.
(project).asn: Contains information on material type for each object. Created after Setup Materials is performed.
(project).bnd: (.bnd - boundary) Contains the boundary information for each object. Created after Setup Boundaries is performed.

(project).avl: Contains information (triangles, time, etc.) for each pass.

(project).cnd: Lists whether an object (in matrix) is signal or ground. Created after Setup Executive Parameters: Matrix is performed.

(project).prm: Lists values for the project after nominal solving, such as frequency value, percent energy, and number of passes.

(project).cap: (.cap - capacitance) Lists the values from the capacitance matrix.

(project).adm: (.adm - admittance) Lists the values from the admittance matrix.

9.5 Step-by-step Guide to Optimization Interface

1. Open *Matlab*.

2. Type "maxgui88" (for version 8.8) to open optimization module.

3. Enter Home Directory in text box, e.g. "c:\matlab\maxgui".

4. Enter Project Path in text box, e.g. "c:\ansoft\projects\jason\lambda1.pjt". This should renew the variables and set all their initial values to zero. The stored initial values for the project variables can be restored by clicking on the load button next to the "Initial Value" box.

5. Enter Maxwell Path in text box, e.g. "c:\ansoft". A *Maxwell* window should start up if you entered the correct path.

6. Enter Cost Function in text box, e.g. "cost1". Use the edit button to edit the function if necessary. New creates a new function, which must be named in the *Matlab* editor window which opens. The cost function ought to be a function of vector inputs and outputs, with the single input vector being the variables calculated by *Maxwell*'s parametric module, in that same order, and the output being the result of the vector cost function of the input. For cases with constraints, a second output is needed. This second output is the constraint function, which will be kept less than zero in the search for an optimal solution.

7. Select Optimization algorithm, e.g. "fminu BGFS", from the list-menu. If "constr" is selected, a dialogue box will appear asking for the absolute maxima-minima of the solution search. These are to be defined as vectors, in the same order as the included variables are listed in the variables list-box. Notice, only included variables are to have these constraints.

8. Edit the initial value as well as inclusion/exclusion of each variable, e.g. click on "frequency"; select "exclude from optimization"; click on "epsilon1"; enter "3" in "Initial Value" box; select "sigma1"; enter "1e-11" in "Initial Value" box. Notice these values can be saved and loaded using the buttons next to the text box.

9. Enter the number of output variables, e.g. "2". This is the number of actual output variables desired counting from the end of the *Maxwell* parametric mode spreadsheet. Notice that complex-numbered values, such as admittance, count as two output variables.

10. Click on "Start Maxwell" to begin optimization process.

9.6 Applications

This section presents a simple example of solving the inverse problem with the developed software. Figure 9.7 shows the convergence process of finding dielectric permittivity and conductivity of a homogeneous material using the interdigital sensor. The initial guesses for capacitance C_{12} and conductance G_{12} are somewhat different from the correct values. It took almost 40 iterations to converge to correct values of dielectric properties with a specified accuracy of the cost function Y:

$$Y = |(C_m - C_c)/C_m|^2 + |(G_m - G_c)/G_m|^2 , \tag{9.1}$$

where C_c and G_c are calculated and C_m and G_m are measured values of capacitance and conductance, respectively.

More complicated cases of inverse problems are treated in consecutive chapters, especially for moisture dynamics. In several cases, the optimization with *Maxwell* has been used for those problems, as pointed out later, where appropriate. For example, a moisture diffusion problem has been solved in Chapter 11.

9.7 Summary

A brief summary of the results of this project follows:

1. A versatile tool for solving a variety of optimization problems through adaptive finite element analysis has being developed.

2. Applications include power equipment design, insulation coordination, management of electric and magnetic field distribution, MEMS and sensor optimization, etc.

3. Problems already solved involved up to 6 variables (including a moisture diffusion problem and not included in this thesis a magnetic field minimization problem).

4. The computation time varies between minutes and weeks.

5. Future work should concentrate on the stability of highly intensive computational tasks and development of tools for treating discrete problems.

The code for the optimization with *Maxwell* and related problems is given in Appendix H.

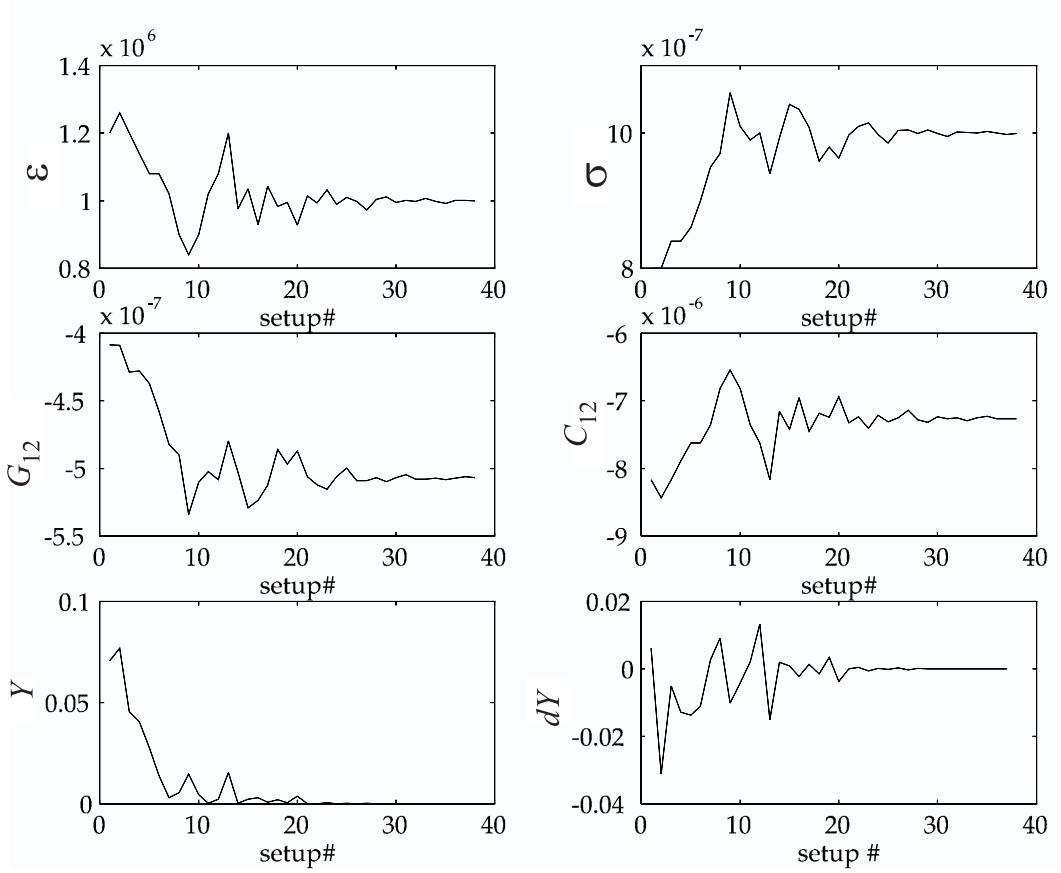

Figure 9.7: Material properties can be determined by guessing at the values of material properties until they match the measured values. This inverse problem can be formulated as an optimization problem. Relative dielectric permittivity ε and conductivity σ are scaled in this example by 10^6 in order to avoid the low conductivity threshold in Maxwell at about 10^{-9} S/m. Y is the cost function and $dY = Y_{i+1} - Y_i$ is the differential value of the consecutive cost function values that is used as a convergence criterion.

Chapter 10

Dielectric Spectroscopy

10.1 Introduction

Mechanical and rheological methods address macroscopic properties, while spectroscopic methods address properties on the microscopic molecular level [65]. Many simple versions of chemical sensors perform measurements at a single operating point, for example, using DC conduction measurements or AC capacitive measurements at a single frequency. In these cases, it is usually not possible to differentiate between the change of the signal caused by the chemical of interest and the change of the signal caused by an interference process, such as moisture absorption, variation of ambient temperature, electrical noise, etc. A variety of spectroscopy techniques is available to improve differentiation between signal change sources and, thus, extend capabilities of existing sensing techniques without introducing changes in the physical design of the sensor itself.

10.2 Impedance Spectroscopy

In contrast to other spectroscopy techniques, such as, for example, Fourier transform infrared spectroscopy, the impedance, admittance, and dielectric spectroscopy do not

usually exhibit extremely sharp gradients at the resonant points in the frequency response. The topic of dielectric spectroscopy is very broad by itself and is the subject of separate books, such as [167, 172]. Some aspects of dielectric spectroscopy are specialized to dielectric materials only, such as measurement of Warburg impedance (frequency dependent resistive and capacitive components due to polarization under low current conditions in the double layer) and distortion of the Debye semi-circle in Cole-Cole plots when plotting ε'' vs. ε' [231]. Other aspects are common to broadband spectroscopies in general. For example, a normalized difference Fourier transform magnitude spectrum [67] helps to differentiate between different chemicals that are being absorbed by the sensitive layer. The impedance spectra has been used for evaluation of moisture absorption in solar panel encapsulations [225].

Figures 10.1 and 10.2 are extracted from a study dedicated to measurement of electrochemical double layer properties that was reported in [209]. The properties of liquid dielectric were found by immersing a parallel plate capacitor with a variable gap in the liquid and measuring the impedance over a range of frequencies. These impedances were then used to determine element values in an equivalent electrical circuit, where each element was a lumped parameter representation of the liquid dielectric properties. The test cell impedance was determined by connecting the cell to the circuit shown in Figure 10.1 and measuring the voltage gain across the circuit (v_o/v_s) as a function of frequency.

A lumped element model for the impedance is then used to determine the bulk conductivity and permittivity of the liquid. While the simplest model for the dielectric is a resistor R_1 in parallel with a capacitor C_1, this model is inadequate for describing the data. If the unknown impedance were formed by a resistor in parallel with a capacitor, a plot of the imaginary part of the impedance against the real part of the impedance would be a Cole-Cole semi-circle plot [174]. While this applies at the lower temperatures, the semi-circular shape is lost at the higher temperatures, as illustrated by the Cole-Cole plots in Figure 10.2. This is consistent with capacitive elements at the electrodes and motivates the form of the test cell impedance illustrated in Figure 10.1.

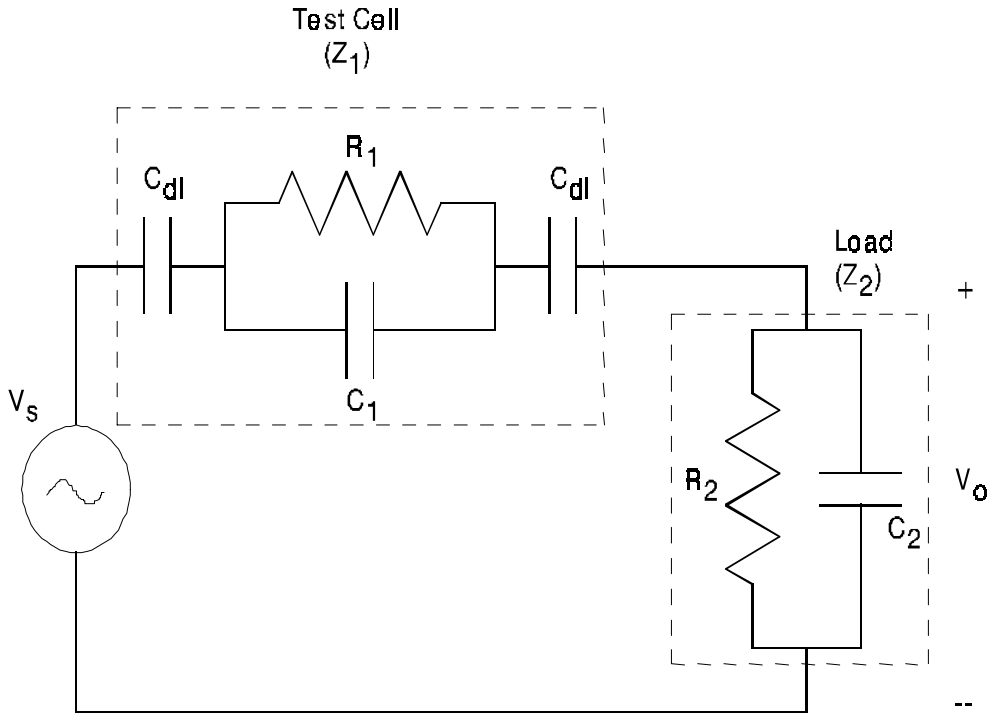

Figure 10.1: An electrical equivalent circuit diagram for the gain and phase measurements in transformer oil including capacitors C_{dl} near each electrode to account for the electrical double layer. [14].

The electrode capacitances C_{dl} result from the space-charge polarization associated with the electrical double layer while the bulk properties of the liquid conductivity σ and permittivity ε are given by R_1 and C_1. The lumped elements are related to the liquid dielectric properties by

$$C_1 = \frac{\epsilon A}{d - 2\lambda_D} \; ; \; R_1 = \frac{d - 2\lambda_D}{\sigma A} \; ; \; C_{dl} = \frac{\epsilon A}{\lambda_D} \tag{10.1}$$

with A the area, d the electrode spacing, σ the liquid conductivity, ϵ the liquid permittivity and with λ_D the characteristic Debye length over which the space-charge is distributed near each electrode. The geometric factor A/d is determined by measuring the capacitance of the structure in air, $C_{air} = \varepsilon_0 A/d$.

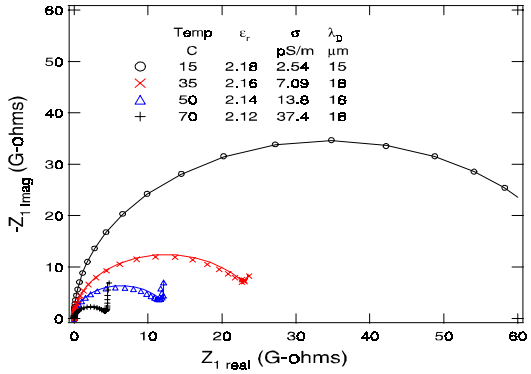

Figure 10.2: Representative Cole-Cole plots of real and imaginary parts of the complex impedance for Shell Diala A transformer oil at four temperatures. The lines give the calculated impedances for the listed estimated parameters. [14].

10.3 Data Visualization: Case Study

The following example on data visualization of dielectric spectroscopy measurements with oil-free transformer pressboard presents a gallery of plots to demonstrate the variety of possible representations of dielectric data and to provide a reference sequence of possible plots that can be used in the future. The measurement was done using a guarded parallel plate sensor with a sensing electrode square of 25 mm on a side, with a floating voltage dielectrometry interface with $C_L = 101.4$ pF (channel two of the controller). The ambient humidity was 60%, the temperature was 25°C, and the pressboard thickness (the distance between the driven and sensing electrodes) was 1.52 mm.

Figure 10.3 shows the measured gain and phase as a function of frequency. The phase valley with a minimum at about 0.5 Hz indicates that the frequency range has been properly selected to characterize the critical transition in the dielectric properties in the high to low frequency response. Figure 10.4 shows the values of transcapacitance and transconductance estimated from gain and phase by solving (4.3). Figures 10.5-10.15 show alternative ways to visualize the dielectric spectroscopy data. Some of the code used for plotting is listed in Appendix F as SpecStart.m.

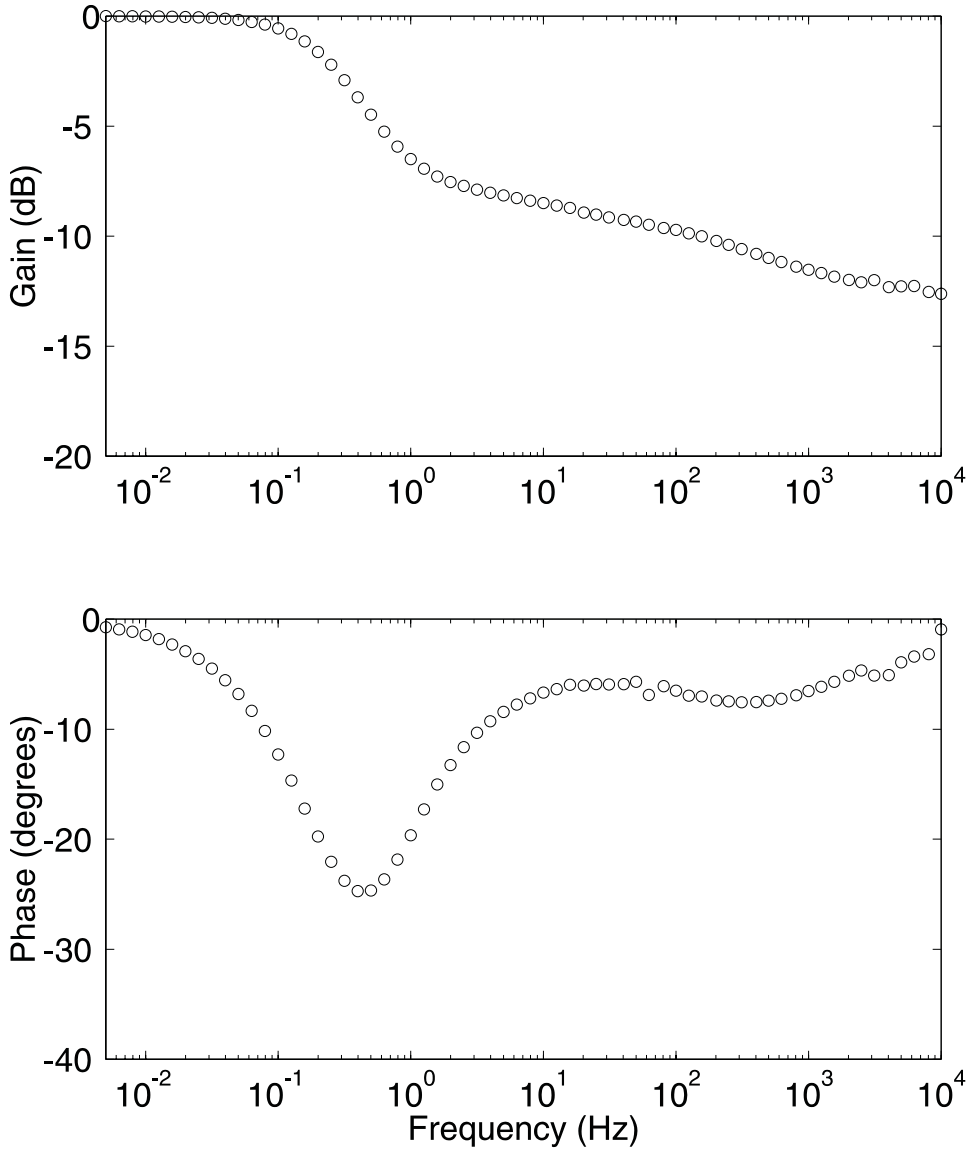

Figure 10.3: Measured gain and phase of the parallel-plate dielectrometry interface output with 1.52 mm thick oil-free transformer pressboard in air at 25°C and 60% relative humidity with $C_L = 101.4$ pF.

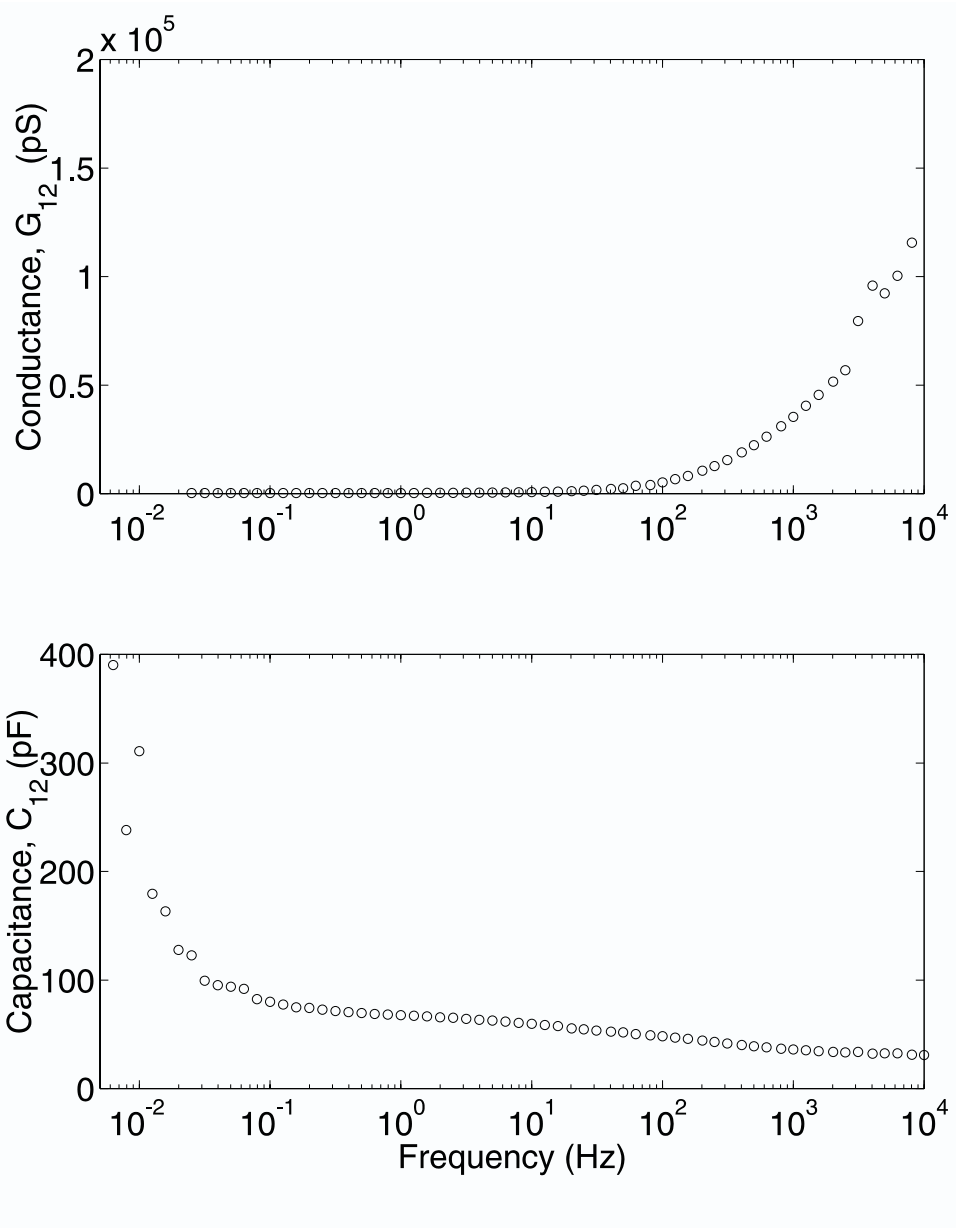

Figure 10.4: Measured transcapacitance C_{12} and transconductance G_{12} as a function of frequency for the data in Figure 10.3. Since the conductance values change over a very wide range, they are not identifiable from the plot at frequencies below 100 Hz. A log-log plot is often more appropriate in this case. The datapoints in this case correspond to actual values, as opposed to values produced by numerical uncertainties.

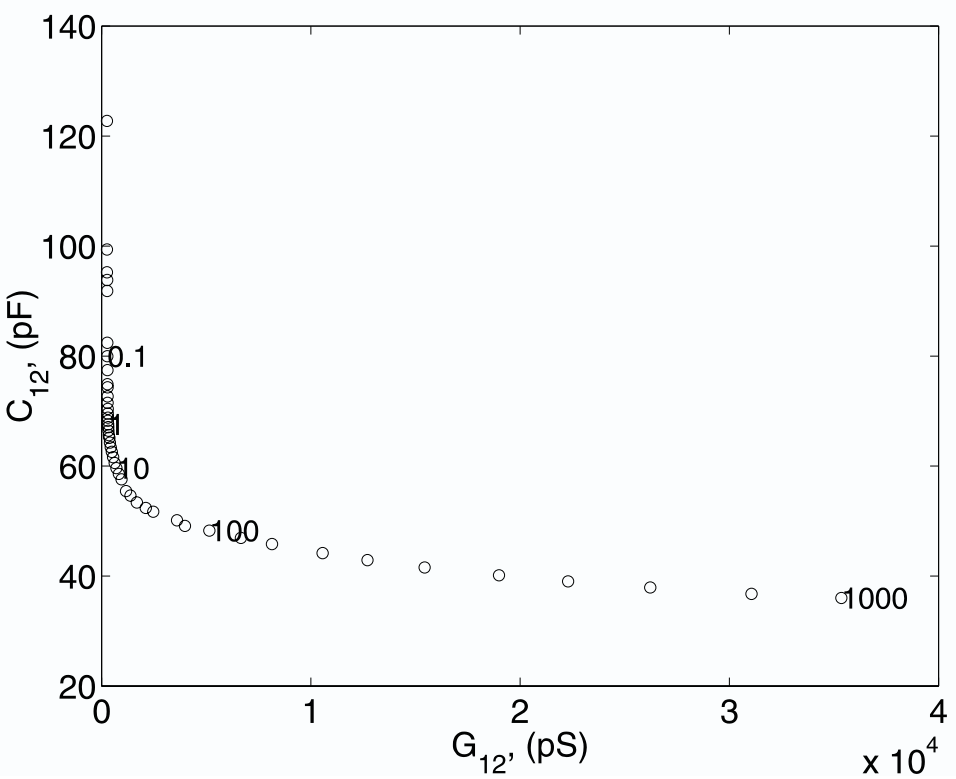

Figure 10.5: Oil-free transformer pressboard transcapacitance vs. transconductance with frequency (Hz) as a parameter.

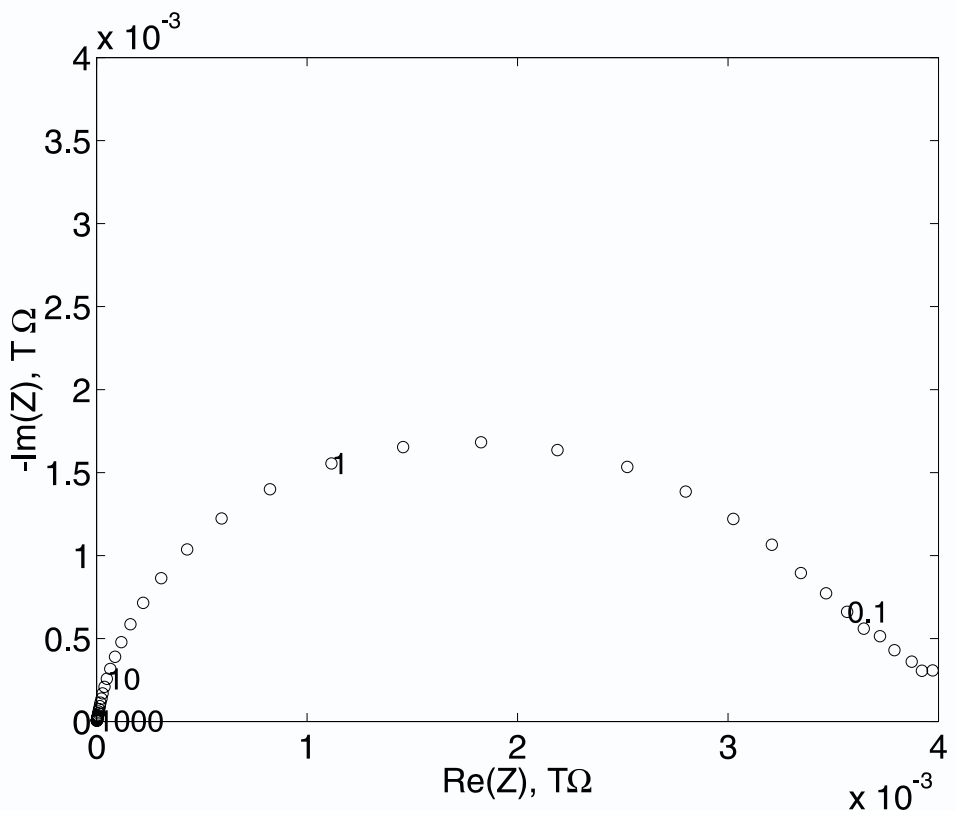

Figure 10.6: A negative imaginary part of transimpedance versus the real imaginary part of transimpedance, analogous to Cole-Cole plots, is often used for displaying data on frequency dispersive materials.

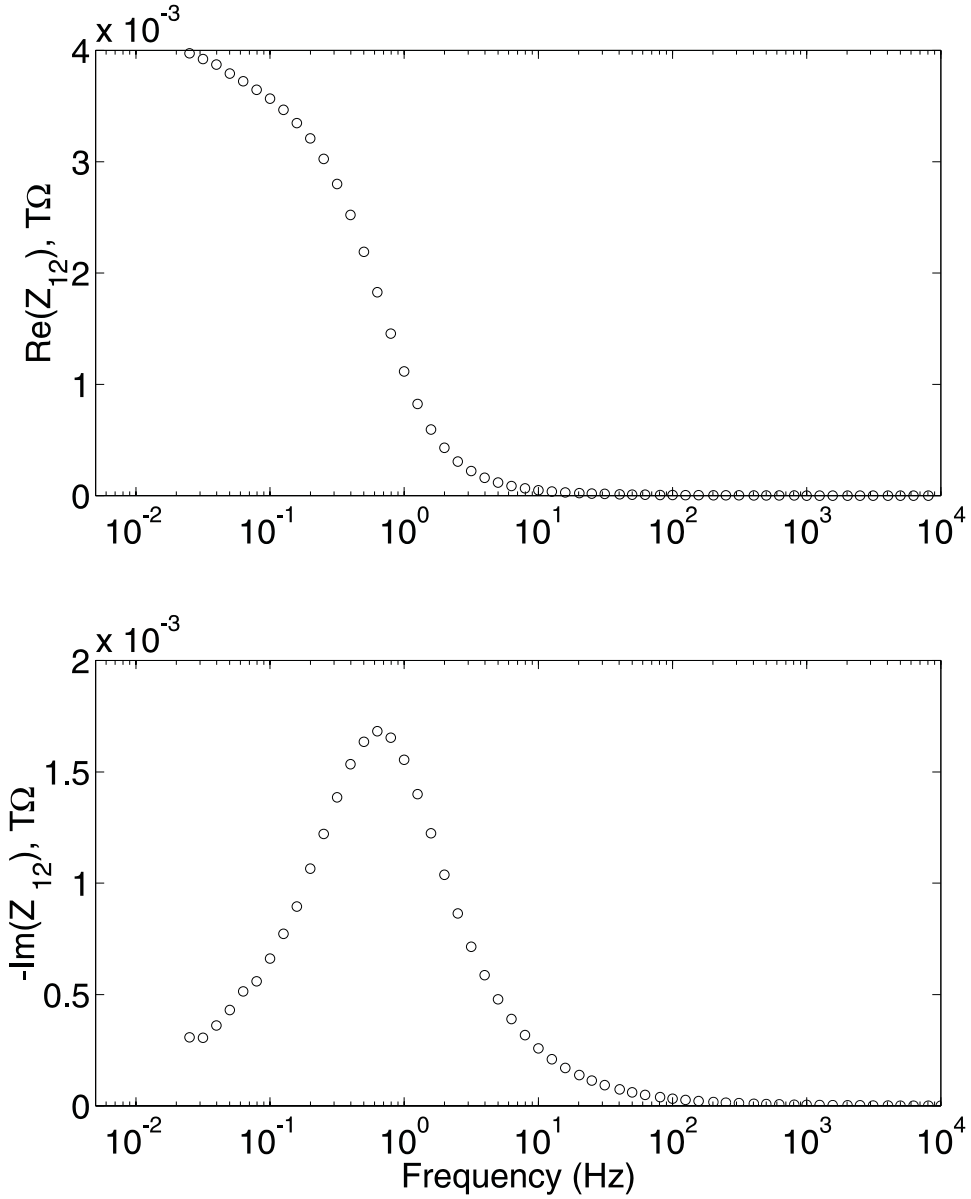

Figure 10.7: Oil-free transformer pressboard real and imaginary parts of impedance as functions of frequency.

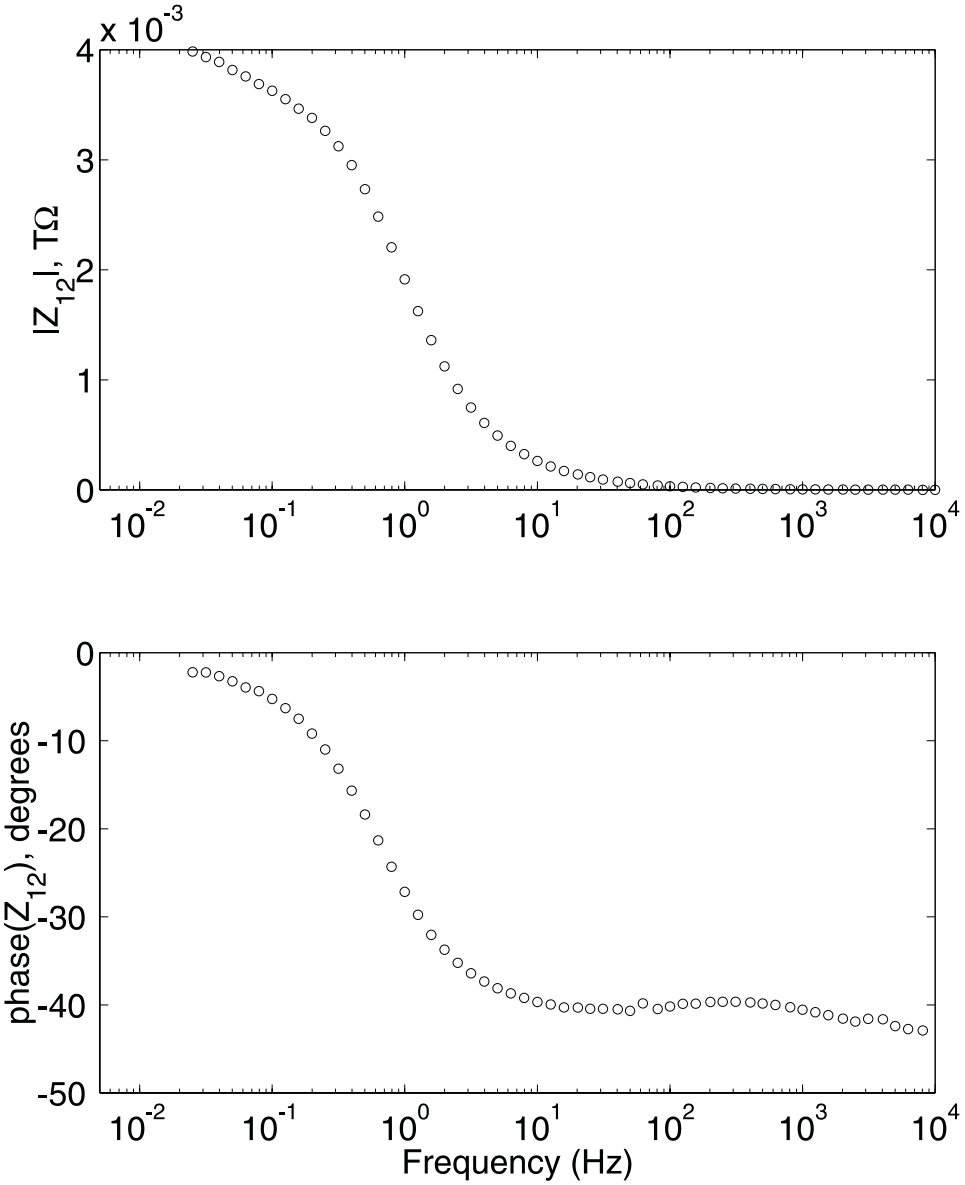

Figure 10.8: Oil-free transformer pressboard absolute value and phase angle of impedance as a function of frequency.

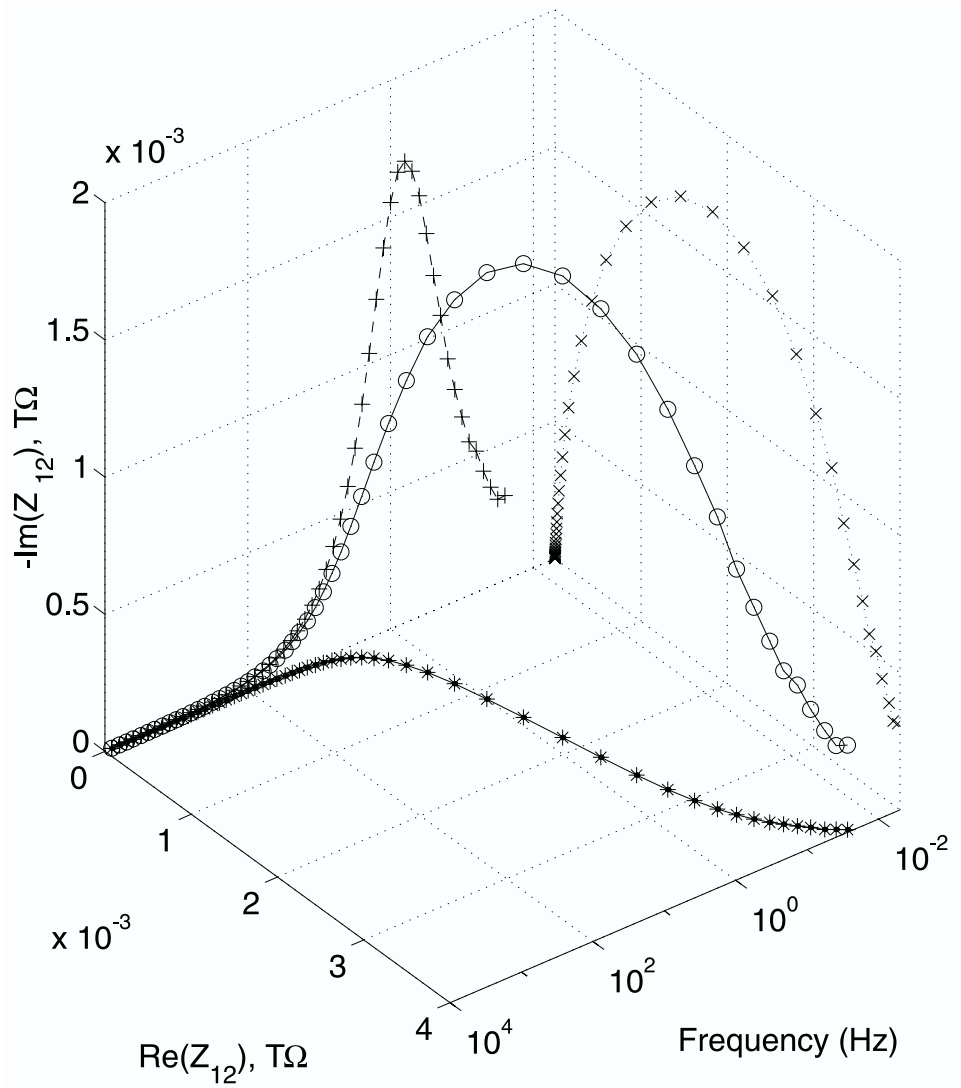

Figure 10.9: A three-dimensional representation of measured oil-free transformer pressboard impedance as a function of frequency. Circles show the data in three dimensions and pluses, x's, and asterisks visualize projections of this three-dimensional curve onto orthogonal planes formed by the axes of frequency, real part of impedance, and negative imaginary part of impedance. This type of plot is frequently used in electrochemistry to effectively visualize dielectric spectroscopy measurement data.

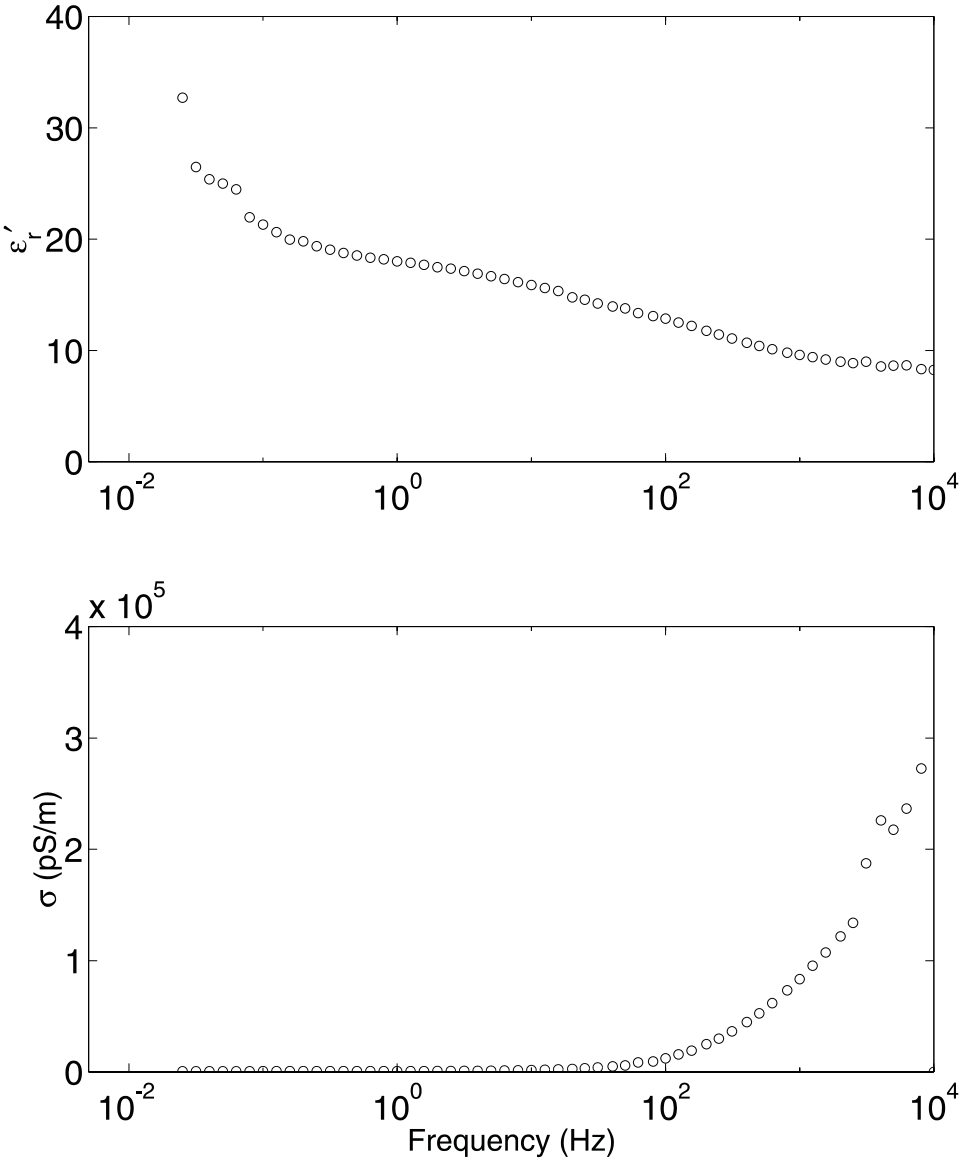

Figure 10.10: Measured oil-free transformer pressboard relative dielectric permittivity and conductivity as functions of frequency. Since the conductance values change over a very wide range, they are not identifiable at frequencies below 100 Hz. A log-log plot is often more appropriate in this case.

10.4 Summary

Visualization of electrical quantities as a function of frequency of electrical excitation is a powerful instrument that may help to study system and material properties. Dielectric spectroscopy deals with measurement and visualization of microscopic material properties, such as dielectric permittivity, conductivity, and loss tangent. It is not always possible or necessary to convert sensor response to dielectric properties data. The impedance and admittance spectroscopy techniques are also widely used and are very suitable for multiple penetration depth measurements.

A comprehensive series of examples that show possible ways of visualization of wideband spectroscopy data is included in this chapter for easy reference. Each representation has certain advantages and drawbacks. For example, loss tangent data for a parallel plate capacitor has a great feature of being almost insensitive to errors in geometry modeling. On the other hand, this presentation does not always reflect the loss of sensitivity to changes in conductivity or dielectric permittivity at certain values of the measurement frequency range. Three-dimensional projection representation of dielectric spectroscopy data combines all features in a single convenient plot to accommodate understanding of underlying phenomena.

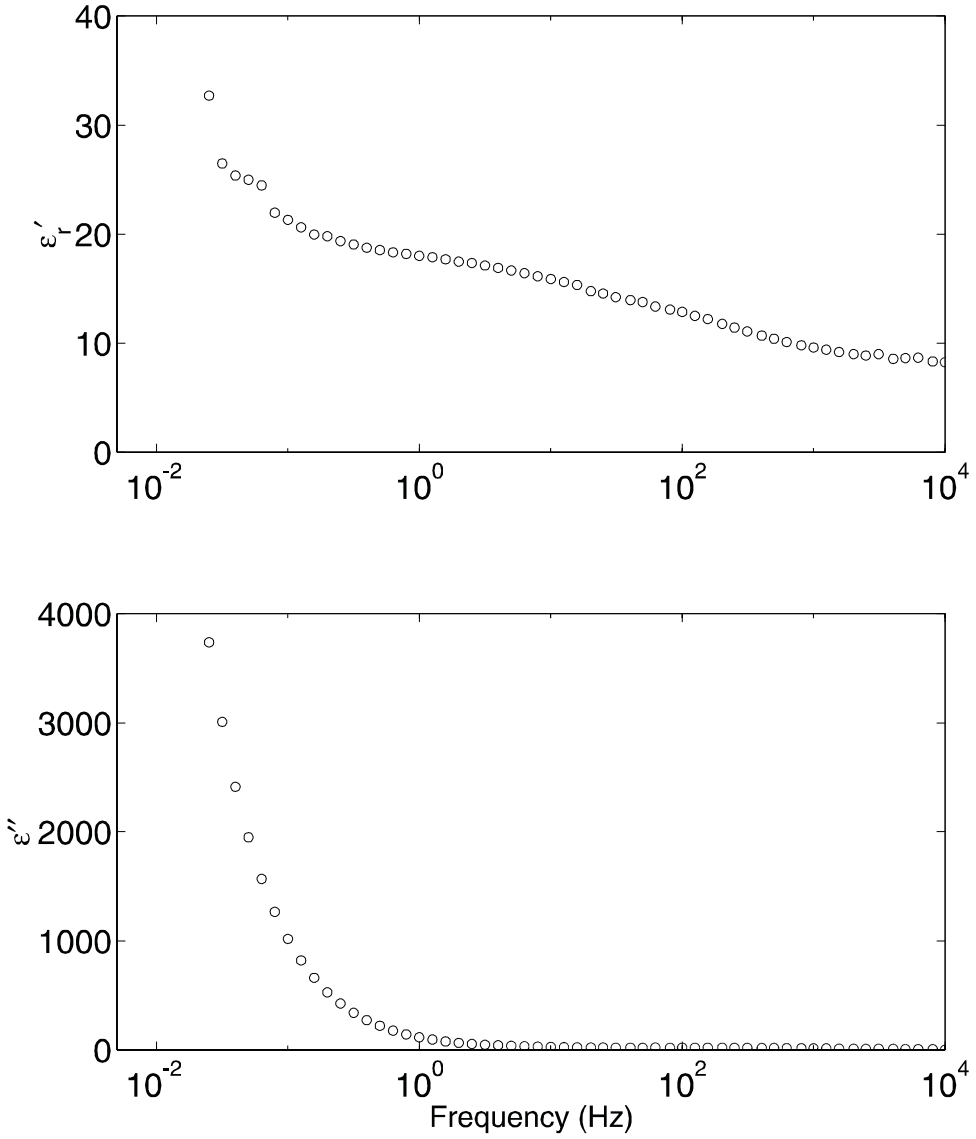

Figure 10.11: Measured oil-free transformer pressboard real and imaginary parts of relative dielectric permittivity on a linear scale as functions of frequency.

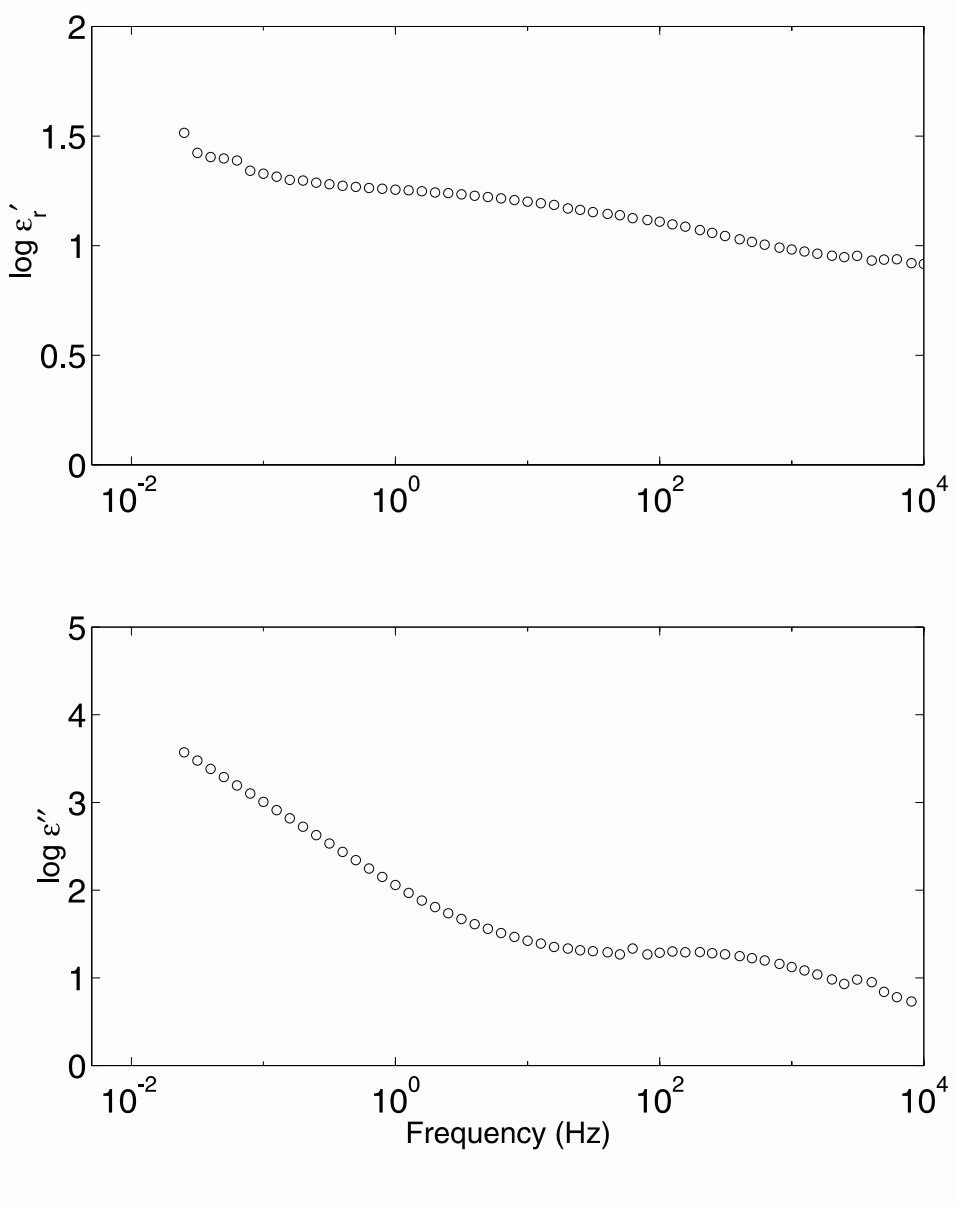

Figure 10.12: Measured oil-free transformer pressboard real and imaginary parts of relative dielectric permittivity on a logarithmic scale as functions of frequency. The slope is not constant for $\log(\varepsilon'')$ throughout the entire frequency range, which indicates that the material is dispersive; the slope is -1 at frequencies below 1 Hz indicates that it is non-dispersive at low frequency.

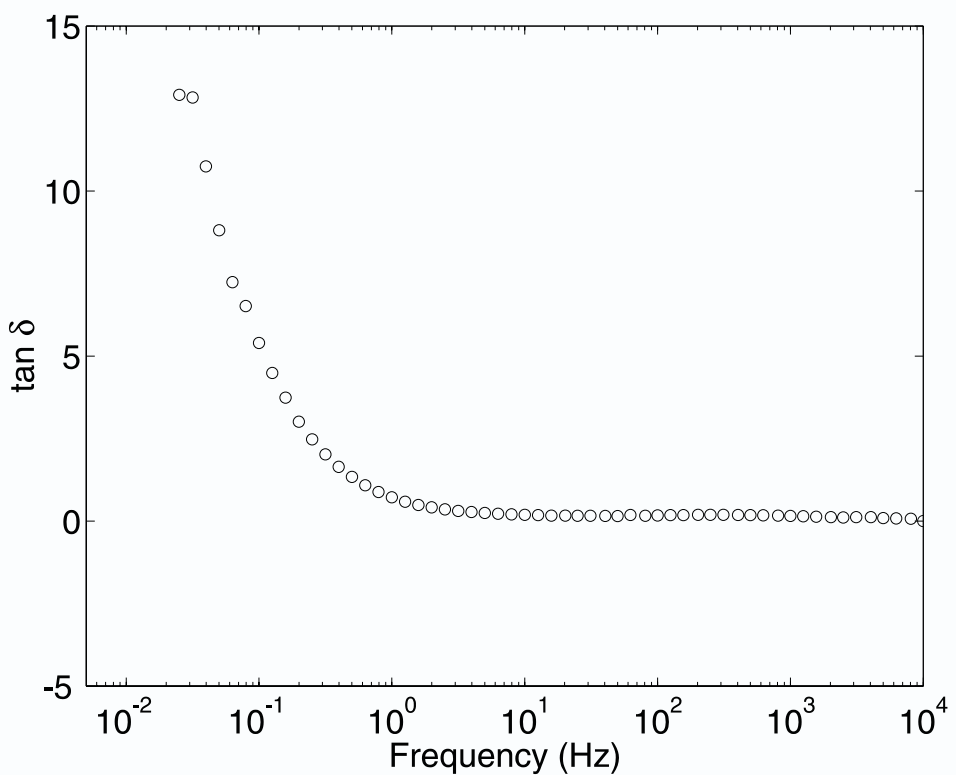

Figure 10.13: Measured oil-free transformer pressboard loss tangent ($tan\delta = \sigma/\varepsilon'$) as a function of frequency.

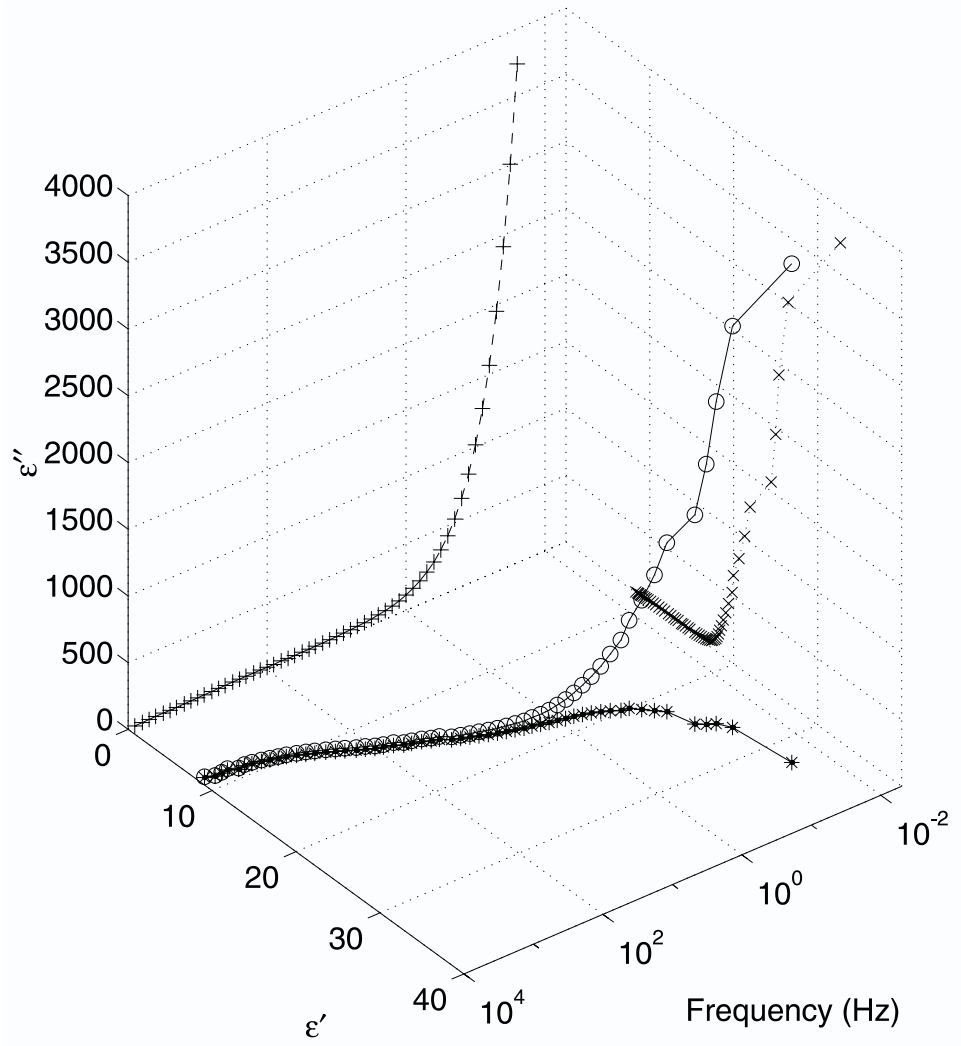

Figure 10.14: A three-dimensional representation of complex dielectric permittivity as a function of frequency for the data in Figure 10.3. Circles show the data in three dimensions and pluses, x's, and asterisks visualize projections of this three-dimensional curve onto orthogonal planes formed by the axes of frequency, real part of dielectric permittivity, and imaginary part of dielectric permittivity. This type of plot is frequently used in electrochemistry to effectively visualize dielectric spectroscopy measurement data.

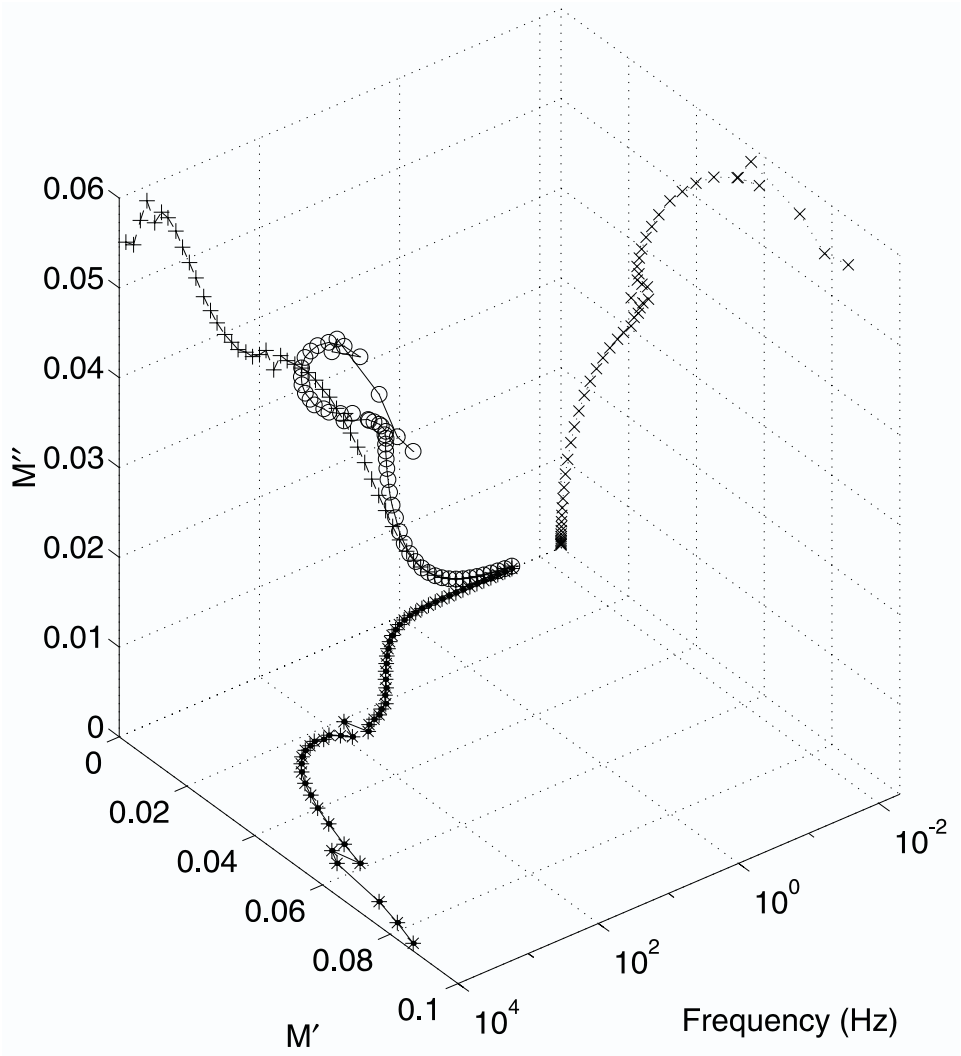

Figure 10.15: A three-dimensional representation of complex dielectric modulus $M = M' - jM'' = 1/\varepsilon^*$ as a function of frequency for the data in Figure 10.3. Circles show the data in three dimensions and pluses, x's, and asterisks visualize projections of this three-dimensional curve onto orthogonal planes formed by the axes of frequency, real part of modulus (M'), and imaginary part of modulus (M''). Modulus spectroscopy tends to emphasize material properties at high frequencies.

Chapter 11

Moisture Dynamics in Transformer Pressboard

11.1 Early Measurements

Throughout this thesis, the dielectric properties have been measured with parallel plate test cells according to [314]. The estimation of true bulk properties is usually complicated by the surface texture. Figure 11.1 shows an optical microscope photograph of the pressboard surface. The high to low dimensions of the surface irregularities are on the order of hundreds of microns.

Results of experiments with oil-free transformer pressboard in air are shown in Figure 11.2. The shape of the phase curve in Figure 11.2 differs from an ideal one-pole system primarily due to the dependence of the dielectric permittivity and conductivity of the pressboard on frequency. Estimation of the numerical values of the parasitic capacitance C_P due to finite electrode thickness and evaluation of its importance can be done based on the leftmost part of the gain curve in Figure 11.2. Solution of the inverse problem and value of a complex dielectric permittivity for this material are shown in Figure 11.3 and Figure 11.4. For a homogeneous material, all three wavelengths should indicate approximately equal values of ε' and ε''.

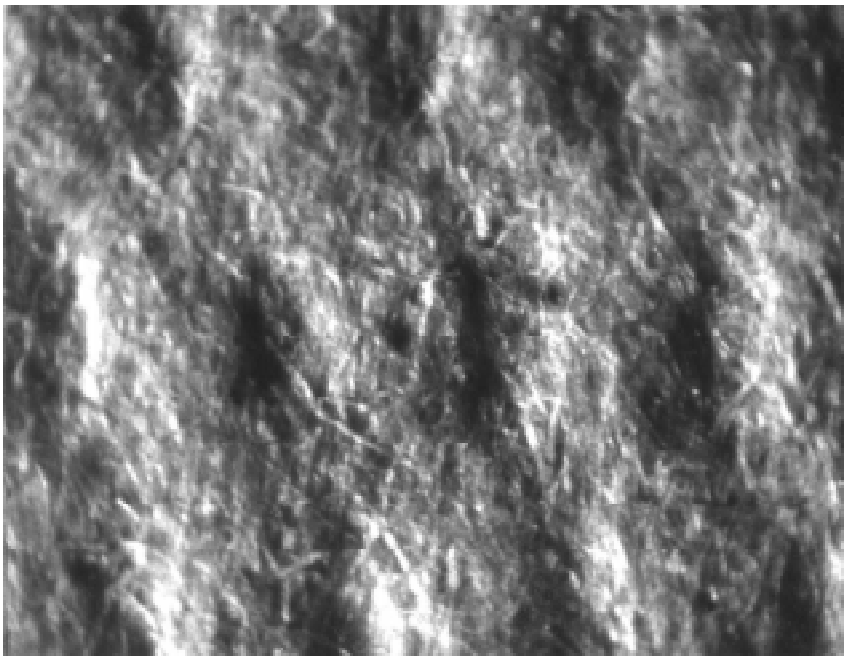

Figure 11.1: An optical microscope photograph of EHV-Weidmann Hi-Val oil-free calendered transformer pressboard surface shows surface texture that strongly affects dielectrometry measurements. Average thickness tolerance is ±5%.

The calibration of ε'' versus G_{12} has been done with a pressboard sample in a parallel plate sensor. However, the results are not very reliable, partially due to low repeatability of the measurement. Only smooth, rigid, slightly compressible materials can be used for precise calibration for σ. In general, intimacy of contact, and, consequently, applied pressure, plays an important role and may potentially introduce very large errors in the parameter estimation process. In addition, surface contamination of the sensor itself may affect calibration, in which case it should be cleaned with solvents.

11.2 Experimental Setups

A large experimental setup build by previous graduate students and modified and maintained mostly by the efforts of graduate students Darrell Schlicker and Yanqing Du and visiting researchers is shown in Figure 11.5. This setup is intended to simulate the environment of oil-filled power transformers. Several sensors are installed to moni-

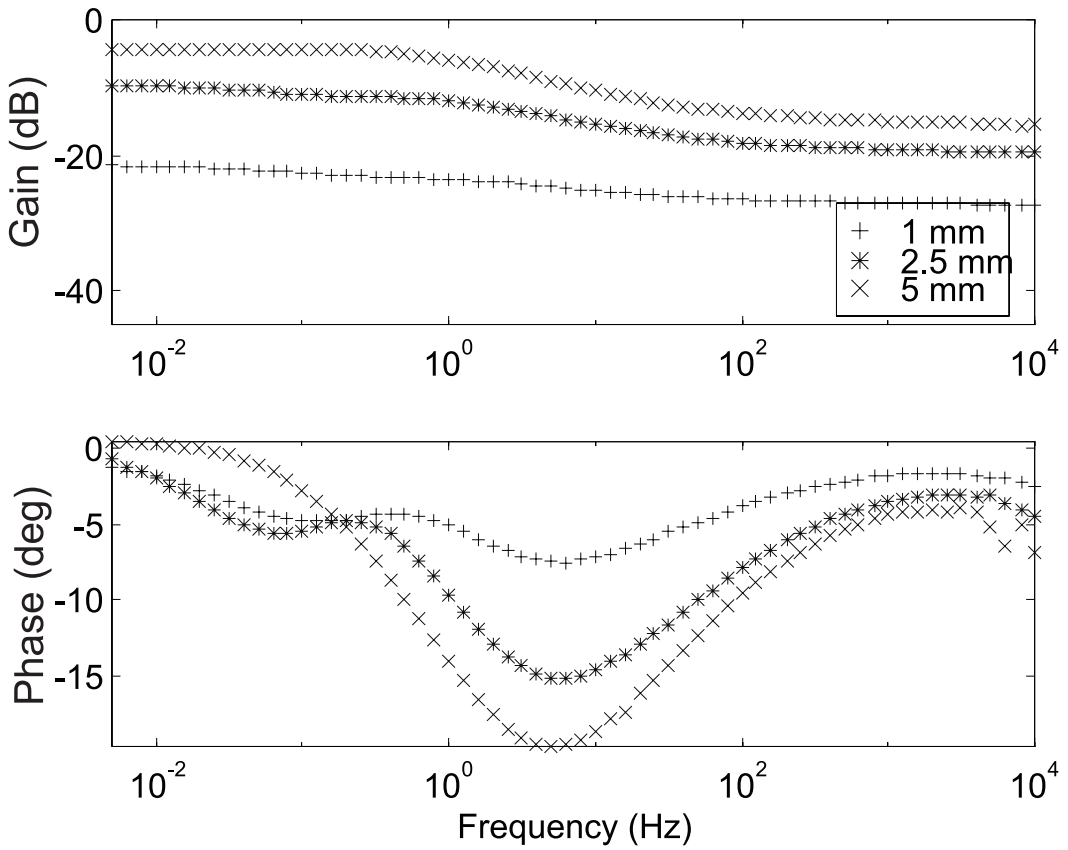

Figure 11.2: Gain and phase for the three-wavelength Kapton sensor of Figure 4.3 with a thick layer (4 mm) of oil-free transformer pressboard in air pressed against the surface of the sensor. The measured load capacitances C_L were equal to 59.2 pF, 23.3 pF, and 23.3 pF for 1 mm, 2.5 mm, and 5 mm wavelengths, respectively.

tor pressure (vacuum gages), temperature (thermocouples), moisture (Harley moisture meter [315]), and electric charge density (absolute charge sensor).

A controlled-environment experimental chamber shown in Figure 11.6 was built by another graduate student, Yanqing Du, to simulate the temperature, moisture, and materials of a power transformer environment [316]. A number of diffusion studies have been performed in this chamber to date. The reported experiment did not involve transformer oil, instead, the ambient air inside the chamber was humidified to a pre-selected value by circulating the moist air through a system of interconnected ducts. A number of experiments with oil-impregnated pressboard is recorded in the MIT doctoral thesis of Yanqing Du [12].

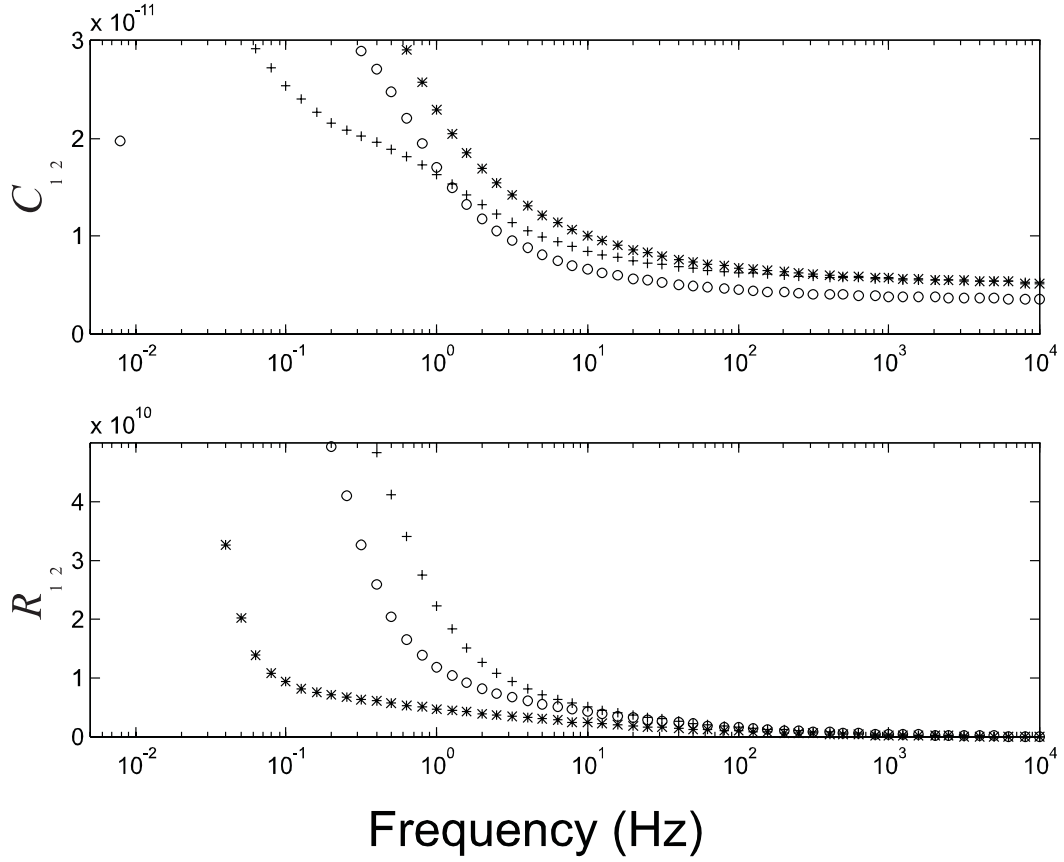

Figure 11.3: Pressboard in air – solution of the inverse problem for a homogeneous material. R_{12} and C_{12} calculated values obtained from floating voltage gain/phase measurements of Figure 11.2 with C_L equal to 59.2 pF, 23.3 pF, and 23.3 pF for 1 mm, 2.5 mm, and 5 mm wavelengths, respectively.

Figure 11.7 shows the critical part of the experimental setup. A piece of 1.5 mm thick oil-free transformer pressboard was positioned next to the sensor. The edges of the pressboard sample were sealed with silicon glue to prevent moisture diffusion from the sides. A number of holes in the metal compression plate provided a path for the moisture molecules to enter the pressboard from the left side (according to the diagram in Figure 11.7).

Even though the change of the pressboard properties through its thickness is gradual in the discussed experiment, the pressboard in the model is represented as a three-layer medium with each layer thickness corresponding to the effective penetration depth of 0.3λ for each wavelength λ of the sensor. In other words, the number of wavelengths

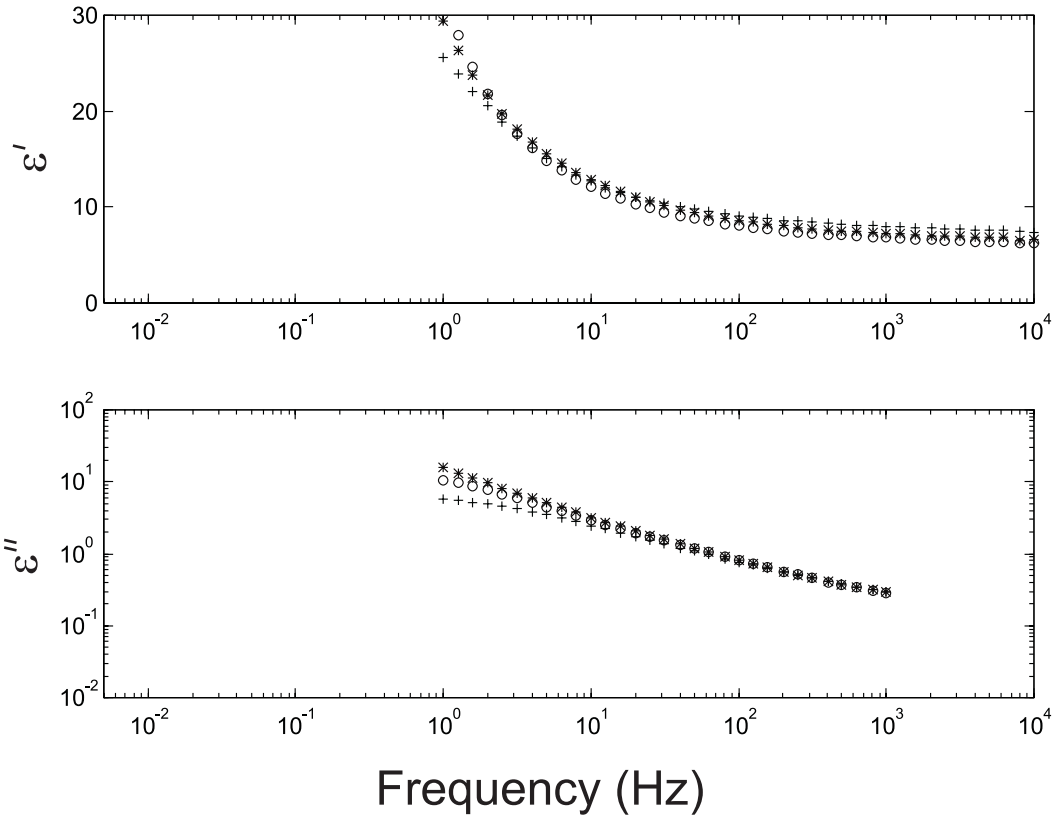

Figure 11.4: Pressboard in air – the values of real part (ε') and imaginary part (ε'') of complex permittivity obtained using the data from Figure 11.3 using calibration with respect to electrode thickness. The slope of log ε'' vs. log f is approximately -0.6, which indicates that pressboard is dispersive.

limits the spatial resolution of the sensor, and only three regions can be distinctively identified with the three wavelength sensor of Figure 4.5. Later in this chapter, Section 11.6, the knowledge of the temporal dynamics of the process helps to improve this representation when plotting moisture profiles.

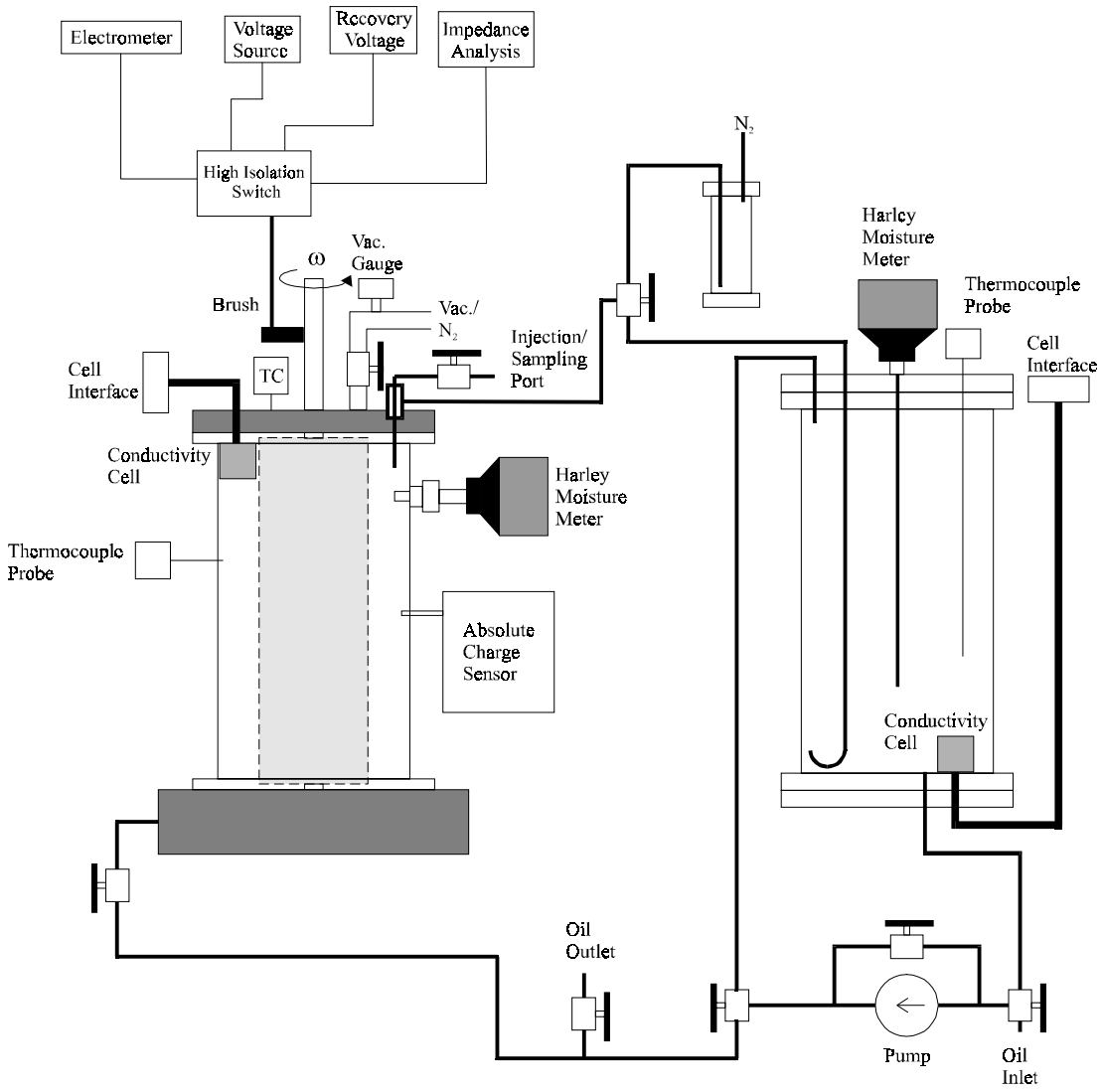

Figure 11.5: Couette facility that simulates transformer environment and is used in our experiments for measurement of transformer insulation properties. [11]

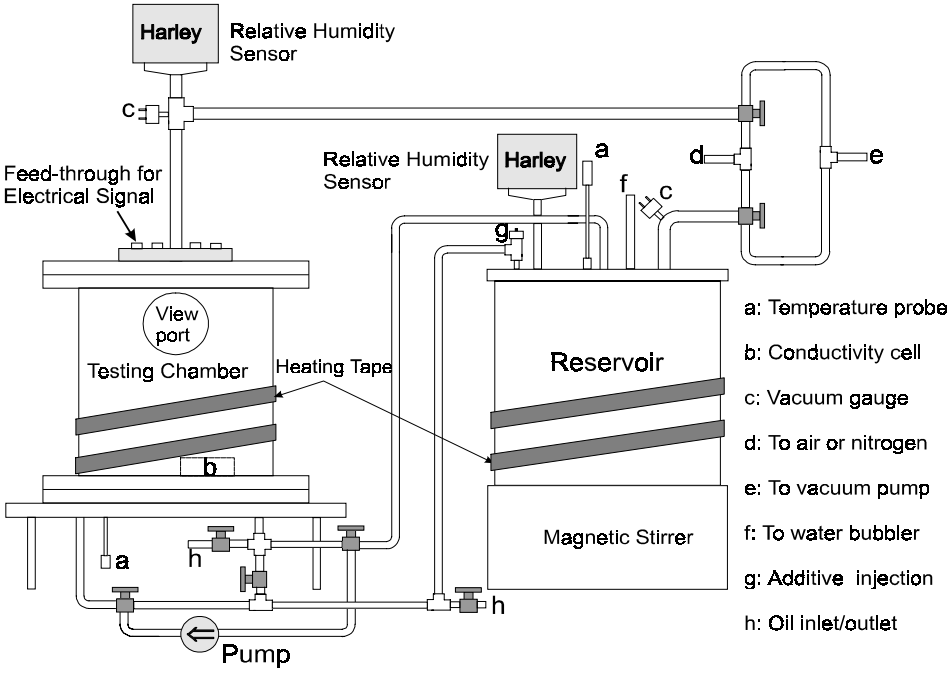

Figure 11.6: A controlled-environment experimental chamber for measurements of moisture dynamics [316].

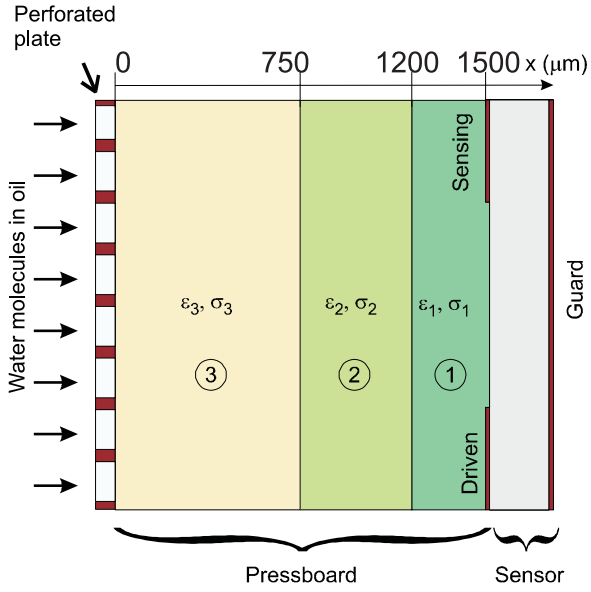

Figure 11.7: A schematic representation of the experimental arrangement. The pressboard is modeled as a three layer medium with distinct properties for each layer related to the quantity of moisture in each layer.

11.3 Forward Problem: Moisture Diffusion

11.3.1 Introduction

The response of a three-wavelength interdigital dielectrometry sensor to the moisture diffusion process in oil-impregnated transformer pressboard has been simulated using an empirical relationship between the moisture concentration and the dielectric properties of transformer pressboard. A benchmark test of the moisture diffusion process has been developed with the purpose of comparing alternative parameter estimation algorithms used in $\omega - k$ (frequency-wavenumber) dielectrometry. The results of simulation highlight characteristic features of the multi-wavelength sensor response, such as the delay of sensor response as a function of sensor wavelength from the start of the transient moisture diffusion process, the influence of moisture boundary conditions, and the relation between the signal magnitude and variations of dielectric properties. One of the parameter estimation algorithms, a linear calibrated admittance-based estimation (LCABE), has been applied to both simulated and measured data. Adequate performance of the LCABE approach in the absence of strong discontinuities of dielectric properties in the electric field penetration region is demonstrated and contrasted to an electrically shielded region case, in which the signal response becomes non-linear. The proposed approach offers significant potential for the measurement of diffusion processes in various dielectrics, especially for cases with highly irregular geometry or material structure. Measurement results from moisture diffusion process monitoring are included. Parameter estimation of measurement results with LCABE confirm its applicability to monitoring of moisture dynamics in transformer pressboard.

The preliminary measurements of the response of the three-wavelength sensor to the molecular diffusion process were presented in [316]. The goal of this study is to continue the development of parameter estimation algorithms to measure the spatial profiles of dynamically varying moisture concentration across the thickness of transformer pressboard in a controlled environment.

In the following sections, the moisture profiles are calculated assuming a nearly linear relationship between the change in sensor transcapacitance and the average amount of moisture in the adjacent pressboard volume [20]. The linearity assumption and terminal circuit parameters are widely used in many designs of relative humidity [60,138,222], gas [221], chemical [231], and biological [232,235] interdigital sensors. From the true physical representation perspective, this approach is inferior to the full-scale model-based inverse problem algorithms that use electric field modeling to relate spatially varying material properties to lumped circuit elements and electrical network terminal parameters of the sensor. However, it offers several advantages, which include simplicity, stability of parameter estimation, speed, and ability to determine moisture profiles in cases of ill-defined geometry and poor surface contact.

11.3.2 Sequence of Computations for LCABE Algorithm

Whenever a new algorithm to solve the inverse problem is being developed, it should first be tested on synthetic data, free of experimental noise and statistical measurement errors. In order to evaluate the performance of the linear calibrated admittance-based estimation (LCABE), the admittance output for various frequencies of the three-wavelength sensor as a function of time during the moisture diffusion process has been simulated using typical values of physical parameters of transformer pressboard. Then, admittance values were supplied to LCABE as the input for the inverse problem to determine moisture profile as a function of time. The sequence of this study is outlined below:

1. Simulate the moisture diffusion process by numerically solving the governing moisture diffusion equation with a finite-difference code.

2. Convert spatial moisture profiles for each measurement frequency at several distinct moments of time to the profiles of dielectric properties using measured relationships from [10].

3. Discretize the calculated dielectric property profiles with a spatial resolution significantly higher than a three layer approximation suggested by the penetration depths of the three-wavelength sensor shown in Figure 11.8.

4. Using the finite element simulation (*Maxwell* by Ansoft Corp.), generate a table of values of transcapacitance C_{12} and transconductance G_{12} for each property profile and each wavelength of the sensor.

5. For each moment of time that has an associated property profile, generate a set of six input variables (G_{12} and C_{12} for each wavelength of the three-wavelength sensor).

6. Use time curves of C_{12} and/or G_{12} to extrapolate the moisture profile at each selected moment of time using the LCABE algorithm.

7. Convert the stair-step moisture profiles to either piecewise-linear or smooth profiles, because the nature of the diffusion process requires that property profiles should not have discontinuities across layer boundaries.

8. Compare the results of the inverse problem solution with the original simulated data of moisture dynamics.

11.3.3 Sequence of Computations for Model-Based Estimation

The following sequence of computer simulation is used to estimate the performance of each specific parameter estimation algorithm using synthetic data.

1. Simulate the moisture diffusion process by solving the moisture diffusion equation for the moisture concentration as a function of time and position.

2. Convert spatial moisture profiles at several moments of time to the profiles of dielectric properties using empirical relationships from [10].

3. Calculate sensor response as a function of time for each dielectric property profile.

4. With the first stage of the parameter estimation algorithm, estimate average dielectric properties of compound layers. Each compound layer includes all individual layers within the effective penetration depth of a given wavelength.

5. Using layer thickness dependent weighting coefficients (second stage of parameter estimation algorithm), compute dielectric properties of individual layers.

6. Using empirical inverse relationships between dielectric properties and moisture from [10], compute stair-step profiles of moisture concentration.

7. Convert stair-step profiles to straight lines or convert to smooth profiles using a polynomial approximation to the stair-step profiles.

8. Compare the results of the inverse problem solution of step 7 with the original simulated data of moisture dynamics from step 1.

11.3.4 Forward Problem Solved Numerically

The forward problem simulation of calculating the equivalent circuit parameters given all material properties includes steps 1 through 5. Several alternative methods could have been used to implement each step. For example, the diffusion equation could have been solved either numerically or analytically. We chose to use a numerical solution to the diffusion equation with a constant diffusion coefficient, because in future work we plan to allow the diffusion coefficient to be a function of moisture concentration, for which analytical solutions are either difficult or not possible. Also, the conversion of moisture profiles into dielectric property profiles depends on empirical data that strongly deviate from the best fit due to a limited spatial resolution of the sensor. However, as long as one is consistent in the assumptions made for the forward problem and for the inverse problem, the performance of the inverse algorithm is assessed properly.

Diffusion Process

Figure 11.9 shows spatial profiles of moisture concentration generated with a finite difference simulation program according to a classic one-dimensional diffusion equation with a constant diffusion coefficient $D = 10^{-11}$ m^2/s:

$$\frac{\partial m}{\partial t} = D\frac{\partial^2 m}{\partial x^2}, \tag{11.1}$$

where m is moisture concentration, t is time, and x is the spatial coordinate in the direction of diffusion. The profiles are shown at 10 distinct moments of time, and the number next to each curve represents time in hours elapsed since the beginning of the diffusion process. The left boundary condition at $x = 0$ is that the moisture concentration is at a constant value, chosen to be 10 percent throughout the process. This boundary condition corresponds to the case when a relatively small amount of pressboard is placed in a very large oil container or when it is open to the atmosphere and the relative humidity of air does not vary significantly during the experiment. Since the total moisture concentration in a sealed transformer is fixed, a change in moisture level in pressboard also changes the moisture level in oil. However, a constant boundary condition is more desirable for the benchmark problem to insure simplicity and consistency of subsequent analysis. The right boundary condition at $x = 1$ mm is the zero flux across the boundary. This condition exists when the pressboard faces an impermeable wall on one side. The sensor attached to the side of pressboard provides this type of an interface.

The diffusion process starts at time zero and continues for about 30 hours. After 30 hours, a nearly flat profile is obtained. The sensor should detect nearly homogeneous properties across the entire pressboard thickness in the beginning and at the end of the simulated period of time.

The imposed boundary conditions cause steep gradients close to the left boundary and almost flat profiles close to the right boundary. Consequently, smaller wavelengths see a nearly homogeneous region, while the fringing fields from the longer wavelengths penetrate through highly inhomogeneous regions. The signal indicating the change of

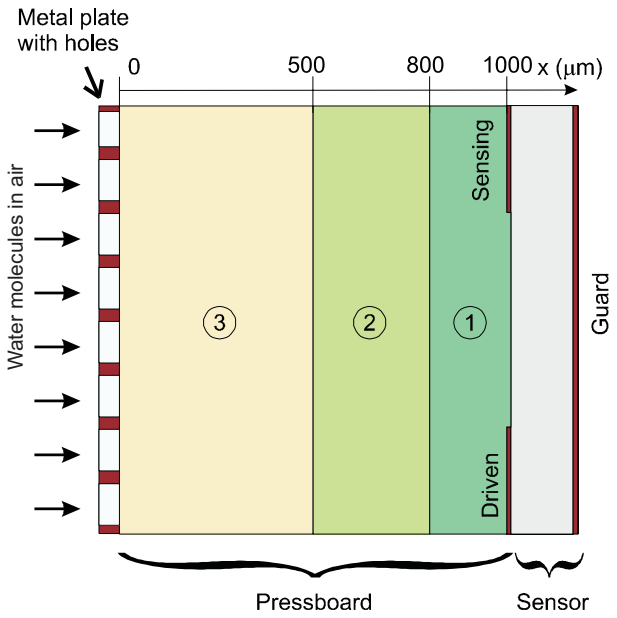

Figure 11.8: The cross-section of pressboard may be discretized into three layers. For each layer the distance from the sensor to far interface corresponds to one-fifth of each of the three spatial wavelengths of the sensor.

moisture concentration after it was stepped up at the left boundary is expected to be practically the same in regions seen by the 1.0 mm and 2.5 mm wavelengths. Since the penetration depth $\approx 0.2\lambda$ of the longest wavelength (5.0 mm) is approximately equal to the 1 mm thickness of pressboard, the signal delay for this wavelength is essentially zero.

Dielectrometry Profiles

In the next step, moisture profiles are converted into profiles of dielectric properties using semi-empirical relationships (11.2) and (11.3) available for oil-impregnated pressboard from [10, 73]:

$$\varepsilon' = \varepsilon_\infty + \varepsilon_0 \cdot 10^{-\gamma(f_T + c_m)} \cdot 10^{c_1} \left(\frac{m}{f}\right)^{-\gamma} \tag{11.2}$$

$$\varepsilon'' = \varepsilon_0 \cdot 10^{-\gamma(f_T + c_m)} \cdot 10^{c_2} \left(\frac{m}{f}\right)^{-\gamma}, \tag{11.3}$$

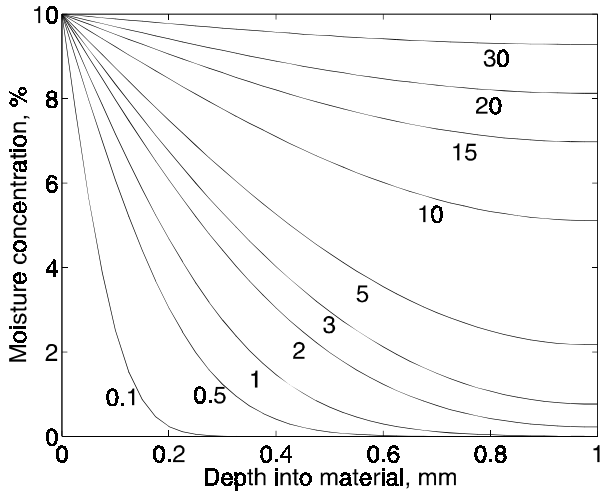

Figure 11.9: Calculated spatial profiles of moisture concentration across the 1 mm thickness of pressboard from dielectrometry measurements using $D = 10^{-11}$ m^2/s. Numbers next to the curves correspond to the time in hours at which the profile was calculated.

where $f(T) \sim E_a/kT$ is only a function of temperature T with $E_a = 0.69eV$ being the activation energy and k being Boltzmann's constant. The functional form of these relationships originates in the "universal curve" methodology [163,317,318]. The values of empirical coefficients have been obtained by curve fitting of the experimental data [10]. The following values of coefficients were found from measurements: $c_1 = -0.7798$, $c_2 = -0.4724$, $c_m = -0.684$, $f_T = 0.6$ (for temperature $T = 70°C$), $\gamma = -0.7$. The high frequency relative dielectric permittivity of transformer pressboard is assumed to be $\varepsilon_\infty = 3$. For the parameters analyzed in this problem, the relationships between the moisture and the dielectric properties are not far from linear (linear when $\gamma = -1$). Not surprisingly, the time-dependent theoretical profiles of dielectric properties look very similar to the moisture profiles. Figure 11.10 shows profiles of relative dielectric permittivity during the diffusion process using (11.2). The maximum value of $\varepsilon_r = 3.72$ is determined by the left boundary condition for moisture concentration $m = 10\%$. Clearly, this simulation excludes low frequency dispersion effects due to an electrochemical double layer, when the values of dielectric permittivity are very high in comparison with the high frequency permittivity. The moisture concentration is found

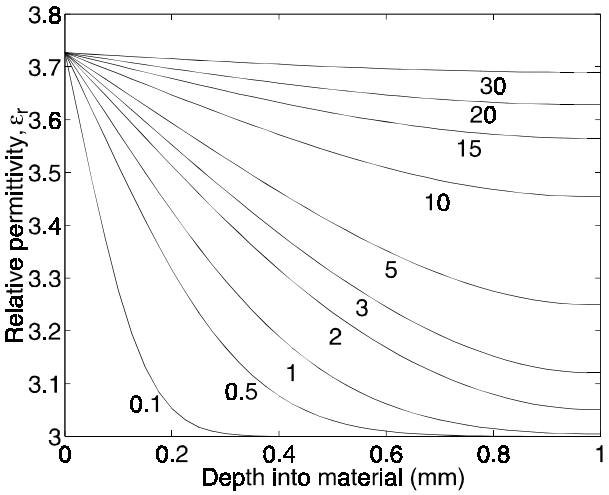

Figure 11.10: Calculated spatial profiles of relative dielectric permittivity ($\varepsilon_r = \varepsilon'/\varepsilon_0$) at 1 Hz across the thickness of pressboard from the empirical correlation of (11.2). Numbers next to the curves correspond to the time in hours for which the profile was calculated.

from (11.2)-(11.3) as

$$m = \left[\frac{\varepsilon' - \varepsilon_\infty}{\varepsilon_0} 10^{[\gamma(f_T + c_m) - c_1]}\right]^{\left(-\frac{1}{\gamma}\right)} \cdot f \tag{11.4}$$

$$m = \left[\frac{\varepsilon''}{\varepsilon_0} 10^{[\gamma(f_T + c_m) - c_2]}\right]^{\left(-\frac{1}{\gamma}\right)} \cdot f \tag{11.5}$$

Figure 11.11 shows spatial profiles of the imaginary part of complex dielectric permittivity (loss factor) obtained using (11.3). They are similar in shape to those of the real part of complex dielectric permittivity, but they span a larger range of values. For that reason, and also since the minimum value of ε'' is zero, the profiles of the loss angle, $\tan\delta = \varepsilon''/\varepsilon'$, (not shown here) are also similar in shape. For measurements at frequency f, the loss factor profiles can readily be re-calculated into conductivity profiles as $\sigma = 2\pi f \varepsilon''$. The conductivity profiles are presented separately in Figure 11.12 because they are directly related to the time variation of the transconductance G_{12} discussed later.

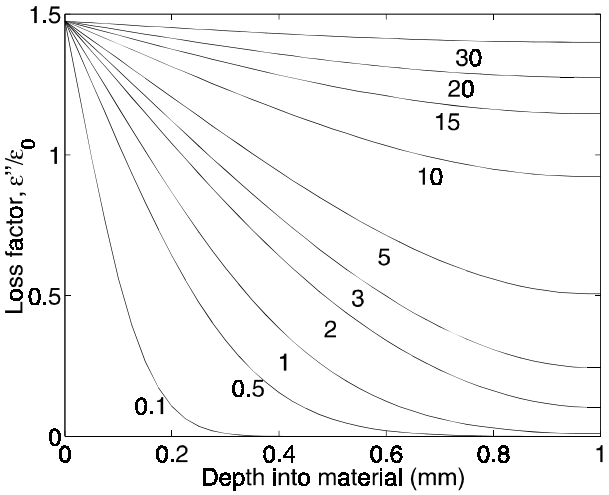

Figure 11.11: Calculated spatial profiles of loss factor at 1 Hz across the thickness of pressboard from the empirical correlation of (11.3). Numbers next to the curves correspond to the time in hours for which the profile was calculated.

Stair-step Approximation

The sensor response to gradual changes of moisture concentration has been simulated using the commercial finite-element software *Maxwell* by Ansoft Corp. The cross-section of pressboard has been broken into 20 equally thick layers, each with specified distinct values of relative permittivity and conductivity, so that for each moment of time this spatial profile would be approximated in a fashion shown in Figure 11.13. The broken curve shows the original profile of relative dielectric permittivity of pressboard at $t = 1$ hour, and the solid line shows a corresponding 20 layer stair-step approximation. This representation is significantly more accurate than a three-step representation available from the three-wavelength sensor. The computational error introduced by the stair-step representation is negligible considering the maximum accuracy available from the three-wavelength sensor.

Figure 11.14 shows the finite element mesh generated by *Maxwell* for the cross-section of the 2.5 mm wavelength sensor. The density of the mesh is higher at the electrode edges, in the regions of significant electrical field enhancement. The location and shape of triangles in the upper part of the pressboard cross-section reflects the

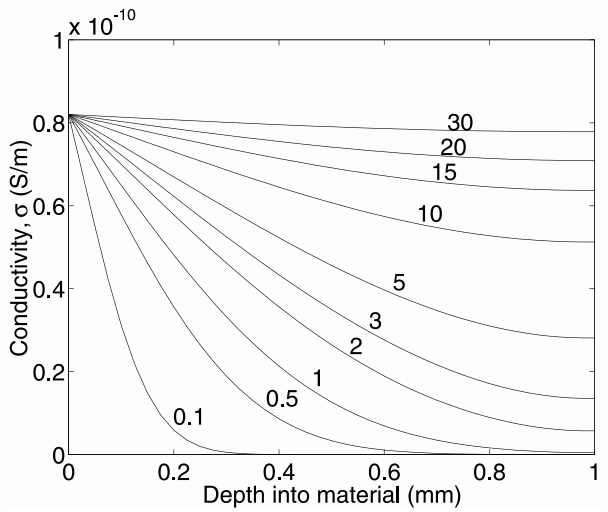

Figure 11.12: Calculated spatial profiles of conductivity at 1 Hz across the thickness of pressboard from dielectrometry measurements. Numbers next to the curves correspond to the time in hours for which the profile was calculated.

layered representation illustrated in Figure 11.13. For the purposes of this simulation, the thin layer between the driven and sensing electrodes whose thickness is equal to the electrode height (14 μm) is assigned the same properties as the insulation layer directly above it. Other simulations could allow this cavity to have dielectric properties of oil for oil-impregnated pressboard or air for oil-free pressboard.

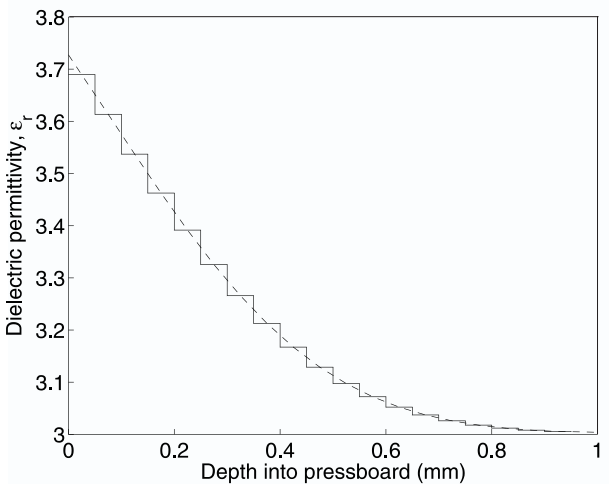

Figure 11.13: Twenty layer stair-step representation of a continuous spatial profile of relative dielectric permittivity of pressboard at $t = 1$ hour.

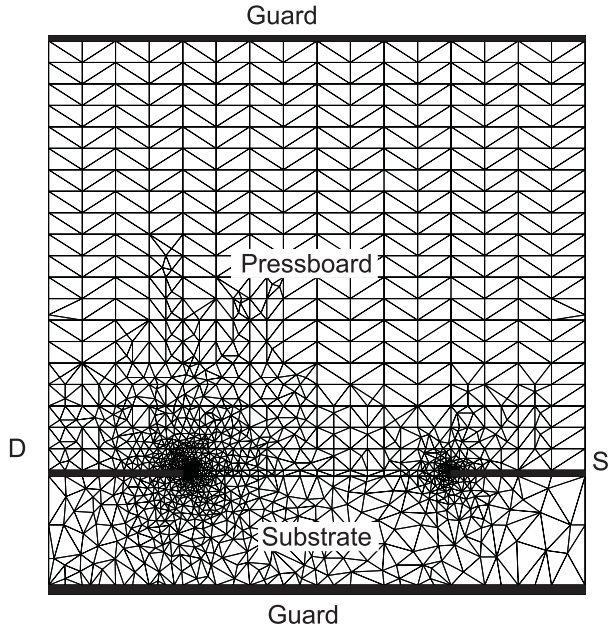

Figure 11.14: Finite-element mesh for the 2.5 mm wavelength electrode cross-section with the guard electrodes at the same potential as the sensing electrode and where spatially varying properties of transformer pressboard are modeled through a twenty layer representation.

11.3.5 Results of Numerical Simulation

The admittance between the driven and sensing electrodes for each spatial wavelength is calculated for each moment of time indicated in Figure 11.9. Two cases are considered, corresponding to our experimental setups. The first case assumes that the region above the pressboard is of semi-infinite extent and has dielectric properties of Teflon, $\varepsilon_r = 2.1$. The second case assumes that a guard plane at the same potential as the sensing electrode is positioned at the top of pressboard (for the sensor and pressboard orientation shown in Figure 11.14). One experimental setup uses a guarded perforated steel plate to provide mechanical support while allowing access of the external fluid (usually air or transformer oil) to pressboard. Alternatively, a perforated Teflon plate has been used. A third case, not analysed here, is direct access of the external fluid to the pressboard-fluid interface, without a perforated plate. In this case, the signal dynamics should be similar to that in case one, as the Teflon plate is closer in dielectric properties to a dielectric fluid than to a metal plate.

A major distinction exists for the conductors and insulators positioned at the top of the 1 mm thick pressboard cross-section. The presence of a conducting sheet significantly alters the distribution of fringing electric fields throughout the thickness of pressboard, especially in the upper region. This, in turn, affects the values of transcapacitance C_{12} and transconductance G_{12} between the driven and sensing electrodes. Table 11.1 shows values of transconductance G_{12} and transcapacitance C_{12} computed for all three wavelengths assuming a 50 percent metallization ratio (equal width drive and sense electrodes), one meter long meander length, and a top insulating layer of infinite thickness with a relative dielectric permittivity $\varepsilon_r = 2.1$ (Teflon). Table 11.2 shows the values of G_{12} and C_{12} computed for the same case, but with the top insulating layer being replaced by a perfect conductor. Although graphical representation of this data is also included and analyzed below, the response is tabulated because these cases are expected to serve as benchmark tests for alternative parameter estimation algorithms.

	$\lambda = 1.0$ mm		$\lambda = 2.5$ mm		$\lambda = 5.0$ mm	
Time, t (h)	G_{12} (pS)	C_{12} (pF)	G_{12} (pS)	C_{12} (pF)	G_{12} (pS)	C_{12} (pF)
0	0.0000	16.5209	0.0000	10.3963	0.0000	7.0421
0.1	-0.0107	16.5195	0.1381	10.4090	0.6713	7.1047
0.5	0.0011	16.5197	0.6135	10.4520	1.8974	7.2173
1	0.4254	16.5529	1.6345	10.5389	3.2680	7.3356
2	3.5564	16.7989	4.8608	10.7960	5.9749	7.5466
3	7.8792	17.1368	8.4096	11.0657	8.4174	7.7200
5	15.7712	17.7502	14.4998	11.5137	12.3269	7.9809
10	28.3175	18.7188	24.1318	12.2030	18.4244	8.3686
15	35.0905	19.2391	29.4096	12.5739	21.8070	8.5771
20	39.0242	19.5407	32.5008	12.7893	23.8041	8.6982
30	42.8133	19.8306	35.4947	12.9967	25.7488	8.8146

Table 11.1: Nominal values of transconductance G_{12} and transcapacitance C_{12} for all three wavelengths calculated for 11 distinct moments of time during the diffusion process assuming a top insulating layer of semi-infinite extent with $\varepsilon_r = 2.1$ (Teflon).

	$\lambda = 1.0$ mm		$\lambda = 2.5$ mm		$\lambda = 5.0$ mm	
Time, t (h)	G_{12} (pS)	C_{12} (pF)	G_{12} (pS)	C_{12} (pF)	G_{12} (pS)	C_{12} (pF)
0	0.0000	14.0861	0.0000	5.6639	0.0000	1.3092
0.1	-0.5872	14.0140	-0.9099	5.5501	-0.4919	1.2453
0.5	-1.3645	13.9306	-1.8895	5.4387	-0.9159	1.1922
1	-1.5941	13.9055	-2.1000	5.4152	-0.9600	1.1869
2	0.5577	14.0798	-0.8331	5.5293	-0.5285	1.2321
3	4.1422	14.3718	1.1481	5.7023	0.0800	1.2904
5	10.9672	14.9225	4.8925	6.0143	1.2252	1.3886
10	21.9644	15.7952	11.0511	6.4958	3.1819	1.5320
15	27.9077	16.2604	14.4556	6.7488	4.3084	1.6043
20	31.3596	16.5289	16.4557	6.8938	4.9841	1.6448
30	34.6853	16.7866	18.3975	7.0324	5.6495	1.6829

Table 11.2: Nominal values of transconductance G_{12} and transcapacitance C_{12} for all three wavelengths calculated for 11 distinct moments of time during the moisture diffusion process assuming a perfectly conducting top layer.

To avoid confusion, we should comment on the fact that the transconductance G_{12} in column 2 of Table 11.1 and in columns 2, 4, and 6 of Table 11.2 sometimes assumes negative values. This does not violate any physical laws and does not require any special assumptions about the physics or electrochemistry of the process. The negative values of transconductance (as well as transcapacitance) arise from the fact that a multi-electrode distributed system with spatially varying material properties is being represented as the simple lumped element circuit of Figure 1.4 that does not have the same topology as the sensor. In particular, there is a parallel capacitance and conductance from the interface between drive and sense electrodes to the backplane guard electrodes that at low frequencies can result in negative values of C_{12} and G_{12} in the π-equivalent circuit. Additional discussion to clarify this issue is available in [27] and in Section 8.2 of this thesis.

The simulated change of capacitance with time, from values in Tables 11.1 and 11.2 are shown for each wavelength in Figures 11.15(a) and 11.15(b), respectively without and with a metal top plate. The absolute value of transcapacitance increases as the spatial wavelength decreases for the same total meander length. Also, the absolute value of C_{12} decreases with the introduction of the perfect conductor as a top plate. Intuition supports this result: the conductor terminates some of the electric field lines originating at the driven electrode which would have otherwise reached the sensing electrode. So, even though the total capacitive energy stored in the system increases, the capacitive coupling between the driven and sensing electrodes decreases because of redirection of fringing electric field lines.

For the purposes of employing the LCABE algorithm, the time varying capacitive sensor response should be normalized to common base values, which would later be related to moisture concentration base values. First, consider normalization to the starting value, shown in Figure 11.16:

$$C_{12ns} = \frac{C_{12}(t)}{C_{12}(t=0)}. \tag{11.6}$$

The *a priori* number at $t = 0$ is available because the entire pressboard region is

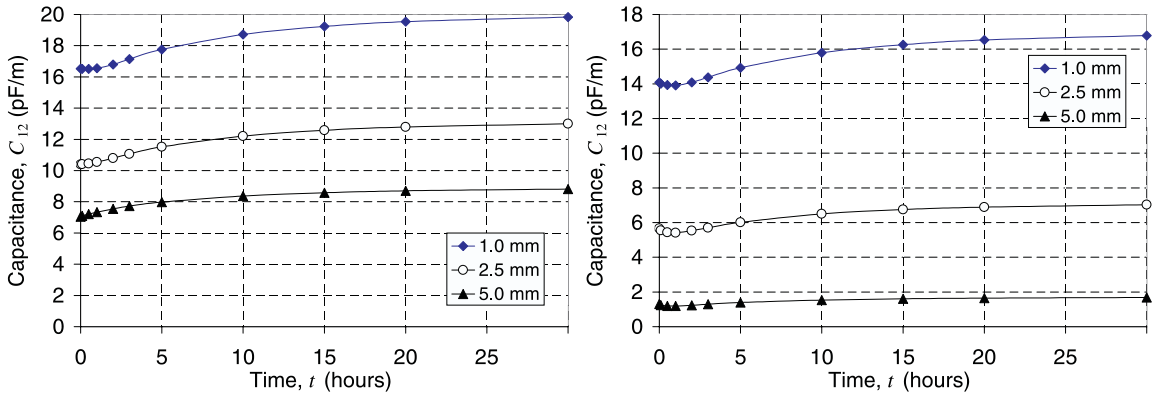

(a) without metal top plate

(b) with metal top plate

Figure 11.15: Simulated variation of capacitance per one meter length during moisture diffusion calculated using the half-cell presentation as shown in Figure 11.14.

considered uniform before the diffusion process starts. Therefore, one may want to use the starting value of capacitance of each wavelength as the normalization factor. Each curve in Figure 11.16 was obtained by dividing entries in Figure 11.15 by the corresponding curve starting value, for example, by $C_{12} = 7.0421$ pF/m in Table 11.1 for the 5.0 mm wavelength curve in Figure 11.16(a). This way of plotting emphasizes some salient features of the process dynamics. The relative change of capacitance increases with wavelength because the ratio of the spatial wavelength to the substrate thickness approximately determines what fraction of energy is stored in the pressboard. Since the substrate thickness does not change with the wavelength in this sensor design, the final normalized values of capacitance differ at the end of the diffusion process. The only exceptions are the 5.0 mm and 2.5 mm wavelengths in Figure 11.16(a), whose values are approximately equal at $t = 30$ hours. This happens because a small part of capacitive energy associated with the 5.0 mm wavelength is stored in the top insulating layer, which reduces the fraction of the electric field lines that go only through the pressboard. In other words, if the thickness of pressboard was higher, the distribution of the final normalized values of capacitance C_{12ns} in Figure 11.16(a) would be similar to that observed in Figure 11.16(b).

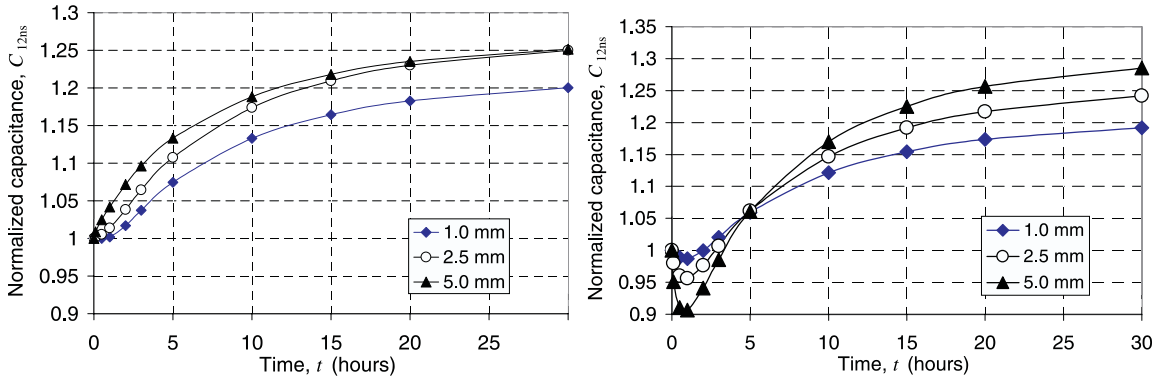

(a) without metal top plate

(b) with metal top plate

Figure 11.16: Change of normalized capacitance C_{12ns} during the diffusion process with normalization to the starting value for each of the three wavelengths as given in (11.6).

Figure 11.16 illustrates the delay difference with wavelength. In case (a), the 5.0 mm wavelength reacts to changes in moisture concentration immediately, whereas the 1.0 mm wavelength goes through the inflection point, experiencing a delay on the order of 0.5 hours. In case (b), all wavelengths respond immediately, although with different intensity, because the zero order spatial Fourier harmonic is strongly affected by the large increase in conductivity and permittivity due to the presence of moisture in the upper region of the pressboard cross-section. Another way to look at this is to say that the fringing electric field lines from the drive electrode to the top plate are affected immediately by the increase of conductivity and dielectric permittivity at the top.

Another important feature of the time profiles in Figure 11.16(b) is the initial decrease of capacitance during the first three hours of the diffusion process. It may seem counter-intuitive at first, because the average value of the relative dielectric permittivity grows continuously. In this case, the initial reduction of capacitance is due to increasing conductivity in the upper region. Some fringing electric field lines that would previously follow an arc between the driven and sensing electrode now are drawn into the high conductivity region and terminate on the top plate.

Another possible way to normalize the change of capacitance is by using *a pos-*

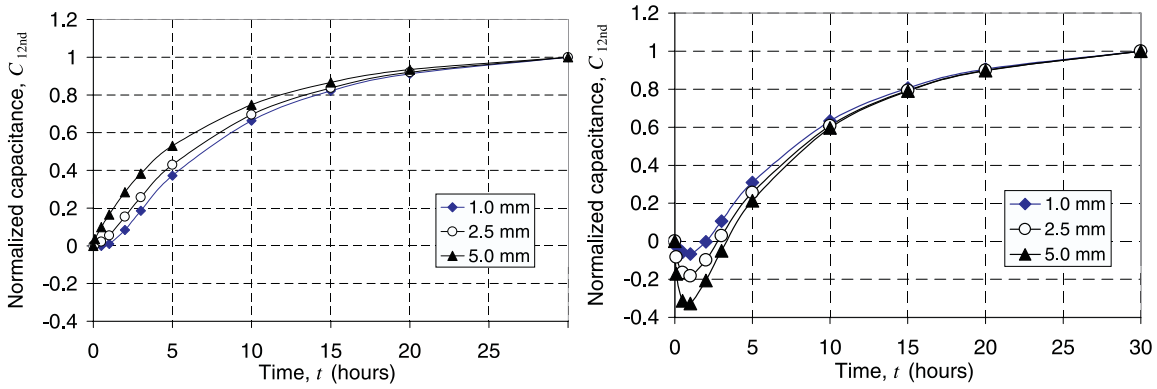

(a) without metal top plate

(b) with metal top plate

Figure 11.17: Change of normalized capacitance C_{12nd} during the diffusion process with normalization to the difference between the final and the starting values for each of the three wavelengths as given in (11.7).

teriori information. Figure 11.17 shows the same signal curve linearly normalized to the difference between the final and the starting value, so that the final value of the normalized signal is equal to 1 and the starting value is equal to 0:

$$C_{12nd} = \frac{C_{12}(t) - C_{12}(t=0)}{C_{12}(t=\infty) - C_{12}(t=0)}. \tag{11.7}$$

Figure 11.17(a) exhibits similar features as Figure 11.16(a). The speed of the response growth increases with the spatial wavelength. At each moment of time, except for the initial and final values, the magnitude of the normalized capacitance C_{12nd} is the highest for the 5.0 mm wavelength and the lowest for the 1.0 mm wavelength. From the perspective of mapping the range of capacitance values to the range of moisture values, the representation in Figure 11.17(a) is more advantageous than that in Figure 11.16(a) because it allows direct linear mapping in which the average signals from each region of the pressboard retain their relative relationships. On the other hand, the relative positioning of normalized signal amplitude is reversed in Figure 11.17(b) with respect to their counterparts in Figure 11.17(a). A direct linear mapping to moisture values would result in non-physical negative moisture concentration values early in the simulation.

Before we turn our attention to mapping of capacitance dynamics to moisture dynamics, we should also review the changes of the interelectrode transconductance during the same diffusion process. It is well known that the local bulk conductivity of transformer pressboard changes by several orders of magnitude during typical moisture concentration transients [73], whereas the real part of the complex dielectric permittivity varies in a comparatively narrow range (at a given frequency). Figure 11.18 reflects this difference. The initial conductance values are zero, whereas the final values are on the order of tens of picosiemens.

The effect of the metal top plate is clearly pronounced. The distribution of the final values of G_{12} is much wider for case (b) in Figure 11.18. This same effect has been observed in Figure 11.15 for the capacitance C_{12} values. The intersection of curves in Figure 11.18(a) at about three hours from the beginning of the diffusion process that leads to the reversal of the wavelength sequence in their signal's relative magnitude for each period of time is easy to interpret. Given an infinitely thick homogeneous material, the conductance decreases with the wavelength increase, so when the property distribution becomes nearly homogeneous at time $t = 30$ hours, the conductance increases from the 5.0 mm wavelength to the 1.0 mm wavelength. However, in the beginning of the process, when the moisture has only partially diffused into the pressboard, the conductivity in the upper layers is only seen by the longer wavelengths. The two competing factors equalize at time $t \approx 3$ hours.

To parallel data representation shown in Figure 11.17, the conductance plots are normalized to their final value (since the starting value is zero). Figure 11.19 shows that the results of the conductance normalization are very similar to the results of the capacitance normalization, including the reversal of the curve sequence between cases (a) and (b). The difference between the curves for individual wavelengths within the same top plate case is slightly less pronounced for the conductance, primarily because the growth over several orders of magnitude has been normalized to the linear [0;1] interval. Logarithmic representation of such data will be explored separately.

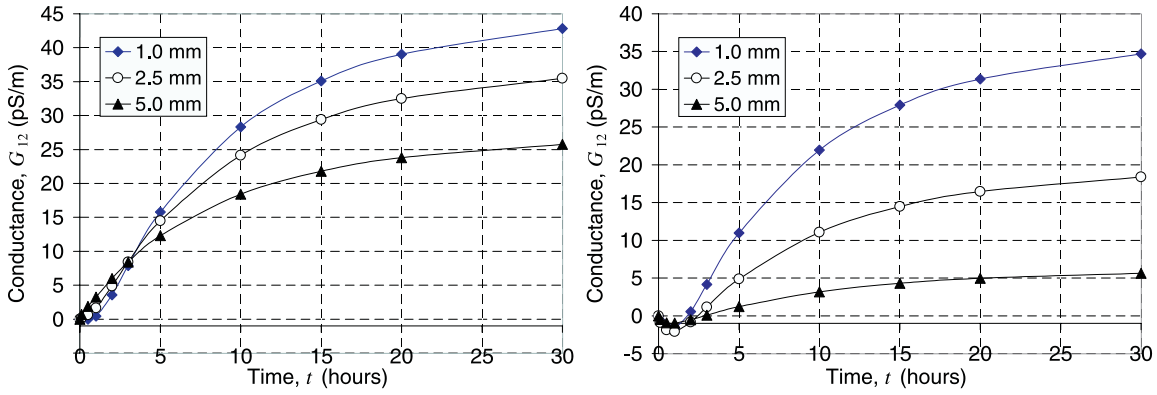

(a) without metal top plate (b) with metal top plate

Figure 11.18: Simulated variation of conductance during moisture diffusion on per meter length basis calculated using a half-cell representation as shown in Figure 11.14.

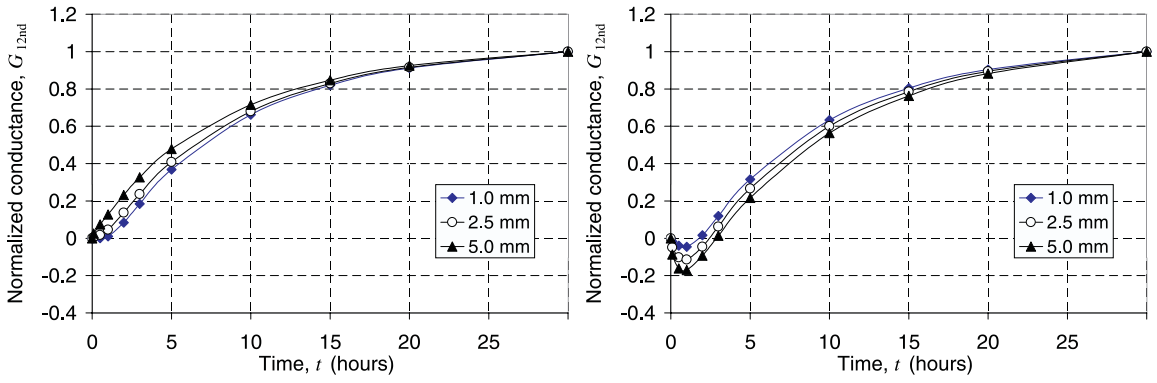

(a) without metal top plate (b) with metal top plate

Figure 11.19: Change of conductance during the diffusion process with normalization to the final value for each of the three wavelengths, $G_{12nd} = G_{12}(t)/G_{12}(t = \infty)$.

11.4 Estimation with LCABE Algorithm

11.4.1 Assumption of Linearity

The simplest type of mapping from the interdigital sensor output usually assumes a linear relationship between the sensor capacitance, conductance, impedance, admittance, or resistance and the physical variable of interest (e.g. [225, 226, 233]). The advantages of such an approach include its inherent simplicity, stability, and speed. The disadvantages are numerous. Only relatively simple cases of spatial property distributions can be treated; the physics and chemistry of underlying phenomena are not fully represented; *a posteriori* information about the signal and frequent re-calibration may be necessary; mass transfer in the bulk of material is reflected in the signal hysteresis.

The assumption of linearity for the case analyzed here is reasonable for relatively small variations for moisture concentration, and when the outer boundary moisture concentration is available from auxiliary sensor measurements. Bringing a perfect conductor in the vicinity of the sensor head significantly distorts the otherwise adequate linear relationship between moisture concentration and capacitance C_{12} as was illustrated in Figures 11.15 through 11.19. Figure 11.20 shows the time variation of average moisture concentration detected by different electrode pairs. These profiles have been generated by a linear mapping of time profiles of the normalized capacitance C_{12nd} in Figure 11.17 from the [0; 1] interval to moisture concentration in the interval [0;10 %]. In the field measurement, the upper limit of moisture concentration can be provided by an auxiliary moisture sensor immersed in transformer oil, using oil-pressboard equilibrium curves.

Figure 11.20 shows that such a mapping performs adequately for case (a), but produces negative, non-physical values of moisture concentration in case (b). Also, the sequence of curves in case (b) does not reflect average moisture concentrations in each layer of transformer pressboard because the normalized values decrease below the starting value initially. For that reason, only case (a) is analyzed from this point.

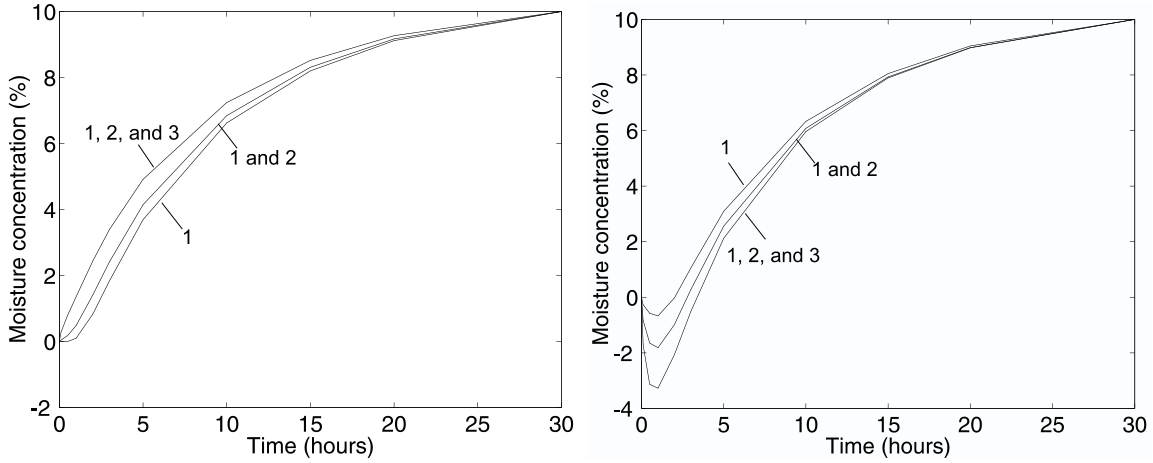

(a) without metal top plate

(b) with metal top plate

Figure 11.20: Time profiles of average moisture concentration calculated from simulated capacitance curves in Figure 11.17. The numbers next to the curves indicate the regions shown in Figure 11.8 penetrated with a corresponding spatial wavelength. The calculated moisture in part (b) is not physical at early time because of the negative moisture concentration values.

By the nature of the mapping, the initial ($t = 0$) and final ($t = 30$ hours) moisture concentration profiles are guaranteed to be flat and assume extreme values of the moisture concentration interval [0;10 %].

11.4.2 Stair-Step Profiles

From three-wavelength computer simulations, Figure 11.21 shows the calculated three-layer stair-step spatial profiles of moisture concentration at selected moments of time that directly correspond to the time profiles in Figure 11.20a. Time in hours is indicated above each curve at each of the three layers of Figure 11.8 selected to represent pressboard thickness. The stair-step profiles provide intermediate, crude estimates of moisture concentration. For clarity of graphical presentation, the steps are plotted so that the level in the region 500 – 800 μm shows the average level at the 500 – 1,000 μm region. Similarly, the level in the region 0 – 500 μm shows the average level at the 0 – 1,000 μm region. The 800 – 1000 μm region shows the average moisture level in

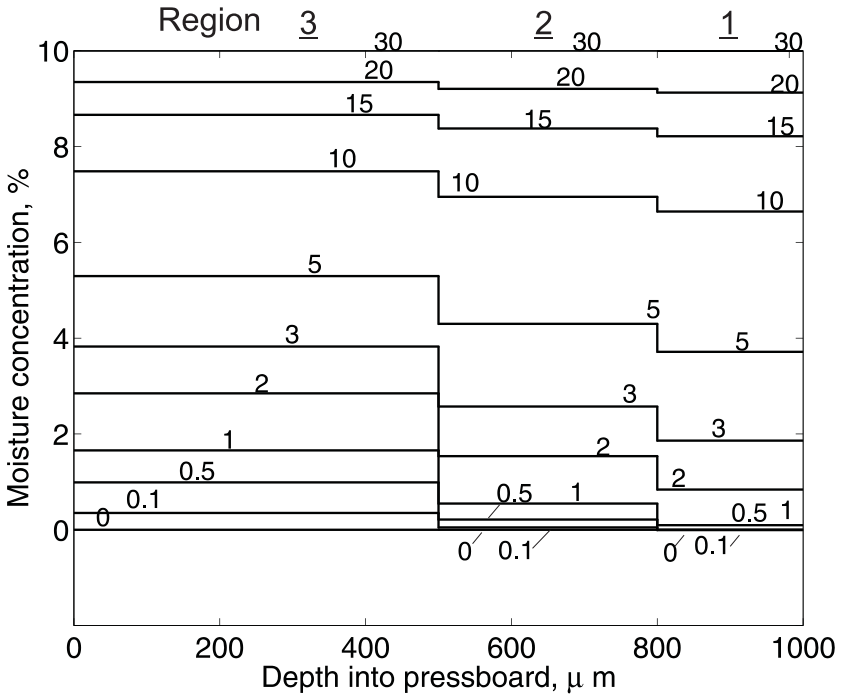

Figure 11.21: Stair-step profiles of average moisture concentration for selected moments of time in hours plotted using the results in Figure 11.20(a), where the moisture values in Region 3 are obtained from curve (1, 2, and 3), in Region 2 from curve (1 and 2), and in region 1 from curve (1).

the layer adjacent to the sensor. Appropriate weighting of these levels to reflect actual changes in each region is achieved in the next step by exploiting the outer boundary condition value at x=0. However, even at this point, the adequacy of the proposed approach is demonstrated as the moisture concentration decreases from left to right, as expected from the physical model.

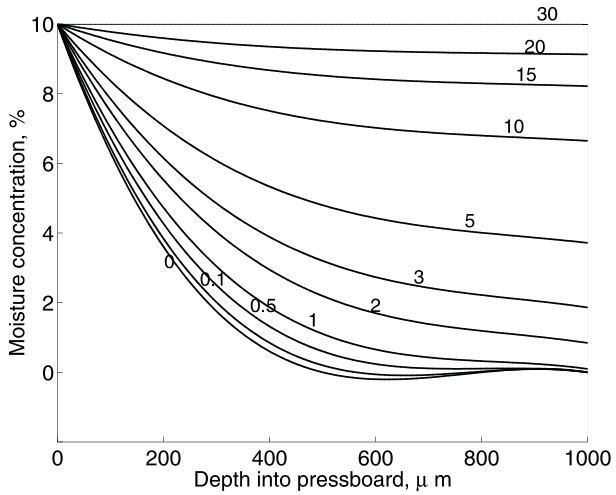

Figure 11.22: Smoothed continuous profiles of moisture concentration with an imposed 10% constant moisture concentration boundary condition at $x = 0$ using a polynomial approximation of profiles in Figure 11.21. Profiles do not agree well with those of Figure 11.9 at early times ($t < 1$ hour) because of the large gradients near $x = 0$ that are not resolvable by the TWS.

11.4.3 Continuous Profiles

Additional information about the physical process is always valuable when solving inverse problems. Since the diffusion of moisture is being analyzed, we can impose a continuity requirement on each moisture profile. The discontinuities in Figure 11.21 are due to the spatial discretization of profile representation with the three-wavelength sensor shown in Figure 11.8. Also, the left boundary condition at $x = 0$ may be available from auxiliary sensor measurements of oil moisture. In this benchmark problem, the left boundary condition is a constant moisture concentration of 10 percent. Stair-step profiles in Figure 11.21 are first converted into point-wise profiles by assuming average concentration values at the region boundaries and a 10% concentration at the left boundary. Then the moisture profiles are approximated with a fourth-order polynomial in x. The result of this process is presented in Figure 11.22. The resultant profiles are close to the original ones shown in Figure 11.9 for all times except the very early ones. Very high gradients in the outer regions could not be accurately characterized due to the limited spatial resolution of the three-wavelength sensor.

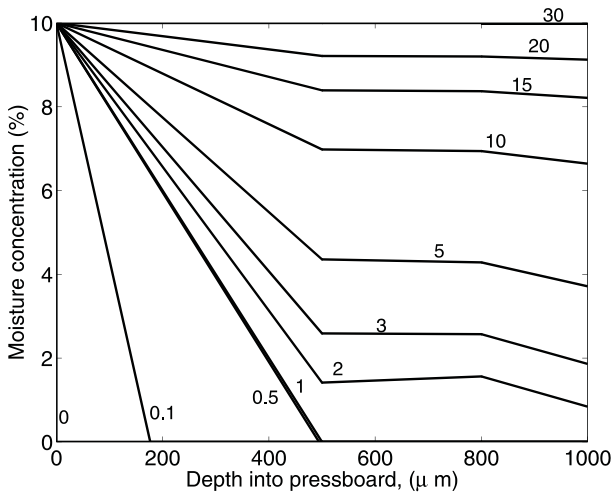

Figure 11.23: Piecewise-continuous moisture concentration profiles generated with the imposed additional signal magnitude conservation requirement.

To address the steep gradients issue, one can incorporate a conservation of signal magnitude requirement while interpreting the stair-step parameter estimation provided by the three-wavelength sensor. It may be necessary to move the coordinates of the point that separates regions with dissimilar properties, which we will refer to as the collocation point (see Section 11.5.8 for more details on collocation points). Figure 11.23 shows piecewise-continuous spatial profiles in which the collocation point departs from the region boundary and shifts to the left if the corresponding flat profile region in Figure 11.21 is at a very low moisture value. For example, the area of the triangle in Figure 11.23(a) at time 0.5 hours is proportional to the area under the corresponding rectangle in Figure 11.21 that extends from $x = 0$ to $x = 500\mu$m. On the other hand, if the area of the triangle is larger than the rectangle area times the proportionality factor, the collocation point remains at the interlayer boundary. The proportionality factor should be selected based on the spatial rate of decay of the electrical field in the material at increasing distances from the sensor head. In the first approximation chosen here, the triangle area has to be five times as large as the rectangle area. The proportionality factor is somewhat dependent on material properties and has been selected empirically based on several simulations.

11.5 Model-Based Estimation

11.5.1 Background

This section of this thesis concentrates on several aspects of solving the multi-wavelength interdigital dielectrometry inverse problem. This is an ill-posed problem that requires estimation of properties of multiple material layers using values of terminal capacitance and conductance between interdigital electrodes of varying spatial periodicity. The limitations of existing algorithms are discussed. The performance of a new parameter estimation algorithm is evaluated using a benchmark forward problem computed previously. The algorithm is used to estimate smooth profiles of dielectric properties and moisture concentration across the thickness of oil-impregnated transformer pressboard using stair-step, piecewise linear, and polynomial approximations. Application of this technological approach to other problems where diffusion processes must be monitored holds significant potential.

11.5.2 Sequence of Simulation

The following sequence of computer simulations is used to estimate the performance of each specific parameter estimation algorithm using synthetic data.

1. Simulate the moisture diffusion process by solving the moisture diffusion equation for the moisture concentration as a function of time and position.

2. Convert spatial moisture profiles at several moments of time to the profiles of dielectric properties using empirical relationships from [10].

3. Calculate sensor response as a function of time for each dielectric property profile.

4. With the first stage of the parameter estimation algorithm, estimate average dielectric properties of compound layers. Each compound layer includes all individual layers within the effective penetration depth of a given wavelength.

5. Using layer thickness dependent weighting coefficients (second stage of parameter estimation algorithm), compute dielectric properties of individual layers.

6. Using empirical inverse relationships between dielectric properties and moisture from [10], compute stair-step profiles of moisture concentration.

7. Convert stair-step profiles to straight lines (using signal magnitude conservation requirements) or convert to smooth profiles using a polynomial approximation to the stair-step profiles.

8. Compare the results of the inverse problem solution of step 7 with the original simulated data of moisture dynamics from step 1.

11.5.3 Alternative Algorithms

For the purpose of moisture profiling, it is also possible to use adaptive optimization. The stair-step moisture profiles shown in Figure 11.24 have been estimated from three-wavelength sensor simulations using a marching optimization algorithm with a different set of simulated data [20]. A successful estimation, however, required that smooth dielectric property profiles are approximated with three-layer stair-step profiles before computing interelectrode capacitance, otherwise the errors accumulated due to stair-step representation lead to either a lack of convergence or completely erroneous estimations for outer layers. In other words, even when measurements are made with absolute precision and the geometry of the sensor is modeled with no error, one should expect differences between the simulations and the measurements because a stair-step representation of property profiles that are smooth in reality introduces a systematic error in the simulations.

The approximate stair-step profiles shown in Figure 11.24 do not reflect well the actual distribution of moisture. In reality, the moisture concentration profile is a continuous function. A piecewise linear approximation would be better than a stair-step approximation. The transformation from the discontinuous to the continuous function

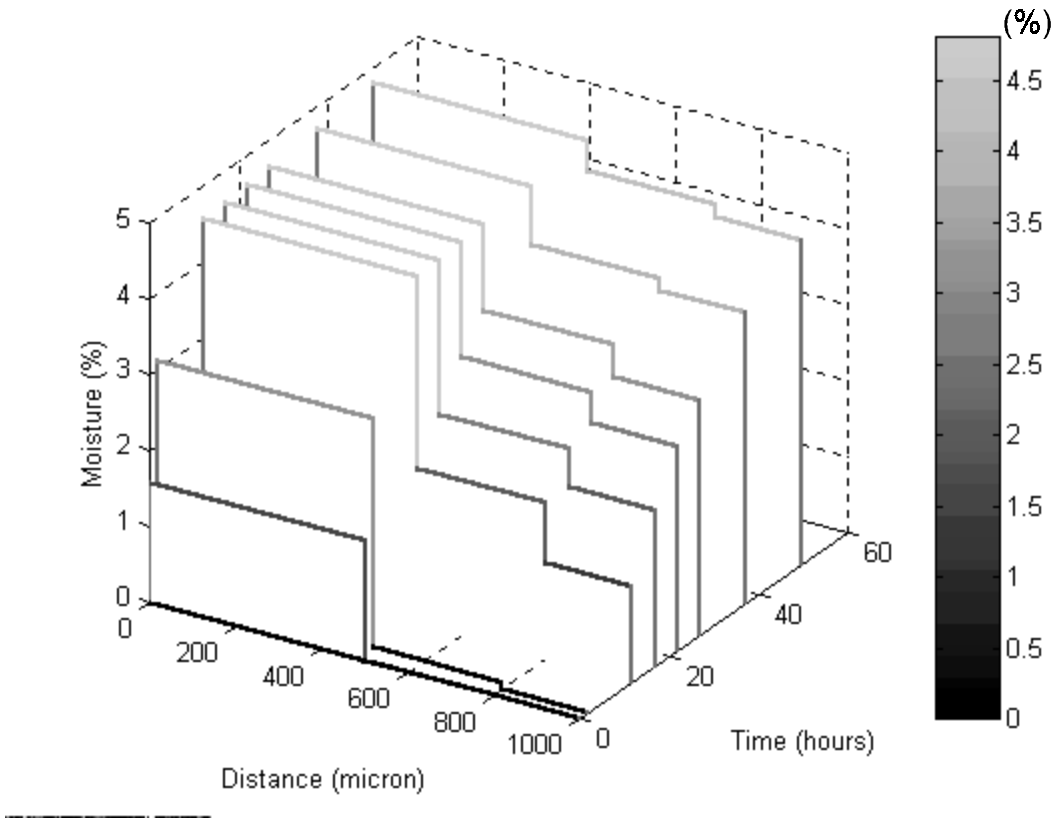

Figure 11.24: A successful case of a three-region inverse problem calculation using an iterative optimization approach with synthetic data. The gray scale refers to the local pressboard moisture concentration in %.

should be made taking signal magnitude conservation into account. The outside moisture boundary concentration is known from separate moisture measurements in the oil using an oil moisture sensor and from standard equilibrium curves between the oil and pressboard.

11.5.4 Simulated Measurement Setup

Figure 11.25 shows the critical part of the experimental setup simulated in this study. The 1 mm thick oil-impregnated transformer pressboard is positioned next to the sensor head. The holes in the compression plate provide a path for moisture molecules to enter

the pressboard from the left side (x=0).

Even though the change of the pressboard properties through its thickness is gradual in the discussed experiment, the pressboard in the model is represented as a three-layer medium with each layer thickness corresponding to the effective penetration depth of $\lambda/5$ for each wavelength λ of the sensor. In other words, the number of wavelengths limits the spatial resolution of the sensor, and only three regions can be distinctively identified with the three-wavelength sensor. Later in this thesis, the knowledge of the physics of the process helps to improve this representation when plotting moisture profiles (Section 11.5.8). At the first stage of parameter estimation, we evaluate properties of compound layers, shown in Figure 11.25(a). The compound layers occupy the region between the sensor and the $\lambda/5$ penetration depth into pressboard. At the second stage, the compound layer properties are decomposed into the properties of individual layers, shown in Figure 11.25(b). The individual layers occupy the space between two neighboring $\lambda/5$ penetration depths.

11.5.5 Compound Layers

In Figure 11.25(a) the 1 mm sensor determines the average dielectric properties (ε_1, σ_1) of the 200 μm thick layer; the 2.5 mm sensor determines the average dielectric properties (ε_{12}, σ_{12}) of the 500 μm thick layer; and the 5 mm sensor determines the average dielectric properties (ε_{123}, σ_{123}) of the 1000 μm thick layer. Figure 11.26 shows calculated time profiles of relative dielectric permittivity ε_r estimated for each wavelength from transcapacitance simulations, assuming a homogeneous pressboard within the sensing distance of each wavelength as shown in Figure 11.25a. Since in reality the dielectric permittivity is highest near the interface where moisture enters the pressboard, longer wavelengths at this point underestimate the average value of the relative dielectric permittivity in a corresponding compound layer. Nevertheless, the dynamics of the process is properly reflected. The 1 mm wavelength exhibits a signal delay of about 0.5 hour until the moisture reaches the inner parts of pressboard,

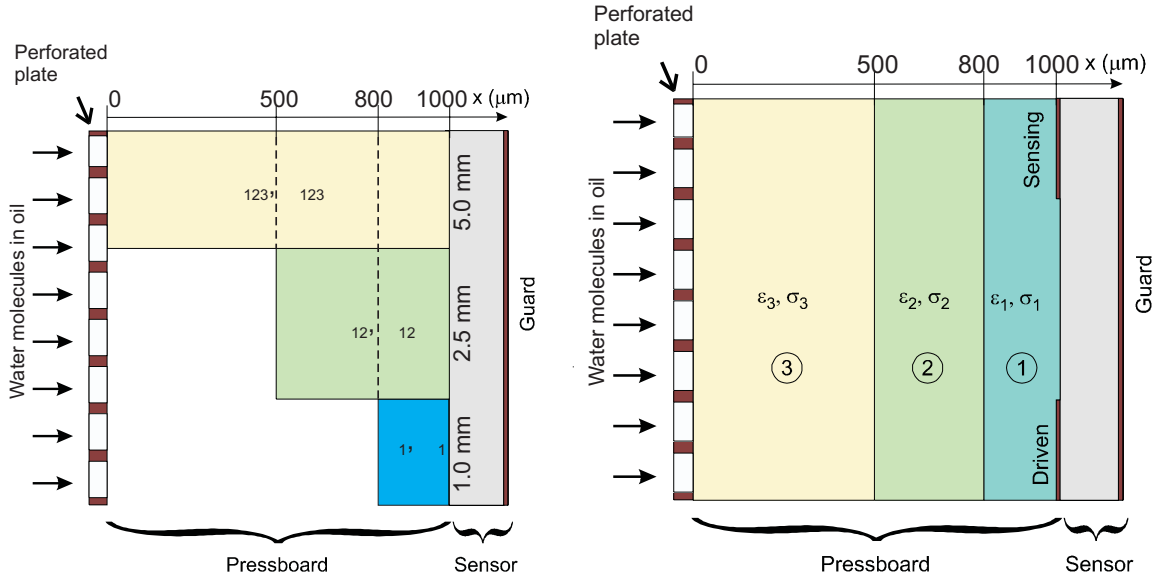

(a) compound layers as seen by each of three wavelengths

(b) individual layers for the half-period cell

Figure 11.25: A schematic representation of the experimental arrangement. The pressboard is modeled as a three layer medium with distinct properties for each layer related to the quantity of moisture in each layer. In experiments and computer simulations the perforated plate is made of Teflon ($\varepsilon_r = 2.1$ and $\sigma = 0$).

whereas the longest wavelength immediately responds to the moisture diffusion. The ceiling and bottom values for each wavelength are determined correctly.

Similarly, as shown in Figure 11.27(a), the estimated values of conductivity are all within an expected range and longer wavelengths respond faster to the diffusion process. The starting values of conductivity are zero, as required by the initial conditions, and the final values (ceiling values) are close to those expected from the moisture concentration equations (11.3). The final values estimated by different wavelengths are not exactly the same for two reasons. First, at 30 hours, the moisture concentration has not completely yet reached a new equilibrium, so, in fact, the estimate will be larger for increasing wavelength. Second, unlike dielectric permittivity, the conductivity has been changing over several orders of magnitude during the diffusion process, so, plotting such a drastic variation on a linear scale augments small numerical noise. In other words, the conductivity has a stronger dependence on the moisture concentration than

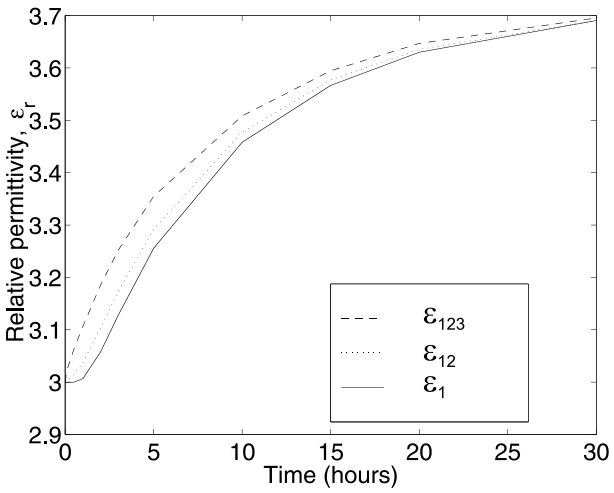

Figure 11.26: Calculated time profiles of average relative dielectric permittivity of compound layers of oil-impregnated transformer pressboard estimated by individual wavelengths using homogeneous region models for synthetic data in Figure 11.15.

the relative dielectric permittivity, which affects the relative accuracy of the inverse problem estimates. The meshing of the solution space along the conductivity axis is logarithmically distributed over seven decades, so, the accuracy of the local function approximation is limited by the distance between the adjacent points. Figure 11.27(b) displays the same data as Figure 11.27(a), but with a vertical logarithmic axis. On the logarithmic scale, the difference between the estimated curves is highest at the beginning of the process, when the highest spatial gradients of the moisture concentration exist.

Figure 11.28 shows stair-step profiles of the relative dielectric permittivity and conductivity for selected moments of time, which are derived from corresponding time profiles in Figures 11.26 and 11.27. Both profile plots have very similar shape, and either of them could be used to derive spatial moisture profiles. Before doing that, one should try to extract the maximum amount of information from the experimental (or, in this case, simulation) data. In order to convert from the homogeneous compound layer estimation to the individual layer estimation, appropriate weighting coefficients may be used. For the diffusion problem, the compound layer averaging overestimates material dielectric properties near the sensor and underestimates properties near the

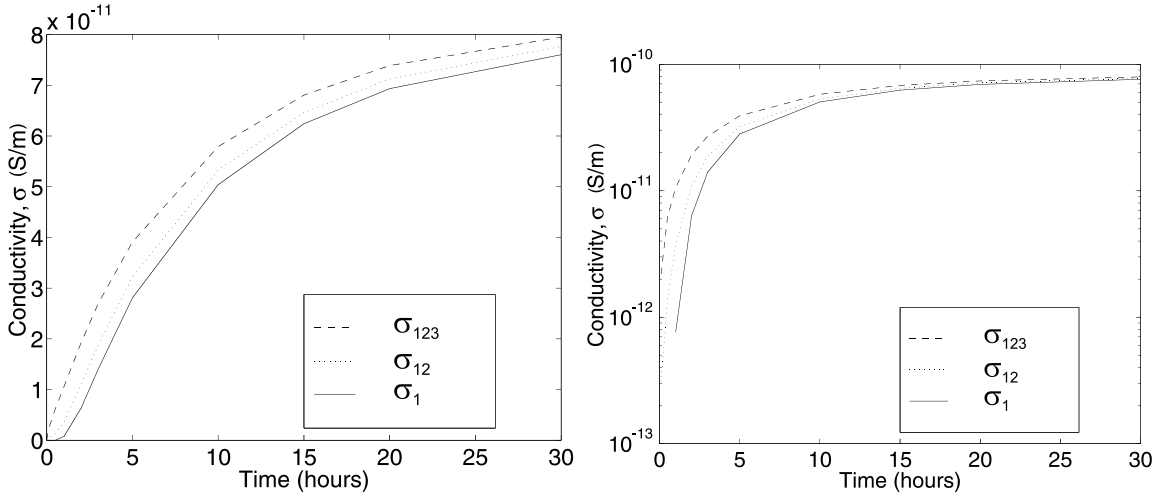

(a) linear conductivity scale

(b) logarithmic conductivity scale

Figure 11.27: Calculated time profiles of average conductivity of compound layers of oil-impregnated transformer pressboard estimated by individual wavelengths using homogeneous region models.

$x = 0$ interface.

11.5.6 Weighting Coefficients

Figures 11.29 and 11.30 illustrate the process of generating the weighting coefficients for the considered case. The capacitance C_{12} is calculated and shown in Figure 11.29 for each wavelength as the thickness of dielectric with the relative dielectric permittivity $\varepsilon_r = 2.1$ placed next to the sensor head increases. The space outside the dielectric is filled with air. The same data is normalized in Figure 11.30 to the difference between the maximum and minimum values of the corresponding curve, so that the change of capacitance in percent $\Delta C_{\%}$ is equal to

$$\Delta C_{\%} = \frac{C - C_{\min}}{C_{\max} - C_{\min}} \times 100\%, \tag{11.8}$$

where C, $C_{\max}$, and $C_{\min}$ are respectively current, maximum, and minimum values of capacitance for each curve. The percentage change of capacitance at each thickness value for each wavelength is proportional to the relative weight of the contribution

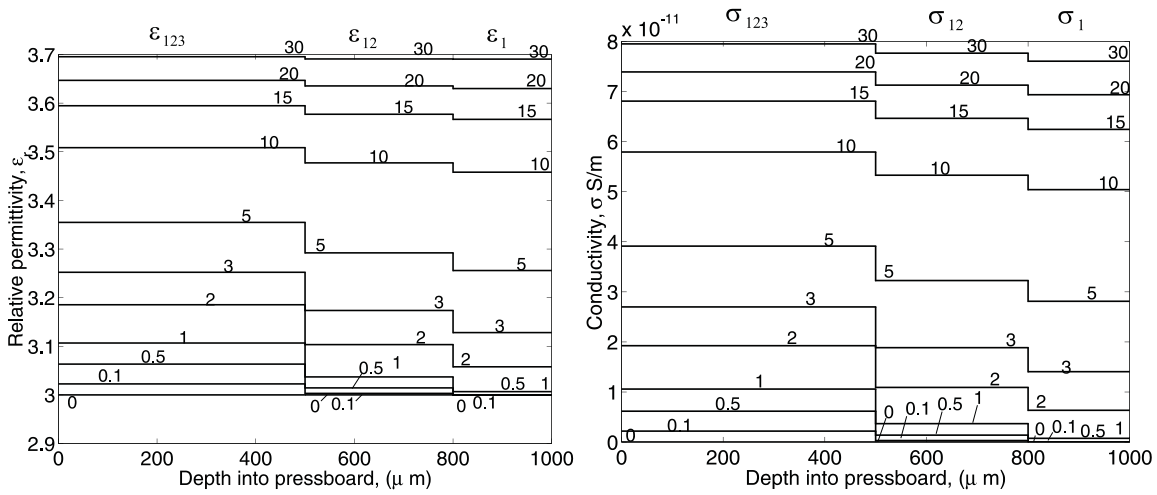

(a) relative dielectric permittivity

(b) conductivity

Figure 11.28: Stair-step spatial profiles of average relative dielectric permittivity and conductivity in oil-impregnated transformer pressboard at selected moments of time in hours based on permittivity profiles shown in Figure 11.26 and conductivity profiles of Figure 11.27. Each level corresponds to the average estimated value in the compound regions of Figure 11.25(a) within reach of a given penetration depth.

from the increase of thickness of the dielectric material at this coordinate to the total capacitance value. The coefficients selected for the given problem are found for the middle location of each region shown in Figure 11.25 and listed in Table 11.3. For the layer thicknesses chosen in Figure 11.25 the middle of each layer are at 100 μm, 350 μm, and 750 μm. These locations are indicated in Figure 11.30 by dashed vertical lines. The corresponding weighting coefficients are the ordinate values at the intersection of these vertical lines with the respective curves for each wavelength as shown by horizontal lines in Figure 11.30. Since the first layer has thickness equal to the penetration depth of the 1 mm wavelength, there is no weighting and the weighted permittivity of the first layer adjacent to the sensor remains unchanged. The difference between the second and the first individual layers should be larger than the difference between the second and the first compound layers as long as the derivative of the permittivity profile with respect to position does not change its sign in the entire region of interest. The increase of the difference between the two neighboring layers is governed by the sensitivity of

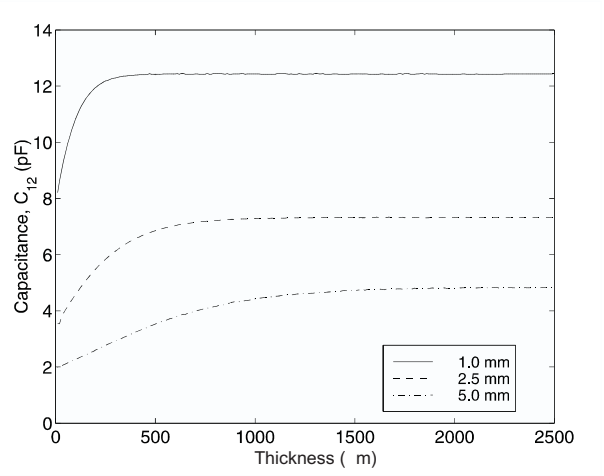

Figure 11.29: Calculated change of the interelectrode capacitance C_{12} per one meter length with the increase of the dielectric thickness ($\varepsilon_r = 2.1$), with air above the dielectric, for each wavelength of the three-wavelength sensor.

each wavelength to the differential change in dielectric properties at a given depth. The weighting coefficients provided in Table 11.3 reflect differences in sensitivity. Therefore, the permittivity difference between two individual layers is equal to the permittivity difference between two corresponding compound layers times the ratio of the weighting coefficients. Thus, the permittivity of the second individual layer is defined by:

$$\varepsilon_2 = \varepsilon_1 + (\varepsilon_{12} - \varepsilon_1)\frac{k_2(\lambda = 2.5)}{k_1(\lambda = 2.5)} \tag{11.9}$$

The same argument holds for the third individual layer:

$$\varepsilon_3 = \varepsilon_{12} + (\varepsilon_{123} - \varepsilon_{12})\frac{k_3(\lambda = 5)}{k_2(\lambda = 5)} + (\varepsilon_{123} - \varepsilon_1)\frac{k_2(\lambda = 5)}{k_1(\lambda = 5)} \tag{11.10}$$

These equations indicate that the difference between the dielectric permittivities of adjacent individual layers is larger than the difference between the dielectric permittivity of corresponding compound layers, and the increase of these differences is proportional to the ratio of corresponding weighting coefficients.

11.5.7 Individual Layers

After weighting, the time profiles of the relative dielectric permittivity and conductivity change shape to what is shown in Figures 11.31 and 11.32. The most drastic change

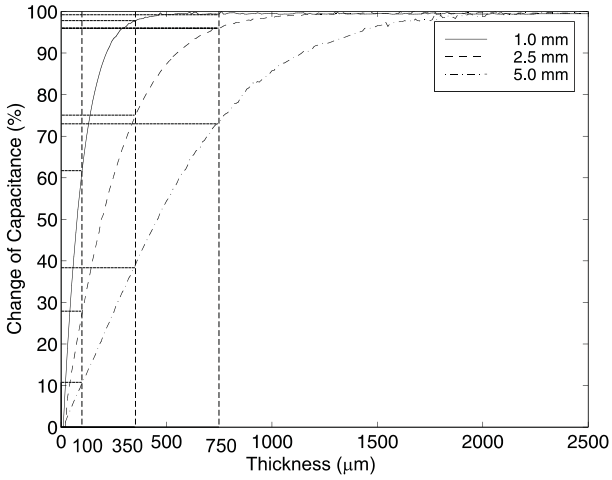

Figure 11.30: Calculated change of the interelectrode capacitance C_{12} of the three-wavelength sensor normalized to the highest and lowest capacitance values as given by (11.8) clearly illustrates the variation of the effective penetration depth.

Thickness (μm)	Coefficient	$\lambda = 1.0$ mm	$\lambda = 2.5$ mm	$\lambda = 5.0$ mm
100	$k_1(\%)$	61.7	27.9	10.8
350	$k_2(\%)$	97.8	75.1	38.4
750	$k_3(\%)$	99.2	96.0	73.0

Table 11.3: Percent change of interelectrode capacitance (weighting coefficients) at different thicknesses. The values of thickness are selected to be in the middle of each insulating region. The weighting coefficients for each wavelength are found in Figure 11.30 by the intersection of the change in capacitance curves with thicknesses of 100, 350, and 750 μm.

from Figures 11.26 and 11.27 is with the ε_3 and ε_{123} signals associated with the 5 mm wavelength as the signal delay becomes more pronounced, reflecting the true nature of the diffusion dynamics. Effectively, the weighted profiles plotted for individual layers provide higher spatial resolution than those for compound layers which average over the entire pressboard thickness. Because the steady-state conductivity values σ_1, σ_2, and σ_3 should be the same, the error between the conductivity values for each individual layer at the end of the diffusion process becomes larger than found for compound layers in Figure 11.27, as seen in Figure 11.32(a), but it is still relatively small on the logarithmic scale, as seen in Figure 11.32(b).

The corresponding stair-step profiles of dielectric properties are shown in Figure

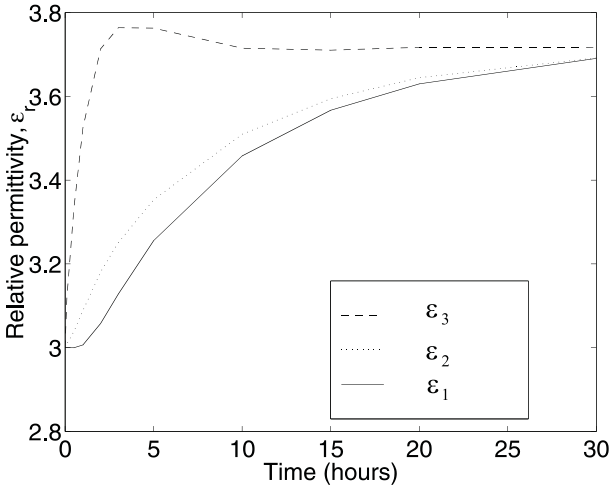

Figure 11.31: Time profiles of average relative dielectric permittivity in each individual layer of oil-impregnated transformer pressboard estimated using weighting coefficients.

11.33. This time, the moisture level at each step indicates the estimated value at the corresponding individual layer. In comparison with profiles for the compound layers shown in Figure 11.28, the new profiles exhibit less homogeneous distribution of material properties, as expected. The moisture concentration in the individual layer 1 (nearest to the sensor) is kept exactly the same as the moisture concentration in the compound layer 1. The differences are most significant between individual layer 3 and compound layer 3. The process of weighting tends to increase differences between neighboring layers. As an unfortunate side effect, the estimated values of dielectric properties are too high in region 3 for the end part of the diffusion process, which can be seen by comparing Figure 11.33(a) with Figure 11.10 and comparing Figure 11.33(b) with Figure 11.12. Potentially, additional information from the auxiliary sensors might be used for improvement of the parameter estimation algorithm output in nearly uniform distributions of permittivity and conductivity.

11.5.8 Moisture Profiles

The stair-step profiles of the dielectric properties can be converted into stair-step moisture profiles shown in Figure 11.34 using relationships (11.4) and (11.5). Ideally, mois-

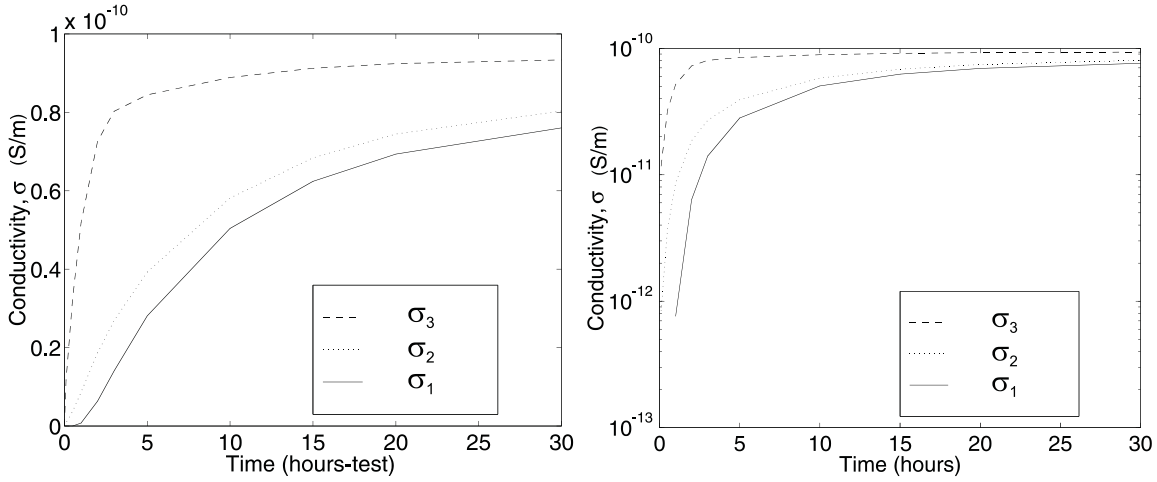

(a) linear conductivity scale

(b) logarithmic conductivity scale

Figure 11.32: Time profiles of average conductivity in each individual layer of oil-impregnated transformer pressboard estimated using weighting coefficients.

ture profiles estimated from ε_r and from σ should be the same. The differences observed between Figures 11.34(a) and 11.34(b) are mostly due to the limited resolution of the three-region representation of continuous profiles. Naturally, the differences increase as one moves away from the sensor. The largest differences are in region 3, because the variations of properties there are blurred by changes of properties in regions 1 and 2, and it is most difficult to deconvolve properties in the individual region 3 from the properties of the compound region "123". Also, region 3 for most of the diffusion process time has high gradients of moisture concentration, which is least similar to the flat stair-step representation employed at this juncture. Exactly the opposite is true for region 1. Here, the match between moisture concentration values derived from permittivity and from conductivity are almost ideal. This region is immediately adjacent to the sensor and the moisture concentration is nearly flat at all times, which makes the inversion more accurate. In general, the moisture dynamics are captured properly, but it is desirable to increase the resolution of spatial profiling using available information about the system.

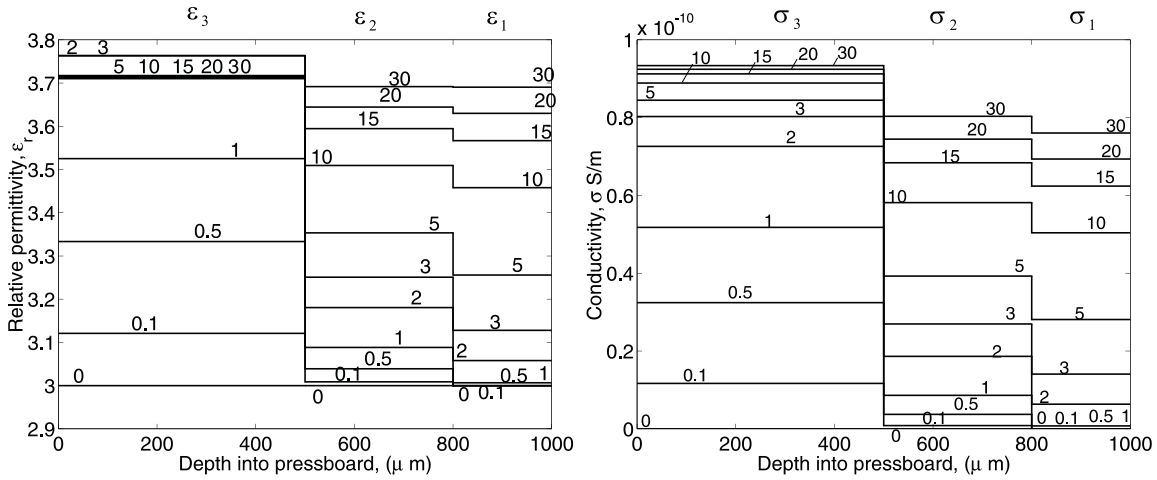

(a) relative dielectric permittivity

(b) conductivity

Figure 11.33: Stair-step spatial profiles of relative dielectric permittivity and conductivity in each individual layer in Figure 11.25(b) of transformer pressboard at selected moments of time.

Piecewise Linear Approximation

The approximate stair-step profiles shown in Figure 11.34 do not reflect well the actual distribution of the moisture. In reality, the moisture concentration profile is a continuous function. A piece-wise linear approximation would be better than a stair-step approximation. The transformation from the discontinuous to the continuous function should be made taking the signal magnitude conservation into account. The outside moisture boundary concentration is known from separate moisture measurements in the surrounding oil using an oil moisture sensor and from standard equilibrium curves between the oil and pressboard [20].

The moisture profile at each moment of time must satisfy the following minimum requirements: the external boundary value is known, the profile is continuous, and it is differentiable everywhere except across boundaries. The moisture concentration at the $x = 0$ external boundary of the pressboard is known from the measurements in oil using commercially available moisture sensors and equilibrium curves.

Once we change the shape of the moisture profile from a flat line to a line with non-

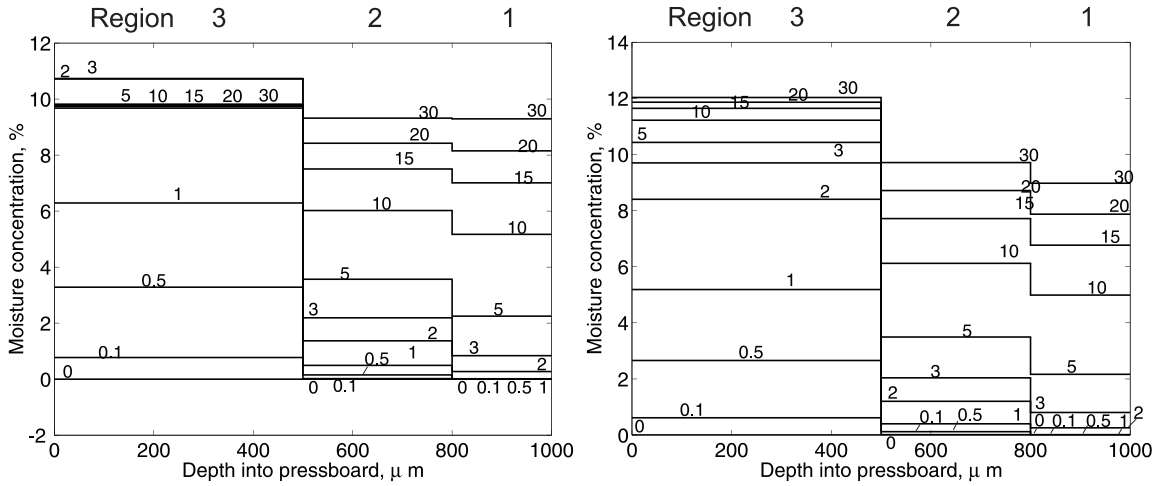

(a) estimated from ε_r (b) estimated from σ

Figure 11.34: Stair-step profiles of moisture concentration estimated from profiles of dielectric properties using (11.4) and (11.5). Ideally, both profiles should be the same.

zero slope, we should expect the area under the curves of both profiles to be in a certain ratio to each other. If the sensitivity of the sensor to the differential amount of moisture is the same for every position, the ratio of the two areas would have been equal to 1. Since the electric field strength reduces as we move away from the sensor, the ratio of the two areas must be different. The coefficient α is introduced to account for the fact that the change of the sensor output due to a nominal change in material properties of a narrow incremental layer is larger closer to the sensor (which has been illustrated in Figure 11.30). The coefficient value $\alpha = 0.2$ is found empirically by comparing forward and inverse problem results at high gradient regions visually. At this point, the technique is approximate and additional accuracy should be sought in the sensor design rather than in the search of exact coefficient values. If one chooses $\alpha = 1$, the area under the triangles and trapezoids obtained with (11.11)- (11.16) is equal to the area under respective rectangles in the stair-step profile. The notation for the process of transition from stair-step to continuous profiles is illustrated in Figure 11.35. In order to satisfy both signal magnitude conservation and continuity, the currently employed profile shaping algorithm moves the collocation point (the $t = 0$ coordinates

of the point between two regions with dissimilar properties) between the two adjacent regions towards the $x = 0$ exterior interface. The collocation point is normally placed at the interface between individual layers, but it is moved in order to achieve higher spatial resolution in case of high spatial moisture concentration gradients. Using the definitions shown in Figure 11.35, the new coordinate of the collocation point $(x_{i,n}, y_{i,n})$ is found from the old collocation points $(x_{i,o}, y_{i,o})$ and $(x_{e,o}, y_{e,o})$ (see curve 1 in Figure 11.35 for reference). The following equations guarantee that the ratio of areas under the triangle and the rectangle remains the same.

If

$$y_{e,n} > \frac{2}{\alpha} y_{e,o} \tag{11.11}$$

then

$$x_{i,n} = x_{e,o} + \frac{(2/\alpha)\, y_{e,o}}{y_{e,n}} \left(x_{i,o} - x_{e,o}\right) \tag{11.12}$$

and

$$y_{i,n} = 0 \tag{11.13}$$

where the x coordinate refers to the distance axis, the y coordinate refers to the moisture concentration axis with the origin at the pressboard-oil interface, subscript "i" stands for interior boundary, subscript "e" stands for exterior boundary, subscript "o" refers to the old collocation point, and subscript "n" refers to the new collocation point.

As the amount of moisture in the pressboard grows with time, curve 1 in Figure 11.35 shifts to the right until it reaches the critical position indicated by curve 2. At this point, the ratio of the rectangle area to the triangle area is still equal to α, and further increase in the amount of moisture can no longer be accommodated by a triangular profile. The boundary condition at the right boundary at $x_{i,0}$ now requires a non-zero moisture concentration. Therefore, when the average value of the moisture concentration exceeds the critical value determined by curve 2, the collocation point starts shifting upwards rather than to the right, and the rectangular profile is replaced with a trapezoid, which can be expressed algebraically as: If

$$y_{e,n} < \frac{2}{\alpha} y_{e,o} \tag{11.14}$$

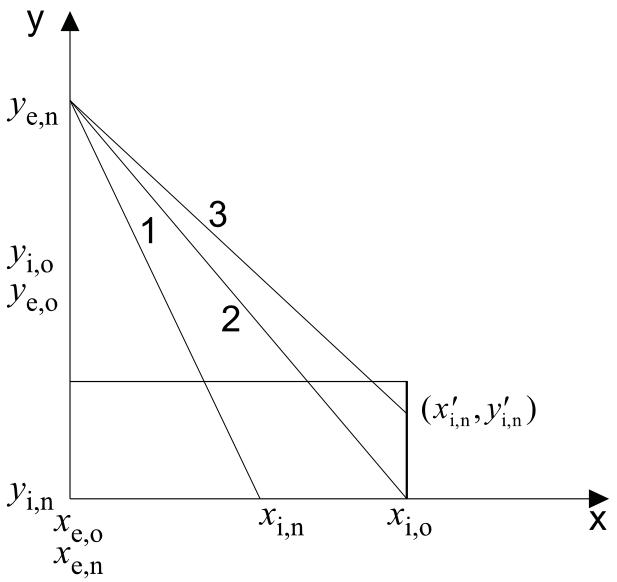

Figure 11.35: Illustration of transition from stair-step to piecewise linear continuous profiles. 1: low moisture concentration, 2: critical moisture concentration, 3: high moisture concentration. To the first approximation, the area under the old rectangular profile (horizontal line) to the new triangular or trapezoidal profiles remains at the ratio of α.

then

$$x'_{i,n} = x_{i,o} \tag{11.15}$$

and

$$y'_{i,n} = \frac{2}{\alpha} y_{e,o} - y_{e,n} \tag{11.16}$$

(see curve 3 in Figure 11.35 for reference). Figure 11.36 shows piecewise linear continuous profiles of moisture concentration obtained with the imposed signal magnitude conservation requirements of (11.11)-(11.16). Even though the estimated profiles resemble the original synthetic ones, this approach is very sensitive to small errors introduced to the input of the inverse problem by trying to represent smooth continuous profiles with a stair-step function. The open boundary for moisture diffusion at $x = 0$ in Figures 11.36(a) and 11.36(b) has moisture concentration pinned at 10 percent, which increases the overshoot of the trapezoids at depth 500 μm.

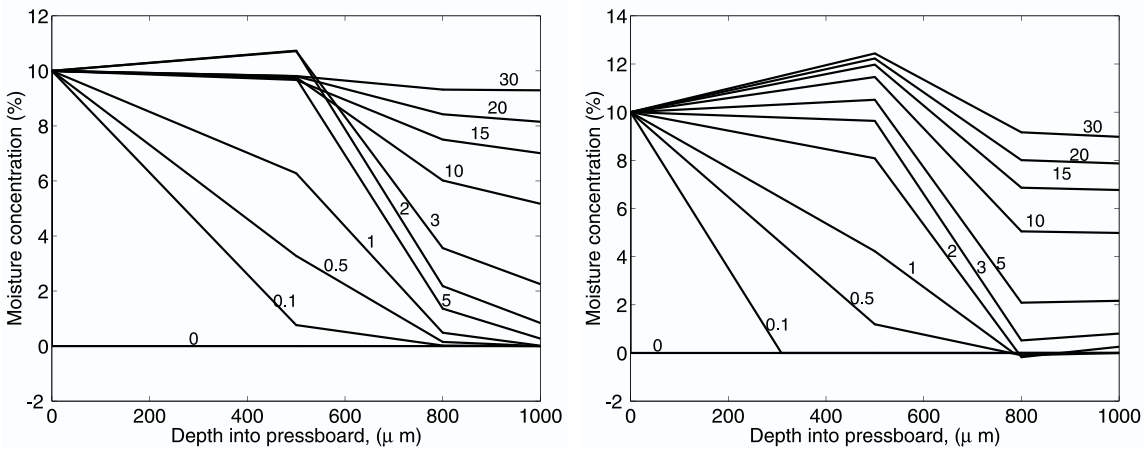

(a) estimated from ε_r (b) estimated from σ

Figure 11.36: Piecewise linear continuous profiles of moisture concentration obtained with (11.11)-(11.16) at different moments of time in hours.

Polynomial Approximations

Ideally, polynomial approximations to property profiles should have all the features suggested by the physics of a studied process. The concentration profiles and their spatial derivatives due to moisture diffusion in otherwise macroscopically homogeneous media are expected to have no discontinuities. Clearly, in this study moisture concentration profiles obtained from simulated interdigital dielectrometry data should maximally resemble the profiles obtained by solving the diffusion equation, shown in Figure 11.9. Figure 11.37 shows smooth profiles that have been generated from the stair-step profiles by using a third order polynomial approximation. In this case, no attempt is made to capture the high gradients close to the open boundary. Even though it may be possible with numerical data, the measurement errors in the experimental data will most likely not provide such an opportunity. Moisture concentration distributions derived from the real part of the complex dielectric permittivity (Figure 11.37(a)) are very similar to those derived from the imaginary part (Figure 11.37(b)). Bulging above the maximum concentration at intermediate moments of time is due to enforcing the 10 percent concentration open boundary condition at $x = 0$ and slight overshooting on

the moisture concentration estimate in individual layer 3 after using weighting coefficients in Table 11.3. Alternatively, the boundary condition could have been relaxed to avoid bulging. In this case, the trade-off is sought between the functional shape of the moisture profile and the accuracy of determining the moisture concentration at the point immediately adjacent to the boundary. The bulging can be viewed as a result of a sharp discontinuity in the expected measurement error value as a function of pressboard depth. The error increases continuously as one moves away from the sensor towards the pressboard-oil interface, but it is near zero at the interface. One of the trade-offs between the stability and the accuracy of parameter estimation is the margin of error assigned to the auxiliary sensor and moisture equilibrium curves.

Several elements could be altered to increase the resolution of accuracy of this technology. The number of wavelengths could be increased to obtain a larger number of equations corresponding to the larger number of approximating layers in the pressboard; a sensor could be made with moving mechanical parts to vary the electrode periodicity and thus the effective penetration depth; the sensor could be combined with other types of non-destructive measurement sensors, such as ultrasonic or chemical; an ultra-thin selectively absorbing layer could be used for verification of moisture concentration at the closed boundary; etc. At this point, however, the expected accuracy is adequate for the problem of moisture monitoring in transformer pressboard.

Summary

Each type of approximation, piecewise linear and polynomial has its advantages. The piecewise linear approximation has better performance for high gradient profile regions, but it does not reflect the smoothness of the real profiles. The polynomial approximation is smooth, but it gives rise to high numerical errors in case of high gradients. Given the three region resolution of the three wavelength sensor, either approximation is usable. Other approaches are also possible, some of them are very obvious. As sensors become more accurate and sophisticated, spline approximation could be used. At

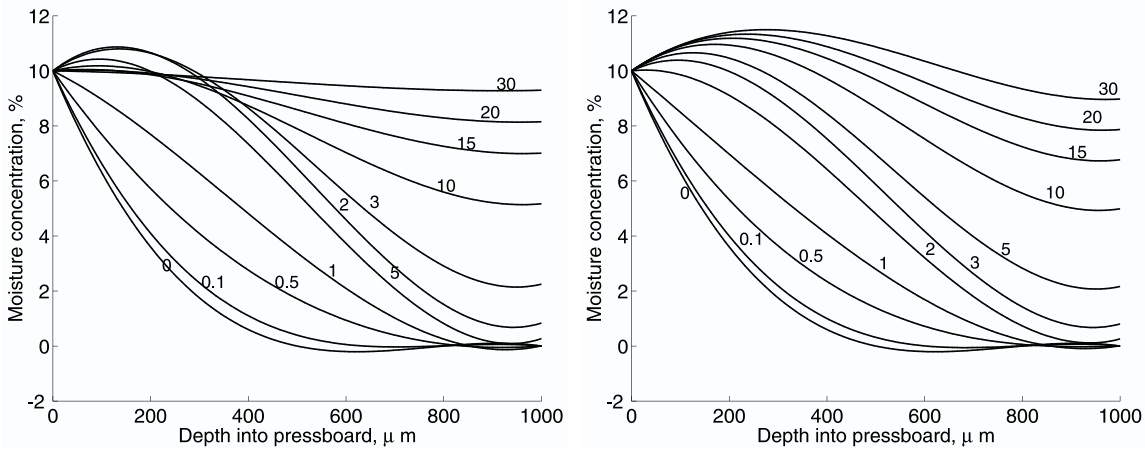

(a) estimated from ε_r

(b) estimated from σ

Figure 11.37: Smooth continuous profiles of moisture concentration calculated from Figure 11.36 using a third order polynomial approximation.

this point, other approaches have not been investigated because it would have had no effect on the overall sensor performance and there are far more significant areas that deserve attention. See Conclusions (Chapter 14) for this discussion.

11.6 Experimental Results

The results discussed in this section, also presented in [25], are representative of many studies of moisture dynamics in transformer pressboard. The moisture concentration was measured in a 1.5 mm thick oil-free transformer pressboard as a function of time and position during the moisture diffusion process. A flexible interdigital three-wavelength sensor shown in Figure 4.5 was used to gather information regarding pressboard dielectric properties at different depths from the sensor-pressboard interface. Data was obtained by processing the signals from the three-wavelength sensor, air humidity sensor, and thermocouple installed in the experimental chamber. Air-pressboard equilibrium curves were used to provide boundary conditions and the relative moisture level magnitude.

A controlled-environment experimental chamber was built to simulate the temperature, moisture, and materials of a power transformer environment [316]. A number of diffusion studies were performed in this chamber to date. The ambient air inside the chamber was humidified to a pre-selected value by circulating moist air through a system of interconnected ducts.

Initially, the pressboard was vacuum-dried. The moisture diffusion process started with a step change in the ambient air humidity from 0% to about 12% with temperature being held at 70°C. Air-pressboard equilibrium relationships [319] were used to provide boundary conditions at the air-pressboard interface and relative moisture level information needed for the parameter estimation algorithms. According to these relationships, a 12% humidity level in air at 70°C corresponds to 1.8% equilibrium moisture concentration in the transformer pressboard. Thus, the left side boundary condition at x=0 for this experiment is that the moisture level is equal to 1.8% for the duration of the entire experiment.

The signals from the sensing electrodes of the three wavelengths were recorded at three frequencies: 0.1 Hz, 1 Hz, and 10 Hz. This analysis utilizes the signals only taken at the frequency of 1 Hz, since the transcapacitance and transconductance were similar at 0.1 Hz and 10 Hz. Figure 11.38 shows the values of measured transcapacitance for each of the three electrode pairs. Each signal follows approximately the same pattern dictated by the diffusion dynamics. After a small initial delay, the signal grows at a high rate, after which it flattens off, indicating the end of the diffusion process experiment. The initial delay time is the shortest for the longest wavelength, because it can "see" deepest into the pressboard.

Similar results hold for the measured transconductance vs. time for each of the three wavelengths. The relative amplitude of change of transconductance is normally larger than that of the transcapacitance due to the high electric conductivity growth with the increase of the moisture concentration. Nevertheless, as demonstrated in the next section, the transcapacitance provides sufficient sensitivity for the moisture profile measurements.

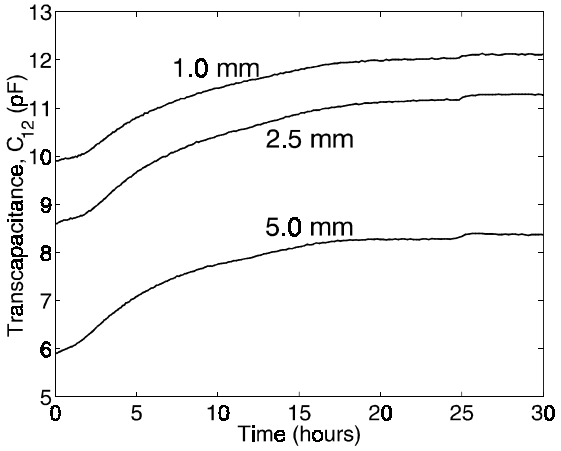

Figure 11.38: Measured capacitance between each electrode pair throughout the moisture diffusion experiment for each sensor wavelength at 1 Hz.

11.7 Moisture Profiles

The transcapacitance signals in Figure 11.38 were used to generate the curves of moisture concentration in the pressboard layers, assuming a linear relationship between the non-dimensional difference capacitance values of (11.7) and the moisture levels at each moment of time,

$$m(t) = m(t=0) + [m(t=\infty) - m(t=0)]\, C_{12nd}(t), \tag{11.17}$$

where for our experiment $m(t=0) = 0$ and $m(t=\infty) = 1.8\%$. Note that conversion of measured capacitance values to moisture does not require any empirical relationship relating moisture to dielectric properties like those in (11.2) and (11.3).

Figure 11.39 shows the change in the average values of moisture concentration in the three regions that correspond to the penetration depths of the three wavelengths of the sensor. The average value corresponds to the cumulative amount of moisture in all regions within reach of a given penetration depth. The fact that the difference of the moisture concentration measured by the 2.5 mm and the 1.0 mm wavelengths is very small is related to a relatively small signal delay difference in the detection time analysis. Since the right side blocked boundary condition eliminates the moisture escape, the gradient-driven diffusion process results in a nearly flat moisture concentration profile

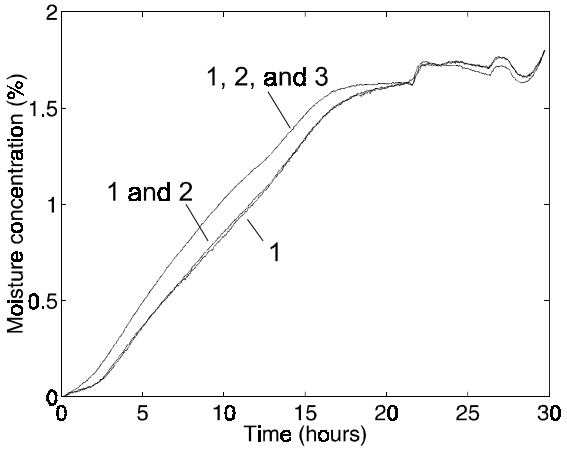

Figure 11.39: Average moisture level measured by each wavelength: region 1 (1 mm), regions 1 and 2 (2.5 mm), and regions 1, 2, and 3 (5 mm) using Figure 11.38 with (11.17).

across regions 1 and 2 of the pressboard indicated in Figure 11.8.

Figure 11.40 shows calculated moisture profiles from dielectrometry measurements for 14 distinct moments of time. The moisture spatial profiles were calculated from the measurement data using multi-variable parameter estimation algorithms for the three-wavelength sensor combined with the moisture measurement data of the ambient environment (air relative humidity of 12%) together with moisture equilibrium curves to give the pressboard moisture concentration of 1.8% at $x = 0$. Early time profiles for t $<$ 2 hours are not shown because as earlier shown in the simulated analysis of Figure 11.22, the three wavelength sensor has insufficient resolution for high gradients near the x=0 interface.

The process starts with a step change in moisture concentration to 1.8% at the left boundary at time zero. The first two profiles (at the time moments of two hours and four hours) continue to show a slightly overestimated amount of moisture in the middle region of the pressboard because the sensor resolution is insufficient to capture high profile gradients. Future work should include better use of signal magnitude conservation requirements in order to improve the spatial resolution without adding more electrode pairs of different spatial periodicity. In this case, it may be possible

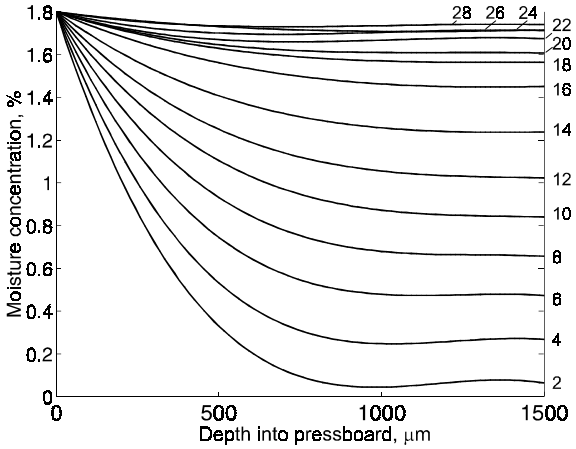

Figure 11.40: Calculated spatial profiles of moisture concentration across the thickness of pressboard from dielectrometry measurements using $D \approx 2.3 \times 10^{-11}$ m^2/s. Numbers next to the curves correspond to the time in hours at which the profile was measured. These curves were obtained using a polynomial approximation of the stair-step representation similar to that shown in Figure 11.21.

to combine advantages of an approximate smooth profile representation and a straight line representation with moving collocation points.

The experiment is stopped at about 30 hours, when the signals essentially stop changing. At this point, the moisture profile is expected to be almost uniform and at the maximum value of 1.8%. The profile at 28 hours has these characteristics.

Now, it is possible to evaluate the moisture diffusion coefficient from the moisture dynamics presented in Figure 11.40. By simulating the diffusion process using a standard finite difference technique, one can match the measured profiles. The estimated value of the diffusion coefficient is $D \approx 2.3 \times 10^{-11}$ m^2/s. Figure 11.41 shows theoretical moisture profiles generated using the estimated value of diffusion coefficient that are in reasonable agreement with the measured profiles in Figure 11.40.

11.8 Pseudo-Simulation Case

The optimal range of frequencies at which measurement should be taken depends on several factors. Normally, the most information about the system can be extracted at

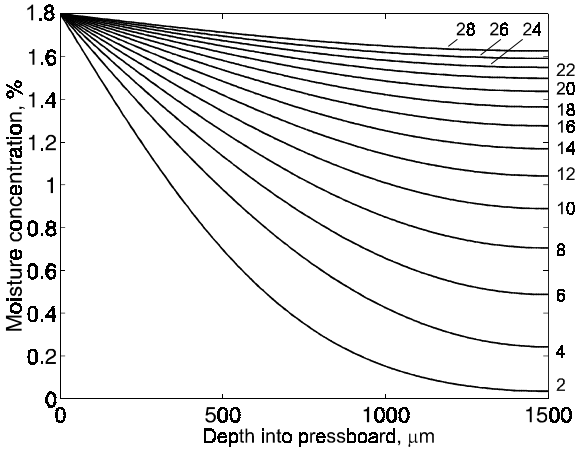

Figure 11.41: Theoretical spatial profiles of moisture concentration across the thickness of pressboard calculated using a diffusion coefficient of $D = 2.3 \times 10^{-11}$ m^2/s, selected based on the best visual match of the curves in the low gradient region. Numbers next to the curves correspond to the time in hours after the moisture was stepped on to 1.8% at $x = 0$.

frequencies which lead to a comparable magnitude of the real and imaginary components of the signal gain, which is defined here as the ratio of the voltage on the sensing and the driven electrodes. Figure 11.42 shows a typical frequency sweep of the driving voltage signal from 0.005 Hz to 10 kHz. In the high frequency range, the conduction currents are negligibly small, and only capacitance between the electrodes can be measured reliably. At the low frequency limit, the displacement currents are negligibly small and only the conductance between the electrodes can be measured reliably. So, the range from 10 Hz to 0.1 Hz is usually chosen for continuous measurements in order to view the transition from high to low frequency behavior.

A fairly sophisticated numerical algorithm was developed to relate the response of the three wavelength sensor to the spatial distribution of dielectric permittivity and conductivity. This algorithm provides estimates of the complex dielectric permittivity in the stratified media adjacent to the sensor. In order to verify the validity of the algorithm, the process of diffusion of water molecules was simulated using a finite difference technique. Then, the curves of the concentration of moisture were transformed into spatial profiles of the complex dielectric permittivity using a semi-empirical functional

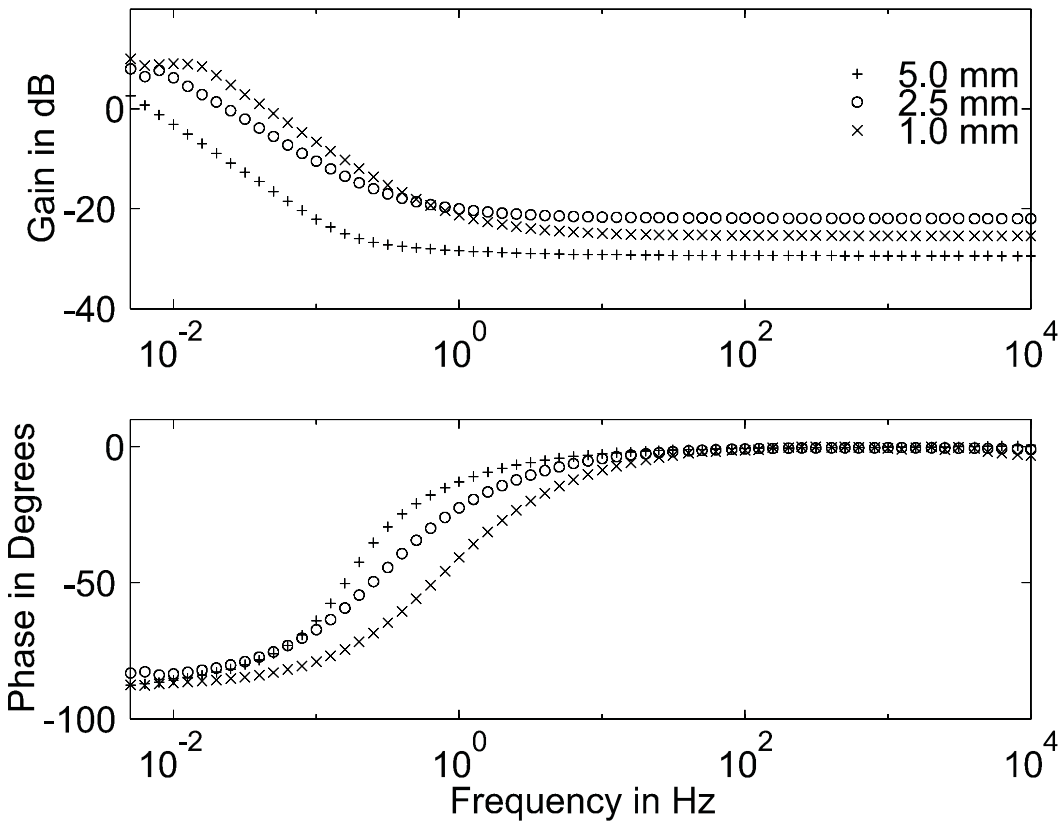

Figure 11.42: Frequency spectrometry results for oil-impregnated Hi-Val 1 mm thick pressboard at 70° C.

dependence determined earlier [10]. Table 11.4 lists values of dielectric permittivity and conductivity for this case, processed with Matlab code *datent03.m* (Appendix G) for moisture profile calculation and plotting.

11.9 Summary

For the first time, the experimental results presented in this section show a successful case of the monitoring of moisture dynamics in transformer pressboard using a multiple penetration depth interdigital sensor. The stability of the parameter estimation algorithms has been achieved by sacrificing the maximum achievable accuracy. The first presented approach (LCABE) lacks generality of a more conventional parameter estimation through an accurate evaluation of the dielectric properties of stratified

	Relative dielectric permittivity			Conductivity, (pS/m)		
Time (hours)	$\lambda = 1$mm	$\lambda = 2.5$mm	$\lambda = 5$mm	$\lambda = 1$mm	$\lambda = 2.5$mm	$\lambda = 5$mm
0	3	3	3	0	0	0
0.1439	3	3	3.2	0	0	3.54
1.858	3	3.03	3.32	0	5.31	5.66
11.86	3.17	3.24	3.42	3.01	4.25	7.43
16.86	3.24	3.28	3.421	4.25	4.96	7.45
21.86	3.29	3.32	3.422	5.13	5.66	7.47
26.86	3.32	3.35	3.425	5.66	6.20	7.52
37.38	3.37	3.39	3.43	6.55	6.90	7.61
49.88	3.4	3.41	3.435	7.08	7.26	7.70

Table 11.4: Relative dielectric permittivity and conductivity as a stair-step function of time and space constructed from calculated smooth moisture diffusion profiles and transformed into stair-step moisture diffusion profiles shown in Figure 11.24. The accuracy of the marching approach is adequate for solving simulated diffusion problem as long as conversion from smooth to stair-step profiles is included in the simulation prior to solving forward problem.

media, but it has the advantage of adequate performance for any type of pressboard through self-calibration and linearity assumptions. The second presented approach, model-based estimation, is more general and versatile, but it also requires extensive and reliable experimental data accumulated with parallel-plate sensors to provide the transition from the complex dielectric permittivity to moisture concentration.

Chapter 12

Detection of Buried Landmines

12.1 Problem Statement

Detection and discrimination of buried landmines can be accomplished using interdigital dielectrometry technology. In general, dielectrometry is capable of detecting and discriminating both plastic and metal objects in the ground, whereby the presence of low dielectric constant plastic landmines in a high dielectric constant sand will decrease the measured capacitance, while a metal landmine would increase the capacitance for most configurations. Further improvements in measurement selectivity will be gained from low frequency measurement of terminal conductance as well as capacitance and their variation with frequency.

The technical background information in this subsection is publicly available. Most of the data is adapted from [320]. An example of a commonly used antipersonnel surface burst plastic landmine is shown in Figure 12.1. The M14 mine is produced in the United States, but its copies are also manufactured in Vietnam (MN-79, MD82B) and India (M-14). It is a relatively small mine with height 40 mm, diameter 56 mm, and total weight of about 100 grams. The explosive charge, 29 grams of tetryl, is positioned at the lower portion of the mine. The M14 contains almost no metal, except for the striker tip and the detonator, which makes it difficult to detect with

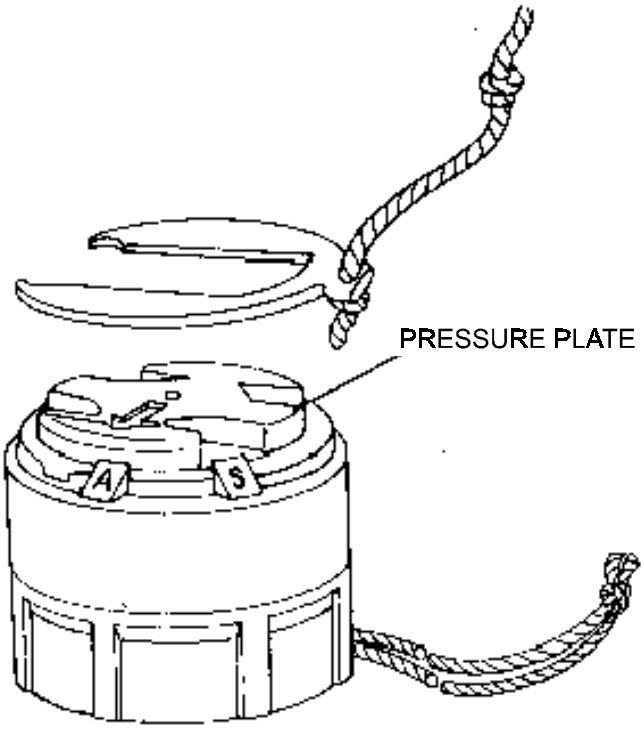

Figure 12.1: The antipersonnel plastic landmine M14.

conventional inductive coil mine detectors. Due to its small size, it may also be missed using conventional probing techniques. This landmine is usually installed manually. It does not self-destruct or self-neutralize with time. Once identified, it can be neutralized by placing an explosive charge adjacent to the mine.

12.2 Sensor Design and Response

For fringing electric field sensors with co-planar driven and sensing electrodes, the depth of electric field penetration is approximately proportional to the distance between the electrodes. For the interdigital electrode setup, such as shown in Figure 4.5, the penetration depth has been found equal to approximately one-fifth to one-third of the spatial wavelength. It is reasonable then for the landmine detector to use technology, instrumentation, and algorithms originating from the previous work, but with

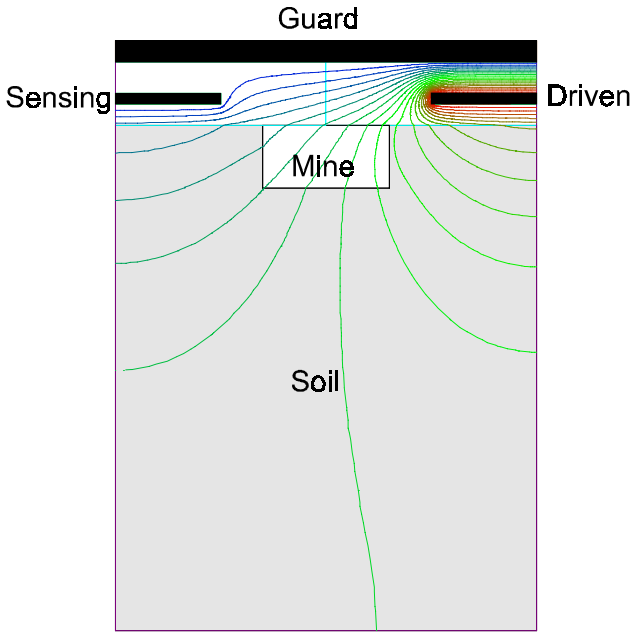

Figure 12.2: A two-dimensional cross-section of the half-wavelength cell of the interdigital landmine detector with equipotential lines for the (ε_r=2.7) landmine in sand (ε_r=6). The wavelength is 80 cm and the distance from the sensor electrodes to the sand is 2 cm.

layer wavelengths increased to approximately 20 cm, 40 cm, and 80 cm. This allows penetration depth into the ground of about 6 cm, 12 cm, and 24 cm, respectively. The fringing electric field penetrating the ground in the direct vicinity of the sensor can be created either by a sinusoidal voltage with swept frequency or by a step or pulsed signal in time. In order to insure sufficient sensitivity, the driving voltage may need to be as high as several hundred volts.

A larger (in size) version of the sensor with a smaller number of electrode fingers can be used for the detection of buried landmines. Figure 12.2 shows a cross-section of a half-wavelength of the 80 cm wavelength sensor. The sensor is placed 2 cm above the ground level, and the landmine is assumed to be just under the surface. The landmine relative dielectric constant is taken to be $\varepsilon_r = 2.7$, which is that of acrylonitrile-butadiene-styrene (ABS), a typical material used in plastic landmines.

First, let us consider the high-frequency case, when the conduction currents are

negligible in comparison with capacitive currents. The relative dielectric constant of soil is taken to be 6, corresponding to our measurement of sand, and that of the landmine to be 2.7, corresponding to the reported value of ABS. Figure 12.2 shows the distribution of the equipotential lines in this arrangement. The voltage between the neighboring equipotential lines is 0.05 V when the driven electrode is at 1 V, and the sensing and guard electrodes are at ground potential. All calculations are made on a per meter basis.

12.3 Capacitive Response

Figures 12.3-Figure 12.7 show the change in capacitance for the non-conductive (high frequency) cases for three wavelengths (20 cm, 40 cm, and 80 cm) as the sensor is moved laterally along the surface or the landmine is buried deeper along the center line. Figures 12.3 and 12.4 show that the sensitivity to the landmine presence is the smallest for the 80 cm wavelength because the ratio of the landmine volume to the penetration volume are the smallest. The smallest half-wavelength, whose response is shown in Figure 12.7 is shorter than the horizontal dimension of the modeled landmine, for which reason there is hardly any output variation due to the horizontal displacement of the landmine and is thus not plotted. Case studies are presented for ABS or metal landmines as being representative of real landmines, as well as for a landmine with relative permittivity of ε_r=1 (air) to show the lower limit sensitivity for landmine permittivity much less than sand. The metal landmine also provides an upper limit result for landmines with much higher permittivity or conductivity than the sand.

12.4 Frequency Response

A potential weak spot in the amplitude-based detection considered in the previous section is the fact that the amplitude of the response will change with irregularities of the surface, presence of other objects in the studied area, and vertical movement of

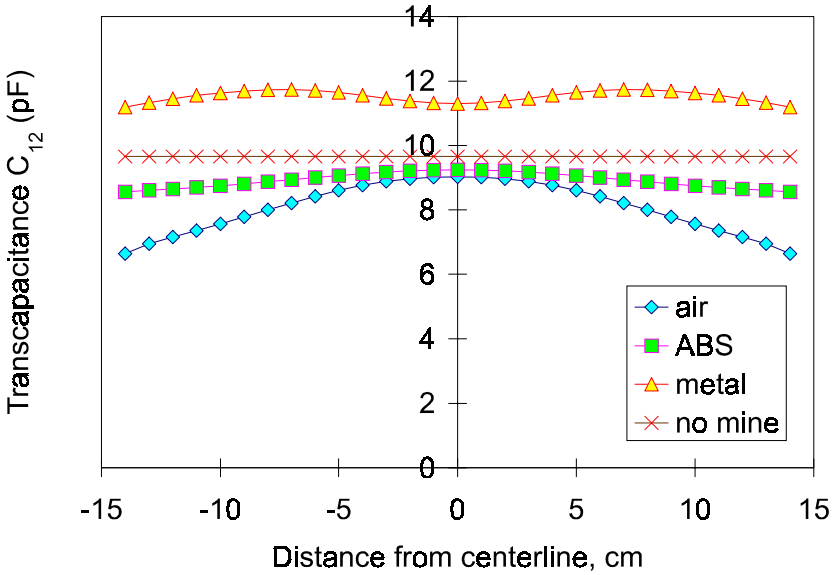

Figure 12.3: Calculated response of the 80 cm wavelength sensor to the horizontal displacement above the landmine at zero buried depth with 2 cm between the sensor and soil for various landmine materials.

Material	Relative permittivity	Conductivity (S/m)
Soil	6	10^{-9}
Landmine	2.7	10^{-8}
Electrodes	-	5.8×10^{7}
Ambient (air)	1	0

Table 12.1: Dielectric properties of materials assumed in the simulation.

the sensor. In other words, although detection of the landmine is very straightforward, its discrimination from other sources of signal perturbation is a more challenging task. More sophisticated algorithms should be used to reduce the false alarm rate. One such algorithm is presented in this section. Most of the materials under consideration (soil, landmine, small pieces of metal) are far from being perfectly insulating. Their conductivity varies over many orders of magnitude. For every landmine, the combination of capacitive and conduction currents leaves a specific frequency response signature which we will illustrate with the following simulation. Consider the same system, shown in Figure 12.2, but driven with a frequency sweep from 0.005 Hz to 10 kHz. The assumed dielectric properties of the materials are described in Table 12.1.

Suppose that the landmine is centered as in Figure 12.2, and the signal frequency

is swept from 0.005 Hz to 10 kHz. A more narrow sweep will suffice once properties of the specific landmines are determined. Figure 12.8 and Figure 12.9 clearly show the signature left by the landmine. The peaks in the frequency derivative plots can be predicted once the complex dielectric permittivities of the composing materials are known.

One of the most important points which need to be understood about these figures is that the irregularity of the surface would change the amplitude curve shapes shown in Figure 12.3, but will not introduce additional humps into the responses shown in Figures 12.8-12.11. A combination of both types of information will be the most valuable. In order to make the measurements faster, a single impulse voltage signal in the time domain can be applied instead of the frequency sweep. As long as the complex dielectric permittivity is constant with the electric field intensity (which is almost true for voltages below the kV range), the information gained by the frequency sweep and the step response are almost identical. An impulse voltage has an infinite frequency spectrum.

12.5 Effects of Uneven Terrain

One of the major advantages of the frequency derivative spectroscopy is the relatively low sensitivity of this technique to the errors introduced by irregularities of the soil surface. The amplitude-based recognition, on the other hand, is strongly susceptible to such errors. In order to illustrate this concept, we consider the situation shown in Figure 12.12. Here, the movement of an 80-cm wavelength interdigital sensor over an indentation in an otherwise flat sand surface is simulated. Figure 12.12 is drawn to scale, the distance between adjacent grid dots is 2 cm. The void created by the indentation is filled with air. The dielectric properties of sand are the same as in the previous examples, that is $\varepsilon_r = 6$ and $\sigma = 10^{-9}$ S/m. Figure 12.13 repeats Figure 12.3 with the new case superimposed over previous cases. The response to the presence of the indent is similar to the response of the presence of a buried ABS material

simulating the landmine. However, the frequency derivative response in the case of the surface irregularity remains practically unchanged from the flat surface case and is distinctly different from the ABS case. In reality, the surface would contain numerous irregularities of various shapes. Similarly to the case just considered, the frequency derivative response will not contain secondary peaks. For ease of comparison, different cases for the 80 cm wavelength are combined in Figure 12.14 and Figure 12.15.

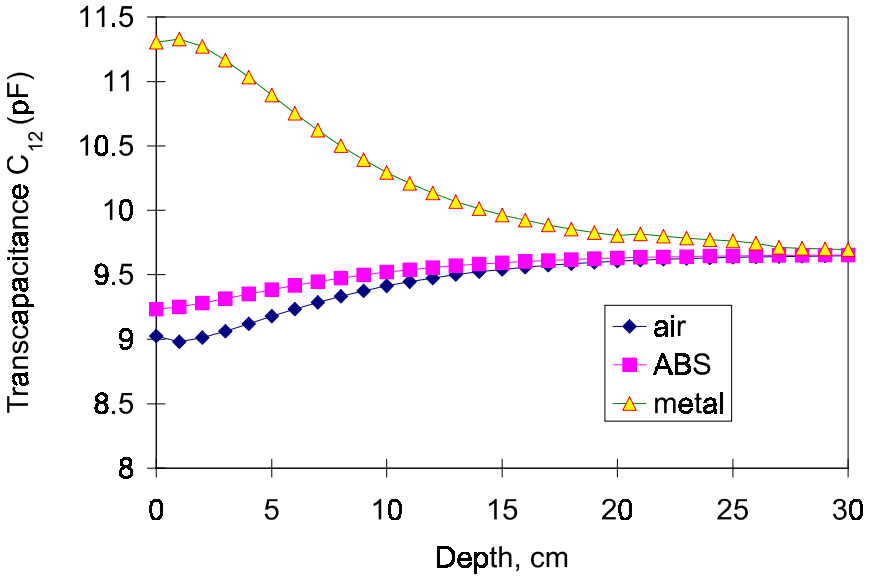

Figure 12.4: Calculated response of the 80 cm wavelength sensor to the change in the landmine buried depth with the landmine at the centerline of the half wavelength at zero buried depth with 2 cm between the sensor and soil for various landmine materials.

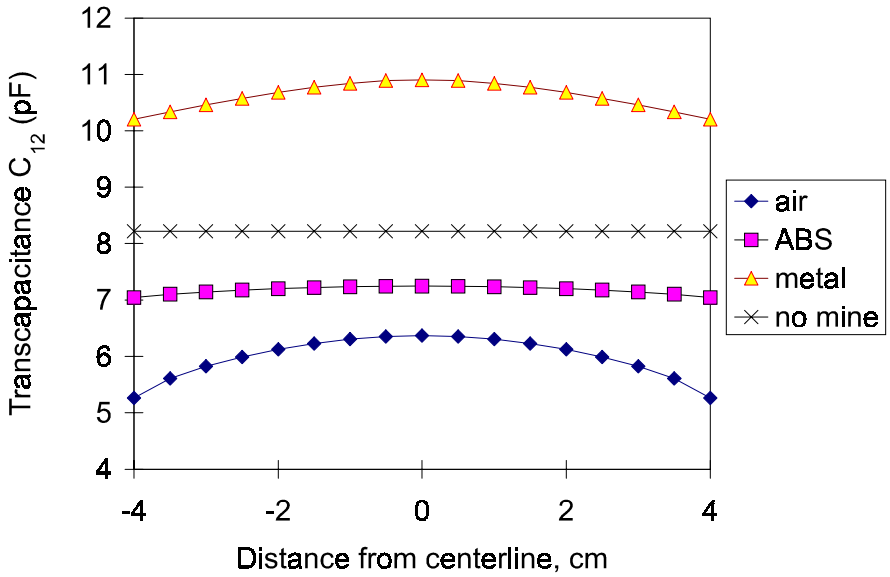

Figure 12.5: Calculated response of the 40 cm wavelength sensor to the horizontal displacement above the landmine at zero buried depth with 2 cm between the sensor and soil for various landmine materials.

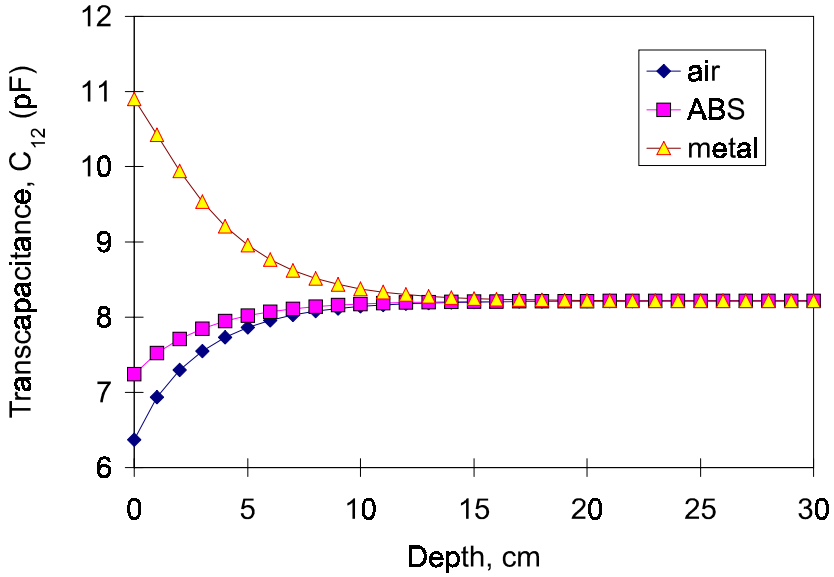

Figure 12.6: Calculated response of the 40 cm wavelength sensor to the change in the landmine buried depth with the landmine at the centerline of the half wavelength at zero buried depth with 2 cm between the sensor and the ground for various landmine materials.

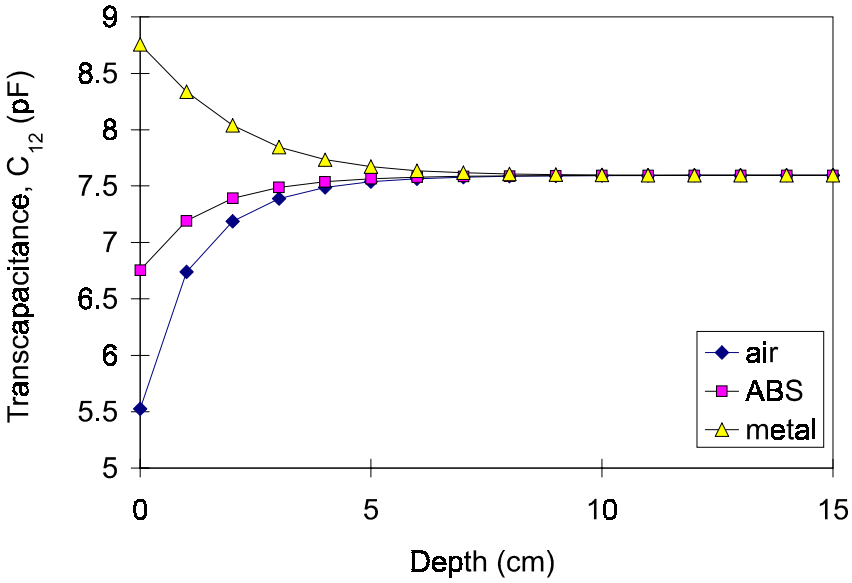

Figure 12.7: Calculated response of the 20 cm wavelength sensor to the change in the buried depth with landmine at the centerline of the half wavelength at zero buried depth with 2 cm between the sensor and soil for various landmine materials.

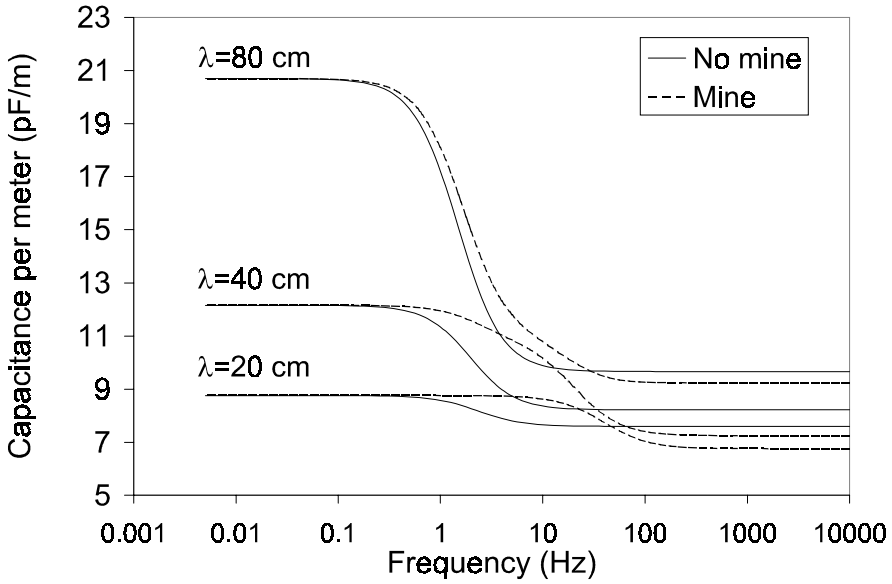

Figure 12.8: Simulated capacitance per meter length with and without landmine for three spatial wavelengths of interdigital electrodes.

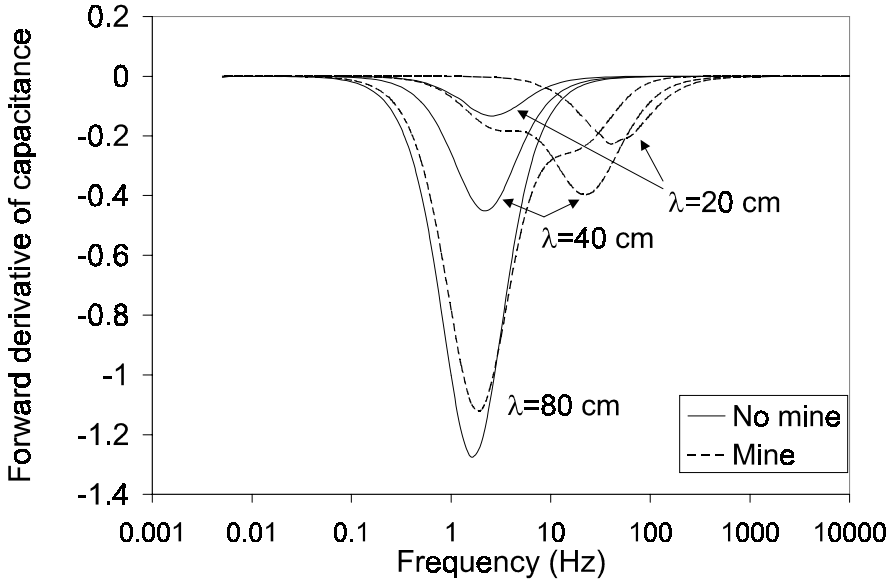

Figure 12.9: Simulated capacitance derivative with respect to the logarithm of frequency accentuates the characteristic signature of the landmine. The experimental data requires classic smoothing of derivative based on five-point local approximation.

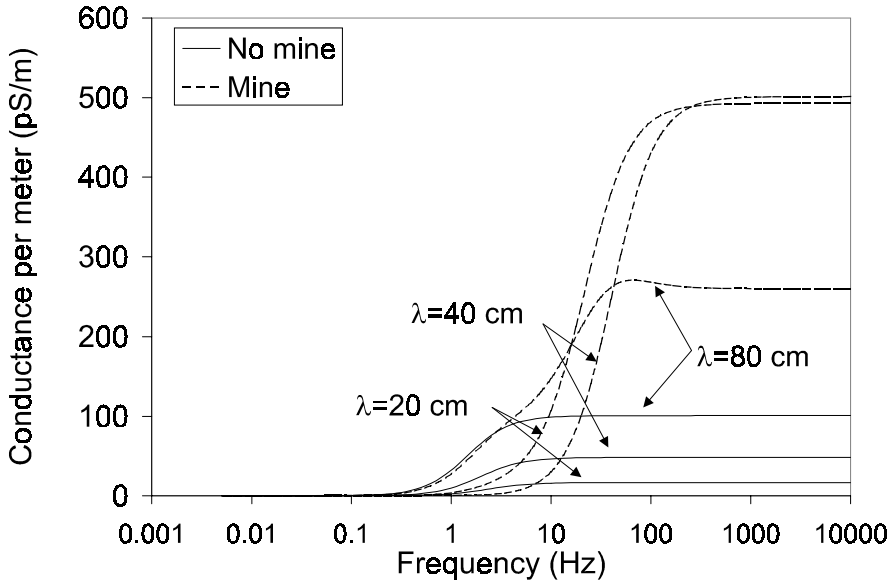

Figure 12.10: Simulated conductance per meter length with and without landmine for three spatial wavelengths of interdigital electrodes.

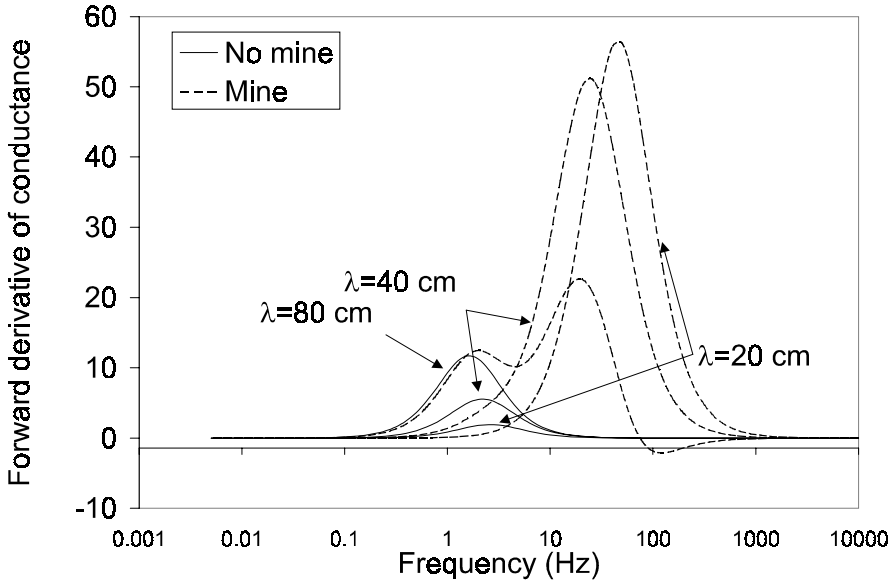

Figure 12.11: Simulated conductance derivative with respect to the logarithm of frequency accentuates the characteristic signature of the landmine.

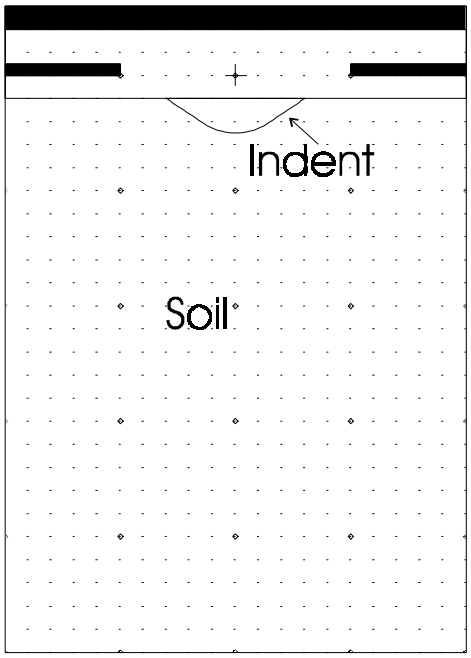

Figure 12.12: Irregularity of terrain complicates the task of mine search if the recognition algorithms are based solely on the amplitude measurement.

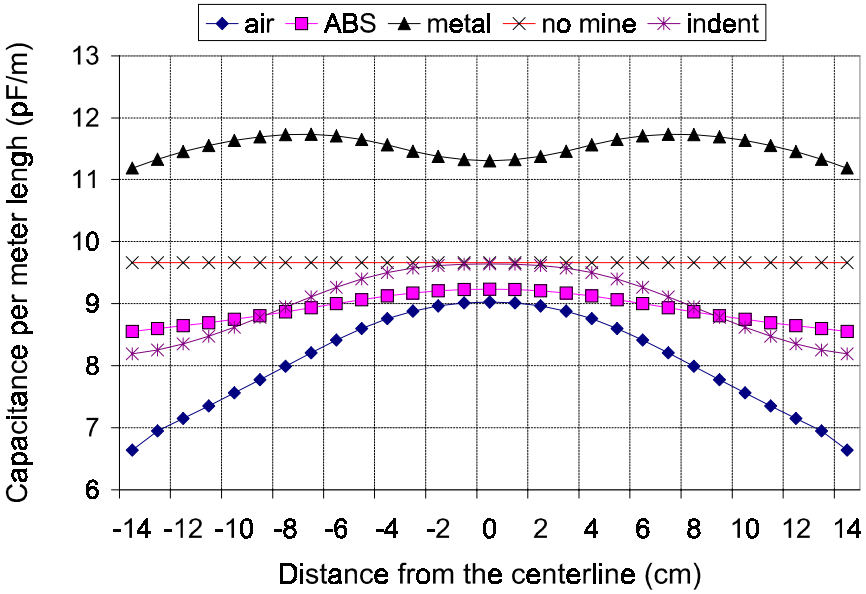

Figure 12.13: The amplitude sensor response (λ = 80 cm) to the movement in the horizontal plane is very similar for the cases of the buried ABS block (landmine) and uneven surface shown in Figure 12.12. All lines are for the flat surface except for the asterisks.

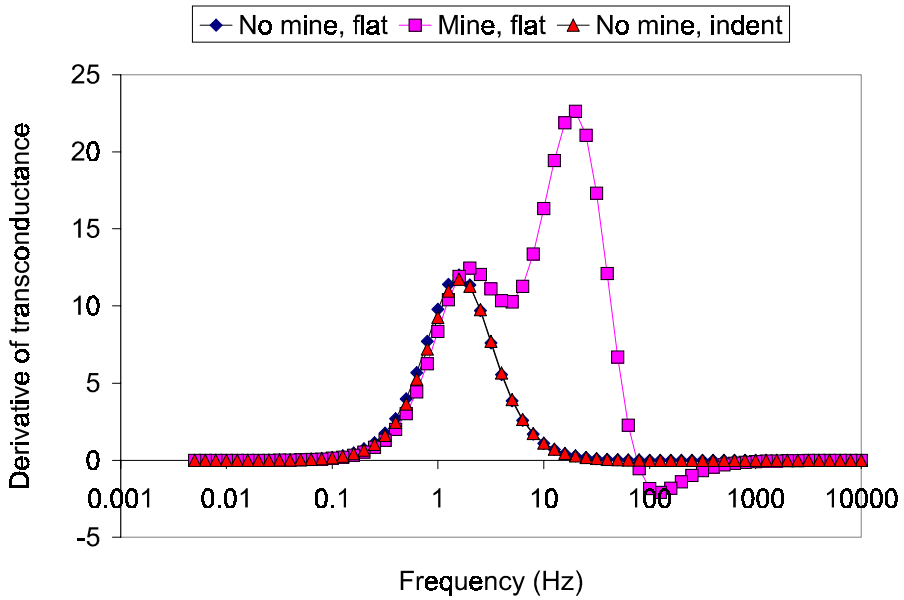

Figure 12.14: Frequency derivative spectroscopy analysis for the case of surface irregularity shown in Figure 12.12 for the 80 cm wavelength sensor. Comparison of cases with flat and with irregular soil surface.

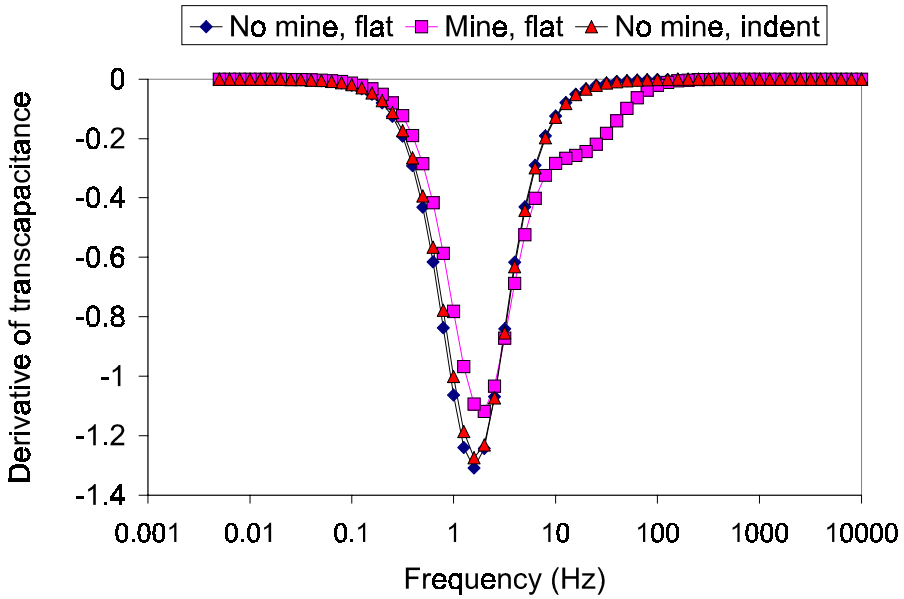

Figure 12.15: Frequency derivative spectroscopy analysis for the case of surface irregularity shown in Figure 12.12 for the 80 cm wavelength sensor. Comparison of cases with flat and with irregular soil surface.

12.6 Dielectric Properties of Sand and Sugar

This section documents measurement of dielectric properties of sand and sugar measured with a parallel plate capacitor. Sand has been tested as a typical soil where landmines are buried, and sugar was used as an explosive simulant. Sugar (chemical formula of fructose is $C_6H_{12}O_6$) is used as a stimulant of such explosives as HMX (High Melting eXplosive, also known as octogen and cyclotetramethylene-tetranitramine, $C_7H_5O_6N_3$) and TNT (2,4,6-trinitrotoluene, $C_7H_5O_6N_3$) [321]. Sugar is known to have similar dielectric properties to these explosives. The advantages of using sugar include the fact that it is inert, and, therefore, a safe material; it is also organic, as are TNT and HMX; and that it is readily available. These measurements were done together with an MIT UROP student Ricky Debnath [47].

12.6.1 Measurements in Air

The parallel plate sensor measurements were done in air using a guarded parallel plate capacitor with a sensing electrode area of about 25 cm^2 and the gap distance between the electrodes on the order of 0.6 cm. The sand was in direct contact with the copper electrodes of the capacitor cell. Figure 12.16 shows an example of a Mathcad worksheet for determining load capacitance and then a parallel plate sensor capacitance using the floating voltage measurement mode, included here for clarity and easy future reference. Figure 12.17 shows the gain and phase response of the parallel plate capacitor in air for the entire frequency range. A nearly zero phase indicates no conductivity between the electrodes (as should be expected). Figure 12.18 shows the capacitance of the parallel plate sensor estimated from the data in Figure 12.17. Based on geometric dimensions in the beginning of this paragraph, the relative dielectric permittivity of air is correctly estimated to be equal to 1.

Determine Load Capacitance

$GdB := -12.32$

$Ctest := 32.4$

$Gv := 10^{\frac{GdB}{20}}$

$Gv = 0.242$

$Cload := \frac{1 - Gv}{Gv} \cdot Ctest$

$Cload = 101.427$

Determine Capacitance of Parallel Plate Sensor in Air

$GdB := -28.95$

$Gv := 10^{\frac{GdB}{20}}$

$Gv = 0.036$

$Cair := \frac{Gv}{1 - Gv} \cdot Cload$

$Cair = 3.754$

Figure 12.16: A Mathcad worksheet example for converting gain and phase output of the parallel plate sensor for measurements in floating voltage measurement mode with no conductivity present. Included here for easy reference.

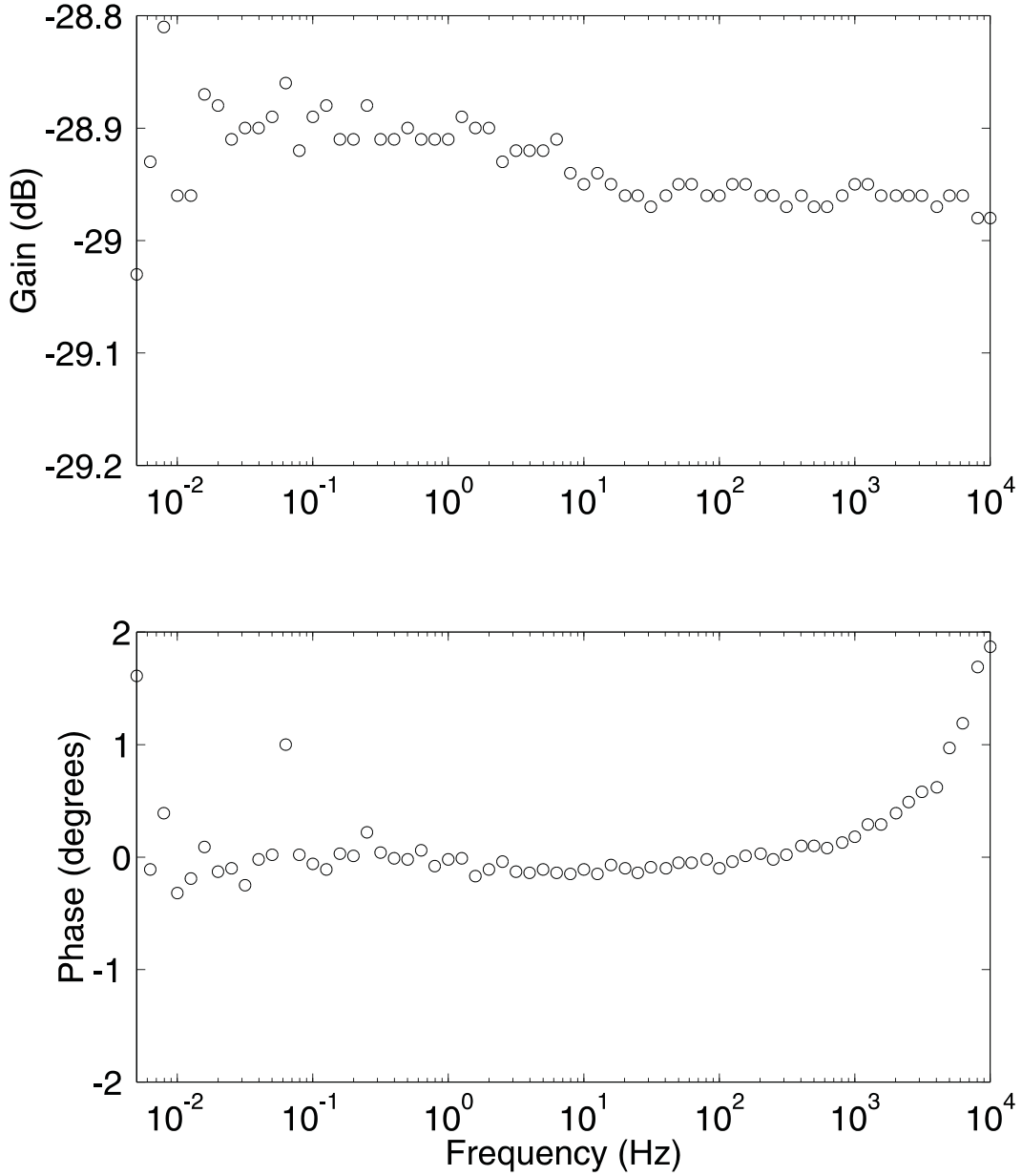

Figure 12.17: Gain and phase output of the parallel plate sensor for measurements in air in floating voltage mode, $C_L = 101.4$ pF.

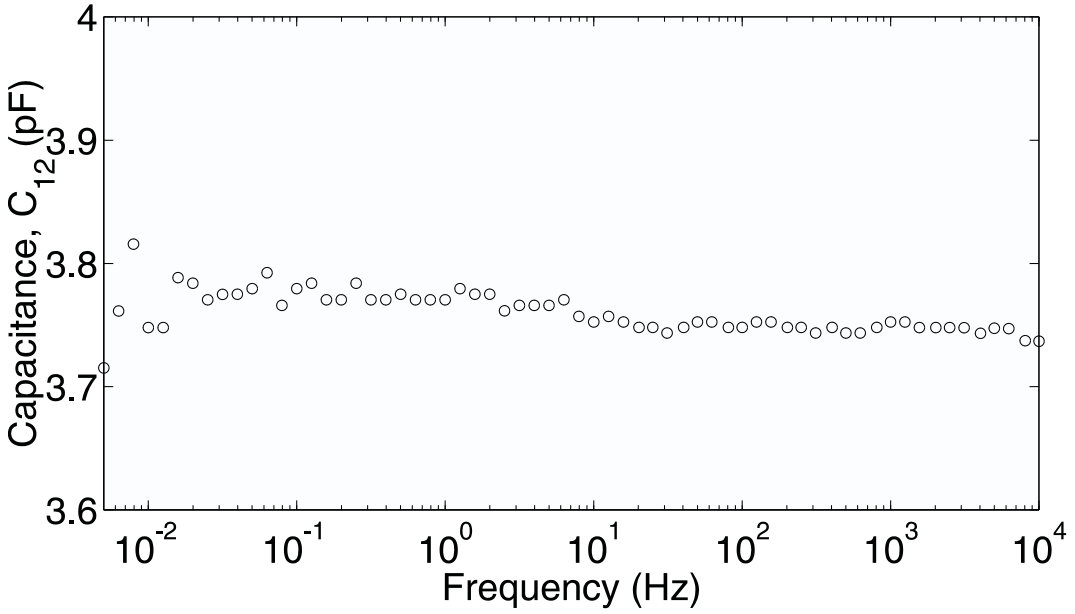

Figure 12.18: Capacitance of the parallel plate sensor in air estimated from the data in Figure 12.17.

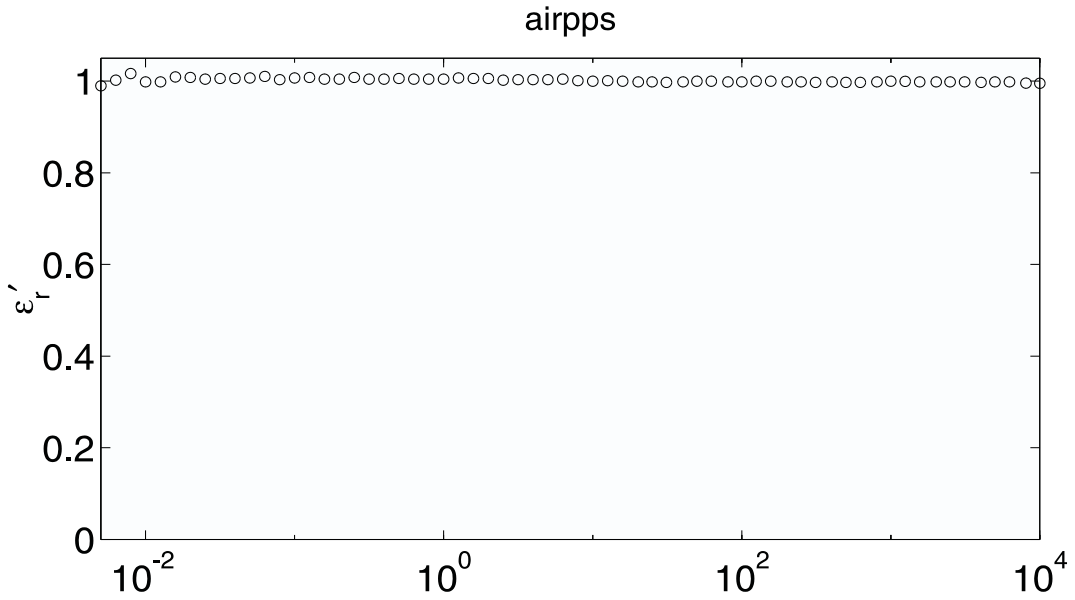

Figure 12.19: Relative dielectric permittivity of air estimated using calibration parameters and data in Figure 12.18.

12.6.2 Measurements in Sand

The following gallery of plots (Figure 12.20-Figure 12.29) is mostly self-explanatory. They represent a variety of ways to display dielectric spectroscopy data and could serve as a starting point for someone who wants to pursue dielectric spectroscopy as a means of enhancing detection and discrimination of plastic landmines. Each representation has individual characteristics that might be advantageous for increasing sensitivity and selectivity of the landmine detector without changing the sensor design. For example, one might discover that measurements around 1 Hz frequency are too slow for field application. In this case, a logical step may be to explore data display and analysis in terms of dielectric modulus $M = \varepsilon^{-1}$ rather than dielectric permittivity or conductivity because it tends to emphasize high frequency data as shown in Figure 12.29.

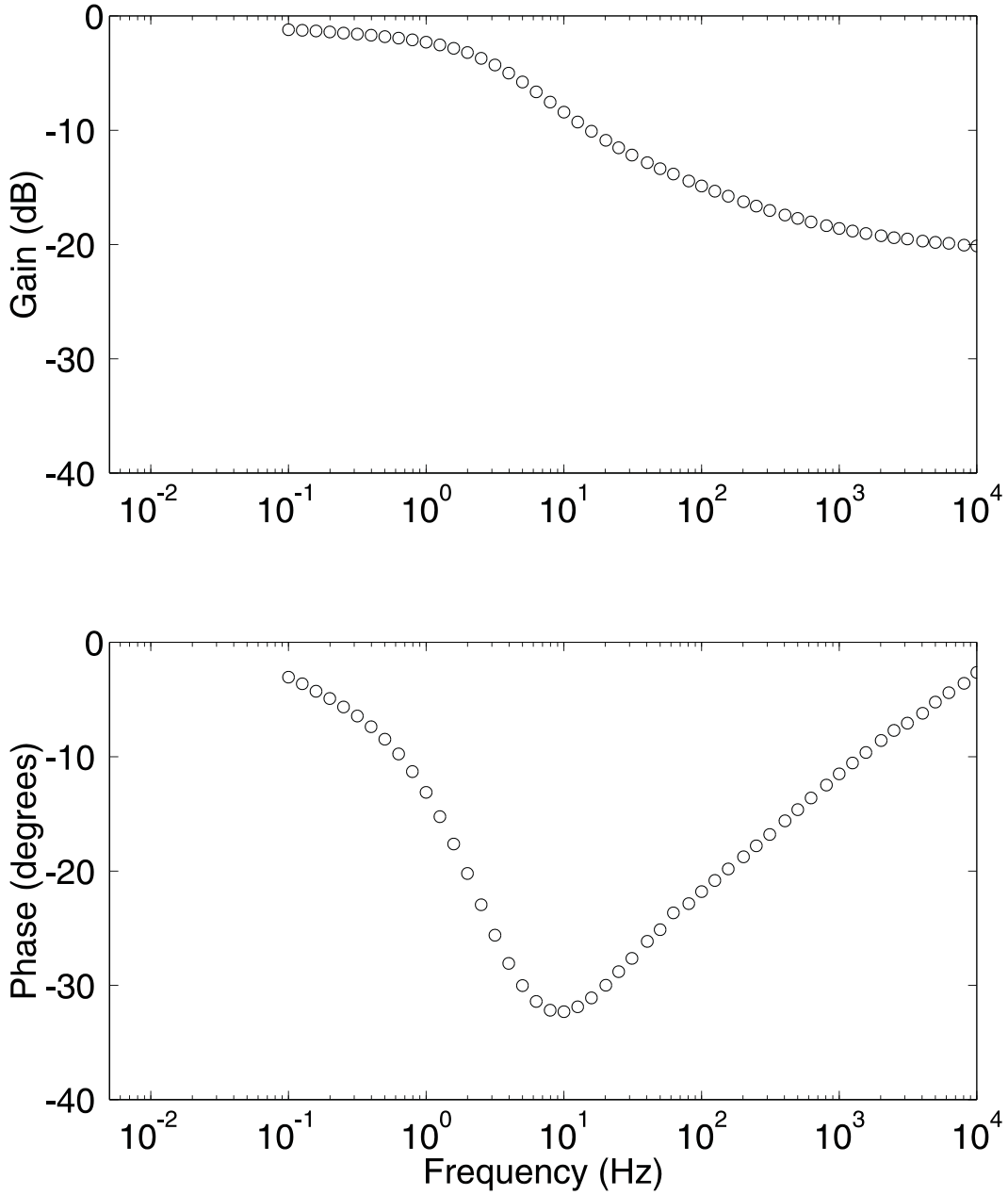

Figure 12.20: Gain and phase of sand vs. frequency estimated using the parallel plate sensor. The phase breakpoint and the frequency around 10 Hz suggests that it might be a good frequency for searching individual signatures of buried objects.

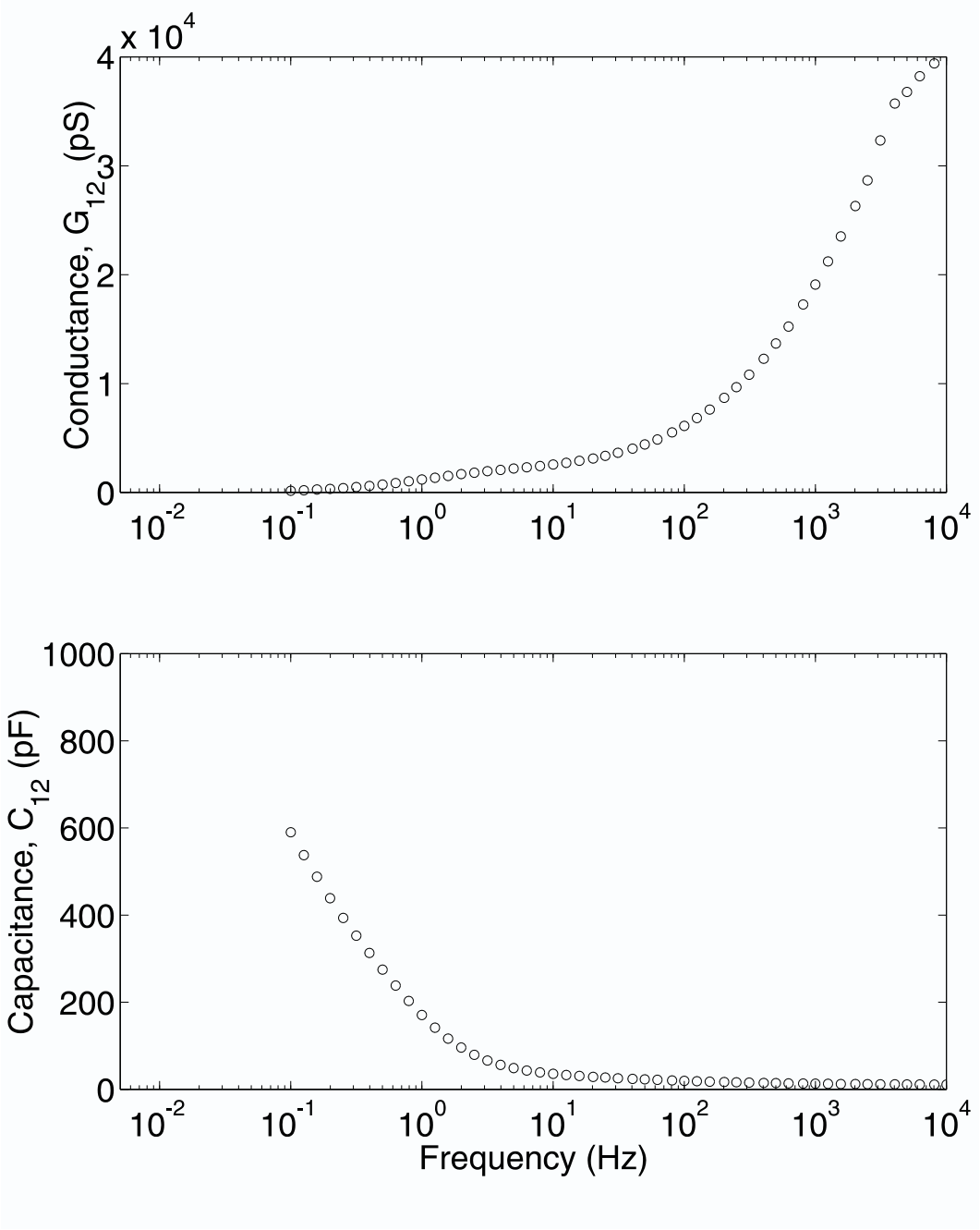

Figure 12.21: Capacitance and conductance of sand vs. frequency estimated from data in Figure 12.20. One can see that with this traditional representation the dielectric response does not have significant distinct features, but rather shows conductance growth and capacitance decay with increasing frequency.

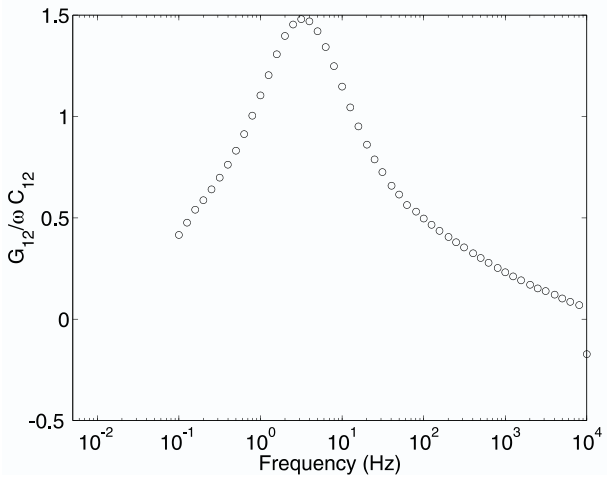

Figure 12.22: Loss angle tan δ of sand vs. frequency for the data in Figure 12.21. For a parallel plate capacitor geometry, tan δ is exactly equal to the ratio $C_{12}/\omega G_{12}$, but it is not true for fringing field geometry. Interestingly, for the parallel plate geometry the error in the estimation of the geometrical dimensions does not introduce errors into the estimation of tan δ.

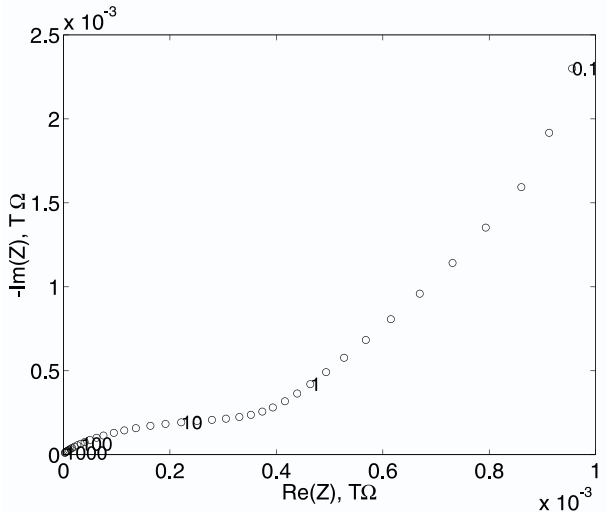

Figure 12.23: Real part of impedance vs. negative imaginary part of impedance for the data in Figure 12.21. Notice that in comparison with the sugar data which will be presented in Figure 12.33, high conductivity values at low frequencies dominate approximately the semi-circular shape of the Nyquist plot with a breakpoint frequency at about 10 Hz.

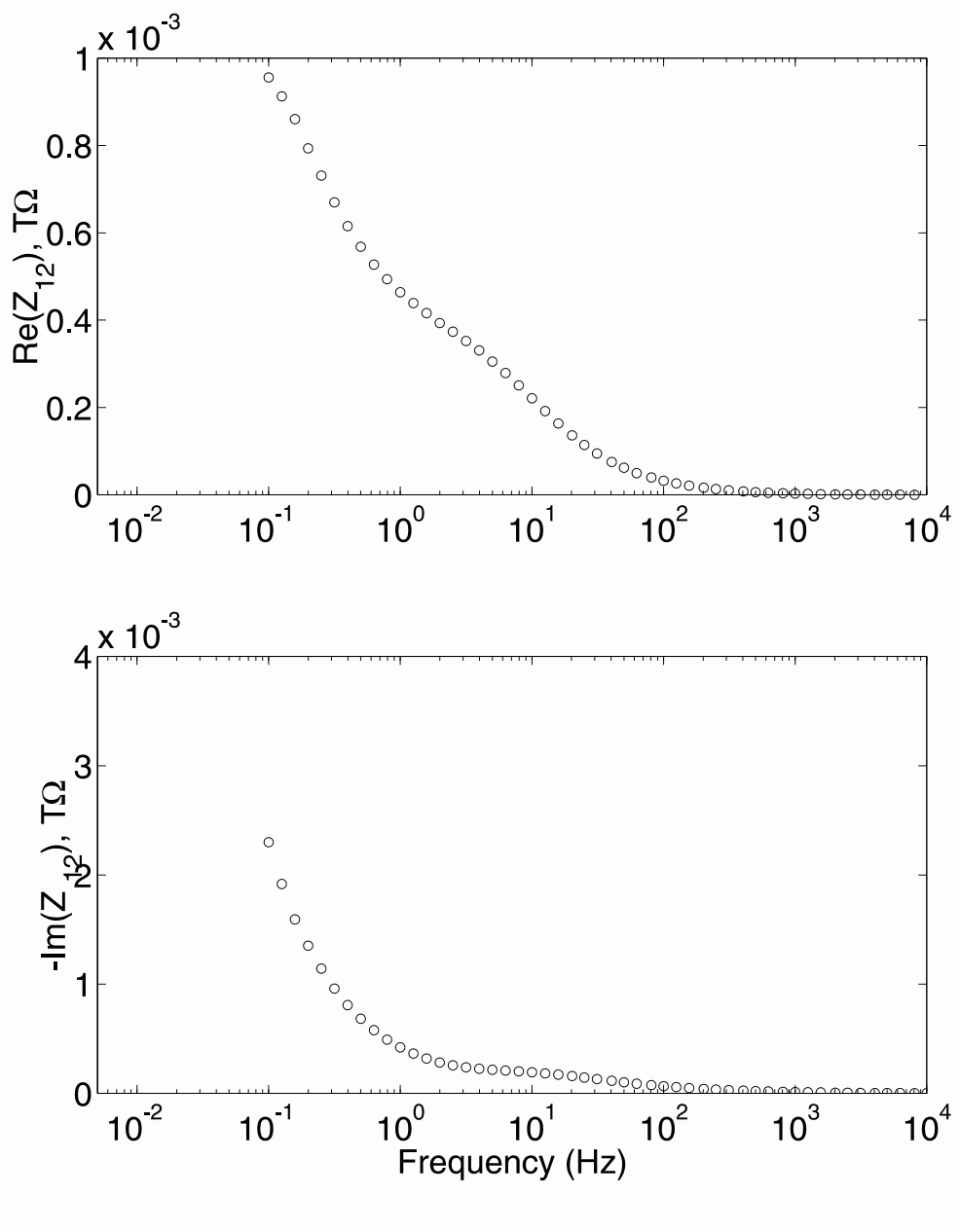

Figure 12.24: Real and imaginary parts of impedance of sand vs. frequency estimated based on the data in Figure 12.21. Impedance spectroscopy also tends to emphasize lower frequencies. Since it generally is used more frequently than the admittance spectroscopy, it should not be overlooked in the search process for reliable landmine detection techniques.

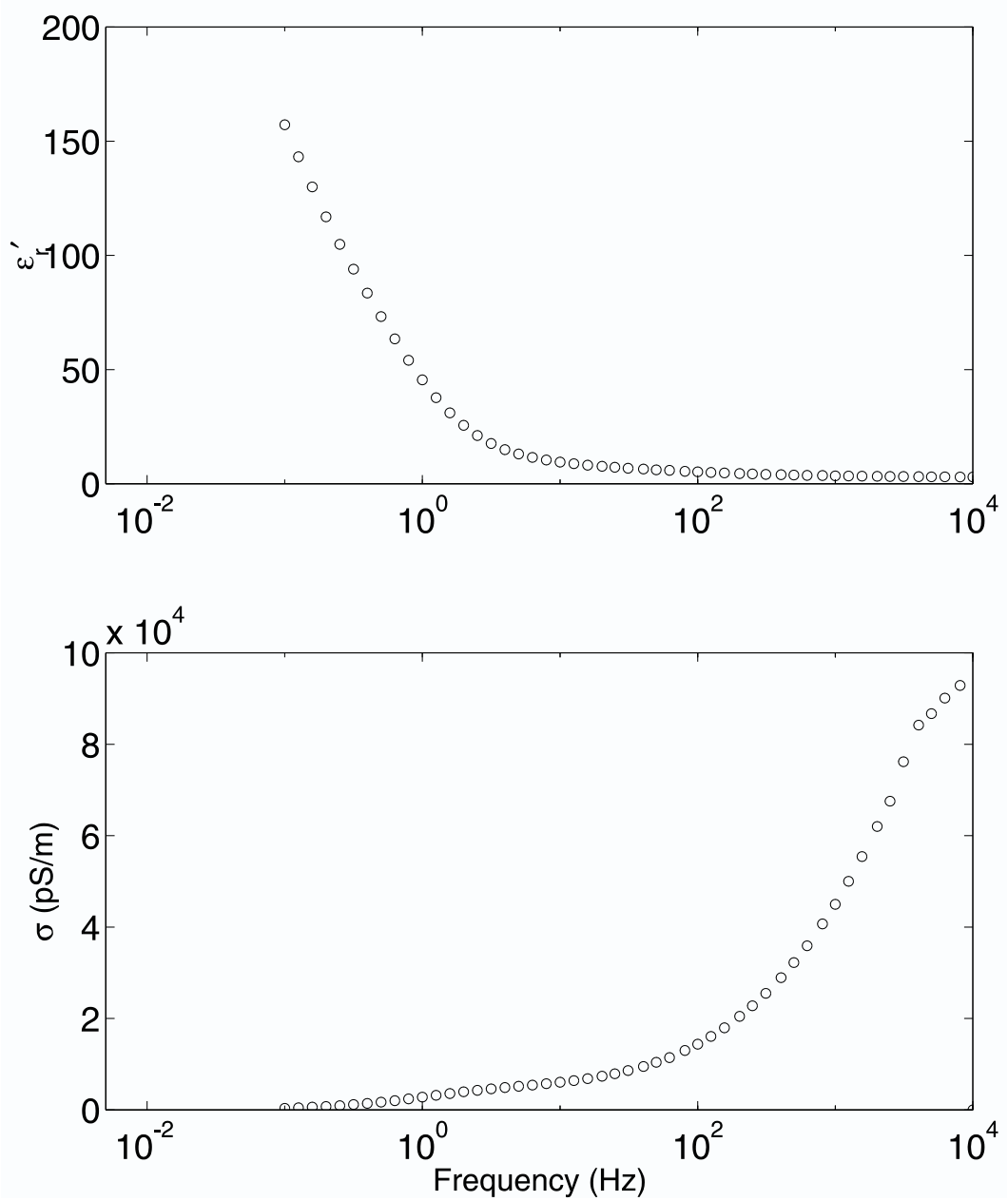

Figure 12.25: Relative dielectric permittivity and conductivity of sand estimated from Figure 12.21 data. A decrease of relative dielectric permittivity with frequency is characteristic for all materials (although not necessarily in the shown frequency range). The large increase of apparent conductivity with frequency is frequently observed in granular materials. It is important to know whether plastic explosives are expected to appear in granular or solid form and the size of the grains.

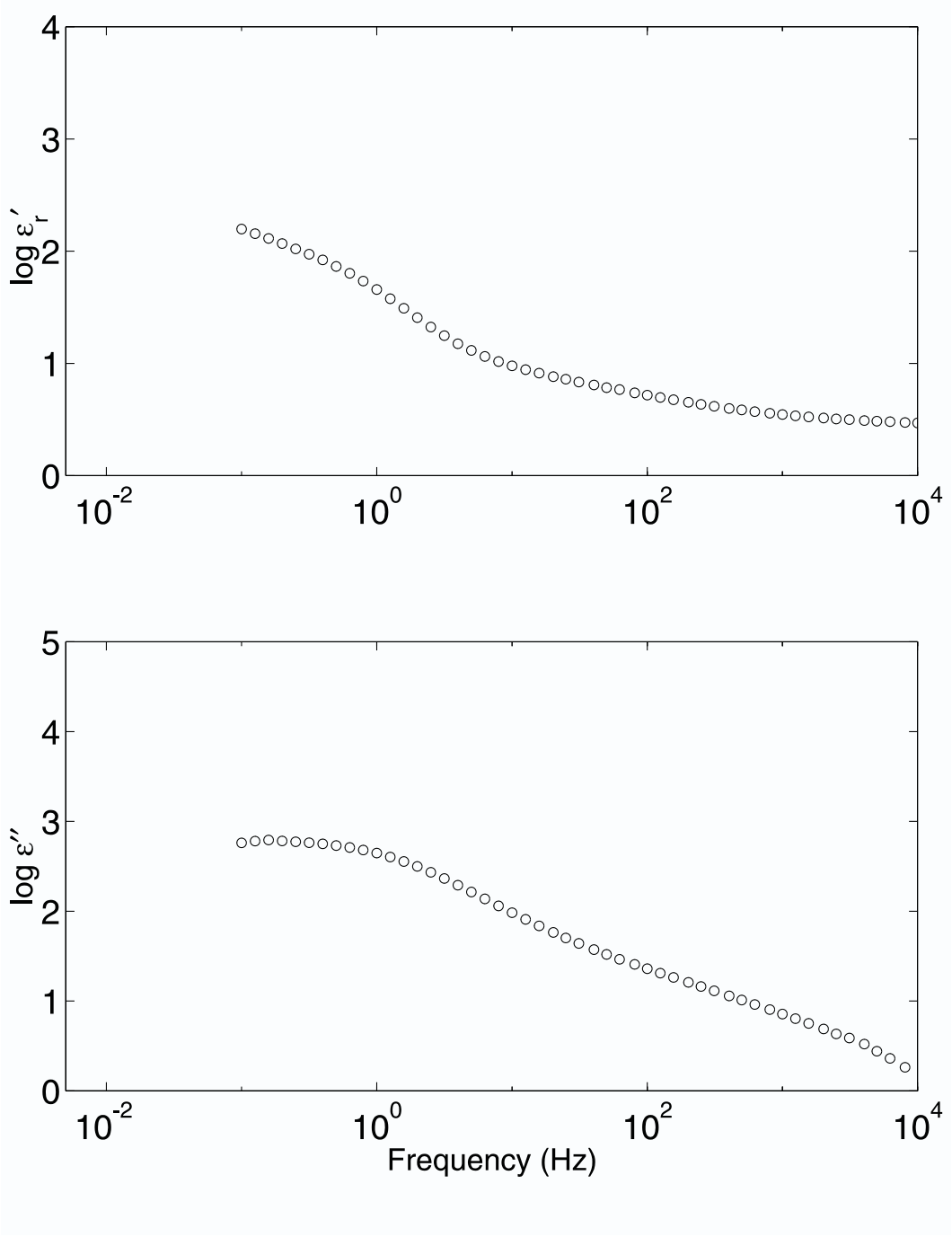

Figure 12.26: Relative dielectric permittivity and loss factor of sand vs. frequency estimated from Figure 12.21 data. The slope of log ε'' is approximately -0.6 in the linear region, which indicates the dispersive nature of the material response.

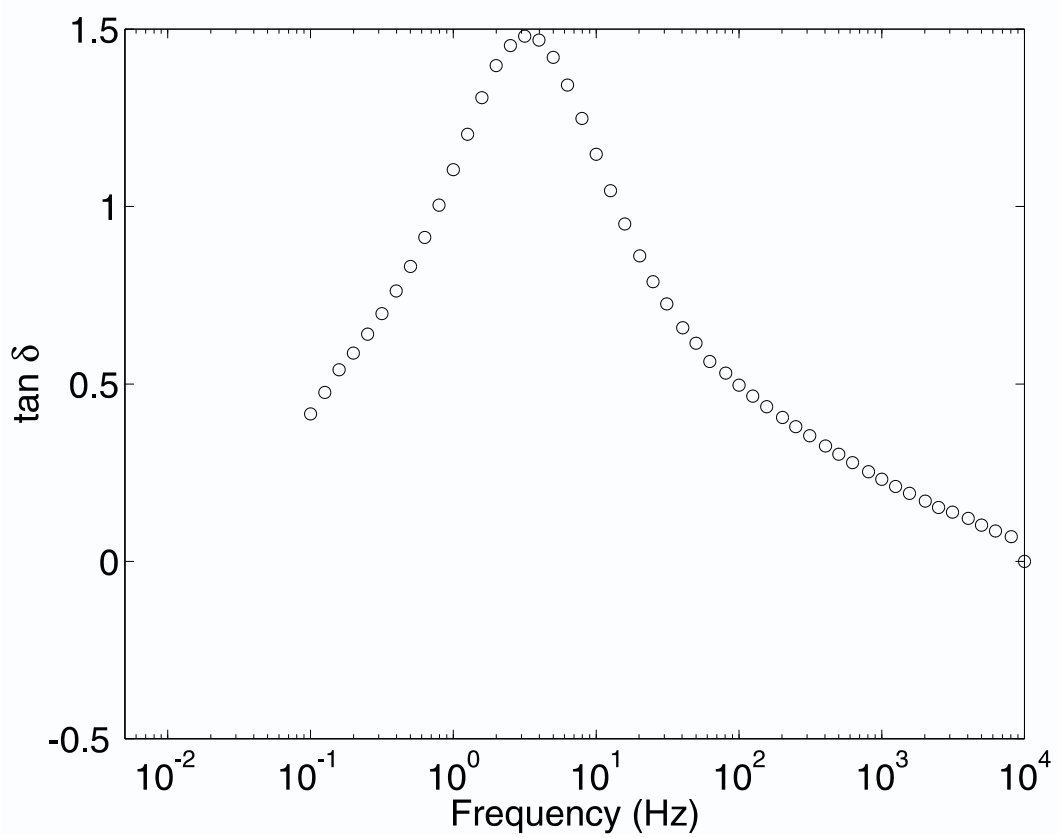

Figure 12.27: Loss tangent of sand vs. frequency using parallel plate sensor with the data from Figure 12.21.

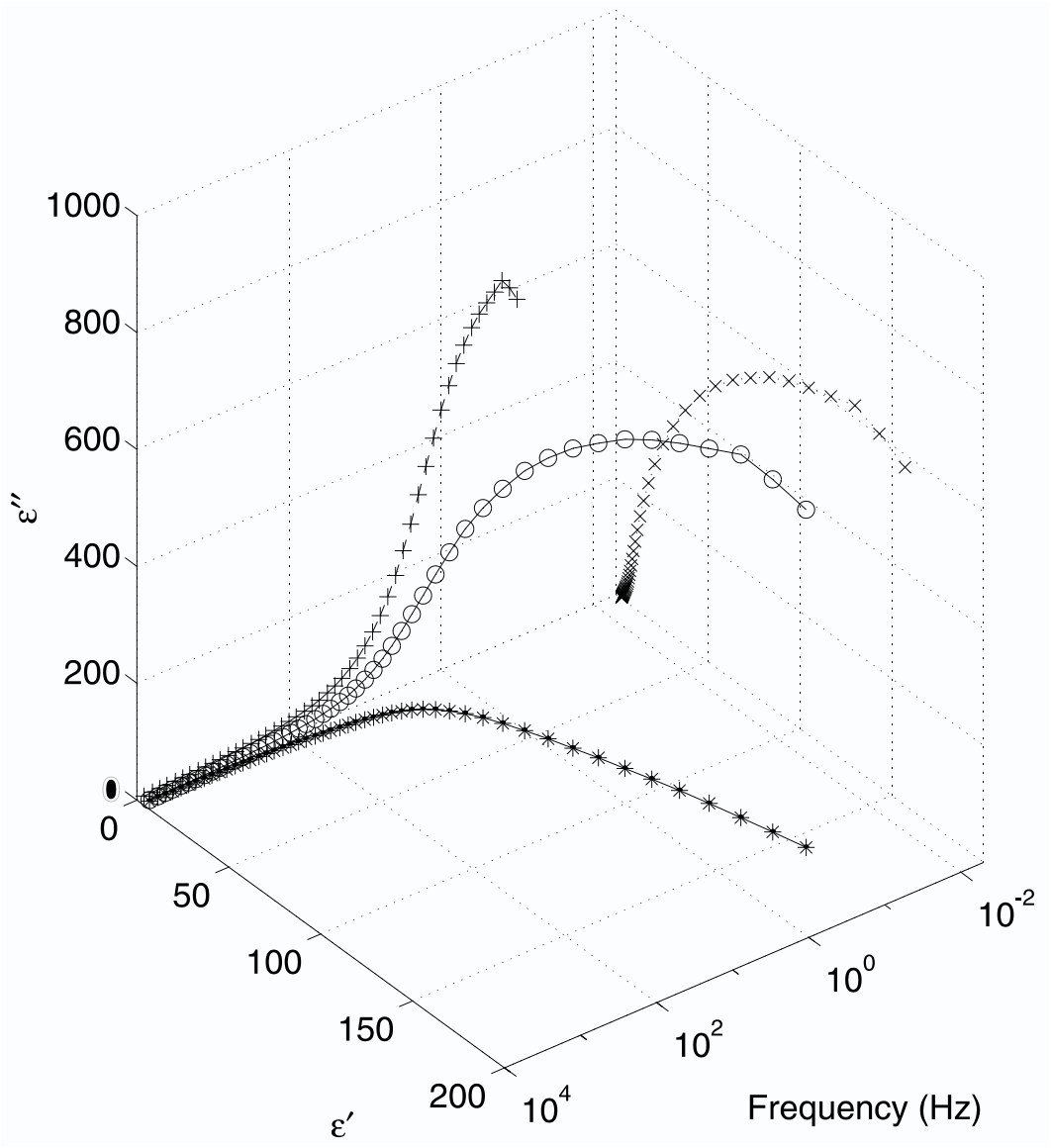

Figure 12.28: Relative dielectric permittivity and loss factor of sand vs. frequency (circles) estimated from Figure 12.21 data. The projection on the backplane (x's) is a Cole-Cole plot, of a nearly semi-circular shape. Modeling of Cole-Cole plots using constant value circuit equivalent elements and constant phase elements (CPE) helps the understanding of micro- and macro-structure of the material under test.

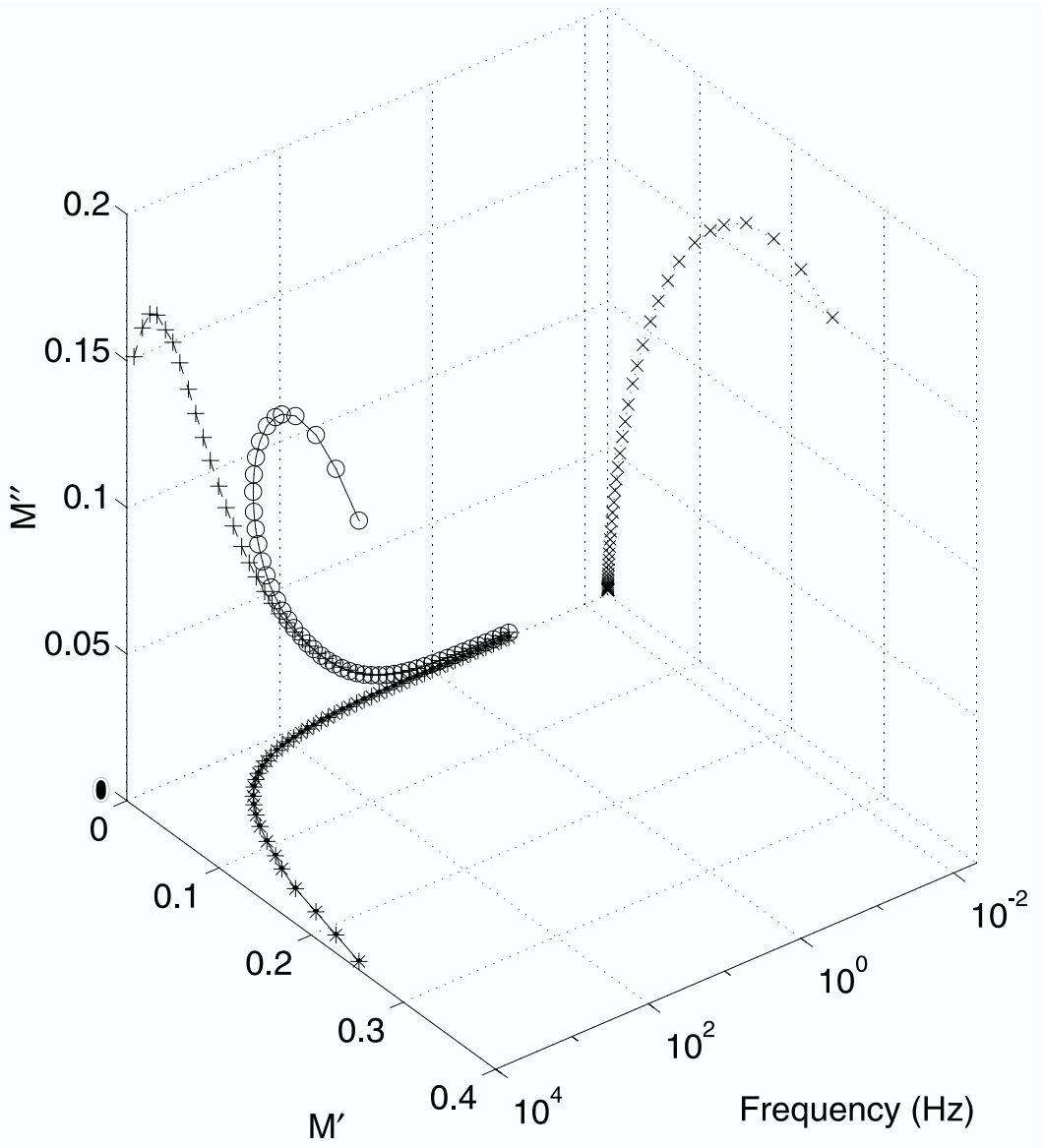

Figure 12.29: Real and imaginary parts of the complex modulus $M = M' - jM'' = 1/\varepsilon^*$ of sand vs. frequency for Figure 12.21 data. Modulus spectroscopy plots usually emphasize high frequency features of dielectric data, which makes it potentially a very valuable tool for high-speed field applications. In this plot one of the most salient features is the maximum of M'' at about 5 kHz.

12.6.3 Measurements in Sugar

The results of dielectric measurements of sugar properties show a great deal of similarity to the sand properties. Part of the reason is that the grain size is approximately equal in both cases. Undoubtedly, a fine powder would exhibit a significantly different response, but the experimental verification of that goes beyond the scope of the current study. Some of the plots analogous to those already presented for sand are given in Figures 12.30-12.38.

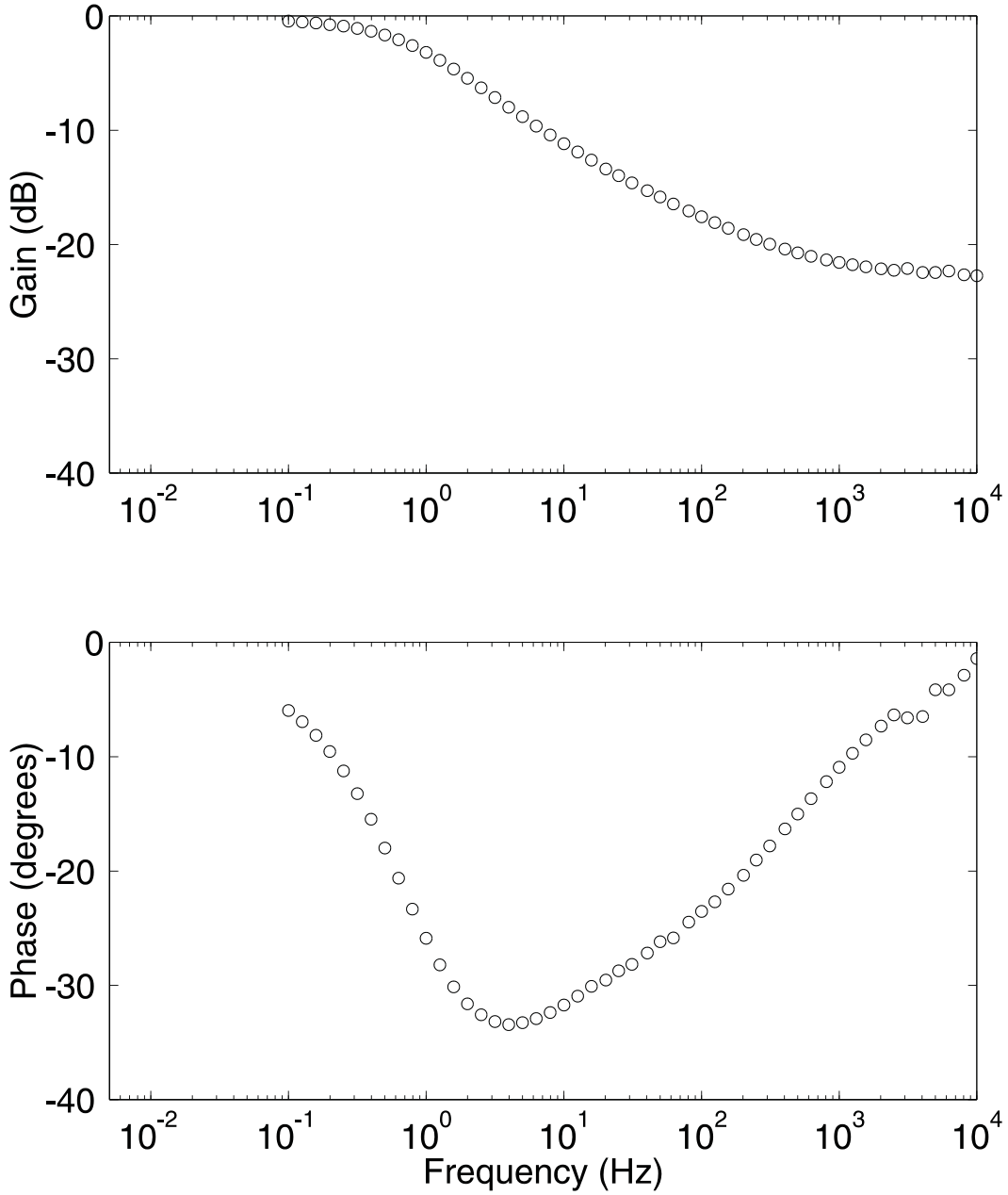

Figure 12.30: Measured gain and phase of sugar vs. frequency using the parallel plate sensor in floating voltage mode with load capacitance $C_L = 101.4$ pF. This response is very similar to that of sand in Figure 12.20, except the minimum phase point is located at about 4 Hz.

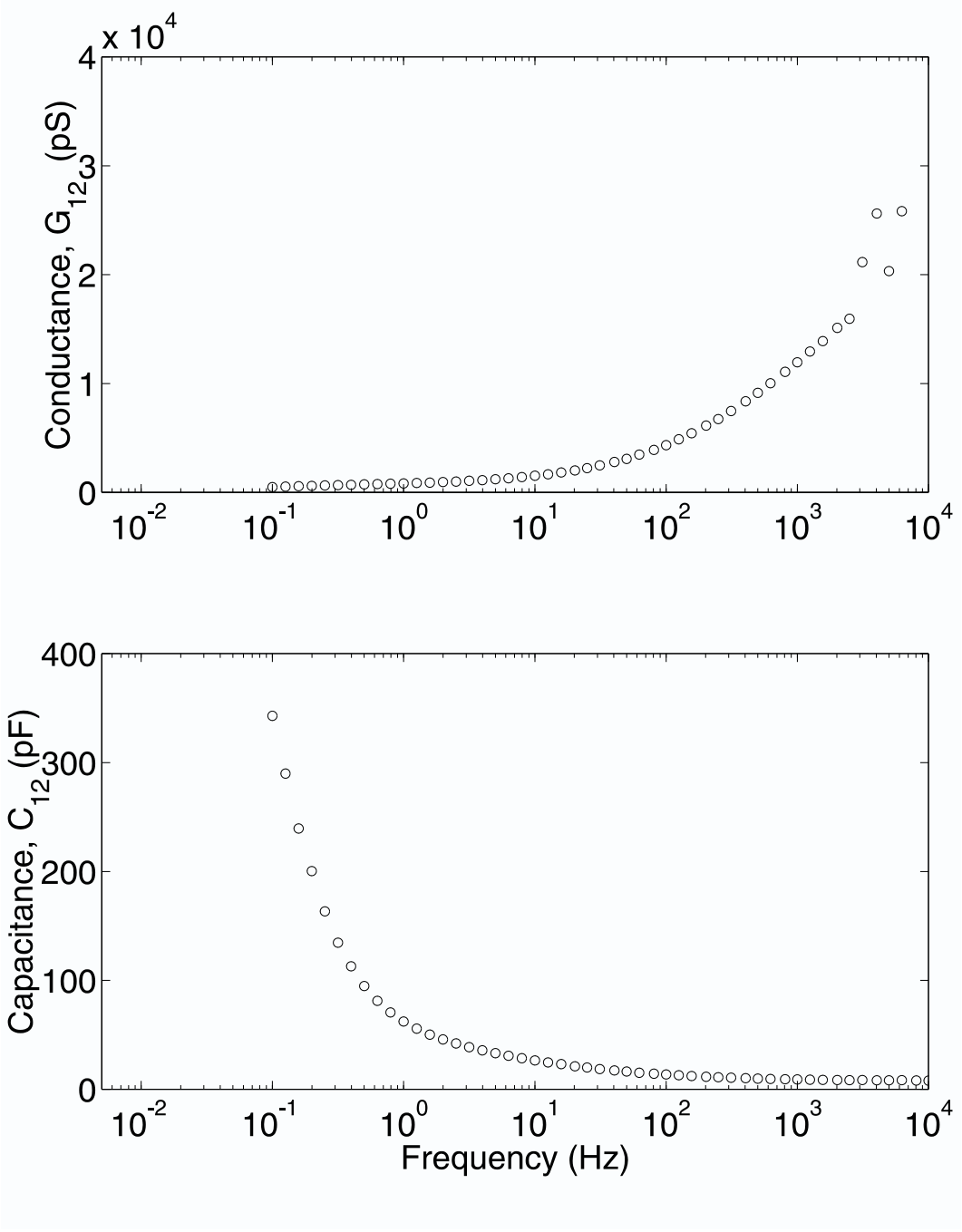

Figure 12.31: Capacitance and conductance of sugar vs. frequency calculated from Figure 12.30 with load capacitance $C_L = 101.4$ pF.

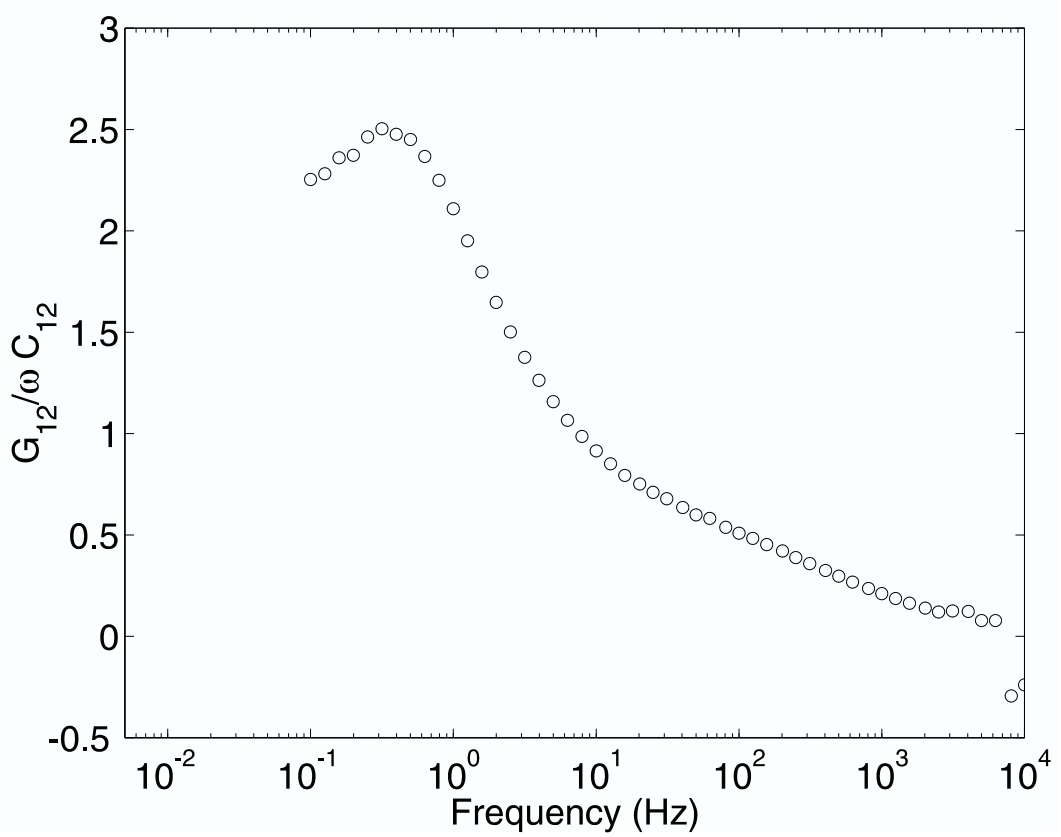

Figure 12.32: Loss tangent $\tan\delta = G_{12}/\omega C_{12}$ *for the data in Figure 12.31.*

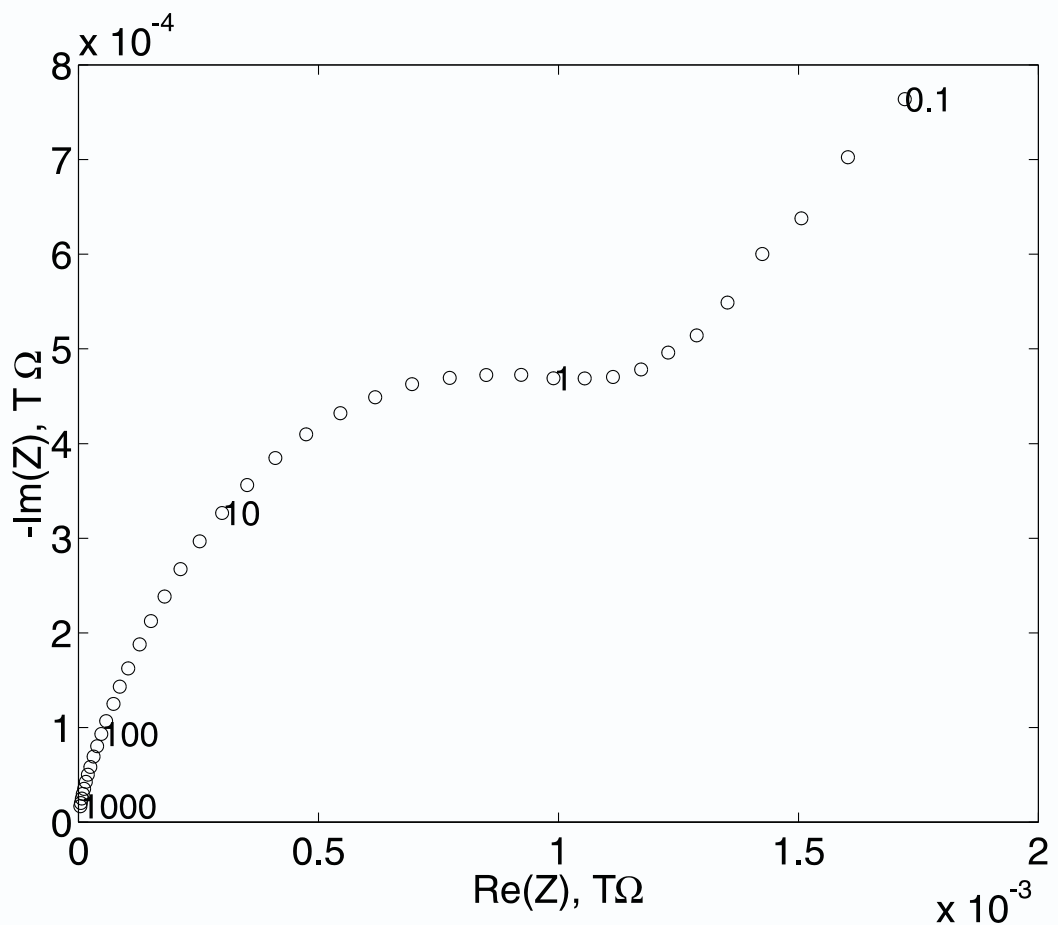

Figure 12.33: Real part of impedance vs. negative imaginary part of impedance for the data in Figure 12.31. Notice that in comparison with the sand data in Figure 12.23, the lower conductivity values at low frequencies result in a clearly visible semi-circular shape of the Nyquist plot with a breakpoint frequeny at 1 Hz.

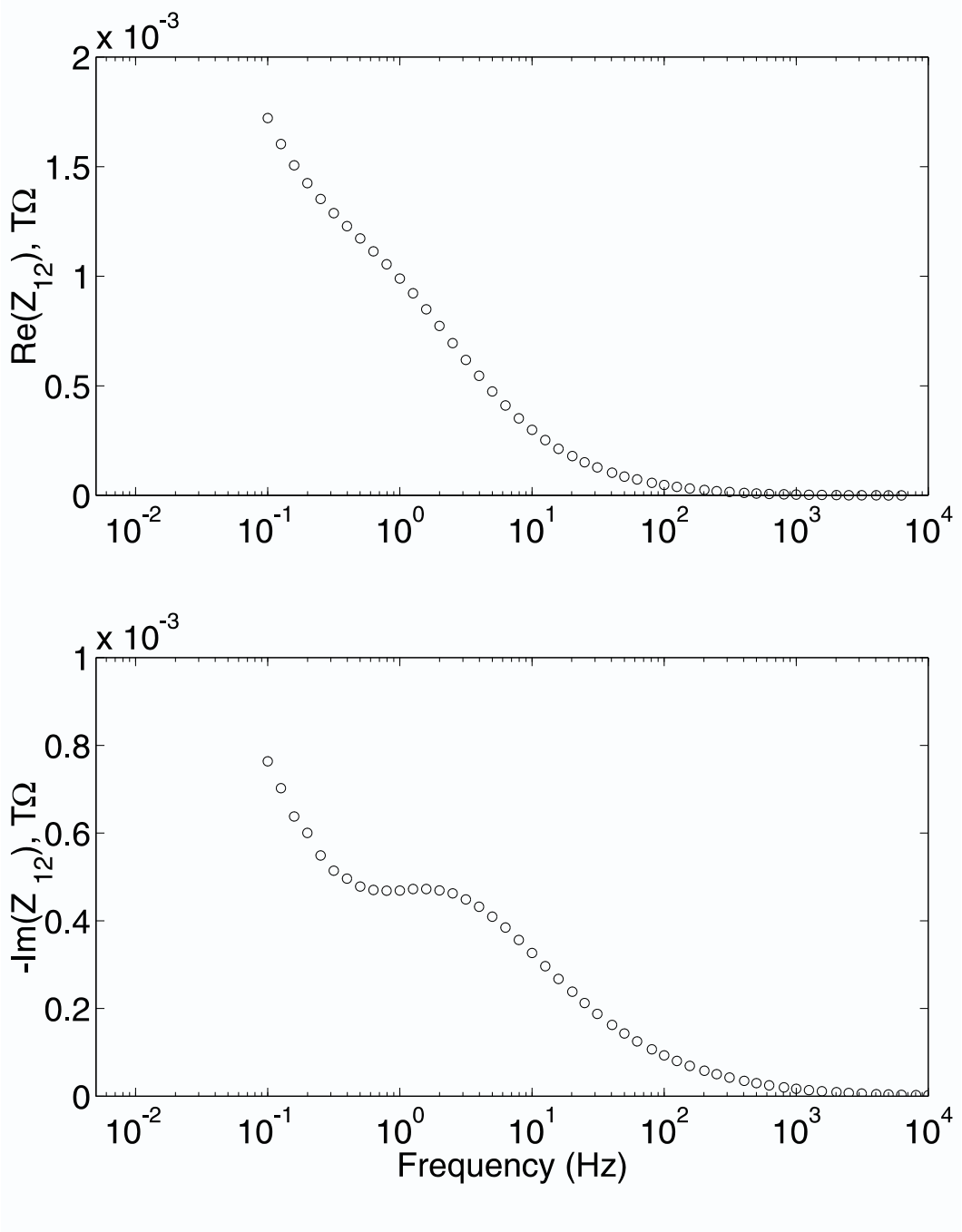

Figure 12.34: Real and imaginary parts of impedance of sugar vs. frequency for the data in Figure 12.31. Notice that this representation has more salient features than the admittance representation in Figure 12.31.

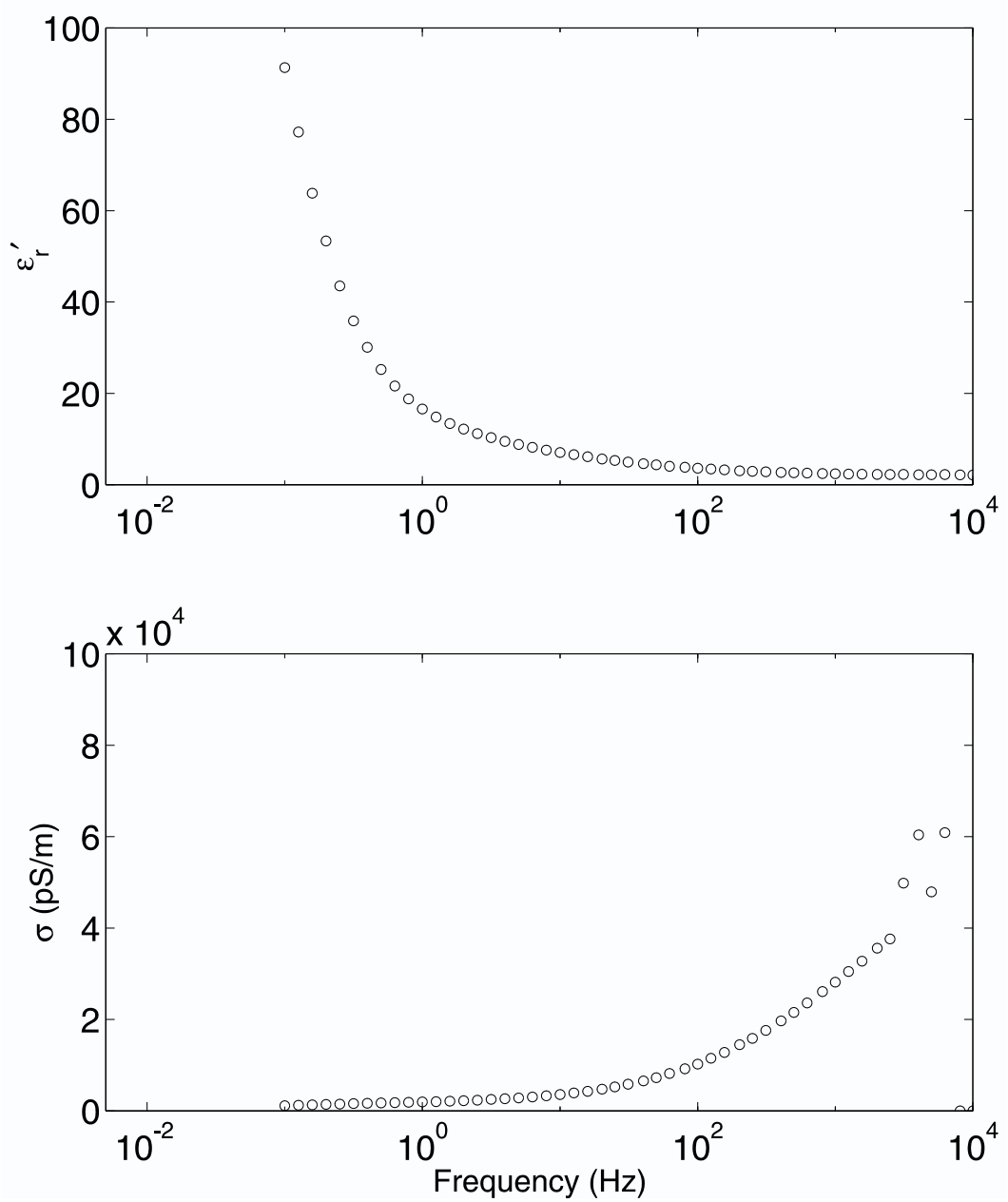

Figure 12.35: Relative dielectric permittivity and conductivity of sugar for the data in Figure 12.31. Again, a large increase in conductivity and decay in dielectric permittivity with increasing frequency dominates the frequency response.

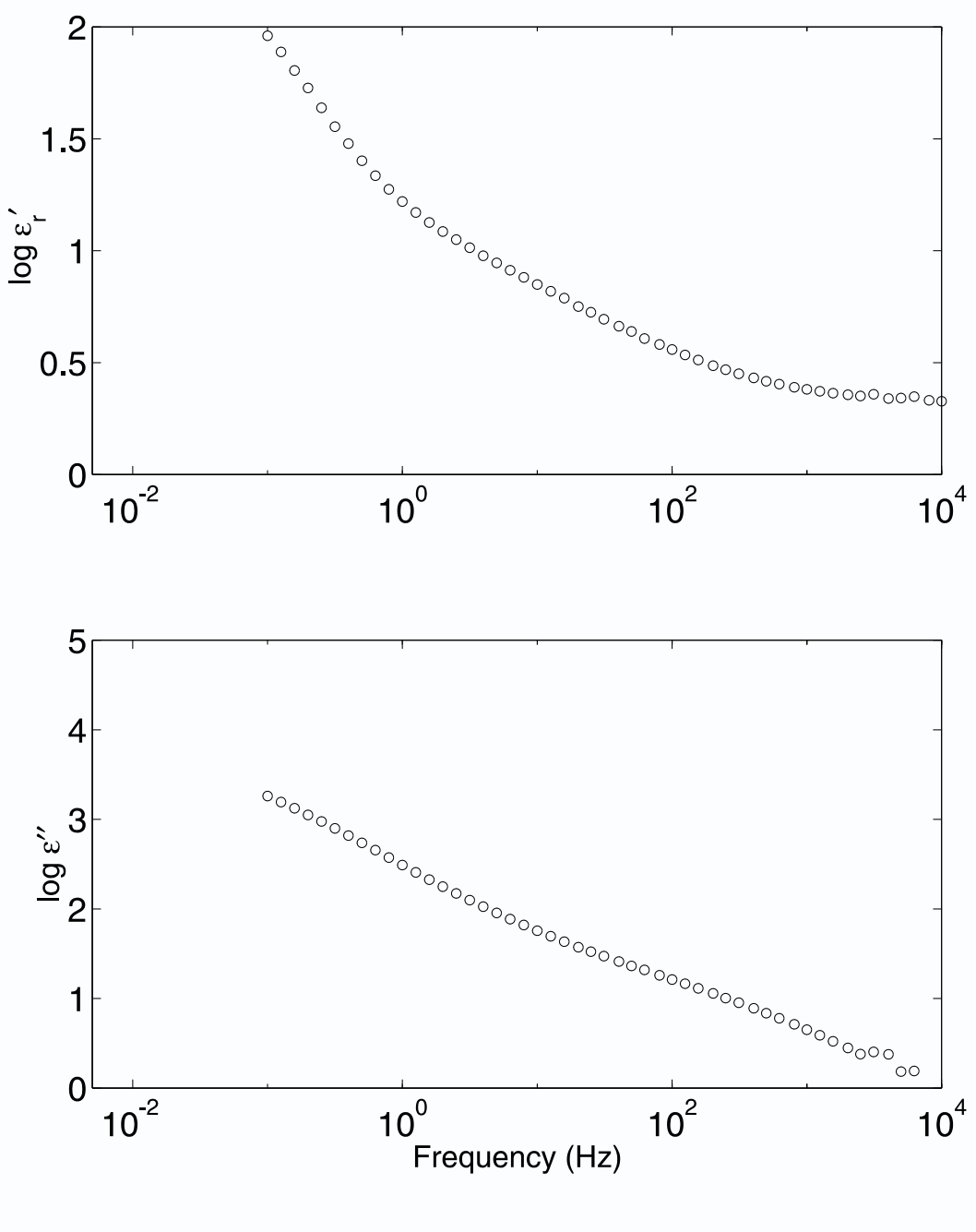

Figure 12.36: Relative dielectric permittivity and loss factor of sugar vs. frequency for the data in Figure 12.31. The log ε'' plot is nearly linear for the entire measured frequency range with a negative slope of about -0.5 showing that sugar is frequency dispersive in this frequency range.

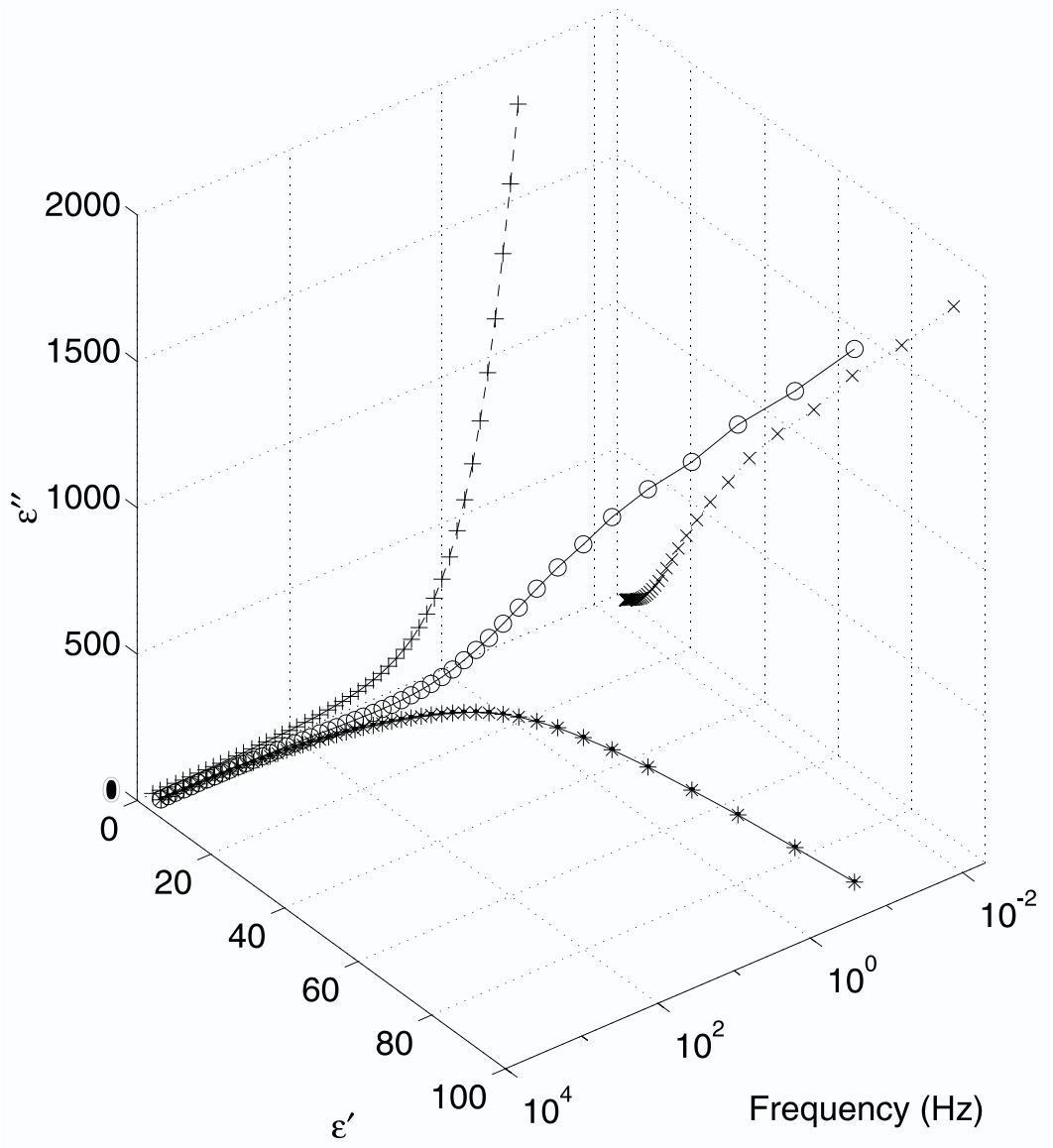

Figure 12.37: Relative dielectric permittivity and loss factor of sugar vs. frequency estimated for Figure 12.31 data. The projection on the backplane is a Cole-Cole plot with shape that significantly departs from a semi-circle. Compare with analogous data for sand in Figure 12.37. Modeling of Cole-Cole plots using constant value circuit equivalent elements and constant phase elements (CPE) helps in the understanding of micro- and macrostructure of the material under test.

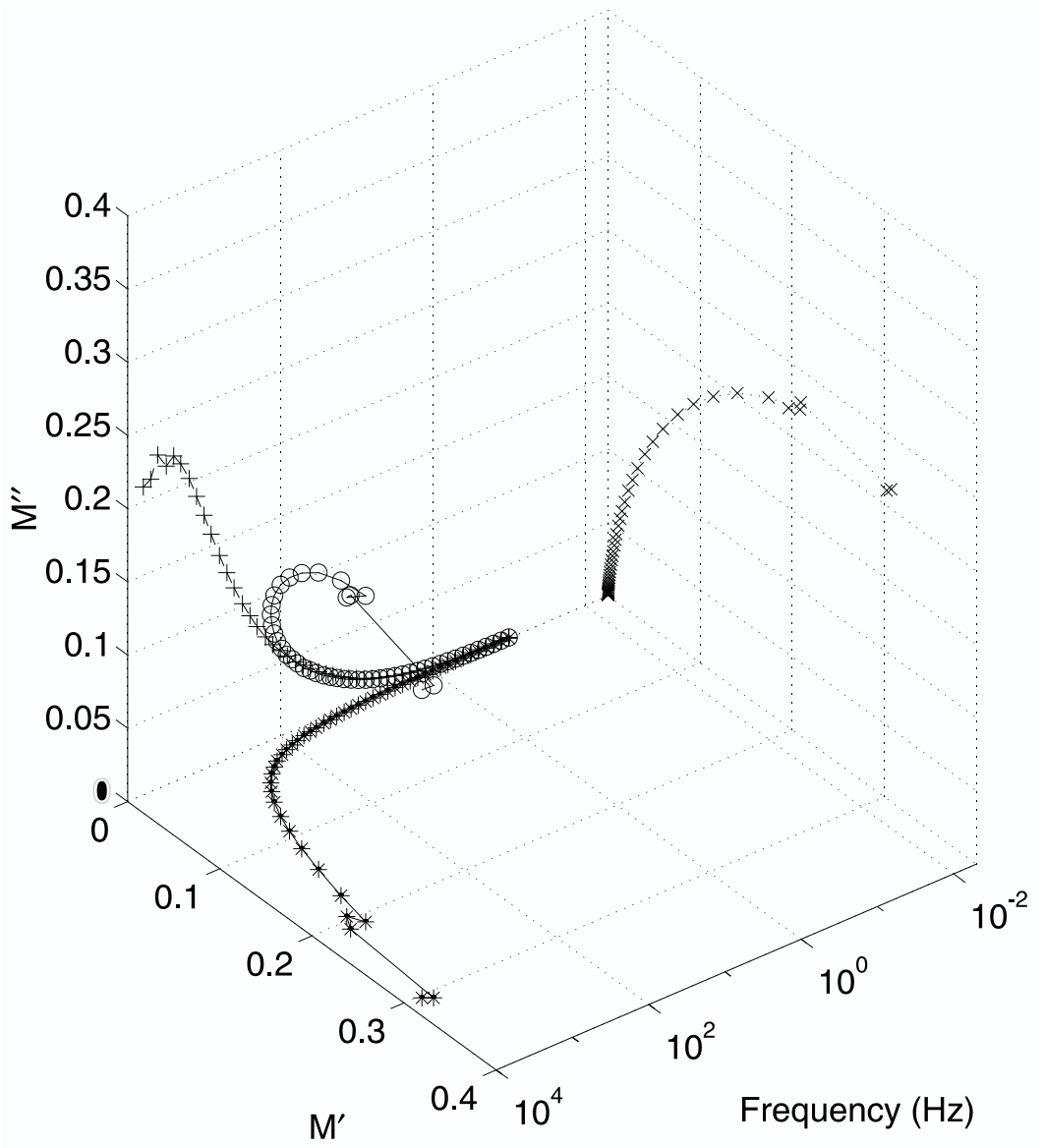

Figure 12.38: Real and imaginary parts of the complex modulus $M = 1/\varepsilon^* = M' - jM''$ of sugar vs. frequency for Figure 12.31 data. Modulus spectroscopy plots usually emphasize high frequency features of dielectric data, which makes it potentially a very valuable tool for high-speed field applications. In this plot one of the most salient features is the maximum of M'' at about 3 kHz. The noise above 5 kHz is due to speed limitations of the high input impedance operational amplifier AD509 in the dielectrometry interface circuitry. If needed, a faster op-amp can be used at these frequencies.

12.6.4 Simulations of Landmine Sensor

Optimization of Sensor Design

The sensitivity of the fringing field dielectrometry sensor can be increased by positioning driving, sensing, and guard electrodes so that the relative change of the signal is maximum when the land mine is present. The analysis given here is not novel, it simply illustrates an obvious and very common approach in the designing of fringing field sensors. One example of this type of sensor geometry modification is given in Figure 16 of [60]. Two cases are considered in this section. The first case uses parallel positioning of the sensing and guard electrodes, as shown in Figure 12.39. The width of each electrode is 5 cm, the distance between the driven electrode and bottom guard electrode is 10 cm, and the distance between the sensing and guard electrodes is 0.5 cm. Only field plots for air are included here for compactness of presentation, so that the sand is not shown in the field plots. For simulations with sand, the flat sand surface is 3 cm below the sensing and drive electrodes. The region size is large enough to ignore the effects of the outside boundaries. In the field plots, the boundary conditions have zero normal electric field component, which is the *Maxwell* default Neumann condition. This is the design that is currently used. An alternative design, not necessarily the best, but better than the one currently used is shown in Figure 12.40. A different pattern of electric field lines is designed to increase the sensitivity of the sensor to the presence of dielectric materials in the fringing field region. The results of simulations with the first design are presented in Table 12.2 (air in the fringing field region) and in Table 12.3 (sand, dielectric permittivity equal to 6 and conductivity is zero, in the fringing field region). The ratio of capacitances between the driven and the sensing electrodes in sand and in air is 6.81/3.67=1.86.

The results of simulations with the second design are presented in Table 12.4 (air in the fringing field region) and in Table 12.5 (sand, dielectric permittivity equal to 6 and conductivity is zero, in the fringing field region). The ratio of capacitances between the driven and the sensing electrodes in sand and in air is 6.41/2.91=2.20, about 20 percent better than for the first design.

	Drive	GroundPlate	Sense	Senseguard
Drive	19.184	-13.44	-3.6695	-2.071
GroundPlate	-13.444	28.075	-5.0889	-9.5423
Sense	-3.6695	-5.0889	133.54	-124.78
Senseguard	-2.071	-9.5423	-124.78	136.4

Table 12.2: Capacitance matrix in pF/m for the design shown in Figure 12.39, with air in the fringing field region.

	Drive	GroundPlate	Sense	Senseguard
Drive	23.485	-13.79	-6.8069	-2.8884
GroundPlate	-13.79	28.87	-5.6053	-9.4752
Sense	-6.8069	-5.6053	137.09	-124.67
Senseguard	-2.8884	-9.4752	-124.67	137.04

Table 12.3: Capacitance matrix in pF/m for the design shown in Figure 12.39, with sand $\varepsilon_r = 6$ in the fringing field region 3 cm from the sensing electrode.

	Drive	GroundPlate	Sense	Senseguard
Drive	21.679	-9.7704	-2.9116	-8.9965
GroundPlate	-9.7704	64.349	-10.051	-44.528
Sense	-2.9116	-10.051	22.43	-9.4669
Senseguard	-8.9965	-44.528	-9.4669	62.991

Table 12.4: Capacitance matrix in pF/m for the design shown in Figure 12.40, with air in the fringing field region.

	Drive	GroundPlate	Sense	Senseguard
Drive	25.86	-10.043	-6.4053	-9.4118
GroundPlate	-10.043	66.884	-10.138	-46.704
Sense	-6.4053	-10.138	26.116	-9.5725
Senseguard	-9.4118	-46.704	-9.5725	65.688

Table 12.5: Capacitance matrix in pF/m for the design shown in Figure 12.40, with sand $\varepsilon_r = 6$ in the fringing field region 3 cm from the sensing electrode.

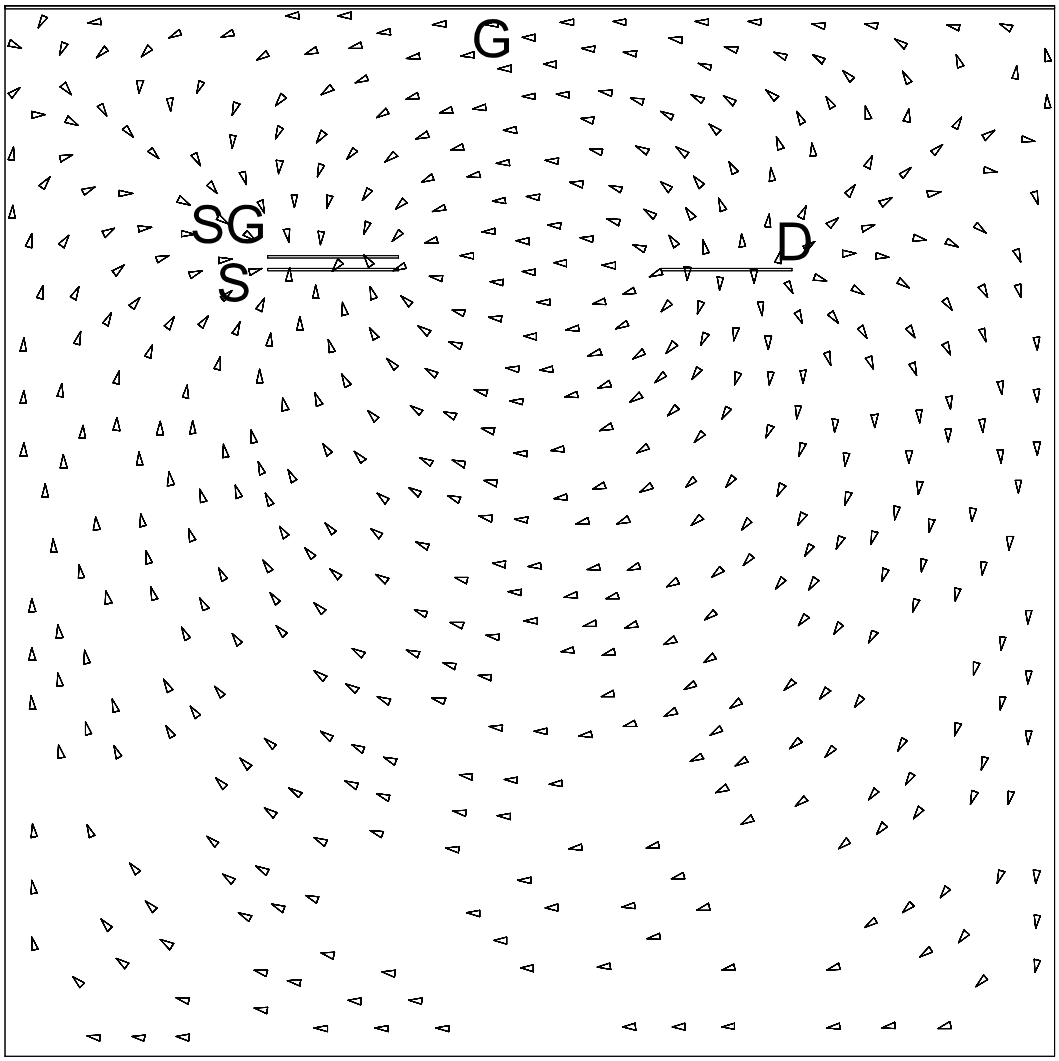

Figure 12.39: Present design of the fringing field landmine detector showing computed electric field arrows in air. D - drive, S - sense, SG - sense guard, G - guard. SG and G are at the same node from the electronic circuit point of view. Many electric field arrows go straight from the driven to sensing electrode without reaching the fringing field region of interest below the drive and sense electrodes.

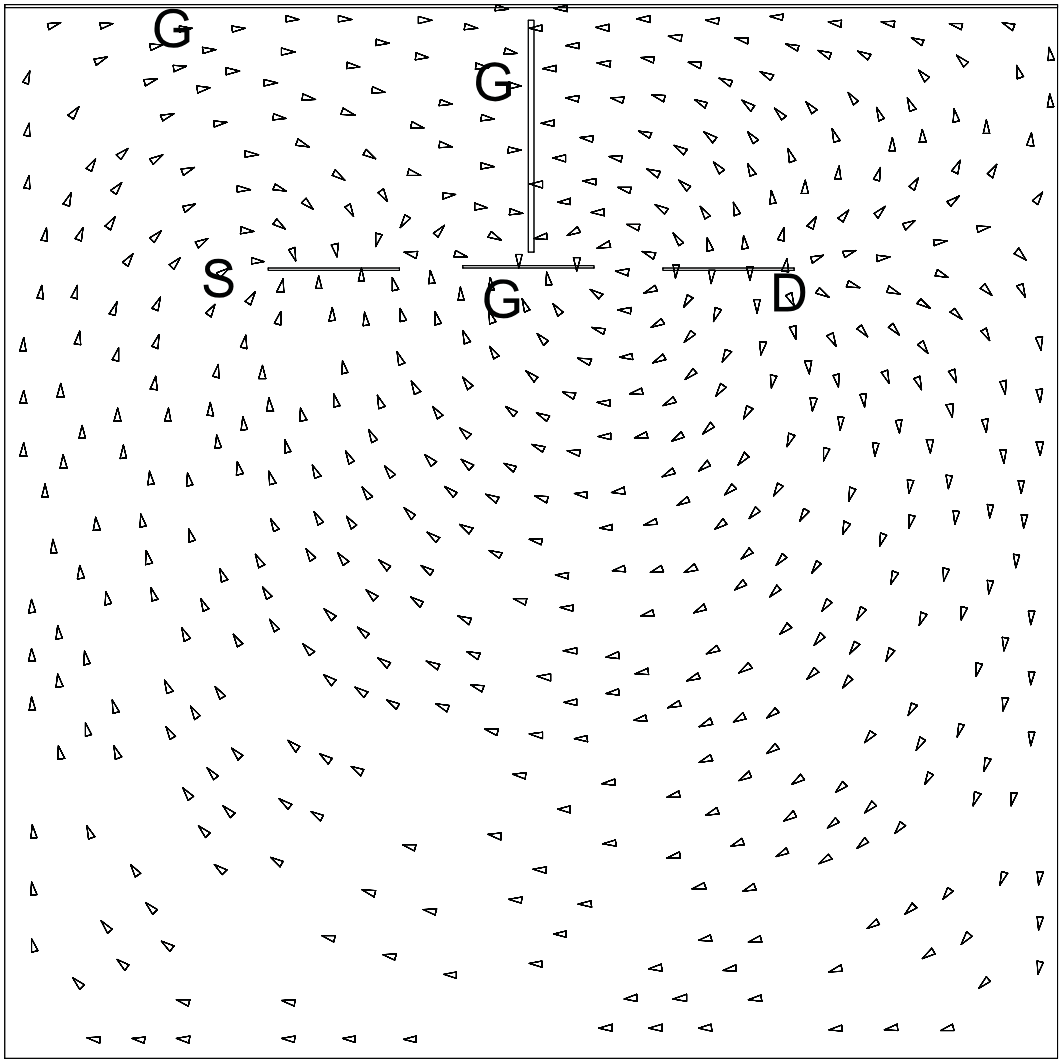

Figure 12.40: Improved design of the fringing field landmine detector showing computed electric field arrows in air. D - drive, S - sense, G - guard. All G electrodes are at the same node from the electronic circuit point of view. In this design, the capacitance between the driven and sensing electrodes is smaller than in the case shown in Figure 12.39, however the percent increase of the capacitance due to the presence of high permittivity sand dielectric in the fringing field region 3 cm below the drive and sense electrodes is higher.

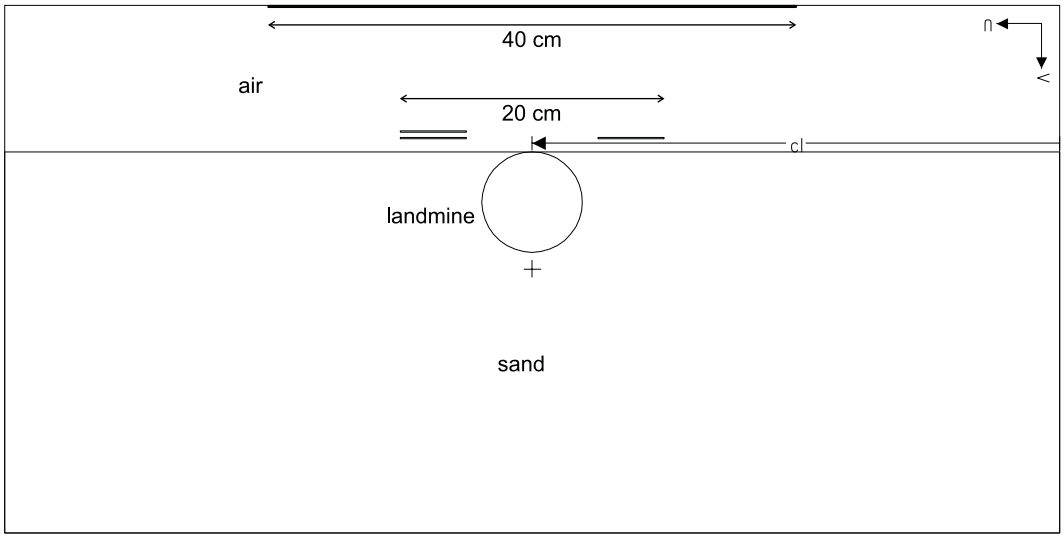

Figure 12.41: Sensor and landmine model used in simulations. The total sensor width is 40 cm.

Two-dimensional Simulation of Buried Landmines

Since some of the measurements performed in the lab include two-dimensional long cylindrical landmine surrogates of circular cross-section, the following simulations, performed with the help of Ricky Debnath [47] are helpful in preliminary estimation of the sensor response to the presence of a buried landmine. The sensor has been supplied by Jentek Sensors, Inc. [51]. Movement of the sensor above the landmine has been simulated with *Maxwell*. In all simulations, the sand is assumed to have dielectric properties that do not vary with frequency, $\varepsilon_r = 6$ and $\sigma = 10^{-9}$ S/m. The landmine has a radius of 3.8 cm, and the sensor is shown in Figure 12.41. Figures 12.42 and 12.43 show that in this case the sensor has a reasonable sensitivity to the presence of a Teflon landmine. The capacitance response has numerical noise for the case of a similar simulation for an aluminum landmine surrogate shown in Figure 12.44, which deserves additional investigation, but has a clean and easily identifiable signature for the conductance shown in Figure 12.45. The results suggest that this approach holds significant promise for humanitarian landmine detection, in which case the soil is allowed to be sufficiently dry and the terrain is sufficiently flat.

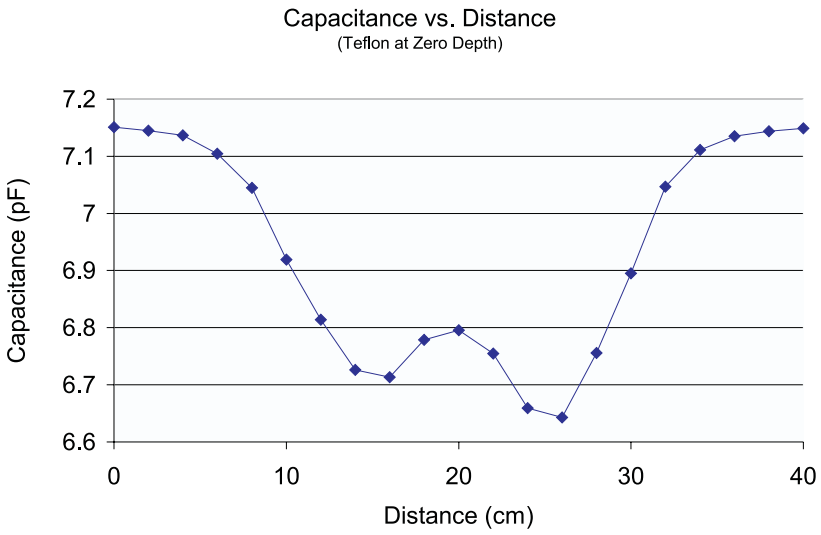

Figure 12.42: Measured capacitance vs. lateral distance for a Teflon landmine surrogate at zero depth. The capacitance achieves its extremum values when the mine is closest to the inner edges of sensing and drive electrodes.

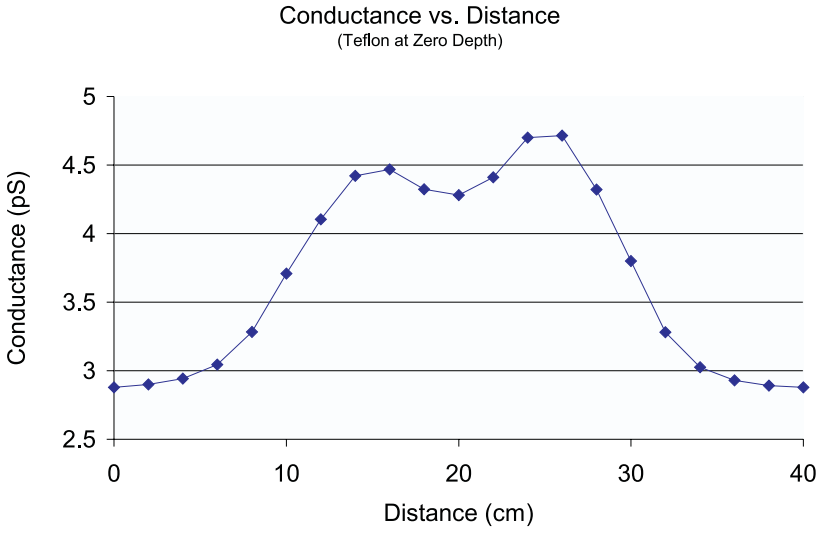

Figure 12.43: Measured conductance vs. lateral distance for a Teflon landmine surrogate at zero depth. The response is not symmetrical due to the presence of the guard electrode directly under the sensing electrode. The conductance achieves its extremum values when the mine is closest to the inner edges of sensing and drive electrodes.

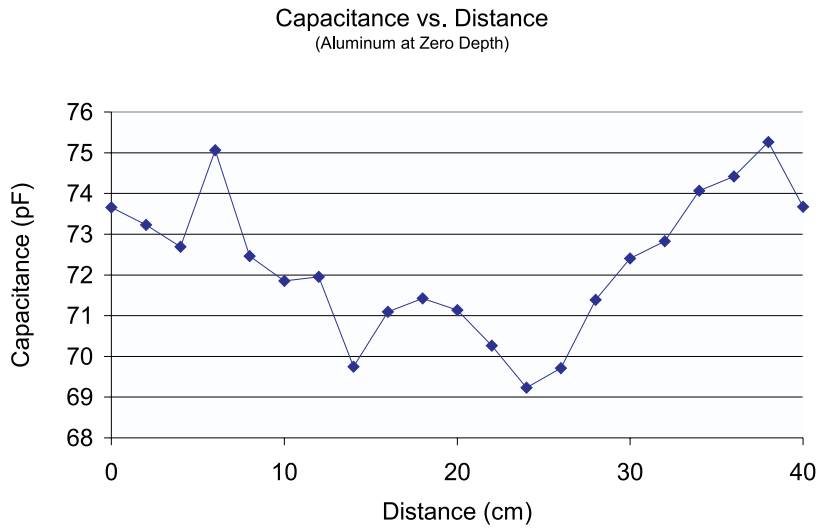

Figure 12.44: Measured capacitance vs. distance for an aluminum landmine surrogate at zero depth. The capacitance achieves its extremum values when the mine is closest to the inner edges of sensing and drive electrodes.

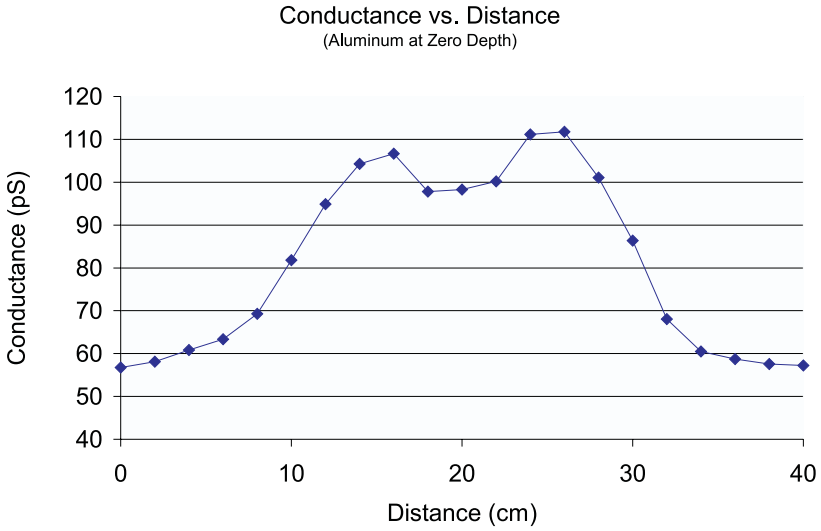

Figure 12.45: Measured conductance vs. distance for an aluminum landmine surrogate at zero depth. The response is not symmetrical due to the presence of a guard electrode directly under the sensing electrode. The conductance achieves its extremum values when the mine is closest to the inner edges of sensing and drive electrodes.

12.7 Summary

A feasibility study of fringing electric field dielectrometry techniques for detection and discrimination of plastic and metal landmines in relatively dry soils has generated mostly positive results. As long as the landmines are buried no deeper than 2 to 3 inches from the surface, they are detectable with fringing electric field sensors.

This Chapter provided an extensive example sequence of visualization of frequency-dependent data and suggested possible solutions for pattern recognition to enhance discrimination of plastic landmine dielectric signatures from the signatures of other objects. Since it is desirable to operate at frequencies above 1 Hz, the complex dielectric modulus is more efficient for wideband dielectric frequency data presentation than the complex dielectric permittivity.

Very extensive additional research is needed to bring this technology to practical use. Possible approaches to landmine discrimination should include differential capacitive sensing, frequency and pulse excitation dielectrometry spectroscopy, a combination of electric and magnetic field penetration, and cross-correlation or measurement data with other sensing approaches.

Chapter 13

Miscellaneous Applications

Many applications of interdigital sensors have been explored in cooperation with Jentek Sensors, Inc. [50, 51]. Most of these are currently company proprietary information. A brief non-comprehensive overview of the following selected applications serve to indicate the commercial and scientific potential of this technology.

13.1 Chemical Protective Garments

Protective garments are used to reduce human exposure to toxic gases present in the environment in an industrial emergency or battlefield conditions. The lifetime of these garments is determined by the remaining sorptive capacity of the active carbon layer, which, in turn, strongly depends on the levels of exposure, therefore, it is desirable to develop a relatively simple method for characterization of current status and prediction of remaining lifetime of these garments. Two materials used in chemical protective garments are Saratoga and BDO (Battle Dress Overgarment). BDO has a higher sorptive capacity of activated carbon materials using impregnated polyurethane foam and affords extended protection against toxic vapor and against the more concentrated challenge of liquid droplets [322]. Saratoga is a newer material, more mechanically stable and rigid, with foam replaced by activated carbon microspheres. Toluene is selected

as a simulant of toxic gases for our experiments because it has similar properties, but is less toxic and readily available.

Experiments with gas sensitive low conduction polymers demonstrate that sensitive materials are practically never purely and exclusively selective to a specific chemical. Instead, they usually respond to changes in concentration of several gas components present in the ambient [259]. In our case, the adsorption of toluene in chemical protection suit garments has been monitored through the change in dielectric spectrum of the active carbon particle layer. The levels of adsorption were stepped from high to low by holding the experimental parts under vacuum for increasing amounts of time and by increasing the temperature of the heating element.

The reversibility of the material saturation process depends on electrical and chemical interactions between the challenge gas molecules and the sensitive adsorbing material. The surface adsorption tends to be reversible with heating and/or vacuum-driven degassing, whereas the true bulk diffusion process either exhibits a very strong hysteresis or can not be reversed at all [323]. The reversibility of response with hysteresis has been investigated, similar to the approach taken in [231].

Adsorption of toluene can potentially also be characterized by x-ray analysis with electron microscopes. Experiments with SEM demonstrated that a high vacuum sample chamber cannot be used due to extensive sample outgassing. Measurements in an environmental SEM in the low vacuum chamber under nearly atmospheric pressure may be adequate. At this point, several SEM images have been taken with Saratoga material samples. Figure 13.1 shows that the microspheres are nearly ideal in shape and are normally separated by dimensions far less than their radius. Figures 13.2 and 13.3 show the microsphere surface at higher magnification.

13.1.1 Preliminary Measurements with Toluene

A test chamber, shown in Figure 13.4, has been built to control the experiment temperature, pressure, humidity, and chemical environment. This chamber was used in

Figure 13.1: An SEM micrograph of the carbon microsphere. The white line is 100 μm (23 mm in the image). Garment fibers are seen in the upper left corner.

several series of experiments, and a small subset of data is reported below. It is currently possible to measure saturation levels of toluene in materials which contain an active layer of microspheres, such as Saratoga. The active layer consisting of the carbon based foam, such as the black layer in the BDO sample, presents significant measurement challenges. The difficulties include compression of the foam, relatively high conductivity of the material, and lack of structural strength.

Somewhat noisy results of the measurements of the Saratoga sample can be explained by variability of micro-cavities, the effects of temperature, moisture concentration, pressure distribution, and non-uniform distribution of the contaminant over the sample volume. The average conductivity of the Saratoga material increases several times from the non-impregnated to the fully impregnated state. The average dielectric permittivity changes by a factor of less than two.

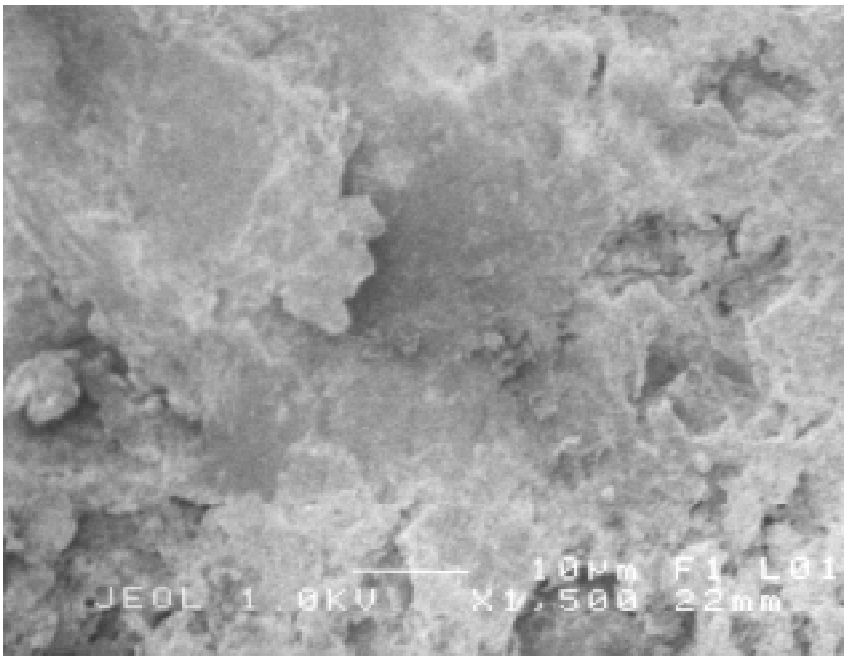

Figure 13.2: An SEM micrograph of the carbon microsphere surface at 1,500 magnification. The toluene molecules attach to the surface of activated carbon, therefore a large surface area is important for this application.

13.1.2 Experimental Setup and Procedures

The experimental procedures were similar to those described earlier, except for the sequence of the impregnation states. It was originally suggested that the level of impregnation is controlled by exposing the sample to increasingly larger amounts of toluene. However, this procedure was difficult to implement because most of the toluene would condense on the walls of the desiccant vessel used for impregnation. Consequently, this procedure was modified. The sample was first measured after being put into a 300 mTorr vacuum for 24 hours. Then, it was toluene impregnated to saturation for another 24 hours. Probably, less time is needed for impregnation, but due to the limited access to the special lab facilities, 24 hours was a minimum useful time period. Then, the sample was gradually outgassed. In the beginning, outgassing was natural, then, by vacuum, then, by heating. A vacuum alone was not sufficient to bring the sample back to its original weight.

Figure 13.5 shows a typical frequency sweep of the three-wavelength Teflon sensor

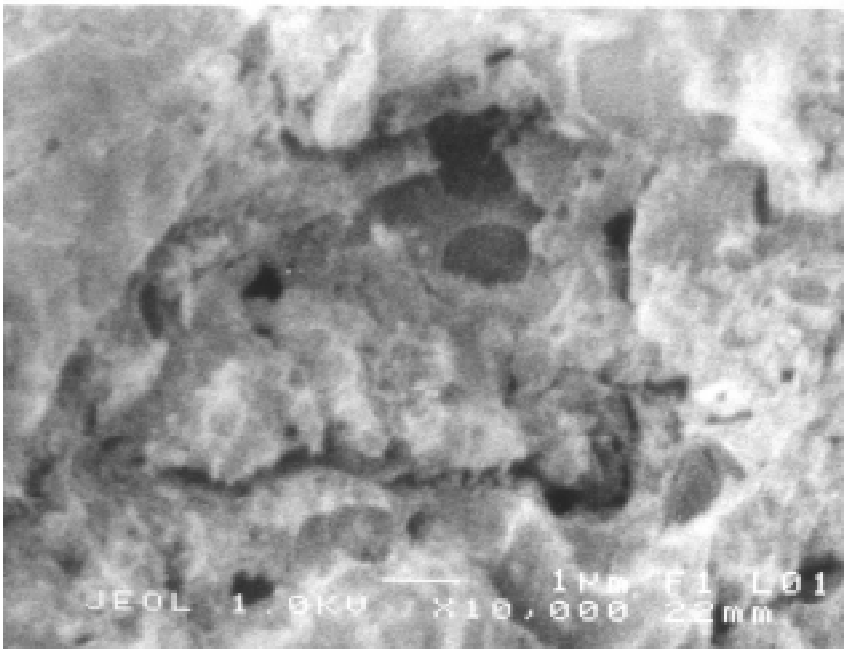

Figure 13.3: An SEM micrograph of the carbon microsphere surface at 10,000 magnification reveals material porosity.

with a garment sample. The 1 Hz frequency has been selected for consecutive measurements based on this sweep. Figure 13.6 shows that the change in the concentration of the absorbed toluene is detected by all three wavelengths after it exceeds 5 mg/sq. cm. Figure 13.7 shows that at 10 Hz phase changes are larger while gain changes are smaller for the same change in saturation levels. Figures 13.7 shows that transconductance and transcapacitance are the most reliable indicators of the saturation level.

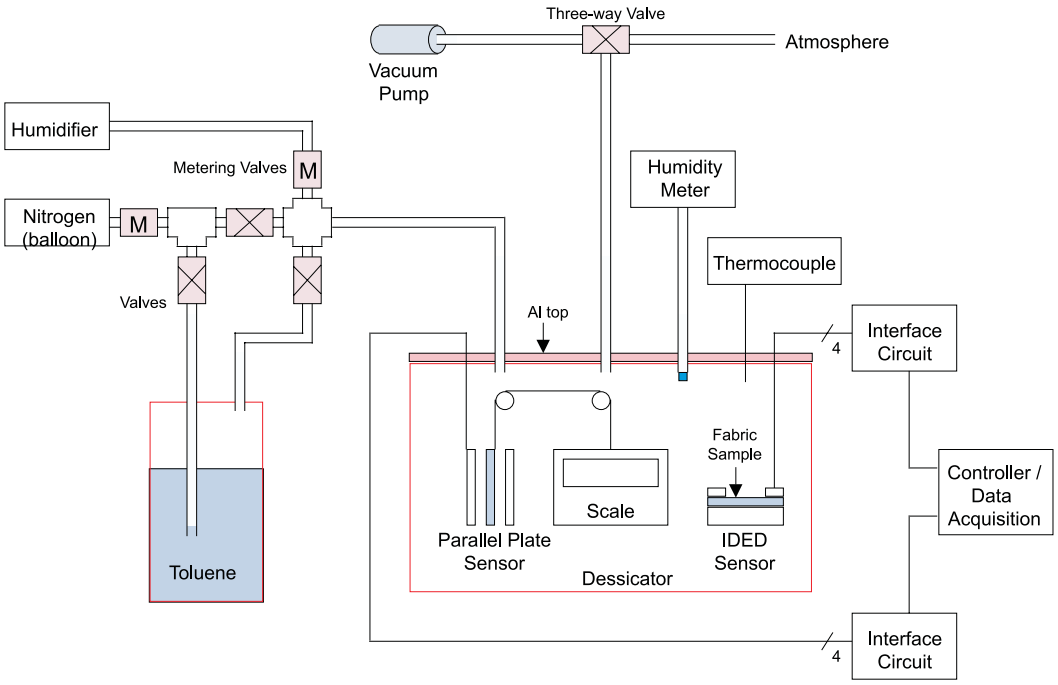

Figure 13.4: A schematic of the experimental vacuum test chamber for simultaneous measurements with interdigital sensor, parallel plate sensor, weight monitoring of samples, and control of pressure, temperature, and humidity. (Final version drawn by Andy Washabaugh of Jentek Sensors).

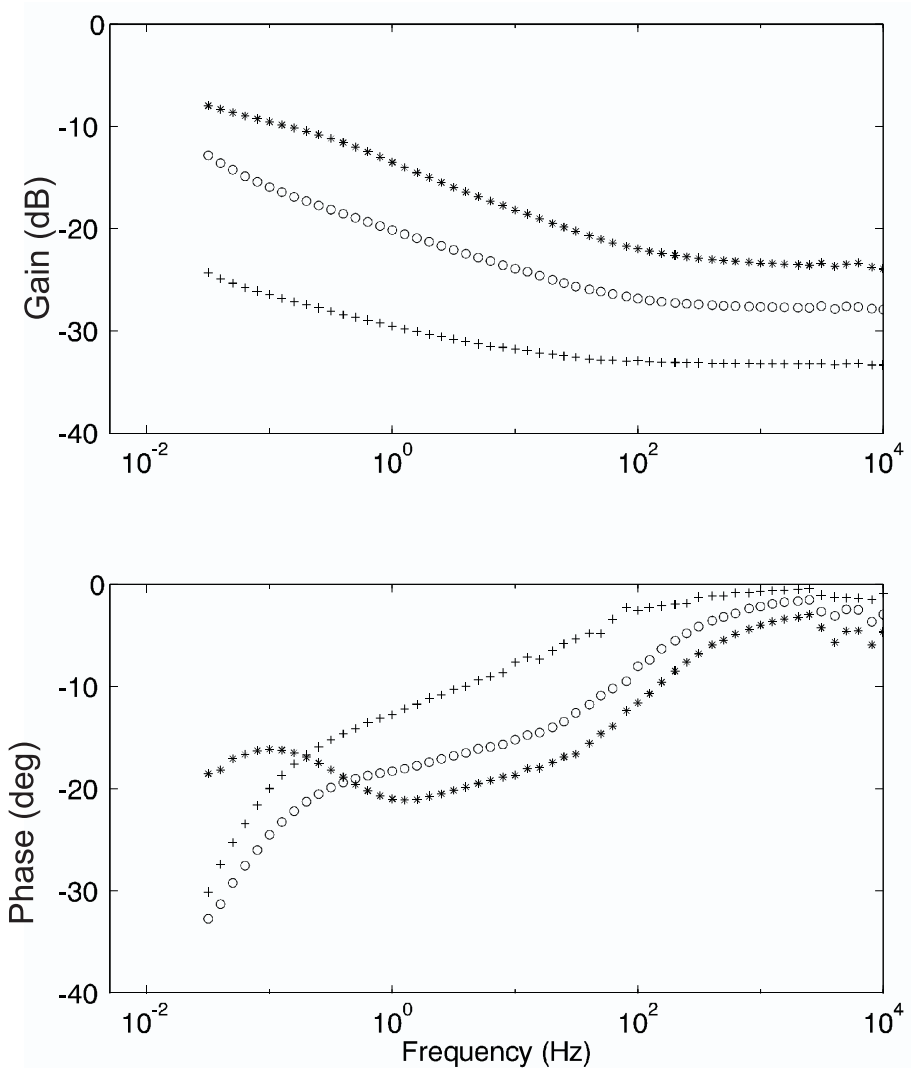

Figure 13.5: Frequency response of the Teflon TWS in air with a Saratoga sample pressed against it. Gain/phase frequency sweep shows that measurement of outgassing at 1 Hz is unlikely to produce a noticeable phase change on the 5 mm wavelength measurement because the phase curve has a nearly zero derivative at that frequency. Legend: "+"-1 mm,"o"-2.5 mm,""-5 mm.*

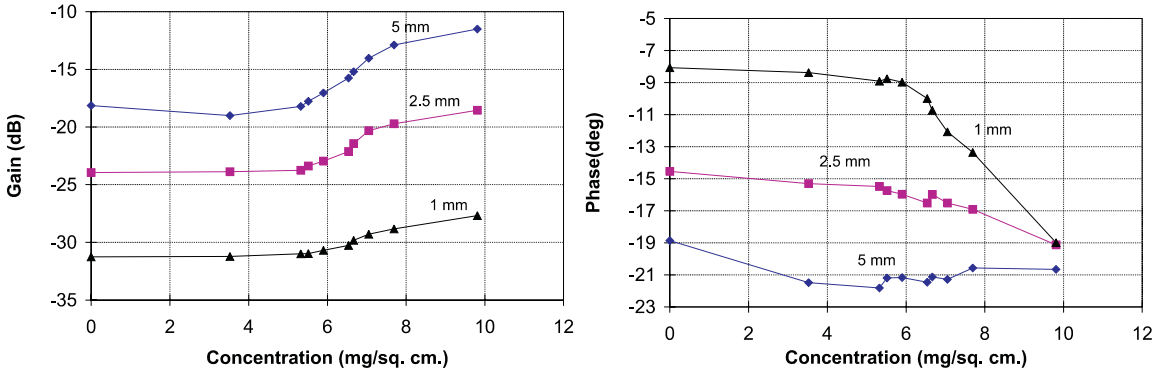

(a) gain (b) phase

Figure 13.6: The change in the concentration of the absorbed toluene is detected by all three wavelengths after it exceeds 5 mg/sq. cm. Measurement is done at 1 Hz. The frequency of 1 Hz is not optimal for phase detection on the 5 mm wavelength channel.

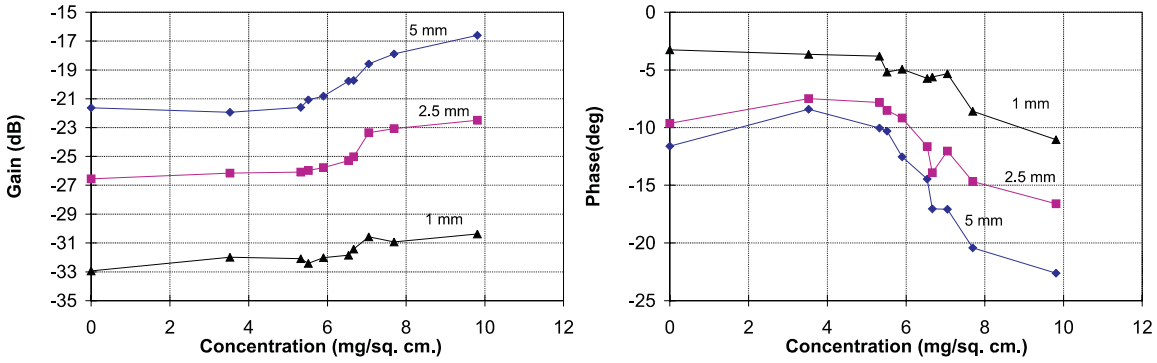

(a) gain (b) phase

Figure 13.7: The same sample as in Figure 13.6 with measurements at 10 Hz. The change in the concentration of the absorbed toluene is detected by all three wavelengths after it exceeds ≈5 mg/sq. cm.

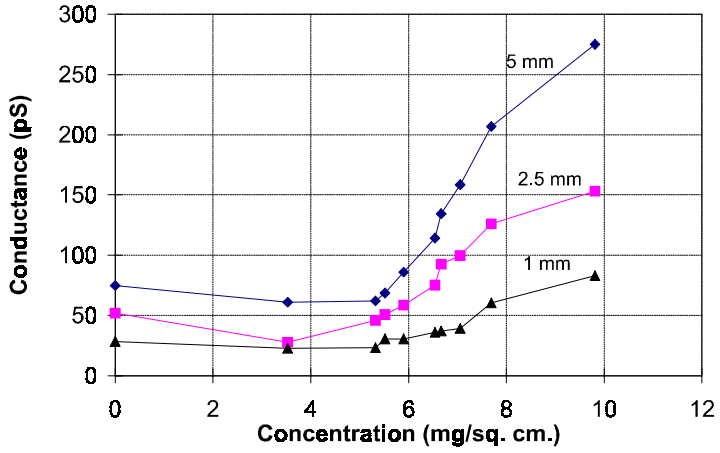

Figure 13.8: The data in Figure 13.7 (for 10 Hz) converted into terminal transconductance, which seems to be the most reliable indicator of saturation.

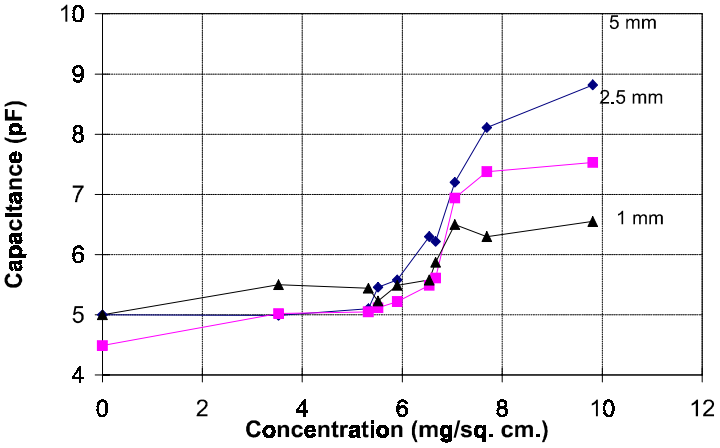

Figure 13.9: The data in Figure 13.7 (for 10 Hz) converted into terminal transcapacitance. The change is more abrupt above 6 mg/cm^2, possibly due to a shielding layer of toluene bonds formed on the surface of the microspheres, which changes the grain boundary conditions.

13.2 Detection of Flaws

Monitoring of the structural integrity of fiberglass flywheels has been another application of fringing field capacitive sensors. This is a simple application in which no effort is made to determine dielectric properties of materials. Instead, a sensor is applied to the surface of a material at different locations. If bulk and surface properties of the sample are homogeneous, the sensor response would remain the same, within measurement noise. A crack introduces a discontinuity in the sensor response. Figure 13.10 shows a typical response when a 2.5 mm wavelength sensor is moved along the material surface. The crack located at 38 mm from the edge of the sample can be easily identified by looking at the three-point moving average of the sensor capacitance response. Due to a limited spatial resolution of the sensor, a narrow (less than 1 mm) crack produces a dip in the sensor response, which is approximately as wide spatially (about 10 mm) as the active sensing area. Deconvolution could be applied in the future to achieve higher resolution without loss of penetration depth. This type of measurement methodology falls into a broader category of capacitive sensors and usually does not require extensive theoretical modeling. The potential applications for structural integrity control are numerous and the implementation is very economical.

13.3 Summary

The applications of interdigital dielectrometry described in this chapter briefly represent only a small part of potential uses of this technique. Wearable sensing is becoming increasingly important with the recent trend towards wearable computing. The experimental data with chemical garments shows that the major difficulty with direct measurements of garments may come from insufficient sensitivity of dielectrometry to changes in the material chemistry. An optimized sensitive layer deposited on the sensor surface and correlated with the bare electrodes data might provide adequate sensitivity and selectivity. The selectivity to a particular chemical is very important in the

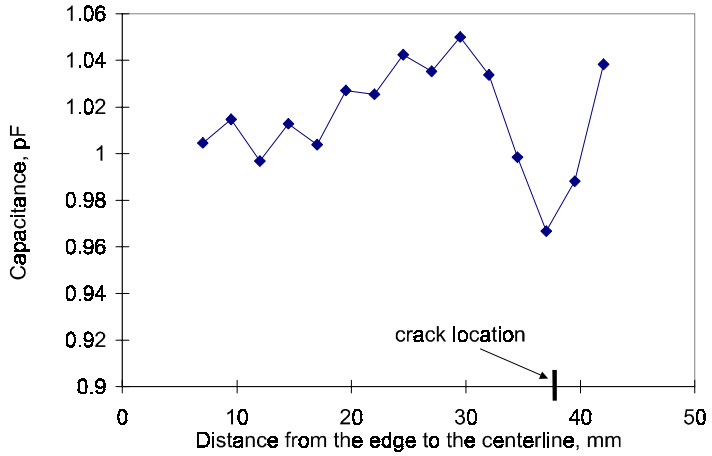

Figure 13.10: Three-point moving average of capacitance as a function of surface position for a 2.5 mm wavelength sensor indicates sufficient sensitivity to the presence of cracks in fiberglass flywheels.

natural environment, where humidity, temperature, and chemical composition change drastically.

Capacitive sensors for on-line monitoring of structural integrity of fiber composites under high mechanical stress provides a very economical and reliable way of non-contact sensing. The presented data for fiberglass flywheels indicates sufficient sensitivity to the presence of incipient cracks prior to the delamination due to centripetal forces.

Chapter 14

Conclusions and Future Work

14.1 Main Contributions

The tasks that have been accomplished in the course of the doctoral program research described in this thesis are listed in this section. The summaries in the individual chapters provide additional information regarding specific accomplishments, contributions, and conclusions.

14.1.1 Sensor Design and Fabrication

Several new interdigital sensors have been designed, fabricated, and characterized. The three-wavelength interdigital sensor with Teflon substrate has been used most successfully for several applications. Other sensors, such as the comb-serpentine-comb (CSC) fringing electric field sensor, curved interdigital sensor, and twin-sensor arrays, have been designed to address specific problems encountered with the classic design.

The following improvements were incorporated into the new three-wavelength sensor design:

- New fabrication and cleaning procedures suitable for dielectrometry analysis of highly insulating materials have been developed. A hydrophobic Teflon substrate has been introduced to eliminate moisture absorption into previously used polyimide sub-

strate.

- The capacitive coupling of the sensor leads to the sensing electrode has been reduced through changes in geometrical layout, use of coaxial cables, and modification of sensor mounting.

- The cross-coupling between individual wavelengths has been reduced through changes in geometrical layout (for high frequencies) and through guarding of inactive wavelength or switching to a short-circuit measurement mode (for low frequencies).

- When necessary, the parasitic capacitance due to electrode thickness has been reduced by forming thinner electrodes.

- The departure from the two-dimensional theoretical model due to fringing electric fields at the sensor perimeter regions has been reduced by introducing guarded fingers and measuring the differential signal change at the finger end regions.

- For selected cases, the chemical stability of the electrodes has been enhanced with gold-plating.

- Higher signal-to-noise ratio in guarded mode has been achieved by eliminating substrate capacitance effects by guarding the backplane and increasing effective meander length.

14.1.2 Experimental Techniques

Some algorithms for the inverse problem developed in the course of this study require special experimental arrangements, such as liquid or viscous dielectric fillers, mechanical displacement of the sensor head, and uniform pressure distribution over the sensor head area. While making measurement techniques more complicated, these approaches offer higher accuracy and reliability of measurements, as demonstrated in this thesis.

The statistical analysis of multiple wavelength measurements has shown the significance of a high-level of cross-correlation between individual wavelengths due to erratic air gap between the sensor head and solid dielectric material. A new type of a multiple penetration depths sensor, the CSC sensor has been designed, fabricated and applied

to test materials to provide a proof of concept.

14.1.3 Parameter Estimation Algorithms

It has been shown here that the previously advocated "marching approach" and parameter estimation algorithms based on adaptive optimization do not perform adequately due to high sensitivity to measurement noise. Several parameter estimation algorithms have been developed for different applications to address this issue.

The parameter estimation algorithm based on a linear relationship between moisture concentration and terminal capacitance and conductance has been developed and successfully applied to simulated as well as experimental data.

An overview of forward problem models and algorithms has been compiled based on a literature search and our own research. The selection of the forward problem algorithm strongly depends on the desired characteristics required by the inverse problem, most significantly speed and versatility. For that reason, no single forward problem approach can be viewed as the best one for all applications.

14.1.4 Moisture Dynamics

For the first time, moisture diffusion processes in oil-free and oil-impregnated transformer pressboard has been monitored non-destructively. Theoretical simulations confirmed the validity and reliability of the selected instrumentation and parameter estimation technology. Together with Yanqing Du [12], the moisture diffusion coefficient in transformer pressboard has been estimated for several scenarios.

14.1.5 New Areas of Application

New areas of application of this technology have been investigated, including estimation of remaining sorptive capacity of chemical garments and evaluation of structural integrity of fiberglass flywheels. Most of the data of these studies has been acquired

during summer work at Jentek Sensors, Inc., and is not included here due to its proprietary nature. Overall, preliminary measurements confirmed significant potential of this technology.

The preliminary study on applicability of fringing electric field sensing technology for detection of buried plastic and metal landmines for the purposes of humanitarian demining has been conducted. It should be made clear that the goals of this study did not include any full-scale development of a sensing technology. The feasibility simulations and measurements have confirmed adequate sensitivity and selectivity of this approach for relatively dry soils. When the moisture content of soils is high, its high electric conductivity effectively shields the landmine from the penetrating electric field lines. Frequency impedance spectroscopy plots generated from measurement data revealed a rich in features spectrum that could potentially be used for landmine discrimination.

14.2 Conclusions and Recommendations

14.2.1 Forward and Inverse Problems

A number of numerical and analytical techniques are available to solve the forward problem of interdigital dielectrometry. Two-dimensional approximations are no longer necessary for forward problem solution because of increased computer speed and availability of tools for three-dimensional electromagnetic analysis. In this aspect, interdigital dielectrometry can be easily converted into fringing field dielectrometry, so that the spatial periodicity is not maintained. However, the adaptive solution of inverse problems is still computationally too expensive even for numerical modeling of two-dimensional geometry representations, let alone three-dimensional representations. For that reason, analytical expressions still continue to play a significant role. Major difficulties, however, in solving the inverse problem are not posed by electric field modeling issues. The inverse problem has been found to be extremely sensitive to small statisti-

cal errors in input parameters, which is a common characteristic for all ill-posed inverse problems. The parameter estimation algorithms developed in this thesis form a compromise between accuracy and stability of solutions to achieve reasonable inversion. The use of pre-computed solution spaces speeds up parameter estimation algorithms, but does not, by itself, provide additional stability of inversion. Future work should probably take a step away from direct development of parameter estimation algorithms, but rather should concentrate on sensor optimization and sensitivity analysis. A rigorous approach should be developed for analysis of various disturbance factors, some of which have been discussed in this thesis, including cross-coupling effects, assumptions or infinite length and infinite periodicity, electrode thickness and width, surface contact quality, cross-correlation between signals of individual wavelengths, electronic measurement noise, input capacitance of the high impedance operational amplifier, thermal expansion and stability, miscibility of dissimilar fluids, aging and wear of instrumentation, surface contamination, and accuracy on numerical simulation.

Specifically, future research should also continue to minimize the effects of contact quality. It would be worthwhile to investigate other sensor substrate and coating materials for selective absorption of particular materials to be measured, elastic conducting materials, and, possibly, liquid electrodes.

14.2.2 Dielectrometry Analysis

Once the practical problems of sensor manufacturing and the theoretical problems of appropriate modeling and sensitivity analysis are resolved, it should be possible to apply the full arsenal of tools used with parallel plate dielectrometry measurements, such as dielectric spectroscopy, data fitting to reveal material microstructure, etc., to analyze the response of interdigital dielectrometry sensors. Frequency-dependent data contains more information than had so far been used in interdigital dielectrometry. One promising application of dielectric spectroscopy is the development of signal processing routines for invariant quantification of the output signal change due to the presence of

selected input factors, such as, for example, a selected chemical.

14.2.3 Estimation of Smooth Profiles of Material Properties

Linear Mapping Based Estimation

Measurement of moisture diffusion processes in transformer pressboard has been made possible using multi-wavelength dielectrometry. The parameter estimation algorithm based on terminal characteristics of interdigital comb electrodes has been developed and tested against synthetic data. As a part of the algorithm testing process, the solution to a benchmark problem of a transient diffusion process has been calculated using FE software. The benchmark problem can be used in the future to compare the performance of alternative parameter estimation algorithms. It also helps to develop intuition for analysis of multi-wavelength dielectrometry measurements and provides insights into improved experimental practices.

The algorithm tested here has demonstrated adequate performance for experimental setups which do not have sharp gradients of dielectric properties within the sensor penetration depth region of a wavelength. The algorithm has been successfully applied to experimental data. The moisture diffusion coefficient in oil-free transformer pressboard has been evaluated assuming that it is independent of moisture concentration.

Future work may include testing of algorithms that determine spatially inhomogeneous dielectric properties as an intermediate step before evaluating the moisture concentration distribution. Measurements of moisture diffusion in oil-impregnated pressboard in a simulated transformer environment should be reported as well. The understanding of moisture-related processes in power transformers can be enhanced with this methodology.

Model-Based Estimation

Limited spatial resolution of the three-wavelength dielectrometry sensor affects the performance of model-based parameter estimation algorithms, especially when material properties vary gradually. A parameter estimation algorithm designed for smooth profiles of material properties has been developed and tested using synthetic data. This algorithm does not use adaptive optimization to solve the interdigital dielectrometry inverse problem due to its inherent lack of stability when applied to smooth spatial profiles. Instead, semi-empirical weighting coefficients are used to separate contributions from individual layers of materials to the overall sensor response. The advantages of such an approach include increased stability, reduced computational cost, and ability to analyze anomalous experimental data. On the other hand, the maximum achievable accuracy with this approach is lower than that with adaptive algorithms, mostly because the weighting coefficients are used separately on real and imaginary parts of complex dielectric permittivity and because the values of weighting coefficients are weakly dependent on material and substrate permittivity. In other words, in the algorithm presented here we sacrificed accuracy of the solution for its stability.

14.2.4 Landmine Detection

While fringing field dielectrometry has confirmed reasonable sensitivity to plastic and metal objects in relatively dry soil, it is still unclear what is the best approach for field applications. For practical purposes, two approaches seem most promising. First, one can scan the surface with a single pair, or with an array of electrodes, record the signals, and plot the magnitude image on a computer screen, as is done with most scanning probe microscope techniques. The second promising approach is to record dielectric spectroscopy signatures of target landmines in the soil of each geographical region and to use pattern recognition techniques for detecting this signature during a scan.

14.3 Future Work

14.3.1 Sensor Combinatorics

Future applications of fringing field dielectrometry sensors are likely to include on-chip amplification, a temperature measuring element, a power source, and an antenna to eliminate a need for connecting wires. Both interdigital dielectrometry sensors and surface acoustic wave devices have essentially identical electrode topology, but they use different physical phenomena to detect changes in the material under test. Each technology has inherent advantages and drawbacks. A natural step in the sensor development is to combine positive aspects of each sensing technology in a single design. One such design uses a SO_2-sensitive material (heteropolysilaxane, NND/PTMS) to reduce the overall cross-sensitivity of the sensor to humidity interference [238]. One should expect development of a wide range of sensor arrays, wearable and embedded self-powered sensor systems, and sensors with moving parts, with interdigital or fringing field electrodes at a core of many applications.

14.3.2 Chemical Sensors

Theoretically, the composition of an air sample can be measured with traditional gas chromatography, ion mobility spectroscopy, and similar high-end laboratory equipment. However, these approaches are not suitable for wearable sensing due to their bulkiness, inherently high cost, high power consumption requirements, etc. [324]. An array of microelectronic chemical sensors is far more suited for field application [69].

Interdigital sensors are well-suited for detection and measurement of concentration of various chemical components in a liquid and gaseous state. The majority of sensors operate on the same principles, as briefly described below. Usually, the planar region that contains the interdigital electrodes is covered with a sensitive material. The coating is chosen so that it selectively adsorbs selectively the molecules of interest. Presence of these molecules in the regions of electric field penetration alters the sensors response,

because either the dielectric properties of the adsorbed material are different from those of the sensitive layer, or because the sound transmission characteristics of the region changed with the adsorption process. In the first case, the measurement of impedance between the electrodes is efficient, and in the second case, the piezoelectric transducers can be used. This smart coating approach is often particularly effective when the conductivity of the material is related to the concentration of the contaminant. Ideally, a highly selective smart coating combined with a simple interdigital structure could be sufficient for the measurement of the concentration of a specific chemical. However, in reality, most coatings respond to several types of chemicals, and are also susceptible to changes in humidity, temperature, dust, light, radiation, atmospheric pressure, etc. Consequently, the efforts of the research community in this area could be divided into two distinct stages: manufacturing techniques and interpretation of the sensor output. In order to make sensors highly selective and reliable, the researchers in this field introduce a variety of modifications and improvements to the basic idea.

One of the most successful techniques is to introduce additional layers to the original coating. While being an excellent solution from the chemical and the mass transfer point of view, the multi-layered coatings complicate significantly the interpretation of the sensor response. When the material of the coating changes from uniform in its properties to being stratified, the basic planar interdigital electrode structure no longer provides enough equations to solve for all variables of interest.

It is also reported in the field that the humidity of the ambient air alters significantly the response of the coated sensors [229]. Consider the sensor topology in Figure 14.1. A hydrophobic membrane is transparent for the contaminant of interest while keeping the moisture molecules from entering the volume of the sensitive coating. Ideally, the amplitude of the capacitance or conductance between the electrodes can be mapped to measure the concentration of the contaminant. Measurement of capacitance is quite common, for example see [218]. However, any type of contamination or damage of the hydrophobic membrane would produce a response similar to that from contaminant adsorption. Of course, the impedance spectroscopy could provide additional information

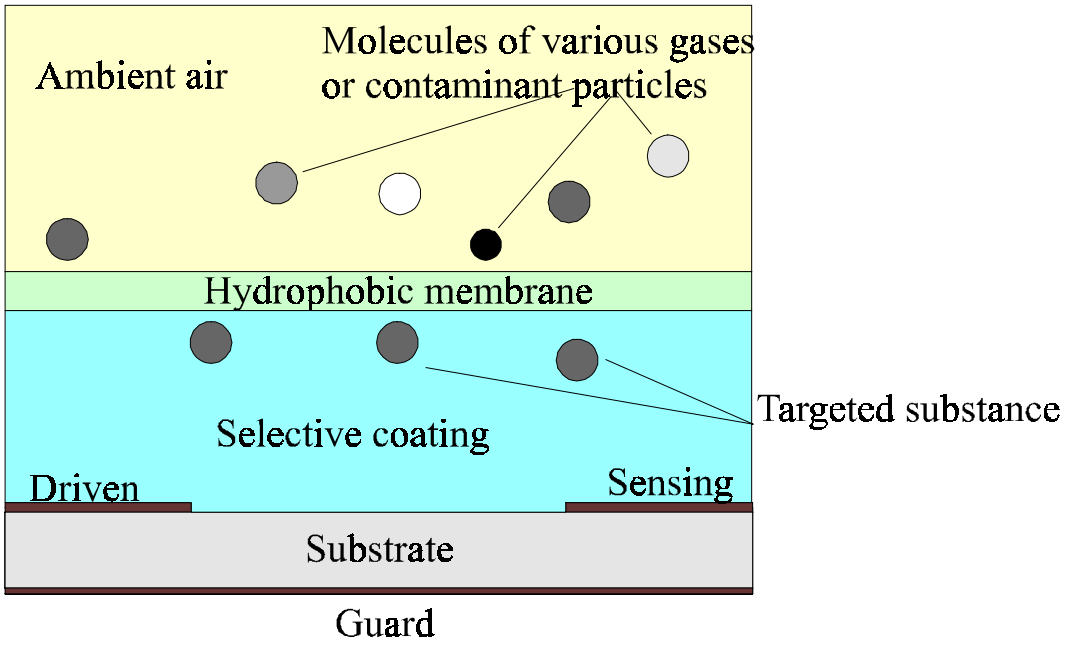

Figure 14.1: A schematic representation of the interdigital sensor used in conjunction with a selective coating and a hydrophobic membrane. Only designated molecules are attached to the selective coating, and moisture can not penetrate into the bulk of the coating. The interpretation of the sensor response, however, becomes more difficult.

about the system [325]. Yet, a conventional planar interdigital sensor does not usually supply a sufficient number of independent variables to evaluate the exact distribution in the high field region.

Furthermore, multiple penetration depths make it possible to monitor diffusion processes and resolve spatial profiles of contaminant concentration across the coating [20]. Nowadays, calibrated sensors are used in chemically active environments [220]. The diffusion dynamics type of measurement would be particularly useful for dynamic environments, when the relaxation time of the sensor response is comparable to the relaxation time of the contaminant concentration increase.

14.3.3 Characterization and Active Control of Electrochemical Boundary Layers

Ion boundary layers control the rates of electrochemical processes in batteries, fuel cells, and capacitors. A better understanding of boundary layer electrochemical processes may improve performance of these devices. This may be done using multi-wavelength interdigital $\omega - k$ dielectrometry.

Because multi-wavelength dielectrometry is capable of measuring a layer thickness of stratified materials, it holds a significant potential for process monitoring of vacuum chemical vapor deposition of various polymer materials, providing feedback information for quality control, especially for complex, multi-layered structures.

The family of dielectrometry sensors developed in this program has the potential of use in other fields dealing with characterization of surfaces of thin films. Feasibility studies on this technology were done for monitoring of performance of solar cell batteries, thin film curing processes, high-speed energy storing flywheels, and hydropower turbine blades.

The technology for non-destructive measurement of spatial profiles of dielectric properties of insulating materials is in its fledgling stage. Once the successful property estimation is achieved, the applications of the technology will be numerous and will eventually outgrow the scope of this work.

14.3.4 Aging and Corrosion in Civil Infrastructures

Future research may also use dielectrometry sensors for inspection of structures such as painted metals, to monitor and characterize age related degradation. This includes correlation of electrical properties to variations with damage caused by moisture, heat, oxidation, corrosion, and fatigue for painted, wooden, and concrete structures using dielectrometry. Applications include poles, bridges, pipes, concrete structures, towers, boilers, steam generator tubing, ceramic and metallic coated turbine blades, pipelines,

railroad rails, welds, and steel drums for waste storage.

The dielectrometry sensors can be used to profile moisture within and beneath the barrier paint coatings such as epoxies, urethanes, and alkyds. Information about the degree to which the coating is breached by moisture could be used to estimate the coating remaining life and to determine whether the metal substrate is actively corroding. A means of determining the depth of moisture penetration within a visibly sound coating and of detecting the presence of non-conducting corrosion oxides at the interface of the coating and metal would represent a significant advance in corrosion detection and paint integrity analysis. Another possible application for monitoring aging and deterioration due to moisture in paper concerns preservation of books, journals, and other archival papers.

14.3.5 Flow Electrification

Simulation of the transformer environment for moisture dynamics and flow electrification can be done using a multiple wavelength dielectrometry sensor in the MIT Couette Facility to measure complex permittivity profiles as a function of time in oil-impregnated pressboard as a function of oil moisture levels that are larger and smaller than the equilibrium moisture levels. Specifically, the formation of surface dry zones in pressboard should be investigated when moisture is leaving and its transient effect on static electrification, and of the formation of surface wet zones when moisture is entering pressboard and its effect on charge leakage.

Modeling moisture dynamics may involve physical, mathematical, and computer modeling of moisture diffusion processes in oil-impregnated pressboard and calculation of the response of multi-wavelength dielectrometry sensors. In particular, computer algorithms can perform the inverse problem of parameter estimation of the time and space distributions of permittivity, conductivity, and moisture concentration from dielectrometry gain/phase measurements.

Appendix A

Initial Conditioning of Sensors Manufactured by Polyflon

A.1 Introduction

Sensors produced by Polyflon Company [269] arrive from the manufacturer in large sheets, typically 12 inches by 18 inches (approximately 30 cm by 45 cm). The color of the insulating surface of these sheets is not white, as would be expected from virgin PTFE material, but is rather brownish due to a layer of a proprietary chemical that is used to increase the adhesion force between the copper layer and the PTFE substrate. The surface conductivity of this residue is non-negligible in the low frequency range. It is possible to remove this brownish layer using the procedures outlined below.

These procedures and know-how tips are given in a very detailed form. Experience with several students shows that a person who is given a short basic set of instructions and who follows them precisely without paying attention to a number of minor details usually ends up damaging the sensor. Most often, the sensor will be in a working condition, but not in the best achievable working condition. Minor defects introduced by improper variation of the process parameters eventually result in early sensor failure due to cracking of the sensor leads or the working area electrodes themselves. Many of

the precautions described in this document are prompted by the fact that the copper layer is very thin, ranging from 9 μm to 35 μm, depending on the batch parameters. The style of these instructions is geared towards an inexperienced student. For example, given these instructions, an undergraduate student should be able to process newly manufactured sensors without additional instructions or supervision.

A.2 Ultrasound Cleaning

A.2.1 Before You Start

First, read the entire set of instructions before doing anything. When following the instructions, use your judgment, think about the properties of the materials you are using, the primary effects of your actions and possible side effects.

Constantly check the sensors' surface visually. Use latex or vinyl gloves, and change them whenever you feel that they are becoming contaminated. Never touch the sensor surface with bare fingers, do not sneeze on it, do not drop it or put it in dusty locations. It is better to process sensors one at a time. If you process several of them simultaneously, never let their surfaces touch each other. For example, if you dry them in the oven by putting one on the top of the other, water will be trapped between the two surfaces, and the copper will oxidize heavily. Another advantage of processing sensors one at a time is that if you do something wrong, the damage will not be too great.

A.2.2 Step 0. Cut Out Sensors

Usually, sensors arrive in larger sheets that have to be cut into individual sensors. A paper cutter usually works well, unless you have some complex shapes, in which case a sharp blade or knife can be used. If you use some hard object (for example, a steel ruler) to guide your knife or blade, put a napkin under this object to avoid imprints on the sensor surface. The maximum size of the sensor board after cutting is limited by the size of the glass container which is inserted into an ultrasonic cleaner. Smaller

shapes are better, because they make it easier to spot problems on the surface.

A.2.3 Step 1. Pre-Clean sensors

Do the initial pre-cleaning well and thoroughly; it will pay off. When sensor sheets arrive from the manufacturer, they may have fingerprints, dust, or some other contaminants on the surface besides the brown residue itself. These contaminants must be removed. A general procedure is to clean the substrate with acetone and methanol. Acetone leaves more dry residue than methanol, so, methanol should be the last step in the rinsing. Acetone is generally a stronger solvent, that's why we use it in conjunction with methanol.

Wiping

Rinsing, by itself, may not be sufficient. Instead, soak a blob of cotton or some soft tissue in acetone or methanol. Wipe the sensor surface with this tissue. Do not apply too much force, as it may lift off the copper traces or leave imprints on the surface. Do not apply too little force, otherwise your wiping will be futile. If you wipe with acetone, follow-up immediately with methanol. Do not let acetone dry out, it will make it harder to remove the residue.

Before you wipe, form a cushion of clean napkins on a clean horizontal surface. If you do not create a soft cushion, every little hard particle below the sensor will leave an imprint on the sensors' surface as you apply the force to the surface when you wipe. Use several layers of napkins, because you will have to throw them away whenever the top napkin becomes dirty. Usually they become dirty at the perimeter of the sensor. Do not make the mistake of turning the sensor over and putting it on the napkin that has been soiled a minute before.

Rinsing

After you finish wiping, rinse. Do not forget that you have to wipe and rinse both sides of the sensor. Use marked bottles of acetone and methanol; make sure you know what is inside. Both acetone and methanol have to be of high grade purity; anhydrous solutions are the best. Keep the sensor at a 30 to 60 degree angle with respect to a vertical plane, hold it with your latex glove, and, with the bottle in the other hand, rinse in a sweeping motion from upper edge downwards. Repeat if necessary.

Baking

After you finished rinsing, bake the sensor in the oven. For this stage of cleaning, 10 to 15 minutes is enough. All you need to do is to wait until methanol evaporates from the sensor surface. There is no need to overheat the oven, in fact, it can be detrimental. The thermal expansion coefficient of Teflon is greater than that of copper. Avoid subjecting the sensor to high temperature gradients. Keep the temperature of the oven at around 50°C. Make sure that air has access to both sides of the sensor, and that the sensor does not touch any heating elements directly. Again, never put sensors on top of each other. Trapped moisture causes very strong oxidation and corrosion.

A.2.4 Step 2. Prepare the Bleach and the Ultrasonic Cleaner

For ultrasoung cleaning, we use the brand ULTRAsonik (TM) 104x by NEY. It helps to the read instructions for this cleaner to better understand what is going on. Fill the cleaner with regular hot water and turn the heater on. Fill the glass container with an undiluted regular strength bleach. Do not mix regular bleach with other brands, like Ultra-Clorox 2, for example. The latter is a detergent and is totally inadequate for this task.

Heat the bleach solution to 60-70°C using a separate heater, and then move the container into the ultrasonic cleaner. Put the glass container in the water like a boat and rest the handles on the sides of the tank. Do not put bleach in the cleaner tank

directly because it will damage the stainless steel walls of the tank. The hot water is used for transmitting the power of the ultrasound waves to the bleach. You always need to keep the level of water high. If the water evaporates, even only half-way, the cleaner will burn out, because the heating elements are placed underneath the tank, and the temperature sensor is at the top part of the tank. Without water, the feedback to the temperature controller is lost.

Degas the solution at maximum setting of degassing and average power in the ultrasonic cleaner for 10 minutes. The degassing is needed to reduce the mechanical impact of ultrasonic cleaning on the copper electrodes. The effect of degassing is rather mild, do not rely on it too much and do not aim to overdo it.

The higher the temperature of the bleach solution, the faster the brown residue will come off. It is actually possible to clean the sensor without using the ultrasound, just by soaking it in the hot Clorox. In my experience, the quality of cleaning by soaking is always lower than that achieved with ultrasound, while tarnishing of the copper surface would be almost the same.

If you clean several sensors in a queue, one at a time, it is advisable that you use a fresh bleach solution for every sensor, because the cleaning time increases when the solution becomes saturated with the brown residue, and, as was already mentioned, one of the goals is to reduce the time of the ultrasound cleaning to the minimum.

A.2.5 Step 3. Clean off the Brown Residue

To clean off the residue, reduce the power setting of the ultrasonic cleaner to a minimum, and turn on the degassing feature. In this regime, the damage to the copper by the power of the ultrasound waves is minimal. Sensors are placed inside the ultrasonic tank for a time period between 30 seconds and 2 minutes. Just lift the sensor from the bleach with your gloved hand and see if it has turned white. Do not rely on the color information when the sensor is submerged into the bleach, because the bleach itself is yellowish. Never insert metal objects into bleach, because they may start a chemical

reaction with the copper.

The ultrasound forms standing waves in the bulk of the liquid. Certain points become more destructive than others. For that reason, during the ultrasound cleaning, the sensor needs to be constantly moved around with a stick or your finger (gets a little hot though). Usually, the corner areas of the copper electrodes are affected more than inside areas. You can see the spots which get too much acoustic pressure by observing the bubbles which form there. Move the sensor and sweep the bubbles away with your finger or any non-sharp non-metallic object you are using.

A.2.6 Step 4. Rinse off the Bleach

Remove the sensors from the cleaning tank and flush with running warm water, then rinse with acetone, immediately follow by rinsing with methanol. Each consecutive rinsing must be done before the sensor dries off, otherwise, a residue remains deposited on the surface. Make sure that there is no water left on the surface before you put the sensor in the oven. For this step, wiping is not needed, but would not hurt either. Be aware that drops of bleach will readily discolor your clothes.

A.2.7 Step 5. Bake the sensor

Bake the sensor in the oven for 10 to 15 min at 50°C. See earlier comments on baking procedures. If the oven is not available, air drying is sufficient. Naturally, the drying time is several times longer than the baking time. Try to find a dust-free area and avoid direct sunlight.

A.2.8 Step 6. Remove Tarnish

If all previous steps were done properly, you should have little or no tarnish on the surface of the copper. Still, you might end up with some tarnish, which may look like dots of rust, fingerprints, traces of drops of water, etc. If these are surface effects,

and they did not go into the bulk of copper (on the micron scale), they can be easily removed by appropriate agents. A number of products is available for this purpose in any hardware store. I tried several and picked the two which work best for me, but other brands worked well too.

Nevr-Dull (TM) wadding by The George Basch Co., and Tarni-Shield (TM) lotion by 3M company perform well. Nevr-Dull is a little stronger, so it should be used when you have a lot of tarnish. Tarni-Shield is supposed to create an ultra-thin protecting layer for the copper to keep it from oxidation for a long time. So, use Nevr-Dull if you feel that it is necessary, or skip it if you don't have much tarnish, then apply Tarni-Shield with a non-lint napkin, and dry off with a cotton tissue. See comments for wiping above.

Several things to watch for when you remove tarnish. As you apply any of the two products, your tissue quickly becomes black with the substance you removed from the copper surface. Change your tissue often, otherwise the black residue will smear the surface of Teflon when you keep rubbing it. Do not forget to change the napkins underneath the sensor, because they will quickly become soiled with the black residue. Do not forget that you need to apply the agents to both surfaces of the sensor. When you turn the sensor over, make sure you put it on a clean surface.

A.2.9 Step 7. Clean Sensors with Acetone and Methanol

Thoroughly wipe the surface to remove any black residue from the Teflon surface. Methanol removes it better, but a more reliable way is to wipe with both acetone and methanol. Then rinse with acetone and methanol. Same instructions on wiping and rinsing as above apply.

A.2.10 Step 8. Final Bake

Sensors are baked in the oven at 50°C for two hours. This is a final dry-off of the sensors. Since you are going to use the sensor after this step for actual measurements, you are

now concerned with electrical properties. The goal is to achieve zero conductivity at the lowest frequency of interest. The minimum baking time depends on many factors, among which the most important are the temperature in the oven and the relative humidity of the air. Of course, several hours of baking will give you a solid reliability margin, but you will often have results which are just as good with only 15 minutes in the oven.

A.2.11 Step 9. Plating (Optional)

If desired, the sensor electrodes can be plated with an inert metal. Gold plating, silver plating, or tin plating can be applied both in the lab or by sending to an outside plating company. For example, Immersion Tin Plating solution is available from Kepro (catalog No.: ITP-1QT). The thickness of the tin layer formed by this product is usually less than one μm. Naturally, step 7 and step 8 have to be repeated after step 9.

Subsequent routine cleaning of the sensor can be done with regular solvents, such as acetone and methanol, with little or no heating required afterwards, depending on your task.

Appendix B

Continuum Model

A major portion of the earlier development efforts of frequency-wavelength dielectrometry was dedicated to solving the forward problem with a "continuum model". This model provides a mathematical description of the stratified media in terms of known values of the complex dielectric permittivity for each layer.

The continuum model was not used in this thesis because commercial finite element software is now available to perform the same tasks. This Appendix does not represent an original contribution. Instead, the model, as it was developed by previous students [8–10], is included here for completeness and to provide a link to previous work. This Appendix is based primarily on [10]. For a more complete description see [8, 71, 76].

The task of finding the complex impedance between interdigital electrodes is not a trivial one. Traditional analytical methods can provide closed-form solutions only for a limited number of classic electrode shapes, such as parallel-plate, cylindrical, and spherical electrodes [153].

Even a two-dimensional approximation of the interdigital structure results in the electric field distribution that is too complex to be described rigorously by simple algebraic expressions. The potential distribution along the sensor-material interface between the driven and sensing electrodes is not known in advance, and depends on the material properties and geometric parameters of the structure. The potential dis-

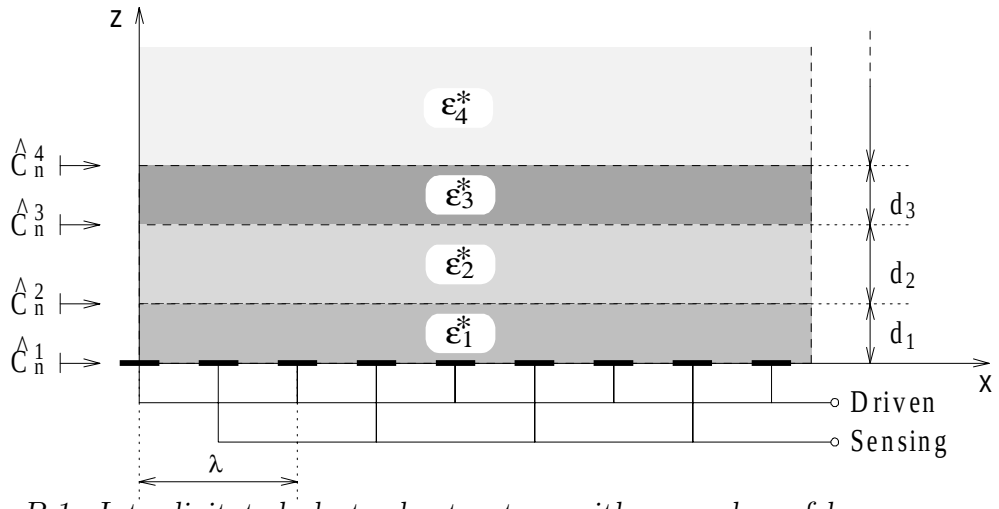

Figure B.1: Interdigitated electrode structure with a number of homogeneous layers above it [10].

tribution must be calculated using the principle of charge conservation at the interfaces.

Figure B.1 shows the idealized view of the interdigital structure with a multi-layered material above it. In order to validate a two-dimensional analysis, the electrodes are assumed to be infinitely long in the y-direction and possess infinite periodicity in the x-direction. The axes orientation in Figure B.1 is the same as in the rest of this document whenever the interdigital structures are discussed. An additional idealized assumption in the original model was the negligible thickness of the sensor electrodes. This assumption introduces a non-negligible error into parameter estimation algorithms, as discussed in Section 6.4. If desired, it can be removed by assuming an additional insulating layer between the side walls of interdigital electrodes that have finite thickness. For the simplicity of discussion, the following model also assumes that there is no surface conductivity at the interfaces between material layers. The reader is referred to [8] to learn how surface conductivity can be incorporated into the continuum model.

The continuum model was developed for steady-state AC excitation. Impulse or step responses are of great interest because they provide equivalent information to that received from the AC excitation frequency sweep while significantly reducing the required measurement time. The issues related to transformation between time and frequency domains are treated separately. In this discussion we use the following con-

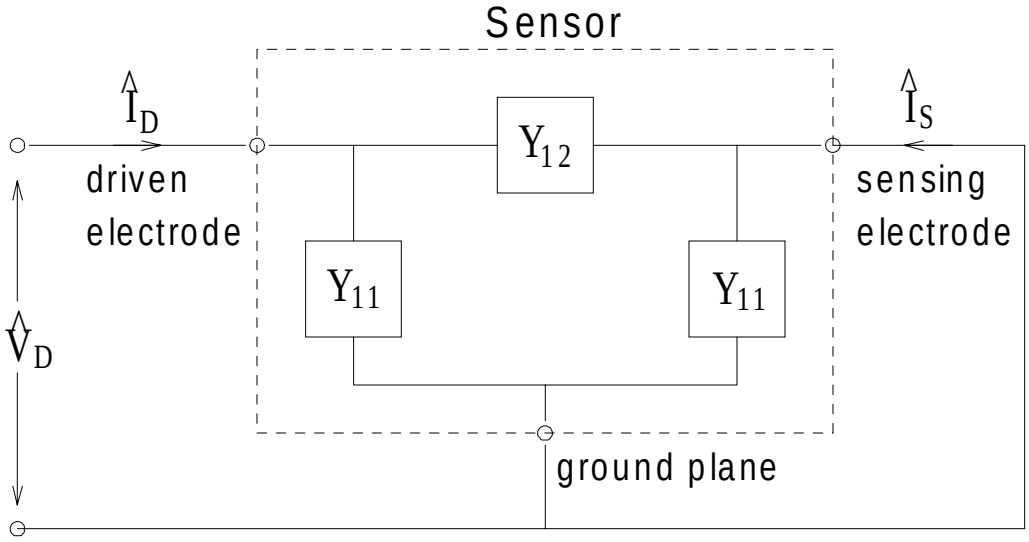

Figure B.2: Lumped circuit model for the interdigitated sensor structure within the dashed box and shown with grounded sensing electrode [10].

vention: All quantities are complex since only a single time sinusoidal mode $e^{j\omega t}$ is assumed. The remaining complex amplitudes that are functions of space are denoted by a 'tilde' ($\tilde{}$). The complete time and space dependence of the corresponding physical quantity is obtained from

$$F(x,z,t) = \Re\left\{\tilde{F}(x,z)e^{j\omega t}\right\} \tag{B.1}$$

where ω is the steady-state radian frequency. If a quantity's spatial x-dependence is also sinusoidal, then it can be represented by a complex phasor denoted by a 'hat' ($\hat{}$):

$$\tilde{F}(x,z) = \hat{F}(z)e^{-jkx} \tag{B.2}$$

$$F(x,z,t) = \Re\left\{\hat{F}(z)e^{j(\omega t-kx)}\right\} \tag{B.3}$$

where k is the wave number, related to the wavelength λ as

$$k = \frac{2\pi}{\lambda} \tag{B.4}$$

Earlier designs of interdigital sensors and associated electronic circuitry used the three-terminal symmetrical pi-equivalent circuit model shown in Figure B.2. Strictly speaking, every individual wavelength section of an interdigital sensor has four electrical

terminals: driven electrode, sensing electrode, ground electrode, and guard electrode. By means of an operational amplifier follower circuit, the guard electrode is always held at the same potential as the sensing electrode, so that any current between them is effectively eliminated. As long as the amplifier can provide the necessary current magnitude, the admittance between the guard electrode and the other three electrodes has no influence on the measurement. We may therefore leave the guard electrode out of the circuit model. The goal is to be able to calculate the admittances between these three terminals from the parameters of the layer structure.

The circuit model of the structure is shown in Figure B.2. Ideally, the admittance Y_{11} of the driven electrode to ground is the same as the admittance of the sensing electrode to ground because the two electrodes should have an identical geometry. In reality, especially when the total number of fingers is small, these two admittances may be somewhat different because the number of fingers is not always exactly the same. However, admittance per unit length quantities are indeed the same. Y_{12} represents the admittance between the driven and the sensing electrodes. It has much stronger dependence on the material under test properties than the other two equivalent circuit elements. Y_{11} primarily depends on substrate properties with some fringing field dependence on the material under test. Y_{12} primarily depends on the material under test properties with some fringing field dependence on substrate properties. We may calculate the admittances by applying test voltages at the terminals and calculating the resulting terminal currents. Since the equivalent circuit is independent of electrical terminal constraints, the simplest form of test circuit is to ground the sensing electrode and apply a voltage $\widehat{V}_D$ to the driven electrode as shown in Figure B.2. Then the unknown admittances can be calculated in the following way:

$$Y_{12} = -\frac{\widehat{I}_S}{\widehat{V}_D} \tag{B.5}$$

$$Y_{11} = \frac{\widehat{I}_D + \widehat{I}_S}{\widehat{V}_D} \tag{B.6}$$

In order to calculate $\widehat{I}_D$, we need to know the normal component of the total (displacement plus conduction) current density $j\omega\epsilon^*\widetilde{E}_z(x)$, which is integrated over

the area of the driven electrode to give the total terminal current. It is therefore necessary to solve for the electric field distribution.

The entire interdigitated structure is periodic in the x-direction with a wavelength λ. This means that for every quantity that depends on x we may use Fourier series expansions to write:

$$\tilde{\Phi}(x,z) = \sum_{n=-\infty}^{\infty} \hat{\Phi}_n(z) e^{-jk_n x} \tag{B.7}$$

$$\tilde{E}_z(x,z) = \sum_{n=-\infty}^{\infty} \hat{E}_{zn}(z) e^{-jk_n x} \tag{B.8}$$

where n is the Fourier mode number and

$$k_n = \frac{2\pi n}{\lambda} \tag{B.9}$$

It is convenient to define the *complex surface capacitance density* $\hat{C}_n$, which relates $\epsilon^* \hat{E}_{zn}$ at a planar surface $z =$ constant to the potential $\hat{\Phi}_n$ at that surface for every Fourier mode n in the following way:

$$\hat{C}_n = \frac{\epsilon^* \hat{E}_{zn}}{\hat{\Phi}_n} \tag{B.10}$$

Knowing $\hat{C}_n$ at the electrode surface will let us calculate the terminal currents from the potential distribution at that surface.

We have assumed that each layer of material in Figure B.1 is uniform, so that within a layer the complex permittivity $\epsilon^* = \epsilon - j\sigma/\omega$ is independent of the spatial coordinates. This means that Laplace's equation

$$\nabla^2 \Phi = 0 \tag{B.11}$$

is satisfied everywhere in space except at the interfaces between the layers. At these interfaces, however, the boundary conditions require continuity of $\hat{\Phi}$ (tangential component of $\vec{E}$ is continuous) and $\epsilon^* \hat{E}_z$ (normal component of conduction plus displacement current density is continuous). This means that at these interfaces $\hat{C}$ may be uniquely defined. Let $\hat{C}_n^m$ be the complex surface capacitance density at the interface between

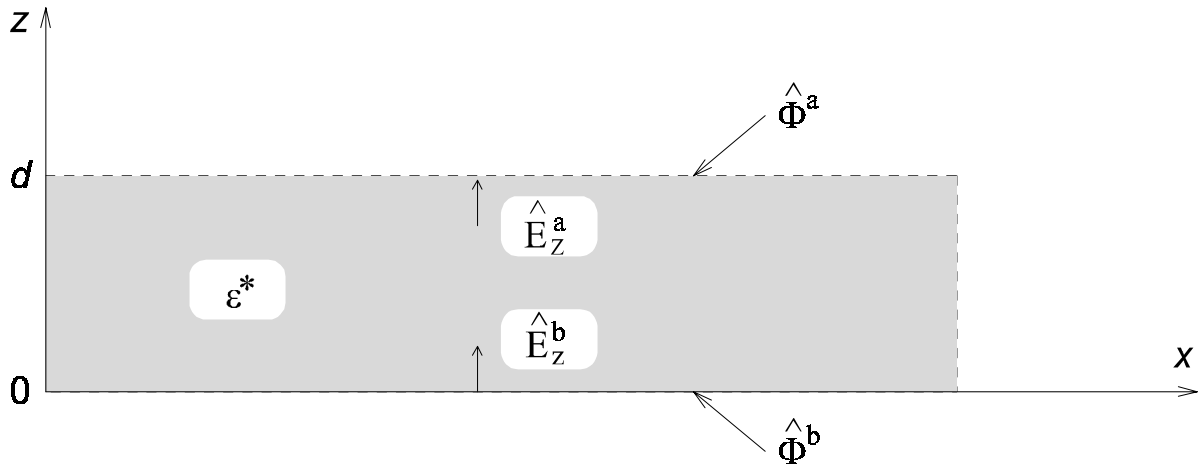

Figure B.3: A representative layer of homogeneous material [10].

the mth layer and the one below it (see Figure B.1), i.e. the surface at $z = \sum_{i=1}^{m-1} d_i$, with n referring to the Fourier mode. If we can express $\widehat{C}_n^m$ in terms of $\widehat{C}_n^{m+1}$, d_m, and ϵ_m^*, then we could apply this relationship recursively, beginning at the topmost layer N, to obtain $\widehat{C}_n^N$, then $\widehat{C}_n^{N-1}$, etc. and ultimately find $\widehat{C}_n^1$, the complex surface capacitance density at the electrode surface.

Consider the slab of uniform material in Figure B.3. We would like to find $\widehat{C}_n^b = \epsilon^* \widehat{E}_{zn}^b / \Phi_n^b$ as a function of $\widehat{C}_n^a = \epsilon^* \widehat{E}_{zn}^a / \Phi_n^a$, ϵ^*, k_n, and d. Since equation B.11 is satisfied, and since the potential is periodic in the x-direction with a wave number of k_n, the z-dependence of $\hat{\Phi}_n$ must be exponential. We therefore guess the following form:

$$\hat{\Phi}_n(z) = \hat{A} \sinh k_n z + \hat{B} \cosh k_n z \tag{B.12}$$

We have the boundary conditions

$$\hat{\Phi}_n(z=0) = \hat{\Phi}_n^b \tag{B.13}$$

$$\hat{\Phi}_n(z=d) = \hat{\Phi}_n^a \tag{B.14}$$

which leads by inspection to the final solution for $\hat{\Phi}_n$:

$$\hat{\Phi}_n(z) = \frac{\hat{\Phi}_n^a \sinh k_n z - \hat{\Phi}_n^b \sinh k_n (z-d)}{\sinh k_n d} \tag{B.15}$$

The z-directed electric field can be obtained from equation B.15 by differentiation as follows:

$$\widehat{E}_{zn} = -\frac{d\widehat{\Phi}_n}{dz} = k_n \left[\frac{-\widehat{\Phi}_n^a \cosh k_n z + \widehat{\Phi}_n^b \cosh k_n (z-d)}{\sinh k_n d} \right] \tag{B.16}$$

from which we obtain

$$\widehat{E}_{zn}^a = \widehat{E}_{zn}(z=d) \quad = \quad -k_n \widehat{\Phi}_n^a \coth k_n d + k_n \widehat{\Phi}_n^b \frac{1}{\sinh k_n d} \tag{B.17}$$

$$\widehat{E}_{zn}^b = \widehat{E}_{zn}(z=0) \quad = \quad -k_n \widehat{\Phi}_n^a \frac{1}{\sinh k_n d} + k_n \widehat{\Phi}_n^b \coth k_n d \tag{B.18}$$

$$\widehat{C}_n^a = \frac{\varepsilon^* \hat{E}_{zn}^a}{\hat{\Phi}_n^a} = \epsilon^* k_n \left(-\coth k_n d + \frac{\widehat{\Phi}_n^b}{\widehat{\Phi}_n^a \sinh k_n d} \right) \tag{B.19}$$

$$\widehat{C}_n^b = \frac{\varepsilon^* \hat{E}_{zn}^b}{\hat{\Phi}_n^b} = \epsilon^* k_n \left(-\frac{\widehat{\Phi}_n^b}{\widehat{\Phi}_n^a \sinh k_n d} + \coth k_n d \right) \tag{B.20}$$

From equation B.19 we obtain

$$\frac{\widehat{\Phi}_n^b}{\widehat{\Phi}_n^a} = \left(\frac{\widehat{C}_n^a}{\epsilon^* k_n} + \coth k_n d \right) \sinh k_n d \tag{B.21}$$

which we can then substitute into equation B.20 to yield:

$$\widehat{C}_n^b = \epsilon^* k_n \left(\frac{\widehat{C}_n^a \cosh k_n d + \epsilon^* k_n \sinh k_n d}{\widehat{C}_n^a \sinh k_n d + \epsilon^* k_n \cosh k_n d} \right) \tag{B.22}$$

Let us test the validity of equation B.22 in the limits $d = 0$ and $d = \infty$. For a layer of zero width this equation reduces to $\widehat{C}_n^b = \widehat{C}_n^a$, as required. For $d \to \infty$ both the hyperbolic sine and cosine approach the exponential function, i.e.

$$\lim_{d \to \infty} \left(\frac{\widehat{C}_n^a \cosh k_n d + \epsilon^* k_n \sinh k_n d}{\widehat{C}_n^a \sinh k_n d + \epsilon^* k_n \cosh k_n d} \right) = 1 \tag{B.23}$$

which reduces equation B.22 to $\widehat{C}_n^b = \epsilon^* k_n$. This is a useful result, as it directly applies to the semi-infinite topmost layer in Figure B.1. If its index number is N, then

$$\widehat{C}_n^N = \epsilon_N^* k_n \tag{B.24}$$

We now have the means of calculating $\widehat{C}_n^1$ from equations B.22 and B.24 by recursively descending down the layer structure. If on the bottom side of the electrode plane we had a similar set of layers, we would obtain a value for the surface capacitance density from that side too.

Instead of a structure of layers similar to the one in Figure B.1, the bottom side of the three-wavelength sensor has a single substrate layer of thickness h and permittivity ϵ_S which is typically purely real because the substrate's conductivity is negligible in typical substrate materials such as the polymers Kapton and Teflon. On the other side of the substrate the metal backplane is deposited which is typically grounded or guarded. We cannot use the equations developed so far to obtain the surface capacitance density due to the bottom side of the electrodes, because the potential at the ground plane is forced to zero. We may, however, use equation B.19 with $\widehat{\Phi}^b = 0$ to obtain

$$\widehat{C}_n^{-1} = -\epsilon_S k_n \coth k_n h \tag{B.25}$$

where the negative superscript indicates layers below the surface.

Since the surface capacitance density is known, it could be integrated over the areas of the driven and the sensing electrodes to obtain the currents $\widehat{I}_D$ and $\widehat{I}_S$ if the potential is known at the electrode plane. While the potential is indeed known along the electrodes, where it is constrained by them to be $\widehat{V}_D$ (driven electrode) or zero (grounded sensing electrode), in the space between the electrodes along the interface it is not known and must be determined by a different boundary condition, namely conservation of charge.

$$\vec{n} \cdot \left[\vec{J}_1 - \vec{J}_2 + \varepsilon_1 \frac{\partial \vec{E}_1}{\partial t} - \varepsilon_2 \frac{\partial \vec{E}_2}{\partial t} \right] = 0 \tag{B.26}$$

The potential between the electrodes is approximated by a piecewise-linear function, which divides the space between the electrodes into $k_c + 1$ intervals, delimited by k_c *collocation points*, as shown in Figure B.4. In every interval the potential is assumed to vary linearly between the potentials at the two end points. The potential distribution is thus fully determined by the potential at the k_c collocation points. Now that we have a form for $\widetilde{\Phi}(y)$, we can use the Fourier integral to obtain an expression for $\widehat{\Phi}_n$, which is an algebraically linear function of the unknown potentials at the collocation points. In order to find these potentials $\widehat{\Phi}_j$, we need a set of k_c equations, which can be obtained by applying conservation of charge to k_c intervals centered around

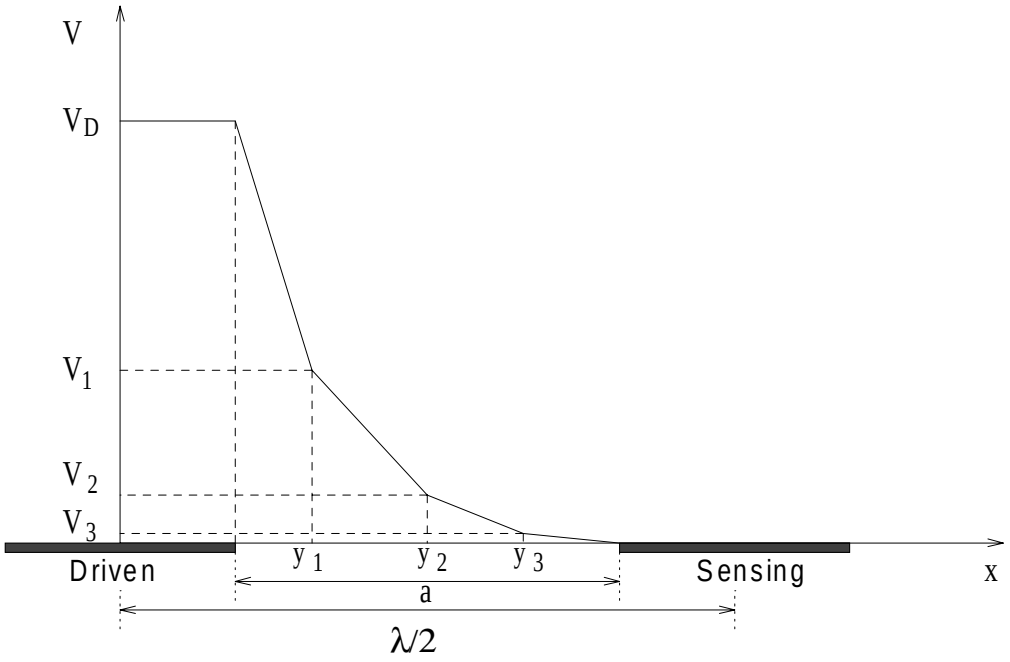

Figure B.4: Piecewise-smooth collocation-point approximation to the potential between the electrodes of an interdigitated structure. Three collocation points at y_1, y_2, and y_3 are shown [10].

the collocation points. Reference [8] presents this process in detail, carrying out all integrations, etc. What is important to us is that this numerical process yields the potential distribution at the electrode surface and ultimately makes it possible to find Y_{11} and Y_{12}.

Finally, if the admittances in Figure B.2 are known and if the sensor is loaded by an interface box of input admittance Y_L (see Appendix D), the magnitude and phase of the voltage ratio are given by

$$\frac{\widehat{V}_S}{\widehat{V}_D} = \frac{Y_{12}}{Y_{12} + Y_{11} + Y_L} \tag{B.27}$$

The subsidiary parameter estimation routines implement the numerical calculations presented in this section. The function **gp()**, defined in **gp.c** listed in [10] gives the gain and phase of the voltage ratio of an interdigitated sensor when it is supplied with the parameters of the sensor and with the properties of the layers above it. The C code

of [10] used in its implementation is an almost direct translation from the FORTRAN code written by Dr. M. Zaretsky [8].

In some cases, measurements with a metal plate were used to squeeze the materials against the surface of the interdigitated sensor. In those cases the topmost layer had to be approximated as infinitely conducting. The presence of a conductor at the top does not introduce anything new to the analysis, provided it is left floating, as the model assumes. If the conductor is grounded, the admittance network of Figure B.2 would be altered and this change must be included in the mathematical model unless the top conducting plate is sufficiently far away from the sensor. The contribution of the higher order modes to the total capacitance value decays exponentially with the distance, but the contribution of the zero order mode decays inversely to the distance to the top plate.

Appendix C

Controller

C.1 Background

The *controller*, a microprocessor-based data acquisition system commonly used in our dielectrometry measurements, was originally developed by Mr. David Otten [326] and later enhanced by Mr. Darrell Schlicker. The information contained in [10] is repeated and updated here. The description of the firmware enhancements is included at the end of this Appendix. The original software for the communication with the controller was altered by many users (Y. Sheiretov, Y. Du, B. Berdnikov, and others) to suit their specific purposes.

The controller constitutes an integral part of the standard measurement system shown in Figure 1.6. The controller is capable of two types of data acquisition: the Data Logger and Gain-Phase Measurements (GPM). The former is used to record time domain signals from the sensor and the latter is used for frequency domain measurements.

C.2 Communication and Operation

The controller itself can be controlled by a terminal or computer over an RS-232 interface or over a telephone line with a 300 baud modem. The communication line is used in both directions: to send commands and to receive data.

The controller has a total of four *channels* for its GPM operation, i.e. it is capable of processing four independent inputs. It provides all four channels with a *driven* AC voltage of complex amplitude $\widehat{V}_d$. It performs a *frequency scan*, i.e. measurements at all frequencies in a specified range. The maximal range of frequencies at which the controller is capable of performing GPM measurements is from $10^{-2.3}$ Hz (≈ 0.005 Hz) to 10^4 Hz. Two consecutive measurements are at frequencies 0.1 apart on a logarithmic scale, corresponding to a ratio of $10^{0.1} \approx 1.259$. At every frequency, the controller waits for a certain number (3–7) of cycles to complete so as to ensure that sinusoidal steady state is reached, at which point it records the magnitude and phase angle of the ratio between the input voltage and the driven voltage, in decibels and degrees respectively:

$$\text{Gain} = 20 \log \left| \frac{\widehat{V}_{sense}}{\widehat{V}_d} \right| \tag{C.1}$$

$$\text{Phase} = \frac{180}{\pi} \angle \left(\frac{\widehat{V}_{sense}}{\widehat{V}_d} \right) \tag{C.2}$$

The input impedance of the controller is not high enough for applications in which very insulating materials are studied. Therefore buffering of the input signal is needed and that is provided by the interface box, described in Appendix D. In addition to gain and phase data, another piece of information recorded by the controller is the offset voltage, which is the DC component of the input voltage, and the multiplication gain of the measured signal. The DC buildup is due to charge accumulated on the input capacitance from the input current of the operational amplifier. The larger the D.C. offset the lower is the measurement precision. A 12 bit analog-to-digital converter provides a maximum resolution of about 0.001 V for a 5 V signal. However, this requires a zero D.C. offset. This phenomenon is further discussed in Appendix D describing the interface box.

The entire frequency sweep takes anywhere between one and three hours depending on characteristics of the measured signals. If the signals are unstable, the measurement is re-triggered at the same frequency point until a satisfactory reading is taken.

All measurement parameters are stored in non-volatile memory and remain unchanged even if the electric power supply is disconnected. An on-board lithium battery maintains time and date information. A reset push button for the controller is located inside the metal enclosure on the main printed circuit board. If the controller does not operate properly, it may be reset by pressing this button or removing the AC power and re-applying it.

C.3 Commands

Table C.1 presents a summary of commands recognized by all versions of the controller firmware. The version 1.7 additions by Darrell Schlicker are also included.

Both upper case and lower case letters are acceptable for the command entry. All commands return some type of acknowledgement if they are entered correctly. No acknowledgement means that the command was not recognized as valid. The acknowledgement always begins with a left bracket "[", followed by the two letters of the command. The remainder of the response depends on the command and the status of the instrument at the time the command was entered. All error messages follow the two letters of the command with the word "error:" and then a brief description of the problem.

Fixed parameters - not supported, not supported, channel 1 delay, channel 2 delay, channel 3 delay, channel 4 delay

GPM parameters - starting logarithmic frequency, ending logarithmic frequency, excitation level, channel 1 enable, channel 2 enable, channel 3 enable, channel 4 enable, diagnostic enable, auto trigger enable

Data Logger Parameters - channel 1 gain, channel 2 gain, channel 3 gain, channel 4 gain,

All commands are made up of an opening bracket "[", two letters of the command, optional parameters for some commands, and a closing bracket "]". For those commands which allow parameters, the current status of the parameters will be displayed if they are omitted. If the parameters are included, they will be updated. All the parameters or none of them must be used.

Command	Description
[FP,parameters]	read/set fixed parameters
[GP,parameters]	read/set GPM parameters
[LP,parameters]	read/set data logger parameters
[TG]	trigger gain phase meter
[TL]	trigger data logger
[GD]	read GPM data
[LD]	read logger data
[CS]	check status
[AM]	abort data logger and GPM measurements in progress
[CM]	clear memory buffer
[DT,parameters]	read/set date and time
[CP,parameters]	read/set communication parameters
[ME]	master auto-trigger flag enable
[MD]	master auto-trigger flag disable
[VE]	software version number
[SP,parameters]	read/set ACS port parameters [11]
[DE,parameters]	control output port of the ACS connector [11]

Table C.1: Summary of controller commands.

channel 5 gain, channel 6 gain, channel 7 gain, auto zero enable, auto trigger enable

Date and Time parameters - year, month, day, hour, minute, second

Communication Parameters - RS-232 baud rate, telephone number, data storage interval, data dump interval, call enable

GPM Header - channel number, temperature, year, month, day, hour, minute, second

GPM Data - frequency, magnitude, phase, offset, gain

Data Logger data - channel 1 data, channel 2 data, channel 3 data, channel 4 data, channel 5 data, channel 6 data, channel 7 data, year, month, day, hour, minute, second

Status Parameters- master auto-trigger flag, not supported, Data Logger measurement, not supported, GPM measurement, not supported, not supported

SP- pin 13, pin 12, pin 14, pin 11 to read ASC port parameters [11]

DE- Ch1 Excite, Ch1 Discharge, Ch1 Attenuate, Ch2 Excite, Ch2 Discharge, Ch2 Attenuate, Ch3 Excite, Ch3 Discharge, Ch3 Attenuate to control output port of the ASC connector [11]

As data is collected by the controller, it is stored in its internal memory until this memory buffer is explicitly cleared. The controller may be set to begin new measurements periodically, which is extremely useful if the experiment requires monitoring a process as it evolves with time. However, in this mode the controller will quickly run out of memory, after which it will stop recording data. If a single channel is enabled, the controller will run out of memory after thirteen full frequency scans. If, on the other hand, three channels are enabled, e.g. for three-wavelength sensor measurements, the memory will be enough to store data for only five full frequency scans.

To avoid this problem, a program was developed by Yanko Sheiretov. It automatically stores the data from every scan into a file and clears the memory. It is called **tw.c** (for three-wavelength) and is presented in Section "Data Acquisition" of Appendix G in [10]. The other way of communicating with the controller is the program **kermit**,

available on most UNIX systems. If the automatic program **tw.c** is used, it is recommended that a low baud rate is set, e.g. 1200, so that transmission errors are reduced to a minimum. It is usually all right to use a baud rate of 9600 when using **kermit**, because any communication problems would be easily detected visually.

Since the gain measured by the controller may vary greatly in the range of frequencies of interest, the controller may have to switch between different modes of pre-amplification. It has been noted that such transitions between modes may result in erroneous data at a specific frequency, manifested as "kinks" in the otherwise smooth curves relating the gain and phase response of a system to the frequency. These events are merely experimental artifacts and no physical significance should be attributed to them.

C.4 Troubleshooting

When the controller is used in a new measurement setup, a catch-22 situation may arise: one must know the communication speed to be able to send commands to the controller and the communication speed can be retrieved only by sending a proper command ([FP]). The workaround is to try sequentially all possible communication speeds from the computer end pushing the reset button every time. The controller will not send a readable message unless the communication speed is right.

Appendix D

Interface Boxes

The interface box, as shown in Figure 1.6, has two functions: to raise the input impedance of the measurement electronics and to buffer a voltage signal before it is processed by the controller. A very high input impedance is needed for the low frequency dielectrometry measurements with highly insulating materials.

The buffering is accomplished with a unity-gain-connected ultralow input bias current operational amplifier (AD549) that provides a very high input impedance at the sensing node. Sometimes an additional buffer stage is used to ensure that sufficient current is generated by the buffering circuit. The buffered signal is used to guard the sensing electrode and the cable that connects the sensing electrode with the interface box. In multi-wavelength sensors, each sensing electrode has an individual guard unless the short-circuit measurement mode is used. In the latter case, all guard electrodes can be combined because they are all held at the ground potential.

D.1 Parallel-Plate Sensor Interface Box

The schematic diagram of the high impedance interface circuit is shown in Figure D.1. The input of the interface is loaded either with a parallel RC pair, or with a single resistor or capacitor. A pure capacitance is used most often because it simplifies the

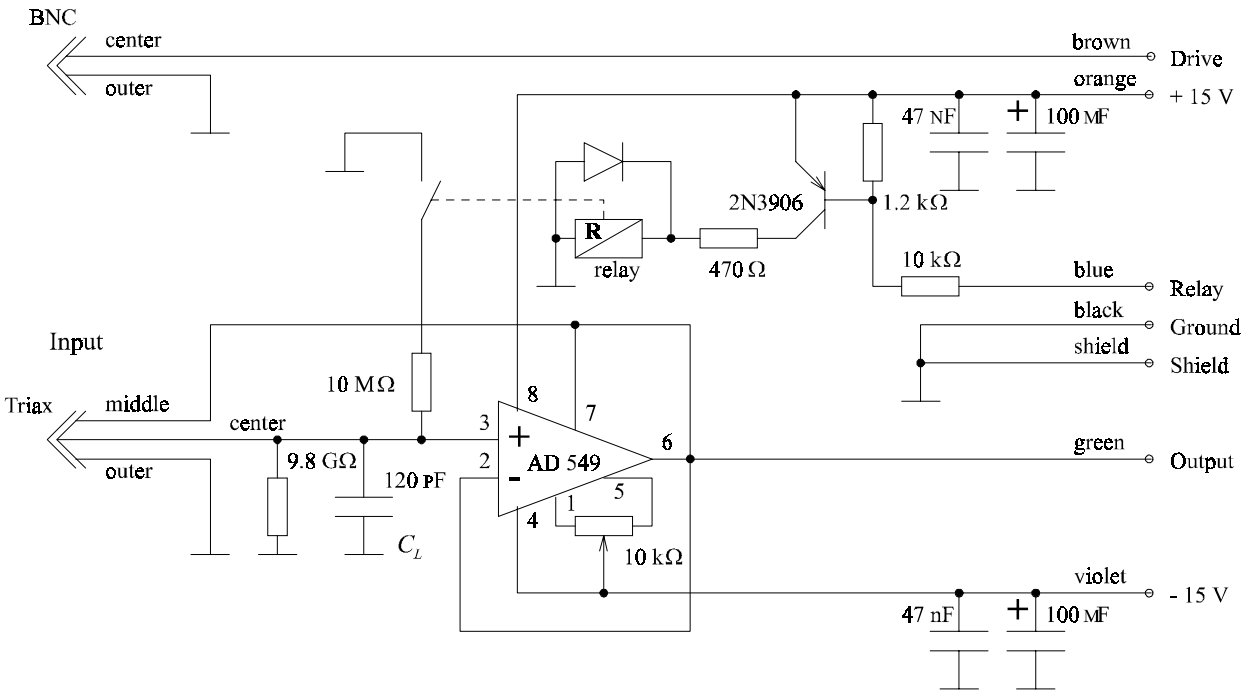

Figure D.1: High impedance dielectrometry interface circuit diagram used for floating voltage mode measurements [10].

interpretation of the raw measurement data. The value of this load capacitance, C_L, must be known precisely. It differs slightly from the nominal value of the capacitor because it is effectively connected in parallel with the capacitance associated with the operational amplifier and some of the wiring. The best way to guarantee a correct interpretation of the measurement results is to precisely evaluate the load capacitance in advance. This can be done by connecting a well-shielded high precision capacitor of a known value between the driven and the sensing electrode inputs of the interface box. Then, the load capacitance can be determined from the values of the test capacitance and the measured gain. See Section 4.6 for equations that should be used in different cases. The judicious choice of the load element values requires that they are significantly higher than the parasitics, yet to load enough to insure a measurable signal amplitude with a wide dynamic range.

The relay is used to discharge the load capacitor every time a measurement is completed, in order to prevent saturation from leakage current. For low frequency dielec-

trometry measurements, this relay must provide a very high open circuit impedance in order to prevent signal contamination by the conductive currents leakage. The 2N3906 transistor is used to drive the relay.

D.2 Three-Wavelength Sensor Interface

The circuit of this interface box is essentially identical to that shown in Figure D.1, but repeated three times, one circuit for each channel. Several types of connectors were used throughout the last few years to connect the sensor electrodes and the measurement circuitry. The latest version of the interface box uses gold-plated SMA connectors which are a miniature version of the standard BNC connectors. More than a dozen interface boxes were built for different projects. Each of them has a different set of load capacitances, which makes bookkeeping of the changes particularly important for data interpretation. Normally, the values of the load capacitance would be chosen so that the gain of the three-wavelength sensor in air is close to -40 dB.

D.3 Short-Circuit Mode Interface

The interface for a short circuit mode has been developed as a joint effort (in the order of contribution level) of D. E. Schlicker [11], Y. Du, and myself. Due to increased complexity and in order to reduce electronic interference, the circuit has been separated into three boards. The schematics for the three boards are shown in Figures D.2-D.4. The sensing board provides a high input impedance measurement of short circuit current into the sensing electrodes, the driving board provides the driven electrode signals, and the digital control board makes possible an independent drive signal of each channel as well as a software-controlled gain of the measurement circuit through the change of op-amp feedback capacitors. For more details see the doctoral thesis of Yanqing Du [12].

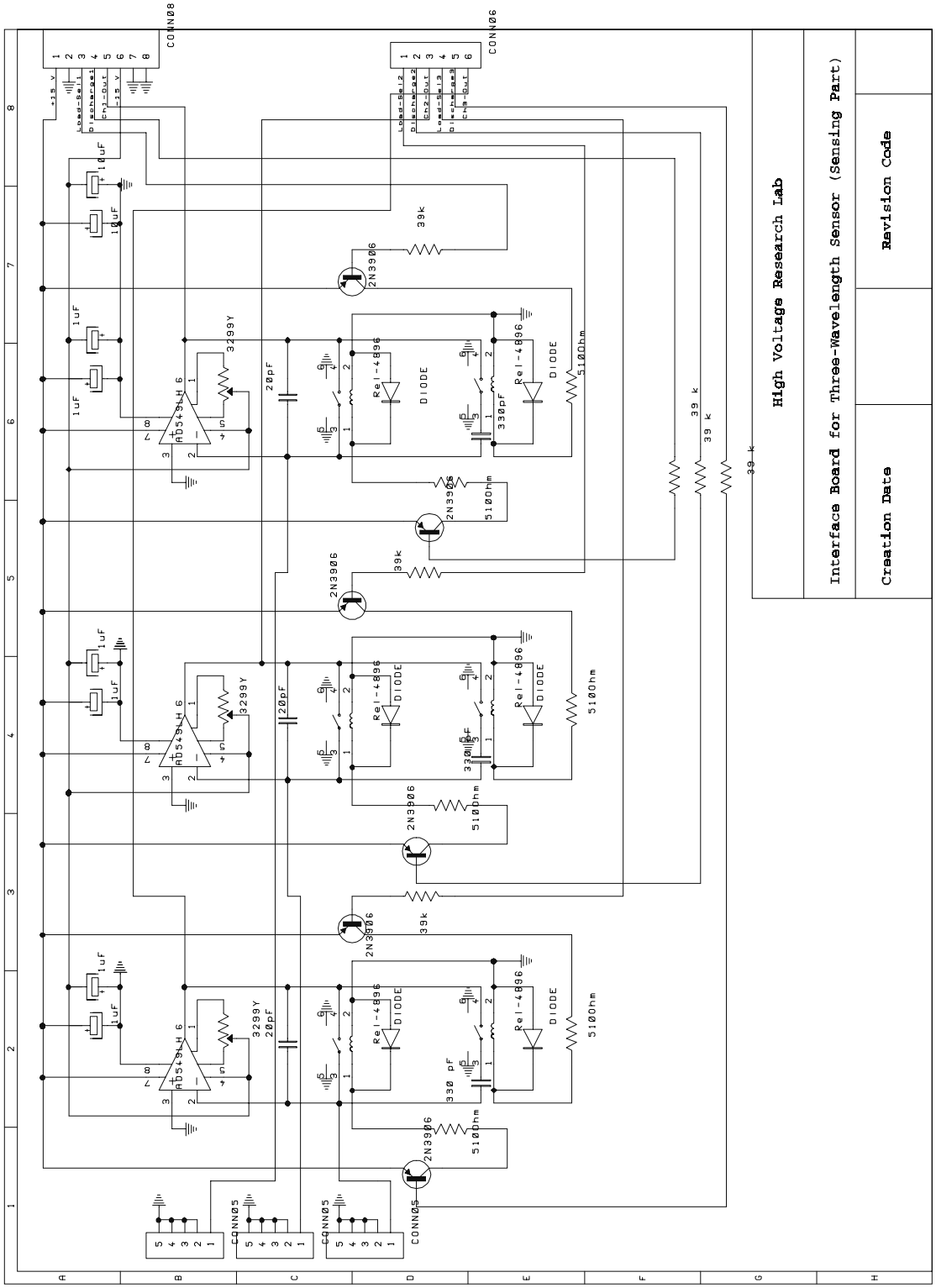

Figure D.2: Sensing board of the short-circuit interface box [11, 12].

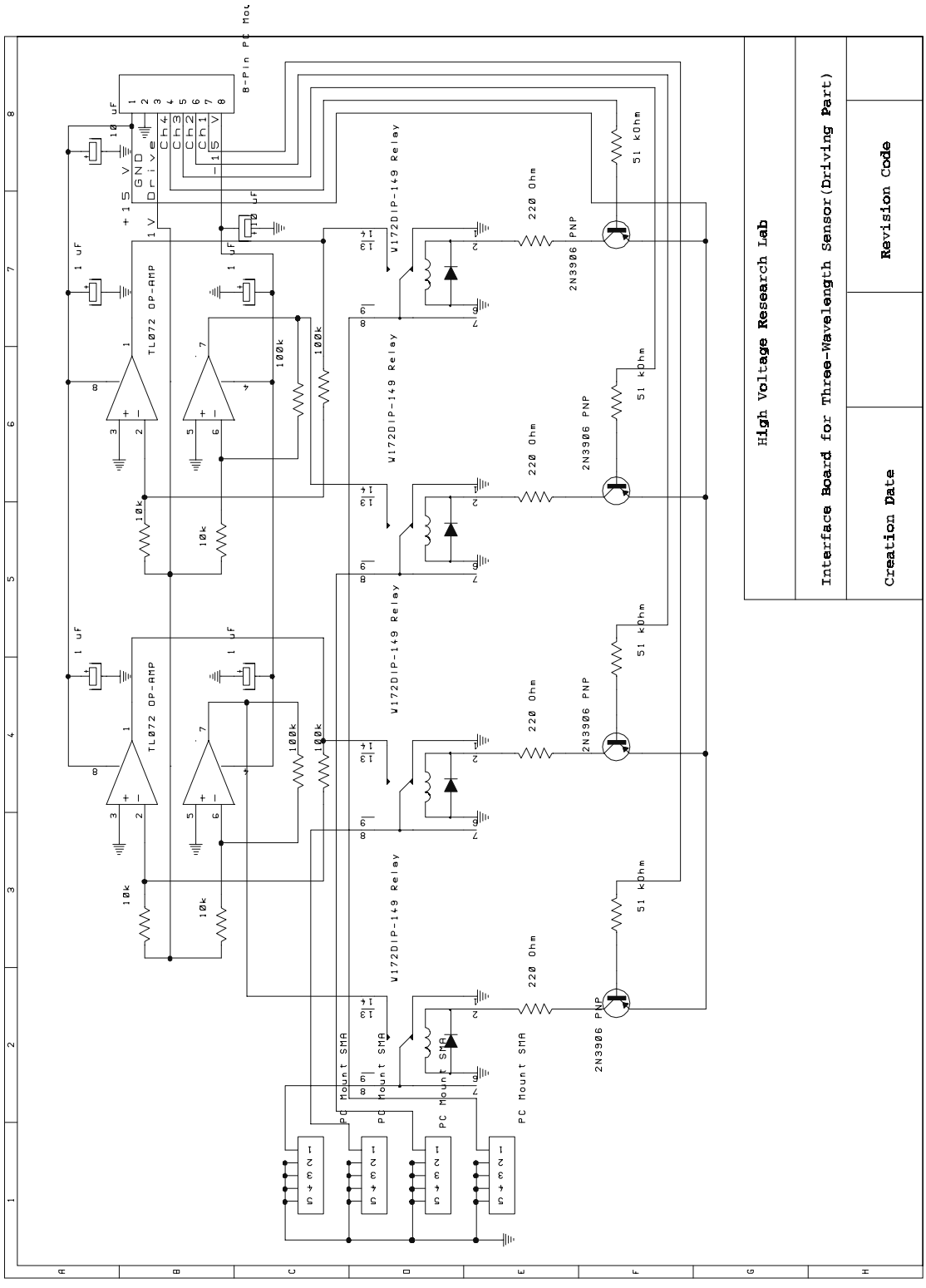

Figure D.3: Driving board of the short-circuit interface box [11, 12].

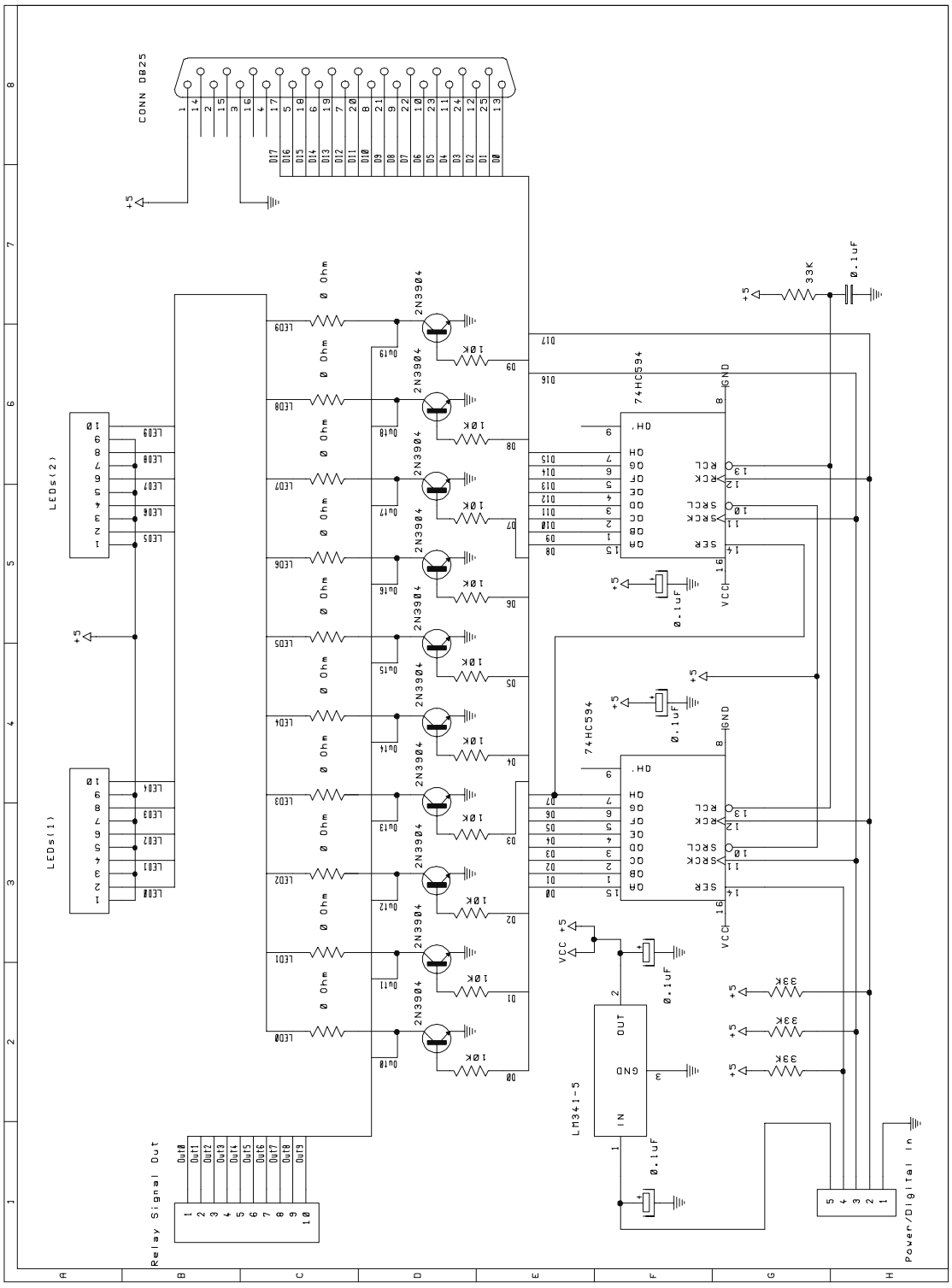

Figure D.4: Digital control board of the short-circuit interface box [11, 12].

Appendix E

Ansoft *Maxwell* Software

E.1 Tips and Tricks

A number of know-how tricks has been accumulated after performing a number of numerical simulations with *Maxwell* software by Ansoft Corp. The following tips list was started by Andrew Takahashi and later expanded by other students and myself. The features are version dependent. The latest version available at the time of writing this manuscript was 1.7.66.

1. Running a *Maxwell* parametric solution can be very tricky since there are apparently some conventions within *Maxwell* which will cause some problems. However, as always, you should begin by drawing your model, selecting materials/boundary conditions as for your nominal problem.

2. The quantities which you wish to vary in *Maxwell* must be declared as variables when you are drawing your model and selecting materials. In the Draw Model phase, this is done by adding point to point constraints or adding angle constraints. Each of these constraints is given a name which you can refer to later. We observed on several occasions that point to point constraints do not always behave as they should. Always make sure that you animate variables in the Setup Variables dialog in order to insure the proper behavior. Also, even though the model may animate correctly, the solution

may not solve correctly without the addition of more constraints. (i.e. you may receive an out of range error.)

3. In the Setup Materials phase, you may select to have a material's property represented by a function. This function will have a name which can later be added to your variable table in the setup solution dialog box. Likewise you can define boundary/source conditions as functions and these will be available in the setup solution dialog box.

4. The older versions of *Maxwell* had thresholds for conductivity beyond which the material is considered a perfect conductor or perfect insulator. The low threshold is about 10^{-9} S/m, and the high threshold is 10000 S/m. One way of getting around this *Maxwell* feature is to multiply the dielectric permittivity and conductivity by a large number. This works for highly insulating materials whose conductivity is below the low threshold. The multiplication gets the conductivity above the low threshold. Then the resulting capacitance and conductance must be divided by the same factor. The new version (1998, version 1.7.66) is free from this drawback in some projects and still has it in others. It is not currently clear when the scaling may be omitted.

5. In the setup variables table, from the menu bar, select Variables. You should be able to add any variables which have been previously defined to the solution table. Any geometric constraints should be added first as maintaining the geometry will result in the fewest number of recalculated meshes. After all required variables have been added to the table you may select Sweep from the menubar to define the ranges and sampling.

6. Also keep in mind that *Maxwell* always operates a parametric solution with the adaptive analysis feature set to on even if the checkbox is off. That is, if you want to preserve a mesh generated by the nominal problem and use the same mesh for the entire parametric solution then you must set the number of passes to 1 and make sure that the Current mesh is selected.

7. As far as we can tell, there really is no correlation between what *Maxwell* displays as the current mesh and the actual mesh that *Maxwell* uses when it calculates

the parametric solution. The only way to be sure that *Maxwell* uses the correct mesh is to be certain that no mesh has been generated yet or to clear all meshes by making a trivial change in the Setup Materials Dialog box and saving it.

8. Sometimes the *Maxwell* parametric solution will hang at a certain point for an unusually long period of time. As strange as it sounds, if you click on the close window icon at the top right of the *Maxwell* 2D Modeler, the program will ask if you wish to exit the 2D Modeler. If you reply yes, the system will unhang and continue to process the solution normally. This has no observable detrimental effect on the simulation data.

9. I have also received a few errors that the solution failed to converge even though the nominal problem is solved correctly. Strangely, this error goes away if the nominal mesh is generated in two cycles. For example, I requested 10 passes on the first cycle and when that mesh was generated I requested an additional pass on the current mesh. When I then ran the parametric problem with one pass, the solution did converge and the simulation was able to proceed as normal.

10. If you are going to be running the simulation on multiple machines, attempt to have the minimum amount of repetition. For example if you are copying the project from one machine to another you should save the solution data (.ptd file) for the project and delete it from the current project directory. Solution setups can count for several megabytes of data that will just be deleted when the next solution is generated. The easiest way I've seen to delete the solution setups is to alter the setup variables table and delete all rows. After saving the new setup all old setup data will be deleted.

11. You'll probably want to concatenate and sort the multiple data files in order to use them with some analysis package such as Matlab.

12. When specifying parametric sweeps, try to avoid unnecessary re-calculation of the finite element mesh. The mesh does not change from one setup to another if only material properties or frequency change. However, the change in geometric properties always requires a new mesh. The adaptive mesh calculation may increase the total

program execution time by as much as a factor of four. An additional disadvantage of improper sequencing of variables in the parametric module is the numerical noise due to a varying number of triangles in the geometrically identical setups.

Appendix F

Service Code

F.1 Data Acquisition

F.1.1 Description of Programs

tw2.c (For three-wavelength). This program is used for automated data acquisition and display on the ASCII screen. Primarily for use on the omega-k computer in the MIT High Voltage Research Lab. The goal of this program is to display on the ASCII screen the results of the multi-wavelength measurements with the controller, as they become available. The program checks the measurements status at exponentially increasing intervals of time and displays new data, if any.

data.c This program serves to acquire data from the controller in a variety of scenarios. The instructions are provided in the function usage().

F.1.2 tw2.c

```
/*****************************************************************/
/* */
/*    tw2.c */
/* */
/*  11/12/90 */
/*   Based on code by Yanko Sheiretov */
/*   Modified by Boris Berdnikov, 7/18/96 */
/*   Modified by Alex Mamishev Oct. 96 */
/* */
/*      Usage:  tw <filename> [<-Pparameter line>] [<-Ddelay>] */
/* Parameter line format: from,to,voltage,ch1,ch2,ch3 */
/* */
/*****************************************************************/
/* The goal of this program is to display on the ASCII screen
the results of the multi-wavelength, measurements with the controller,
as they become available. The progam checks the measurements status
at exponentially increasing intervals of time and displays new data,
if any */

# include <string.h>
# include <stdlib.h>
# include <stdio.h>/* define standard I/O routines    */
# include <sgtty.h>/* define stty and gtty calls    */
# include <fcntl.h>/* define access modes    */
# include <time.h>
# include <math.h>

# define BAUD B4800
# define LINE "/dev/ttyag"
# define BUSY -1
# define MAXSCANS 99

char ss[80];
char param[30] = "[GP,";
int delay = 10;
float last = 5.0;
FILE *fpi,*fpo,*fpd,*fopen();

printnewdata();
wait(int);

main(argc,argv)
int argc;
char *argv[];
{
int port, ext;
struct sgttyb tty;
char status, sleep[20], filename[80];

if (argc > 4 || argc < 2 || argv[1][0] == '-')
```

```
{
fprintf(stderr, "usage: tw <filename> ");
fprintf(stderr, "[<-Pparameter line>] ");
fprintf(stderr, "[<-Ddelay>]\n");
fprintf(stderr, "Parameter line format: from,to,");
fprintf(stderr, "voltage,ch1,ch2,ch3\n");
exit(1);
}

/*
parse parameter line
*/
if ((fpd = fopen(argv[1],"r")) != NULL)
{
fprintf(stderr, "File %s already exists, overwrite? ",
argv[1]);
if (tolower(getchar()) != 'y') exit(1);
}
fclose(fpd);
if ((fpd = fopen(argv[1],"w")) == NULL)
{
fprintf(stderr, "Cannot open file %s", argv[1]);
exit(1);
}
/*
set port baud rate, no echo, and raw mode
*/
if ((port = open(LINE,O_RDWR)) == BUSY)
{
fprintf(stderr, "Error: line busy\n");
exit(1);
}
gtty (port,&tty);
tty.sg_flags &= (~ECHO);
tty.sg_flags |= (RAW);
tty.sg_ispeed = tty.sg_ospeed = BAUD;
stty(port,&tty);

fpo = fdopen(port,"r");
fpi = fdopen(port,"w");
/*
Initialize control box
*/
wait(1);
command("[AM]");
wait(1);
command("[MD]");
wait(1);
command("[AM]");
wait(1);
command("[CM]");
```

```
/*
Extract initial delay time and control box parameters from
the parameter line
*/
if (argc >= 3)
{
if (argv[2][0] == '-' && (tolower(argv[2][1]) == 'p'))
strcat(param,argv[2]+2);
else if (argc == 4 && argv[3][0] == '-' &&
(tolower(argv[3][1]) == 'p'))
strcat(param,argv[3]+2);
else strcat(param, "4.0,-2.3,1.0,E,E,E");

if (argv[2][0] == '-' && (tolower(argv[2][1]) == 'd'))
delay = atoi(argv[2]+2);
else if (argc == 4 && argv[3][0] == '-' &&
(tolower(argv[3][1]) == 'd'))
delay = atoi(argv[3]+2);
if (!delay)
{
fprintf(stderr, "Wrong delay value\n");
exit(1);
}
}
if (strlen(param) < 5) strcat(param,"4.0,-2.3,1.0,E,E,E");
strcat(param,",D,D,D]");

command(param);
wait(1);
command("[TG]");

do      {
wait(delay);
printnewdata();

/*
Get control box status, exit if measurements have been completed
*/
fprintf(fpi,"[CS]");
fgets(ss,80,fpo);
sscanf(ss,"[CS,%*c,%*c,%*c,%*c,%c,%*c,%*c]",&status);
}
while (status != 'D');

fclose(fpd);
fclose(fpi);
fclose(fpo);
close(port);

}
```

```
/*
executes a control box command
*/
command(s)
char s[];
{
printf("%s", s);
fprintf(fpi,s);
fgets(ss,80,fpo);
printf("\t%s", ss);
}



/*
chacks for the new data, measured by the control box;
if there is any, prints it to the stdout and the output file
*/
printnewdata()
{
char buffer[10];
float l;

fprintf(fpi,"[GD]");
fgets(ss,80,fpo);
if (last > 4) fprintf(fpd,ss);
while (fgets(ss,80,fpo) && ss[3] != ']')
{
strncpy(buffer,ss+6,5);
if (last > (l = atof(buffer)) + 0.02)
{
printf(ss);
fprintf(fpd,ss);
}
}

if (l < last)
{
delay = (int) (delay * 1.5 );/*exp(log(10) * (last - l))*/
last = l;
}
}

/*
waits t seconds; unlike "sleep", can accept non-constant
parameters
*/
wait(t)
int t;
{
time_t st;
```

```
st = time(NULL);
while ((int)(time(NULL) - st) < t) ;
}
```

F.1.3 data.c

```
/* data.c
This program serves to acquire data from the controller in
a variety of scenarios. The instructions are provided in the
function usage().
Written mostly by Boris Berdnikov, with participation of
Alex Mamishev, reusing code of Yanko Sheiretov and previous
LEES students

Summer 1996  */

# include <string.h>
# include <stdlib.h>
# include <stdio.h>/* define standard I/O routines    */
# include <sgtty.h>/* define stty and gtty calls    */
# include <fcntl.h>/* define access modes    */
# include <time.h>

# define BAUD B9600
# define LINE "/dev/ttyag"
# define BUSY -1
# define MAXSCANS 99

# define SERIAL 1
# define PARALLEL 0

char header[80];
int totalstart = 0, totalstop = 63, order = SERIAL;
int wl1mm = 1, wl25mm = 1, wl5mm = 1;
int  print = 1;
FILE *fpi, *fpo, *fpd;

measure(int, int, int);
float fabs(float);
usage();
wait(int);

typedef struct
{
int chnum;
float freq, gain, phase, offset;
int amp;
} data_record;

data_record results[3][64];

float freqs[65] = {
 4.0,  3.907, 3.796, 3.699, 3.606, 3.495, 3.398, 3.305, 3.194, 3.097,
 3.0,  2.907, 2.796, 2.699, 2.606, 2.495, 2.398, 2.305, 2.194, 2.097,
 2.0,  1.907, 1.796, 1.699, 1.606, 1.495, 1.398, 1.305, 1.2,   1.1,
 1.0,  0.9,   0.8,   0.7,   0.6,   0.5,   0.4,   0.3,   0.2,   0.1,
```

```
 0.0, -0.1,  -0.2,  -0.3,  -0.4,  -0.5,  -0.6,  -0.7,  -0.8,  -0.9,
-1.0, -1.1,  -1.2,  -1.3,  -1.4,  -1.5,  -1.6,  -1.7,  -1.8,  -1.9,
-2.0, -2.1,  -2.2,  -2.3,  -2.3 };

float waves[3] = {5, 1, 2.5};

main(argc, argv)
int argc;
char *argv[];
{
float f, g;
struct sgttyb tty;
int port, ext, i, j;
char ss[80], outfname[80], *chp;

if (argc != 2 && argc != 4 || argc == 2 && argv[1][0] == '-')
{
fprintf(stderr, "Usage: \t%s ", argv[0]);
usage();
exit(1);
}

if (argc == 4)
{
argv[1][1] = tolower(argv[1][1]);
switch (argv[1][1]) {
case 'f': break;

case 'i':

if (chp = strchr(argv[2], ',')) *chp++ = '\0';
f = atof(argv[2]);
argv[2] = chp;

if (f < freqs[63] || f > freqs[0])
{
fprintf(stderr, "Wrong 'from' value\n");
exit(1);
}

while (freqs[i++] > f);
if (fabs(freqs[i+1]-f) < fabs(freqs[i]-f))
totalstart = i+1;
else if (i-1 && fabs(freqs[i-1]-f) < fabs(freqs[i]-f))
totalstart = i-1;

if (chp = strchr(argv[2], ',')) *chp++ = '\0';
f = atof(argv[2]);
argv[2] = chp;
if (f < freqs[63] || f > freqs[0])
{
fprintf(stderr, "Wrong 'to' value\n");
```

```
exit(1);
}

while (freqs[i++] > f);
if (fabs(freqs[i+1]-f) < fabs(freqs[i]-f))
totalstop = i+1;
else if (i-1 && fabs(freqs[i-1]-f) < fabs(freqs[i]-f))
totalstop = i-1;

break;

case 's':

if (chp = strchr(argv[2], ',')) *chp++ = '\0';
f = atof(argv[2]);
argv[2] = chp;

if (f < freqs[63] || f > freqs[0])
{
fprintf(stderr, "Wrong frequency value\n");
exit(1);
}

while (freqs[i++] > f);
if (fabs(freqs[i+1]-f) < fabs(freqs[i]-f))
totalstart = i+1;
else if (i-1 && fabs(freqs[i-1]-f) < fabs(freqs[i]-f))
totalstart = i-1;
totalstop = totalstart;
break;

default:

fprintf(stderr, "Usage: \t%s", argv[0]);
usage();
exit(1);
}


if (strlen(argv[2]))
{
if ((chp = strchr(argv[2], ','))
&& *(strchr(argv[2], ',') + 2))
{
fprintf(stderr, "Usage: \t%s ", argv[0]);
usage();
exit(1);
}

if (chp) *chp++ = '\0';
if (strlen(argv[2]))
{
```

```
wl1mm  = !(!strchr(argv[2], '1'));
wl25mm = !(!strchr(argv[2], '2'));
wl5mm  = !(!strchr(argv[2], '5'));
}

if (*chp) if (tolower(*chp) == 'p') order = PARALLEL;
     else if (tolower(*chp) == 's') order = SERIAL;
else {
fprintf(stderr, "Usage: \t%s ", argv[0]);
usage();
exit(1);
}
}

if (wl1mm + wl25mm + wl5mm == 1) order = SERIAL;
if (totalstart == totalstop) order = PARALLEL;
}

strcpy(outfname, argv[argc-1]);

if ((fpd = fopen(outfname, "r")) != NULL)
{
fprintf(stderr, "File %s already exists, overwrite? ",
outfname);
if (tolower(getchar()) != 'y') exit(1);
}
fclose(fpd);
if ((fpd = fopen(outfname, "w")) == NULL)
{
fprintf(stderr, "Cannot open file %s", outfname);
exit(1);
}

/*
set port baud rate, no echo, and raw mode
*/

if ((port = open(LINE,O_RDWR)) == BUSY)
{
fprintf(stderr, "Error: line busy\n");
exit(1);
}
gtty (port,&tty);
tty.sg_flags &= (~ECHO);
tty.sg_flags |= (RAW);
tty.sg_ispeed = tty.sg_ospeed = BAUD;
stty(port, &tty);

fpo = fdopen(port, "r");
fpi = fdopen(port, "w");

/*
```

```
Initialize control box
*/

printf("Initializing, please wait... ");
wait(1);
fprintf(fpi, "[MD]");
fgets(ss, 80, fpo);
wait(1);
fprintf(fpi, "[AM]");
fgets(ss, 80, fpo);
wait(1);

printf("done\n");
memset((void *) results, 0, sizeof(results));

if (order == SERIAL) for (i = 0; i < 3; i++)
{
if (i == 0 && !wl5mm || i == 1 && !wl1mm || i == 2 && !wl25mm)
continue;
printf("Measuring wavelength %.1f mm from frequency %.3f to frequency %.3f... ",
waves[i], freqs[totalstart], freqs[totalstop]);
measure(totalstart, totalstop, i);
printf("done\n");
}
else for (i = totalstart; i <= totalstop; i++)
    for (j=0; j < 3; j++)
if (!(j == 0 && !wl5mm || j == 1 && !wl1mm || j == 2 && !wl25mm))
{
printf("Measuring wavelength %.1f mm at the frequency %.3f... ",
waves[j], freqs[i]);
measure(i, i, j);
printf("done\n");
}

fprintf(fpi, "[AM]");
fgets(ss, 80, fpo);
wait(1);
fprintf(fpi, "[CM]");
fgets(ss, 80, fpo);

fputs(header, fpd);
for (i = totalstart; i<=totalstop; i++) for (j=0; j<3; j++)
{
if (j == 0 && !wl5mm || j == 1 && !wl1mm || j == 2 && !wl5mm)
continue;
fprintf(fpd, "[GD,%i,%.3f,%.2f,%.2f,%.3f,%i]\n", j+1,
results[j][i].freq, results[j][i].gain,
results[j][i].phase, results[j][i].offset,
results[j][i].amp);
}

fclose(fpd);
```

```
fclose(fpi);
fclose(fpo);
close(port);

}



measure(start, stop, chan)
int start, stop, chan;
{
char status, ss[80];
int delay = 10, k, l;

fprintf(fpi, "[GP,%.3f,%.3f,1.0,E,D,D,D,D,D]",
freqs[start], freqs[stop]);
fgets(ss, 80, fpo);
wait(1);

fprintf(fpi, "[CM]");
fgets(ss, 80, fpo);
wait(1);

fprintf(fpi, "[SW,4]");
fgets(ss, 80, fpo);
wait(1);

fprintf(fpi, "[SW,%d]", chan+1);
fgets(ss, 80, fpo);
wait(1);

fprintf(fpi, "[TG]");
fgets(ss, 80, fpo);
wait(1);

l = start;
if (start != stop) delay = 1;


do      {

wait(delay);

if (print)
{
fprintf(fpi, "[GD]");
if (l == totalstart)
{
fgets(header, 80, fpo);
printf("\n");
} else fgets(ss, 80, fpo);
```

```
k = start;
while (k++ < l) fgets(ss, 80, fpo);
while (fgets(ss, 80, fpo) && ss[3] != ']')
{
sscanf(ss, "[GD,%*i,%f,%f,%f,%f,%i]\n",
  &results[chan][l].freq, &results[chan][l].gain,
  &results[chan][l].phase, &results[chan][l].offset,
  &results[chan][l++].amp);
ss[4] = (char)(chan + 0x31);
printf(ss);
}
}

delay = (int) (delay * 1.5);

/*
Get control box status, exit if measurements have been completed
*/
fprintf(fpi, "[CS]");
fgets(ss, 80, fpo);
sscanf(ss, "[CS,%*c,%*c,%*c,%*c,%c,%*c,%*c]", &status);
}
while (status != 'D');

}


/*
waits t seconds; unlike "sleep", can accept non-constant
parameters
*/
wait(t)
int t;
{
time_t st;

st = time(NULL);
while ((int)(time(NULL) - st) < t) ;

}



usage()
{
fprintf(stderr, "<-i [<from>[,<to>[,<wavelengths>[,<mode>]]]]> |\n\t");
fprintf(stderr, "    <-f <wavelengths>[,<mode>]> |\n\t");
fprintf(stderr, "    <-s <frequency>[,<wavelengths>]> <filename>\n");
fprintf(stderr, ...
"-i  --\ttake measurements over the [from .. to] frequency interval\n");
fprintf(stderr, "\t(by default -- the entire control box diapasone\n");
fprintf(stderr, "-f  --\ttake full measurement cycle over the entire ");
```

```
fprintf(stderr, "control box diapasone\n");
fprintf(stderr, "-s  --\ttake measurements on the specific frequency\n\n");
fprintf(stderr, "Parameter <wavelengths>: <[1][2][5]>\n");
fprintf(stderr, "If <wavelengths> is empty or absent, all three wavelengths");
fprintf(stderr, " are measured;\nif <wavelengths> is present and ");
fprintf(stderr, "not empty, measurements are taken only for\nthe specified");
fprintf(stderr, " wavelengths (1 mm wavelength is denoted by digit '1',");
fprintf(stderr, " 2.5 mm --\ndigit '2', and 5 mm -- digit '5').\n");
fprintf(stderr, "Parameter <mode> may be either 'p' or 's', referring to the ");
fprintf(stderr, "parallel and serial\nmode of measurents, correspondingly.\n");
fprintf(stderr, "Parameters are separated by commas, no spaces are allowed.\n");

}



float fabs(f)
float f;
{
return f > 0 ? f : -f;
}
```

F.2 Data Manipulation

PlotSolSpace.m plots the solution space for non-dimensionalized capacitance, conductance, permittivity, and conductivity.

SpecStart.m This program is used for conversion of standard gain-phase data into conductance, capacitance, susceptance, impedance, and, in the case of parallel plate sensor measurements, the dielectric permittivity, conductivity, loss factor, and loss angle associated with a given frequency sweep.

combine.m This program is used to combine individual frequency sweeps into one frequency sweep.

PlotSolSpace.m This program is used for plotting the solution space of two variables using *Maxwell* output.

SpecStart.m This is the first part of the versatile plotting routine for dielectric spectroscopy. Particularly interesting are 3D plots with orthogonal projections. This program is continued with SpecCont.m, which has very similar code and is not included here to save space.

F.2.1 combine.m

```
function combine(file1,file2,file5,outputFile)

%file1 contains 1mm info
%file2 contains 2.5mm info
%file5 contains 5mm info

% open data file1

DatID1 = fopen(file1,'rt');
if (DatID1 == -1)
  disp(' ');
error('Error Opening Data File!');
end;

% Read off Header Data Line
[Head] = fscanf(DatID1,'[GH,%f,%i,%i,%i,%i,%i]',7);

% Read Data to Matrix
[Data1,Number] = fscanf(DatID1,'[GD,%i,%f,%f,%f,%f,%i]',[6,inf]);

% Close File

fclose(DatID1);

% open data file2

DatID2 = fopen(file2,'rt');
if (DatID2 == -1)
  disp(' ');
error('Error Opening Data File!');
end;

% Read off Header Data Line
[Head] = fscanf(DatID2,'[GH,%f,%i,%i,%i,%i,%i]',7);

% Read Data to Matrix
[Data2,Number] = fscanf(DatID2,'[GD,%i,%f,%f,%f,%f,%i]',[6,inf]);

% Close File

fclose(DatID2);

% open data file5

DatID5 = fopen(file5,'rt');
if (DatID5 == -1)
  disp(' ');
error('Error Opening Data File!');
end;
```

```
% Read off Header Data Line
[Head] = fscanf(DatID5,'[GH,%f,%i,%i,%i,%i,%i,%i]',7);

% Read Data to Matrix
[Data5,Number] = fscanf(DatID5,'[GD,%i,%f,%f,%f,%f,%i]',[6,inf]);
Number = Number / 6;

% Close File

fclose(DatID5);

out = zeros(Number,6);

k = 1;

Data1 = Data1';
Data2 = Data2';
Data5 = Data5';

while k<Number
   out(k,1:6) = Data5(k,1:6);
   k = k+1;
   out(k,1:6) = Data2(k,1:6);
   k = k+1;
   out(k,1:6) = Data1(k,1:6);
   k = k+1;
end

out = out';

FileName = [outputFile];

DatID = fopen(outputFile, 'w');
fprintf(DatID,'[GH,%f,%i,%i,%i,%i,%i,%i]\n', Head);
fprintf(DatID,'[GD,%i,%f,%f,%f,%f,%i]\n', out);

fclose(DatID);
```

F.2.2 PlotSolSpace.m

```
function plotSolSpace(Solspacename);
% function plotSolSpace(Solspacename);
% This function will plot the solution space given in Solspacename given the
% the solution space is organized as a 4 column matrix [eps, sig, G12, C12]
% Solution spaces are generally formatted according to the GCSORT01 Program.

close all;
Plotvector=[1 1 1 1 0]
Nonshaded=1
% load solution space
load(Solspacename);

Data=DataTrans;
% Extract/Organize Data
RowCol=size(Data);
% Attempt to nondimensionalize plots, end up dividing
%by epsilon of substrate which is 2.1e6
Epsilon = Data(1:RowCol(1),1)/2.1e6;
Sigma = Data(1:RowCol(1),2)/(2.1e6*8.05e-12)/6.28;

G12 = Data(1:RowCol(1),3)/(2.1e6*8.05e-12)/6.28;
C12 = Data(1:RowCol(1),4)/(2.1e6*8.05e-12);
% end

numberOfPointsg=25;
numberOfPointsc=25;

% Define the axis spacing and grids
mig = linspace(min(log10(G12)),max(log10(G12)) ,numberOfPointsg);
mic = linspace(min(C12),max(C12),numberOfPointsc);
[mpig,mpic] = meshgrid(mig,mic);
if Plotvector(1)
   iEpsilon = griddata(log10(G12),C12,Epsilon,mpig,mpic);
end;
if Plotvector(2)
   iSigma = griddata(log10(G12),C12,log10(Sigma),mpig,mpic);
end;

%iEpsilon = interp2(log10(G12),C12,iEpsilon,mpig,mpic);
% Draw the surface and contour plots
if Plotvector(1)
   figure;
   shading interp;
   %surfc(mpig, mpic , iEpsilon);
   plot3(log10(G12),C12,Epsilon,'.');
   zlabel('\epsilon/\epsilon_s','fontname','arial','fontsize',16);
   xlabel('log_1_0 (G_1_2/\epsilon_s\omega)','fontname','arial','fontsize',16);
   ylabel('C_1_2/\epsilon_s ','fontname','arial','fontsize',16);
   %colormap(gray);
   %colorbar('vert');
```

```
   grid on;
   set(gca,'fontname','arial','fontsize',16);
end;

if Plotvector(2)
   figure;
   %surf(mpig,mpic,iSigma);
   plot3(log10(G12),C12,log10(Sigma),'.');
   zlabel('log_1_0(\sigma/\epsilon_s\omega)','fontname','arial','fontsize',16);
   xlabel('log_{10} (G_1_2/\epsilon_s\omega)','fontname','arial','fontsize',16);
   ylabel('C_1_2/\epsilon_s','fontname','arial','fontsize',16);
   %colorbar('vert');
   %colormap(gray);
   grid on;
   set(gca,'fontname','arial','fontsize',16);
end;
% The following section is the tmgrid program modified
%to plot the contours of the inverse problem.
MovUp=[0.0 0.00];
MovRight=[0 .00];

% Form Conductance and Capacitance Vectors (check the negatives)
ConductanceVec1 = G12;
CapacitanceVec1=C12;

% Form Conductance and Capacitance Vectors (check the negatives)
ConductanceVec2 = C12;
CapacitanceVec2=log10(G12);


grid = [CapacitanceVec1, CapacitanceVec2];
sigma = linspace(1/2.1,20/2.1,39);
sigma = round(sigma*100)/100;
delta = linspace(log10(1e-14/2.1/8.05e-12/6.28),log10(1e-7/2.1/8.05e-12/6.28),71);
delta = round(delta*100)/100;
CapacitanceVec1(1:300,1);
delta=delta';
sigma=sigma';
length(CapacitanceVec1)

% Function to plot Grid
% grid = gain/phase data in array form
% sigma = conductivites
% delta = liftoff


% Grid Array form
%
% [mag1 phase1]; for delta 1, sigma 1
% [mag2 phase2]; for delta 2, sigma 1

% Get Array Sizes
```

```
SigSize = size(sigma,1)
deltSize = size(delta,1)

% Build Matrix Grid
MatrixGain  = zeros(SigSize,deltSize);
MatrixPhase = zeros(SigSize,deltSize);
for SigIndex = 1:SigSize
lineStartIndex = (SigIndex-1)*deltSize  + 1;
lineEndIndex = lineStartIndex + deltSize - 1;
MatrixGain(SigIndex,:) = grid(lineStartIndex:lineEndIndex,1)';
MatrixPhase(SigIndex,:) = grid(lineStartIndex:lineEndIndex,2)';
end


% Plot Standard Grid

figure
%subplot(2,1,1)

% Plot Lines of Constant Sigma
for SigLine = 1:4:SigSize
plot(MatrixGain(SigLine,:),MatrixPhase(SigLine,:))
   hold on
   xlabel('C_{12}/\epsilon_s','fontname','arial','fontsize',16);
   ylabel('log_{10} (G_{12}/\epsilon_s\omega)','fontname','arial','fontsize',16);

%   pause
end
ax=axis;

% Indicate Lines of Constant Sigma
for SigLine = 1:4:SigSize
        text(ax(2)*MovRight(1)+min(MatrixGain(SigLine,:)),...
ax(4)*MovUp(1)+max(MatrixPhase(SigLine,:)),...
num2str(sigma(SigLine)),'fontname','arial','fontsize',16);
end
title('                                                                                ...
 \epsilon/\epsilon_s','fontname','arial','fontsize',16);
set(gca,'fontname','arial','fontsize',16);
figure
% Plot Lines of Constant Liftoff
for LiftLine = 1:10:deltSize
plot(MatrixGain(:,LiftLine)',MatrixPhase(:,LiftLine)')
hold on
end

% labels
xlabel('C_{12}/\epsilon_s','fontname','arial','fontsize',16);
ylabel('log_{10} (G_{12}/\epsilon_s\omega)','fontname','arial','fontsize',16);


        ax=axis;
```

```
% Indicate Lines of Constant Liftoff
for LiftLine = 1:10:deltSize
        text(ax(2)*MovRight(2)+max(MatrixGain(:,LiftLine)),...
        ax(4)*MovUp(2)+max(MatrixPhase(:,LiftLine)),...
num2str(delta(LiftLine)),'fontsize',16,'fontname','arial');
end
title('                                                                    ...
    log_{10}(\sigma/\epsilon_s\omega)','fontname','arial','fontsize',16);
set(gca,'fontname','arial','fontsize',16);


% this is the end of the tmgrid section.

% Attempt to represent C12 and G12 as functions of eps and sig
mis = linspace(min(log10(Sigma)),max(log10(Sigma)),numberOfPointsg);
mie = linspace(min(Epsilon),max(Epsilon),numberOfPointsg);
%mis(14)
%mie(1)
[mpis,mpie] = meshgrid(mis,mie);
if Plotvector(3)
   iC12 = griddata(log10(Sigma),Epsilon,C12,mpis,mpie);
end;
if Plotvector(4)
   iG12 = griddata(log10(Sigma),Epsilon,log10(G12),mpis,mpie);
   %sum(log10(G12))
end;
if Plotvector(5)
   i2G12=griddata(log10(Sigma),Epsilon,G12,mpis,mpie);
end;


if Plotvector(3)
   if Nonshaded
      figure;
      mesh(mpis,mpie,iC12,zeros(25,25));
      zlabel('C_1_2/\epsilon_s','Fontsize',18);
      xlabel('log_1_0 (\sigma /\epsilon_s\omega)','Fontsize',18);
      ylabel('\epsilon/\epsilon_s','Fontsize',18);
      %BarHandle=colorbar('vert');
      %set(BarHandle,'Fontsize',16);
      colormap(gray);
      set(gca,'Fontsize',16);
      %view([-37.5 10]);
      figure;
      [C,H]=contour(mpis,mpie,iC12,'k-');
      ax=axis;
      axis([ax(1) ax(2) 0 10]);
      CL=clabel(C,H);
      set(CL,'Fontname','arial','fontsize',16);
      title('                                                    ...
                                C_1_2/\epsilon_s','Fontsize',18);
```

```
      xlabel('log_1_0 (\sigma /\epsilon_s\omega)','Fontsize',18);
      ylabel('\epsilon/\epsilon_s','Fontsize',18);
      set(gca,'Fontsize',16,'Fontname','Arial');
   else
      figure;
      H=surfc(mpis-6,mpie/1e6,iC12/1e6);
      title('C_1_2','Fontsize',18);
      xlabel('log_1_0 Sigma','Fontsize',18);
      ylabel('Epsilon','Fontsize',18);
      C=contourc(mis-6,mie/1e6,iC12/1e6);
      %[FCD,CDat,V,X,Y,Z,VN,index1,index2]=protectObj(H);
      %clabel(C,H(2:end),'manual');
      %RestoreObj(H,FCD,CDat,V,X,Y,Z,VN,index1,index2);
      BarHandle=colorbar('vert');
      set(BarHandle,'Fontsize',16);
      colormap(gray);
      set(gca,'Fontsize',16);
      view([-37.5 10]);
   end;
end;

if Plotvector(4)
   if Nonshaded
      figure;
      mesh(mpis,mpie,iG12,ones(25,25));
      caxis([0.1 10]);
      zlabel('log_1_0 (G_1_2/\epsilon_s\omega)','Fontsize',18);
      xlabel('log_1_0 (\sigma/\epsilon_s\omega)','Fontsize',18);
      ylabel('\epsilon/\epsilon_s','Fontsize',18);
      %BarHandle=colorbar('vert');
      %set(BarHandle,'Fontsize',16);
      colormap(gray);
      set(gca,'Fontsize',16);
      %view([-37.5 10]);
      figure;
      [C,H]=contour(mpis,mpie,iG12,'k-');
      CL=clabel(C,H);
      set(CL,'fontsize',16,'fontname','arial');
      title('                                                    ...
  log_1_0 (G_1_2/\epsilon_s\omega)','Fontsize',18);
      xlabel('log_1_0 (\sigma/\epsilon_s\omega)','Fontsize',18);
      ylabel('\epsilon/\epsilon_s','Fontsize',18);
      set(gca,'fontsize',16,'fontname','arial');
   else
      figure;
      H=surfc(mpis-6,mpie/1e6,iG12-6);
      title('log_1_0 G_1_2','Fontsize',18);
      xlabel('log_1_0 Sigma','Fontsize',18);
      ylabel('Epsilon','Fontsize',18);
      %C=contourc(mis-6,mie/1e6,iG12-6);
      %[FCD,CDat,V,X,Y,Z,VN,index1,index2]=protectObj(H);
      %clabel(C,H(2:end),'manual');
```

```
      %RestoreObj(H,FCD,CDat,V,X,Y,Z,VN,index1,index2);
      BarHandle=colorbar('vert');
      set(BarHandle,'Fontsize',16);
      set(gca,'Fontsize',16);
      view([-37.5 10]);
      colormap(gray);
   end;
end;

if Plotvector(5)
   if Nonshaded
      figure;
      mesh(mpis,mpie,i2G12,zeros(25,25));
      title('G_1_2/\epsilon_s\omega','Fontsize',18);
      xlabel('log_1_0 (\sigma/\epsilon_s\omega)','Fontsize',18);
      ylabel('\epsilon/\epsilon_s','Fontsize',18);
      %BarHandle=colorbar('vert');
      %set(BarHandle,'Fontsize',16);
      colormap(gray);
      set(gca,'Fontsize',16);
      view([-37.5 10]);
      figure;
      [C,H]=contour(mpis,mpie,i2G12,'k-');
      clabel(C,H);
      title('G_1_2/\epsilon_s\omega','Fontsize',18);
      xlabel('log_1_0 (\sigma/\epsilon_s\omega)','Fontsize',18);
      ylabel('\epsilon/\epsilon_s','Fontsize',18);

   else
      figure;
      H=surfc(mpis-6,mpie/1e6,i2G12/1e6);
      title('G_1_2','Fontsize',18);
      xlabel('log_1_0 Sigma','Fontsize',18);
      ylabel('Epsilon','Fontsize',18);
      C=contourc(mis-6,mie/1e6,i2G12/1e6);
      %[FCD,CDat,V,X,Y,Z,VN,index1,index2]=protectObj(H);
      %clabel(C,H(2:end),'manual');
      %RestoreObj(H,FCD,CDat,V,X,Y,Z,VN,index1,index2);
      BarHandle=colorbar('vert');
      set(BarHandle,'Fontsize',16);
      colormap(gray);
      set(gca,'Fontsize',16);
      view([-37.5 10]);
   end;
end;
```

F.2.3 SpecStart.m

```
function SpecStart(DatFileName,ttl,mm1,mm2,mm5)
% Plots many spectroscopy plots for standard 3-channel output
%    of the controller box
% Sizing of characters is for double-column print
% When values of G12 cannot be determined, they are not printed
%    (instead of being zeroed out or assigned negative values).
%
% Alex Mamishev, Ricky Debnath, May-August 1998

close all
% make fonts appropriate size
set(0,'DefaultAxesFontSize',18)
size set((0,'DefaultTextFontSize',18))

%specify which plots to plot
% sequence: 1)Gain/Phase 2)C12/G12 vs. Freq 3) G12 vs. C12
%4) G12/omega*C12) (tan delta for PP) vs. Frequency 5) Re(Z) vs -Im(Z)

plotIt = [1 1 0 1 1 1 1 1 1 1 1 1 1 1 1];

plotIt = [1 1 0 0 0 1 1 1 1 1 1 1 1 0 0 0];




% specify "1" if you want to print
printIt = 0;

% Load capacitances

 %Cl1mm = 214; CL1mm = Cl1mm;
 %Cl2mm = 97.9; CL2mm = Cl2mm;
 %Cl5mm = 57.54; CL5mm = Cl5mm;

 Cl1mm = 223.15; CL1mm = Cl1mm;
 Cl2mm = 101.7; CL2mm = Cl2mm;
 Cl5mm = 58.7; CL5mm = Cl5mm;

 Cl1mm = 101.9; CL1mm = Cl1mm;
 Cl2mm = 101.4; CL2mm = Cl2mm;
 Cl5mm = 50.0; CL5mm = Cl5mm;

   interface=['OCV, ','C_{L}(5mm) = ',num2str(Cl5mm),' pF, ',...
         'C_{L}(2.5mm) = ',num2str(Cl2mm),' pF, '...
      'C_{L}(1mm) = ',num2str(Cl1mm),' pF, ',DatFileName];

 CH15mm = '5.0 mm';
 CH22mm = '2.5 mm';
 CH31mm = '1.0 mm';
```

```
 Cair1mm = 3.754;
 Cair25mm = 3.754;
 Cair5mm = 3.754 ;

 % open data file

DatID = fopen(DatFileName,'rt');
if (DatID == -1)
disp(' ');
error('Error Opening Data File!');
end;

% Read off Header Data Line
[Head] = fscanf(DatID,'[GH,%f,%i,%i,%i,%i,%i,%i]',7);

% Read Data to Matrix
[Data,Number] = fscanf(DatID,'[GD,%i,%f,%f,%f,%f,%i]',[6,inf]);
Number = Number / 6;
% Close File
fclose(DatID);

% Extract/Organize Data

Freq = 10.^Data(2,3:3:Number);
Omega = Freq.*2.*pi;

Gain1mm  = Data(3,3:3:Number);
Gain25mm = Data(3,2:3:Number);
Gain5mm  = Data(3,1:3:Number);

Phase1mm  = Data(4,3:3:Number);
Phase25mm = Data(4,2:3:Number);
Phase5mm  = Data(4,1:3:Number);

% Identify small phase
PhaseLimit = 3;
SmallPhase1mm = (sign(abs(Phase1mm)-PhaseLimit)+1)./2;
SmallPhase25mm = (sign(abs(Phase25mm)-PhaseLimit)+1)./2;
SmallPhase5mm = (sign(abs(Phase5mm)-PhaseLimit)+1)./2;

semilogx(Freq,SmallPhase25mm,'*')
% Recalculate gain into volts, phase into radians
 Gr1mm = 10.^(Gain1mm./20);
 Gr25mm = 10.^(Gain25mm./20);
 Gr5mm = 10.^(Gain5mm./20);

 Fi1mm = Phase1mm.*pi./180;
 Fi25mm = Phase25mm.*pi./180;
 Fi5mm = Phase5mm.*pi./180;

% Recalculate into real and imaginary parts of gain
 GRe1mm = Gr1mm.*(cos(Fi1mm));
```

```
 GRe2mm = Gr25mm.*(cos(Fi25mm));
 GRe5mm = Gr5mm.*(cos(Fi5mm));

 GIm1mm = Gr1mm.*(sin(Fi1mm));
 GIm2mm = Gr25mm.*(sin(Fi25mm));
 GIm5mm = Gr5mm.*(sin(Fi5mm));

 G12m1 = zeros(1,Number/3)-1;
 G12m2 = zeros(1,Number/3)-1;
 G12m5 = zeros(1,Number/3)-1;

 Sigma1    = zeros(1,Number/3);
 Epsilon1  = zeros(1,Number/3);
 Sigma25   = zeros(1,Number/3);
 Epsilon25 = zeros(1,Number/3);
 Sigma5    = zeros(1,Number/3);
 Epsilon5  = zeros(1,Number/3);


 % Solve system of equations

 for ii = 1:Number/3,
 A1 = [ GRe1mm(ii)-1 -Omega(ii)*GIm1mm(ii);
GIm1mm(ii)  Omega(ii)*(GRe1mm(ii)-1)];
 B1 = [ Omega(ii)*GIm1mm(ii)*CL1mm;
-GRe1mm(ii)*Omega(ii)*CL1mm];

 A2 = [ GRe2mm(ii)-1 -Omega(ii)*GIm2mm(ii);
GIm2mm(ii)  Omega(ii)*(GRe2mm(ii)-1)];
 B2 = [ Omega(ii)*GIm2mm(ii)*CL2mm;
-GRe2mm(ii)*Omega(ii)*CL2mm];

 A5 = [ GRe5mm(ii)-1 -Omega(ii)*GIm5mm(ii);
GIm5mm(ii)  Omega(ii)*(GRe5mm(ii)-1)];
 B5 = [ Omega(ii)*GIm5mm(ii)*CL5mm;
-GRe5mm(ii)*Omega(ii)*CL5mm];

 X1 = A1\B1;
 X2 = A2\B2;
 X5 = A5\B5;

 C12m1(ii) = X1(2);
 C12m2(ii) = X2(2);
 C12m5(ii) = X5(2);

lC12m1(ii) = log10(C12m1(ii));
lC12m2(ii) = log10(C12m2(ii));
lC12m5(ii) = log10(C12m5(ii));


%%% Make sure G12 can be measured - that is the phase (in degrees) differs
%%% sufficiently from 0, and that we are not in high frequency range
```

```
%%% where phase delay is caused by the op-amps

% Phase limit when G12 can be detected
% change upper frequency limit to eliminate
% the effects of HF A/D rolloff

PhaseLimit = 3;

if (abs(Phase1mm(ii)) > PhaseLimit & Freq(ii)<100000)
   G12m1(ii) = X1(1);
lG12m1(ii) = log10(G12m1(ii));
end

if (abs(Phase25mm(ii)) > PhaseLimit & Freq(ii)<100000)
   G12m2(ii) = X2(1);
lG12m2(ii) = log10(G12m2(ii));
end

if (abs(Phase5mm(ii)) > PhaseLimit & Freq(ii)<100000)
   G12m5(ii) = X5(1);
lG12m5(ii) = log10(G12m5(ii));
end

end


if mm1~=0
    Epsilon1 = C12m1./Cair1mm;
    lEpsilon1 = log10(Epsilon1);
    Sigma1 = G12m1./Cair1mm.*8.85;
    EpsilonDoublePrime1  = Sigma1./Omega;
    lEpsilonDoublePrime1 = log10(lEpsilonDoublePrime1);
    tand1 = EpsilonDoublePrime1./(Epsilon1*8.85);
    m12m1 = 1./(Epsilon1 - j.*EpsilonDoublePrime1);
 end

 if mm2~=0
    Epsilon25 = C12m2./Cair25mm;
    lEpsilon25 = log10(Epsilon25);
    Sigma25 = G12m2./Cair25mm*8.85;
    EpsilonDoublePrime25 = Sigma25./Omega;
    lEpsilonDoublePrime25 = log10(EpsilonDoublePrime25);
    tand25 = EpsilonDoublePrime25./(Epsilon25*8.85);
    m12m25 = 1./(Epsilon25 - j.*EpsilonDoublePrime25);
 end

 if mm5~=0
    Epsilon5=C12m5./Cair5mm;
    lEpsilon5 = log10(Epsilon5);
    Sigma5=G12m5./Cair5mm*8.85;
    EpsilonDoublePrime5  = Sigma5./Omega;
    lEpsilonDoublePrime5 = log10(EpsilonDoublePrime5);
```

```
    tand5 = EpsilonDoublePrime5./(Epsilon5*8.85);
    m12m5 = 1./(Epsilon5 - j.*EpsilonDoublePrime5);
 end

 % Compute Z12

 y12m1=G12m1+i.*Omega.*C12m1;
 y12m2=G12m2+i.*Omega.*C12m2;
 y12m5=G12m5+i.*Omega.*C12m5;

 z12m1=1./y12m1;
 z12m2=1./y12m2;
 z12m5=1./y12m5;

 lz12m1 = log10(z12m1);
 lz12m2 = log10(z12m2);
 lz12m5 = log10(z12m5);



%Save C12/G12

Results = [Freq;   G12m1;   C12m1;   G12m2;   C12m2;   G12m5;   C12m5];

FileName = [DatFileName '.res'];
DatID = fopen(FileName, 'w');
fprintf(DatID, 'Frequency\t\tG12 - 1mm\tC12 - 1mm\tG12 -
... 2.5 mm\tC12 - 2.5mm\tG12 - 5 mm\tC12 - 5 mm\n');
%fprintf(DatID,'%e\t\t%e\t%e\t%e\t%e\t%e\t%e\n', Results);
fprintf(DatID,'%f\t\t%f\t%f\t%f\t%f\t%f\t%f\n', Results);


fclose(DatID);


% ------------------------------------------------------
% PlotNow Gain and Phase vs. Freq
if plotIt(1)==1

   figure ('PaperPosition', [.25 .75 8 9.5])

   subplot(2,1,1)
   if mm1~=0
      semilogx(Freq,Gain1mm,'+','MarkerSize',6)
   end;
   if mm2~=0
      if mm1~=0
         hold on
      end;
      semilogx(Freq,Gain25mm,'o','MarkerSize',6)
      hold off
   end;
```

```
   if mm5~=0
      if (mm1+mm2)~=0
         hold on
      end;
      semilogx(Freq,Gain5mm,'*','MarkerSize',6)
      hold off;
   end;
  set(gca,'FontSize',18,'XTick', [0.01 0.1 1 10 100 1000 10000])
  title(ttl);
  xlabel(interface,'FontSize',14)
  ylabel('Gain (dB)')
  ax = axis;
  axis([(10^(-2.3)) (10^4) ax(3) ax(4)])
  %axis([(10^(-2.3)) (10^4) -28 -22])


  subplot(2,1,2)
  if mm1~=0
     semilogx(Freq,Phase1mm,'+','MarkerSize',6)
  end;
  if mm2~=0
     if mm1~=0
        hold on
     end;
semilogx(Freq,Phase25mm,'o','MarkerSize',6)
   hold off
  end;
 if mm5~=0
if (mm1+mm2)~=0
hold on
end;
h=semilogx(Freq,Phase5mm,'*','MarkerSize',6)
hold off;
 end;
  set(gca,'FontSize',18,'XTick', [0.01 0.1 1 10 100 1000 10000])
  ylabel('Phase (degrees)')
  xlabel('Frequency (Hz)')
  ax = axis;
  axis([(10^(-2.3)) (10^4) ax(3) ax(4)])
  if printIt==1
     print;
  end
end


%-------------------------------------------------------

%PlotNow C12 and G12 vs. Freq.
if plotIt(2) == 1
   figure ('PaperPosition', [.25 .75 8 9.5])
   subplot(2,1,1)
   if mm1~=0
```

```
      semilogx(Freq,G12m1,'+','MarkerSize',5)
   end;
   if mm2~=0
      if mm1~=0
         hold on
      end;
      semilogx(Freq,G12m2,'o','MarkerSize',5)
      hold off
   end;
   if mm5~=0
      if (mm1+mm2)~=0
         hold on
      end;
      semilogx(Freq,G12m5,'*','MarkerSize',5)
      hold off;
   end;
   ax = axis;

   G12m1new=G12m1+(3*(ax(4)-ax(3)).*(SmallPhase1mm-1));
   G12m2new=G12m2+(3*(ax(4)-ax(3)).*(SmallPhase25mm-1));
   G12m5new=G12m5+(3*(ax(4)-ax(3)).*(SmallPhase5mm-1));

   subplot(2,1,1)
   if mm1~=0
      semilogx(Freq,G12m1new,'+','MarkerSize',5)
   end;
   if mm2~=0
      if mm1~=0
         hold on
      end;
      semilogx(Freq,G12m2new,'o','MarkerSize',5)
      hold off
   end;
   if mm5~=0
      if (mm1+mm2)~=0
hold on
   end;
   semilogx(Freq,G12m5new,'*','MarkerSize',5)
   hold off;
end;

axis([(10^(-2.3)) (10^4) ax(3) ax(4)])
set(gca,'XTick', [0.01 0.1 1 10 100 1000 10000])
%legend('+','1 mm','o','2.5 mm','*','5 mm')

title(ttl);
ylabel('Conductance, G_{12}  (pS)')

subplot(2,1,2)
if mm1~=0
   semilogx(Freq,C12m1,'+','MarkerSize',5)
end;
```

```
if mm2~=0
if mm1~=0
      hold on
   end;
semilogx(Freq,C12m2,'o','MarkerSize',5)
hold off
end;
if mm5~=0
if (mm1+mm2)~=0
hold on
end;
semilogx(Freq,C12m5,'*','MarkerSize',5)
hold off;
end;
xlabel('Frequency (Hz)')
ylabel('Capacitance, C_{12} (pF)')
ax = axis;
axis([(10^(-2.3)) (10^4) ax(3) ax(4)])
set(gca,'XTick', [0.01 0.1 1 10 100 1000 10000])
  if printIt==1
     print;
  end
end

%-------------------------------------------------------

%PlotNow log C12 and log G12 vs. Freq.
if plotIt(3) == 1
   figure%('PaperPosition', [.25 .75 8 9.5])
   subplot(2,1,1)
   if mm1~=0
      semilogx(Freq,lG12m1,'+','MarkerSize',5)
   end;
   if mm2~=0
      if mm1~=0
         hold on
      end;
      semilogx(Freq,lG12m2,'o','MarkerSize',5)
      hold off
   end;
   if mm5~=0
      if (mm1+mm2)~=0
         hold on
      end;
      semilogx(Freq,lG12m5,'*','MarkerSize',5)
      hold off;
   end;
   ax = axis;

   lG12m1new=lG12m1+(3*(ax(4)-ax(3)).*(SmallPhase1mm-1));
   lG12m2new=lG12m2+(3*(ax(4)-ax(3)).*(SmallPhase25mm-1));
   lG12m5new=lG12m5+(3*(ax(4)-ax(3)).*(SmallPhase5mm-1));
```

```
   subplot(2,1,1)
   if mm1~=0
      semilogx(Freq,lG12m1new,'+','MarkerSize',5)
   end;
   if mm2~=0
      if mm1~=0
         hold on
      end;
      semilogx(Freq,lG12m2new,'o','MarkerSize',5)
      hold off
   end;
   if mm5~=0
      if (mm1+mm2)~=0
hold on
   end;
   semilogx(Freq,lG12m5new,'*','MarkerSize',5)
   hold off;
end;

axis([(10^(-2.3)) (10^4) ax(3) ax(4)])
set(gca,'XTick', [0.01 0.1 1 10 100 1000 10000])
%legend('+','1 mm','o','2.5 mm','*','5 mm')

title(ttl);
ylabel('log (Cond.), G_{12}  (pS)')

subplot(2,1,2)
if mm1~=0
   semilogx(Freq,lC12m1,'+','MarkerSize',5)
end;
if mm2~=0
if mm1~=0
      hold on
   end;
semilogx(Freq,lC12m2,'o','MarkerSize',5)
hold off
end;
if mm5~=0
if (mm1+mm2)~=0
hold on
end;
semilogx(Freq,lC12m5,'*','MarkerSize',5)
hold off;
end;
xlabel('log (Frequency) (Hz)')
ylabel('log(Cap.), C_{12} (pF)')
ax = axis;
axis([(10^(-2.3)) (10^4) ax(3) ax(4)])
set(gca,'XTick', [0.01 0.1 1 10 100 1000 10000])
  if printIt==1
     print;
```

```
  end
end




%-----------------------------------------------------------

% PlotNow G12 vs. C12
if plotIt(4)==1

   figure%('PaperPosition', [.25 .75 8 9.5])
   if mm1~=0
      for ii=1:length(Freq)
         if SmallPhase1mm(ii)==1
            plot(G12m1(ii),C12m1(ii),'+','MarkerSize',6);
if Freq(ii)==.01 | Freq(ii)==.1 | Freq(ii)==1 | ...
Freq(ii)==10 | Freq(ii)==100 | Freq(ii)==1000 | Freq(ii)==10000
               text(G12m1(ii),C12m1(ii),num2str(Freq(ii)),...
                  'FontSize',16);
            hold on;
         end
end
      end
   end;
   if mm2~=0
      if mm1~=0
         hold on
      end;
      for ii=1:length(Freq)
         if SmallPhase25mm(ii)==1
            plot(G12m2(ii),C12m2(ii),'o','MarkerSize',6);
if Freq(ii)==.01 | Freq(ii)==.1 | Freq(ii)==1 | ...
Freq(ii)==10 | Freq(ii)==100 | Freq(ii)==1000 | Freq(ii)==10000
               text(real(G12m2(ii)),C12m2(ii),num2str(Freq(ii)),...
                  'FontSize',16);
            hold on;
      end
end
      end
      hold off
   end;
   if mm5~=0
      if (mm1+mm2)~=0
         hold on
      end;
      for ii=1:length(Freq)
         if SmallPhase5mm(ii)==1
            plot(G12m5(ii),C12m5(ii),'*','MarkerSize',6);
if Freq(ii)==.01 | Freq(ii)==.1 | Freq(ii)==1 |...
 Freq(ii)==10 | Freq(ii)==100 | Freq(ii)==1000 | Freq(ii)==10000
```

```
               text(G12m5(ii),C12m5(ii),num2str(Freq(ii)),...
                  'FontSize',16);
 hold on;
         end
      end
      end
      hold off;
   end;
  title(ttl);
  xlabel('G_{12}, (pS)')
  ylabel('C_{12}, (pF)')
  if printIt==1
     print;
  end
end

%-------------------------------------------------

% PlotNow (G12/omega*C12) (tan delta for PP) vs. Frequency
if plotIt(5)==1

   figure%('PaperPosition', [.25 .75 8 9.5])
   if mm1~=0
      semilogx(Freq,G12m1new./C12m1./Omega,'+','MarkerSize',6)
   end;
   if mm2~=0
      if mm1~=0
         hold on
      end;
      semilogx(Freq,G12m2new./C12m2./Omega,'o','MarkerSize',6)
      hold off
   end;
   if mm5~=0
      if (mm1+mm2)~=0
         hold on
      end;
      semilogx(Freq,G12m5new./C12m5./Omega,'*','MarkerSize',6)
      hold off;
   end;
  set(gca,'FontSize',18,'XTick', [0.01 0.1 1 10 100 1000 10000])
  title(ttl);
  xlabel('Frequency (Hz)')
  ylabel('G_{12}/\omega C_{12}')
  ax = axis;
  axis([(10^(-2.3)) (10^4) ax(3) ax(4)])
  if printIt==1
     print;
  end
end


%-----------------------------------------------------------------
```

```
% PlotNow Zreal vs -ZImag
if plotIt(6)==1

   figure %('PaperPosition', [.25 .75 8 9.5])

   if mm1~=0
      for ii=1:length(Freq)
         if SmallPhase1mm(ii)==1
            plot(real(z12m1(ii)),-imag(z12m1(ii)),'+','MarkerSize',6);
            if Freq(ii)==.01 | Freq(ii)==.1 | Freq(ii)==1 |...
Freq(ii)==10 | Freq(ii)==100 | Freq(ii)==1000 | Freq(ii)==10000
               text(real(z12m1(ii)),-imag(z12m1(ii)),num2str(Freq(ii)),...
                  'FontSize',16);
            hold on;
      end
         end
      end
   end;
   if mm2~=0
      if mm1~=0
         hold on
      end;
      for ii=1:length(Freq)
         if SmallPhase25mm(ii)==1
            plot(real(z12m2(ii)),-imag(z12m2(ii)),'o','MarkerSize',6);
            if Freq(ii)==.01 | Freq(ii)==.1 | Freq(ii)==1 |...
 Freq(ii)==10 | Freq(ii)==100 | Freq(ii)==1000 | Freq(ii)==10000
               text(real(z12m2(ii)),-imag(z12m2(ii)),num2str(Freq(ii)),...
                  'FontSize',16);
            hold on;
end
         end
      end
      hold off
   end;
   if mm5~=0
      if (mm1+mm2)~=0
         hold on
      end;
      for ii=1:length(Freq)
         if SmallPhase5mm(ii)==1
            plot(real(z12m5(ii)),-imag(z12m5(ii)),'*','MarkerSize',6);
            if Freq(ii)==.01 | Freq(ii)==.1 | Freq(ii)==1 | Freq(ii)==10 |...
 Freq(ii)==100 | Freq(ii)==1000 | Freq(ii)==10000
               text(real(z12m5(ii))+.005,-imag(z12m5(ii)),num2str(Freq(ii)),...
                  'FontSize',16);
            hold on;
end
         end
      end
      hold off;
```

```
   end;
   title(ttl);
   xlabel('Re(Z), T\Omega')
   ylabel('-Im(Z), T\Omega')

   if printIt==1
      print;
   end
end



%-----------------------------------------------------------
%PlotNon Re(Z) and -Im(Z) vs. Freq.
if plotIt(7) == 1
   figure ('PaperPosition', [.25 .75 8 9.5])
   subplot(2,1,1)
   if mm1~=0
semilogx(Freq,real(z12m1),'+','MarkerSize',5)
end;
if mm2~=0
if mm1~=0
hold on
end;
semilogx(Freq,real(z12m2),'o','MarkerSize',5)
hold off
end;
if mm5~=0
if (mm1+mm2)~=0
hold on
end;
semilogx(Freq,real(z12m5),'*','MarkerSize',5)
hold off;
end;
ax = axis;

RealZ12m1new=real(z12m1)+(3*(ax(4)-ax(3)).*(SmallPhase1mm-1));
RealZ12m2new=real(z12m2)+(3*(ax(4)-ax(3)).*(SmallPhase25mm-1));
RealZ12m5new=real(z12m5)+(3*(ax(4)-ax(3)).*(SmallPhase5mm-1));


subplot(2,1,1)
if mm1~=0
semilogx(Freq,RealZ12m1new,'+','MarkerSize',5)
end;
if mm2~=0
if mm1~=0
hold on
end;
semilogx(Freq,RealZ12m2new,'o','MarkerSize',5)
hold off
end;
```

```
if mm5~=0
if (mm1+mm2)~=0
hold on
end;
semilogx(Freq,RealZ12m5new,'*','MarkerSize',5)
hold off;
end;

axis([(10^(-2.3)) (10^4) ax(3) ax(4)])
set(gca,'FontSize',18,'XTick', [0.01 0.1 1 10 100 1000 10000])
%legend('+','1 mm','o','2.5 mm','*','5 mm')


title(ttl);
ylabel('Re(Z_{12}), T\Omega')

subplot(2,1,2)
if mm1~=0
semilogx(Freq,-imag(z12m1),'+','MarkerSize',5)
end;
if mm2~=0
if mm1~=0
hold on
end;
semilogx(Freq,-imag(z12m2),'o','MarkerSize',5)
hold off
end;
if mm5~=0
if (mm1+mm2)~=0
hold on
end;
semilogx(Freq,-imag(z12m5),'*','MarkerSize',5)
hold off;
end;
xlabel('Frequency (Hz)')
ylabel('-Im(Z_{12}), T\Omega')
ax = axis;
axis([(10^(-2.3)) (10^4) ax(3) ax(4)])
set(gca,'FontSize',18,'XTick', [0.01 0.1 1 10 100 1000 10000])
  if printIt==1
     print;
  end
end


%-------------------------------------------------------

%PlotNow |Z| and angle(Z) vs. Freq.
if plotIt(8) == 1
   figure ('PaperPosition', [.25 .75 8 9.5])
   subplot(2,1,1)
   if mm1~=0
```

```
   semilogx(Freq,abs(z12m1),'+','MarkerSize',5)
end;
if mm2~=0
   if mm1~=0
      hold on
   end;
   semilogx(Freq,abs(z12m2),'o','MarkerSize',5)
   hold off
end;
if mm5~=0
   if (mm1+mm2)~=0
      hold on
   end;
   semilogx(Freq,abs(z12m5),'*','MarkerSize',5)
   hold off;
end;

ylabel('|Z_{12}|, T\Omega')
ax = axis;
axis([(10^(-2.3)) (10^4) ax(3) ax(4)])
set(gca,'XTick', [0.01 0.1 1 10 100 1000 10000])

title(ttl);

subplot(2,1,2)
if mm1~=0
   semilogx(Freq,angle(z12m1)*180/2/pi,'+','MarkerSize',5)
end;
if mm2~=0
   if mm1~=0
      hold on
   end;
   semilogx(Freq,angle(z12m2)*180/2/pi,'o','MarkerSize',5)
   hold off
end;
if mm5~=0
   if (mm1+mm2)~=0
      hold on
   end;
   semilogx(Freq,angle(z12m5)*180/2/pi,'*','MarkerSize',5)
   hold off;
end;
ax = axis;
AngleZ12m1new=angle(z12m1)*180/2/pi+(3*(ax(4)-ax(3)).*(SmallPhase1mm-1));
AngleZ12m2new=angle(z12m2)*180/2/pi+(3*(ax(4)-ax(3)).*(SmallPhase25mm-1));
AngleZ12m5new=angle(z12m5)*180/2/pi+(3*(ax(4)-ax(3)).*(SmallPhase5mm-1));
subplot(2,1,2)
if mm1~=0
   semilogx(Freq,AngleZ12m1new,'+','MarkerSize',5)
end;
if mm2~=0
   if mm1~=0
```

```
         hold on
      end;
      semilogx(Freq,AngleZ12m2new,'o','MarkerSize',5)
      hold off
   end;
   if mm5~=0
      if (mm1+mm2)~=0
         hold on
      end;
      semilogx(Freq,AngleZ12m5new,'*','MarkerSize',5)
      hold off;
   end;
   axis([(10^(-2.3)) (10^4) ax(3) ax(4)])
   set(gca,'XTick', [0.01 0.1 1 10 100 1000 10000])
   %legend('+','1 mm','o','2.5 mm','*','5 mm')
   xlabel('Frequency (Hz)')
   ylabel('phase(Z_{12}), degrees')
   if printIt==1
      print;
   end
end
```

```
%-------------------------------------------------------------

%PlotNon Re(Z) and -Im(Z) vs. Freq.
if plotIt(9) == 1
    figure ('PaperPosition', [.25 .75 8 9.5])
    flag = 0;
if mm1~=0
      for ii=1:length(Freq)
         if SmallPhase1mm(ii)==1
            view(142.5,30)
            plot3(Freq(ii),real(z12m1(ii)),0,'*',...
               Freq(ii),0,-imag(z12m1(ii)),'+'...
               ,.005,real(z12m1(ii)),-imag(z12m1(ii)),'x',...
               Freq(ii),real(z12m1(ii)),-imag(z12m1(ii)),'o','MarkerSize',9)
            hold on
            h=get(gcf,'CurrentAxes');
            set(h,'XScale','log')
            xl=xlabel('Frequency (Hz)');
            yl=ylabel('Re(Z_{12}), T\Omega');
            zl=zlabel('-Im(Z_{12}), T\Omega');
            set([xl,yl,zl],'units','normalized')
            if flag == 1
```

```
plot3(Freq(ii-1:ii),real(z12m1(ii-1:ii)),[0 0],'.-',...
               Freq(ii-1:ii),[0 0],-imag(z12m1(ii-1:ii)),'--'...
               ,[.005 .005],real(z12m1(ii-1:ii)),-imag(z12m1(ii-1:ii)),':',...
               Freq(ii-1:ii),real(z12m1(ii-1:ii)),-imag(z12m1(ii-1:ii)),'-'...
,'MarkerSize',9)
end
          flag = 1;
    end
      end

      hold off
   end;
   if mm2~=0
      if mm1~=0
         hold on
      end;
      for ii=1:length(Freq)
         if SmallPhase25mm(ii)==1
            view(142.5,30)
            plot3(Freq(ii),real(z12m2(ii)),0,'*',...
               Freq(ii),0,-imag(z12m2(ii)),'+'...
               ,.005,real(z12m2(ii)),-imag(z12m2(ii)),'x',...
               Freq(ii),real(z12m2(ii)),-imag(z12m2(ii)),'o','MarkerSize',9)
            hold on
            h=get(gcf,'CurrentAxes');
            set(h,'XScale','log')
            xl=xlabel('Frequency (Hz)');
            yl=ylabel('Re(Z_{12}), T\Omega');
            zl=zlabel('-Im(Z_{12}), T\Omega');
            set([xl,yl,zl],'units','normalized')
if flag == 1
             plot3(Freq(ii-1:ii),real(z12m2(ii-1:ii)),[0 0],'.-',...
                Freq(ii-1:ii),[0 0],-imag(z12m2(ii-1:ii)),'--'...
                ,[.005 .005],real(z12m2(ii-1:ii)),-imag(z12m2(ii-1:ii)),':',...
                Freq(ii-1:ii),real(z12m2(ii-1:ii)),-imag(z12m2(ii-1:ii)),'-'...
,'MarkerSize',9)
end
flag = 1;
         end
      end

   end;
   if mm5~=0
      if (mm1+mm2)~=0
         hold on
      end;
      for ii=1:length(Freq)
         if SmallPhase5mm(ii)==1
            view(142.5,30)
            plot3(Freq(ii),real(z12m5(ii)),0,'*',...
               Freq(ii),0,-imag(z12m5(ii)),'+'...
               ,.005,real(z12m5(ii)),-imag(z12m5(ii)),'x',...
```

```
               Freq(ii),real(z12m5(ii)),-imag(z12m5(ii)),'o','MarkerSize',9)
            hold on
            h=get(gcf,'CurrentAxes');
            set(h,'XScale','log')
            xl=xlabel('Frequency (Hz)');
            yl=ylabel('Re(Z_{12}), T\Omega');
            zl=zlabel('-Im(Z_{12}), T\Omega');
            set([xl,yl,zl],'units','normalized')
            if flag == 1
plot3(Freq(ii-1:ii),real(z12m5(ii-1:ii)),[0 0],'.-',...
               Freq(ii-1:ii),[0 0],-imag(z12m5(ii-1:ii)),'--'...
               ,[.005 .005],real(z12m5(ii-1:ii)),-imag(z12m5(ii-1:ii)),':',...
               Freq(ii-1:ii),real(z12m5(ii-1:ii)),-imag(z12m5(ii-1:ii)),'-'...
,'MarkerSize',9)
            end
flag = 1;
   end
      end
      hold off;
   end;

   %legend('+','1 mm','o','2.5 mm','*','5 mm')
   ax = axis;
   axis([(10^(-2.3)) (10^4) ax(3) ax(4) ax(5) ax(6)]);
   set(h,'XTick', [0.01 1 100 10000]);
   grid;
   title(ttl);
   if printIt==1
      print;
   end
end



%-----------------------------------------------------------
%Plot Epsilon/Sigma
if plotIt(10)==1
   figure ('PaperPosition', [.25 .75 8 9.5])

   subplot(2,1,1)
   if mm1~=0
      semilogx(Freq,Epsilon1,'+','MarkerSize',5)
   end;
   if mm2~=0
      if mm1~=0
         hold on
      end;
      semilogx(Freq,Epsilon25,'o','MarkerSize',5)
      hold off

      if mm5~=0
         if (mm1+mm2)~=0
```

```
            hold on
         end;
         semilogx(Freq,Epsilon5,'*','MarkerSize',5)
         hold off;
      end;

      title(ttl,'FontSize',16);
      ylabel('{\epsilon_r}\prime','FontSize',16)
      ax = axis;
      axis([(10^(-2.3)) (10^4) 0 max(ax(4), 1e-20)])

      subplot(2,1,2)
      if mm1~=0
         semilogx(Freq,Sigma1,'+','MarkerSize',5)
      end;
      if mm2~=0
         if mm1~=0
            hold on
         end;
         semilogx(Freq,Sigma25,'o','MarkerSize',5)
         hold off
      end;
      if mm5~=0
         if (mm1+mm2)~=0
            hold on
         end;
         semilogx(Freq,Sigma5,'*','MarkerSize',5)
         hold off;
      end;
   end
   ylabel('{\sigma} (pS/m)','FontSize',16)
   xlabel('Frequency (Hz)','FontSize',16)
   ax = axis;
   axis([(10^(-2.3)) (10^4) 0 max(ax(4), 1e-20)])
   %extra = strcat('Filename: ', DatFileName);
   %axa = axis;
   %text(axa(1),axa(3)-0.38*(axa(4)-axa(3)),extra);
   if printIt==1
      print;
   end
end
specCont
```

Appendix G

Parameter Estimation Code

G.1 Calibration-Based Algorithms

G.1.1 Description of Programs

Many of these programs has been written with the help of Chris Lin as a part of his UROP project [44].

sigeps.m This program is the Matlab 5.0 version. It reads TWS data and produces gain/phase and C_{12} and G_{12} graphs as functions of frequency. It also records the C_{12} and G_{12} values in a ".res" file. The input arguments are DatFileName, ttl, mm1, mm2, and mm5. DatFileName is a string that contains the data filename. If it has a filename extension, sigeps.m will not be able to record data in the ".res" file. ttl is a string that contains the title for the graphs. The mm1, mm2, and mm5 arguments correspond to each wavelength of the TWS and specify whether or not those data series should be plotted. When using this program, one needs to keep track of the C_L values and whether or not the input data file starts with the characters "[gd]". Forgetting to delete these characters will result in a file opening error. It also has the ability to calculate ε and σ for parallel plate capacitors. The capacitance values in air for the parallel plate capacitors are needed and the user must keep track of where and in what format the

values are stored. The program will compute ε and σ values for interdigital sensor data as well, but those should be ignored since the algorithm is intended for only parallel plate geometries.

csigeps.m This is a close relative of sigeps.m. It is also written for use with Matlab 5.0. The difference between the two programs is that csigeps.m reads and analyzes constant frequency sweeps. It takes two additional arguments: f and interval. f is the log10 of the frequency used and interval is the number of seconds between measurements. This program reads data differently since it receives data differently from the previous programs. When the GPM is in repeat trials mode, it inserts a header line before each trial. This means that every fourth line contains measurement time data in a constant frequency sweep and must be treated separately. Of particular note is that the horizontal axis of the plots generated by this program indicate the number of trials passed, not the total time. This program, like sigeps.m, plots ε and σ for parallel plate capacitors.

se.m This program calculates dielectric properties for highly insulating materials measured using a TWS. It only works on very good insulators, but they can be solids or liquids. DatFileName and ttl are used as described in previous programs. However, the mm1, mm2, and mm5 arguments are actually fairly irrelevant in this program. It will probably malfunction if they are not all set to 1. The gainInAir1, gainInAir2, and gainInAir5 arguments are the gain in air (dB) measured by the GPM. They are used to calculate the metallization ratio of the sensor. This metallization ratio is then used to determine what the ε vs. C_{12} relationship for liquids is. The materialType parameter (a string: either "l" for liquid or "s" for solid) tells the program what set of equations to use. If materialType = "l", then it will use the equations it just computed. If materialType = "s", then the program computes the tangent at $\varepsilon = 1$ of the liquids curves and changes the slope by an empirically determined offset angle. The program also takes the arguments actualEpsilon and otherPlots. actualEpsilon is used to draw a horizontal line across the frequency sweep to indicate the theoretical value of ε and provide a reference. otherPlots specifies whether the gain/phase and C_{12},G_{12} graphs

should be plotted (1 means yes and 0 means no). The key plot generated by this program shows the actual and average ε values on the top axes and the ε values from each wavelength along with the average ε value on the bottom axes. se.m also provides statistical information about the error, standard deviations, and mean values below this plot.

twoliq.m This program was used for the two-fluids measurements. DataFileName and ttl are used as described previously. The mm1, mm2, and mm5 parameters are permanently set to 1. This was done because the program will always use the data from all three channels. The parameters were not eliminated completely because they appear frequently in the code and while efficiency is reduced by keeping them around, a lot of potential debugging time is avoided. capType specifies what type of parallel plate capacitor is used in conjunction with the two single wavelength sensors. The flag 1 means YCap (aluminum capacitor) and 0 means PPCap (tuning capacitor). The exact values of the air capacitance values for these devices must be known or the program will produce erroneous results. gainInAira and gainInAirb are the measured gain in air of the two different single wavelength sensors and enable the program to compute metallization ratios and determine the appropriate ε vs. C_{12} relationships to use. The same algorithm used in se.m is used. otherPlots specifies whether the gain/phase and C_{12}/ε data should be plotted in addition to the permittivity data (1 means yes and 0 means no). lambda specifies the wavelength in mm of the sensors used. Currently, the program can only handle inputs of 1 or 2.5. In fact, for any value other than 1, the program will treat lambda as if it were equal to 2.5. This program also generates a lot of useful statistical information about capacitance and permittivity. It uses the mean permittivity calculated from the parallel plate capacitor as the "actual permittivity" for error and standard deviation purposes. It is questionable whether this should be done. These statistics are printed at the bottom of the C_{12}/ε (capacitance statistics) and permittivity (ε statistics) plots.

solliq.m solliq.m is actually a collection of programs and data files (generated using *Maxwell*) used to analyze filled air gap measurements data. solliq.m is the parent

function and calls readsim.m to generate a look-up table and runs child.m iteratively on the input data. waveLength1 and waveLength2 specify the wavelengths (1, 2.5, or 5) with which the input data were taken. fluid1 and fluid2 specify which liquid (air, corn oil, or castor oil) was used to fill the gap between the sensor and the sample. inputData is a two column matrix of the measured C_{12} values. The first column corresponds to waveLength1 and fluid1 and the second column corresponds to waveLength2 and fluid2. resolution specifies the number of contour lines drawn on the generated contour plots. The program generates contour plots for each row of inputData. If the last three lines of solliq.m are uncommented, the program will prompt the user to continue after generating each individual contour plot and close that plot before the next iteration. The return argument results is a four column matrix that contains the data from inputData along with the computed h and ε values (h is the effective air gap). These values are sometimes NaN or not a number.

child.m child.m does all the computation. The specific algorithms and steps are described in section 5.2. Besides generating contour plots, child.m returns rEpsilon and rH to solliq.m. These values are used to construct the results matrix returned by solliq.m. If the C_{12} pair passed to child.m is not close enough to the interpolated patch generated by child.m, rEpsilon and rH will not be numbers and NaN (not a number) will be returned. However, the C_{12} pair will still be plotted (mapped on the C_{12}-1-C_{12}-2 plane of two different wavelengths) and will show up possibly on the interpolated surface of the contour plot. Some insight into the ε and h values can be gleaned from this.

readSim.m This routine reads the *Maxwell* simulation data files specified by the input parameters and returns a four column matrix: [ε h C_{12}-1 C_{12}-2] where each entry is actually a column vector. h varies from 0 to 66 at intervals of 6 and ε varies from 1 to 5 at intervals of 0.2 for each value of h. So, there are 231 rows. These data are used by child.m to generate the monotonic and plaid data needed to enable child.m to estimate ε and h for the arbitrary input C_{12} pair.

G.1.2 sigeps.m

```
function sigeps(DatFileName,ttl,mm1,mm2,mm5)

%%% Plots Gain, Phase, C12, G12, Epsilon, and Sigma for a Frequency Run
%%% Last Modified June 10, 1997 by Christopher Lin.


% Load capacitances

% These are the values for trials between 2/97 and 5/30/97
% Cl1mm = 101.2; CL1mm = Cl1mm;
% Cl2mm = 58.0; CL2mm = Cl2mm;
% Cl5mm = 50.0; CL5mm = Cl5mm;

% These are the values for trials after 6/10/97 (Interface box was rebuilt)
% Cl1mm = 98.0; CL1mm = Cl1mm;
% Cl2mm = 59.1; CL2mm = Cl2mm;
% Cl5mm = 49.1; CL5mm = Cl5mm;

% These are the values for trials after 7/23/97 (Cloads were recalibrated)
Cl1mm = 100.5; CL1mm = Cl1mm;
Cl2mm =  58.1; CL2mm = Cl2mm;
Cl5mm =  49.4; CL5mm = Cl5mm;

% open data file

DatID = fopen(DatFileName,'rt');
if (DatID == -1)
  disp(' ');
error('Error Opening Data File!');
end;

% Read off Header Data Line
[Head] = fscanf(DatID,'[GH,%f,%i,%i,%i,%i,%i,%i]',7);

% Read Data to Matrix
[Data,Number] = fscanf(DatID,'[GD,%i,%f,%f,%f,%f,%i]',[6,inf]);
Number = Number / 6;

% Close File

fclose(DatID);

% open reference file (contains values of C12 and G12 in air)
RefFileName = 'aircal3.res';
DatID = fopen(RefFileName,'rt');
if (DatID == -1)
disp(' ');
error('Error Opening Reference File!');
end;
```

```
% Read off Header Data Line
fread(DatID,78);

% Read Reference Data to Matrix
[Ref, N] = fscanf(DatID,'%f\t%f\t%f\t%f\t%f\t%f\t%f\n',[7,inf]);
% Close File
fclose(DatID);


% Extract/Organize Data

Freq = 10.^Data(2,3:3:Number);
Omega = Freq.*2.*pi;

Gain1mm  = Data(3,3:3:Number);
Gain25mm = Data(3,2:3:Number);
Gain5mm  = Data(3,1:3:Number);

Phase1mm  = Data(4,3:3:Number);
Phase25mm = Data(4,2:3:Number);
Phase5mm  = Data(4,1:3:Number);

% Recalculate gain into volts, phase into radians
Gr1mm = 10.^(Gain1mm./20);
Gr25mm = 10.^(Gain25mm./20);
Gr5mm = 10.^(Gain5mm./20);

Fi1mm = Phase1mm.*pi./180;
Fi25mm = Phase25mm.*pi./180;
Fi5mm = Phase5mm.*pi./180;

% Recalculate into real and imaginary parts of gain
GRe1mm = Gr1mm.*(cos(Fi1mm));
GRe2mm = Gr25mm.*(cos(Fi25mm));
GRe5mm = Gr5mm.*(cos(Fi5mm));

GIm1mm = Gr1mm.*(sin(Fi1mm));
GIm2mm = Gr25mm.*(sin(Fi25mm));
GIm5mm = Gr5mm.*(sin(Fi5mm));

G12m1 = zeros(1,Number/3);
G12m2 = zeros(1,Number/3);
G12m5 = zeros(1,Number/3);

Sigma1   = zeros(1,Number/3);
Epsilon1 = zeros(1,Number/3);
Sigma2   = zeros(1,Number/3);
Epsilon2 = zeros(1,Number/3);
Sigma5   = zeros(1,Number/3);
Epsilon5 = zeros(1,Number/3);

G12m1 = zeros(1,Number/3)-10;
```

```
G12m2 = zeros(1,Number/3)-10;
G12m5 = zeros(1,Number/3)-10;

% Solve system of equations
for ii = 1:Number/3,
 A1 = [ GRe1mm(ii)-1 -Omega(ii)*GIm1mm(ii);
GIm1mm(ii)  Omega(ii)*(GRe1mm(ii)-1)];
 B1 = [ Omega(ii)*GIm1mm(ii)*CL1mm;
-GRe1mm(ii)*Omega(ii)*CL1mm];

 A2 = [ GRe2mm(ii)-1 -Omega(ii)*GIm2mm(ii);
GIm2mm(ii)  Omega(ii)*(GRe2mm(ii)-1)];
 B2 = [ Omega(ii)*GIm2mm(ii)*CL2mm;
-GRe2mm(ii)*Omega(ii)*CL2mm];

 A5 = [ GRe5mm(ii)-1 -Omega(ii)*GIm5mm(ii);
GIm5mm(ii)  Omega(ii)*(GRe5mm(ii)-1)];
 B5 = [ Omega(ii)*GIm5mm(ii)*CL5mm;
-GRe5mm(ii)*Omega(ii)*CL5mm];

 X1 = A1\B1;
 X2 = A2\B2;
 X5 = A5\B5;

 C12m1(ii) = X1(2);
 C12m2(ii) = X2(2);
 C12m5(ii) = X5(2);

%%% Make sure G12 can be measured - that is the phase (in degrees) differs
%%% sufficiently from 0, and that we are not in high frequency range
%%% where phase delay is caused by the op-amps.  Otherwise, G12 remains
%%% equal to -10.

% Phase limit when G12 can be detected
PhaseLimit = 1;

if (abs(Phase1mm(ii)) > PhaseLimit & Freq(ii)<1000)
G12m1(ii) = X1(1);
end
if (abs(Phase25mm(ii)) > PhaseLimit & Freq(ii)<1000)
  G12m2(ii) = X2(1);
end
if (abs(Phase5mm(ii)) > PhaseLimit & Freq(ii)<1000)
G12m5(ii) = X5(1);
end

end

% For aircal.res,  PPCap is in column 3 and YCap is in column 5.
% aircal.res should be used for the 5mm calibration trials (in
% corn oil).  Also, the capacitance of YCap is about 8 (vs. 4 in
% the other aircal files).
```

```
% For aircal2.res, PPCap is in column 3 and YCap is in column 7.
% aircal2.res should be used for the 1mm and 2.5mm calibration
% trials in corn oil.

% For aircal3.res, PPCap is in column 3 and YCap is in column 5.
% aircal3.res should be used for the calibration trials in
% transformer oil (type AX).

if mm1~=0
Epsilon1 = C12m1./Ref(5:7:N);
Sigma1 = G12m1./Ref(5:7:N).*8.85;
end
if mm2~=0
Epsilon2 = C12m2./Ref(3:7:N);
Sigma2 = G12m2./Ref(3:7:N).*8.85;
end
if mm5~=0
Epsilon5 = C12m5./Ref(3:7:N);
Sigma5 = G12m5./Ref(3:7:N).*8.85;
end

%Save C12/G12
Results = [Freq;   G12m1;   C12m1;    Sigma1;   Epsilon1;  ...
G12m2;   C12m2;    Sigma2;   Epsilon2;  G12m5;   C12m5;   Sigma5;   Epsilon5];
FileName = [DatFileName '.eps'];
DatID = fopen(FileName, 'w');
fprintf(DatID, 'Frequency\t\tG12 - 1mm\tC12 - 1mm\tSigma - 1mm\tEpsilon - ...
1mm\tG12 - 2.5mm\tC12 - 2.5mm\tSigma - 2.5mm\tEpsilon 2.5mm\tG12 - 5mm\tC12...
 - 5mm\tSigma - 5mm\tEpsilon - 5mm\n');
fprintf(DatID,'%f\t\t%f\t%f\t%f\t%f\t%f\t%f\t%f\t%f\t%f\t%f\t%f\t%f\t%f\t%f\n', Results);
fclose(DatID);

% ------------------------------------------------------------------
% These variables dictate what gets printed in the legend.

CH15mm = '5mm Sensor';
CH22mm = 'PPCap';
CH31mm = 'YCap';

% Plot Gain/Phase
figure('PaperPosition', [.25 .75 8 9.5])
subplot(2,1,1)
if mm1~=0
semilogx(Freq,Gain1mm,'+','MarkerSize',5)
end;
if mm2~=0
if mm1~=0
hold on
end;
semilogx(Freq,Gain25mm,'o','MarkerSize',5)
hold off
```

```
end;
if mm5~=0
if (mm1+mm2)~=0
hold on
end;
semilogx(Freq,Gain5mm,'*','MarkerSize',5)
hold off;
end;
title(ttl,'FontSize',16);
ylabel('Gain (dB)','FontSize',16)
ax = axis;
axis([(10^(-2.3)) (10^4) ax(3) ax(4)])

subplot(2,1,2)
if mm1~=0
semilogx(Freq,Phase1mm,'+','MarkerSize',5)
end;
if mm2~=0
if mm1~=0
hold on
end;
semilogx(Freq,Phase25mm,'o','MarkerSize',5)
hold off
end;
if mm5~=0
if (mm1+mm2)~=0
hold on
end;
semilogx(Freq,Phase5mm,'*','MarkerSize',5)
hold off;
end;
ylabel('Phase (degrees)','FontSize',16)
xlabel('Frequency (Hz)','FontSize',16)
ax = axis;
axis([(10^(-2.3)) (10^4) ax(3) ax(4)])

[legh, objh]=legend(CH31mm,CH22mm,CH15mm);

xdata1 = get(objh(1), 'XData');
ydata1 = get(objh(1), 'YData');
xdata2 = get(objh(2), 'XData');
ydata2 = get(objh(2), 'YData');
xdata3 = get(objh(3), 'XData');
ydata3 = get(objh(3), 'YData');

set(objh(1), 'xdata', (xdata1(1)+xdata1(2))/2, 'ydata', ydata1(1))
set(objh(2), 'xdata', (xdata2(1)+xdata2(2))/2, 'ydata', ydata2(1))
set(objh(3), 'xdata', (xdata3(1)+xdata3(2))/2, 'ydata', ydata3(1))

extra = strcat('Filename: ' DatFileName);
axa = axis;
text(axa(1),axa(3)-0.38*(axa(4)-axa(3)),extra);
```

```
%Plot C12/G12

figure('PaperPosition', [.25 .75 8 9.5])

subplot(2,1,1)
if mm1~=0
semilogx(Freq,C12m1,'+','MarkerSize',5)
end;
if mm2~=0
if mm1~=0
hold on
end;
semilogx(Freq,C12m2,'o','MarkerSize',5)
hold off
end;
if mm5~=0
if (mm1+mm2)~=0
hold on
end;
semilogx(Freq,C12m5,'*','MarkerSize',5)
hold off;
end;
title(ttl,'FontSize',16);
ylabel('C_{12} (pF)','FontSize',16)
ax = axis;
axis([(10^(-2.3)) (10^4) ax(3) ax(4)])

subplot(2,1,2)
if mm1~=0
semilogx(Freq,G12m1,'+','MarkerSize',5)
end;
if mm2~=0
if mm1~=0
hold on
end;
semilogx(Freq,G12m2,'o','MarkerSize',5)
hold off
end;
if mm5~=0
if (mm1+mm2)~=0
hold on
end;
semilogx(Freq,G12m5,'*','MarkerSize',5)
hold off;
end;
ylabel('G_{12} (pS)','FontSize',16)
xlabel('Frequency (Hz)','FontSize',16)
ax = axis;
axis([(10^(-2.3)) (10^4) 0 max(ax(4), 1e-20)])

[legh, objh]=legend(CH31mm,CH22mm,CH15mm);
```

```
xdata1 = get(objh(1), 'XData');
ydata1 = get(objh(1), 'YData');
xdata2 = get(objh(2), 'XData');
ydata2 = get(objh(2), 'YData');
xdata3 = get(objh(3), 'XData');
ydata3 = get(objh(3), 'YData');

set(objh(1), 'xdata', (xdata1(1)+xdata1(2))/2, 'ydata', ydata1(1))
set(objh(2), 'xdata', (xdata2(1)+xdata2(2))/2, 'ydata', ydata2(1))
set(objh(3), 'xdata', (xdata3(1)+xdata3(2))/2, 'ydata', ydata3(1))

extra = strcat('Filename: ' DatFileName);
axa = axis;
text(axa(1),axa(3)-0.38*(axa(4)-axa(3)),extra);

%Plot Epsilon/Sigma

figure('PaperPosition', [.25 .75 8 9.5])

subplot(2,1,1)
if mm1~=0
semilogx(Freq,Epsilon1,'+','MarkerSize',5)
end;
if mm2~=0
if mm1~=0
hold on
end;
semilogx(Freq,Epsilon2,'o','MarkerSize',5)
hold off
end;
if mm5~=0
if (mm1+mm2)~=0
hold on
end;
semilogx(Freq,Epsilon5,'*','MarkerSize',5)
hold off;
end;

title(ttl,'FontSize',16);
ylabel('{\epsilon}','FontSize',16)
ax = axis;
axis([(10^(-2.3)) (10^4) 0 max(ax(4), 1e-20)])

subplot(2,1,2)
if mm1~=0
semilogx(Freq,Sigma1,'+','MarkerSize',5)
end;
if mm2~=0
if mm1~=0
hold on
end;
```

```
semilogx(Freq,Sigma2,'o','MarkerSize',5)
hold off
end;
if mm5~=0
if (mm1+mm2)~=0
hold on
end;
semilogx(Freq,Sigma5,'*','MarkerSize',5)
hold off;
end;

ylabel('{\sigma} (pS/m)','FontSize',16)
xlabel('Frequency (Hz)','FontSize',16)
ax = axis;
axis([(10^(-2.3)) (10^4) 0 max(ax(4), 1e-20)])

[legh, objh]=legend(CH31mm,CH22mm,CH15mm);

xdata1 = get(objh(1), 'XData');
ydata1 = get(objh(1), 'YData');
xdata2 = get(objh(2), 'XData');
ydata2 = get(objh(2), 'YData');
xdata3 = get(objh(3), 'XData');
ydata3 = get(objh(3), 'YData');

set(objh(1), 'xdata', (xdata1(1)+xdata1(2))/2, 'ydata', ydata1(1))
set(objh(2), 'xdata', (xdata2(1)+xdata2(2))/2, 'ydata', ydata2(1))
set(objh(3), 'xdata', (xdata3(1)+xdata3(2))/2, 'ydata', ydata3(1))

extra = strcat('Filename: ' DatFileName);
axa = axis;
text(axa(1),axa(3)-0.38*(axa(4)-axa(3)),extra);
```

G.1.3 csigeps.m

```
function sigeps(DatFileName,ttl,mm1,mm2,mm5,f,interval)

% Load capacitances

% These are the values for trials between 2/97 and 5/30/97
% Cl1mm = 101.2; CL1mm = Cl1mm;
% Cl2mm = 58.0; CL2mm = Cl2mm;
% Cl5mm = 50.0; CL5mm = Cl5mm;

% These are the values for trials after 6/10/97 (Interface box was rebuilt)
% Cl1mm = 98.0; CL1mm = Cl1mm;
% Cl2mm = 59.1; CL2mm = Cl2mm;
% Cl5mm = 49.1; CL5mm = Cl5mm;

% These are the values for trials after 7/23/97 (Cloads were recalibrated)
Cl1mm = 100.5; CL1mm = Cl1mm;
Cl2mm =  58.1; CL2mm = Cl2mm;
Cl5mm =  49.4; CL5mm = Cl5mm;

% open data file

DatID = fopen(DatFileName,'rt');
if (DatID == -1)
  disp(' ');
error('Error Opening Data File!');
end;

status = fseek(DatID,0,'eof');
endOfFile = ftell(DatID);
status = fseek(DatID,0,'bof');
% Read off Header Data Line
[Head] = fscanf(DatID,'[GH,%f,%i,%i,%i,%i,%i,%i]',7);

Data = zeros(6,1);
index = 0;
while (ftell(DatID) < (endOfFile - 5))
%while (index < 7)
   fscanf(DatID,'[GH,%f,%i,%i,%i,%i,%i,%i]',7);
   index = index + 1;
   [Data(:,index)] = fscanf(DatID,'[GD,%i,%f,%f,%f,%f,%i]',6);
   index = index + 1;
   [Data(:,index)] = fscanf(DatID,'[GD,%i,%f,%f,%f,%f,%i]',6);
   index = index + 1;
   [Data(:,index)] = fscanf(DatID,'[GD,%i,%f,%f,%f,%f,%i]',6);
   end

Number = index;
fclose(DatID);

% open reference file
```

```
RefFileName = 'aircal.res';
DatID = fopen(RefFileName,'rt');
if (DatID == -1)
disp(' ');
error('Error Opening Reference File!');
end;

% Read off Header Data Line
fread(DatID,78);

% Read Reference Data to Matrix
[Ref, N] = fscanf(DatID,'%f\t%f\t%f\t%f\t%f\t%f\t%f\n',[7,inf]);
% Close File
fclose(DatID);

% Extract/Organize Data

Trial = 1:Number/3;
Freq = 10^(f);
Omega = Freq*2*pi;

C1air = 0;
C2air = 0;
C5air = 0;

reference = (4 - f + .1)*10;
      C1air = Ref(3,reference);
      C2air = Ref(5,reference);
      C5air = Ref(7,reference);

Gain1mm  = Data(3,3:3:Number);
Gain25mm = Data(3,2:3:Number);
Gain5mm  = Data(3,1:3:Number);

Phase1mm  = Data(4,3:3:Number);
Phase25mm = Data(4,2:3:Number);
Phase5mm  = Data(4,1:3:Number);

% Recalculate gain into volts, phase into radians
Gr1mm = 10.^(Gain1mm./20);
Gr25mm = 10.^(Gain25mm./20);
Gr5mm = 10.^(Gain5mm./20);

Fi1mm = Phase1mm.*pi./180;
Fi25mm = Phase25mm.*pi./180;
Fi5mm = Phase5mm.*pi./180;

% Recalculate into real and imaginary parts of gain
GRe1mm = Gr1mm.*(cos(Fi1mm));
GRe2mm = Gr25mm.*(cos(Fi25mm));
GRe5mm = Gr5mm.*(cos(Fi5mm));
```

```
GIm1mm = Gr1mm.*(sin(Fi1mm));
GIm2mm = Gr25mm.*(sin(Fi25mm));
GIm5mm = Gr5mm.*(sin(Fi5mm));

G12m1 = zeros(1,Number/3);
G12m2 = zeros(1,Number/3);
G12m5 = zeros(1,Number/3);

Sigma1   = zeros(1,Number/3);
Epsilon1 = zeros(1,Number/3);
Sigma2   = zeros(1,Number/3);
Epsilon2 = zeros(1,Number/3);
Sigma5   = zeros(1,Number/3);
Epsilon5 = zeros(1,Number/3);

G12m1 = zeros(1,Number/3)-10;
G12m2 = zeros(1,Number/3)-10;
G12m5 = zeros(1,Number/3)-10;

% Solve system of equations
for ii = 1:Number/3,
 A1 = [ GRe1mm(ii)-1 -Omega*GIm1mm(ii);
GIm1mm(ii)  Omega*(GRe1mm(ii)-1)];
 B1 = [ Omega*GIm1mm(ii)*CL1mm;
-GRe1mm(ii)*Omega*CL1mm];

 A2 = [ GRe2mm(ii)-1 -Omega*GIm2mm(ii);
GIm2mm(ii)  Omega*(GRe2mm(ii)-1)];
 B2 = [ Omega*GIm2mm(ii)*CL2mm;
-GRe2mm(ii)*Omega*CL2mm];

 A5 = [ GRe5mm(ii)-1 -Omega*GIm5mm(ii);
GIm5mm(ii)  Omega*(GRe5mm(ii)-1)];
 B5 = [ Omega*GIm5mm(ii)*CL5mm;
-GRe5mm(ii)*Omega*CL5mm];

 X1 = A1\B1;
 X2 = A2\B2;
 X5 = A5\B5;

 C12m1(ii) = X1(2);
 C12m2(ii) = X2(2);
 C12m5(ii) = X5(2);

%%% Make sure G12 can be measured - that is the phase (in degrees) differs
%%% sufficiently from 0, and that we are not in high frequency range
%%% where phase delay is caused by the op-amps.  Otherwise, G12 remains
%%% equal to -10.

% Phase limit when G12 can be detected
PhaseLimit = 1;
```

```
if (abs(Phase1mm(ii)) > PhaseLimit)
G12m1(ii) = X1(1);
end
if (abs(Phase25mm(ii)) > PhaseLimit)
  G12m2(ii) = X2(1);
end
if (abs(Phase5mm(ii)) > PhaseLimit)
G12m5(ii) = X5(1);
end

end

if mm1~=0
Epsilon1 = C12m1./C1air;
Sigma1 = G12m1./C1air.*8.85;
end
if mm2~=0
Epsilon2 = C12m2./C2air;
Sigma2 = G12m2./C2air.*8.85;
end
if mm5~=0
Epsilon5 = C12m5./C5air;
Sigma5 = G12m5./C5air.*8.85;
end

%Save C12/G12

Results = [Trial;   G12m1;   C12m1;    Sigma1;   ...
Epsilon1;  G12m2;   C12m2;    Sigma2;   Epsilon2;  ...
G12m5;   C12m5;   Sigma5;   Epsilon5];

FileName = [DatFileName '.ces'];
DatID = fopen(FileName, 'w');
fprintf(DatID, 'Frequency\t\tG12 - 1mm\tC12 - 1mm\tSigma - 1mm\tEpsilon ...
- 1mm\tG12 - 2.5mm\tC12 - 2.5mm\tSigma - 2.5mm\tEpsilon 2.5mm\tG12 - ...
5mm\tC12 - 5mm\tSigma - 5mm\tEpsilon - 5mm\n');
fprintf(DatID,'%f\t\t%f\t%f\t%f\t%f\t%f\t%f\t%f\t%f\t%f\t%f\t%f\t%f\t%f\t%f\n', Results);

fclose(DatID);

% ------------------------------------------------------------------
% Plot Gain/Phase
figure('PaperPosition', [.25 .75 8 9.5])
subplot(2,1,1)
if mm1~=0
plot(Trial,Gain1mm,'+','MarkerSize',5)
end;
if mm2~=0
if mm1~=0
hold on
end;
plot(Trial,Gain25mm,'o','MarkerSize',5)
```

```
hold off
end;
if mm5~=0
if (mm1+mm2)~=0
hold on
end;
plot(Trial,Gain5mm,'*','MarkerSize',5)
hold off;
end;
ylabel('Gain (dB)','FontSize',16)

subplot(2,1,2)
if mm1~=0
plot(Trial,Phase1mm,'+','MarkerSize',5)
end;
if mm2~=0
if mm1~=0
hold on
end;
plot(Trial,Phase25mm,'o','MarkerSize',5)
hold off
end;
if mm5~=0
if (mm1+mm2)~=0
hold on
end;
plot(Trial,Phase5mm,'*','MarkerSize',5)
hold off;
end;
ylabel('Phase (degrees)','FontSize',16)
xlabel('Trial Number','FontSize',16)

[legh, objh]=legend('PPCap','YCap','5 mm');

xdata1 = get(objh(1), 'XData');
ydata1 = get(objh(1), 'YData');
xdata2 = get(objh(2), 'XData');
ydata2 = get(objh(2), 'YData');
xdata3 = get(objh(3), 'XData');
ydata3 = get(objh(3), 'YData');

set(objh(1), 'xdata', (xdata1(1)+xdata1(2))/2, 'ydata', ydata1(1))
set(objh(2), 'xdata', (xdata2(1)+xdata2(2))/2, 'ydata', ydata2(1))
set(objh(3), 'xdata', (xdata3(1)+xdata3(2))/2, 'ydata', ydata3(1))

%Plot C12/G12

figure('PaperPosition', [.25 .75 8 9.5])

subplot(2,1,1)
if mm1~=0
plot(Trial,C12m1,'+','MarkerSize',5)
```

```
end;
if mm2~=0
if mm1~=0
hold on
end;
plot(Trial,C12m2,'o','MarkerSize',5)
hold off
end;
if mm5~=0
if (mm1+mm2)~=0
hold on
end;
plot(Trial,C12m5,'*','MarkerSize',5)
hold off;
end;

ylabel('C_{12} (pF)','FontSize',16)

subplot(2,1,2)
if mm1~=0
plot(Trial,G12m1,'+','MarkerSize',5)
end;
if mm2~=0
if mm1~=0
hold on
end;
plot(Trial,G12m2,'o','MarkerSize',5)
hold off
end;
if mm5~=0
if (mm1+mm2)~=0
hold on
end;
plot(Trial,G12m5,'*','MarkerSize',5)
hold off;
end;
ylabel('G_{12} (pS)','FontSize',16)
xlabel('Trial Number','FontSize',16)

[legh, objh]=legend('PPCap','YCap','5 mm');

xdata1 = get(objh(1), 'XData');
ydata1 = get(objh(1), 'YData');
xdata2 = get(objh(2), 'XData');
ydata2 = get(objh(2), 'YData');
xdata3 = get(objh(3), 'XData');
ydata3 = get(objh(3), 'YData');

set(objh(1), 'xdata', (xdata1(1)+xdata1(2))/2, 'ydata', ydata1(1))
set(objh(2), 'xdata', (xdata2(1)+xdata2(2))/2, 'ydata', ydata2(1))
set(objh(3), 'xdata', (xdata3(1)+xdata3(2))/2, 'ydata', ydata3(1))
```

```
%Plot Epsilon/Sigma

figure('PaperPosition', [.25 .75 8 9.5])

subplot(2,1,1)
if mm1~=0
plot(Trial,Epsilon1,'+','MarkerSize',3)
end;
if mm2~=0
if mm1~=0
hold on
end;
plot(Trial,Epsilon2,'o','MarkerSize',3)
hold off
end;
if mm5~=0
if (mm1+mm2)~=0
hold on
end;
plot(Trial,Epsilon5,'*','MarkerSize',3)
hold off;
end;

title(ttl,'FontSize',16);
ylabel('{\epsilon}','FontSize',16)

subplot(2,1,2)
if mm1~=0
plot(Trial,Sigma1,'+','MarkerSize',3)
end;
if mm2~=0
if mm1~=0
hold on
end;
plot(Trial,Sigma2,'o','MarkerSize',3)
hold off
end;
if mm5~=0
if (mm1+mm2)~=0
hold on
end;
plot(Trial,Sigma5,'*','MarkerSize',3)
hold off;
end;

ylabel('{\sigma} (pS/m)','FontSize',16)
xlabel('Trial Number','FontSize',16)
[legh, objh]=legend('PPCap','YCap','5 mm');

xdata1 = get(objh(1), 'XData');
ydata1 = get(objh(1), 'YData');
xdata2 = get(objh(2), 'XData');
```

```
ydata2 = get(objh(2), 'YData');
xdata3 = get(objh(3), 'XData');
ydata3 = get(objh(3), 'YData');

set(objh(1), 'xdata', (xdata1(1)+xdata1(2))/2, 'ydata', ydata1(1))
set(objh(2), 'xdata', (xdata2(1)+xdata2(2))/2, 'ydata', ydata2(1))
set(objh(3), 'xdata', (xdata3(1)+xdata3(2))/2, 'ydata', ydata3(1))

extra = strcat('Filename: ', DatFileName);
axa = axis;
text(axa(1),axa(3)-0.38*(axa(4)-axa(3)),extra);
```

G.1.4 se.m

```
function se(DatFileName,ttl,mm1,mm2,mm5,gainInAir1,gainInAir2,gainInAir5,...
materialType,actualEpsilon,otherPlots)

%%% Plots Gain, Phase, C12, and Epsilon for a High Frequency Run.
%%% Specifically, Phase is Approximately Zero (good insultator).
%%% Last Modified July 6, 1997 by Christopher Lin.

gainInAir(1) = gainInAir1;
gainInAir(2) = gainInAir2;
gainInAir(3) = gainInAir5;

% Load capacitances

% These are the values for trials between 2/97 and 5/30/97
% Cl1mm = 101.2; CL1mm = Cl1mm;
% Cl2mm = 58.0; CL2mm = Cl2mm;
% Cl5mm = 50.0; CL5mm = Cl5mm;

% These are the values for trials after 6/10/97 (Interface box was rebuilt)
Cl1mm = 98.0; CL1mm = Cl1mm;
Cl2mm = 59.1; CL2mm = Cl2mm;
Cl5mm = 49.1; CL5mm = Cl5mm;


% These are the values for trials after 7/23/97 (Interface box was rebuilt)
Cl1mm = 100.5; CL1mm = Cl1mm;
Cl2mm = 58.1; CL2mm = Cl2mm;
Cl5mm = 49.4; CL5mm = Cl5mm;
% open data file

DatID = fopen(DatFileName,'rt');
if (DatID == -1)
  disp(' ');
error('Error Opening Data File!');
end;

% Read off Header Data Line
[Head] = fscanf(DatID,'[GH,%f,%i,%i,%i,%i,%i]',7);

% Read Data to Matrix
[Data,Number] = fscanf(DatID,'[GD,%i,%f,%f,%f,%f,%i]',[6,inf]);
Number = Number / 6;

% Close File

fclose(DatID);

% Extract/Organize Data

Freq = 10.^Data(2,3:3:Number);
```

```
Omega = Freq.*2.*pi;

Gain1mm  = Data(3,3:3:Number);
Gain25mm = Data(3,2:3:Number);
Gain5mm  = Data(3,1:3:Number);

Phase1mm  = Data(4,3:3:Number);
Phase25mm = Data(4,2:3:Number);
Phase5mm  = Data(4,1:3:Number);

% Recalculate gain into volts, phase into radians
Gr1mm = 10.^(Gain1mm./20);
Gr25mm = 10.^(Gain25mm./20);
Gr5mm = 10.^(Gain5mm./20);

Fi1mm = Phase1mm.*pi./180;
Fi25mm = Phase25mm.*pi./180;
Fi5mm = Phase5mm.*pi./180;

% Recalculate into real and imaginary parts of gain
GRe1mm = Gr1mm.*(cos(Fi1mm));
GRe2mm = Gr25mm.*(cos(Fi25mm));
GRe5mm = Gr5mm.*(cos(Fi5mm));

GIm1mm = Gr1mm.*(sin(Fi1mm));
GIm2mm = Gr25mm.*(sin(Fi25mm));
GIm5mm = Gr5mm.*(sin(Fi5mm));

% Solve system of equations
for ii = 1:Number/3,
 A1 = [ GRe1mm(ii)-1 -Omega(ii)*GIm1mm(ii);
GIm1mm(ii)  Omega(ii)*(GRe1mm(ii)-1)];
 B1 = [ Omega(ii)*GIm1mm(ii)*CL1mm;
-GRe1mm(ii)*Omega(ii)*CL1mm];

 A2 = [ GRe2mm(ii)-1 -Omega(ii)*GIm2mm(ii);
GIm2mm(ii)  Omega(ii)*(GRe2mm(ii)-1)];
 B2 = [ Omega(ii)*GIm2mm(ii)*CL2mm;
-GRe2mm(ii)*Omega(ii)*CL2mm];

 A5 = [ GRe5mm(ii)-1 -Omega(ii)*GIm5mm(ii);
GIm5mm(ii)  Omega(ii)*(GRe5mm(ii)-1)];
 B5 = [ Omega(ii)*GIm5mm(ii)*CL5mm;
-GRe5mm(ii)*Omega(ii)*CL5mm];

 X1 = A1\B1;
 X2 = A2\B2;
 X5 = A5\B5;

 C12m1(ii) = X1(2);
 C12m2(ii) = X2(2);
 C12m5(ii) = X5(2);
```

```
end

%Compute Metallization of Sensor from gainInAir:
gAir1 = 10^(gainInAir(1)/20);
gAir2 = 10^(gainInAir(2)/20);
gAir5 = 10^(gainInAir(3)/20);

cAir1 = gAir1*CL1mm/(1-gAir1);
cAir2 = gAir2*CL2mm/(1-gAir2);
cAir5 = gAir5*CL5mm/(1-gAir5);

metal1 = 0.7934*sqrt(cAir1) - 0.0966*cAir1 - 0.6502
metal2 = 0.8419*sqrt(cAir2) - 0.1545*cAir2 - 0.3157
metal5 = 0.9099*sqrt(cAir5) - 0.1954*cAir5 - 0.2040

%Compute line (slope and intercept) from metallization:
line1 = 0.2090*metal1^2 - 0.7148*metal1 + 0.6928;
line2 = 0.1855*metal2^2 - 0.6165*metal2 + 0.6534;
line5 = 0.1874*metal5^2 - 0.5751*metal5 + 0.6102;

sqrt1 = 0.9290*metal1^2 - 1.7726*metal1 + 0.8006;
sqrt2 = 2.2988*metal2^2 - 4.5944*metal2 + 2.2768;
sqrt5 = 3.5109*metal5^2 - 7.1093*metal5 + 3.7179;

inter1 = -0.1260*metal1^2 - 0.2474*metal1 - 0.4904;
inter2 = -0.2679*metal2^2 + 0.3955*metal2 - 0.4511;
inter5 =  0.9312*metal5^2 - 0.4282*metal5 - 0.3935;

%Compute epsilon from C12 and the appropriate slope and intercept:
 Epsilon1 = zeros(Number/3,1);
 Epsilon2 = zeros(Number/3,1);
 Epsilon5 = zeros(Number/3,1);
 aEpsilon = zeros(Number/3,1);
 aEpsilon = aEpsilon + actualEpsilon;

if (materialType == 'l')
    Epsilon1 = C12m1.^0.5*sqrt1+C12m1*line1+inter1;
    Epsilon2 = C12m2.^0.5*sqrt2+C12m2*line2+inter2;
    Epsilon5 = C12m5.^0.5*sqrt5+C12m5*line5+inter5;
else
    c1a = (sqrt(1/line1 - inter1/line1 + (sqrt1/(2*line1))^2) - sqrt1/(2*line1))^2;
    c1b = (sqrt(1.1/line1 - inter1/line1 +...
 (sqrt1/(2*line1))^2) - sqrt1/(2*line1))^2;
    slopeLiquids1 = 0.1/(c1b - c1a);
    atan1 = atan(slopeLiquids1);
    atan1 = atan1 + 0.096;
    slopeSolids1 = tan(atan1);
    Epsilon1 = (C12m1-c1a)*slopeSolids1+1;

    c2a = (sqrt(1/line2 - inter2/line2 + (sqrt2/(2*line2))^2) - sqrt2/(2*line2))^2;
    c2b = (sqrt(1.1/line2 - inter2/line2...
 + (sqrt2/(2*line2))^2) - sqrt2/(2*line2))^2;
```

```
    slopeLiquids2 = 0.1/(c2b - c2a);
    atan2 = atan(slopeLiquids2);
    atan2 = atan2 + 0.041;
    slopeSolids2 = tan(atan2);
    Epsilon2 = (C12m2-c2a)*slopeSolids2+1;

    c5a = (sqrt(1/line5 - inter5/line5 + (sqrt5/(2*line5))^2) - sqrt5/(2*line5))^2;
    c5b = (sqrt(1.1/line5 - inter5/line5...
 + (sqrt5/(2*line5))^2) - sqrt5/(2*line5))^2;
    slopeLiquids5 = 0.1/(c5b - c5a);
    atan5 = atan(slopeLiquids5);
    atan5 = atan5 + 0.0002;
    slopeSolids5 = tan(atan5);
    Epsilon5 = (C12m5-c5a)*slopeSolids5+1;
end

% Statistical Information
averageEpsilon = (Epsilon1+Epsilon2+Epsilon5)/3;
meanEpsilon = num2str(mean(averageEpsilon));
stdEpsilon = num2str(std(averageEpsilon));
mm1Mean = num2str(mean(Epsilon1));
mm2Mean = num2str(mean(Epsilon2));
mm5Mean = num2str(mean(Epsilon5));
mm1Error = Epsilon1 - actualEpsilon;
mm2Error = Epsilon2 - actualEpsilon;
mm5Error = Epsilon5 - actualEpsilon;
mm1STDError = num2str(std(mm1Error));
mm2STDError = num2str(std(mm2Error));
mm5STDError = num2str(std(mm5Error));
errort = num2str(((mean(averageEpsilon) - actualEpsilon)/actualEpsilon)*100);
error1 = num2str(((mean(Epsilon1) - actualEpsilon)/actualEpsilon)*100);
error2 = num2str(((mean(Epsilon2) - actualEpsilon)/actualEpsilon)*100);
error5 = num2str(((mean(Epsilon5) - actualEpsilon)/actualEpsilon)*100);

%Save C12/epsilon
Results = [Freq; C12m1; Epsilon1; C12m2; Epsilon2; C12m5; Epsilon5];
FileName = [DatFileName '.sem'];
DatID = fopen(FileName, 'w');
fprintf(DatID, 'Frequency\t\tC12 - 1mm\tEpsilon - 1mm\tC12...
 - 2.5mm\tEpsilon 2.5mm\tC12 - 5mm\tEpsilon - 5mm\n');
fprintf(DatID,'%e\t\t%e\t%e\t%e\t%e\t%e\t%e\n', Results);
fclose(DatID);

if (otherPlots == 1)
% Plot Gain/Phase
figure('PaperPosition', [.25 .75 8 9.5])
subplot(2,1,1)
if mm1~=0
semilogx(Freq,Gain1mm,'+','MarkerSize',5)
end;
if mm2~=0
if mm1~=0
```

```
hold on
end;
semilogx(Freq,Gain25mm,'o','MarkerSize',5)
hold off
end;
if mm5~=0
if (mm1+mm2)~=0
hold on
end;
semilogx(Freq,Gain5mm,'*','MarkerSize',5)
hold off;
end;
title(ttl,'FontSize',16);
ylabel('Gain (dB)','FontSize',16)
ax = axis;
axis([(10^(-2.3)) (10^4) ax(3) ax(4)])

subplot(2,1,2)
if mm1~=0
semilogx(Freq,Phase1mm,'+','MarkerSize',5)
end;
if mm2~=0
if mm1~=0
hold on
end;
semilogx(Freq,Phase25mm,'o','MarkerSize',5)
hold off
end;
if mm5~=0
if (mm1+mm2)~=0
hold on
end;
semilogx(Freq,Phase5mm,'*','MarkerSize',5)
hold off;
end;
ylabel('Phase (degrees)','FontSize',16)
xlabel('Frequency (Hz)','FontSize',16)
ax = axis;
axis([(10^(-2.3)) (10^4) ax(3) ax(4)])

[legh, objh]=legend('1mm','2.5mm','5mm');

xdata1 = get(objh(1), 'XData');
ydata1 = get(objh(1), 'YData');
xdata2 = get(objh(2), 'XData');
ydata2 = get(objh(2), 'YData');
xdata3 = get(objh(3), 'XData');
ydata3 = get(objh(3), 'YData');

set(objh(1), 'xdata', (xdata1(1)+xdata1(2))/2, 'ydata', ydata1(1))
set(objh(2), 'xdata', (xdata2(1)+xdata2(2))/2, 'ydata', ydata2(1))
set(objh(3), 'xdata', (xdata3(1)+xdata3(2))/2, 'ydata', ydata3(1))
```

```
%extra = strcat('Filename: ' DatFileName);
%axa = axis;
%text(axa(1),axa(3)-0.38*(axa(4)-axa(3)),extra);

%Plot C12/epsilon

figure('PaperPosition', [.25 .75 8 9.5])

subplot(2,1,1)
if mm1~=0
semilogx(Freq,C12m1,'+','MarkerSize',5)
end;
if mm2~=0
if mm1~=0
hold on
end;
semilogx(Freq,C12m2,'o','MarkerSize',5)
hold off
end;
if mm5~=0
if (mm1+mm2)~=0
hold on
end;
semilogx(Freq,C12m5,'*','MarkerSize',5)
hold off;
end;
title(ttl,'FontSize',16);
ylabel('C_{12} (pF)','FontSize',16)
ax = axis;
axis([(10^(-2.3)) (10^4) ax(3) ax(4)])

subplot(2,1,2)
if mm1~=0
semilogx(Freq,Epsilon1,'+','MarkerSize',5)
end;
if mm2~=0
if mm1~=0
hold on
end;
semilogx(Freq,Epsilon2,'o','MarkerSize',5)
hold off
end;
if mm5~=0
if (mm1+mm2)~=0
hold on
end;
semilogx(Freq,Epsilon5,'*','MarkerSize',5)
hold off;
end;

title(ttl,'FontSize',16);
```

```
ylabel('{\epsilon}','FontSize',16)
ax = axis;
axis([(10^(-2.3)) (10^4) 0 max(ax(4), 1e-20)])

[legh, objh]=legend('1mm','2.5mm','5mm');

xdata1 = get(objh(1), 'XData');
ydata1 = get(objh(1), 'YData');
xdata2 = get(objh(2), 'XData');
ydata2 = get(objh(2), 'YData');
xdata3 = get(objh(3), 'XData');
ydata3 = get(objh(3), 'YData');

set(objh(1), 'xdata', (xdata1(1)+xdata1(2))/2, 'ydata', ydata1(1))
set(objh(2), 'xdata', (xdata2(1)+xdata2(2))/2, 'ydata', ydata2(1))
set(objh(3), 'xdata', (xdata3(1)+xdata3(2))/2, 'ydata', ydata3(1))

%extra = strcat('Filename: ' DatFileName);
%axa = axis;
%text(axa(1),axa(3)-0.38*(axa(4)-axa(3)),extra);

end

%Plot epsilon/average epsilon

%figure('PaperPosition', [0 1 8.25 9.75])
figure

subplot(2,1,1)
semilogx(Freq,averageEpsilon,'kx','MarkerSize',3)
hold on
semilogx(Freq,aEpsilon,'k-','MarkerSize',3)
hold off
title(ttl,'FontSize',18);
ylabel('Mean and actual {\epsilon}','FontSize',14);
ax = axis;
axis([(10^(-2.3)) (10^4) 0 5]);

subplot(2,1,2)
if mm1~=0
semilogx(Freq,Epsilon1,'k+','MarkerSize',3)
end;
if mm2~=0
if mm1~=0
hold on
end;
semilogx(Freq,Epsilon2,'ko','MarkerSize',3)
hold off
end;
if mm5~=0
if (mm1+mm2)~=0
hold on
```

```
end;
semilogx(Freq,Epsilon5,'k*','MarkerSize',3)
hold off;
end;
hold on
semilogx(Freq,averageEpsilon,'kx','MarkerSize',3)


ylabel('{\epsilon}','FontSize',18)
ax = axis;
axis([(10^(-2.3)) (10^4) 0 5])
xlabel('Frequency','FontSize',18);


[legh, objh]=legend('1mm','2.5mm','5mm','Average',3);

xdata1 = get(objh(1), 'XData');
ydata1 = get(objh(1), 'YData');
xdata2 = get(objh(2), 'XData');
ydata2 = get(objh(2), 'YData');
xdata3 = get(objh(3), 'XData');
ydata3 = get(objh(3), 'YData');
xdata4 = get(objh(4), 'XData');
ydata4 = get(objh(4), 'YData');

set(objh(1), 'xdata', (xdata1(1)+xdata1(2))/2, 'ydata', ydata1(1))
set(objh(2), 'xdata', (xdata2(1)+xdata2(2))/2, 'ydata', ydata2(1))
set(objh(3), 'xdata', (xdata3(1)+xdata3(2))/2, 'ydata', ydata3(1))
set(objh(4), 'xdata', (xdata4(1)+xdata4(2))/2, 'ydata', ydata4(1))

set(gcf,'Color','White')

%line1 = strcat('Filename:', DatFileName, '     ...
Mean:', meanEpsilon, '     STD:', stdEpsilon, '     %Error:', errort, '%');
%line2 = strcat('1.0mm Mean:', mm1Mean, '     ...
STD Error:', mm1STDError, '     %Error:', error1, '%');
%line3 = strcat('2.5mm Mean:', mm2Mean, '     ...
STD Error:', mm2STDError, '     %Error:', error2, '%');
%line4 = strcat('5.0mm Mean:', mm5Mean, '     ...
STD Error:', mm5STDError, '     %Error:', error5, '%');

%axa = axis;
%text(axa(1),-1.0,line1);
%text(axa(1),-1.3,line2);
%text(axa(1),-1.6,line3);
%text(axa(1),-1.9,line4);
```

G.1.5 twoliq.m

```
function twoliq(DatFileName,ttl,capType,gainInAira,gainInAirb,otherPlots,lambda)

%%% Plots Gain, Phase, C12, and Epsilon for a Two Fluid Run.
%%% Specifically, Phase is Approximately Zero (good insultator).
%%% Last Modified July 17, 1997 by Christopher Lin.

mm1 = 1;
mm2 = 1;
mm5 = 1;

gainInAir(1) = capType;
gainInAir(2) = gainInAira;
gainInAir(3) = gainInAirb;

% Load capacitances

Cl1mm = 100.5; CL1mm = Cl1mm;
Cl2mm =  58.1; CL2mm = Cl2mm;
Cl5mm =  49.4; CL5mm = Cl5mm;


% open data file

DatID = fopen(DatFileName,'rt');
if (DatID == -1)
  disp(' ');
error('Error Opening Data File!');
end;

% Read off Header Data Line
[Head] = fscanf(DatID,'[gd][GH,%f,%i,%i,%i,%i,%i,%i]',7);

% Read Data to Matrix
[Data,Number] = fscanf(DatID,'[GD,%i,%f,%f,%f,%f,%i]',[6,inf]);
Number = Number / 6;

% Close File

fclose(DatID);


% Extract/Organize Data

Freq = 10.^Data(2,3:3:Number);
Omega = Freq.*2.*pi;

Gain1mm  = Data(3,3:3:Number);
Gain25mm = Data(3,2:3:Number);
Gain5mm  = Data(3,1:3:Number);
```

```
Phase1mm  = Data(4,3:3:Number);
Phase25mm = Data(4,2:3:Number);
Phase5mm  = Data(4,1:3:Number);

% Recalculate gain into volts, phase into radians
 Gr1mm = 10.^(Gain1mm./20);
 Gr25mm = 10.^(Gain25mm./20);
 Gr5mm = 10.^(Gain5mm./20);

 Fi1mm = Phase1mm.*pi./180;
 Fi25mm = Phase25mm.*pi./180;
 Fi5mm = Phase5mm.*pi./180;

%
% Recalculate into real and imaginary parts of gain
 GRe1mm = Gr1mm.*(cos(Fi1mm));
 GRe2mm = Gr25mm.*(cos(Fi25mm));
 GRe5mm = Gr5mm.*(cos(Fi5mm));

 GIm1mm = Gr1mm.*(sin(Fi1mm));
 GIm2mm = Gr25mm.*(sin(Fi25mm));
 GIm5mm = Gr5mm.*(sin(Fi5mm));

% Solve system of equations
 for ii = 1:Number/3,
 A1 = [ GRe1mm(ii)-1 -Omega(ii)*GIm1mm(ii);
GIm1mm(ii)  Omega(ii)*(GRe1mm(ii)-1)];
 B1 = [ Omega(ii)*GIm1mm(ii)*CL1mm;
-GRe1mm(ii)*Omega(ii)*CL1mm];

 A2 = [ GRe2mm(ii)-1 -Omega(ii)*GIm2mm(ii);
GIm2mm(ii)  Omega(ii)*(GRe2mm(ii)-1)];
 B2 = [ Omega(ii)*GIm2mm(ii)*CL2mm;
-GRe2mm(ii)*Omega(ii)*CL2mm];

 A5 = [ GRe5mm(ii)-1 -Omega(ii)*GIm5mm(ii);
GIm5mm(ii)  Omega(ii)*(GRe5mm(ii)-1)];
 B5 = [ Omega(ii)*GIm5mm(ii)*CL5mm;
-GRe5mm(ii)*Omega(ii)*CL5mm];

 X1 = A1\B1;
 X2 = A2\B2;
 X5 = A5\B5;

 C12m1(ii) = X1(2);
 C12m2(ii) = X2(2);
 C12m5(ii) = X5(2);
end

C12m1;
C12a = C12m2;
C12b = C12m5;
```

```
%Compute Metallization of Sensor from gainInAir:

 gAira = 10^(gainInAir(2)/20);
 gAirb = 10^(gainInAir(3)/20);

 cAira = gAira*CL2mm/(1-gAira);
 cAirb = gAirb*CL5mm/(1-gAirb);

if (lambda == 1)
 metala = 0.7934*sqrt(cAira) - 0.0966*cAira - 0.6502;
 metalb = 0.7934*sqrt(cAirb) - 0.0966*cAirb - 0.6502;
 linea = 0.2090*metala^2 - 0.7148*metala + 0.6928;
 lineb = 0.2090*metalb^2 - 0.7148*metalb + 0.6928;
 sqrta = 0.9290*metala^2 - 1.7726*metala + 0.8006;
 sqrtb = 0.9290*metalb^2 - 1.7726*metalb + 0.8006;
 intera = -0.1260*metala^2 - 0.2474*metala - 0.4904;
 interb = -0.1260*metalb^2 - 0.2474*metalb - 0.4904;
else
 metala = 0.8419*sqrt(cAira) - 0.1545*cAira - 0.3157;
 metalb = 0.8419*sqrt(cAirb) - 0.1545*cAirb - 0.3157;
 linea = 0.1855*metala^2 - 0.6165*metala + 0.6534;
 lineb = 0.1855*metalb^2 - 0.6165*metalb + 0.6534;
 sqrta = 2.2988*metala^2 - 4.5944*metala + 2.2768;
 sqrtb = 2.2988*metalb^2 - 4.5944*metalb + 2.2768;
 intera = -0.2679*metala^2 + 0.3955*metala - 0.4511;
 interb = -0.2679*metalb^2 + 0.3955*metalb - 0.4511;
end

%Compute epsilon from C12 and the appropriate slope and intercept:



 Epsilon1 = zeros(Number/3,1);
 Epsilona = zeros(Number/3,1);
 Epsilonb = zeros(Number/3,1);

RefFileName = 'aircal4s.res';
DatID = fopen(RefFileName,'rt');
if (DatID == -1)
disp(' ');
error('Error Opening Reference File!');
end;

% Read off Header Data Line
fread(DatID,78);

% Read Reference Data to Matrix
[Ref, N] = fscanf(DatID,'%f\t%f\t%f\t%f\t%f\t%f\t%f\n',[7,inf]);
% Close File
fclose(DatID);
```

```
% For aircal4s.res, PPCap is in column 3 and YCap is in column 5.
% aircal4s.res should be used for the calibration trials in
% transformer oil (type AX).
% capType = 1 <=> YCap
% capType = 0 <=> PPCap


if(capType == 1)
Epsilon1 = C12m1./Ref(5:7:N);
else
Epsilon1 = C12m1./Ref(3:7:N);
end

Epsilona = C12a.^0.5*sqrta+C12a*linea+intera;
Epsilonb = C12b.^0.5*sqrtb+C12b*lineb+interb;

 actualEpsilon = mean(Epsilon1);
 aEpsilon = zeros(Number/3,1);
 aEpsilon = aEpsilon + actualEpsilon;


% Statistical Information

averageEpsilon = (Epsilona+Epsilonb)/2;
meanEpsilon = num2str(mean(averageEpsilon));
stdEpsilon = num2str(std(averageEpsilon));
mm1Mean = num2str(mean(Epsilon1))
mmaMean = num2str(mean(Epsilona))
mmbMean = num2str(mean(Epsilonb))
mm1Error = Epsilon1 - actualEpsilon;
mmaError = Epsilona - actualEpsilon;
mmbError = Epsilonb - actualEpsilon;
mm1STDError = num2str(std(mm1Error));
mmaSTDError = num2str(std(mmaError));
mmbSTDError = num2str(std(mmbError));
errort = num2str(((mean(averageEpsilon) - actualEpsilon)/actualEpsilon)*100);
error1 = num2str(((mean(Epsilon1) - actualEpsilon)/actualEpsilon)*100);
errora = num2str(((mean(Epsilona) - actualEpsilon)/actualEpsilon)*100);
errorb = num2str(((mean(Epsilonb) - actualEpsilon)/actualEpsilon)*100);

c12astr = num2str(mean(C12a))
c12bstr = num2str(mean(C12b))
c12ratio = num2str(mean(C12a)/mean(C12b))

%ttl
%error1
%errora
%errorb

%Save C12/epsilon

Results = [Freq; C12m1; Epsilon1; C12a; Epsilona; C12b; Epsilonb];
```

```
FileName = [DatFileName '.tlq'];

DatID = fopen(FileName, 'w');

fprintf(DatID, 'Frequency\t\tC12 - Cap\tEpsilon - Cap\tC12...
 - A\tEpsilon A\tC12 - B\tEpsilon - B\n');
fprintf(DatID,'%e\t\t%e\t%e\t%e\t%e\t%e\t%e\n', Results);

fclose(DatID);

if (otherPlots == 1)
% --------------------------------------------------------------------
% Plot Gain/Phase
figure('PaperPosition', [0 1 8.25 9.75])
subplot(2,1,1)
if mm1~=0
semilogx(Freq,Gain1mm,'+','MarkerSize',5)
end;
if mm2~=0
if mm1~=0
hold on
end;
semilogx(Freq,Gain25mm,'o','MarkerSize',5)
hold off
end;
if mm5~=0
if (mm1+mm2)~=0
hold on
end;
semilogx(Freq,Gain5mm,'*','MarkerSize',5)
hold off;
end;
title(ttl,'FontSize',16);
ylabel('Gain (dB)','FontSize',16)
ax = axis;
axis([(10^(-2.3)) (10^4) ax(3) ax(4)])

subplot(2,1,2)
if mm1~=0
semilogx(Freq,Phase1mm,'+','MarkerSize',5)
end;
if mm2~=0
if mm1~=0
hold on
end;
semilogx(Freq,Phase25mm,'o','MarkerSize',5)
hold off
end;
if mm5~=0
if (mm1+mm2)~=0
hold on
```

```
end;
semilogx(Freq,Phase5mm,'*','MarkerSize',5)
hold off;
end;
ylabel('Phase (degrees)','FontSize',16)
xlabel('Frequency (Hz)','FontSize',16)
ax = axis;
axis([(10^(-2.3)) (10^4) ax(3) ax(4)])

if (capType == 1)
device1 = 'YCap';
else
device1 = 'PPCap';
end

if (lambda == 1)
devicea = '1mm A';
deviceb = '1mm B';
else
devicea = '2.5mm A';
deviceb = '2.5mm B';
end

[legh, objh]=legend(device1,devicea,deviceb);

xdata1 = get(objh(1), 'XData');
ydata1 = get(objh(1), 'YData');
xdata2 = get(objh(2), 'XData');
ydata2 = get(objh(2), 'YData');
xdata3 = get(objh(3), 'XData');
ydata3 = get(objh(3), 'YData');

set(objh(1), 'xdata', (xdata1(1)+xdata1(2))/2, 'ydata', ydata1(1))
set(objh(2), 'xdata', (xdata2(1)+xdata2(2))/2, 'ydata', ydata2(1))
set(objh(3), 'xdata', (xdata3(1)+xdata3(2))/2, 'ydata', ydata3(1))

extra = strcat('Filename: ', DatFileName);
axa = axis;
text(axa(1),axa(3)-0.38*(axa(4)-axa(3)),extra);

%Plot C12/epsilon

figure('PaperPosition', [0 1 8.25 9.75])

subplot(2,1,1)
if mm1~=0
semilogx(Freq,C12m1,'+','MarkerSize',5)
end;
if mm2~=0
if mm1~=0
hold on
end;
```

```
semilogx(Freq,C12a,'o','MarkerSize',5)
hold off
end;
if mm5~=0
if (mm1+mm2)~=0
hold on
end;
semilogx(Freq,C12b,'*','MarkerSize',5)
hold off;
end;
title(ttl,'FontSize',16);
ylabel('C_{12} (pF)','FontSize',16)
ax = axis;
axis([(10^(-2.3)) (10^4) ax(3) ax(4)])

subplot(2,1,2)
if mm1~=0
semilogx(Freq,Epsilon1,'+','MarkerSize',5)
end;
if mm2~=0
if mm1~=0
hold on
end;
semilogx(Freq,Epsilona,'o','MarkerSize',5)
hold off
end;
if mm5~=0
if (mm1+mm2)~=0
hold on
end;
semilogx(Freq,Epsilonb,'*','MarkerSize',5)
hold off;
end;

title(ttl,'FontSize',16);
ylabel('{\epsilon}','FontSize',16)
ax = axis;
axis([(10^(-2.3)) (10^4) 0 max(ax(4), 1e-20)])

[legh, objh]=legend(device1,devicea,deviceb);

xdata1 = get(objh(1), 'XData');
ydata1 = get(objh(1), 'YData');
xdata2 = get(objh(2), 'XData');
ydata2 = get(objh(2), 'YData');
xdata3 = get(objh(3), 'XData');
ydata3 = get(objh(3), 'YData');

set(objh(1), 'xdata', (xdata1(1)+xdata1(2))/2, 'ydata', ydata1(1))
set(objh(2), 'xdata', (xdata2(1)+xdata2(2))/2, 'ydata', ydata2(1))
set(objh(3), 'xdata', (xdata3(1)+xdata3(2))/2, 'ydata', ydata3(1))
```

```
line1 = strcat('Filename:', DatFileName);
line2 = strcat('Sensor A Capacitance:', c12astr);
line3 = strcat('Sensor B Capacitance:', c12bstr);
line4 = strcat('Capacitance Ratio:', c12ratio);

axa = axis;
text(axa(1),(axa(3)-axa(4))/5,line1);
text(axa(1),1.2*(axa(3)-axa(4))/5,line2);
text(axa(1),1.4*(axa(3)-axa(4))/5,line3);
text(axa(1),1.6*(axa(3)-axa(4))/5,line4);
end

%Plot epsilon/average epsilon

figure('PaperPosition', [0 1 8.25 9.75])

subplot(2,1,1)
semilogx(Freq,averageEpsilon,'x','MarkerSize',5)
hold on
semilogx(Freq,aEpsilon,'-','MarkerSize',5)
hold off
title(ttl,'FontSize',16);
ylabel('Average and actual {\epsilon}','FontSize',16);
xlabel('Frequency','FontSize',16);
ax = axis;
axis([(10^(-2.3)) (10^4) 0 5]);

subplot(2,1,2)
if mm1~=0
semilogx(Freq,Epsilon1,'+','MarkerSize',5)
end;
if mm2~=0
if mm1~=0
hold on
end;
semilogx(Freq,Epsilona,'o','MarkerSize',5)
hold off
end;
if mm5~=0
if (mm1+mm2)~=0
hold on
end;
semilogx(Freq,Epsilonb,'*','MarkerSize',5)
hold off;
end;
hold on
semilogx(Freq,averageEpsilon,'x','MarkerSize',5)


title(ttl,'FontSize',16);
ylabel('{\epsilon}','FontSize',16)
```

```
ax = axis;
axis([(10^(-2.3)) (10^4) 0 5])
xlabel('Frequency','FontSize',16);


[legh, objh]=legend(device1,devicea,deviceb,'Average');

xdata1 = get(objh(1), 'XData');
ydata1 = get(objh(1), 'YData');
xdata2 = get(objh(2), 'XData');
ydata2 = get(objh(2), 'YData');
xdata3 = get(objh(3), 'XData');
ydata3 = get(objh(3), 'YData');
xdata4 = get(objh(4), 'XData');
ydata4 = get(objh(4), 'YData');

set(objh(1), 'xdata', (xdata1(1)+xdata1(2))/2, 'ydata', ydata1(1))
set(objh(2), 'xdata', (xdata2(1)+xdata2(2))/2, 'ydata', ydata2(1))
set(objh(3), 'xdata', (xdata3(1)+xdata3(2))/2, 'ydata', ydata3(1))
set(objh(4), 'xdata', (xdata4(1)+xdata4(2))/2, 'ydata', ydata4(1))


line1 = strcat('Filename:', DatFileName, '    ...
 Mean:', meanEpsilon, '     STD:', stdEpsilon, '     %Error:', errort, '%');
line2 = strcat('Capacitor Mean:', mm1Mean, '    ...
 STD Error:', mm1STDError, '     %Error:', error1, '%');
line3 = strcat('Sensor A   Mean:', mmaMean, '    ...
 STD Error:', mmaSTDError, '     %Error:', errora, '%');
line4 = strcat('Sensor B   Mean:', mmbMean, '     ...
STD Error:', mmbSTDError, '     %Error:', errorb, '%');

axa = axis;
text(axa(1),-1.0,line1);
text(axa(1),-1.3,line2);
text(axa(1),-1.6,line3);
text(axa(1),-1.9,line4);
```

G.1.6 solliq.m

```
function [results] = ...
solliq(waveLength1,waveLength2,fluid1,fluid2,inputData,resolution)

%inputData should be a two column matrix

%initialize results matrix
results = '';

%read simulation data
simData = readSim(waveLength1,waveLength2,fluid1,fluid2);

data1 = inputData(:,1);
data2 = inputData(:,2);

meaData = [data1, data2];
points = size(meaData,1);

%loop through measurement data
for index=1:points
   [epsilon,h] = child(simData,meaData(index,:),fluid1,fluid2,resolution);
   results = [results;meaData(index,:),epsilon,h];
%   results(index,:)
%   input('press enter to continue');
%   close all;
end
```

G.1.7 child.m

```
function [rEpsilon,rH] = child(simulationData,measurementPoint,...
fluid1,fluid2,numberOfContours)

%simulationData will be a four column matrix [epsilon, h, cap1, cap2]
%measurementPoint will be a two column row vector [cap1, cap2]

%Calculate distance from each measurement point to each of the simulation points
simDataSize = size(simulationData,1);
for n=1:simDataSize
   temp = sqrt((simulationData(n,3)-measurementPoint(1))^2 +...
 (simulationData(n,4)-measurementPoint(2))^2);
   distance(n,1:5) = [simulationData(n,1:4),temp];
end

%Sort by distance (column 5 of distance matrix)
distance = sortrows(distance,5);

%Find 'n' closest points (try 10)
numberOfPoints = 10;
localData = distance(1:numberOfPoints,:);

%Plot using Delaunay triangulation
epsilon = localData(:,1);
h = localData(:,2);
cap1 = localData(:,3);
cap2 = localData(:,4);

%subplot(2,1,1);
%tri = delaunay(cap1,cap2);
%trisurf(tri, cap1, cap2, epsilon);
%title('Epsilon');
%xlabel(strcat('C_1_2 ',fluid1));
%ylabel(strcat('C_1_2 ',fluid2));

%subplot(2,1,2);
%tri = delaunay(cap1,cap2);
%trisurf(tri, cap1, cap2, h);
%title('h');
%xlabel(strcat('C_1_2 ',fluid1,num2str(waveLength1)));
%ylabel(strcat('C_1_2 ',fluid2,num2str(waveLength2)));


%Transform selected simulation points into plaid and monotonic form
micap1 = linspace(min(cap1),max(cap1),numberOfPoints);
micap2 = linspace(min(cap2),max(cap2),numberOfPoints);
[mpicap1,mpicap2] = meshgrid(micap1,micap2);
iEpsilon = griddata(cap1,cap2,epsilon,mpicap1,mpicap2);
iH = griddata(cap1,cap2,h,mpicap1,mpicap2);
```

```
%Interpolate to find h and epsilon for measurement data
rEpsilon = ...
interp2(mpicap1,mpicap2,iEpsilon,measurementPoint(1),measurementPoint(2));
rH = interp2(mpicap1,mpicap2,iH,measurementPoint(1),measurementPoint(2));

figure;

subplot(2,1,1);
contourf(mpicap1,mpicap2,iEpsilon,numberOfContours);
colorbar;
hold on;
plot3(measurementPoint(1),measurementPoint(2),1,'k*','MarkerSize',5);
title('Epsilon');
xlabel(strcat('C_1_2 ',fluid1,' 1'));
ylabel(strcat('C_1_2 ',fluid2,' 2'));


subplot(2,1,2);
contourf(mpicap1,mpicap2,iH,numberOfContours);
colorbar;
hold on;
plot3(measurementPoint(1),measurementPoint(2),1,'k*','MarkerSize',5);
title('h');
xlabel(strcat('C_1_2 ',fluid1,' 1'));
ylabel(strcat('C_1_2 ',fluid2,' 2'));
```

G.1.8 readSim.m

```
function [simData] = readSim(waveLength1,waveLength2,fluid1,fluid2)

if (waveLength1==1)
   if (strcmp(fluid1,'air'));
      fileName1 = 'air1.ptd';
   elseif (strcmp(fluid1,'corn'));
      fileName1 = 'corn1.ptd';
   elseif (strcmp(fluid1,'castor'));
      fileName1 = 'castor1.ptd';
   else
      error('Invalid fluid type');
   end
elseif (waveLength1==2.5)
   if (strcmp(fluid1,'air'));
      fileName1 = 'air2.ptd';
   elseif (strcmp(fluid1,'corn'));
      fileName1 = 'corn2.ptd';
   elseif (strcmp(fluid1,'castor'));
      fileName1 = 'castor2.ptd';
   else
      error('Invalid fluid type');
   end
elseif (waveLength1==5)
   if (strcmp(fluid1,'air'));
      fileName1 = 'air5.ptd';
   elseif (strcmp(fluid1,'corn'));
      fileName1 = 'corn5.ptd';
   elseif (strcmp(fluid1,'castor'));
      fileName1 = 'castor5.ptd';
   else
      error('Invalid fluid type');
   end
else
   error('Invalid wavelength');
end


if (waveLength2==1)
   if (strcmp(fluid2,'air'));
      fileName2 = 'air1.ptd';
   elseif (strcmp(fluid2,'corn'));
      fileName2 = 'corn1.ptd';
   elseif (strcmp(fluid2,'castor'));
      fileName2 = 'castor1.ptd';
   else
      error('Invalid fluid type');
   end
elseif (waveLength2==2.5)
   if (strcmp(fluid2,'air'));
      fileName2 = 'air2.ptd';
```

```
   elseif (strcmp(fluid2,'corn'));
      fileName2 = 'corn2.ptd';
   elseif (strcmp(fluid2,'castor'));
      fileName2 = 'castor2.ptd';
   else
      error('Invalid fluid type');
   end
elseif (waveLength2==5)
   if (strcmp(fluid2,'air'));
      fileName2 = 'air5.ptd';
   elseif (strcmp(fluid2,'corn'));
      fileName2 = 'corn5.ptd';
   elseif (strcmp(fluid2,'castor'));
      fileName2 = 'castor5.ptd';
   else
      error('Invalid fluid type');
   end
else
   error('Invalid wavelength');
end


% open data files
DatID1 = fopen(fileName1,'rt');
if (DatID1 == -1)
  disp(' ');
error('Error Opening Data File!');
end;

[data1,number] = fscanf(DatID1,'setup%*i %*i %i %f %*s %*s ...
%*s %*i %*f %*f (%*f,%*f)(%*f,%*f) %*f %*f %*f %*f (%*f,%f)',[3,inf]);
data1 = data1';
h = data1(:,1);
epsilon = data1(:,2);
data1 = -data1(:,3).*10^9.*(500+waveLength1/.8);


DatID2 = fopen(fileName2,'rt');
if (DatID2 == -1)
  disp(' ');
error('Error Opening Data File!');
end;

[data2,number] = fscanf(DatID2,'setup%*i %*i %*i %*f %*s %*s %*s...
 %*i %*f %*f (%*f,%*f)(%*f,%*f) %*f %*f %*f %*f (%*f,%f)',[1,inf]);
data2 = data2';
data2 = -data2.*10^9.*(500+waveLength2/.8);

simData = [epsilon,h,data1,data2];
```

G.2 Diffusion: Forward Problem

G.2.1 Description of Programs

diffr01.m solves the diffusion problem using the finite differences approach.

Moi2EpEx.m converts moisture profiles into profiles of relative dielectric permittivity, conductivity, and loss factor, providing their plots and 4-th order polynomial approximations. Outputs data in Matlab binary file *AllProfiles*.

PolAppro.m This function fits the simulated data from moisture diffusion programs with a polynomial and returns polynomial fit coefficients.

eps2mo01.m converts moisture matrix into an ε matrix.

datent03.m This function contains data to be plotted for the stair-step diffusion case.

G.2.2 diffr01.m

```
%       Function diffr01.m
%       This function solves explicitely the diffusion equation in 1-D
%       using finite difference simulation
%       The diffusion coefficient is assumed to be constant
%       Left boundary value of concentration is constant

%       By Alex Mamishev, December 1997
%       Modified throughout 1998

%%%  INITIAL PARAMETERS

% To plot several profile curves on one graph, pick time in hours:
timeHours=[0.1 0.5 1 2  3 5 10 15 20 30];
timeSec=timeHours*3600;
% diffusion coefficient in m^2/sec
D=1e-11;
% Thickness of material in meters
Thickness = 0.001;

% Pick the number of time steps Time Steps in sec large enough
%to prevent loss of stability
% The larger is the number of XSteps, the larger should be the
%number of TimeSteps
% XSteps = number of nodes in space
% TimeSteps = number of Time Steps in sec
XSteps=41; TimeSteps=4000;
% Process input parameters
distance=linspace(0,Thickness,XSteps);
% initialize the vector that contains all profiles
FuncP1Array = zeros(length(timeHours),XSteps);

% set font size in all figures
set(0,'DefaultAxesFontSize',20);
set(0,'DefaultTextFontSize',20);

% OUTER LOOP FOR PLOTTING MOISTURE PROFILES AT DIFFERENT MOMENTS OF TIME
for i1=1:length(timeSec)
   timeHours(i1)
   TotalTime=timeSec(i1);
   dx=Thickness/XSteps;
   dt=TotalTime/TimeSteps;
   coef=D*(dt/dx^2);

   Func=1:XSteps;

   % Set initial conditions and boundary values
   % Boundary values are constant here
   Func(1)=1.0;
   Func(XSteps)=0.0;
   %  Set interior points to 0
```

```
   Func(2:XSteps-1)=0.0;

   FuncP1=Func;

%  begin marching forward in time
   for K=1:TimeSteps
      FuncP1(2:XSteps-1)=Func(2:XSteps-1)+coef*(Func(3:XSteps)-...
2*Func(2:XSteps-1)+Func(1:(XSteps-2)));

%     update function Func
      Func(2:XSteps-1)=FuncP1(2:XSteps-1);

%    update boundary value
      Func(XSteps)=FuncP1(XSteps-1);
      FuncP1(XSteps)=FuncP1(XSteps-1);

%     update time
      TKP1=K*dt;

%      Plot Solution
   end
   plot(distance*1000, FuncP1)
   pause(0.5)
   hold on
   FuncP1Array(i1,:) =  FuncP1;
end
xlabel('Depth into material, mm');
ylabel('Moisture concentration, %');

% execute if want to label the profiles
if 1
   for i2 = 1:length(timeHours)
      gtext(num2str(timeHours(i2)))
   end
end
save AllProfiles FuncP1Array -ascii -double;
```

G.2.3 Mois2Eps.m

```
function Mois2Eps(MoistProfiles)
%   Function to determine dielectric permittivity profiles from
% moisture profiles in pressboard
%  Also computes 4-th order polynomial approximation of these profiles and
% print the coefficients into the file polCoef
%   Uses function PolAppro
%   Takes input file generated by diffr01.m, such as AllProfiles
%   Generates output

%   By Alex Mamishev, August 97

%  INPUT VARIABLES
% specify dimensions of the region
XSteps = 41;
distance=linspace(0,0.001,XSteps);

% set font size in all figures
set(0,'DefaultAxesFontSize',20);
set(0,'DefaultTextFontSize',20);

load(MoistProfiles);

% parameter values from Sheiretov thesis
m = allprofiles;
Freq = 1;
einf = 3*8.85e-12;
e0   =   8.85e-12;
cm    =  -0.684;
fT   =   0.6;
c1   =   -0.7798;
c2   =   -0.4724;
g    =  -0.7;

epsilon = einf + e0.*10.^(-g.*(fT+cm)).*10.^(c1).*(m./Freq).^(-g);
EpsilonRel = epsilon/e0;

epsilondp = e0.*10.^(-g.*(fT+cm)).*10.^(c2).*(m./Freq).^(-g);
sigma = epsilondp*(2*pi*Freq);
lossFactor = epsilondp/e0;

size(epsilon)

figure
for i1=1:10
plot(distance*1000, EpsilonRel(i1,:))
   pause(0.5)
   hold on
EpsilonRel(i1,2:2:40)
end
xlabel('Depth into material (mm)');
```

```
ylabel('Relative permittivity, \epsilon_r');

% to mark the curves manually:
timeHours=[0.1 0.5 1 2  3 5 10 15 20 30];
if 1
if 0
   for i2 = 1:length(timeHours)
      gtext(num2str(timeHours(i2)))
   end
end

figure
for i1=1:10
plot(distance*1000, sigma(i1,:))
   pause(0.5)
   hold on
end
xlabel('Depth into material (mm)');
ylabel('Conductivity, \sigma (S/m)');

% to mark the curves manually:
if 0
   for i2 = 1:length(timeHours)
      gtext(num2str(timeHours(i2)))
   end
end


figure
for i1=1:10
plot(distance*1000, lossFactor(i1,:))
   pause(0.5)
   hold on
end
xlabel('Depth into material (mm)');
ylabel('Loss factor, \epsilon\prime\prime/\epsilon_0');

% to mark the curves manually:
if 0
   for i2 = 1:length(timeHours)
      gtext(num2str(timeHours(i2)))
   end
end
end

% POLYNOMIAL APPROXIMATION
% polynomial approximation - epsilon
polEps=PolAppro(distance, EpsilonRel, timeHours, XSteps);
xlabel('Depth into material (mm)');
ylabel('Dielectric permittivity, \epsilon_r');

% polynomial approximation -sigma
```

```
polSig=PolAppro(distance, sigma, timeHours, XSteps);
xlabel('Depth into material (mm)');
ylabel('Conductivity, \sigma (S/m)');


% polynomial approximation - epsilon double prime
polEpsDP=PolAppro(distance, lossFactor, timeHours, XSteps);
xlabel('Depth into material (mm)');
ylabel('Loss factor, \epsilon\prime\prime/\epsilon_0');

EpsPrec=EpsilonRel(:,2:2:40);
SigPrec=sigma(:,2:2:40);
save polCoef polEps polSig polEpsDP -ascii;
save EpsPrec EpsPrec -ascii;
save SigPrec SigPrec -ascii;
save EpsPrec EpsPrec   -ascii;
```

G.2.4 PolAppro.m

```
function polFun=PolAppro(xFunction, yFunction,timeHours, XSteps)
% This function fits the simulated data from moisture diffusion programs
%   with a 4-th degree polynomial
%   Function returns polynomial fit coefficiens
% Takes input: xFunction - vector of x values
%              yFunction - vector of y values
%              timeHours - sequence of simulated profile times
%              XSteps - discretization of x axis
% change parameter "spacer" to skip data points used in approximation

% Alex Mamishev, March 1998

% initialize the array for storage of coefficients
polFun=zeros(length(timeHours),5);
spacer = 1; % increase value to skip data points
FittedFunction = zeros(length(timeHours),(XSteps-1)/spacer);

for i3 = 1:length(timeHours)
   % compute coefficients and store them in an array
   polFun(i3,:)=...
polyfit(xFunction(1:spacer:XSteps),yFunction(i3,1:spacer:XSteps),4);
   % recompute the fitted data
   FittedFunction(i3,1:spacer:XSteps)=...
      polFun(i3,1).*xFunction(1:spacer:XSteps).^4+...
      polFun(i3,2).*xFunction(1:spacer:XSteps).^3+...
      polFun(i3,3).*xFunction(1:spacer:XSteps).^2+...
      polFun(i3,4).*xFunction(1:spacer:XSteps)+...
      polFun(i3,5);
end

figure
for i1=1:10
plot(xFunction(1:spacer:XSteps)*1000, FittedFunction(i1,1:spacer:XSteps))
   pause(0.5)
   hold on
end

% to mark the curves manually:
if 0
   for i2 = 1:length(timeHours)
      gtext(num2str(timeHours(i2)))
   end
end
```

G.2.5 eps2mo01.m

```
function [m]=eps2mo01(er1, Freq)
% Function to determine moisture content in % from
% relative dielectric permittivity at different frequencies
% By Alex Mamishev, August 97

einf = 3*8.85e-12;
e0   =   8.85e-12;
cm    =  -0.684;
fT   =   0.6;
c1   =   -0.7798;
c2   =   -0.4724;
g    =  -0.7;

m = (((er1-einf)/e0).^(-1/g)).*(10^(-(fT+cm)+c1/g)).*Freq;
```

G.2.6 datent03.m

```
function datent03()
% this function contains data to be plotted
% for stair step diffusion case

EpsPrimeMatr =...
[3 3 3 3 3 3;...
3.2 3.2 3 3 3 3;...
3.32 3.32 3.03 3.03 3 3;...
3.41 3.41 3.24 3.24 3.17 3.17;...
3.421 3.421 3.29 3.29 3.24 3.24;...
3.422 3.422 3.325 3.325 3.29 3.29;...
3.425 3.425 3.35 3.35 3.32 3.32;...
3.43 3.43 3.38 3.38 3.37 3.37;...
3.435 3.435 3.41 3.41 3.4 3.4...
];

for ii=1:9
  mostep01(EpsPrimeMatr(ii,:));
end

 figure
[x,y]=size(EpsPrimeMatr);

for ii=1:x
  xMat(ii)=ii;
end
for ii=1:y
  yMat(ii)=ii;
end

xMat=[0 0.1439 1.858 11.86 16.86 21.86 26.86 37.38 49.88];
yMat=[0 500 500 800 800 1000];

 waterfall(yMat,xMat,EpsPrimeMatr)
colormap(jet);
colorbar;
xlabel('Distance (micron)');
ylabel('Time (hours)');
zlabel('Moisture (%)');

Freq=ones(size(EpsPrimeMatr));
m=eps2mo01(EpsPrimeMatr*8.85e-12,Freq);

a= waterfall(yMat(1:6),xMat(1:9),m(1:9,1:6))
set(a,'LineWidth',2)
colormap(copper);
set(gcf,'Color',[1 1 1])
%colorbar;
xlabel('Distance (micron)');
ylabel('Time (hours)');
```

```
zlabel('Moisture (%)');

%%% Apply continuity conditons
% We will need more data points for y axis, in fact, three more intermediate points
% Upper boundary value for epsilon:
% These values come from figure J1.9
%UpperLeftEpsPrime=[3, 3.62, 3.62, 3.51, 3.49, 3.47, 3.465, 3.455, 3.45];
UpperLeftEpsPrime=[3, 3.62, 3.615, 3.52, 3.5, 3.485, 3.48, 3.47, 3.46];
% convert using the conversion equations to moisture
Freq2=ones(size(UpperLeftEpsPrime));
UpperLeftMoist=eps2mo01(UpperLeftEpsPrime*8.85e-12,Freq2)

coef=1;

% Recalculate rectangular profile into a continous profile
figure

yMatNew=yMat;
yMatNew2=ones(size(yMat)+[0 1]);
size(yMatNew2)
moistOld=m;
moistNew=moistOld;
for ii=1:length(xMat)
   %recreate thickness of the layers initial vector
   yMatNew=yMat;
   %define left boundary
   moistNew(ii,1)=UpperLeftMoist(ii);
   %scroll through all moments of time
   if((UpperLeftMoist(ii)/2)>m(ii,1))
      %convert first region to a triangle
      moistNew(ii,2)=0;
      yMatNew(2)=yMat(1)+(2*m(ii)/UpperLeftMoist(ii))*(yMat(2)-yMat(1));
   else
      %convert first region to a trapesoid
      moistNew(ii,2)=(2*m(ii,1)-UpperLeftMoist(ii))*coef;
   end
   %do the same operation on the second region
   moistNew(ii,3)=moistNew(ii,2);
   if moistNew(ii,2)==0
      moistNew(ii,4)=0;
   else
      if((moistNew(ii,3)/2)>m(ii,4))
         %convert second region to a triangle
         moistNew(ii,4)=0;
         yMatNew(4)=yMat(3)+(2*m(ii)/moistNew(ii,3))*(yMat(4)-yMat(3));
      else
         %convert second region to a trapesoid
         moistNew(ii,4)=(2*m(ii,3)-moistNew(ii,3))*coef;
      end
   end

   %do the same operation on the third region
```

```
   moistNew(ii,5)=moistNew(ii,4);
   if moistNew(ii,4)==0
      moistNew(ii,6)=0;
   else
      if((moistNew(ii,5)/2)>m(ii,6))
         %convert third region to a triangle
         moistNew(ii,6)=0;
         yMatNew(6)=yMat(5)+(2*m(ii,5)/moistNew(ii,5))*(yMat(6)-yMat(5));
      else
         %convert third region to a trapesoid
         moistNew(ii,6)=(2*m(ii,5)-moistNew(ii,5))*coef;
      end
   end

   %a= waterfall(yMatNew(1:6),xMat(ii:ii),moistNew(ii:ii,1:6));
   a=plot(yMatNew(1:6),moistNew(ii:ii,1:6));
   set(a,'LineWidth',2);
   set(gca,'FontSize',18)
   hold on;
end

%ax=axis;
%axis([ax(1) ax(2) ax(3) ax(4) 0 ax(6)])
b=xlabel('Distance (micron)');
%   ylabel('Time (hours)');
    ylabel('Moisture (%)');
```

G.3 Three-layer Inverse Problem - Fast Algorithm

G.3.1 Description of Programs

gcsort01.m converts a .ptb file of Maxwell output into a .mat file specified by the user, later to be used by **convertGCtoES.m**. Must be executed manually, separately from other programs. The input .ptb file has the following sequence of active variables: ε_r, σ, Y_{12}, Y_{11}. If the sequence of active variables is different, it should be adjusted in the fscanf command line.

Ngpimpvc.m is a routine provided by Yanqing Du to sort out the raw data from the controller.

ReadInGCSim.m reads a 6-column file of alternating conductance and capacitance values and selects two specified columns.

eps2mo01.m converts dielectric permittivity to moisture concentration.

sig2mo01.m converts conductivity to moisture concentration.

convertGCtoES.m converts conductance-capacitance data into sigma-epsilon data. All data is assumed to have been converted to a 1 Hz solution space (unless the solution spaces had been generated for other frequencies).

convertGPtoGC.m converts gain-phase data into conductance-capacitance data.

TimeToProfile.m converts time-varying data into space-varying data.

G.3.2 gcsort01.m

```
function gcsort01(DatFileName,OutFileName)
% InFileName,OutFileName
% This function reads in the unsorted output
% from Ansoft and writes the sorted (first by sigma
% and then by epsilon) data into a matlab binary
% file

% clean up the workspace
clear all; close all;
%profile gcsort;

%%% Initial data, not used in all versions
% Length of Epsilon column
NEpsilon=39;
% Length of Sigma column
NSigma=105;
% Nominal Sigma
NominalSigma = 1e-8;

%names of the input and output datafiles
%DatFileName='newlat5.ptd';
%OutFilName='newlat5';

% open data file

DatID = fopen(DatFileName,'rt');
if (DatID == -1)
disp(' ');
error('Error Opening Data File!');
end;

% Read Data to Matrix
[Data,Number] = fscanf(DatID,'setup%*i %f%f %*s%*s%*s ...
%*f %*f %*f %*s,%*s%*s,%*s %*f%*f%*f%*f (%f,%f) (%f,%f)',[6,inf]);
Number = Number / 6;
% Close File
fclose(DatID);

% Multiply -C's and -G's by -1
Data(3:6,1:Number)=(-1)*Data(3:6,1:Number);


%    sort the data first by Epsilon, if Epsilons are equal - then by Sigma

% first, sort by Sigma
[temp index] = sort(Data(2,:));

% rearrange the matrix according to this sort
SigmaSorted=Data(:,index);
```

```
% now, sort by epsilon
[temp2 index2]=sort(SigmaSorted(1,:));

% arrange according to new indexing:
DataSorted=SigmaSorted(:,index2);
DataTrans=DataSorted';
% write sorted data to a file
save (OutFilName,'DataTrans');
%load OutFilName;
```

G.3.3 Ngpimpvc.m

```
function ngpimpVc(DatFileName,filebegin,fileend,ttl,fno,Num,CL1mm,...
 CL2mm,CL5mm,VoltageBoostOrNot)
% Function ngpimpVc plots  raw data of all frequency
% data in a multi-frequency measurement in one figure using the
% time in the Head, given the frequency started at 10^fmax, ended
% at 10^fmin and the relative humidity using the new interface box.
% Data collected using Code NA*SIN1C.e
% It also computes C12 and G12.
% VoltageBoostOrNot=0, means 1 volt excitation
% VoltageBoostOrNot=1, means 10 volts boost

% Data aquisition by D.E. Schlicker
% Modified by Y. Du
% 11/11/97

% open data file

%no. of data in one measurement (between each time header
dno=2;
col=0;
fileno=fileend-filebegin+1;

for file=filebegin:fileend
file
    if (fileno==1) DatID=fopen(DatFileName,'rt');
else if(file<=9)  DatID = fopen([DatFileName '00' num2str(file) '.gpd'],'rt');
     else if(file<=99) DatID= fopen([DatFileName '0' num2str(file) '.gpd'],'rt');
else DatID=fopen([DatFileName '1' num2str(file) '.gpd'],'rt');
     end
    end
    if (DatID == -1)
disp(' ');
error('Error Opening Data File!');
    end;
    for k=1:Num*3*fno
Head(:,k+col) = fscanf(DatID,'[GH,%f,%i,%i,%i,%i,%i,%i]',7);
Data(:,col*dno+(k-1)*dno+1:col*dno+(k-1)*dno+dno)=...
fscanf(DatID,'[GD,%i,%f,%f,%f,%f,%i]',[6,dno]);
    end

    fclose(DatID);
    [row col]=size(Head);
    end
end
col=col/fno;

dno=dno*fno;

for k=1:fno
Gain1(k,:)=Data(3,k*2-1+dno*2:dno*3:col*dno-1);
```

```
Gain25(k,:)=Data(3,k*2-1+dno:dno*3:col*dno-1);
Gain5(k,:)=Data(3,k*2-1:dno*3:col*dno-1);

Offset1(k,:)=Data(5,k*2-1+dno*2:dno*3:col*dno-1);
Offset25(k,:)=Data(5,k*2-1+dno:dno*3:col*dno-1);
Offset5(k,:)=Data(5,k*2-1:dno*3:col*dno-1);
Amp1(k,:)=Data(6,k*2-1+dno*2:dno*3:col*dno-1);
Amp25(k,:)=Data(6,k*2-1+dno:dno*3:col*dno-1);
Amp5(k,:)=Data(6,k*2-1:dno*3:col*dno-1);

Phase1(k,:)=Data(4,k*2-1+dno*2:dno*3:col*dno-1);
Phase1(k,:)=Phase1(k,:)+360*(Phase1(k,:)<0)*(VoltageBoostOrNot==0);
Phase25(k,:)=Data(4,k*2-1+dno:dno*3:col*dno-1);
Phase25(k,:)=Phase25(k,:)+360*(Phase25(k,:)<0)*(VoltageBoostOrNot==0);
Phase5(k,:)=Data(4,k*2-1:dno*3:col*dno-1);
Phase5(k,:)=Phase5(k,:)+360*(Phase5(k,:)<0)*(VoltageBoostOrNot==0);

%RH for oil
RH(k,:)=(Data(5,k*4:dno*3:col*dno)-1)/4*100-2.575;

Freq(k,:)=10.^(Data(2,k*2-1+dno*2:dno*3:col*dno-1));
end


%Determine the relative time

T1=Head(3,1)*30*24+Head(4,1)*24+Head(5,1)+Head(6,1)/60+Head(7,1)/3600;
T22=T1;
for k=1:col/3
kk=k*3*fno-8;
T2=Head(3,kk)*30*24+Head(4,kk)*24+Head(5,kk)+Head(6,kk)/60+Head(7,kk)/3600;
time(k)=T2-T1;
end

% Output the Gain in dB, phase in degrees
fid=fopen('andrew1.out','w')
fprintf(fid,'%f %f %f %f %f %f %f %f %f\n',...
[Freq(1,:);Gain1(1,:);Phase1(1,:);Freq(2,:);Gain1(2,:);Phase1(2,:);Freq(3,:);...
Gain1(3,:);Phase1(3,:)]);
fclose('all')

fid=fopen('andrew2.out','w')
fprintf(fid,'%f %f %f %f %f %f %f %f %f\n',[Freq(1,:);Gain25(1,:);Phase25(1,:);...
Freq(2,:);Gain25(2,:);Phase25(2,:);Freq(3,:);Gain25(3,:);Phase25(3,:)]);
fclose('all')

fid=fopen('andrew5.out','w')
fprintf(fid,'%f %f %f %f %f %f %f %f %f\n',[Freq(1,:);Gain5(1,:);Phase5(1,:);...
Freq(2,:);Gain5(2,:);Phase5(2,:);Freq(3,:);Gain5(3,:);Phase5(3,:)]);
fclose('all')

%Impedance calculation
```

```
Gr1mm = 10.^(Gain1./20);
Fi1mm = Phase1*pi/180;

Gr25mm = 10.^(Gain25./20);
Fi25mm = Phase25*pi/180;

Gr5mm = 10.^(Gain5./20);
Fi5mm = Phase5*pi/180;

% Recalculate into real and imaginary parts of gain
Gre1 = Gr1mm.*(cos(Fi1mm));
Gim1 = Gr1mm.*(sin(Fi1mm));
cGain1=Gre1+j*Gim1;


Gre2 = Gr25mm.*(cos(Fi25mm));
Gim2 = Gr25mm.*(sin(Fi25mm));
cGain25=Gre2+j*Gim2;

Gre5 = Gr5mm.*(cos(Fi5mm));
Gim5 = Gr5mm.*(sin(Fi5mm));
cGain5=Gre5+j*Gim5;

for k=1:fno

Omega = Freq (k,1)*2*pi;
Y12m1(k,:)=(-1)^((VoltageBoostOrNot==0))*cGain1(k,:)*j*Omega*CL1mm/...
(1+9*VoltageBoostOrNot);
GG12m1(k,:)=real(Y12m1(k,:));
CC12m1(k,:)=imag(Y12m1(k,:))/Omega;

Y12m25(k,:)=(-1)^((VoltageBoostOrNot==0))*cGain25(k,:)*j*Omega*CL2mm/...
(1+9*VoltageBoostOrNot);
GG12m25(k,:)=real(Y12m25(k,:));
CC12m25(k,:)=imag(Y12m25(k,:))/Omega;

Y12m5(k,:)=(-1)^((VoltageBoostOrNot==0))*cGain5(k,:)*j*Omega*CL5mm/...
(1+9*VoltageBoostOrNot);
GG12m5(k,:)=real(Y12m5(k,:));
CC12m5(k,:)=imag(Y12m5(k,:))/Omega;
end

% Output Capacitance and Conductance Data
fid=fopen('gcdata1.out','w');
fprintf(fid,'%f %f %f %f %f %f %f %f %f\n',....
   [Freq(1,:);CC12m1(1,:);GG12m1(1,:);.....
      Freq(2,:);CC12m1(2,:);GG12m1(2,:);....
      Freq(3,:);CC12m1(3,:);GG12m1(3,:)]);
fclose(fid);

fid=fopen('gcdata2.out','w');
fprintf(fid,'%f %f %f %f %f %f %f %f %f\n',....
```

```
   [Freq(1,:);CC12m25(1,:);GG12m25(1,:);.....
      Freq(2,:);CC12m25(2,:);GG12m25(2,:);....
      Freq(3,:);CC12m25(3,:);GG12m25(3,:)]);
fclose(fid);

fid=fopen('gcdata5.out','w');
fprintf(fid,'%f %f %f %f %f %f %f %f %f\n',....
   [Freq(1,:);CC12m5(1,:);GG12m5(1,:);.....
      Freq(2,:);CC12m5(2,:);GG12m5(2,:);....
      Freq(3,:);CC12m5(3,:);GG12m5(3,:)]);
fclose(fid);


for k=1:fno
figure('PaperPosition',[0.25 0.75 8 9.5])
subplot(3,2,1), plot(time, Gain1(k,:))
xlabel('Time(hours)')
ylabel('Gain of 1.0mm (dB)')
ax=axis;
axis([0 max(time) ax(3) ax(4)]);

subplot(3,2,2), plot(time, Phase1(k,:))
xlabel('Time(hours)')
ylabel('Phase of 1.0mm (deg)')
ax=axis;
axis([0 max(time) ax(3) ax(4)]);


subplot(3,2,3) ,plot(time, Gain25(k,:))
xlabel('Time(hours)')
ylabel('Gain of 2.5mm (dB)')
ax=axis;
axis([0 max(time) ax(3) ax(4)]);

subplot(3,2,4) ,plot(time, Phase25(k,:))
xlabel('Time(hours)')
ylabel('Phase of 2.5mm (deg)')
ax=axis;
axis([0 max(time) ax(3) ax(4)]);

subplot(3,2,5), plot(time, Gain5(k,:))
xlabel('Time(hours)')
ylabel('Gain of 5.0mm (dB)')
ax=axis;
axis([0 max(time) ax(3) ax(4)]);

text('String',ttl,'Fontsize',18,'HorizontalAlignment','center','Units','Inches',...
'Position',[3 8.5])
text('String', [ num2str(Head(3)) '/' num2str(Head(4)) '/' num2str(Head(2)) ' ' ...
num2str(Head(5)) ':' num2str(Head(6)) ],'Fontsize',10,'HorizontalAlignment',...
'left','Units','Inches','Position',[5 8.2] )
text('String',  ['f= ' num2str(Freq(k)) ''] ,'Fontsize',10,...
```

```
'HorizontalAlignment','left','Units','Inches','Position',[5 8.05] )
text('String', ['File:' DatFileName ],'Fontsize',10,'HorizontalAlignment','left',...
'Units','Inches','Position',[5 7.9] )

subplot(3,2,6), plot(time, Phase5(k,:))
xlabel('Time(hours)')
ylabel('Phase of 5.0mm (deg)')
ax=axis;
axis([0 max(time) ax(3) ax(4)]);

%************************************ Plot Impedance
figure('PaperPosition',[0.25 0.75 8 9.5])
subplot(3,2,1), plot(time, CC12m1(k,:))
xlabel('Time(hours)')
ylabel('C12 of 1.0mm (pF)')
ax=axis;
axis([0 max(time) ax(3) ax(4)]);

subplot(3,2,2), plot(time, GG12m1(k,:))
xlabel('Time(hours)')
ylabel('G12 of 1.0mm (pS)')
ax=axis;
axis([0 max(time) ax(3) ax(4)]);


subplot(3,2,3) ,plot(time, CC12m25(k,:))
xlabel('Time(hours)')
ylabel('C12 of 2.5mm (pF)')
ax=axis;
axis([0 max(time) ax(3) ax(4)]);

subplot(3,2,4) ,plot(time, GG12m25(k,:))
xlabel('Time(hours)')
ylabel('G12 of 2.5mm (pS)')
ax=axis;
axis([0 max(time) ax(3) ax(4)]);

subplot(3,2,5), plot(time, CC12m5(k,:))
xlabel('Time(hours)')
ylabel('C12 of 5.0mm (pF)')
ax=axis;
axis([0 max(time) ax(3) ax(4)]);

text('String',ttl,'Fontsize',18,'HorizontalAlignment','center','Units','Inches',...
'Position',[3 8.5])
text('String', [ num2str(Head(3)) '/' num2str(Head(4)) '/' num2str(Head(2)) ' ' ...
num2str(Head(5)) ':' num2str(Head(6)) ],'Fontsize',10,'HorizontalAlignment',...
'left','Units','Inches','Position',[5 8.2] )
text('String',  ['f= ' num2str(Freq(k)) ''] ,'Fontsize',10,...
'HorizontalAlignment','left','Units','Inches','Position',[5 8.05] )
text('String', ['File:' DatFileName ],'Fontsize',10,'HorizontalAlignment','left',...
'Units','Inches','Position',[5 7.9] )
```

```
subplot(3,2,6), plot(time, GG12m5(k,:))
xlabel('Time(hours)')
ylabel('G12 of 5.0mm (pS)')
ax=axis;
axis([0 max(time) ax(3) ax(4)]);
end



figure
plot(time,RH(1,:))
ax=axis;
axis([0 max(time) ax(3) ax(4)])
xlabel('Time (hours)')
ylabel('%')
ax=axis;
if ((ax(4)-ax(3))<3) ax(4)=ceil((ax(4)-ax(3))/2+ax(3)+2);
ax(3)=floor((ax(4)-ax(3))/2+ax(3)-2);
elseif (max(RH(k,:))-min(RH(k,:))>10)
ax(4)=ceil(max(RH(k,:)));
ax(3)=floor(min(RH(k,:)));
end
axis([0 max(time) ax(3) ax(4)]);
text('String','','Fontsize',18,'HorizontalAlignment','center','Units','Inches',...
'Position',[3 6.5])
text('String', [ num2str(Head(3)) '/' num2str(Head(4)) '/' num2str(Head(2)) ' ' ...
num2str(Head(5)) ':' num2str(Head(6)) ],'Fontsize',10,'HorizontalAlignment',...
'left','Units','Inches','Position',[5 5.8] )
text('String', ['File:' DatFileName ],'Fontsize',10,'HorizontalAlignment','left',...
'Units','Inches','Position',[5 5.5] )
```

G.3.4 ReadInGCSim.m

```
function [G,C]=ReadInGCSim(Datafile,col1,col2)
% example: ReadInGCSim('MaxOut.dat',1,2)
% assigns values in the columns 1 and 2 of datafile MaxOut.dat to conductance and
% capacitance on the left
% This function will read the simulation results arranged in columns in ascii format
% Six columns are required (two for each wavelength)
% output format from the analyze.m program written by Yanqing.
% Datafile is a string referring to the name of the datafile in the matlab path.
%
% Alex Mamishev, June 1998

% Open Datafile
DatID = fopen(Datafile,'rt');
if (DatID == -1)
disp(' ');
error('Error Opening Data File!');
end;

% Read Data to Matrix
[Data,Number] = fscanf(DatID,'%f %f %f %f %f %f',[6,inf]);
Number = Number / 6;

% Close data file
fclose(DatID);

% form the requested columns

G = -1*Data(col1,:);
C = -1*Data(col2,:);
```

G.3.5 eps2mo01.m

```
function [m]=eps2mo01(er1, Freq)
% Function to determine moisture content in % from
% relative dielectric permittivity at different frequencies
% [m] = function eps2mo01(er1, Freq)
% By Alex Mamishev, August 97
einf = 3*8.85e-12;
e0   =   8.85e-12;
cm    =  -0.684;
fT   =   0.6;
c1   =   -0.7798;
c2   =   -0.4724;
g    =  -0.7;

m = (((er1-einf)/e0).^(-1/g)).*(10^(-(fT+cm)+c1/g)).*Freq;
```

G.3.6 sig2mo01.m

```
function [m]=sig2mo01(sigma, Freq)
% Function to determine moisture content in % from
% relative dielectric permittivity at different frequencies
% [m] = function eps2mo01(er1, Freq)
% By Alex Mamishev, August 97
einf = 3*8.85e-12;
e0   =   8.85e-12;
cm    =  -0.684;
fT   =   0.6;
c1   =   -0.7798;
c2   =   -0.4724;
g    =  -0.7;

m = (((sigma/(2*pi*Freq))/e0).^(-1/g)).*(10^(-(fT+cm)+c2/g)).*Freq;
```

G.3.7 convertGPtoGC.m

```
function [rEpsilon, rSigma]=...
   convertGCtoES(SolSpaceFileName,Gvector,Cvector,Lmeander,lambda)
%function [rEpsilon, rSigma]=...
%%%convertGCtoES(SolSpaceFileName,Gvector,Cvector,Lmeander)
%%% converts Capacitance/Conductance data into epsilon/sigma data
%%% input variables: binary file that contains the  ...
%%% GCES solution space (SolSpaceFileName),
%%%  vector of conductances(Gvector), vector of capacitances (Cvector),
%%% Lmeander is the meandering length of the sensor in m,
%%% lambda is an index equal to 1, 2.5, or 5
%%% Conductance data should be in picosiemens and
%%% Capacitance should be in picofarads
%
%%% example of usage: [Epsilon, Sigma]=convertGCtoES('solspace.mat',Gexp,Cexp).
%%% In this example the file 'solspace.mat' has been generated by the routine
%%% gcsort01('inputfile.ptd','solspace'), where
%%% the file 'inputfile.ptd is generated with
%%% the parametric sweep option of Maxwell
%%% Alex Mamishev, January 1998
% Modified by Andrew Takahashi

% Initialize
  numberOfContours=10;
  numberOfPoints = 10; % This is the number of points to use in determining the
                       % local surface

% load the solution space file
load(SolSpaceFileName);

Data=DataTrans;
% Extract/Organize Data
%  The division by 1e6 used to occurs because the Solution space is generated
% with relative permittivity and conductivity   multiplied by 1e6
% It is no longer necessary with the new version of Maxwell.
RowCol=size(Data);
Epsilon = Data(1:RowCol(1),1);
Sigma = Data(1:RowCol(1),2);

G12 = Data(1:RowCol(1),3)*Lmeander;
C12 = Data(1:RowCol(1),4)*Lmeander;

% Prepare data for linear approximation of non-conductive data
C12ForLinear=Cvector*0.5e12/Lmeander;


% G11 and C11 are not used but are kept for future reference
G11 = Data(1:RowCol(1),5);
C11 = Data(1:RowCol(1),6);

% calculate the epsilon value from each GC pair
```

```
%simulationData will be a four column matrix [epsilon, sigma, G12, C12]
simulationData = [Epsilon, Sigma, G12, C12];
measurementPoint = [Gvector; Cvector];

%Calculate distance from each measurement point to each of the simulation points
simDataSize = size(simulationData,1);
size(simulationData);

% EuclDistance is a 5 column vector
EuclDistance=[simulationData,zeros(simDataSize,1)];
rEpsilon=zeros(1,length(Gvector));
rSigma=zeros(1,length(Gvector));

%%%% Calculate interpolated data for each measurement datapoint
for n=1:length(Gvector)
   n
   GDistanceNorm=(EuclDistance(:,3)-Gvector(n))/Gvector(n);
   CDistanceNorm=(EuclDistance(:,4)-Cvector(n))/Cvector(n);
   temp=sqrt(GDistanceNorm.^2+CDistanceNorm.^2);
   EuclDistance(:,5) = temp;

   %Sort by distance (column 5 of distance matrix)
   EuclDistance = sortrows(EuclDistance,5);

   %Find 'n' closest points (as defined in numberOfPoints variable).
   localData = EuclDistance(1:numberOfPoints,:);
   %  %Find the closest point
   localClosest=EuclDistance(1,:);

   % select local data
   epsilonLoc = localData(:,1);
   sigmaLoc = localData(:,2);
   G12Loc = localData(:,3);
   C12Loc = localData(:,4);

   %Transform selected simulation points into plaid and monotonic form
   mig = linspace(min(G12Loc),max(G12Loc),numberOfPoints);
   mic = linspace(min(C12Loc),max(C12Loc),numberOfPoints);
   [mpig,mpic] = meshgrid(mig,mic);
   iEpsilon = griddata(G12Loc,C12Loc,epsilonLoc,mpig,mpic);
   iH = griddata(G12Loc,C12Loc,sigmaLoc,mpig,mpic);

   %Interpolate to find h and epsilon for measurement data
   rEpsilon(n) = interp2(mpig,mpic,iEpsilon,Gvector(n),Cvector(n));
   rSigma(n) = interp2(mpig,mpic,iH,Gvector(n),Cvector(n));

   % if detecting NaN, use the interpolation only with epsilon data

   if (isnan(rEpsilon(n))==1)

   % Sort epsilonLoc into a monotonically increalsing vector
    SigmaSorted=sortrows(simulationData,2);
```

```
   epsSorted=SigmaSorted(1:39,1);
   C12Sorted=SigmaSorted(1:39,4);
   Cvector(n)
   rEpsilon(n)= interp1q(C12Sorted, epsSorted, Cvector(n));
end

   if isnan(rSigma(n))==1
      rSigma(n)=0;
   end

if 0
    % if detecting NaN, use the closest point
   if (isnan(rEpsilon(n))==1 & lambda==5)
      rEpsilon(n)= 1.05*sqrt(C12ForLinear(n))+0.37*C12ForLinear(n)+(-0.38);
   end
   if (isnan(rEpsilon(n))==1 & lambda==2.5)
      rEpsilon(n)= 0.55*sqrt(C12ForLinear(n))+0.39*C12ForLinear(n)+(-0.32);
   end
   if (isnan(rEpsilon(n))==1 & lambda==1)
      rEpsilon(n)= 0.1467*sqrt(C12ForLinear(n))+0.38*C12ForLinear(n)+(-0.647);
   end

   if isnan(rSigma(n))==1
      rSigma(n)=0;
   end

 end
end

if 0

 %Plot using Delaunay triangulation
% Plot delaunay surface of simulation solution space
figure;
subplot(2,1,1);
tri = delaunay(log10(G12),C12);
trisurf(tri, log10(G12), C12, Epsilon);
title('Epsilon', 'FontName','Arial');
xlabel('log10 G_1_2','FontName','Arial');
ylabel('C_1_2 ','FontName','Arial');

subplot(2,1,2);
tri = delaunay(log10(G12),C12);
trisurf(tri, log10(G12), C12, log10(Sigma));
title('log10 Sigma','FontName','Arial');
xlabel('log10 G_1_2','FontName','Arial');
ylabel('C_1_2','FontName','Arial');
end;

if 0
   % This is used to show a contour plot of the local interpolated surface.
   % Currently only works for the last point generated since it requires the
```

```
   % use of iH and iEpsilon which are generated inside the loop.
   figure;

   subplot(2,1,1);
   contour(mpig,mpic,iEpsilon,numberOfContours);
   colorbar;
   hold on;
   plot3(measurementPoint(1,238),measurementPoint(2,238),1,'k*','MarkerSize',5);
   title('Epsilon','FontName','Arial');
   xlabel('G_1_2','FontName','Arial');
   ylabel('C_1_2','FontName','Arial');

   subplot(2,1,2);
   contour(mpig,mpic,iH,numberOfContours);
   colorbar;
   hold on;
   plot3(measurementPoint(1,238),measurementPoint(2,238),1,'k*','MarkerSize',5);
   title('Sigma','Fontname','Arial');
   xlabel('G_1_2 ','Fontname','Arial');
   ylabel('C_1_2 ','Fontname','Arial');
end
```

G.3.8 convertGCtoES.m

```
function [rEpsilon, rSigma]=...
   convertGCtoES(SolSpaceFileName,Gvector,Cvector,Lmeander,lambda)
%function [rEpsilon, rSigma]=...
%%%convertGCtoES(SolSpaceFileName,Gvector,Cvector,Lmeander)
%%% converts Capacitance/Conductance data into epsilon/sigma data
%%% input variables: binary file that contains the  ...
%%% GCES solution space (SolSpaceFileName),
%%%  vector of conductances(Gvector), vector of capacitances (Cvector),
%%% Lmeander is the meandering length of the sensor in m,
%%% lambda is an index equal to 1, 2.5, or 5
%%% Conductance data should be in picosiemens and
%%% Capacitance should be in picofarads
%
%%% example of usage: [Epsilon, Sigma]=convertGCtoES('solspace.mat',Gexp,Cexp).
%%% In this example the file 'solspace.mat' has been generated by the routine
%%% gcsort01('inputfile.ptd','solspace'), where
%%% the file 'inputfile.ptd is generated with
%%% the parametric sweep option of Maxwell
%%% Alex Mamishev, January 1998
% Modified by Andrew Takahashi

% Initialize
  numberOfContours=10;
  numberOfPoints = 10; % This is the number of points to use in determining the
                       % local surface

% load the solution space file
load(SolSpaceFileName);

Data=DataTrans;
% Extract/Organize Data
%  The division by 1e6 used to occurs because the Solution space is generated
% with relative permittivity and conductivity   multiplied by 1e6
% It is no longer necessary with the new version of Maxwell.
RowCol=size(Data);
Epsilon = Data(1:RowCol(1),1);
Sigma = Data(1:RowCol(1),2);

G12 = Data(1:RowCol(1),3)*Lmeander;
C12 = Data(1:RowCol(1),4)*Lmeander;

% Prepare data for linear approximation of non-conductive data
C12ForLinear=Cvector*0.5e12/Lmeander;


% G11 and C11 are not used but are kept for future reference
G11 = Data(1:RowCol(1),5);
C11 = Data(1:RowCol(1),6);

% calculate the epsilon value from each GC pair
```

```
%simulationData will be a four column matrix [epsilon, sigma, G12, C12]
simulationData = [Epsilon, Sigma, G12, C12];
measurementPoint = [Gvector; Cvector];

%Calculate distance from each measurement point to each of the simulation points
simDataSize = size(simulationData,1);
size(simulationData);

% EuclDistance is a 5 column vector
EuclDistance=[simulationData,zeros(simDataSize,1)];
rEpsilon=zeros(1,length(Gvector));
rSigma=zeros(1,length(Gvector));

%%%% Calculate interpolated data for each measurement datapoint
for n=1:length(Gvector)
   n
   GDistanceNorm=(EuclDistance(:,3)-Gvector(n))/Gvector(n);
   CDistanceNorm=(EuclDistance(:,4)-Cvector(n))/Cvector(n);
   temp=sqrt(GDistanceNorm.^2+CDistanceNorm.^2);
   EuclDistance(:,5) = temp;

   %Sort by distance (column 5 of distance matrix)
   EuclDistance = sortrows(EuclDistance,5);

   %Find 'n' closest points (as defined in numberOfPoints variable).
   localData = EuclDistance(1:numberOfPoints,:);
   %  %Find the closest point
   localClosest=EuclDistance(1,:);

   % select local data
   epsilonLoc = localData(:,1);
   sigmaLoc = localData(:,2);
   G12Loc = localData(:,3);
   C12Loc = localData(:,4);

   %Transform selected simulation points into plaid and monotonic form
   mig = linspace(min(G12Loc),max(G12Loc),numberOfPoints);
   mic = linspace(min(C12Loc),max(C12Loc),numberOfPoints);
   [mpig,mpic] = meshgrid(mig,mic);
   iEpsilon = griddata(G12Loc,C12Loc,epsilonLoc,mpig,mpic);
   iH = griddata(G12Loc,C12Loc,sigmaLoc,mpig,mpic);

   %Interpolate to find h and epsilon for measurement data
   rEpsilon(n) = interp2(mpig,mpic,iEpsilon,Gvector(n),Cvector(n));
   rSigma(n) = interp2(mpig,mpic,iH,Gvector(n),Cvector(n));

   % if detecting NaN, use the interpolation only with epsilon data

   if (isnan(rEpsilon(n))==1)

   % Sort epsilonLoc into a monotonically increalsing vector
    SigmaSorted=sortrows(simulationData,2);
```

```
   epsSorted=SigmaSorted(1:39,1);
   C12Sorted=SigmaSorted(1:39,4);
   Cvector(n)
   rEpsilon(n)= interp1q(C12Sorted, epsSorted, Cvector(n));
end

   if isnan(rSigma(n))==1
      rSigma(n)=0;
   end

if 0
    % if detecting NaN, use the closest point
   if (isnan(rEpsilon(n))==1 & lambda==5)
      rEpsilon(n)= 1.05*sqrt(C12ForLinear(n))+0.37*C12ForLinear(n)+(-0.38);
   end
   if (isnan(rEpsilon(n))==1 & lambda==2.5)
      rEpsilon(n)= 0.55*sqrt(C12ForLinear(n))+0.39*C12ForLinear(n)+(-0.32);
   end
   if (isnan(rEpsilon(n))==1 & lambda==1)
      rEpsilon(n)= 0.1467*sqrt(C12ForLinear(n))+0.38*C12ForLinear(n)+(-0.647);
   end

   if isnan(rSigma(n))==1
      rSigma(n)=0;
   end

 end
end

if 0

 %Plot using Delaunay triangulation
% Plot delaunay surface of simulation solution space
figure;
subplot(2,1,1);
tri = delaunay(log10(G12),C12);
trisurf(tri, log10(G12), C12, Epsilon);
title('Epsilon', 'FontName','Arial');
xlabel('log10 G_1_2','FontName','Arial');
ylabel('C_1_2 ','FontName','Arial');

subplot(2,1,2);
tri = delaunay(log10(G12),C12);
trisurf(tri, log10(G12), C12, log10(Sigma));
title('log10 Sigma','FontName','Arial');
xlabel('log10 G_1_2','FontName','Arial');
ylabel('C_1_2','FontName','Arial');
end;

if 0
   % This is used to show a contour plot of the local interpolated surface.
   % Currently only works for the last point generated since it requires the
```

```
   % use of iH and iEpsilon which are generated inside the loop.
   figure;

   subplot(2,1,1);
   contour(mpig,mpic,iEpsilon,numberOfContours);
   colorbar;
   hold on;
   plot3(measurementPoint(1,238),measurementPoint(2,238),1,'k*','MarkerSize',5);
   title('Epsilon','FontName','Arial');
   xlabel('G_1_2','FontName','Arial');
   ylabel('C_1_2','FontName','Arial');

   subplot(2,1,2);
   contour(mpig,mpic,iH,numberOfContours);
   colorbar;
   hold on;
   plot3(measurementPoint(1,238),measurementPoint(2,238),1,'k*','MarkerSize',5);
   title('Sigma','Fontname','Arial');
   xlabel('G_1_2 ','Fontname','Arial');
   ylabel('C_1_2 ','Fontname','Arial');
end
```

G.3.9 TimeToProfile.m

```
function TimeToProfile(V5mm,V2mm,V1mm, moistLim, VLim, Interval)
set(0,'DefaultTextFontSize',16);

V5mmAdj=(V5mm*V1mm(1)/V5mm(1));
V2mmAdj=V2mm*V1mm(1)/V2mm(1);
V1mmAdj=V1mm*V1mm(1)/V1mm(1);

% create the time vector in hours
tHours = ones(1,length(V5mm));
for ii=1:length(V5mm)
   tHours(ii) = ii/(Interval/2);
end

% overwrite the time vector if data is not equally spaced
%(still have to use Interval = 1)
if 1
   tHours=[0 0.1 0.5 1 2 3 5 10 15 20 30];
end

if 0
figure
plot(V5mmAdj,'*')
hold on
plot(V5mmAdj)
plot(V2mmAdj)
plot(V2mmAdj,'o')
plot(V1mmAdj)
plot(V1mmAdj,'.')
end

Mo5mm=(V5mmAdj-V5mmAdj(1))/(max(V5mmAdj)-V5mmAdj(1))*moistLim(2);
Mo2mm=(V2mmAdj-V2mmAdj(1))/(max(V2mmAdj)-V2mmAdj(1))*moistLim(2);
Mo1mm=(V1mmAdj-V1mmAdj(1))/(max(V1mmAdj)-V1mmAdj(1))*moistLim(2);

if 1
figure
a= plot(tHours,Mo5mm); hold on; % plot(Mo5mm)
%set(a,'LineWidth',1.2);
plot(tHours,Mo2mm); % plot(Mo2mm,'o')
%set(a,'LineWidth',1.2);
plot(tHours,Mo1mm); % plot(Mo1mm,'.-')
%set(a,'LineWidth',1.2);
size(tHours)

set(gca,'FontSize',20)
xlabel('Time (hours)','FontSize',20)
ylabel('Moisture concentration (%)','FontSize',20)
%axis([0 30 0 2])

end
```

```
% plot a stair-step profile

if 1
   figure
   for n=1:Interval:length(V5mm)
   ySdata(1)=Mo5mm(n);
   ySdata(2)=Mo5mm(n);
   ySdata(3)=Mo2mm(n);
   ySdata(4)=Mo2mm(n);
   ySdata(5)=Mo1mm(n);
   ySdata(6)=Mo1mm(n);
   PlotSteps(ySdata)
   hold on
end
if 0
   for iii=1:3
   for ii=1:length(tHours)
      gtext(num2str(tHours(ii)))
   end
   end
end
end

% plot a continuous profile
 for n=1:Interval:length(V5mm)
    MoiMat(1,:)=Mo5mm;
    MoiMat(2,:)=Mo5mm;
    MoiMat(3,:)=Mo2mm;
    MoiMat(4,:)=Mo2mm;
    MoiMat(5,:)=Mo1mm;
    MoiMat(6,:)=Mo1mm;
 end
 MoiMat=MoiMat';

% Plot mass conservation line profile
   yMat=[0  500 500 800 800 1000];
   boundary=10*ones(size(V5mm))
   PlotTriangles2(tHours,yMat,MoiMat,boundary);
   xlabel('Depth into pressboard, (\mu m)')
   ylabel('Moisture concentration (%)')
if 1
      for ii=1:length(tHours)
          gtext(num2str(tHours(ii)))
      end
end


if 1
   figure
   for n=1:Interval:length(V5mm)
   ySdata(1)=Mo5mm(n);
   ySdata(2)=Mo5mm(n);
```

```
   ySdata(3)=Mo2mm(n);
   ySdata(4)=Mo2mm(n);
   ySdata(5)=Mo1mm(n);
   ySdata(6)=Mo1mm(n);
   PlotSteps(ySdata)
   hold on
end
if 0
   for iii=1:3
   for ii=1:length(tHours)
      gtext(num2str(tHours(ii)))
   end
   end
end

% go from region values to the boundary values

Mo01=2*Mo1mm-Mo2mm;
Mo01=Mo1mm;
Mo12=(Mo1mm+Mo2mm)/2;
Mo25=(Mo2mm+Mo5mm)/2;

if 1
   figure
   plot(Mo25,'*'); hold on; plot(Mo25)
   plot(Mo12); plot(Mo12,'o')
   plot(Mo01); plot(Mo01,'.')
end


figure
for n=1:Interval:length(V5mm)
   ydata(1)=moistLim(2);
   ydata(2)=Mo25(n);
   ydata(3)=Mo12(n);
   ydata(4)=Mo01(n);
   PlotProfile([0 500 800 1000],ydata)
   hold on
end
if 0
   for ii=1:length(tHours)
      gtext(num2str(tHours(ii)))
   end
end
end
```

Appendix H

Matlab Code For Maxwell Optimization GUI

Most of this code has been written by undergraduate students Binh Truong [42], John Miller [43], Gaurav Tewari [46], and Jason Bau [48] under my close supervision. All routines are commented inside the code. See top of each file for the function description.

H.1 Matlab Code For Preliminary Steps

H.1.1 autsens3.m

```
%this is the function that did the first sub-project.  This
%extracted the data from the parametric sweep to give us our
%non-dimensionalized plot of C12

function [out1,out2,out3,out4]=autsens3(InpFile,OutFile,lambda,eps)


% clean up the workspace
%clear all; close all;
close all
set(0,'DefaultAxesFontSize',18)
size set(0,'DegaultTextFontSize',18)

% open data file
```

```
DatID = fopen(InpFile,'rt');
if (DatID == -1)
disp(' ');
error('Error Opening Data File!');
end;

% Read Data to Matrix
[Data,Number] = fscanf(DatID,'setup%i %f %f %*s%*s%*s %*f %*f %*f...
 %*s,%*s %*s,%*s %*f %*f %*f %*f %f %f',[5,inf]);
Number = Number / 5;
% Close File
fclose(DatID);

Col1=Data(2,:);
Col2=Data(3,:);

% Find dimension of variable columns
Var2Len=0;
ii=1;

while Data(2,1) == Data(2,ii)
  Var2Len = Var2Len+1;
  ii=ii+1;
end

Var1Len = Number/Var2Len;
lambda=sscanf(lambda,'%f');
eps=sscanf(eps,'%f');
% Form Variable Vectors
Var1 = Data(2,Var2Len:Var2Len:Number);
Var1 = inv(lambda).*Var1;
Var2 = Data(3,1:Var2Len);
Var2 = inv(eps).*Var2;
% Form Capacitance Vectors
Cap12Vec = Data(4,:)*(-1e11);
Cap13Vec=Data(5,:)*(-1e11);
Var1Len
% Form rectangular arrays
Cap12Matr = zeros(Var1Len, Var2Len);
for ii=1:Var1Len
   Cap12Matr(ii,:) = Cap12Vec(1+(ii-1)*Var2Len:Var2Len+(ii-1)*Var2Len);
end
Cap13Matr = zeros(Var1Len, Var2Len);
for ii=1:Var1Len
   Cap13Matr(ii,:) = Cap13Vec(1+(ii-1)*Var2Len:Var2Len+(ii-1)*Var2Len);
end

Cap12hf=zeros(Var1Len/2,Var2Len);
Cap13hf=Cap12hf;
Var1hf=zeros(1,Var1Len/2);
for ll=1:Var1Len/2
   Var1hf(ll)=Var1(ll);
```

```
   Cap12hf(ll,:)=Cap12Matr(ll,:);
   Cap13hf(ll,:)=Cap13Matr(ll,:);
end


Var1thin=zeros(1,Var1Len/4);
Var2thin=zeros(1,Var2Len/4);
Cap12thintmp=zeros(Var1Len/4,Var2Len);
Cap13thintmp=Cap12thintmp;
Cap12thin=zeros(Var1Len/4,Var2Len/4);
Cap13thin=Cap12thin;

for jj=2:2:Var1Len/2
   Var1thin(jj/2)=Var1(jj);
   Cap12thintmp(jj/2,:)=Cap12Matr(jj,:);
   Cap13thintmp(jj/2,:)=Cap13Matr(jj,:);
end

for kk=2:2:Var2Len
   Var2thin(kk/2)=Var2(kk);
   Cap12thin(:,kk/2)=Cap12thintmp(:,kk);
   Cap13thin(:,kk/2)=Cap13thintmp(:,kk);
end
%out1=Var1thin;
%out2=Var2thin;
%out3=Cap12thin;
%out4=Cap13thin;
figure
mesh(Var2thin,Var1thin,Cap12thin);
axis([0,10,0,.5,0,50]);
zlabel('C_1_2/\epsilon_s')
xlabel('\epsilon_m/\epsilon_s');
ylabel('{\it d}/\lambda');
%title('C_1_2/\epsilon_s')


Var1s=zeros(1,.3*Var1Len);
Var2s=zeros(1,.2*Var2Len);
Cap12stmp=zeros(.3*Var1Len,Var2Len);
Cap12s=zeros(.3*Var1Len,.2*Var2Len);

for ll=1:Var1Len*.3
   Var1s(ll)=Var1(ll);
   Cap12stmp(ll,:)=Cap12Matr(ll,:);
end

for mm=1:Var2Len*.2
   Var2s(mm)=Var2(mm);
   Cap12s(:,mm)=Cap12stmp(:,mm);
end
figure
hold on
```

```
v=linspace(1,10,10);
[g,b]=contour(Var2s,Var1s,Cap12s,v);
y=clabel(g,b);
set(y,'FontSize',18);
xlabel('Normalized dielectric constant, \epsilon_m/\epsilon_s');
ylabel('Normalized substrate thickness, {\it d}/\lambda');
axis([0,2,0,.3]);
o=[.47 .47 .47 ];
a=[.254 .1016 .0508];
plot(o,a,'b*','MarkerSize',8);
o1=[1.0476 1.0476 1.0476];
a1=[.254 .1016 .0508];
plot(o1,a1,'bv','MarkerSize',8);
hold off
%title('C_1_2');


v=linspace(3,45,15);
figure
[c,h]=contour(Var2,Var1hf,Cap12hf,v);
w=clabel(c,h);
set(w,'FontSize',18);
xlabel('Normalized dielectric constant, \epsilon_m/\epsilon_s');
ylabel('Normalized substrate thickness, {\it d}/\lambda');
title('C_1_2')
figure
vv=[2,3,4,6,8,10,15,20,30,40,60,100,120,150];
[d,j]=contour(Var2,Var1hf,Cap13hf,vv);
x=clabel(d,j);
set(x,'FontSize',18);
xlabel('Normalized dielectric constant, \epsilon_m/\epsilon_s');
ylabel('Normalized substrate thickness, {\it d}/\lambda');
title('C_1_3')
figure
mesh(Var2,Var1hf,Cap13hf);
axis([0,10,0,.5,0,200])
zlabel('C_1_3/\epsilon_s')
xlabel('\epsilon_m/\epsilon_s');
ylabel('{\it d}/\lambda');
title('C_1_3/\epsilon_s')

Var1spc=Var1(6);
Cap12spct=Cap12Matr(6,:);
Cap13spct=Cap13Matr(6,:);
for i = 8:2:Var1Len
   Var1spc = [Var1spc Var1(i)];
   Cap12spct = [Cap12spct; Cap12Matr(i,:)];
   Cap13spct = [Cap13spct; Cap13Matr(i,:)];
end
Cap12spc=Cap12spct(:,3);
Cap13spc=Cap13spct(:,3);
Var2spc = Var2(3);
```

```
for j=4:1:Var2Len-2
   Var2spc = [Var2spc Var2(j)];
   Cap12spc = [Cap12spc Cap12spct(:,j)];
   Cap13spc = [Cap13spc Cap13spct(:,j)];
end


%out1=Cap12Matr;
%out2=Cap13Matr;
out1=Var1spc;
out2=Var2spc;
out3=Cap12spc;
out4=Cap13spc;
```

H.1.2 approx.m

```
%This is the m-file which does the 3rd order polynomial
%Approximation of the Normalized Capacitance plot

set(0,'DefaultAxesFontSize',18)
size set(0,'DegaultTextFontSize',18)

p=polyfit2d(e,f,c,3,3);
z=polyval2d(p,e,f);
diff=(c-z)./c*100;
figure
mesh(thin(b),thin(half(a)),thin(half(z')'));
axis([0,10,0,.5,0,50]);
zlabel('C_1_2/\epsilon_s')
xlabel('\epsilon_m/\epsilon_s');
ylabel('{\it d}/\lambda');
title('C_1_2/\epsilon_s, 3rd-order-polynomial approximation')

figure
mesh(b,a,z);
figure
mesh(b,a,diff);
clear('u','v','x','v1');
figure
 for sl=3:length(a)
 u(sl)=a(sl);
 v(sl,:)=diff(sl,:);
end
for jw=3:length(b)
   x(jw)=b(jw);
   v1(:,jw)=v(:,jw);
end
mesh(x,u,v1);
xlabel('\epsilon_m/\epsilon_s');
ylabel('{\it d}/\lambda');
zlabel('Deviation (%)')
title('Error of 3rd-order-polynomial')
```

H.1.3 lastdir.m

```
%a little helper function that finds
%the last directory listed in a path

function s=lastdir(path)
[c d]= strtok(path, '\');
[e f]= size(d);
if (f == 0)
   s = c;
else s=lastdir(d);
end
```

H.1.4 paracoef.m

```
%This is the parametric coefficent routine described in the
%report.

function [e,s]=paracoef(epsfile,sigfile,projpath)
projname=lastdir(projpath);
[projname b]= strtok(projname, '.');
ptdID = fopen(strcat(projpath,'\',projname,'.ptd'),'rt+');
ptbID = fopen(strcat(projpath,'\',projname,'.ptb'),'rt+');

if ptdID == -1 | ptbID == -1
error('Error Opening Data File!');
end;

[n1 n2]=setupnums(ptbID,ptdID);

epsname=lastdir(epsfile)
[epsname b] = strtok(epsname, '.');
load(epsfile)
eps=eval(epsname);

signame=lastdir(sigfile)
[signame b] = strtok(signame, '.');
load(sigfile)
sig=eval(signame);

c=size(sig);
d=size(eps);

c1=c(1);
[final junk]=ptbscan(ptbID);
fseek(ptbID,-9,1);
for i=1:c1
   epsstr=num2str(eps(i,:),'%8g ');
   sigstr=num2str(sig(i,:),'%8g ');
   n1=n1-1;
   n2=n2+1;
   s1=num2str(n1);
   s2=num2str(n2);
   o=strcat('setup',s2,'1 ',epsstr,sigstr,'F F T',final);
   fprintf(ptdID,'%s\n',o);
   fprintf(ptbID,' B_ROW %s \n  \n E_ROW \n',s1);
end
fseek(ptbID,-15,1)
fprintf(ptbID,'33 \n  \n E_ROW \nE_DATA \n');


e=eps;
s=o;
```

```
fclose(ptdID);
fclose(ptbID);
```

H.1.5 setupnums.m

```
%This function looks through the .ptd and .ptb
%files to find the current setup number, which
%is the first line of the parametric sweeps screen.


function [o1, o2]=setupnums(ptbfid,ptdfid)
o1=0;
o2=0;
fseek(ptbfid,0,-1);
fseek(ptdfid,0,-1);
while ~feof(ptbfid)
   line1=fgetl(ptbfid);
   if length(findstr(line1,'B_ROW'))==1
      o1=sscanf(line1,'B_ROW %i');
   end
end
while ~feof(ptdfid)
   line2=fgetl(ptdfid);
   if length(findstr(line2,'setup'))==1
      o2=sscanf(line2,'setup%i');
   end
end
```

H.2 Code for Graphical User Interface

H.2.1 Guifunc.m

This is the function which handles all of the GUI actions.

```
function guifunc(action)

%Function "guifunc" interfaces the GUI with Maxwell, and handles all
% callbacks in the interface.


%callback function for the Maxwell GUI

global homed; %Global home directory containing all relevant programs to solve the
              %  optimization problem at hand
global project1; %Wavelength we are really interested in solving for
                 %creating more "projects" will create more wavelengths
global varvals;   %the values of all the variables, in a vector
global varnames;  %the corresponding names of variables, also in vector format
global varexc;   %whether to exclude the respective variable in optimization.
global opt_routine;%Stores user-specified name of optimization routine
global costfunction; %Name of the cost function which the optimization routine
                     %will use
global ansoft_dir; %Directory which contains Ansoft application program
global optchoice; %the optimization routine
global numouts; %the number of output variables (not a string)
global vlb; %the absolute upper and lower bounds, used in constr
global vub;
%The following "switch" structure constitutes the backbone of this program
% The cases of the statement are comprised of the "actions" requested by the
% callback functions of the GUI. (the various callback functions corresponding
% to each graphic in the GUI may be seen readily using the Callback editor in
% GUIDE

switch action

case 'FuncFile' %Specification of Optimization fuction file
   opt_func_file = get(gcbo, 'String');

case 'AnsoftDir'%Specification of the Ansoft application program directory
   ansoft_dir = get(gcbo, 'String');
   %Start Maxwell from here
   cd (ansoft_dir);
   !maxwell

case 'HomeDir'%Specification of the 'home' directory (where all subroutines
              % are placed together)
   homed = get(gcbo, 'String');
   cd (homed);
case 'ProjectDir1'%Specification of the directory corresponding to the first
```

```
                % wavelength
   project1 = get(gcbo, 'String');

   varnames=scanvars(project1);
   [m n]=size(varnames);
   varvals=zeros(1,m);
   varexc=zeros(1,m);
   vub=[];
   vlb=[];
   Var_popup_handle = findobj(gcbf,'Tag','Variables');
   set(Var_popup_handle,'Value',1)
   set(Var_popup_handle,'String',varnames)
   set(Var_popup_handle,'Enable','on')
   Val_box_handle=findobj(gcbf,'Tag','VarInit');
   set(Val_box_handle,'Enable','on')
   guifunc InitVars



%case 'SigmaVal'   %Initialization of Sigma and Epsilon values
%   sig_init = get(gcbo, 'String');
%   sig_init = eval(sig_init)
%case 'EpsilonVal'
%   eps_init = get(gcbo, 'String');
%   eps_init = eval(eps_init)

%Activate the "Start Maxwell" button only after the appropriate values
% above have been entered

   StartHndl = findobj(gcbf, 'String', 'Start Maxwell');
   set(StartHndl, 'Enable', 'on')

%By having made the initial values of Sigma and Epsilon globals, I have
%  effectively eliminated the necessity of using initgues.m; this function
%  is now no longer used.
case 'CostFun'
   costfunction=get(gcbo,'String')

case 'NewCost'
   edit;

case 'Editor'
   edit(costfunction)

case 'NumOuts'
   numouts=get(gcbo,'String');
   numouts=str2num(numouts)

case 'OptRoutine'

  % User is now given choice of optimization routines to choose from
  choices = get(gcbo, 'String');
```

```
  optchoice = get(gcbo, 'Value');
  opt_routine = choices(optchoice,:)
  if optchoice == 9;
     promptstr={'Upper Bound Vector', 'Lower Bound Vector'};
     titlestr='Absolute Boundary Vectors';
     initstr={mat2str(vub) mat2str(vlb)};
     result=inputdlg(promptstr, titlestr, 1,initstr);


     if ~isempty(result)
        vub=eval(result{1});
        vlb=eval(result{2});
     end
  end

case 'InitVars'
   Var_Popup_Handle=findobj(gcbf,'Tag','Variables');
   VarNum=get(Var_Popup_Handle,'Value');
   Init_Box_Handle=findobj(gcbf,'Tag','VarInit');
   str=num2str(varvals(VarNum));
   set(Init_Box_Handle,'String',str);
   Exc_Handle=findobj(gcbf,'Tag','Exclude');
   exc=varexc(VarNum);
   set(Exc_Handle,'Value',exc);
case 'VarInit'
   Var_Popup_Handle=findobj(gcbf,'Tag','Variables');
   VarNum=get(Var_Popup_Handle,'Value');
   text=get(gcbo,'String');
   val=str2num(text);
   varvals(VarNum)=val;

case 'SaveInits'
   file1=strcat(project1,'\varvals');
   file2=strcat(project1,'\varexc');
   file3=strcat(project1,'\vlb');
   file4=strcat(project1,'\vub');
   save(file1,'varvals','-ascii');
   save(file2,'varexc','-ascii');
   save(file3,'vlb','-ascii');
   save(file4,'vub','-ascii');
case 'LoadInits'
   file1=strcat(project1,'\varvals');
   file2=strcat(project1,'\varexc');
   file3=strcat(project1,'\vlb');
   file4=strcat(project1,'\vub');
   load(file1);
   load(file2);
   load(file3);
   load(file4);
   guifunc InitVars
case 'ExcludeVar'
   Var_Handle=findobj(gcbf,'Tag','Variables');
```

```
   VarNum=get(Var_Handle,'Value');
   yn=get(gcbo,'Value');
   varexc(VarNum)=yn;
   varexc
case 'StartMaxwell'
   cd (homed)
%Since we are now only interested in one wavelength the "z:/..." arguments being
% passed to sweep are just dummy arguments (there is no such directory!). It was
% thought better to do this, since it allows us greater flexibilty if we ever
% wish to switch back to analyzing 2 or 3 wavelengths, without incurring any
% drawbacks in the case at hand

% Enable the following buttons:

RestartHndl = findobj(gcbf, 'String', 'Restart');
set(RestartHndl, 'Enable', 'on')

ContinueHndl = findobj(gcbf, 'String', 'Continue');
set(ContinueHndl, 'Enable', 'on')

AbortHndl = findobj(gcbf, 'String', 'Abort');
set(AbortHndl, 'Enable', 'on')

Maxrun(homed,project1);


%Invoke start3 with appropriate parameters and 'mode' to begin execution
%Start3(homed,project1,1);

 %Change i: to d: and k: to c: when needed (when shifting to Couette)


case 'ContinueMaxwell'%the "ContinueMaxwell" button has been pressed
   cd (homed);
   Start3(homed, project1,1);


case 'RestartMaxwell'%the "RestartMaxwell" button has been pressed

   cd (homed);
   Start3(homed, project1,2);


case 'Abort'         %the "Abort" button has been pressed
   warning('All Computations Terminated...Exiting Matlab')
   pause(3)
   warning('You will need to abort Maxwell separately')
   pause(3)
   exit

end
```

H.2.2 maxrun.m

```
%This is the function that calls the optimization routines.
%This function is called by GUIfunc once the Start Maxwell
%button is pushed.  It then handles the inclusion/exclusion
%of variables, normalizes them, and calls the optimization
%function with 'iter' as the cost function.

function Maxrun(h1,p1)

global ansoft_dir
global homed
global project1
global varvals
global varexc
global ptdfile
global ptbfile
global ptdID
global ptbID
global normal
global opt_routine
global optchoice
global projname
global vlb
global vub

projname=lastdir(project1);
[projname b]= strtok(projname, '.');
ptdfile = strcat(project1,'\',projname,'.ptd');
ptdID = fopen(ptdfile,'rt+');
ptbfile=strcat(project1,'\',projname,'.ptb');
ptbID = fopen(ptbfile,'rt+');

[a b]=posscan(ptbID,ptdID);


freqflag=0;

homed=h1;
project1=p1;

%this is to handle the inclusion/exclusion of variables.
l=length(varvals);
incvar = [];
for i = 1 : l
   test=varexc(i);
   if test==1
      incvar=incvar;
   else incvar=[incvar varvals(i)];
   end
end
```

```
%this will allow us to run the optimization routine with values
%of the same order of magnitude

[runval normal]=normalize(incvar)

%this will make the lower and upper bounds the correct order
%of magnitude, as well.
vlb1=vlb./10.^normal
vub1=vub./10.^normal

options=foptions;
options(1)=1;
options(16)=.00001;
options(2)=.0001;
options(3)=.0001;

%setting these options would get the proper opt routine to run.
switch optchoice

case 1
   opt_routine='fminu';
   options(6)=0;
case 2
   opt_routine='fminu';
   options(6)=1;
case 3
   opt_routine='fminu';
   options(6)=2;
case 4
   opt_routine='fmins';
case 5
   opt_routine='fsolve'
   options(5)=0;
case 6
   opt_routine='fsolve'
   options(5)=1;
case 7
   opt_routine='leastsq'
   options(5)=1;
case 8
   opt_routine='leastsq'
   options(5)=0;
case 9
   opt_routine='constr'

end
options(5)
options(6)

%this is to handle the strange case of the constraints.
```

```
if optchoice==9
  runstr=strcat(opt_routine,'(''iter2'',runval,options,vlb1,vub1)')
else
   runstr=strcat(opt_routine,'(''iter'',runval,options)')
end


soln=eval(runstr);

%making our solutions their original orders of magnitude
soln=soln.*10.^normal;


%This code is to reconstruct the entire solution vector, putting
%the variables excluded from optimization back.

newsoln=[];
l = length(varvals);
j=1;

for i = 1:l
   test=varexc(i);
   if test == 1
      newsoln(i)=varvals(i);
   else
      newsoln(i)=soln(j)
      j=j+1;
   end
end


varvals=newsoln;

guifunc InitVars
```

H.2.3 iter.m

```
%This is the function which is called over and over again by
%the matlab optimization routine in order to derive the results
%of the parametric sweep.  It takes in a single vector as an
%input, and also outputs a single vector, as per the specifications
%of the optimization toolbox.

function outvec=iter(invec)

global ansoft_dir
global homed
global project1
global projname
global ptdfile
global ptbfile
global ptdID
global ptbID
global normal
global costfunction
global numouts
global varvals
global varexc



%putting the normalized values back to regular for maxwell's sake
invec=invec.*(10.^normal);


%This code is to reconstruct the entire variable vector, putting
%the variables excluded from optimization back.

newinvec=[];
l = length(varvals);
j=1;
for i = 1:l
   test=varexc(i);
   if test == 1
      newinvec(i)=varvals(i);
   else
      newinvec(i)=invec(j);
      j=j+1;
   end
end
newinvec
projname=lastdir(project1);
[projname b]= strtok(projname, '.');
ptdfile = strcat(project1,'\',projname,'.ptd');
ptdID = fopen(ptdfile,'rt+');
```

```
ptbfile=strcat(project1,'\',projname,'.ptb');
ptbID = fopen(ptbfile,'rt+');

if ptdID == -1 | ptbID == -1
error('Error Opening Data File!');
end

[n1 n2]=setupnums(ptbID,ptdID);
n1=n1-1;
n2=n2+1;
s1=num2str(n1);
s2=num2str(n2);
valstr=num2str(newinvec,'%8g ');
valstr=['     ', valstr];
[finalstr ptdform]=ptbscan(ptbID);

%[bpos dpos]=posscan(ptbID,ptdID);

o=strcat('setup', s2,valstr,'F F T',finalstr);

%write ptb and ptd files
fseek(ptbID,-9,1);
fprintf(ptdID,'%s\n',o);
fprintf(ptbID,' B_ROW %s \n  \n E_ROW \n',s1);
fseek(ptbID,-15,1);
fprintf(ptbID,'33 \n  \n E_ROW \nE_DATA \n');

fclose(ptdID);
fclose(ptbID);

cd(ansoft_dir);

len=length(project1);
prj=' ';
for i=2:len+1
   prj(i)=project1(i-1);
end
maxcmd=strcat('m2dfs -batch variables' , prj);
dos(maxcmd,'-echo');
pause(5)
test=0;
%This is a loop to test if "lock.inf" exists in the project
%directory.  If it does, it means the project is still
%running.  Otherwise, it's done and we can proceed to read
%the results out.
while test~=-1
   pause(5)
   test=fopen(strcat(project1,'\lock.inf'));
   if test~=-1
      fclose(test);
   end
end
```

```
ptdID=fopen(ptdfile);
line1=fgetl(ptdID);
c=sscanf(line1,ptdform);
[d e]=size(c);
frewind(ptdID);
a=fscanf(ptdID,ptdform,[d,inf]);
[f g]=size(a);
fclose(ptdID);

%This collects the output variables into outvec
d=numouts-1;
for k = 1:numouts
   outvec(k)= a(f-d,g);
   d=d-1;
end

%This is where we use our simplified cost function
%to derive the output vector!

costfunstr=strcat(costfunction,'(outvec)');
outvec=eval(costfunstr);
```

H.2.4 iter2.m

```
%nearly the same functionality as iter, but this one handles
%the 'constr' matlab optimization function, which deals with
%constraints

function [outvec,cstr]=iter(invec)

global ansoft_dir
global homed
global project1
global projname
global ptdfile
global ptbfile
global ptdID
global ptbID
global normal
global costfunction
global numouts
global varvals
global varexc
global optvars


%putting the normalized values back to regular for maxwell's sake
invec=invec.*(10.^normal);

optvars=invec;
%This code is to reconstruct the entire variable vector, putting
%the variables excluded from optimization back.

newinvec=[];
l = length(varvals);
j=1;
for i = 1:l
   test=varexc(i);
   if test == 1
      newinvec(i)=varvals(i);
   else
      newinvec(i)=invec(j);
      j=j+1;
   end
end
newinvec
projname=lastdir(project1);
[projname b]= strtok(projname, '.');
ptdfile = strcat(project1,'\',projname,'.ptd');
ptdID = fopen(ptdfile,'rt+');
ptbfile=strcat(project1,'\',projname,'.ptb');
ptbID = fopen(ptbfile,'rt+');
```

```
if ptdID == -1 | ptbID == -1
error('Error Opening Data File!');
end

[n1 n2]=setupnums(ptbID,ptdID);
n1=n1-1;
n2=n2+1;
s1=num2str(n1);
s2=num2str(n2);
valstr=num2str(newinvec,'%8g ');
valstr=['     ', valstr];
[finalstr ptdform]=ptbscan(ptbID);

%[bpos dpos]=posscan(ptbID,ptdID);

o=strcat('setup', s2,valstr,'F F T',finalstr);

%write ptb and ptd files
fseek(ptbID,-9,1);
fprintf(ptdID,'%s\n',o);
fprintf(ptbID,' B_ROW %s \n  \n E_ROW \n',s1);
fseek(ptbID,-15,1);
fprintf(ptbID,'33 \n  \n E_ROW \nE_DATA \n');

fclose(ptdID);
fclose(ptbID);

cd(ansoft_dir);

len=length(project1);
prj=' ';
for i=2:len+1
   prj(i)=project1(i-1);
end
maxcmd=strcat('m2dfs -batch variables' , prj);
dos(maxcmd,'-echo');
pause(5)
test=0;
%This is a loop to test if "lock.inf" exists in the project
%directory.  If it does, it means the project is still
%running.  Otherwise, it's done and we can proceed to read
%the results out.
while test~=-1
   pause(5)
   test=fopen(strcat(project1,'\lock.inf'));
   if test~=-1
      fclose(test);
   end
end


ptdID=fopen(ptdfile);
```

```
line1=fgetl(ptdID);
c=sscanf(line1,ptdform);
[d e]=size(c);
frewind(ptdID);
a=fscanf(ptdID,ptdform,[d,inf]);
[f g]=size(a);
fclose(ptdID);

%This collects the output variables into outvec
d=numouts-1;
for k = 1:numouts
   outvec(k)= a(f-d,g);
   d=d-1;
end

costfunstr=strcat(costfunction,'(outvec,optvars)');
[outvec cstr]=eval(costfunstr);
```

H.2.5 normalize.m

```
%this is the function which does the normalization of
%vectors.  It takes in two vectors as input and
%then outputs their orders as well as their value
%in that order.
function [vals ,orders]=normalize(in)

l=length(in);

for i =1:l
   num=in(i);
   logthm=log10(num);
   orders(i)=floor(logthm);
   vals(i)=num/(10^orders(i));
end
```

H.2.6 cost2.m

```
%this is a Sample cost function used by the GUI
%Note this one does not handle constraints

function o=cost2(i)


o=((i(1)+4.45583e-12)/1e-12)^2+((i(2)+1.10751e-11)/1e-11)^2;
```

H.2.7 ptbscan.m

```
%this is the function that scans through the .ptb file to find
%variable names and also the form of the 'fscanf' for the
%.ptd file.

function [outstr, outform]=ptbscan(fid)
frewind(fid);
flg=0;
outstr='';
outform='setup';
while ~feof(fid)
   line1=fgetl(fid);
   if ~isempty(findstr(line1,'Solve'))
      flg=1;
   end
   if flg==1
      if ~isempty(findstr(line1,'Type'))
         type=sscanf(line1,'Type %s');
         if strcmp(type, 'LONG') | strcmp(type, 'DBL')
            outstr=strcat(outstr,'0 ');
         elseif strcmp(type, 'VEC2') | strcmp(type, 'CPLX')
            outstr=strcat(outstr,'(0 , 0) ');
         end
      end
   end
   if ~isempty(findstr(line1,'Type'))
      type=sscanf(line1,'Type %s');
      if strcmp(type, 'LONG') | strcmp(type, 'DBL')
         outform=strcat(outform,' %f');
      elseif strcmp(type, 'VEC2') | strcmp(type, 'CPLX')
         outform=strcat(outform,' (%f,%f)');
      elseif strcmp(type,'STR')
         outform=strcat(outform,'%i');
      elseif strcmp(type,'BOOL')
         outform=strcat(outform,' %*s');
      end
   end

end
```

H.2.8 scanvars.m

```
%this function also looks through the .ptb files.  It
%it is interfaced with Guifunc to get the names of all the
%relevant variables, which we later display in a list-menu

function o=scanvars(path);

varnames = [''];
projname=lastdir(path);
[projname b]= strtok(projname, '.');
ptbID = fopen(strcat(path,'\',projname,'.ptb'),'rt+');

a=1;
frewind(ptbID);
while a==1
   line1=fgetl(ptbID);
   if ~isempty(findstr(line1,'Type'))
      if isempty(findstr(line1,'BOOL'))
         if isempty(findstr(line1,'STR'))
            line2=fgetl(ptbID);
            name = sscanf(line2,'Name %s');
            varnames=char(varnames,name);
         end
      else a=0;
      end
   end
end
fclose(ptbID);
[i j]=size(varnames);

for c=2:i
   o(c-1,:)=varnames(c,:);
end
```

H.2.9 posscan.m

```
%This routine writes the new data to
%new .ptd and .ptb files.  It removes existing
%data so the files don't get unmanagably large.

function [ptb,ptd]=posscan(ptbid,ptdid)

global project1
global projname
global ptdfile
global ptbfile

newfile1=strcat(project1,'\',projname,'.bnw');
newfile2=strcat(project1,'\',projname,'.dnw');

newbid=fopen(newfile1,'wt+');
newdid=fopen(newfile2,'wt+');

frewind(ptbid);
frewind(ptdid);
flg1=0;
flg2=0;

while ~feof(ptbid) & flg1==0
   line1=fgetl(ptbid);
   fprintf(newbid,'%s\n',line1);
   if ~isempty(findstr(line1,'E_ROW'))
      ptb=ftell(ptbid);
      flg1=1;
   end
end
fprintf(newbid,'E_DATA \n');

line2=fgetl(ptdid);
fprintf(newdid,'%s\n',line2);
ptd=ftell(ptdid);
fclose(newbid);
fclose(newdid);
fclose(ptbid);
fclose(ptdid);

copy1=['copy ' newfile1 ' ' ptbfile];
copy2=['copy ' newfile2 ' ' ptdfile];
dos(copy1);
dos(copy2);
```

Bibliography

[1] J. P. Rivenc, "Theoretical and experimental aspects of $\omega - k$ dielectrometry with interdigitated sensors," tech. rep., High Voltage Research Laboratory, Massachusetts Institute of Technology, Cambridge, MA, Dec. 1996.

[2] S. L. Garverick, *A.C. Measurements with a Depletion-mode Charge-flow Transistor*. PhD thesis, Massachusetts Institute of Technology, Cambridge, MA, 1980.

[3] H. L. Lee, *Optimization of a Resin Cure Sensor*. PhD thesis, Department of Electrical Engineering and Computer Science, Massachusetts Institute of Technology, Cambridge, MA, Aug. 1982.

[4] S. M. Gasworth, *Electrification by Liquid Dielectric Flow*. PhD thesis, Massachusetts Institute of Technology, Cambridge, MA, Feb. 1985.

[5] M. C. W. Coln, *A High Performance Dielectric Measurement System*. PhD thesis, Massachusetts Institute of Technology, Cambridge, MA, June 1985.

[6] L. Mouayad, "*Monitoring of Transformer Oil Using Microdielectrometric Sensors*," Master's thesis, Department of Electrical Engineering and Computer Science, Massachusetts Institute of Technology, Cambridge, MA, May 1985.

[7] P. Li, *Low Frequency, Millimeter Wavelength, Interdigital Dielectrometry of Insulating Media in a Transformer Environment*. PhD thesis, Department of Electrical Engineering and Computer Science, Massachusetts Institute of Technology, Cambridge, MA, May 1987.

[8] M. C. Zaretsky, *Parameter Estimation Using Microdielectrometry with Application to Transformer Monitoring*. PhD thesis, Department of Electrical Engineering and Computer Science, Massachusetts Institute of Technology, Cambridge, MA, Nov. 1987.

[9] P. A. von Guggenberg, *Application of Interdigital Dielectrometry to Moisture and Double Layer Measurements in Transformer Insulation*. PhD thesis, Department of Electrical Engineering and Computer Science, Massachusetts Institute of Technology, Cambridge, MA, June 1993.

[10] Y. K. Sheiretov, "*Dielectrometry Measurements of Moisture Dynamics in Oil-Impregnated Pressboard*," Master's thesis, Department of Electrical Engineering and Computer Science, Massachusetts Institute of Technology, Cambridge, MA, May 1994.

[11] D. E. Schlicker, "*Flow Electrification of Aged Transformer Oils*," Master's thesis, Department of Electrical Engineering and Computer Science, Massachusetts Institute of Technology, Cambridge, MA, Aug. 1996.

[12] Y. Du, *Measurements and Modeling of Moisture Diffusion Processes in Transformer Insulation Materials using Interdigital Dielectrometry Sensors*. PhD thesis, Department of Electrical Engineering and Computer Science, Massachusetts Institute of Technology, Cambridge, MA, June 1999.

[13] A. V. Mamishev, Y. Du, and M. Zahn, "Measurement of dielectric property distributions using interdigital dielectrometry sensors," in *IEEE Conference on Electrical Insulation and Dielectric Phenomena*, (Virginia Beach, VA), pp. 309–312, Oct. 1995.

[14] A. Washabaugh, A. V. Mamishev, Y. Du, and M. Zahn, "Dielectric measurements of semi-insulating liquids and solids," in *International Conference on Conduction and Breakdown in Dielectric Liquids*, (Rome, Italy), pp. 381–384, July 1996.

[15] Y. Du, M. Zahn, A. V. Mamishev, and D. E. Schlicker, "Moisture dynamic measurements of transformer board using a three-wavelength dielectrometry sensor," in *IEEE International Symposium on Electrical Insulation*, (Montreal, Quebec, Canada), pp. 53–56, June 1996.

[16] A. V. Mamishev and M. Zahn, "Techniques for semi-empirical characterization of material and sensor properties in interdigital dielectrometry," in *IEEE International Symposium on Electrical Insulation*, (Montreal, Quebec, Canada), pp. 486–489, June 1996.

[17] A. V. Mamishev, M. Zahn, B. C. Lesieutre, and B. A. Berdnikov, "Influence of geometric parameters on characteristics of an interdigital sensor," in *IEEE Conference on Electrical Insulation and Dielectric Phenomena*, (San Francisco, CA), pp. 550–553, Oct. 1996.

[18] A. V. Mamishev, B. Berdnikov, J. P. Rivenc, B. C. Lesieutre, and M. Zahn, "Surface contact effects in interdigital dielectrometry," in *10th International Symposium on High Voltage Engineering*, vol. 6, (Montreal, Canada), pp. 357–360, Aug. 1997.

[19] A. V. Mamishev, B. C. Lesieutre, and M. Zahn, "Parameter estimation using an interdigital dielectrometry sensor with finite-element software," in *IEEE Conference on Electrical Insulation and Dielectric Phenomena*, (Minneapolis, MN), pp. 234–237, Oct. 1997.

[20] A. V. Mamishev, Y. Du, B. C. Lesieutre, and M. Zahn, "Measurement of stratified distributions of dielectric properties and dependent physical parameters," in *Fall Meeting of Materials Research Society*, (Boston, MA), pp. 29–34, Dec. 1997.

[21] A. V. Mamishev, C. Lin, Y. Du, B. C. Lesieutre, and M. Zahn, "Improvement of algorithms for on-line interdigital dielectrometry measurement of material properties," in *IEEE International Symposium on Electrical Insulation*, (Washington, D.C.), pp. 444–447, June 1998.

[22] A. V. Mamishev, Y. Du, B. C. Lesieutre, and M. Zahn, "Interdigital dielectrometry sensors for measurements of spatial profiles of complex permittivity and related physical properties," in *3rd International Conference on Electric Charge in Solid Insulators*, (Tours, France), June 1998. Poster presentation.

[23] Y. Du, A. V. Mamishev, B. C. Lesieutre, and M. Zahn, "Application of interdigital dielectrometry sensors for monitoring diffusion of moisture into solid dielectrics," in *3rd International Conference on Electric Charge in Solid Insulators*, (Tours, France), June 1998. Poster presentation.

[24] Y. Du, A. V. Mamishev, B. C. Lesieutre, and M. Zahn, "Measurements of moisture diffusion in transformer pressboard," in *IEEE Conference on Electrical Insulation and Dielectric Phenomena*, (Atlanta, GA), pp. 341—344, Oct. 1998.

[25] A. V. Mamishev, Y. Du, B. C. Lesieutre, and M. Zahn, "Measurement of moisture spatial profiles in transformer pressboard," in *IEEE Conference on Electrical Insulation and Dielectric Phenomena*, (Atlanta, GA), pp. 323–326, Oct. 1998.

[26] A. V. Mamishev, Y. Du, B. C. Lesieutre, and M. Zahn, "Development and applications of multi-wavelength interdigital dielectrometry sensors and parameter estimation algorithms," in *Joint Symposium on Electrostatics*, (Stanford University, CA), pp. 169–181, June 1998.

[27] A. V. Mamishev, B. C. Lesieutre, and M. Zahn, "Optimization of multi-wavelength interdigital dielectrometry instrumentation and algorithms," *IEEE Transactions on Dielectrics and Electrical Insulation*, pp. 408–420, 1998.

[28] A. V. Mamishev, A. R. Takahashi, Y. Du, B. C. Lesieutre, and M. Zahn, "Conductivity-frequency relationships applied to dielectrometry parameter estimation," *IEEE Transactions on Dielectrics and Electrical Insulation*, 1999. Submitted for publication.

[29] A. V. Mamishev, A. R. Takahashi, Y. Du, B. C. Lesieutre, and M. Zahn, "Assessment of performance of fringing electric field sensor arrays," *Research in Non-Destructive Evaluation*, 1998. Prepared for publication.

[30] Y. Du, A. V. Mamishev, B. C. Lesieutre, M. Zahn, and S. Lindgren, "A review of moisture equilibrium in the paper-oil system," *Electrical Insulation Magazine*, pp. 1–10, January/February 1999.

[31] A. V. Mamishev, Y. Du, B. C. Lesieutre, and M. Zahn, "One-sided measurement of material dielectric properties a using liquid dielectric immersion technique," in *IEEE International Conference of Dielectric Liquids*, (Nara, Japan), June 1999. Accepted for publication.

[32] Y. Du, A. V. Mamishev, B. C. Lesieutre, and M. Zahn, "Measurements of moisture solubility for differently conditioned transformer oil," in *IEEE International Conference of Dielectric Liquids*, (Nara, Japan), June 1999. Accepted for publication.

[33] A. Washabaugh, D. E. Schlicker, A. V. Mamishev, M. Zahn, and N. Goldfine, "Dielectric sensor arrays for monitoring of aging in composites and other low-conductivity media," in *SPIE Conference*, 1999. Submitted.

[34] A. V. Mamishev, Y. Du, J. H. Bau, B. C. Lesieutre, and M. Zahn, "Evaluation of diffusion-driven material property profiles using three-wavelength interdigital sensor," *IEEE Transactions on Dielectrics and Electrical Insulation*, 1999. In preparation.

[35] A. V. Mamishev, Y. Du, B. C. Lesieutre, and M. Zahn, "Model-based estimation material property profiles with multi-wavelength dielectrometry," *IEEE Transactions on Dielectrics and Electrical Insulation*, 1999. In preparation.

[36] A. V. Mamishev, Y. Du, B. C. Lesieutre, and M. Zahn, "Error propagation in multiple penetration depth fringing electric field sensor measurements," *IEEE Transactions on Instrumentation and Measurements*, 1999. Submitted.

[37] A. V. Mamishev, Y. Du, B. C. Lesieutre, and M. Zahn, "Interdigital sensors and transducers," *Proceedings of the IEEE*, 1999. Abstract accepted.

[38] N. Goldfine, M. Zahn, A. V. Mamishev, and D. Schlicker, "Methods for processing, optimization, calibration, and display of measured dielectrometry signals using property estimation grids." Patent pending, 1999.

[39] B. C. Lesieutre, A. V. Mamishev, E. K. Y. Du, M. Zahn, and G. Verghese, "Forward and inverse parameter estimation algorithms of interdigital dielectrometry sensors," in *Joint Symposium on Electrostatics*, (Boston, MA), June 1999. Accepted.

[40] Y. Du, S. Kang, A. V. Mamishev, B. C. Lesieutre, and M. Zahn, "Measurements of moisture diffusion dynamics in transformer insulation using interdigital dielectrometry measurements," in *Joint Symposium on Electrostatics*, (Boston, MA), June 1999. Accepted.

[41] B. A. Berdnikov and A. V. Mamishev, "Investigation of properties, optimization, and development of parameter estimation algorithms for a three-wavelength interdigital sensor. Final UROP report.," tech. rep., High Voltage Research Laboratory, Massachusetts Institute of Technology, Cambridge, MA, Feb. 1997.

[42] B. Truong, "Software development for the characterization of dielectric properties of insulating materials. Final UROP report.," tech. rep., High Voltage Research Laboratory, Massachusetts Institute of Technology, Cambridge, MA, May 1997.

[43] J. Miller, "Software development for the characterization of dielectric properties of insulating materials. Final UROP report.," tech. rep., High Voltage Research Laboratory, Massachusetts Institute of Technology, Cambridge, MA, Aug. 1997.

[44] C. Lin, "High Voltage Research Laboratory UROP. Final report.," tech. rep., High Voltage Research Laboratory, Massachusetts Institute of Technology, Cambridge, MA, Aug. 1997.

[45] A. Takahashi, "High Voltage Research Laboratory UROP. Final report.," tech. rep., High Voltage Research Laboratory, Massachusetts Institute of Technology, Cambridge, MA, Nov. 1997.

[46] G. T. Tewari, "Development of a GUI optimization module to assist in the utilization of software for the characterization of the dielectric properties of insulating materials. UROP report.," tech. rep., High Voltage Research Laboratory, Massachusetts Institute of Technology, Cambridge, MA, May 1998.

[47] I. Debnath, "Detection of plastic and metal landmines using fringing field dielectrometry. UROP report.," tech. rep., High Voltage Research Laboratory, Massachusetts Institute of Technology, Cambridge, MA, Oct. 1998.

[48] J. Bau, "Generalization a GUI optimization module developed for software characterization of dielectric properties of insulating materials. UROP report.," tech. rep., High Voltage Research Laboratory, Massachusetts Institute of Technology, Cambridge, MA, Oct. 1998.

[49] M. Sarda, "Characterization of airgap between Teflon and an interdigital three-wavelength sensor surface in dielectrometry measurements. AUP report.," tech. rep., High Voltage Research Laboratory, Massachusetts Institute of Technology, Cambridge, MA, Dec. 1998.

[50] A. V. Mamishev, "Measurement of contaminant concentration in the protective chemical gear, internal report," tech. rep., Jentek Sensors, Cambridge, MA, July 1997.

[51] *Enhanced Magnetoquasistatic (Inductive) Metal Detection and New Electroquasistatic (Capacitive) Plastic Detection for Landmine Detection and Identification,*

Jentek Sensors, Inc. Cambridge, MA, June 1997. Jentek Sensors Final Report to the US Army Night Vision Directorate.

[52] I. G. Matis, K. A. Bergmanis, and E. E. Klotinsh, "Device for measuring permittivity or materials." U.S. Patent No. 3,671,857, 1970.

[53] I. G. Matis, K. A. Bergmanis, and E. E. Klotinsh, "Device for measuring permittivity or materials." U.S. Patent No. 3,694,742, 1970.

[54] S. D. Senturia and S. L. Garverick, "Method and apparatus for microdielectrometry." U.S. Patent No. 4,423,371, Dec. 27, 1983.

[55] R. D. Baxter and P. J. Freud, "Humidity sensing element." U.S. Patent No. 4,814,690, Jan. 1986.

[56] J. R. Melcher and M. C. Zaretsky, "Apparatus and methods for measuring permittivity in materials." U.S. Patent No. 4,814,690, Mar. 21, 1989.

[57] F. Waldman and P. von Guggenberg, "Apparatus and methods for measuring the dielectric and geometric properties of materials." U.S. Patent Serial No. 07/706,406, May 28, 1991.

[58] I. G. Matis, "On multiparameter control of dielectric properties of laminate polymer materials," *Latvijas PSR Zinatnu Akademijas Vestis, Fizikas un Tehnisko Zinatnu Serija*, no. 6, pp. 60–67, 1966.

[59] S. D. Senturia and C. M. Sechen, "The use of the charge-flow transistor to distinguish surface and bulk components of thin-film sheet resistance," *IEEE Transactions on Electron Devices*, vol. ED-24, p. 1207, Sept. 1977.

[60] R. S. Jachowicz and S. D. Senturia, "A thin-film capacitance humidity sensor," *Sensors and Actuators*, vol. 2, pp. 171–186, Dec. 1981.

[61] M. C. Zaretsky and J. R. Melcher, "Complex permittivity measurements of thin films using microdielectrometry," in *Conference on Electrical Insulation and Dielectric Phenomena*, (Claymont, DE), pp. 462–471, Nov. 1986.

[62] N. J. Goldfine, A. P. Washabaugh, J. V. Dearlove, and P. A. von Guggenberg, "Imposed $\omega - k$ magnetometer and dielectrometer applications," in *Review of Progress in Quantitative Nondestructive Evaluation* (D. Thompson and D. Chimenti, eds.), vol. 12, (New York), Plenum Press, 1993.

[63] P. A. von Guggenberg and M. C. Zaretsky, "Estimation of one-dimensional complex-permittivity profiles: a feasibility study," *Journal of Electrostatics*, vol. 34, pp. 263–277, Mar. 1995.

[64] V. K. Varadan, V. V. Varadan, and X. Q. Bao, "Integration of interdigital transducers, MEMS and antennas for smart structures," in *Smart Structures and Materials 1996: Smart Electronics and MEMS Conference*, (San Diego, CA), pp. 95–106, Feb. 1996.

[65] S. D. Senturia, N. F. Sheppard, Jr., H. L. Lee, and D. R. Day, "In-situ measurement of the properties of curing systems with microdielectrometry," *Journal of Adhesion*, vol. 15, no. 69, pp. 69–90, 1982.

[66] N. T. Smith and D. D. Shepard, "Dielectric cure analysis: theory and industrial applications," *Sensors*, vol. 12, pp. 42–48, Oct. 1995.

[67] E. S. Kolesar and J. M. Wiseman, "Interdigitated gate electrode field effect transistor for the selective detection of nitrogen dioxide and diisopropyl methylphosphonate," *Analytical Chemistry*, vol. 61, pp. 2355–2361, 1989.

[68] J. W. Gardner, "Intelligent gas sensing using an integrated sensor pair," *Sensors and Actuators B*, vol. 26-27, pp. 261–266, 1995.

[69] G. Niebling and A. Schlachter, "Qualitative and quantitative gas analysis with non-linear interdigital sensor arrays and artificial neural networks," *Sensors and Actuators B*, vol. B 26-27, pp. 289–292, 1995.

[70] M. C. Zaretsky, J. R. Melcher, and C. M. Cooke, "Moisture sensing in transformer oil using thin-film microdielectrometry," *IEEE Transactions on Electrical Insulation*, vol. 24, pp. 1167–1176, Dec. 1989.

[71] M. C. Zaretsky, P. Li, and J. R. Melcher, "Estimation of thickness, complex bulk permittivity and surface conductivity using interdigital dielectrometry," *IEEE Transactions on Electrical Insulation,*, vol. 24, pp. 1159–1166, Dec. 1989.

[72] J. O. Simpson and S. A. Bidstrup, "Modeling conductivity and viscosity changes during epoxy cure using TEA, DMA, and DSC," *Proceedings of the American Chemical Society, Division of Polymeric Materials: Science and Engineering, Fall Meeting*, vol. 69, no. 3, pp. 451–452, 1993.

[73] Y. K. Sheiretov and M. Zahn, "Dielectrometry measurements of moisture dynamics in oil-impregnated pressboard," *IEEE Transactions on Dielectrics and Electrical Insulation*, vol. 2, pp. 329–351, June 1995.

[74] N. F. Sheppard, D. R. Day, H. L. Lee, and S. D. Senturia, "Microdielectrometry," *Sensors and Actuators*, vol. 2, pp. 263–274, July 1982.

[75] Y. K. Sheiretov and M. Zahn, "Dielectrometry measurements of spatial moisture profiles in oil-impregnated pressboard," in *IEEE International Conference on Properties and Applications of Dielectric Materials*, (University of Queensland, Brisbane, Australia), pp. 701–704, July 1994.

[76] M. C. Zaretsky, L. Mouayad, and J. R. Melcher, "Continuum properties from interdigital electrode dielectrometry," *IEEE Transactions on Electrical Insulation*, vol. 23, pp. 897–917, Dec. 1988.

[77] S. D. Senturia, N. F. Sheppard, S. Poh, and H. R. Appelman, "The feasibility of electrical monitoring of resin cure with the charge-flow transistor," *Polymer Engineering and Science*, vol. 21, pp. 113–118, Feb. 1981.

[78] J. R. Melcher, "Electrohydrodynamic surface waves," in *Waves on Fluid Interfaces* (R. E. Meyer, ed.), pp. 167–200, Academic Press: New York, NY, 1983.

[79] J. R. Melcher, "Charge relaxation on a moving liquid interface," *Physics of Fluids*, no. 10, pp. 325–331, 1967.

[80] S. M. Gasworth, J. R. Melcher, and M. Zahn, "Induction sensing of electrokinetic streaming current," in *Conference on Interfacial Phenomena In Practical Insulating Systems*, (National Bureau of Standards, Gaithersburg, MD), Sept. 1983.

[81] J. C. Zuercher and J. R. Melcher, "Double-layer transduction at a mercury-electrolyte interface was imposed temporal and spatial periodicity," *Journal of Electrostatics*, vol. 5, pp. 21–31, Oct. 1978.

[82] M. J. Golis, "Tutorial: Non-destructive materials evaluation – and overview addressing its theory and application," in *Materials Research Society Fall Meeting*, (Boston, MA), Dec. 1997.

[83] P. A. von Guggenberg and J. R. Melcher, "A three-wavelength flexible sensor for monitoring the moisture content of transformer pressboard," in *Proceedings of The 3rd International Conference on Properties and Applications of Dielectric Materials*, vol. 2, (Tokyo, Japan), pp. 1262–1265, July 8–12, 1991.

[84] I. G. Matis, "Method and equipment for determining the dielectric constant of polymer materials with one-sided access," *Polymer Mechanics*, vol. 2, no. 4, pp. 380–383, 1966.

[85] I. G. Matis and E. Klotin'sh, "External capacitive probes for the nondestructive determination of the dielectric properties of polymeric materials," *Polymer Mechanics*, vol. 5, no. 6, pp. 983–987, 1969.

[86] I. G. Matis and K. D. Ozols, "Calculation of the electrostatic capacitance of coplanar annular electrodes with two-layer or three layer dielectric (in Russian)," *Latvijas PSR Zinatnu Akademijas Vestis, Fizikas un Tehnisko Zinatnu Serija*, no. 5, pp. 93–101, 1971.

[87] I. G. Matis, "Calculations of the intensity of the electric field in a conductor of rectangular section (in Russian)," *Latvijas PSR Zinatnu Akademijas Vestis, Fizikas un Tehnisko Zinatnu Serija*, no. 4, pp. 70–74, 1971.

[88] I. G. Matis and K. D. Ozols, "Electrostatic capacity calculation of coplanar circular electrodes (in Russian)," *Latvijas PSR Zinatnu Akademijas Vestis, Fizikas un Tehnisko Zinatnu Serija*, no. 4, pp. 611–69, 1971.

[89] K. A. Bergmanis and I. G. Matis, "Calculation of the electric field of a capacitor with a cylindrical dielectric," *Polymer Mechanics*, vol. 7, no. 3, pp. 461–464, 1971.

[90] I. G. Matis, "Trends in the development of methods of nondestructive testing of composite materials," *Mechanics of Composite Materials*, vol. 25, no. 3, pp. 368–375, 1974.

[91] V. D. Shtraus, "Nondestructive methods of determining the dielectric constants of anisotropic polymeric materials," *Polymer Mechanics*, vol. 10, no. 4, pp. 611–614, 1974.

[92] I. G. Matis, "An electronic computing instrument for measuring dielectric constants (the IDP-6)," *Polymer Mechanics*, vol. 8, no. 4, pp. 670–672, 1976.

[93] V. A. Latishenko and I. G. Matiss, "Methods and means for nondestructive study of damageability of composite materials," in *Proceedings of the First USA-USSR Symposium on Fracture of Composite Materials*, (Riga, USSR), pp. 321–328, 1978.

[94] V. D. Shtraus, "Investigation of curing an epoxy resin by the polarization current method," *Polymer Mechanics*, vol. 14, no. 1, pp. 118–123, 1978.

[95] V. A. Latishenko and I. G. Matis, "Ways and means of studying damage in composites," *Mechanics of Composite Materials*, no. 2, pp. 344–350, 1979.

[96] V. A. Latishenko and I. G. Matis, "Determination of susceptibility to damage of organic and carbon-fiber reinforced plastics by nondestructive methods," *Mechanics of Composite Materials*, no. 3, pp. 523–528, 1982.

[97] I. G. Matis, *Elektroemkostnye Preobrazovateli dlia Nerazrushajuschego Kontrolia.* Riga, Latvia: Zinatne, 2nd ed., 1982.

[98] I. G. Matiss, "A new capacitance technique for quality control of nonmetallic materials and structures," *Materials Evaluation*, vol. 40, no. 3, pp. 299–304, 1982.

[99] E. S. Krichevskii and O. S. Protopopov, "Nomographs for finding the capacitance of coplanar-plate capacitors (used as measuring transducers)," *Measurement Techniques*, vol. 29, no. 5, pp. 437–439, 1986.

[100] I. G. Matiss and V. D. Shtrauss, "Multi-parameter dielectric relaxation spectrometry for quality control of composites," *NDT International*, vol. 21, no. 4, pp. 266–276, 1988.

[101] I. G. Matis, "Trends in the development of methods of nondestructive testing of composite materials," *Mechanics of Composite Materials*, vol. 25, no. 3, pp. 368–375, 1989.

[102] V. D. Shtraus, "Nondestructive relaxation spectrometry of dielectrics," *Mechanics of Composite Materials*, vol. 25, no. 4, pp. 521–534, 1989.

[103] I. G. Matis, "Methods and means of inspecting the quality of composite materials," *Soviet Journal of Nondestructive Testing*, vol. 27, no. 4, pp. 277–285, 1991.

[104] I. G. Matis, "Spectrometric methods of investigation of the structure of composite materials. A review," *Mechanics of Composite Materials*, no. 2, pp. 320–334, 1991.

[105] I. G. Matiss, "Expert systems for nondestructive testing," *Automatic Control and Computer Sciences*, vol. 27, no. 2, pp. 36–39, 1993.

[106] V. Shtrauss, "Information processing technology in the study of relaxation phenomena. Formal theory of relaxation systems," *Automatic Control and Computer Sciences*, vol. 28, no. 4, pp. 35–46, 1994.

[107] V. Shtrauss, "Information processing technology in the study of relaxation phenomena. Formal theory of relaxation systems," *Automatic Control and Computer Sciences*, vol. 28, no. 4, pp. 42–51, 1994.

[108] V. Shtrauss, D. Pablaks, and A. Kalpinsh, "A multiparameter approach to the test procedure generation for evaluation of the structure of materials," *Latvian Journal of Physics and Technical Sciences*, no. 5, pp. 52–62, 1994.

[109] I. G. Matis, "Frequency-dependent mathematical models for capacitive transducers. I. Models of heterogeneous media," *Russian Journal of Nondestructive Testing*, vol. 31, no. 4, pp. 257–265, 1995.

[110] V. Shtrauss, "Functional conversion of signals in the study of relaxation phenomena," *Signal Processing*, vol. 45, no. 3, pp. 293–312, 1995.

[111] V. Shtrauss, A. Kalpinsh, U. Lomanovskis, and J. Rotbahs, "Tomographic imaging by electrical methods," *Latvian Journal of Physics and Technical Sciences*, no. 3, pp. 23–47, 1995.

[112] V. D. Shtraus, "Information processing technology in studies of relaxation phenomena: Relaxation models generated by a fractional-order operator with two sectional parameters," *Avtomatika i Vychislitelnaya Tekhnika*, vol. 29, no. 4, pp. 17–25, 1995.

[113] I. G. Matis, "Theoretical principles for constructing the transfer function of a nondestructive test probe," *Automatic Control and Computer Sciences*, vol. 30, no. 6, pp. 40–50, 1996.

[114] V. D. Shtraus, "Sampling relaxation signals," *Automatic Control and Computer Sciences*, vol. 30, no. 2, pp. 28–36, 1996.

[115] V. D. Shtraus, "Resin cure monitoring system based on nondestructive dielectric spectrometry," *Mechanics of Composite Materials*, vol. 32, no. 3, pp. 279–282, 1996.

[116] V. Shtrauss and U. Lomanovskis, "Multi-frequency capacitance tomography with linear sensors," in *BEC '96. The 5th Biennial Baltic Electronics Conference. Proceedings*, (Tallinn, Estonia), pp. 155–158, 1996.

[117] V. Shtrauss, "Spectrum analysis and synthesis of relaxation signals," *Signal Processing*, vol. 63, no. 2, pp. 107–119, 1997.

[118] S. D. Senturia, C. M. Sechen, and J. A. Wishneusky, "The charge-flow transistor: a new MOS device," *Applied Physics Letters*, vol. 30, pp. 106–108, Jan. 1977.

[119] N. F. Sheppard, Jr., S. L. Garverick, D. R. Day, and S. D. Senturia, "Microdielectrometry: a new method for in situ cure monitoring," in *Proceedings of the 26th SAMPE Symposium*, (Los Angeles, CA), pp. 65–76, Apr. 1981.

[120] S. D. Senturia, S. L. Garverick, and K. Togashi, "Monolithic integrated circuit implementations of the charge-flow transistor oscillator moisture sensor," *Sensors and Actuators*, vol. 2, pp. 59–71, Aug. 1981.

[121] S. D. Senturia, J. Rubinstein, S. J. Azoury, and D. Adler, "Determination of the field effect in low-conductivity materials with the charge-flow transistor," *Journal of Applied Physics*, vol. 52, pp. 3663–3670, May 1981.

[122] T. M. Davidson and S. D. Senturia, "The moisture dependence of the electrical sheet resistance of aluminium oxide thin films with application to integrated moisture sensors," in *International Reliability Physics Symposium. 20th Annual Proceedings*, (New York, NY), pp. 249–252, Mar. 1982.

[123] S. L. Garverick and S. D. Senturia, "An MOS device for AC measurement of surface impedance with application to moisture monitoring," *IEEE Transactions on Electron Devices*, vol. ED-29, pp. 90–101, Jan. 1982.

[124] S. D. Senturia, N. F. Sheppard, Jr., H. L. Lee, and S. B. Marshall, "Cure monitoring and control with combined dielectric/temperature probes," in *Proceedings of the 28th SAMPE Symposium*, (Anaheim, CA), pp. 851–861, Apr. 1983.

[125] T. J. Lewis, "The role of electrodes in conduction and breakdown phenomena in solid dielectrics," *IEEE Transactions on Electrical Insulation*, vol. EI-19, pp. 210–216, June 1984.

[126] D. E. Kranbuehl, S. E. Delos, P. Jue, T. P. Jarvie, and S. A. Williams, "Dynamic dielectric characterization of thermosets and thermoplastics using intrinsic variables," in *Proceedings of the 29th SAMPE Symposium*, (Reno, NV), pp. 1251–1257, Apr. 1984.

[127] N. F. Sheppard, Jr., M. Colin, and S. D. Senturia, "A dielectric study of the time-temperature transformation (TTT) diagram of DGEBA epoxy resins cured with DDS," in *Proceedings of the 29th SAMPE Symposium*, (Reno, NV), pp. 1243–1250, Apr. 1984.

[128] D. R. Day, T. J. Lewis, H. L. Lee, and S. D. Senturia, "The role of boundary layer capacitances at blocking electrodes in the interpretation of dielectric cure data in adhesives," *Journal of Adhesion*, pp. 73–90, 1984.

[129] D. E. Kranbuehl, S. E. Delos, and E. Yi, "Measurement and application of dielectric properties," *SPIE Technical Papers*, vol. 31, no. 311, pp. 73–90, 1985.

[130] D. D. Denton, D. R. Day, D. F. Priore, S. D. Senturia, E. S. Anolick, and D. Scheider, "Moisture diffusion in polyimide films in integrated circuits," *Journal of Electronic Materials*, vol. 14, no. 2, pp. 119–136, 1985.

[131] D. D. Denton, J. B. Camou, and S. D. Senturia, "Effects of moisture uptake on the dielectric permittivity of polyimide films," in *Proceedings of the 1985 International Symposium on Moisture and Humidity*, (Washington, D.C.), pp. 505–513, Apr. 1985.

[132] M. C. W. Coln and S. D. Senturia, "The application of linear system theory to parametric microsensors," in *TRANSDUCERS '85. 1985 International Conference on Solid- State Sensors and Actuators*, (Philadelphia, PA), pp. 118–121, June 1985.

[133] D. D. Denton, S. D. Senturia, E. S. Anolick, and D. Scheider, "Fundamental issues in the design of polymeric capacitive moisture sensors," in *TRANSDUCERS '85. 1985 International Conference on Solid- State Sensors and Actuators*, (Philadelphia, PA), pp. 202–205, June 1985.

[134] S. D. Senturia, "An approach to chemical microsensor packaging," in *TRANSDUCERS '85. 1985 International Conference on Solid- State Sensors and Actuators*, (Philadelphia, PA), pp. 198–201, June 1985.

[135] M. L. Bromberg, D. D. Day, and K. R. Snable, "Measurement and application of dielectric properties," *IEEE Electrical Insulation Magazine*, vol. 2, pp. 18–23, May 1986.

[136] F. W. Smith, H. J. Neuhaus, S. D. Senturia, Z. Feit, D. Day, and T. Lewis, "Electrical conduction in polyimide between 20 and 350°C," *Journal of Electronic Materials*, vol. 16, no. 1, pp. 93–106, 1987.

[137] P. D. Aldrich, S. K. Thurow, M. J. M.Kennon, and M. E. Lyssy, "Dielectric relaxation due to absorbed water in various thermosets," *Polymer*, vol. 28, pp. 2289–2296, Dec. 1987.

[138] D. R. Day and D. D. Shepard, "Dynamic cure and diffusion monitoring in thin encapsulant films," in *Nondestructive Monitoring of Materials Properties Symposium* (J. Holbrook and J. Bussiere, eds.), (Boston, MA), pp. 227–232, Nov. 1988.

[139] F. Bellucci, I. Khamis, S. D. Senturia, and R. M. Latanision, "Moisture effects on the electrical conductivity of Kapton polyimide," *Journal of the Electrochemical Society*, vol. 137, no. 6, pp. 1778–1784, 1990.

[140] K. Nabors, S. Kim, J. White, and S. Senturia, "Fast capacitance extraction of general three-dimensional structures," in *IEEE International Conference on Computer Design: VLSI in Computers and Processors*, (Cambridge, MA), pp. 479–484, Oct. 1991.

[141] D. R. Day, D. D. Shepard, and K. J. Craven, "A microdielectric analysis of moisture diffusion in thin epoxy/amine films of varying cure state and mix ratio," *Polymer Engineering and Science*, vol. 32, pp. 524–528, Apr. 1992.

[142] N. F. Sheppard, Jr., "Design of a conductimetric microsensor based on reversibly swelling polymer hydrogels," in *Proceedings of 6th International Conference on Solid-State Sensors and Actuators (Transducers'91)*, (San Francisco, CA), pp. 773–776, June 1991.

[143] N. F. Sheppard, Jr., R. C. Tucker, and C. Wu, "Electrical conductivity measurements using microfabricated interdigitated electrodes," *Analytical Chemistry*, vol. 65, pp. 1998–2002, May 1993.

[144] S. D. Senturia, "Correlated methods for evaluating polymer properties, interfaces, and adhesion," *International Journal of Microelectronics Packaging, Materials and Technologies*, vol. 1, no. 1, pp. 43–50, 1995.

[145] A. R. K. Ralston, C. F. Klein, P. E. Thoma, and D. D. Denton, "A model for the relative environmental stability of a series of polyimide capacitance humidity sensors," *Sensors and Actuators B (Chemical)*, vol. B34, pp. 343–348, Aug. 1996.

[146] P. A. von Guggenberg and J. R. Melcher, "An immersible relative saturation moisture sensor with application to transformer oil," in *Proceedings of The 3rd International Conference on Properties and Applications of Dielectric Materials*, vol. 2, (Tokyo, Japan), pp. 1258–1261, July 8–12, 1991.

[147] P. A. von Guggenberg, M. Zahn, and J. R. Melcher, "Diagnostic methods for moisture detection in transformer insulation," in *Proceedings of the Third EPRI Workshop: Static Electrification in Power Transformers*, (San Jose, CA), Electric Power Research Institute (EPRI), Jan. 23–24, 1992.

[148] P. A. von Guggenberg, "Experimental investigation of the heterogeneity of the double layer in transformer oil," in *Conference on Electrical Insulation and Dielectric Phenomena*, (Pocono Manor, PA), pp. 68–73, Oct. 23–24, 1993.

[149] Y. K. Sheiretov and M. Zahn, "Study of the temperature and moisture dependent dielectric properties of oil-impregnated pressboard," in *Conference on Electrical Insulation and Dielectric Phenomena*, (Pocono Manor), Oct. 1993.

[150] Y. K. Sheiretov and M. Zahn, "Dielectrometry measurements of moisture dynamics in oil-impregnated pressboard," in *IEEE International Symposium on Electrical Insulation*, (Pittsburgh, PA), pp. 33–36, June 1994.

[151] M. Zahn, "Optical, electrical and electromechanical measurement methodologies of field, charge and polarization in dielectrics (1998 Whitehead Memorial Lecture)," *IEEE Transactions on Dielectrics and Electrical Insulation*, vol. 5, pp. 627–650, Oct. 1998.

[152] H. A. Haus and J. R. Melcher, *Electromagnetic Fields and Energy*. Englewood Cliffs, NJ: Prentice Hall, 1989.

[153] M. Zahn, *Electromagnetic Field Theory: a Problem Solving Approach*. Malabar, FL: Robert E. Krieger Publishing Company, Inc., reprint ed., 1987.

[154] P. Debye, *Polar Molecules*. New York: Chemical Catalog Co., 1929.

[155] A. R. von Hippel, *Dielectrics and Waves*. New York: John Wiley & Sons, 1954.

[156] H. Frölich, *Theory of Dielectrics*. Oxford, United Kingdom: Oxford University Press, 1955.

[157] C. P. Smyth, *Dielectric Behaviour and Structure*. New York, NY: McGraw-Hill, 1955.

[158] V. V. Daniels, *Dielectric Relaxation*. London: Academic Press, 1967.

[159] I. Adamczewski, *Ionization, Conductivity and Breakdown in Dielectric Liquids*. London: Taylor & Francis, 1969.

[160] C. J. F. Böttcher and P. Bordewijk, *Theory of Electric Polarization, Vols. I and II*. Elsevier Scientific Publishing Company, Amsterdam, 1978.

[161] R. Coelho, *Physics of Dielectrics for the Engineer*. Elsevier Scientific Publishing Company, Amsterdam, 1979.

[162] A. R. Blythe, *Electrical Properties of Polymers*. Cambridge University Press, Cambridge, 1979.

[163] A. K. Jonscher, *Dielectric Relaxation in Solids*. Chelsea Dielectrics Press, London, 1983.

[164] A. K. Jonscher, *Universal Relaxation Law*. Chelsea Dielectrics Press, London, 1996.

[165] P. Hedvig, *Dielectric Spectroscopy of Polymers*. Wiley, New York, 1977.

[166] J. R. MacDonald, *Impedance Spectroscopy : Emphasizing Solid Materials and Systems*. Wiley, New York, 1987.

[167] J. P. Runt and J. J. Fitzgerald, eds., *Dielectric Spectroscopy of Polymeric Materials: Fundamentals and Applications*. American Chemical Society, Washington, DC, 1997.

[168] N. F. Mott and E. A. Davis, *Electronic Processes in Non-Crystalline Materials*. Oxford, United Kingdom: Oxford University Press, 1979.

[169] I. S. Zheludev, *Physics of Crystalline Dielectrics, Vols. I and II*. New York: Plenum Press, 1971.

[170] J. van Turnhout, *Thermally Stimulated Discharge of Polymer Electrets*. Amsterdam: Elsevier Scientific Publishing Company, 1975.

[171] G. M. Sessler, *Electrets*. Berlin: Springer-Verlag, 1980.

[172] S. Havriliak Jr. and J. S. Havriliak, eds., *Dielectric and Mechanical Relaxation in Materials*. Munich, Germany: Carl Hanser Verlag, 1997.

[173] J. R. Melcher, *Continuum Electromechanics*. Cambridge, MA: The MIT Press, 1981.

[174] K. S. Cole and R. H. Cole, "Dispersion and absorption in dielectrics," *Journal of Chemical Physics*, vol. 9, pp. 341–351, Apr. 1941.

[175] D. W. Davidson and R. H. Cole, "Dielectric relaxation of glycerol, propylene glycol, and *n*-propanol," *Journal of Chemical Physics*, vol. 19, pp. 1484–1490, 1951.

[176] J. G. Kirkwood and R. M. Fuoss, "Anomalous dispersion and dielectric loss in polar polymers," *Journal of Chemical Physics*, vol. 9, pp. 329–340, 1941.

[177] G. Williams and D. C. Watts, "Non-symmetrical dielectric relaxation behavior arising from a simple empirical decay function," *Transactions of Faraday Society*, vol. 66, pp. 80–85, 1970.

[178] G. Williams, D. C. Watts, S. B. Dev, and A. M. North, "Further considerations of non-symmetrical dielectric relaxation behavior arising from a simple empirical decay function," *Transactions of Faraday Society*, vol. 67, pp. 1323–1335, 1970.

[179] A. K. Vijh, "Electrochemical nature of metal-insulator interfaces," in *IEEE International Symposium on Electrical Insulation*, (Montreal, Que., Canada), pp. 870–873, June 1996.

[180] H. L. Walmsley and G. Woodford, "The generation of electric currents by the laminar flow of dielectric liquids," *Journal of Physics D: Applied Physics*, vol. 14, pp. 1761–1782, Oct. 1981.

[181] H. L. Walmsley, "The generation of electric currents by the turbulent flow of dielectric liquids: I. Long pipes," *Journal of Physics D: Applied Physics*, vol. 15, pp. 1907–1934, Oct. 1982.

[182] H. L. Walmsley, "The generation of electric currents by the turbulent flow of dielectric liquids: II. Pipes of finite length," *Journal of Physics D: Applied Physics*, vol. 16, pp. 553–572, Apr. 1983.

[183] W. H. Hagman, T. H. Crowley, R. D. Tabors, and F. C. Schweppe, "An adaptive transformer monitoring system," in *Proceedings of the Hydro-Quebec International Symposium for Demonstration of Expert System Applications to the Power Industry*, (Montreal, Quebec, Canada), May 7–12, 1989.

[184] J. L. Kirtley, W. H. Hagman, B. C. Lesieutre, M. J. Boyd, E. P. Warren, H. P. Chou, and R. D. Tabors, "Monitoring the health of power transformers," *IEEE Computer Applications in Power*, vol. 9, pp. 18–23, Jan. 1996.

[185] W. L. Teague and J. H. McWhirter, "Dielectric measurements on new power transformer insulation," *Transactions of the American Institute of Electrical Engineers (AIEE), Part III: Power Apparatus and Systems*, vol. 71, pp. 743–752, Oct. 1952.

[186] R. T. Rushall, "Dielectric properties of oil-soaked pressboard as affected by water," *Proceedings of The Institution of Electrical Engineers, Part IIA*, vol. 100, pp. 81–88, Mar. 1953.

[187] A. W. Stannett, "The measurement of water in power transformers," in *Proceedings of The Institution of Electrical Engineers, Part A: Power Engineering, Supplement No. 3*, vol. 109, pp. 80–85, June 1962.

[188] T. E. Constandinou, "Relation between moisture content and low-voltage electrical properties of oil-impregnated, resin-coated and unimpregnated papers," in *Proceedings of The Institution of Electrical Engineers*, vol. 112, pp. 1783–1794, Sept. 1965.

[189] I. Gussenbauer, "Examination of humidity distribution in transformers models by means of dielectric measurements," in *Proceedings of the International Conference on Large High Voltage Electric Systems (CIGRÉ)*, vol. I, (Paris, France), Aug. 27–Sept. 4, 1980. Paper No. 135.

[190] Y. Saito and T. Hino, "A study of thermal deterioration of Kraft pulps using a mass spectrometer," *Transactions of the American Institute of Electrical Engineers (AIEE), Part I: Communication and Electronics*, vol. 78, pp. 602–606, Nov. 1959.

[191] J. Fabre and A. Pichon, "Deterioration processes and products of paper and oil. Application to transformers," in *Proceedings of the International Conference on Large High Voltage Electric Systems (CIGRÉ)*, (Paris, France), June 15–25, 1960. Paper No. 137.

[192] D. H. Shroff and A. W. Stannett, "A review of paper aging in power transformers," *IEE Proceedings, Part C: Generation, Transmission and Distribution*, vol. 132, pp. 312–319, Nov. 1985.

[193] F. M. Clark, "Factors affecting the mechanical deterioration of cellulose insulation," *Transactions of Electrical Engineering*, vol. 61, pp. 742–749, Oct. 1942.

[194] H. P. Moser *et. al.*, *Transformerboard*. St. Johnsbury, Vermont: Scientia Electrica, special publication, 1979.

[195] H. P. Moser and V. Dahinden *et. al.*, *Transformerboard II*. Rapperswil, Switzerland: H. Weidmann AG, 1987.

[196] J. D. Piper, "Moisture equilibrium between gas space and fibrous materials in enclosed electric equipment," *Transactions of the American Institute of Electrical Engineers (AIEE)*, vol. 65, pp. 791–797, Dec. 1946.

[197] T. V. Oommen, "Moisture equilibrium charts for transformer insulation drying practice," *IEEE Transactions on Power Apparatus and Systems*, vol. PAS-103, pp. 3063–3067, Oct. 1984.

[198] G. Beer, G. Gasparini, F. Osimo, and F. Rossi, "Experimental data on the drying-out of insulation samples and test coil for transformers," in *Proceedings of the International Conference on Large High Voltage Electric Systems (CIGRÉ)*, vol. II, (Paris, France), June 8–18, 1966. Paper No. 135.

[199] J. F. Lennon, "Vacuum process in drying of power transformer insulation," *Journal of Vacuum Science & Technology*, vol. 20, pp. 1039–1042, Apr. 1982.

[200] A. S. Asem and A. F. Howe, "Drying of power-transformer insulation," *IEE Proceedings, Part C: Generation, Transmission and Distribution*, vol. 129, pp. 228–232, Sept. 1982.

[201] H. Yoshida and T. Suzuki, "Drying process of insulating materials of transformers," *IEEE Transactions on Electrical Insulation*, vol. EI-20, pp. 609–618, June 1985.

[202] A. C. M. Wilson, *Insulating Liquids: Their Uses, Manufacture, and Properties*, ch. 3. London: The Institution of Electrical Engineers, 1980.

[203] T. O. Rouse, "Mineral insulating oil in transformers," *Electrical Insulation Magazine*, vol. 14, pp. 6–16, May 1998.

[204] E. T. Norris, "High voltage power transformer insulation," in *Proceedings of The Institution of Electrical Engineers*, vol. 110, pp. 428–440, Feb. 1963.

[205] K. Miners, "Particles and moisture effect on dielectric strength of transformer oil using VDE electrodes," *IEEE Transactions on Power Apparatus and Systems*, vol. PAS-101, pp. 751–756, Mar. 1982.

[206] A. P. Washabaugh, P. A. von Guggenberg, M. Zahn, and J. R. Melcher, "Temperature and moisture transient flow electrification measurements of transformer pressboard/oil insulation using a Couette facility," in *Proceedings of The 3rd International Conference on Properties and Applications of Dielectric Materials*, vol. 2, (Tokyo, Japan), pp. 867–870, July 8–12, 1991.

[207] D. J. Lyon, J. R. Melcher, and M. Zahn, "Couette charger for measurement of equilibrium and energization flow parameters: Application to transformer insulation," *IEEE Transactions on Electrical Insulation*, vol. 23, pp. 159–176, Feb. 1988.

[208] A. J. Morin, M. Zahn, and J. R. Melcher, "Fluid electrification measurements of transformer pressboard/oil insulation in a Couette charger," *IEEE Transactions on Electrical Insulation*, vol. 26, pp. 870–901, Oct. 1991.

[209] A. P. Washabaugh and M. Zahn, "Fluid electrification measurements of transformer pressboard/oil insulation in a Couette charger," *IEEE Transactions on Dielectrics and Electrical Insulation*, vol. 3, pp. 161–181, Apr. 1996.

[210] W. W. Guidi and H. P. Fullerton , "Mathematical methods for prediction of moisture take-up and removal in large power transformers," *Proceedings of IEEE Winter Power Meeting*, no. C-74, pp. 242–244, 1974.

[211] T. V. Oommen, "Moisture equilibrium in paper-oil insulation systems," in *Proceedings of the 16th Electrical/Electronics Insulation Conference*, (Chicago, IL), pp. 162–166, Oct. 3–6, 1983.

[212] P. J. Griffin, C. M. Bruce, and J. D. Christie, "Comparison of water equilibrium in silicone and mineral oil transformers," in *Minutes of the Fifty-Fifth Annual International Conference of Doble Clients*, 1988. Paper No. 10-9.

[213] R. B. Kaufman, E. J. Shimanski, and K. W. McFaydynen, "Gas and moisture equilibrium in transformer oil," *Communication and Electronics*, pp. 312–318, July 1955.

[214] K. Y. Lee, J. Frost, C. Stanley, W. Patrick, W. S. Mackie, S. P. Beaumont, and C. D. W. Wilkinson, "Fabrication of ultrasmall devices on thin active GaAs membranes," *Journal of Vacuum Science & Technology B (Microelectronics Processing and Phenomena)*, vol. 5, no. 1, pp. 322–325, 1988.

[215] K. Yamanouchi, "GHz-range SAW device using nano-meter electrode fabrication technology," in *IEEE Ultrasonics Symposium*, vol. 1, pp. 421–428, 1994.

[216] A. Leyk and E. Kubalek, "MMIC internal electric field mapping with submicrometre spatial resolution and gigahertz bandwidth by means of high frequency scanning force microscope testing," *Electronics Letters*, vol. 31, no. 24, pp. 2089–2091, 1995.

[217] J. Lin, S. Möller, and E. Obermeier, "Two-dimensional and three-dimensional interdigital capacitors as basic elements for chemical sensors," *Sensors and Actuators B*, vol. 5, pp. 223–226, 1991.

[218] R. Zhou, A. Hiermann, K. D. Schierbaum, K. E. Geckeler, and W. Göpel, "Detection of organic solvents with reliable chemical sensors based on cellulose derivatives," *Sensors and Actuators B*, vol. 24-25, pp. 443–447, 1995.

[219] H.-E. Endres, W. Göttler, H. D. Jander, S. Drost, and G. Sberveglieri, "Improvements in signal evaluation techniques for semiconductor gas sensors," *Sensors and Actuators B*, vol. 27, pp. 267–270, 1995.

[220] F. A. M. Davide, C. D. Natale, A. D'Amico, A. Hierlemann, J. Mitrovics, M. Schweizer, U. Weimar, W. Göpel, S. Marco, and A. Pardo, "Dynamic calibration of QMB polymer-coated sensors by Wiener kernel estimation," *Sensors and Actuators B*, vol. 26-27, pp. 275–285, 1995.

[221] T. Lang, H.-D. Wiemhöfer, and W. Göpel, "Carbonate based CO_2 sensors with high performance," *Sensors and Actuators B*, vol. B34, pp. 382–387, Jan. 1996.

[222] M. Hijikigawa, T. Sugihara, J. Tanaka, and M. Watanabe, "Micro-chip FET humidity sensor with a long-term stability," in *TRANSDUCERS '85. 1985 International Conference on Solid- State Sensors and Actuators*, (Philadelphia, PA), pp. 221–224, June 1985.

[223] J. Crank, *The Mathematics of Diffusion*, p. 54. Oxford: Clarendon Press, 1956.

[224] J. S. Kim and D. G. Lee, "Analysis of dielectric sensors for the cure monitoring of resin matrix composite materials," *Sensors and Actuators B*, vol. B30, pp. 159–164, Jan. 1996.

[225] G. Huyberechts and L. Frisson, "In situ formation of humidity-sensitive devices for the evaluation of solar panel encapsulations," *Sensors and Actuators B*, vol. 26-27, pp. 308–311, 1995.

[226] K. D. Schierbaum, J. Geiger, U. Weimar, and W. Göpel, "Specific palladium and platinum doping for SnO_2-based thin film sensor arrays," *Sensors and Actuators B*, vol. 13-14, pp. 143–147, 1993.

[227] K. Higaki, S. Kudo, and H. Ohnishi, "Highly selective NO detection using Bi_2O_3-based materials," *Electrochemical and Solid-State Letters*, vol. 1, no. 2, pp. 107–109, 1998.

[228] A. Haeusler and J.-U. Meyer, "A novel thick film conductive type CO_2 sensor," *Sensors and Actuators B*, vol. B34, pp. 388–395, Jan. 1996.

[229] J. Pichlmaier, "Compensation of the influence of humidity on the measurement of an SO_2 sensor by signal processing," *Sensors and Actuators B*, vol. 26-27, pp. 286–288, 1995.

[230] H.-E. Endres and S. Drost, "Optimization of the geometry of gas-sensitive interdigital capacitors," *Sensors and Actuators B*, vol. 4, pp. 95–98, 1991.

[231] H. E. Endres, S. Drost, and F. Hunter, "Impedance spectroscopy on dielectric gas sensors," *Sensors and Actuators B*, vol. 22, pp. 7–11, 1994.

[232] R. F. Taylor, I. G. Marenchic, and E. J. Cook, "An acetylcholine receptor-based biosensor for the detection of cholinergic agents," *Analytica Chimica Acta*, vol. 213, pp. 131–138, 1988.

[233] J. M. Fouke, A. D. Wolin, K. G. Sanders, M. R. Neuman, and E. R. McFadden, Jr., "Sensor for measuring surface fluid conductivity *in vivo*," *IEEE Transactions on Biomedical Engineering*, vol. 35, pp. 877–881, Oct. 1988.

[234] M. Nishizawa, T. Matsue, and I. Uchida, "Penicillin sensor based on microarray electrode coated with pH-responsive polypyrrole," *Analytical Chemistry*, vol. 64, pp. 2642–2644, 1992.

[235] D. C. Cullen, R. S. Sethi, and C. R. Lowe, "Multi-analyte miniature conductance biosensor," *Analytica Chimica Acta*, vol. 231, pp. 33–40, 1990.

[236] S. Datta, *Surface Acoustic Wave Devices*. Prentice-Hall, Englewood Cliffs, NJ, 1986.

[237] E. Benes, M. Gröschl, W. Burger, and M. Schmid, "Sensors based on piezoelectric resonators," *Sensors and Actuators A*, vol. 48, pp. 1–21, 1995.

[238] A. Leidl, R. Hartinger, M. Roth, and H.-E. Endres, "A new SO_2 sensor system with SAW and IDC elements," *Sensors and Actuators B*, vol. B34, pp. 339–342, Jan. 1996.

[239] B. A. Auld, *Acoustic Fields and Waves in Solids, Vols. I and II.* New York, NY: Wiley-Interscience, 1973.

[240] H. Matthews, ed., *Surface Wave Filters.* New York, NY: Wiley-Interscience, 1977.

[241] A. A. Oliner, ed., *Acoustic Surface Waves.* New York, NY: Springer-Verlag, 1978.

[242] V. M. Ristic, *Principles of Acoustic Devices.* New York, NY: Wiley-Interscience, 1983.

[243] R. Feinman, "Infinitesimal machinery," *Journal of Microelectromechanical Systems*, vol. 2, pp. 170–178, Mar. 1993.

[244] J. Fluitman, "Microsystems technology: Objectives," *Sensors and Actuators A*, vol. 56, pp. 423–430, 1996.

[245] A. B. Frazier, R. O. Warrington, and C. Friedrich, "The miniaturization technologies: Past, present, and future," *IEEE Transactions on Industrial Electronics*, vol. 42, pp. 423–430, Oct. 1995.

[246] S. D. Senturia, "The future of microsensor and microactuator design," *Sensors and Actuators A*, vol. 56, pp. 151–166, Mar. 1996.

[247] S. F. Bart, T. A. Lobar, R. T. Howe, J. H. Lang, and M. F. Schlecht, "Design considerations for micromachined electric actuators," *Sensors and Actuators*, vol. 14, pp. 269–292, 1988.

[248] W. C. Tang, M. G. Lim, and R. T. Howe, "Electrostatic comb drive levitation and control method," *Journal of Microelectromechanical Systems*, vol. 1, pp. 170–178, Dec. 1992.

[249] S. Kumar, D. Cho, and W. N. Carr, "A proposal for electrically levitating micromotors," *Sensors and Actuators A*, vol. 24, pp. 141–149, 1990.

[250] M. Mehregany, P. Nagarkar, S. D. Senturia, and J. H. Lang, "Operation of microfabricated harmonic and ordinary side-drive motors," in *Proceedings of the IEEE Micro Electro Mechanical Systems Workshop*, (Napa Valley, CA), pp. 1–8, Feb. 1990.

[251] M. G. Lim, J. C. Chang, D. P. Schultz, R. T. Howe, and R. M. White, "Polysilicon micro-structures to characterize static friction," in *Proceedings of the IEEE Micro Electro Mechanical Systems Workshop*, (Napa Valley, CA), pp. 82–88, Feb. 1990.

[252] C. J. Kim, A. P. Pisano, R. S. Muller, and M. G. Lim, "Polysilicon microgripper," in *Technical Digest of the IEEE Solid-State Sensor and Actuator Workshop*, (Hilton Head, SC), pp. 48–51, June 1990.

[253] J. Yun, R. T. Howe, and P. R. Gray, "Surface micromachined, digitally force-balanced accelerometer with integrated CMOS detection circuitry," in *Technical Digest of the IEEE Solid-State Sensor and Actuator Workshop*, (Hilton Head, SC), pp. 126–131, June 1992.

[254] M. J. Daneman, N. C. Tien, O. Solgaard, A. P. Pisano, K. Y. Lau, and R. S. Muller, "Linear microvibromotor for positioning optical components," *Journal of Microelectromechanical Systems*, vol. 5, pp. 159–165, Sept. 1996.

[255] V. K. Varadan and V. V. Varadan, "Smart electronics with interdigital electrodes, antennas, and MEMS for aerospace structures," in *Micromachined Devices and Components Conference*, (Austin, TX), pp. 120–124, Oct. 1995.

[256] V. K. Varadan, V. V. Varadan, and X. Q. Bao, "IDT, SAW, and MEMS sensors for measuring deflection, acceleration, and ice detection of aircraft," in *Smart Structures and Materials 1996: Smart Electronics and MEMS Conference*, (San Diego, CA), pp. 209–219, Mar. 1997.

[257] V. K. Varadan and V. V. Varadan, "Smart electronics and sensors for IVHS and automobile collision warning antenna systems," in *Micromachined Devices and Components Conference*, (Austin, TX), pp. 120–124, Oct. 1995.

[258] B. Diem, P. Rey, S. Renard, S. Viollet Bosson, H. Bono, F. Michel, M. T. Delaye, and G. Delapierre, "SOI 'SIMOX'; from bulk to surface micromachining, a new age for silicone sensors and actuators," *Sensors and Actuators A*, vol. 46–47, pp. 8–16, 1995.

[259] J. W. Gardner, A. Pike, N. F. de Rooij, M. Koudelka-Hep, P. A. Clerc, A. Hierlemann, and W. Göpel, "Integrated array sensor for detecting organic solvents," *Sensors and Actuators B*, vol. 26-27, pp. 135–139, 1995.

[260] V. Tvarožek, H. T. Tien, I. Novotný, T. Hianik, J. Dlugopolstý, W. Ziegler, A. Leitmannová-Ottová, J. Jakabovič, V. Řeháček, and M. Uhlár, "Thin-film microsystems applicable in (bio)chemical sensors," *Sensors and Actuators B*, vol. 18–19, pp. 597–602, 1994.

[261] H. Subramanian, V. V. Varadan, and V. K. Varadan, "Wireless remotely readable microaccelerometer," in *Smart Structures and Materials 1997: Smart Electronics and MEMS*, (San Diego, CA), pp. 220–228, Mar. 1997.

[262] V. V. Varadan, V. K. Varadan, , X. Bao, S. Ramanathan, and D. Piscotty, "Wireless passive IDT strain microsensor [and helicopter blade control application]," *Smart Materials and Structures*, vol. 6, pp. 745–751, Dec. 1997.

[263] L. Savio, "Managing overloads: The utility challenge," in *Proceedings of the EPRI Workshop: Transformer Overload and Bubble Evolution*, (Palo Alto, CA), Electric Power Research Institute (EPRI), Dec. 8–9, 1987. Paper No. 6-3. EPRI Technical Report EL-5807-SR, June, 1988.

[264] J. Melcher, Y. Daben, and G. Arlt, "Dielectric effects of moisture in polyimide," *IEEE Transactions on Electrical Insulation*, vol. 24, pp. 31–38, Feb. 1989.

[265] Du Pont Company, Electronics Department, Component Materials Division, Wilmington, DE 19898, (800) 237-4357, *Kapton Polyimide Film: Summary of Properties*.

[266] G. Delapierre, H. Grange, B. Chambaz, and L. Destannes, "Polymer-based capacitive humidity sensor," *Sensors and Actuators*, vol. 4, no. 1, pp. 97–104, 1983.

[267] W. A. Clayton, P. J. Freud, and R. D. Baxter, "Contamination resistant capacitive humidity sensor," in *Proceedings of the 1985 International Symposium on Moisture and Humidity*, (Washington, D.C), pp. 535–544, Apr. 1985.

[268] P. J. Schubert and J. H. Nevin, "A polyimide-based capacitive humidity sensor," *IEEE Transactions on Electron Devices*, vol. ED-32, no. 7, pp. 1220–1223, 1985.

[269] Polyflon Company, One Willard Road, Norwalk, CT 06851, e-mail: info@polyflon.com, web: www.polyflon.com, phone: 203 840 7555, fax: 203 840 7565, BBS: 203 840 7564.

[270] Paratronix, Inc., 129 Bank Street, Attleboro, MA 02703-1775, (508) 222-8979.

[271] V. Tvarožek, I. Novotný, I. Ćerven, J. Kovać, and T. Lacko, "R. f. reactive sputtering of zinc oxide films on silicon and Si-SiO_2-TiN substrates," *Sensors and Actuators A*, vol. 30, pp. 123–127, 1992.

[272] A. Hierlemann, W. Göpel, J. Mitrovics, S. Schweizer-Berberich, and U. Weimar, "Polymer-based sensor arrays and the multicomponent analysis for the detection of hazardous organic vapours in the environment," *Sensors and Actuators B*, vol. 26-27, pp. 126–134, 1995.

[273] M. S. Tyagi, *Introduction to Semiconductor Materials and Devices*. New York, NY: Wiley, 1991.

[274] A. S. Tenney, III, S. V. Silverthorne, and R. D. Baxter, "Integrated microsensors," in *Process Sensing and Diagnostics*, vol. 85 of *AIChE Symposium Series*, pp. 14–18, 1989.

[275] I. N. Bronshtein and K. A. Semendyayev, *Handbook of Mathematics*. New York: Van Nostrand Reinhold Company, 1985.

[276] Tech-Etch, Inc., 45 Aldrin Road, Plymouth, MA 02360, (617) 747-0300.

[277] Molex International, 2222 Wellington Court, Lisle, IL, 60532, USA, phone (708) 969-4550, fax (708) 969-1352.

[278] J. M. Seifert, U. Stietzel, and H. C. Kärner, "The ageing of composite insulating materials – new possibilities to detect and to classify ageing phenomena with dielectric diagnostic tools," in *IEEE International Symposium on Electrical Insulation*, (Arington, VA), pp. 373–377, June 1998.

[279] Oren Elliott Products, Inc.128 W. Vine St., P.O. Drawer 638, Edgerton, OH 43517 USA, (419) 298-2306.

[280] W. Lin, "Computation of the parallel-plate capacitor with symmetrically placed unequal plates," *IEEE Transactions on Microwave Theory and Techniques*, vol. MTT-33, no. 9, pp. 800–807, 1985.

[281] "AC loss characteristics and permittivity (dielectric constant) of solid electrical insulating materials." Annual Book of ASTM Standards, D150-81, 1986.

[282] S. P. Parker, ed., *McGraw-Hill Encyclopedia of Physics*. New York: McGraw-Hill, second ed., 1993.

[283] Fuji Film, Itocho International, Inc., 335 Madison Avenue, New York, NY 10017, phone 212-818-8238, fax 212-818-8243.

[284] M. Kirsching and R. H. Jansen, "Accurate, wide range design equations for the frequency dependent characteristics of parallel coupled microstrip lines," *IEEE Transactions on Microwave Theory Tech.*, vol. MTT-32, pp. 83–90, Jan. 1984.

[285] P. C. Kohnke and C. Rajakumar, "General-purpose finite-element software for fluid-structure analysis," *International Journal of Computer Applications in Technology*, vol. 5, pp. 199–207, 1992.

[286] R. Y. Scapple, "A trimmable planar capacitor for hybrid applications," in *Proceedings of the 24th Electronic Components Conf.*, (New York, NY), pp. 203–207, 1974.

[287] J. Keller, "Inverse problems," *American Mathematics Monthly*, vol. 83, pp. 107–118, 1976.

[288] H. W. Engl, M. Hanke, and A. Neubauer, *Regularization of Inverse Problems*. Norwell, MA: Kluwer Academic Publishers, 1996.

[289] B. S. Doyle, "Anomalous low-frequency resonance-type behavior and negative capacitance in doped glasses," *J. Phys. D: Appl. Phys.*, vol. 19, pp. 1129–1139, 1986.

[290] A. K. Jonscher, "The physical origin of negative capacitance," *Journal of the Chemical Society Faraday*, vol. 82 pt. 1, pp. 75–86, 1986.

[291] A. K. Jonscher, "Low-frequency dispersion in semi-insulators," in *Second International Conference of Conduction and Breakdown in Solid Dielectrics*, (Erlangen, West Germany), pp. 36–40, 1986.

[292] A. K. Jonscher, C. Pickup, and S. H. Zaidi, "Dielectric spectroscopy of semi-insulating gallium arsenide," *Semiconductor Science and Technology*, vol. 1, pp. 71–92, July 1986.

[293] A. K. Jonscher and M. N. Robinson, "Dielectric spectroscopy of silicon barrier devices," *Solid-State Electronics*, vol. 31, no. 8, pp. 1277–1288, 1988.

[294] R. A. Collins, S. C. Edwards, F. J. Johnson, A. G. Jones, and L. D. McMahon, "Time-dependent reverse negative differential resistance in thin-film MIM devices," *Physica Status Solidi A*, vol. 95, no. 1, pp. 353–359, 1986.

[295] H. R. Zeller, "Breakdown and prebreakdown phenomena in solid dielectrics," *IEEE Transactions on Electrical Insulation*, vol. EI-22, pp. 115–122, Apr. 1986.

[296] A. I. Krymskii and L. K. Popov, "Quasi-stationary negative capacitance in an inhomogeneous MIS structure," *Mikroelektronika*, vol. 19, no. 4, pp. 328–334, 1990.

[297] M. Beale and P. Mackay, "The origins and characteristics of negative capacitance in metal-insulators-metal devices," *Philosophical Magazine B*, vol. 65, no. 1, pp. 47–64, 1992.

[298] M. Beale, "Anomalous reactance behavior during the impedance analysis of time-varying dielectric systems," *Philosophical Magazine B*, vol. 65, no. 1, pp. 65–77, 1992.

[299] N. A. Penin, "Negative capacitance in semiconductor structures," *Semiconductors*, vol. 30, pp. 340–343, Apr. 1996.

[300] M. H. Abdullah and A. N. Yusoff, "Frequency dependence of the complex impedances and dielectric behavior of some Mg-Zn ferrites," *Journal of Materials Science*, vol. 32, pp. 5817–5823, Nov. 1997.

[301] T. J. B. Swanenburg, "Improved geometry for a semiconductor surface-wave oscillator," *Electronics Letters*, vol. 8, no. 14, pp. 351–352, 1972.

[302] T. J. B. Swanenburg, "Negative conductance of an interdigital electrode structure on a semiconductor surface," *IEEE Transactions on Electron Devices*, vol. ED-20, pp. 630–637, 1973.

[303] S. A. Y. Al-Ismail and C. A. Hogarth, "Forming, negative resistance, pressure effect, dielectric breakdown and electrode diffusion in thin SiO_x films with laterally spaced electrodes," *Journal of Materials Science*, vol. 20, pp. 2186–2192, 1985.

[304] V. A. V'yun, "Negative resistance of interdigital system of electrodes on surface of a semiconductor," *Soviet Journal of Communications Technology and Electronics*, vol. 33, no. 12, pp. 158–160, 1988.

[305] I. Omura, H. Ohashi, and W. Fichtner, "IGBT negative gate capacitance and related instability effects," *IEEE Electron Device Letters*, vol. 18, pp. 622–624, Dec. 1997.

[306] R. F. Milsom and M. Redwood, "Interdigital piezoelectric Raleigh-wave transducer; an improved equivalent circuit," *Electronics Letters*, vol. 7, no. 9, pp. 217–218, 1971.

[307] C. A. Desoer and E. S. Kuh, eds., *Basic Circuit Theory*, p. 393. New York: McGraw Hill Book Co., 1969.

[308] Y. Du, "Dielectrometry measurements of solids and liquids in transformer environment using interdigital sensor. Americal Public Power Association DEED Scholarship Final Report.," tech. rep., High Voltage Research Laboratory, Massachusetts Institute of Technology, Cambridge, MA, 1998.

[309] I. Moumine, B. Gosse, J. P. Gosse, R. Clavreul, and C. Hantouche, "Vegetable oil as an impregnant in HV AC capacitors," in *Proceedings of the 1995 IEEE 5th International Conference on Conduction and Breakdown in Solid Dielectrics*, (New York, NY), pp. 611—615, 1995.

[310] Y. Chen and H. Conrad, "Effects of water content on the electrorheology of corn starch/corn oil dispersions," in *Developments in Non-Newtonian Flows* (D. Siginer, W. V. Arsdale, M. Altan, and D. Alexandrou, eds.), New York, NY: ASME, 1993.

[311] H. Conrad, Y. Li, and Y. Chen, "The temperature dependence of the electrorheology and related electrical properties of corn starch/corn oil suspensions," *Journal of Rheology*, vol. 39, no. 5, pp. 1041–1057, 1995.

[312] R. K. Tripathi, M. Gupta, and J. P. Shukla, "Capacitance technique for measuring moisture content using dielectric data – an immersion method," in *International Conference on Conduction and Breakdown in Dielectric Liquids*, (Rome, Italy), pp. 440–441, July 1996.

[313] "Standard test method for relative permittivity (dielectric constant) and dissipation factor of polyethylene by liquid displacement procedure(ASTM D1531-81)." Annual Book of ASTM Standards, 1986.

[314] "Standard methods of sampling and testing electrical insulating board (ASTM D3394-86)." *Annual Book of ASTM Standards*, 1989.

[315] Harley Moisture Sensor, Model CT-880-BN-H-(0–100%)-X, J.W. Harley Inc., Monitoring Products Group, 9177 Dutton Drive, Twinsburg, OH 44087, (800) 635-3030.

[316] Y. Du, B. C. Lesieutre, and M. Zahn, "Dielectrometry measurements of effects of moisture and anti-static additive on transformer board," in *IEEE Conference on Electrical Insulation and Dielectric Phenomena*, (Minneapolis, MN), pp. 226–229, Oct. 1997.

[317] U. Gafvert, A. Jaksts, C. Tornkvist, and L. Walfridsson, "Electrical field distribution in transformer oil," *IEEE Transactions on Electrical Insulation*, vol. 27, pp. 647–660, June 1992.

[318] B. Nettelblad, "Effect of moisture content on the dielectric properties of cellulose," in *NORD-IS-92*, 1992.

[319] R. Jeffries, "The sorption of water by cellulose and eight other textile polymers," *Journal of the Textile Institute*, vol. 51, no. 9, pp. 339–374, 1960.

[320] MineFacts, a CD-ROM interactive database program available from the U.S. Department of Defence (not a classified information).

[321] S. A. Sheffield, R. L. Gustavsen, and R. R. Alcon, "Porous HMX initiation studies: Sugar as an inert simulant," in *Topical Conference on Shock Compression of Condensed Matter*, (Amherst, MA), July 1997. paper N1.06.

[322] S. Kerrin and E. Klemperer, "A portable sorption tester for nondestructive testing of chemical protective parments. Final report.," Tech. Rep. DNTIS ADA-256-941, Tracer Technologies, San Diego, CA, Aug. 1992.

[323] P. B. M. Archer, A. V. Chadwick, J. J. Miasik, M. Tamizi, and J. D. Wright, "Kinetic factors in the response of organometric semiconductor gas sensors," *Sensors and Actuators*, vol. 16, pp. 379–392, 1989.

[324] D. Bednarczuk and S. P. DeWeerth, "Smart chemical sensing arrays using tin oxide sensors and analog winner-take-all signal processing," *Sensors and Actuators B*, vol. 26-27, pp. 271–274, 1995.

[325] M. E. H. Amrani, P. A. Payne, and K. C. Persaud, "Multi-frequency measurements of organic conducting polymers for sensing of gases and vapors," in *The 8th International Conference on Solid-State Sensors and Actuators and EUROSENSOR IX*, (Stockholm, Sweden), 1995.

[326] Laboratory for Electromagnetic and Electronic Systems, MIT, Cambridge, MA 02139, *Moisture Meter Reference Manual*, Apr. 1991.

Biography

Alexander V. Mamishev was born in the Soviet Union in 1971. He received an equivalent of Bachelor of Science degree in Electrical Engineering and Physics from the Kiev Polytechnic Institute, Kiev, Ukraine in 1992, and Master of Science degree in Electrical Engineering from Texas A&M University, College Station, TX in 1994.

From 1989 to 1992 he was employed as a research assistant at the Kiev Polytechnic Institute; he was also a part-time research assistant from 1991 to 1992 in the Institute of Electrodynamics, Kiev, Ukraine; and a part-time software engineer in a high-tech venture SELT, Inc. (Specialized Electrical Technologies), Kiev, Ukraine. He was a research assistant at Texas A&M University Power System Automation Laboratory from 1992 to 1994, a research assistant at the MIT Laboratory for Electromagnetic and Electronic Systems from 1995 to 1998, and a part-time teaching assistant in the MIT Department of Electrical Engineering and Computer Science in the Fall of 1998, and a short course instructor at MIT in January 1999. In the school interim periods of 1997 and 1998 he was employed by Jentek Sensors, Inc. as a research engineer.

During his graduate studies in the United States, he received the following awards (in reverse chronological order): MIT GSC Travel Grant (October 1998), American Vacuum Society Graduate Research Award (July 1998), IEEE ISEI (International Symposium on Electrical Insulation) Scholarship (April 1998), Link Foundation Energy Fellowship (March 1998), Student Poster Contest at PES Winter Meeting, Honorable Mention (February 1998), Power Engineering Education Committee Student Travel Grant for PES Winter Meeting (January 1998), Graduate Student Award finalist in the Materials Research Society Fall Meeting (December 1997), American Public Power Association (APPA) Demonstration of Energy Efficient Developments Scholarship (September 1997), IEEE Dielectric and Electrical Insulation Society Fellowship (January 1995), IEEE CEIDP (Conference on Electrical Insulation and Dielectric Phenomena) Scholarship (Oct. 1994), APPA Demonstration of Energy Efficient Developments Scholarship (September 1994), TAMU Department of Electrical Engineering Scholarship (August 1994), APICS Donald W. Fogarty International Student Paper Contest, 3rd Prize, Houston (June 1994), ISS TAMU Study Grant for Universities Power Engineering Conference, Ireland (June 1994), IEEE Vincent Bendix Research Award (leader of team entry) (March 1994), IEEE Power Engineering Society T. Burke Hayes Best Student Paper Award (February 1994), NSF Student Support Grant for IEEE PES Meetings (January 1994, January 1995, January 1998, and July 1998),

Electrical Engineering Graduate Program Enhancement Scholarship (December 1993), APPA DEED Scholarship (October 1993), Special One-Time EE Scholarship annually awarded by TAMU Department of Electrical Engineering (September 1993), Industrial Scholarship at 8th International Symposium on High Voltage Engineering, Yokohama, Japan (August 1993), TAMU International Student Services Travel Grant (June 1993), Petro Jacyk Scholarship (1992-1993), George Soros Educational Scholarship (September 1992). He also received various awards and honors during undergraduate studies in the Ukraine (1988-1992), including academic excellence scholarship (loose equivalent of Dean's List) for the entire course of education, participated in various academic contests up to a national level, and held some social leadership positions.

Mr. Mamishev is an author of an IEEE encyclopedia chapter; more than 30 technical papers published in archival journals and at international conferences in nine countries, including two invited papers; he delivered about fifteen industrial presentations and filed a patent application.

Alexander Mamishev is a member of the IEEE Dielectrics and Electrical Insulation Society and IEEE Power Engineering Society, Eta Kappa Nu Electrical Engineering Honor Society, Electrostatics Society of America, Materials Research Society, Sigma Xi, American Society for Nondestructive Testing, Electrochemical Society, American Vacuum Society, IEEE Power Engineering Society AC Field Effects Design Guide Task Force, and MIT Humanitarian Demining Group. He is a reviewer for IEEE Transactions on Dielectrics and Electrical Insulation. He is also scheduled for listing in the 5th edition of Who's Who in Science and Engineering in America.

Alexander Mamishev currently lives in Cambridge, MA and is married to Krystyna Szul.

Index